Primordial cosmology and gravitational waves : from phase transitions to cosmic strings and primordial black holes

Pierre Auclair

Université de Paris

École doctorale des Sciences de la Terre et de l'Environnement et Physique de l'Univers - ED560

Laboratoire AstroParticules et Cosmologie (APC) - Groupe Théorie

Primordial cosmology and gravitational waves:
from phase transitions to cosmic strings and primordial black holes

Par Pierre Auclair

Thèse de doctorat de Physique de l'Univers

Dirigée par Danièle Steer
et par Chiara Caprini

présentée et soutenue publiquement le 9 Juillet 2021
devant le jury composé de :

Ruth Durrer	Professeure (Université de Genève)	Rapportrice
Edmund Copeland	Professeur (University of Notthingham)	Rapporteur
Sébastien Clesse	Assistant professeur (Université libre de Bruxelles)	Examinateur
Mark Hindmarsh	Professeur (University of Helsinki)	Examinateur
David Langlois	Directeur de recherche (Université de Paris, APC)	Examinateur
Germano Nardini	Assistant professeur (University of Stavanger)	Examinateur

Abstract

The gravitational force governs the evolution of structures in the Universe, from the smallest scales, those of moons and planets, to galaxies, clusters, and to the evolution of the Universe itself. Its importance to describe the surrounding Universe is no longer to be demonstrated: the successes of general relativity have been accumulating for more than a century now. However, it was not until the first direct detection of gravitational waves in 2015 by LIGO/Virgo that gravity, in the form of gravitational waves, became a direct observational tool to scrutinize the Universe in its darkest and most inaccessible corners, such as the neighbourhood of black holes and the first moments of the Big Bang. The perspectives offered by these new types of observations are comparable to those brought by the cosmic microwave background at the turn of the millennium, thus marking the beginning of *precision cosmology*.

This PhD work is part of the exciting research topic of gravitational wave studies within the LIGO/Virgo/KAGRA collaboration – the network of ground-based gravitational wave detectors currently in place – and the LISA collaboration, the constellation of three satellites, separated by 2.5 million of kilometres, designed to detect low frequency gravitational waves in space. The main subject of this thesis is the study of primordial cosmology – *i.e.* the first instants of the Universe – mainly through the prism of gravitational wave detectors. This manuscript has three independent parts.

The first part of this thesis deals with cosmic strings, one-dimensional topological defects that could be formed during phase transitions in the primordial Universe. If formed, these relics of the early universe would be markers of the upheavals of our early universe. We study the evolution of the cosmic string network, in particular the density of loops and their gravitational wave emission, we make predictions for the future LISA mission, and finally constrain cosmic strings using the results of LIGO/Virgo/KAGRA.

In a second part, we study the formation of primordial black holes at the end of inflation, a period of accelerated expansion in the early Universe. During this so-called *preheating* phase, which precedes the formation of standard model particles, the inflaton oscillates around the minimum of its potential possibly generating a metric instability at the origin of the formation of a large number of primordial black holes. This part of the thesis is therefore devoted to the study of this instability and to quantifying the production of primordial black holes using the *excursion-set* formalism.

The third part is dedicated to first order phase transitions, in particular during the electroweak transition in extensions of the standard model. During the transition, a large amount of energy is transmitted to the ambient medium in the form of kinetic energy which can lead to turbulence. We therefore propose a model for this freely decaying turbulence and the resulting gravitational wave spectrum.

Keywords: gravitational waves, primordial cosmology, cosmic strings, primordial black holes, first order phase transition, preheating

Court résumé de la thèse

La force gravitationnelle régit l'évolution des structures dans l'Univers, depuis les plus petites échelles, celles des lunes et des planètes, jusqu'aux galaxies, aux clusters et jusqu'à l'évolution de l'Univers lui-même. Son importance pour décrire l'Univers qui nous entoure n'est plus à démontrer : les succès de la relativité générale s'accumulent depuis maintenant plus d'un siècle. Cependant, il a fallu attendre les premières détections directes d'ondes gravitationnelles en 2015 par LIGO/Virgo pour que la gravité, sous la forme d'ondes gravitationnelles, devienne un outil direct d'observation pour scruter l'Univers dans ses recoins les plus sombres et inaccessibles, tels l'environnement proche des trous noirs et les premiers instants de l'Univers. Les perspectives qu'offrent ces nouveaux types d'observations sont comparables à ce que l'étude du fond diffus cosmologique a pu apporter au tournant du millénaire, marquant de ce fait le début de la *cosmologie moderne* de précision. Ce travail de doctorat s'inscrit dans ce sujet de recherche particulièrement stimulant qu'est l'étude des ondes gravitationnelles au sein de la collaboration LIGO/Virgo/KAGRA – le réseau de détecteurs terrestres d'ondes gravitationnelles actuellement en place – et de la collaboration LISA, la constellation de trois satellites séparés de 2,5 millions de kilomètres destinée à détecter des ondes gravitationnelles de basse fréquence dans l'espace.

Le sujet principal de cette thèse est l'étude de la cosmologie primordiale – c'est-à-dire les premiers instants de l'Univers – principalement par le prisme des détecteurs d'ondes gravitationnelles. Ce manuscrit comporte trois parties indépendantes.

La première partie de cette thèse porte sur les cordes cosmiques, des défauts topologiques unidimensionnels susceptibles d'être formés lors de transitions de phase dans l'Univers primordial. Si elles étaient formées, ces reliques des premiers instants de l'Univers seraient des marqueurs des bouleversements qu'a connus notre Univers à ses débuts. C'est dans cette perspective que nous étudions l'évolution du réseau de cordes cosmiques, en particulier celle de la densité de boucles et leur émission d'ondes gravitationnelles. Nous formulons des prédictions pour la future mission LISA et mettons des contraintes sur les cordes cosmiques à partir des résultats de LIGO/Virgo/KAGRA.

Dans une seconde partie, nous étudions la formation de trous noirs primordiaux à la fin de l'inflation, une période d'expansion accélérée dans l'Univers primordial. Durant cette phase dite de *preheating*, qui précède la formation des particules du modèle standard, l'inflaton oscillant autour du minimum de son potentiel aurait pu engendrer une instabilité de la métrique à l'origine de la formation d'une grande quantité de trous noirs primordiaux. Cette deuxième partie de la thèse est donc consacrée à l'étude de cette instabilité et à quantifier la production de trous noirs en utilisant le formalisme d'*excursion-set*.

La troisième et dernière partie est, quant à elle, dédiée aux transitions de phase du premier ordre, en particulier durant la transition électro-faible dans des extensions du modèle standard. Durant la transition, une grande quantité d'énergie est transmise au milieu ambiant sous forme d'énergie cinétique et peut générer de la turbulence. Nous proposons dans cette partie, une modélisation de cette turbulence libre et du spectre d'ondes gravitationnelles qui en résulte.

Mots clefs : ondes gravitationnelles, cosmologie primordiale, cordes cosmiques, trous noirs primordiaux, transitions de phase du premier ordre, preheating

Résumé de la thèse

La gravitation régit l'évolution des structures dans l'Univers, depuis les plus petites échelles, celles des lunes et des planètes, jusqu'aux galaxies, aux clusters et jusqu'à l'évolution de l'Univers lui-même. Son importance pour décrire l'Univers qui nous entoure n'est plus à démontrer : les succès de la relativité générale s'accumulent depuis maintenant plus d'un siècle. Cependant, il a fallu attendre les premières détections directes d'ondes gravitationnelles en 2015 par LIGO/Virgo pour que la gravité, sous la forme d'ondes gravitationnelles, devienne un outil direct d'observation. Cet outil nous est très précieux pour scruter l'Univers dans ses recoins les plus sombres et inaccessibles, comme l'environnement proche des trous noirs et les premiers instants de l'Univers. Les perspectives qu'offrent ces nouveaux types d'observations sont comparables à ce que l'étude du fond diffus cosmologique a pu apporter au tournant du millénaire, marquant de ce fait le début de la *cosmologie moderne* de précision. Ce travail de doctorat s'inscrit dans ce sujet de recherche particulièrement stimulant qu'est l'étude des ondes gravitationnelles d'un point de vue théorique et également au sein de la collaboration LIGO/Virgo/KAGRA – le réseau de détecteurs terrestres d'ondes gravitationnelles actuellement en place – et de la collaboration LISA, la constellation de trois satellites séparés de 2,5 millions de kilomètres destinée à détecter des ondes gravitationnelles de basse fréquence dans l'espace.

Le sujet principal de cette thèse est l'étude de la cosmologie primordiale – c'est-à-dire les premiers instants de l'Univers – principalement par le prisme des détecteurs d'ondes gravitationnelles. Si nos observations en ondes lumineuses ne peuvent provenir de plus loin et de plus tôt que la surface de dernière diffusion, les ondes gravitationnelles produites très tôt dans l'Univers pourraient s'être propagées librement jusqu'à aujourd'hui. L'apport des ondes gravitationnelles dans le domaine de la cosmologie primordiale s'annonce donc considérable pour les prochaines années. Le travail contenu dans cette thèse a mené à la publication de huit articles, dont sept sont reproduits dans le présent manuscrit. Celui-ci comporte trois parties indépendantes, chacune dédiée à un phénomène de nature différente qui aurait pu se produire durant les premiers instants de l'Univers et dont l'observation nous permettrait d'en apprendre plus sur la physique à de très hautes énergies.

La première mais aussi la plus longue partie de cette thèse porte sur les cordes cosmiques, des défauts topologiques unidimensionnels susceptibles de s'être formés lors de transitions de phases dans l'Univers primordial. En effet, alors que l'Univers primordial vieillit et s'étend, celui-ci se refroidit. Il peut alors subir des transitions de phases durant lesquelles certaines symétries se brisent. Ce sont les propriétés topologiques de ces brisures de symétries qui déterminent si des cordes cosmiques peuvent se former. Les caractéristiques de ces cordes cosmiques seraient alors déterminées par la physique en vigueur à de très hautes énergies, énergies qui nous sont inaccessibles en laboratoire ou dans les accélérateurs de particules. Ainsi, si des cordes cosmiques étaient formées, ces reliques des premiers instants de l'Univers seraient des marqueurs des bouleversements qu'il a connus. C'est dans cette perspective que nous étudions dans cette partie l'évolution du réseau de cordes cosmiques, leur émission d'ondes gravitationnelles et la dépendance de ce signal aux différentes propriétés des cordes. Nous y étudions aussi d'autres signatures comme le fond diffus de rayons γ et l'abondance de matière noire.

Cette partie commence par une courte introduction aux cordes cosmiques au chapitre 1 dans laquelle nous rappelons le mécanisme à l'origine de leur formation. Nous y exposons leurs principales propriétés ainsi que leurs conséquences observationnelles, aussi bien gravitationnelles que

non-gravitationnelles. Puis dans le chapitre 2, rédigé en collaboration au sein du groupe de travail "Cosmologie" de LISA, nous passons en revue différents modèles présents dans la littérature pour quantifier la densité de boucles de cordes cosmiques ainsi que deux méthodes différentes pour calculer leurs contributions au fond stochastique d'ondes gravitationnelles. Ce faisant, nous montrons que la future mission LISA sera capable de confirmer ou de contraindre l'existence des cordes cosmiques à des échelles d'énergies cinq ordres de grandeurs plus basses que les meilleures contraintes actuelles provenant des analyses de réseaux de pulsars millisecondes.

Au chapitre 3, nous nous intéressons à la fonction de production qui décrit l'interaction entre le réseau de cordes infinies, c'est-à-dire plus grandes que le rayon de Hubble, et les boucles qui contribuent au fond stochastique d'ondes gravitationnelles. En particulier, nous étudions la fonction de production de Polchinski et Rocha qui a la particularité de tenir compte de la structure fractale des cordes. Par conséquent, ce modèle prédit que des boucles peuvent être produites à toutes les échelles avec une certaine loi de puissance. La densité de boucle qui en résulte avait déjà été étudiée dans un régime particulier, que nous avons entrepris d'étendre et que nous comparons avec les résultats numériques d'autres groupes de recherche. L'impact de ce modèle sur le fond stochastique d'ondes gravitationnelles est étudié en détail dans le chapitre 4. En plus de fournir des formules analytiques pour le spectre d'ondes gravitationnelles pouvant être utilisées pour accélérer l'analyse des données de fond stochastique, nous y évaluons de manière systématique la sensibilité des différentes gammes de détecteurs d'ondes gravitationnelles selon leur fréquence.

Le chapitre 5, qui a été rédigé au sein de la collaboration LIGO/Virgo/KAGRA, est dédié à l'analyse des données issues du troisième cycle d'observations. Nous utilisons ces données pour contraindre l'échelle d'énergie des cordes cosmiques en considérant différents scénarios pour l'évolution du réseau de boucles. Pour ce faire, nous cherchons dans ces données à la fois des signaux de nature stochastique et des bouffées très courtes d'ondes gravitationnelles. Parmi les nouveautés de cette analyse, nous introduisons les modèles décrits aux chapitres 3 et 4. Nous avons aussi ajouté les formes d'ondes associées aux collisions de *kinks*, une source jusqu'alors négligée mais qui peut prédominer sur les cordes avec une dimension fractale élevée.

Les premiers chapitres supposent que l'épaisseur des cordes est infiniment petite par rapport à leur taille, et que la dynamique des cordes suit l'action de Nambu-Goto telle qu'introduite au chapitre 1. Cependant, les divergences entre la description Nambu-Goto des cordes cosmiques qui prédit des boucles à longue durée de vie et les simulations numériques de théorie des champs dans lesquelles les boucles se désintègrent rapidement en particules font l'objet d'un long débat dans la communauté des cordes cosmiques. Le chapitre 6 est une tentative pour combler l'écart qui existe entre ces deux descriptions au moyen d'un modèle hybride. Notre hypothèse principale suppose que les boucles isolées évoluent selon les équations de Nambu-Goto jusqu'à atteindre une taille critique en dessous de laquelle elles disparaissent rapidement en émettant des particules. Ce point de vue est motivé par une série de simulations numériques conduites par l'un de nos collaborateurs : Tanmay Vachaspati. Nous résolvons analytiquement ce modèle simplifié et prédisons que l'effet principal de l'émission de particules est de réduire le spectre d'ondes gravitationnelles à haute fréquence. Pour autant, cet effet n'est pas suffisamment fort pour remettre en question les contraintes exprimées par les détecteurs actuels d'ondes gravitationnelles. À partir d'hypothèses simples sur la désintégration de ces particules en rayons γ, nous sommes en mesure d'estimer la contribution des cordes cosmiques au fond diffus de rayons γ et de montrer qu'elle reste quelques ordres de grandeur sous la barre fixée par l'expérience Fermi-LAT.

Enfin, nous évoquons dans le chapitre 7 le cas des cordes cosmiques porteuses de courant et de la formation de configurations stables de boucles, les *vortons*. La stabilité des vortons est due au

moment angulaire porté par le courant qui prévient l'effondrement final de la boucle. Aux yeux d'un observateur distant, ces vortons ressembleraient à des particules ponctuelles avec une masse et un spin, et pourraient donc constituer une partie de la matière noire de notre Univers. En modélisant l'évolution des cordes avec une équation de continuité, nous sommes en mesure de déterminer leur abondance à tout temps et en particulier aujourd'hui, en fonction des échelles d'énergie de la corde et du courant. Finalement, nous montrons qu'ils constituent, sous certaines conditions bien particulières, un candidat viable et original pour expliquer la présence de matière noire dans l'Univers.

Dans la seconde partie, nous nous intéressons à la formation de trous noirs primordiaux à la fin de l'inflation, une période d'expansion accélérée qui est supposée s'être produite dans l'Univers primordial. Durant cette phase dite de *preheating*, qui précède la formation des particules du modèle standard, l'inflaton oscillant autour du minimum de son potentiel aurait pu engendrer une instabilité de la métrique à l'origine de la formation d'une grande quantité de trous noirs primordiaux.

Le chapitre 8 est une très brève introduction au vaste domaine qu'est l'étude des trous noirs primordiaux. Nous commençons par donner quelques ordres de grandeurs pour apprécier la masse des trous noirs primordiaux ainsi que leur durée de vie. En effet, nous savons depuis les travaux pionniers de Hawking et Bekenstein que les trous noirs ont une température et une luminosité et donc qu'ils perdent de l'énergie sous forme de rayonnement. Nous passons ensuite en revue les différentes méthodes utilisées pour contraindre leur abondance. Enfin, nous utilisons l'analyse perturbative multi-échelles pour acquérir une compréhension de la bande d'instabilité de l'équation de Mathieu correspondant à l'instabilité de *preheating*.

Le cœur de cette partie est le chapitre 9 dédié aux différentes techniques utilisées pour calculer la distribution de masse initiale des trous noirs primordiaux dans le contexte de l'instabilité de *preheating*. Après un bref rappel concernant la physique de l'instabilité de *preheating*, nous nous attardons sur les formalismes de Press et Schechter ainsi que d'excursion-set. Nous montrons que ce dernier formalisme est le plus à même de prendre en compte le problème dit de *cloud-in-cloud*, c'est-à-dire le problème de compter plusieurs fois des structures qui seraient incluses dans de plus grands trous noirs. Nous mettons en lumière que ce problème est analogue au système d'une particule soumise à une équation de Langevin avec une barrière mobile. En particulier, nous mettons en évidence que ce système satisfait à un ensemble d'équations intégrales de Volterra dont un choix particulier permet de résoudre très efficacement ce problème. Enfin, nous montrons que si l'inflaton est très faiblement couplé aux particules du Modèle Standard, ce mécanisme produit très efficacement des trous noirs primordiaux dont la masse varie entre dix grammes et une masse solaire.

La troisième et dernière partie est dédiée aux transitions de phase du premier ordre, en particulier durant la transition électro-faible dans des extensions du modèle standard. Durant la transition de phase, une grande quantité d'énergie est transmise au milieu ambiant sous forme d'énergie cinétique et peut générer de la turbulence. Si la transition de phase électro-faible est du premier ordre, le signal en ondes gravitationnelles ainsi créé devrait être localisé dans la bande de fréquences de LISA, ce qui en fait un sujet d'étude d'importance pour préparer le lancement de cette mission. Dans le chapitre 10, nous commençons par rappeler comment calculer le fond stochastique d'ondes gravitationnelles généré par un fluide parfait relativiste dont le mouvement est purement rotationnel. Ce calcul suppose de connaître les caractéristiques spatiales et temporelles du champ de vitesse au cours de la phase de turbulence libre. C'est pourquoi nous construisons un modèle pour décrire cette période de turbulence libre qui suit la transition de phase. En particulier, nous nous intéressons aux corrélations temporelles du champ de vitesse ainsi qu'aux lois d'évolution de

l'énergie cinétique et de l'échelle intégrale du fluide. Le modèle que nous construisons s'appuie sur différents travaux analytiques préexistants et nous les validons avec des simulations de mécanique des fluides massivement parallèles que nous lançons sur des supercalculateurs. Par la suite, nous mettons en avant l'importance de la condition de *Mercer* qui doit, en principe, être satisfaite par toute fonction de corrélation à deux points. En pratique, la fonction de corrélation à deux temps est souvent définie directement sur la base de considérations phénoménologiques, et non à partir d'un processus stochastique. Ainsi, la condition de Mercer est un indice supplémentaire qui nous guide dans la détermination de la fonction de corrélation. Les fonctions qui satisfont à la condition de Mercer sont appelées *noyaux* et nous passons en revue les exemples de noyaux les plus communément employés : les noyaux séparables, stationnaires et localement stationnaires. Dans le cas de la turbulence libre, nous proposons d'utiliser le noyau non-stationnaire de Gibbs qui est en bon accord avec nos simulations numériques. Ce choix nous garantit la positivité des spectres de vitesse et du fond stochastique d'ondes gravitationnelles. Enfin, nous calculons le signal en ondes gravitationnelles en utilisant un algorithme d'échantillonnage préférentiel adapté au calcul d'intégrales à plusieurs dimensions. Les résultats de ce chapitre sont encore préliminaires, mais ils soulignent l'impact que les incertitudes sur la formation de la phase turbulente ont sur le spectre d'ondes gravitationnelles.

Remerciements

Il ne me sera pas aisé de remercier toutes les personnes qui m'ont aidé de près ou de loin à mener cette thèse à son terme. Ce qui suit est une tentative de remercier autant de personnes que l'espace sur cette page me le permet.

Je suis à jamais redevable à mes directrices de thèse, Danièle Steer et Chiara Caprini, pour m'avoir offert la possibilité d'apprendre à pratiquer la recherche à leurs côtés. C'est toujours avec beaucoup de patience et de bienveillance qu'elles m'ont accompagné et encouragé durant ces trois années. Je me sens immensément privilégié d'avoir pu bénéficier de leur soutien et j'espère poursuivre dans une voie qui sera à la hauteur de ce qu'elles m'ont transmis.

Je remercie Edmund Copeland et Ruth Durrer d'avoir consacré de leur temps pour avoir lu et rapporté en détail sur ce manuscrit. Merci également à Sébastien Clesse, Mark Hindmarsh, David Langlois et Germano Nardini d'avoir accepté de figurer dans mon jury de thèse.

La seconde partie de cette thèse sur les trous noirs primordiaux s'appuie en partie sur des travaux antérieurs de Vincent Vennin. Ce fut donc une joie de lui présenter certains de mes résultats et de pouvoir collaborer avec lui. Je le remercie pour sa profonde gentillesse.

Au cours de mon doctorat et avant la pandémie de coronavirus, j'ai eu la chance d'être accueilli régulièrement à l'Université d'Helsinki. J'exprime ma profonde gratitude à Mark Hindmarsh, David Weir, Kari Rummukainen et à Daniel Cutting pour leur accueil, leurs conseils et pour avoir partagé leurs vastes connaissances sur les transitions de phase de premier ordre. Ce fut un privilège de travailler avec eux et je remercie grandement l'ensemble de l'Institut de physique d'Helsinki pour m'avoir fait sentir si bien accueilli au sein du département.

Je souhaiterais aussi remercier tous les collaborateurs avec qui j'ai eu la chance de travailler et qui ont tous grandement contribué à l'élaboration des différents chapitres de cette thèse. Mes sincères remerciements à Nelson Christensen, Patrick Peter, Christophe Ringeval, Florent Robinet, Mairi Sakellariadou, Daichi Tsuna et Yue Zhao. Ce fut un plaisir de rendre visite à Tanmay Vachaspati en Arizona pour collaborer avec lui. Je le remercie spécialement pour cette invitation.

Mes remerciements vont ensuite à l'ensemble des chercheurs que j'ai côtoyés à l'APC. En particulier, je souhaiterais remercier Matteo Barsuglia et Donatella Fiorucci pour leurs éclairages sur le problème de détection des ondes gravitationnelles au début de ma thèse. Merci aussi aux membres de l'école doctorale et de mon comité de thèse pour leur suivi et leur aide. Je pense notamment à Alessandra Tonazzo, Yannick Giraud-Héraud, Alissa Marteau et Stanislas Babak qui ont œuvré au bon déroulement de ces trois années.

Enfin, ces années ont été rendues particulièrement agréables par la présence des autres doctorants de l'APC avec qui j'ai eu la joie d'organiser et de participer à divers évènements comme le Congrès des Doctorants, les Casual Seminars et les Pub Quiz. Merci à Alexandre, Amélie, Aurélien, Baptiste, Bastien, Calum, Catherine, Clara, Dimitri, Edwan, Gabriel, Jani, Jean-Baptiste, Jewel, Hamza, Hugo, Konstantin, Léandro, Louise, Magdy, Makarim, Marc, Marion, Raphaël, Samuël, Théodoros, Thomas, Thibault et Valentin : ce fut un plaisir de passer ces années avec vous.

Je tiens à remercier ma famille pour avoir toujours entretenu ma curiosité et pour leur soutien indéfectible. À mes parents : vous êtes ma source d'inspiration et je vous dois beaucoup.

Mes derniers remerciements sont pour Blandine qui a partagé ma vie de doctorant et d'étudiant, avec ce que cela comporte de joies mais aussi de déceptions et surtout d'imprévus. Je te remercie pour toutes ces années embellies à tes côtés.

Contents

Introduction

> Mais ce n'est pas tout : Lorentz, dans l'Ouvrage cité, a jugé nécessaire de compléter son hypothèse en supposant que toutes les forces, quelle qu'en soit l'origine soient affectées, par une translation, de la même manière que les forces électromagnétiques, et que, par conséquent, l'effet produit sur leurs composantes par la transformation de Lorentz est encore défini par les équations (4).
> Il importait d'examiner cette hypothèse de plus près et en particulier de rechercher quelles modifications elle nous obligerait à apporter aux lois de la gravitation. J'ai d'abord été conduit à supposer que la propagation de la gravitation n'est pas instantannée, mais se fait à la vitesse de la lumière. (...) Quand nous parlerons donc de la position ou de la vitesse du corps attirant, il s'agira de cette position ou de cette vitesse à l'instant où *l'onde gravifique* est partie de ce corps; quand nous parlerons de la position ou de la vitesse du corps attiré, il s'agira de cette position ou de cette vitesse à l'instant où ce corps attiré a été atteint par l'onde gravifique émanée de l'autre corps. (...) Il n'est donc pas, à première vue, absurde de supposer que les observation astronomiques ne sont pas assez précises pour déceler une divergence aussi petite que celle que nous imaginons. Mais c'est ce qu'une discussion approfondie permettra seule de décider.
>
> Henri Poincaré, *"Sur la Dynamique de l'électron"*, 1905 [1]

A (very) brief history of gravitational waves

In his famous paper of 1905 [2], Albert Einstein shattered the traditional notions of space and time with his theory of *special relativity*. The theory is based on two assumptions

1. All laws of physics must be the same for all observers moving at constant speed relative to each other. This first premise may be seen as Galilean relativity (or invariance).

2. The speed of light must be the same for all inertial observers, regardless of their relative motion. This second premise is motivated by the experiments conducted by Michelson and Morley [3] which had failed to measure a significant difference between the speed of light in the direction of movement of the earth and the speed in other directions.

Among other fundamental results, Albert Einstein used his theory of special relativity to derive the transformation law for the passage from one inertial reference frame to another: the *Lorentz transformation*. Hendrik Lorentz and Henri Poincaré had already found them by looking at the transformation laws leaving Maxwell's equation of electromagnetism invariant. However, Albert

Einstein was the first to give a physical significance to these laws, breaking the notions of absolute time and space.

Soon after this pioneering article, the scientific community questioned whether the laws of gravity should also follow the principles of special relativity. We can find this questioning in a note from Henri Poincaré in 1905 [1] (see quotation at the beginning of the chapter) including the first mention of a *"gravific wave"*, a prototype of a gravitational wave. Then in 1915, Albert Einstein published his manuscript on *General Relativity* (GR) [4], a consistent description of both gravity and special relativity. He quickly postulated the existence of *gravitational waves* (GW) [5, 6] based on his theory of general relativity, and this date is most often considered to be the beginning for the history of gravitational waves.

Gravitational waves are perturbations of the metric satisfying a wave equation, *i.e.* they are ripples of space-time curvature propagating unimpeded at the speed of light. Even though they arise naturally from the perturbation of Einstein's equations, the reality of gravitational waves was debated for a long time. Indeed, the plane gravitational waves solution found by Einstein were first classified into three types: longitudinal-longitudinal; longitudinal-transverse; transverse-transverse. In 1922, Arthur Eddington showed [7] that the first two have no fixed velocity, or rather that it depends on the choice of coordinates. Although Eddington found that the transverse-transverse waves propagate at the speed of light in all systems of coordinates, his result raised suspicion as to the objective existence of gravitational waves. Albert Einstein himself had serious doubts on the subject. In 1936, he submitted a paper to Physical Review, together with Nathan Rosen, in which they claimed that gravitational waves cannot exist in a full theory of general relativity because any such solution would have singularities. The article was reviewed by Howard Robertson who reported that the singularities in question were simply the harmless coordinate singularities of the employed cylindrical coordinates (see for instance Ref. [8]). The issue was only settled in the mid 1950s, thanks to the work of Felix Pirani who rephrased gravitational radiation in terms of the manifestly observable Riemann curvature tensor [9]. Finally, in a famous thought experiment presented during the first "GR" conference at Chapel Hill in 1957 known as the *sticky bead argument*, Richard Feynman noted that if one takes a rod with beads then the effect of a passing gravitational wave would be to move the beads along the rod; friction would then produce heat, implying that the passing wave had done work.

After the Chapel Hill conference, Joseph Weber was the first person to realize that it is not utterly hopeless to detect gravitational waves (see Chapter 10 of Ref. [10] for an historical review about the conception of the GW detectors written by Kip Thorne). He designed and built the first gravitational wave detectors known as *Weber bars* [11]: a cylindrical aluminium bar, about two meters long, a half meter in diameter and a ton in weight. The principle is the following: the bar has a natural mode of vibration which can respond resonantly to the oscillating tidal force applied by a passing gravitational wave. To use such a bar, one has to adjust its size so that its natural frequency matches the frequency of the incoming GW. In 1969, Joseph Weber published results announcing the first detection of gravitational waves [12]. Although his claims were received with scepticism by his peers, many groups of scientists built their own gravitational wave detectors to repeat and improve on Weber's measurements.

The first experimental confirmation of the existence of GW came after the measurement of the orbital period decay in the PSR B1913+16 by Hulse and Taylor in 1974 [13, 14]. Not only does this observation confirm the existence of gravitational radiation, it is also a remarkable quantitative test of general relativity. This announcement sparked renewed interest in the field, and Hulse and Taylor received the Nobel prize in 1993 for this discovery.

In the 1970s, several groups of researchers independently devised a new type of GW detector based on interferometry[1]. These *laser interferometric GW detectors* are very similar to the one used by Michelson and Morley in 1887 to search for the motion of Earth through ether, and soon became a serious alternative to Weber bars. Indeed, interferometers present a number of advantages over Weber bars:

- The bar responds only to a narrow frequency band, therefore decoding the full GW signal would require many bars each with different natural frequencies. On the contrary, interferometers respond, in principle, to all frequencies. Thus, they have a wider frequency range.

- Increasing the length of the interferometer arms increases the sensitivity of the detector by roughly the same amount. By contrast, the Weber bar cannot be lengthened much, since its natural frequency depends on its dimensions.

- Because an interferometer can be a thousand times larger than a Weber bar, it is more immune to the quantum noise produced by the measurement process which fundamentally limits the sensitivity of Weber bars.

In parallel to the development of ground-based interferometers, the idea of using millisecond pulsars as low-frequency GW detectors germinated in the late 1970s [15, 16]. Much like a lighthouse, a pulsar is a highly magnetized rotating compact star emitting beams of electromagnetic radiation out of its magnetic poles. We observe a pulse whenever the beam is directed toward the Earth. Millisecond pulsars are amazingly stable rotators and it is possible – after a precise measurement of the pulsar's spin, astrometric and orbital parameters – to predict the pulse time-of-arrival to a very high accuracy. The passage of a gravitational wave would cause the time of arrival of the pulses to vary by a few tens of nanoseconds. The *Pulsar Timing Array* (PTA) experiments usually monitor a collection of tens of pulsars to account for the dispersion effects in the atmosphere and in the space between the observer and the pulsar. At present, there are three active PTA projects: the Parkes Pulsar Timing Array (PPTA) in Australia, the European Pulsar Timing array (EPTA) using the four largest radio telescopes in Europe and the North American Nanohertz Observatory for Gravitational Waves (NANOGRAV) in North America. These three projects have begun collaborating under the title *International Pulsar Timing Array* (IPTA), releasing their first data in 2016 [17].

Finally, in 2015, nearly forty years after the first prototypes of an interferometric detector, the first direct detection of a GW by the LIGO/Virgo collaboration [18] ended this century long quest for GWs and opened the era of *gravitational wave astronomy*.

The first successes of GW astronomy

In 2017, the Nobel prize went to Rainer Weiss, Barry C. Barish and Kip Thorne to reward their research and the first direct detection of GWs. Four years later, the latest catalogue of gravitational-wave detections by LIGO/Virgo listed a total of 50 events [19], from the first detection of a binary black hole merger in 2015 to the end of the first half of the third observing run O3a (the masses of all the detected compact objects are summarized in Fig. 1). We have moved from the quest for

[1] It is not known for sure who invented the interferometer method to detect gravitational waves, possibly because the method had several precursors. See Refs. [10, 8] for a discussion on the subject.

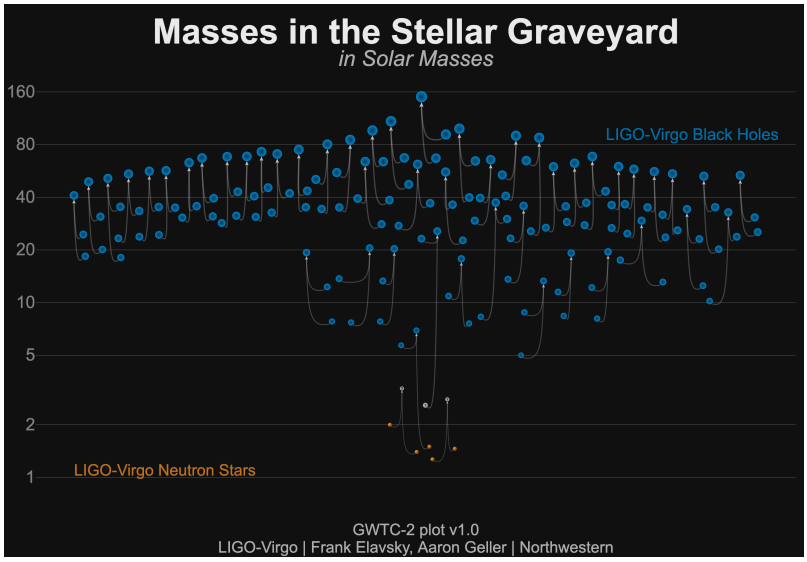

Figure 1: Masses of compact objects detected through gravitational waves [19]. The figure shows black holes (blue), neutron stars (orange), and compact objects of uncertain nature (gray). Each compact binary merger corresponds to three compact objects: the two coalescing objects and the final merger remnant. (Credit: LIGO Virgo Collaboration/Frank Elavsky, Aaron Geller / Northwestern).

GWs to the era of gravitational astronomy, using GW to test the limits of GR and understand the most inaccessible regions of our Universe.

Perhaps the most exceptional GW event of this list is GW170817 [20][2]. It is the first observation of GWs from the inspiraling of two neutron stars, and the electromagnetic counterpart was observed in multiple wavelength bands and localized in the galaxy NGC 4993. In particular, 1.74 ± 0.05 seconds after the GW event, the γ-ray burst (GRB) GRB 170817A was observed independently by the Fermi Gamma-ray Burst Monitor and by the SPectro-meter on board INTEGRAL Anti-Coincidence Shield[3]. This unique *multi-messenger* observation in both GWs and electromagnetic waves has a number of implications for fundamental physics, cosmology and astrophysics [22, 23].

Among the implications for fundamental physics, the temporal offset of 1.74 ± 0.05 s between the GW and the GRB allows one to constrain the speed of GWs, $c_{\rm GW}$, relative to the speed of light $c_{\rm EM}$. The luminosity distance to the source of about 26 Mpc can be accessed through the analysis of the GW signal amplitude. An estimate of the upper bound on the speed difference $\Delta c = c_{\rm GW} - c_{\rm EM}$ can be set by assuming that the GW and GRB were emitted simultaneously. To obtain a lower bound on Δc, one can assume that the two signals were emitted at times differing by more than 1.74 ± 0.05 s with the faster EM signal making up some of the difference. As a conservative bound relative to the few second delays, the authors of Ref. [20] assume that the GRB signal was emitted 10 seconds after the GW signal. The resulting constraint on the speed difference is

$$-3 \times 10^{-15} \leq \frac{\Delta c}{c_{\rm EM}} \leq +7 \times 10^{-16}. \tag{1}$$

This observation has also been used to derive tests for violations of Lorentz invariance, on the polarizations of the GW and of the equivalence principle, finding no deviations from GR and thus constraining tightly models of modified gravity.

Regarding cosmology, the joint observation of GW and EM waves offered a unique and independent measurement of the Hubble constant H_0. If we restrict to the local Universe, the Hubble constant relates the luminosity distance an object d_L with its redshift z (see Ref. [24] for a discussion on distances in cosmology)

$$d_L(z \ll 1) = \frac{cz}{H_0}. \tag{2}$$

Different approaches exist to estimate the Hubble constant. One estimate comes from the measurement of the peaks of the CMB temperature power spectrum, which correspond to the acoustic scale at recombination. The latest Planck result assuming the Λ-CDM model is [25]

$$H_0 = 67.37 \pm 0.54 \text{ km.s}^{-1}\text{Mpc}^{-1}. \tag{3}$$

Other methods using Baryon-acoustic oscillations combined with physics of the big bang nucleosynthesis give similar values for $H_0 = 67.66 \pm 0.42 \text{km.s}^{-1}\text{Mpc}^{-1}$. This is, however, lower than the value obtained by independent measurements at low redshifts, such as the ones of the SH0ES collaboration. This latter measurement involves the complex calibration of a *distance ladder*: a succession of standard rulers to determine distances on a hierarchy of scales. The first ruler is the

[2]The nomenclature for confirmed GW events was initially GWYYMMDD with YY the year, MM the month and DD the day of the detection. In the last catalogue GWTC-2, the events get the UTC time of their detection added to their name. This way, they can have unique names even for two events detected on the same day, as happened three times in O3a.

[3]The network of detectors found another binary neutron star merger in 2019, GW190425, but unfortunately could not find the associated electromagnetic counterpart [21].

measurement of *parallax*, which can be used at the scale of our galaxy. A second ruler comes from *Cepheid variables*, a type of star that pulsates. A direct relationship between a Cepheid variable's luminosity and pulsation period allows one to use them as a ruler for scaling galactic and extragalactic distances. Finally, *type 1a supernovae* are used to measure distances in distant galaxies. Type 1a supernovae have a characteristic light curve after the explosion and it is used to determine their absolute luminosity and hence their distance. This succession of cosmic rulers has been calibrated with increasing accuracy over the past thirty years [26], and the latest measurement of the Hubble constant by the SH0ES collaboration is [27]

$$H_0 = 73.2 \pm 1.3 \text{ km.s}^{-1}\text{Mpc}^{-1}. \tag{4}$$

This 4σ discrepancy between low and high redshift measurements of the Hubble constant is known as the *Hubble tension* and is one of the major lead for physics beyond the Λ-CDM model (see Ref. [28] for a complete review on the Hubble tension). In this context, the gravitational-wave signal of GW170817 gives a direct measurement of the luminosity distance of the source, which, along with the redshift measurement of NGC 4993, can be used to infer cosmological parameters independently of the cosmic distance ladder. From this observation, the LIGO/Virgo collaboration estimated that [20]

$$H_0 = 70^{+12}_{-8} \text{ km.s}^{-1}\text{Mpc}^{-1}. \tag{5}$$

This first measurement paves the way for a new independent and precise determination of the Hubble constant, possibly helping in resolving the Hubble tension.

So far we have discussed the detection of individual GW signals, but it may not be the only GW signals that we can hope to detect. A *stochastic background of gravitational waves* (SGWB) is the superposition of unresolved GW signals, either coming from uncorrelated and unresolved astrophysical mergers, or from cosmological sources in causally disconnected patches in the sky. Some examples of cosmological sources from the early Universe are inflation, phase transitions, primordial black holes and cosmic strings. Each of those sources has different properties and leads to different spectra: standard slow-roll inflation for example leads to a stochastic background which is unobservable [29]. The contribution from cosmic strings and first order phase transition will be the subject of this thesis. Stochastic backgrounds are currently looked for in ground-based detectors [30, 31, 32, 33] and PTA experiments [34]. The latest upper limits on the energy fraction in gravitational waves Ω_{GW} are[4]

$$\Omega_{\text{GW}}^{\text{LIGO/Virgo}}(25 \text{ Hz}) \lesssim 5.8 \times 10^{-9}, \quad \Omega_{\text{GW}}^{\text{NANOGRAV}}(1 \text{ yr}^{-1}) \sim 1.4 - 2.7 \times 10^{-15}. \tag{6}$$

These upper limits already constrain models for the populations of compact objects and of cosmology in the early Universe (see Chapter 5 for cosmic strings). Last year, the NANOGRAV collaboration found strong evidence for a stochastic process across the monitored pulsars, but did not claim a GW detection [36]. Soon after the publication of this article, different interpretations of this signal were proposed (for instance [37, 38, 39, 40, 40, 41, 42, 42, 43, 44] only in the week following the announcement). This clearly shows the excitement in the community, and we can hope that the accumulation of new data will soon make it possible to highlight the true origin of this signal.

[4]The actual limit depends on the shape of the power spectrum and on the prior. See Ref. [35] for a method to reconstruct the spectral shape of a SGWB. For these limits, we assume a flat spectrum for $\Omega_{\text{GW}}(f)$ and a log-uniform prior.

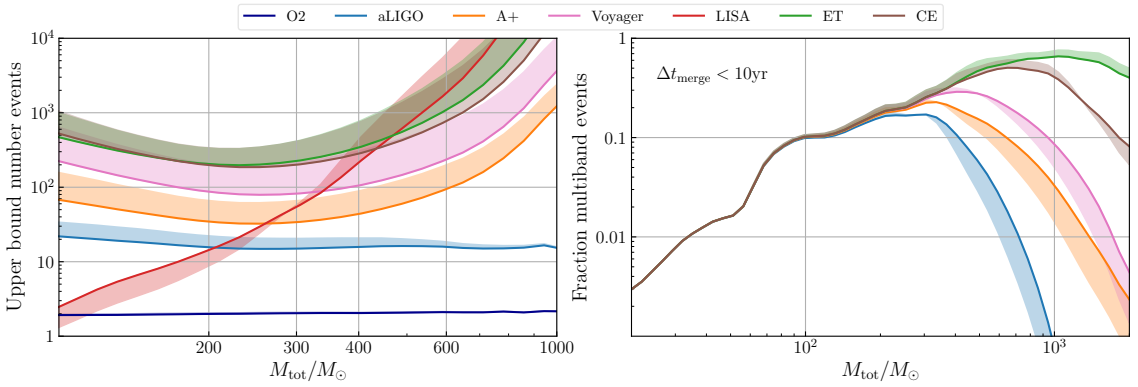

Figure 2: (Left panel) Projection of the maximum number of events detected per year for ground-based detectors (except O2 which is fixed to 9 months) and in 4 years for LISA given the upper bounds from the O1 and O2 runs. (Right panel) Fraction of multi-band events, defined as those LISA detections merging within 10 years and being detected by a ground-based detector. Solid lines represent a constant merger rate with redshift, while the shaded areas delineate the difference resulting from a redshift evolution tracking the star formation rate. The figure is taken from Ref. [45].

The (near) future of gravitational wave astronomy

The next leap in GW astronomy may come from future improvements on the network of ground-based detectors. Between the third and the fourth observing run, the LIGO and Virgo detectors will be upgraded and KAGRA, the Japanese interferometer, will be added. In Ref. [46], the new LIGO/Virgo/KAGRA collaboration estimated that the number of binary black holes (BBH) detected in O3 would be 17^{+22}_{-11}[5], compared to 79^{+89}_{-44} for O4. But perhaps the most impressive gain concerns the sky localization which is expected to be of 280^{+30}_{-23} deg^2 for O3, dropping to 41^{+7}_{-6} for O4 when the four detectors will be operating. Better determination of the sky localization offers the possibility to detect more multi-messenger events such as GW170817 and to infer the redshift of the GW source using galaxy catalogues.

In the not-so-distant future, we can hope that the data accumulated by the PTA experiments will be able to discriminate the origin of the stochastic signal found in NANOGRAV [36]. By the end of the 2020s and the beginning of the 2030s, the two radio-telescopes constituting the *square kilometre array* (SKA) in South Africa and in Australia will start acquiring data and will greatly increase the sensitivity of PTA experiments in the nanohertz frequency band [47]. They will either contribute to detecting GWs, or confirm a detection if a first signal already has been identified.

By the mid 2030s, the *Laser Interferometer Space Antenna* (LISA) – a constellation of three spacecrafts separated by more than a million kilometres – will be able to detect GW signals with frequencies about 0.1 mHz to 1 Hz. The frequency band of LISA is ideally positioned for the study of various cosmological sources [48] (see in Chapter 2 a discussion on cosmic strings and

[5] 21 were eventually detected in during O3a, the first half of O3. The difference with the prediction can be explained by to the more conservative signal-to-noise threshold used to perform these predictions.

Chapter 10 for first order phase transitions at the electroweak scale) and to observe the inspiraling of supermassive black holes among other astrophysical sources [49].

The *Einstein Telescope* (ET), a proposed European ground-based gravitational-wave detector of third-generation, is an evolution of second-generation detectors such as Advanced LIGO, Advanced Virgo, and KAGRA which could be operating in the mid 2030s. The arm length of the detector will be increased to 10 km, compared to 3 km for Virgo and 4 km for LIGO and it will be built a few hundred meters underground. ET's potential is discussed in great details in Ref. [50]. An American equivalent of ET, *Cosmic Explorer* (CE), has been proposed in the US [51].

Fig. 2, taken from Ref. [45], shows the number of events expected per year in the next generations of detectors including the different stages of LIGO (O2, aLIGO, A+ and Voyager), LISA, ET and CE. It illustrates that we are still at the dawn of GW astronomy. By the next 10 to 15 years, we will go from $\mathcal{O}(10)$ events detected per year to over $\mathcal{O}(1000)$ per year. Moreover, a substantial fraction of the inspirals observed by LISA will eventually merge in the frequency band of ground-based detectors, making it possible to track the evolution of individual binaries for years until they merge.

Thesis outline

The main subject of this thesis is the study of primordial cosmology mainly through the prism of gravitational wave detectors. Throughout we work with standard Λ-CDM cosmology, in a flat Universe, assuming General Relativity. Part of this PhD work has been conducted within the Virgo collaboration – Chapter 5 is dedicated on the analysis of the O3 data to constrain cosmic strings – and within the LISA cosmology working group – in Chapter 2, we estimate the capability of LISA to detect GW from cosmic strings. The manuscript is divided into three independent parts, each focusing on a different type of phenomenon in the early Universe.

The first part of this thesis deals with cosmic strings, one-dimensional topological defects that may be formed during phase transitions in the primordial Universe. If formed, these relics would be markers of the upheavals of our early universe. After a short introduction on cosmic strings, we study the evolution of the cosmic string network, in particular the number density of loops. We estimate their gravitational wave emission, make predictions for the future LISA mission, and finally constrain cosmic strings using the results of LIGO/Virgo/KAGRA.

In a second part, we study the formation of primordial black holes at the end of inflation, the period of accelerated expansion of the Universe. During this so-called *preheating* phase, which precedes the formation of standard model particles, the inflaton oscillates around the minimum of its potential possibly generating a metric instability at the origin of the formation of many primordial black holes. This part is therefore devoted to the study of this instability and to quantifying the production of primordial black holes using the *excursion-set* formalism.

The third part is dedicated to first order phase transitions, in particular during the electroweak transition in extensions of the standard model. During the transition, a large amount of energy is transmitted to the ambient medium in the form of kinetic energy thus generating turbulence. We therefore propose a model for this freely decaying turbulence and the resulting gravitational wave spectrum.

Publications resulting from this thesis

The present thesis lead to the publication of seven articles and the prepublication of one article which has been accepted in PRL. In chronological order:

- [52] Pierre Auclair et al. "Cosmic String Loop Production Functions". In: *JCAP* 06.KCL-PH-TH/2019-19 (2019), p. 015. DOI: 10.1088/1475-7516/2019/06/015. arXiv: 1903.06685 [astro-ph.CO]
- [53] Pierre Auclair, Danièle A. Steer, and Tanmay Vachaspati. "Particle Emission and Gravitational Radiation from Cosmic Strings: Observational Constraints". In: *Phys. Rev. D* 101.8 (2020), p. 083511. DOI: 10.1103/PhysRevD.101.083511. arXiv: 1911.12066 [hep-ph]
- [54] Pierre Auclair et al. "Probing the Gravitational Wave Background from Cosmic Strings with LISA". in: *JCAP* 04 (2020), p. 034. DOI: 10.1088/1475-7516/2020/04/034. arXiv: 1909.00819 [astro-ph.CO]
- [55] Manuel Arca Sedda et al. "The missing link in gravitational-wave astronomy: discoveries waiting in the decihertz range". In: *Class. Quant. Grav.* 37.21 (2020), p. 215011. DOI: 10.1088/1361-6382/abb5c1. arXiv: 1908.11375 [gr-qc]
- [56] Pierre G. Auclair. "Impact of the Small-Scale Structure on the Stochastic Background of Gravitational Waves from Cosmic Strings". In: *JCAP* 11 (2020), p. 050. DOI: 10.1088/1475-7516/2020/11/050. arXiv: 2009.00334 [astro-ph.CO]
- [57] Pierre Auclair and Vincent Vennin. "Primordial black holes from metric preheating: mass fraction in the excursion-set approach". In: *JCAP* 02 (2021), p. 038. DOI: 10.1088/1475-7516/2021/02/038. arXiv: 2011.05633 [astro-ph.CO]
- [58] Pierre Auclair et al. "Irreducible cosmic production of relic vortons". In: *JCAP* 03 (2021), p. 098. DOI: 10.1088/1475-7516/2021/03/098. arXiv: 2010.04620 [astro-ph.CO]
- [59] R. Abbott et al. "Constraints on cosmic strings using data from the third Advanced LIGO-Virgo observing run". In: (Jan. 2021). arXiv: 2101.12248 [gr-qc]. To appear in PRL.

Except for Ref. [55], the chapters 2, 3, 4, 5, 6, 7 and 9 of this thesis are based on the above publications. The material presented in Chapter 10 is the result of an ongoing collaboration with Chiara Caprini, Daniel Cutting, Mark Hindmarsh, Kari Rummukainen, Danièle Steer and David Weir. It has not yet been submitted for publication.

Part I

Cosmic strings

Chapter 1

Introduction to cosmic strings

The aim of this section is to give a very generic overview of cosmic strings and their observational consequences, and place my work into context. Many more details, with corresponding calculations, can be found in the subsequent chapters to which I will refer in this introduction. Fig. 1.1 summarizes the specific subjects which I will treat later in this thesis.

1.1 Topological defects

Cosmic strings are a class of stable topological defect solutions of field theories [60] which may form in spontaneous symmetry breaking phase transitions in the early Universe [61, 62]. In a cosmological setting they may lead to interesting observational effects since they concentrate large energy densities. In principle, different types of topological defects can form after a symmetry-breaking phase transition: for example, if the vacuum manifold is disconnected, domain-walls may form at the intersection of different vacua. Indeed, the type of topological defect that forms depends on the topology of the vacuum manifold $\mathcal{M}$, characterized by its homotopy groups [61, 63]. Domain-walls form when $\Pi_0(\mathcal{M})$ is non-trivial, strings when $\Pi_1(\mathcal{M})$ is non-zero whilst a non-vanishing $\Pi_2(\mathcal{M})$ gives point-like monopoles. These defects are stable solutions of the field theory. Textures may form if the homotopy group $\Pi_3(\mathcal{M})$ is non-trivial, but they are unstable and collapse on themselves.

Since this part of the manuscript is devoted to cosmic strings, let me expand on the fundamental group Π_1 of a topological space $\mathcal{M}$. A topological space $\mathcal{M}$ is *simply connected* if it is path-connected and any closed path in $\mathcal{M}$ can be contracted to a point. Equivalently for any $p : [0,1] \to \mathcal{M}$ and $q : [0,1] \to \mathcal{M}$ two closed paths with the same initial and final point ($p(0) = q(0) = p(1) = q(1)$), there exists a homotopy

$$F : [0,1] \times [0,1] \to \mathcal{M}$$
$$\text{such that } F(x,0) = p(x) \text{ and } F(x,1) = q(x).$$

More generally, if such a homotopy exists, p and q are said to be *homotopic*, and this relation is an *equivalence relation*. The fundamental group of a topological space can be seen an indicator of the failure for the space to be simply connected. It is the group formed by the set of the equivalence

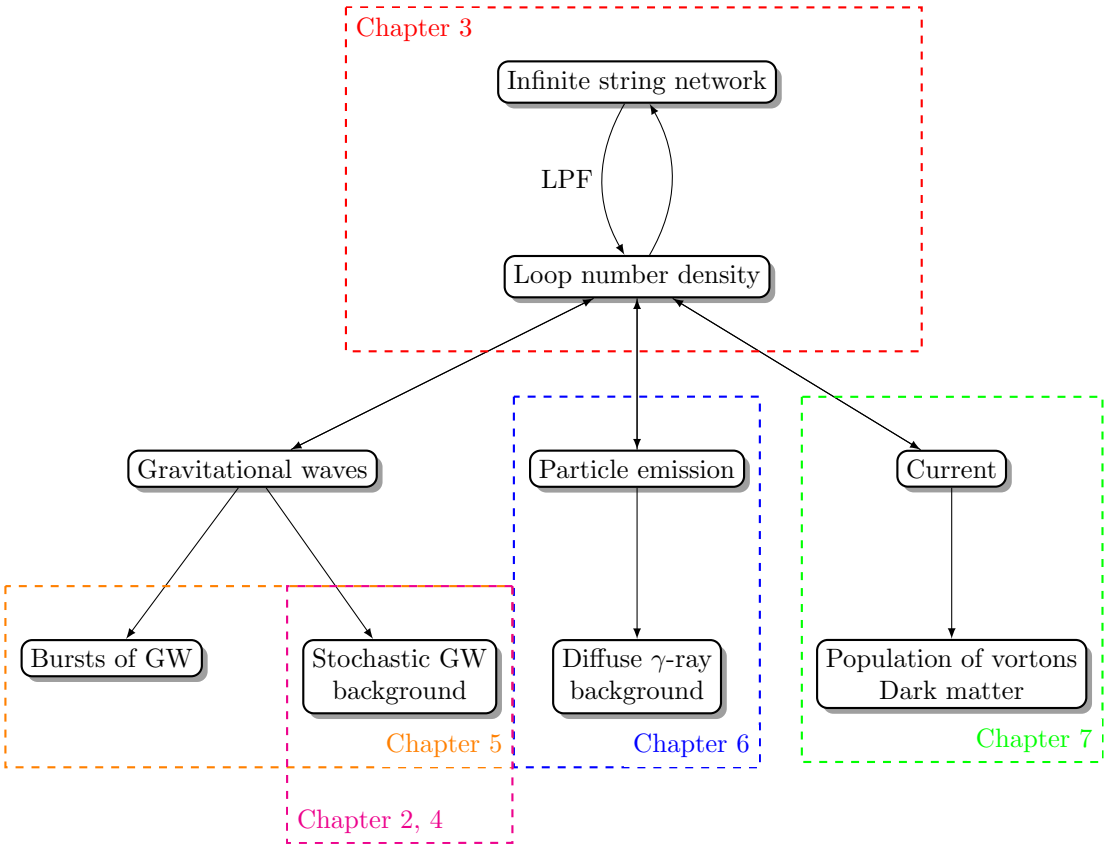

Figure 1.1: Structure for this part of the manuscript.

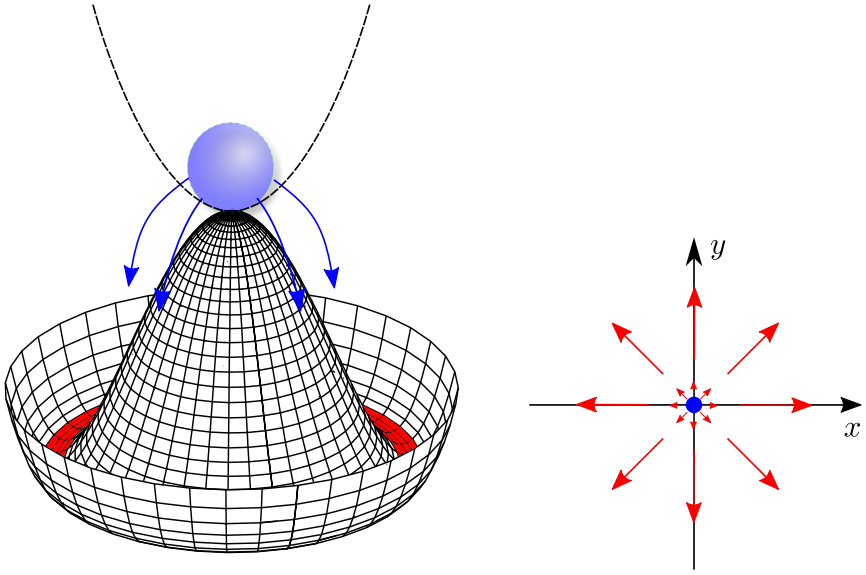

Figure 1.2: Left hand side, Mexican hat potential with a S^1 vacuum manifold. Right hand side, the field configuration for a vortex string. The size of the arrow indicates the expectation value of the order parameter. At the centre of the vortex, the field is necessarily at the top of the Mexican hat potential.

classes of loops up to homotopy, and the concatenation of loops

$$p \circ q : [0,1] \to \mathcal{M}$$
$$(p \circ q)(t) \begin{cases} p(2t) & 0 \leq t \leq 1/2 \\ q(2t-1) & 1/2 \leq t \leq 1 \end{cases}.$$

The elements of the fundamental group classify the different types of admissible string solutions. The simplest example for the formation of cosmic strings is the breaking of an $U(1)$ symmetry, taking a complex scalar field ϕ and a quartic Mexican hat potential with a degenerate circle of minima $|\phi| = \eta$ [64], as shown on Fig. 1.2. In this case, the vacuum manifold $\mathcal{M} = S^1$ is a circle, the fundamental group is $\Pi_1(\mathcal{M}) = \mathbb{Z}$, and the admissible string solutions are labelled by an integer *winding number*.

Topology only tells us about the existence of cosmic strings, not their detailed properties, which in the case of the Abelian-Higgs model will depend on the Higgs and gauge couplings (type I, type II strings) [65, 66, 67, 68]. Furthermore, if the field forming the string is coupled to other fields, it is possible for the latter to condense on the string and give rise to currents [69, 64], see Chapter 7.

1.2 Observational consequences

Alternatively, line-like "cosmic super-strings" can be cosmologically stretched fundamental strings of String Theory, formed for instance at the end of brane inflation [70, 71]. The energy per unit

length of a string μ, is of order η^2, where η is a characteristic energy scale: for topological strings

$$G\mu = 10^{-6}\Big(\frac{\eta}{10^{16}\text{GeV}}\Big)^2 \tag{1.1}$$

with η the energy scale of the phase transition. Generically the string tension is also of order μ, and strings are relativistic objects: the combination of a high energy scale and a relativistic speed clearly indicates that strings are a natural source of GWs. We will discuss the production of GW from strings in details in the following Chapters 2 and 5.

There are other ways one can hope to detect the presence of cosmic strings in the Universe that do not directly involve the observation of the GWs they generate. Multiple potential observational signatures of cosmic string networks have been discussed in the literature, including anisotropies in Cosmic Microwave Background (CMB) [72, 73, 74, 75], lensing events [76, 77], and cosmic rays from the decay of strings into particle radiation [78, 79, 80, 81, 82, 83, 84, 85, 86] (see [69, 64, 87, 88] for a review). Currently, CMB data from the Planck Satellite [72] imply $G\mu < 10^{-7}$ for Nambu-Goto, Abelian-Higgs, and semi-local strings.

The most stringent bounds, however, come from searches for the SGWB, with pulsar timing arrays (PTA) constraining $G\mu$ for Nambu-Goto strings to be $G\mu \lesssim 10^{-11}$ [89, 90], and LIGO-Virgo observations constraining it to as low as $G\mu < 2\times10^{-14}$, depending on the string network model [32, 91, 59] which is one of the main subjects of this thesis.

1.3 Nambu-Goto action

Since the characteristic width $\delta \sim 1/\eta$ of a cosmic string is generally much smaller than the horizon, in this manuscript I mainly assume that strings can be described by the Nambu-Goto (NG) action, which is the leading-order approximation for strings without current when the curvature scale of the strings is much larger than their thickness [69]. Let τ be a time-like and σ a space-like coordinate along the string and $X^\mu(\tau,\sigma)$ the coordinates of the centre of the string. The induced metric on the world-sheet is

$$\gamma_{ab} = g_{\mu\nu}\partial_a X^\mu \partial_b X^\nu \tag{1.2}$$

where $\partial_{a,b}$ denote derivatives with respect to (τ,σ) and $g_{\mu\nu}$ is the background metric evaluated at the position of the string. The Nambu-Goto action which minimizes the area of the world-sheet is then

$$\mathcal{S} = -\mu\int \mathrm{d}\tau\,\mathrm{d}\sigma\,\sqrt{-\det\gamma} \tag{1.3}$$

We refer to such string as NG strings.

The string energy-momentum tensor follows from Eq. (1.3)

$$T^{\mu\nu}(x^\sigma)\sqrt{-\det g} \equiv -2\frac{\delta\mathcal{S}}{\delta g_{\mu\nu}} = \mu\int \mathrm{d}\tau\,\mathrm{d}\sigma\,\sqrt{-\det\gamma}\gamma^{ab}\partial_a X^\mu\partial_b X^\nu\delta^{(4)}(X^\sigma(\tau,\sigma)-x^\sigma) \tag{1.4}$$

using the relation $\delta(\det\gamma) = \det(\gamma)\gamma^{ab}\,\delta\gamma_{ab}$. To find the equations of motion, we vary the action with respect to $X^\mu(\tau,\sigma)$, leading to

$$\delta\mathcal{S} = \frac{\mu}{2}\int \mathrm{d}\tau\,\mathrm{d}\sigma\,\sqrt{-\det\gamma}\gamma^{ab}\left(\frac{\delta\gamma_{ab}}{\delta X^\mu}\,\delta X^\mu + \frac{\delta\gamma_{ab}}{\delta\partial_c X^\mu}\,\delta\partial_c X^\mu\right), \tag{1.5}$$

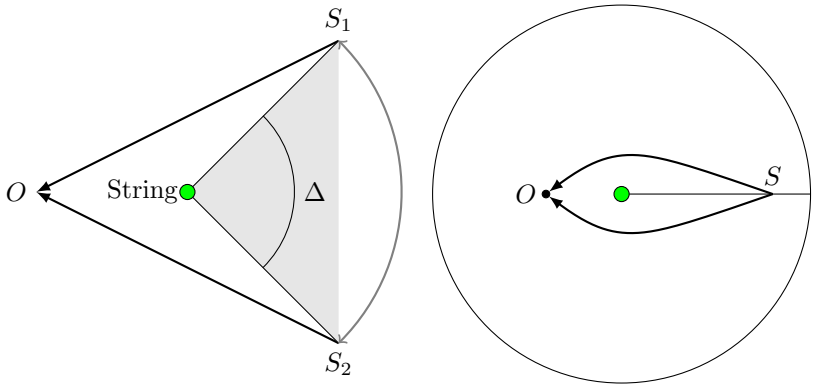

Figure 1.3: Gravitational lensing by a cosmic string. The metric around the string is a cone with a deficit angle $\Delta = 8\pi G\mu$. The observer sees two images S_1 and S_2 of the same source.

with

$$\frac{\delta\gamma_{ab}}{\delta X^\mu} = \frac{\delta g_{\lambda\nu}}{\delta X^\mu}\partial_a X^\lambda \partial_b X^\nu = -2\Gamma_{\mu\lambda\nu}\partial_a X^\lambda \partial_b X^\nu, \tag{1.6}$$

$$\frac{\delta\gamma_{ab}}{\delta\partial_c X^\mu} = g_{\mu\nu}(\gamma^c_b \partial_a X^\nu + \gamma^c_a \partial_b X^\nu). \tag{1.7}$$

Finally the equation of motions becomes

$$\frac{1}{\sqrt{-\det\gamma}}\partial_c\Big(\sqrt{-\det\gamma}\gamma^{ac} g_{\mu\nu}\partial_a X^\nu\Big) + \gamma^{ab}\Gamma_{\mu\lambda\nu}\partial_a X^\lambda \partial_b X^\nu = 0. \tag{1.8}$$

1.4 Cosmic strings in flat space-time

In this section, we study the solutions of the Nambu-Goto action in a flat space-time $g_{\mu_\nu} = \eta_{\mu\nu}$ to gain an understanding of their properties. Since the Nambu-Goto action is, by construction, reparametrization invariant, we fix a specific gauge and choose the *conformal gauge*:

$$\gamma_{01} = \gamma_{00} + \gamma_{11} = 0, \tag{1.9}$$

or equivalently

$$\dot{X}^\mu \cdot X'^\mu = 0 \tag{1.10}$$

$$\dot{X}^2 + X'^2 = 0. \tag{1.11}$$

Here $\cdot = \partial/\partial\tau$ and $' = \partial/\partial\sigma$. The gauge is called *conformal* because the metric is conformally flat

$$\gamma_{ab} = \sqrt{-\det\gamma}\eta_{ab}, \quad \gamma^{ab} = \frac{1}{\sqrt{-\det\gamma}}\eta^{ab}. \tag{1.12}$$

The equations of motion simplify significantly to the wave equation

$$\frac{1}{\sqrt{-\det\gamma}}\partial_a\partial^a X^\mu = \ddot{X}^\mu - X''^\mu = 0. \tag{1.13}$$

However, the conformal gauge does not fix the gauge entirely, and one usually removes the residual freedom by setting $\tau = t = X^0$, which is a solution of Eq. (1.13) with $\mu = 0$. The equations of motion and the gauge conditions give the following system of differential equations for the three-dimensional vector $X^\mu = (t, \mathbf{X})$

$$\dot{\mathbf{X}} \cdot \mathbf{X}' = 0 \tag{1.14}$$

$$\dot{\mathbf{X}}^2 + \mathbf{X}'^2 = 1 \tag{1.15}$$

$$\ddot{\mathbf{X}} - \mathbf{X}'' = 0. \tag{1.16}$$

The solution of the wave equation of Eq. (1.16) is a superposition of left and a right movers

$$\mathbf{X}(t, \sigma) = \frac{1}{2}[\mathbf{a}(t - \sigma) + \mathbf{b}(t + \sigma)], \tag{1.17}$$

where the gauge conditions (1.14) and (1.15) constrain $\mathbf{a}'$ and $\mathbf{b}'$ to be trajectories on a unit sphere, also called the *Kibble sphere*

$$\mathbf{a}'^2 = \mathbf{b}'^2 = 1. \tag{1.18}$$

With the equations of motion, the energy-momentum tensor in flat space-time is rewritten as

$$T^{\mu\nu}(t, \mathbf{x}) = \mu \int \mathrm{d}\sigma \left(\dot{X}^\mu \dot{X}^\nu - X'^\mu X'^\nu \right) \delta^{(3)}(\mathbf{X}(t, \sigma) - \mathbf{x}). \tag{1.19}$$

From this expression, one can directly that calculate the energy contained in the string

$$\mathcal{E} = \int \mathrm{d}^3x \, T^0_0 = \mu \int \mathrm{d}\sigma \, . \tag{1.20}$$

Hence for Nambu-Goto strings, the tension μ is equal to the energy per unit length.

A closed loop of strings is characterized by $\sigma \in [0, \ell[$ where ℓ is the *invariant length*, defined by

$$\ell \equiv \frac{\mathcal{E}}{\mu}. \tag{1.21}$$

In the centre of mass frame, the periodicity of the loop $\mathbf{X}(t, \sigma + \ell) = \mathbf{X}(t, \sigma)$ implies that $\mathbf{a}$ and $\mathbf{b}$ are also periodic and that the loop oscillates with a period

$$T = \frac{\ell}{2}, \tag{1.22}$$

indeed one has $\mathbf{X}(t + \ell/2, \sigma + \ell/2) = \mathbf{X}(t, \sigma)$. This oscillation of the loop is one of the mechanisms through which cosmic string loops emit GW.

For a straight and static string along the z-axis

$$T^\nu_\mu = \mu \delta(x) \delta(y) \mathrm{diag}(1, 0, 0, 1) \tag{1.23}$$

Using this as the right-hand side of the linearized Einstein's equations, the metric around the string is [92]

$$\mathrm{d}s^2 = \mathrm{d}t^2 - \mathrm{d}z^2 - \mathrm{d}r^2 - r^2 \, \mathrm{d}\theta \tag{1.24}$$

with the angle varying in the range $0 \leq \theta < 2\pi(1 - 4G\mu)$. The space-time around the metric is therefore flat and a particle at rest will not experience a gravitational attraction. However, the string introduces a *deficit angle*

$$\Delta = 8\pi G\mu \tag{1.25}$$

and can cause gravitational lensing, as illustrated in Fig. 1.3.

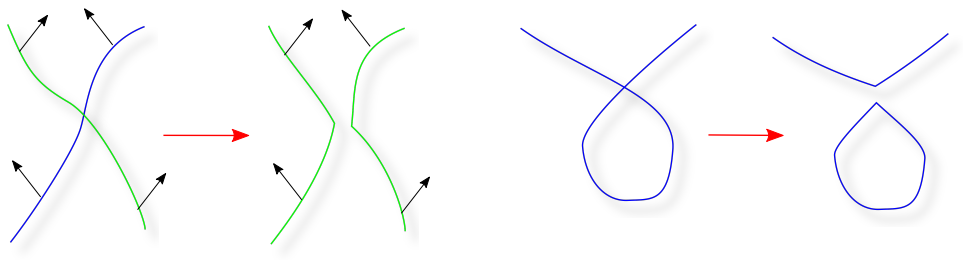

Figure 1.4: Two cosmic string exchange partners when they collide. If a cosmic string intersects itself, it produces a loop.

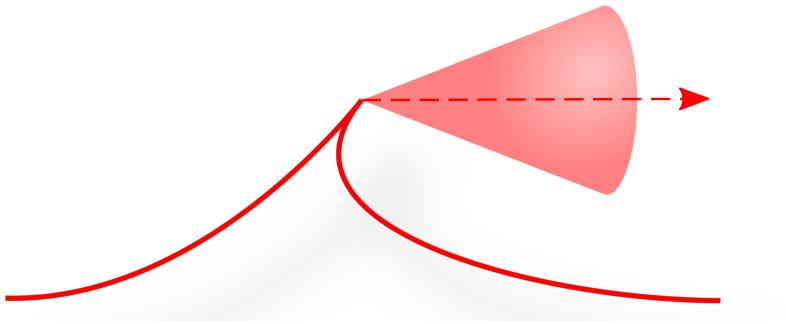

Figure 1.5: Cusps may form periodically on the string and travel instantly at the speed of light in the NG limit. The emission of gravitational waves is concentrated in a localized beam.

1.5 Scaling of the cosmic string network

With the NG equations of motion, one can study the evolution of a string network, from formation until the present time. While the basic picture is simple – a string network is stretched by the cosmological expansion, and the motion of strings leads to multiple interactions and collisions between them – in practice, this is a complicated problem which has been studied in depth in the literature [93, 94, 95, 96, 63, 97, 98, 99, 100]. One often assumes (based on numerical simulations of field theory strings [65, 66]) that when strings collide, they always intercommute, *i.e.*, that they always "exchange partners" and reconnect after a collision. Perhaps the most important conclusion of these studies is that the cosmic string network reaches an attractor *scaling solution* in which its energy density remains a fixed fraction of the background energy density, and all typical loop lengths are proportional to cosmic time (equivalently they scale with the Hubble radius). We will discuss in more detail in Chapter 2 the *Velocity dependent One Scale model* (VOS) and the results of numerical simulations [101, 102, 103, 99] that support the existence of the scaling solution. Most often, we use the scaling variables when studying the properties of the cosmic string network.

$$\gamma \equiv \frac{\ell}{t}$$

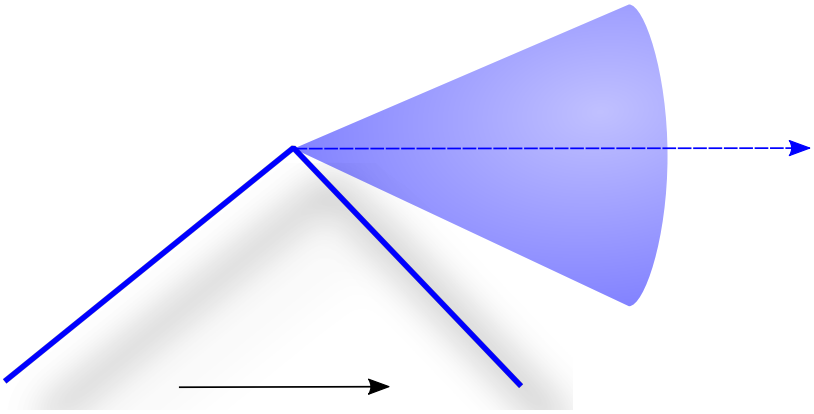

Figure 1.6: Kinks travel along the string at the speed of light. They emit gravitational waves in a localized beam whose direction changes during the propagation of the kink.

1.6 Gravitational wave bursts

Closed loops are formed when a string self-intersects or two curved strings collide. Loops smaller than the horizon decouple from the cosmological evolution and oscillate under their own tension, slowly decaying into GWs. Indeed, in flat space-time, as seen above, loops oscillate with period $\ell/2$. A smooth loop generically develops *cusps*, namely points where the string momentarily moves at the speed of light [104] as in Fig. 1.5. In a flat space-time, using Eq. (1.17)

$$\dot{\mathbf{X}}^2(t,\sigma) = \frac{1}{4}[\mathbf{a}'(t-\sigma) + \mathbf{b}'(t+\sigma)]^2. \tag{1.26}$$

If the two curves intersect on the Kibble sphere $\mathbf{a}'(\zeta_a) = \mathbf{b}'(\zeta_b)$, then $\dot{\mathbf{X}}^2 = 1$ and this happens periodically whenever $2\sigma = -\zeta_a + \zeta_b + n\ell$ and $2t = \zeta_a + \zeta_b + n\ell$ for $n \in \mathbb{Z}$.

Moreover, the intersections of strings generates discontinuities on their tangent vector known as *kinks*, see Fig. 1.6. All loops will contain kinks — either as a result of the intercommutation that produced them, or as historical remnants of past intersections. Cusps and kinks generate gravitational wave bursts [105, 106], and these play a significant role in the stochastic background of GW emitted by string networks. (One should note that a complementary strategy to the detection of the stochastic background is therefore to search for such individual transient signals, see [107, 91] and Chapter 5.) It has also been shown that the collision of kinks produces isotropic bursts of GW [108, 90], see Fig. 1.7. Even though kink-kink collisions produce bursts of GW with relatively low amplitude compared to cusps and kinks; they may dominate the GW emission on very wiggly strings since the number of collisions grows quadratically with the number of kinks on the string. This is why this effect has been added in the third observing run of the LIGO/Virgo/KAGRA collaboration [59], as detailed in Chapter 5.

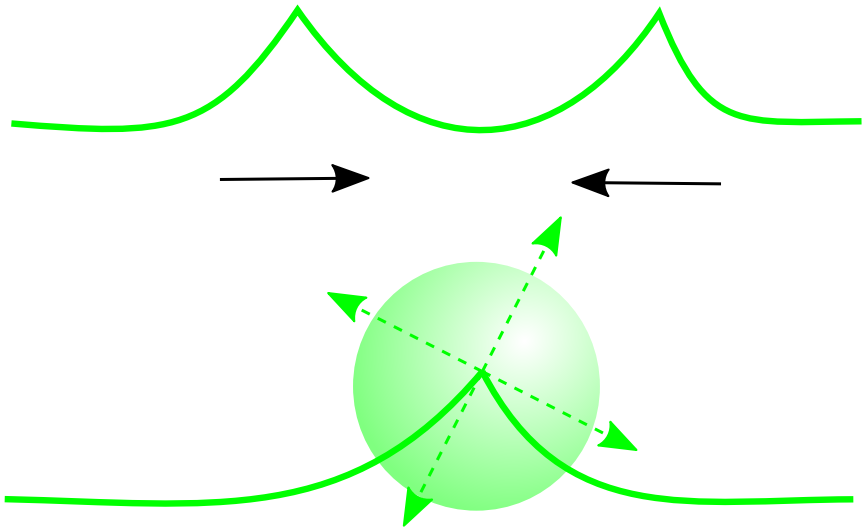

Figure 1.7: Kink-kink collisions emit gravitational waves isotropically. Even though the amplitude of the emitted GW is relatively low, the number of events on a loop grows quadratically with the number of kinks. These collisions may dominate on very wiggly strings.

1.7 Loop production function and loop number density

Although loop production is observed and measured in Nambu-Goto cosmic string simulations [99, 100, 109], it is still a matter of debate whether loops form in the same quantity in field theory simulations [110, 111, 112, 113]. Nambu-Goto simulations from two independent groups have shown that, on *large scales* (see discussion below), where these simulations can be trusted, the loop distribution is a power-law, namely [99, 103, 114]

$$t^4\mathbf{n}(\gamma,t) \propto \gamma^p. \tag{1.27}$$

where $\mathbf{n}$ is the number density distribution of loops of size $[\ell, \ell + \mathrm{d}\ell]$ at cosmic time t, and the time-independence of the combination $t^4\mathbf{n}$ is precisely the scaling regime.

Let us also notice that, due to the huge disparity of scales in the problem (ranging from, for instance, the distance between kinks formed by string intercommutations, to the horizon size), numerical simulations of cosmic string networks cannot incorporate all physical effects. In Nambu-Goto simulations, in particular, effects from GW emission and backreaction onto the string dynamics are ignored[1]. This is why Eq. (1.27) can only be trusted for loops large enough that these effects remain negligible. GW's emission means that loops loose energy and hence become smaller, with an average emitted GW power $P_{\rm gw} = \Gamma G\mu^2$ where Γ is a numerical constant estimated to be $\Gamma = \mathcal{O}(50)$ [117, 118, 114]. Hence, loops decoupled from the Hubble flow shrink at an average rate given by

$$\gamma_{\rm d} \equiv \Gamma G\mu. \tag{1.28}$$

[1]See, however, Ref. [115] and more recently Ref. [116] for an isolated loop.

One therefore expects Eq. (1.27) to hold for loops of length $\ell \gtrsim \ell_{\rm d} = \gamma_{\rm d} t$ (numeric-wise, this is a quite small number already for $G\mu < 10^{-7}$). Emitted GWs will also backreact onto the string thereby affecting its dynamics. The consequences of this process for the network and the loops are still unknown and being studied [119, 120, 121]. However, one expects that loop production should be cut-off below some length scale $\ell_{\rm c} \equiv \gamma_{\rm c} t$, with presumably $\gamma_{\rm c} \leq \gamma_{\rm d}$, which I discuss in Chapters 3 and 4.

As was realized very early on, to include these physical effects one needs to combine results of simulations with analytical modelling [64]. A powerful framework for this is to use a Boltzmann approach to estimate the loop distribution on cosmological time and length scales [96, 122, 123, 124, 125, 126, 127]

$$\left.\frac{\partial}{\partial t}\right|_{\ell} \left(a^3 \mathbf{n}\right) + \left.\frac{\partial}{\partial \ell}\right|_{t} \left(\frac{{\rm d}\ell}{{\rm d}t} a^3 \mathbf{n}\right) = a^3 \mathcal{P} \tag{1.29}$$

in which $\mathcal{P}$ is the loop production function (LPF) and ${\rm d}\ell/{\rm d}t$ is the rate at which the loop shrinks.[2] As we will discuss in Chapter 3, *radically different* assumptions about the loop production function can lead to *similar* powers p on large scales. Indeed, on one hand, motivated by the one-scale model of cosmic string evolution [61, 64], an often studied case is one in which [128, 105, 129, 130, 48, 131, 107, 132, 133]

$$\mathcal{P}(\gamma, t) \propto \delta_{\rm D}(\gamma - \alpha), \tag{1.30}$$

namely all stable loops are formed with size $\ell = \alpha t$ at time t (for constant α) and one can show that in the radiation era $p = -5/2$ while in the matter era $p = -2$ (see Section 3.2.2). On the other hand, all cosmic string simulations show that a lot of small-scale structure, namely kinks generated from string intercommutation, build up on the strings (see Refs. [134, 102, 101, 93, 135, 136, 94] for a discussion of small-scale structure on strings). As a result, one expects loops to be formed on a wide range of scales at any given time. The most recent analytical work along these lines is by Polchinski-Rocha and collaborators [137, 138, 122], who proposed a model of loop production from long strings. It is given by

$$t^5 \mathcal{P}(\gamma > \gamma_{\rm c}, t) \propto \gamma^{2\chi - 3}, \tag{1.31}$$

here the parameter χ will be referred to as the Polchinski-Rocha (PR) exponent[3]. This is clearly very different from a Dirac distribution as a loop production function and the consequences of a power-law loop production function on the loop number density and the SGWB are analysed in Chapters 3 and 4.

1.8 Field-theory strings and particle emission

At a more fundamental level, as discussed above, cosmic strings are not NG but topological solutions of field theories. Their dynamics can therefore also be studied by solving the field theory equations of motions. In studies of large scale field theory string networks [110, 112, 74, 113], loops are observed to decay directly into particles and gauge boson radiation on a short time scale of order of the loop length. Hence, field theory string network simulations predict very different observational consequences — in particular no SGWB from loops. Since field theory and Nambu-Goto strings in principle describe the same physics, and hence lead to the same observational consequences, this is an unhappy situation. Based on high resolution field theory simulations, a possible answer

[2] The explanations for this continuity equation and the link with a Boltzmann equation can be found in Section 7.A

[3] The PR exponent is related to the two-point correlation function of tangent vectors along cosmic strings.

to this long-standing conundrum was proposed in Ref. [139]. In particular, for a loop of length ℓ containing *kinks*, a new characteristic length scale $\ell_{\rm k}$ associated to the collision of kinks was identified, and it was shown that if $\ell \gtrsim \ell_{\rm k}$ gravitational wave emission is the dominant decay mode, whereas for smaller loops $\ell \lesssim \ell_{\rm k}$ particle radiation is the primary channel for energy loss. If a loop contains *cusps*, then one expects that particle radiation is the dominant channel for energy loss below another length-scale $\ell_{\rm c}$ [140, 141]. The observational consequences of this description of particle emission are addressed in Chapter 6. It should be noted that in a recent article [142], Hindmarsh and collaborators have attributed the long lifespan of the loops in Ref. [139] to their particular choice of initial conditions. They argue that the way loops are formed in their simulations is not representative of the actual formation of loops by the infinite string network.

1.9 Current-carrying strings

Most studies of cosmic strings suppose they are structureless, with equal energy per unit length and tension, and therefore they are expected to be well described by a worldsheet action, *i.e.* the Nambu-Goto action. This is no longer the case if, as first realized by Witten [143, 144], particles couple to the string-forming Higgs field can condense in the string core and subsequently propagate along the worldsheet. The resulting strings thus behave like current carrying wires and are endowed with a much richer structure [145, 146].

One of the simplest examples of current-carrying strings is that of a $\mathrm{U}(1)_R \times \mathrm{U}(1)_Q$ gauge theory with an unbroken gauge symmetry Q (which could be for instance electromagnetism) and a broken symmetry R [143]. This model generalizes the prototypical Abelian-Higgs model of cosmic strings behind much of the existing work on cosmic strings. At a temperature $T_{\rm ini}$, and a cosmic time $t_{\rm ini}$, the Higgs field ϕ with $Q = 0$ and $R = 1$ acquires a non-zero vacuum expectation value $|\langle\phi\rangle| \neq 0$, thereby breaking the first component $\mathrm{U}(1)_R$ of the total invariance group; this leads to the formation of vortex lines. The field ϕ vanishes at the core of the string and its phase varies by an integer times 2π along any closed path around the vortex: this is the standard Kibble mechanism. If the theory contains fermions obtaining their masses from the $\mathrm{U}(1)_Q$ broken symmetry, those form zero modes in the string core where the symmetry is restored, thereby forming a superconducting current.

The model also comprises a second scalar field σ with $Q = 1$ and $R = 0$, the coupling potential between ϕ and σ being chosen such that $\langle\sigma\rangle = 0$ in vacuum (where $|\langle\phi\rangle| \neq 0$). Under certain conditions, it is energetically favourable to have $\langle\sigma\rangle \neq 0$ at the core of the string where $\langle\phi\rangle = 0$. At a temperature $T_{\rm cur} < T_{\rm ini}$, and cosmic time $t_{\rm cur} > t_{\rm ini}$, the charged scalar field σ thus condenses on the string and acts as a bosonic charge carrier making the string current-carrying (and in fact actually superconducting). The presence of currents flowing along the strings affects the dynamics of the network, and in Chapter 7 I will particularly focus on vortons [147, 148, 149, 150, 151, 152, 153, 154], namely closed loops of string which are stabilized by the angular momentum carried by the current. Vortons do not radiate classically, and here I make the assumption that they are classically stable as well (see for instance [155, 156, 157] for numerical studies of their stability). On cosmological scales, they appear as point particles having different quantized charges and angular momenta.

1.10 Plan for the part on cosmic strings

The structure of this part of the manuscript is given in Fig. 1.1. To summarize:

- The *infinite string network* consists of all the cosmic strings larger than the Hubble horizon. They are stretched by the expansion of the Universe and lose energy by producing loops. The size and abundance of the produced loops is encoded in the loop production function (LPF)

- The *loop number density* is determined using the Boltzmann equation (1.29). It depends crucially on the loop production function $\mathcal{P}$ and on $\dot{\ell}$ the rate at which the loop shrinks. The influence of the loop production function on the loop number density is the subject of Chapter 3.

- The *emission of GW* is the standard channel by which cosmic string loop lose energy. This emission can be detected either in the form of individual bursts from cusps, kinks and kink-kink collisions, or through the uncorrelated sum of those signals: a stochastic background of GW. In Chapter 2, I review the different methods to calculate the SGWB and assess the capability of LISA, the *Laser Interferometer Space Antenna* to detect a stochastic signal from cosmic strings. Then in Chapter 4, I study the impact of the loop production function on the SGWB from cosmic strings at different frequencies while providing analytical templates for these spectra. And in Chapter 5, I will present the results from the third data observing run by the LIGO/Virgo/KAGRA collaboration on the GW signals of cosmic strings, both in the form of bursts and of a SGWB.

- Numerical simulations of field theory string have shown that loops *emit particles*, thus shortening their lifetime. This energy loss channel modifies significantly the loop number density and the signal in terms of GW. Additionally, this emission of particle may impact other observables such as the Diffuse γ-ray background. This is the subject of Chapter 6.

- Finally, particles coupled to the string-forming Higgs field can condense in the string core and act as charge carriers. One consequence is that closed loop do not shrink indefinitely but are stabilized by the angular momentum of the current. These vortons appear as point-like particles and may be a viable candidate for part of the dark-matter content of the Universe. In Chapter 7, I calculate the abundance of vortons today based on the string tension and the energy-scale of the charge carrier.

Chapter 2

Probing the gravitational wave background from cosmic strings with LISA

This chapter is a reproduction of Ref. [54] which was written in collaboration with the LISA cosmology working group. A significant part of this work, which took a year and a half to complete, involved writing my own code to calculate the stochastic background based on two independent methods (one of which is very useful for bursts constraints, see Chapter 5) which are discussed in sections 2.2.1 and 2.2.2. Other codes already existed and did not always agree amongst each other nor to a sufficient precision. Finding the details and correcting all the codes took a certain time. Thanks to this, I have my own well-tested code which I have also used in the subsequent chapters of this thesis. I have contributed to all the sections of this chapter except for sections 2.6.2 on the agnostic model, 2.5.4 on non-standard cosmologies and 2.6.3 on the gravitational wave bispectrum from long strings.

Abstract

Cosmic string networks offer one of the best prospects for detection of cosmological gravitational waves (GWs). The combined incoherent GW emission of a large number of string loops leads to a stochastic GW background (SGWB), which encodes the properties of the string network. In this paper we analyse the ability of the Laser Interferometer Space Antenna (LISA) to measure this background, considering leading models of the string networks. We find that LISA will be able to probe cosmic strings with tensions $G\mu \gtrsim \mathcal{O}(10^{-17})$, improving by about 6 orders of magnitude current pulsar timing arrays (PTA) constraints, and potentially 3 orders of magnitude with respect to expected constraints from next generation PTA observatories. We include in our analysis possible modifications of the SGWB spectrum due to different hypotheses regarding cosmic history and the underlying physics of the string network. These include possible modifications in the SGWB spectrum due to changes in the number of relativistic degrees of freedom in the early Universe, the presence of a non-standard equation of state before the onset of radiation domination, or changes to the network dynamics due to a string inter-commutation probability less than unity. In the event of a detection, LISA's frequency band is well-positioned to probe such cosmic events. Our results constitute a thorough exploration of the cosmic string science that will be accessible to LISA.

2.1 Introduction

The direct detection of gravitational waves (GWs) by the LIGO and Virgo network [18, 158, 159, 160, 161] marks the dawn of a new era in astronomy, opening a unique window with which to observe the Universe. GWs carry invaluable information about the sources that created them — which could be of astrophysical or cosmological origin — since they propagate unimpeded through space. Gravitational waves therefore constitute one of the most promising new messengers with which we can probe aspects of the Universe so far undetermined by other means.

One of the main targets of GW experiments is the detection of a stochastic gravitational wave background (SGWB) of cosmological origin. The most famous example of such a SGWB is the quasi–scale invariant background from inflation, due to quantum fluctuations [162, 163, 164, 165]. This background is expected to be too small to be detectable by currently planned GW observatories. However, if axion-type species are present during inflation, potentially observable GWs can also be produced with a significant blue-tilt (see *e.g.* [166, 167, 168, 169, 170, 171, 172, 173, 174, 175, 176, 177], or [178] for a general discussion on GWs from inflation). Furthermore, post-inflationary, early-universe phenomena can also generate GWs with a large amplitude, *e.g.* a kination-dominated phase [179, 180, 181, 182, 183], particle production during preheating [184, 185, 186, 187, 188, 189, 190, 191], oscillon dynamics [192, 193, 194, 195, 196], strong first order phase transitions [197, 198, 199, 200, 201, 202, 203], or cosmic defect networks [117, 204, 105, 106, 205, 206, 114]. For a comprehensive review of SGWB signals of cosmological origin, see [29]. In this paper, we focus on precisely one such cosmological source: cosmic strings. We investigate, in particular, the ability of the *Laser Interferometer Space Antenna* (LISA) [207] — which will be the first GW observatory in space — to probe the SGWB emitted by a network of cosmic strings.

Cosmic strings are stable topological defect solutions of field theories [60] which may have formed in symmetry breaking phase transitions in the early Universe [61, 62]. Alternatively, they can be cosmologically stretched fundamental strings of String Theory, formed for instance at the end of brane inflation [70, 71]. The energy per unit length of a string μ, is of order η^2, where η is a characteristic energy scale (for topological strings, the energy scale of the phase transition). In the simplest cases, the string tension is also of order μ, and strings are relativistic objects that typically move at a considerable fraction of the speed of light. The combination of a high energy scale and a relativistic speed clearly indicates that strings should be considered a natural source of GWs.

A network of strings formed in the early Universe emits GWs throughout the history of the Universe, generating a SGWB from the superposition of many uncorrelated sources. In this paper, we forecast the constraints that LISA may put on the dimensionless combination $G\mu$ (where $G = 1/M_{\rm pl}^2$ is Newton's constant, and $M_{\rm pl} = 1.22 \times 10^{19}$ GeV the Planck mass), which is related to the energy scale η through

$$G\mu \sim 10^{-6}\Big(\frac{\eta}{10^{16}\text{GeV}}\Big)^2, \tag{2.1}$$

and which parametrizes the gravitational interactions of the string.

There are other ways one can hope to detect the presence of cosmic strings in the Universe that do not directly involve the observation of the GWs they generate. In fact, several potential observational signatures of cosmic string networks have been discussed in the literature, including anisotropies in Cosmic Microwave Background (CMB) [72, 73, 74, 75], lensing events [76, 77], and cosmic rays from the decay of strings into particle radiation [78, 79, 80, 81, 82, 83, 84, 85, 86] (see [69, 64, 87, 88] for a review). Currently, CMB data from the Planck Satellite [72] imply $G\mu < 10^{-7}$ for Nambu-Goto, Abelian-Higgs, and semi-local strings. The most stringent bounds,

however, come from searches for the SGWB, with pulsar timing arrays (PTA) constraining $G\mu$ for Nambu-Goto strings to be $G\mu \lesssim 10^{-11}$ [89, 90], and LIGO-Virgo observations constraining it to as low as $G\mu < 2 \times 10^{-14}$, depending on the string network model [32, 91]. In this paper we show that LISA will be sensitive to string tensions with $G\mu \gtrsim 10^{-17}$ for Nambu-Goto strings, improving current upper bounds by ~ 10 orders of magnitude relative to CMB constraints, by ~ 6 orders of magnitude relative to current PTA constraints, and even by $\sim$3–4 orders of magnitude relative to future constraints from next generation of PTA experiments.

Since the characteristic width $\delta \sim 1/\eta$ of a cosmic string is generally much smaller than the horizon, in this paper we mainly assume that strings can be described by the Nambu-Goto (NG) action, which is the leading-order approximation when the curvature scale of the strings is much larger than their thickness. We refer to such string as NG strings. Furthermore, we mainly focus on string networks without junctions; comments on cosmic superstring networks with junctions will be made in Section 2.6.2. With the NG action, one can study the evolution of a string network, from formation until the present time. While the basic picture is simple — a string network is stretched by the cosmological expansion, and the motion of strings leads to multiple interactions and collisions between them — in practice, this is a complicated problem which has been studied in depth in the literature. Perhaps the most important conclusion of these studies is that the cosmic string network reaches an attractor *scaling solution* in which its energy density remains a fixed fraction of the background energy density. One often assumes that when strings collide, they always intercommute, *i.e.*, that they always "exchange partners" and reconnect after a collision[1]. As a result, closed loops are formed when a string self-intersects or two curved strings collide. Loops smaller than the horizon decouple from the cosmological evolution and oscillate under their own tension, slowly decaying into GWs. Indeed, in flat space-time, one can show that loops have oscillating trajectories which are periodic in time. The relativistic nature of these strings typically leads to the formation of *cusps*, namely points where the string momentarily moves at the speed of light [104]. Moreover, the intersections of strings will generate discontinuities on their tangent vector known as *kinks*. All loops will contain kinks — either as a result of the intercommutation that produced them, or as historical remnants of past intersections. Cusps and kinks generate gravitational wave bursts [105, 106], and these play a significant role in the SGWB emitted by string networks. (One should note that a complementary strategy to the detection of the stochastic background is therefore to search for such individual transient signals, see [107, 91].)

Other than sub-horizon string loops, the network also contains long strings that that stretch across a Hubble volume. These are either infinite or in the form of super-horizon loops, and are also expected to emit GWs. However, the dominant contribution is generically that produced by the superposition of radiation from many sub-horizon loops along each line of sight. Studying this SGWB and the possibility of observing it with the LISA constellation [207] is the main focus of this paper. We argue that, even though the next round of pulsar timing observations could improve the constraint on the cosmic string tension $G\mu$ in the near future, this will not continue for long. Future tightening of these constraints will necessarily come from GW detectors operating in an intermediate frequency band. This is precisely due to the fact that the GW background expected from strings at lower energy scales will peak at these intermediate frequencies, which are out of reach of PTA experiments. We therefore conclude that LISA is the ideal instrument with which to search for cosmic strings in the future or, at the very least, to further improve constraints on cosmic string scenarios.

[1]This corresponds to an intercommutation probability $P = 1$, which we mainly assume throughout this paper. We comment briefly on $P < 1$, characteristic of cosmic superstrings, in Section 2.6.2.

The paper is organized as follows. In Section 2.2, we briefly review the basic methods and relevant formulae with which to calculate the energy density spectrum of the SGWB emitted by sub-horizon loops in an evolving network of cosmic strings. In Section 2.3, we present different approaches developed in the literature to determine the loop number density, which is a fundamental quantity in the determination the SGWB from any string network. In Section 2.4, we review the emission of GWs by individual strings, in particular the so-called 'loop power spectrum' and the GW waveforms from bursts. These different results are put together in Section 2.5, where we characterize the spectral shape of the SGWB from a cosmic string network. We discuss different (potentially observable) features that can be imprinted in the SGWB spectrum, such as the details of radiation-to-matter transition, the number of relativistic degrees of freedom active during expansion, and the equation of state in the early Universe. In Section 2.6, we analyse in detail the ability of LISA to measure the spectrum of the SGWB from a network of cosmic strings, and in particular we determine the parameter space that is compatible with a detection. Finally, in Section 2.7, we present an overview of our results and state our conclusions.

2.2 The calculation of the SGWB from Cosmic Strings

Several studies in the literature have calculated the SGWB generated by an evolving cosmic string network (see, *e.g.*, [92, 208, 117, 209, 210, 128, 211, 129, 212, 213, 214, 48, 131, 215, 216, 103, 217, 114, 89, 90, 218, 219]). This is often quantified in terms of the fraction of the critical density in GWs per logarithmic interval of frequency,

$$\Omega_{\rm GW}(t_0, f) = \frac{8\pi G}{3H_0^2}\, f\, \frac{{\rm d}\rho_{\rm gw}}{{\rm d}f}\,, \tag{2.2}$$

where H_0 is the Hubble parameter, and ${\rm d}\rho_{\rm gw}/{\rm d}f$ is the energy density in gravitational waves per unit frequency f, observed today (at $t = t_0$). The basic idea is that, given a GW frequency today, one must add up the GW emission from all the loops throughout the entire history of the Universe that contribute to that frequency. To do so, two different and complementary approaches have been developed in the literature, and the aim of this section is to introduce both of them. (These two approaches are also discussed in more detail in Section 2.4.)

Before doing so, we introduce the basic ingredients common to the two approaches. The first is the *number density* $\mathbf{n}(\ell, t)$ of non-self-intersecting, sub-horizon, cosmic string loops of invariant length ℓ at cosmic time t. These are the loops which, through their oscillations, contribute to the SGWB. When the network is scaling — as it is in the radiation and matter eras — $\mathbf{n}(\ell, t)$ can be estimated through different numerical and analytical techniques (see Section 2.3). Scaling, however, cannot be maintained during the radiation-to-matter transition, but analytical estimates can nonetheless be extended to this regime.

The second ingredient is the loop power spectrum, namely the *power $P_{\rm gw}(f, \ell)$ emitted in GWs of frequency f by a cosmic string loop of length ℓ*. It is clear that individual loops of a given length ℓ will radiate in different ways according to their shape. Hence, either one can assume an average (or typical) gravitational loop power spectrum $P_{\rm gw}(f, \ell)$ determined numerically from simulations; or one can focus on particular events on the strings (cusps and kinks) for which $P_{\rm gw}(f, \ell)$ can be determined analytically.

2.2.1 Method I

Let us write the power $P_{\rm gw}(f,\ell)$ in units of $G\mu^2$ and ℓ as

$$P_{\rm gw}(f,\ell) = G\mu^2 \ell \; P(f\ell), \tag{2.3}$$

where we have introduced a function $P(f\ell)$ which in principle takes a different form for each individual loop, depending on its shape. The first method to calculate $\Omega_{\rm GW}(t_0,f)$ assumes the existence of an averaged function, $P(f\ell)$, computed from an ensemble of loops of length ℓ obtained from simulations. Then the energy density in GWs observed at a particular frequency f today is obtained by adding the amount of energy produced at each moment of cosmic evolution for loops of all sizes. On taking into account the redshift of frequencies from the moment of emission until today, one finds

$$\frac{{\rm d}\rho_{\rm gw}}{{\rm d}f} = G\mu^2 \int_0^{t_0} {\rm d}t \left(\frac{a(t)}{a_0}\right)^3 \int_0^\infty {\rm d}\ell \;\; \ell \; \mathbf{n}(\ell,t) \; P\!\left(\frac{a_0}{a(t)} f\ell\right), \tag{2.4}$$

where $a(t)$ is the scale factor which takes the value a_0 today. In order to compute $\Omega_{\rm GW}(t_0,f)$ from Eqs. (2.2) and (2.4), one must specify the cosmological model, the number density of loops $\mathbf{n}(\ell,t)$, and an average power spectrum $P(f\ell)$. This approach has been followed in *e.g.* [92, 208, 117, 209, 210, 128, 213, 214, 48, 216, 103, 217, 114, 89, 218].

2.2.2 Method II

At high frequencies $f\ell \gg 1$, $P_{\rm gw}(f,\ell)$ can be estimated analytically. Indeed, whatever the shape of the loop, one can show that the gravitational waveform sourced by a loop is dominated at high frequency by cusps, kinks, and kink-kink collisions. (See appendix 2.A for an overview of the Nambu-Goto equations and the precise definitions of cusps and kinks). The form of $P_{\rm gw}(f,\ell)$ for these 3 types of events is discussed in Section 2.4.

Cusps, kinks, and kink-kink collisions emit short bursts of GWs. The contribution to the SGWB from the superposition of the unresolved signals from these three types of events is given by

$$\frac{{\rm d}\rho_{\rm gw}}{{\rm d}f} = f^2 \int_0^\infty {\rm d}z \int_0^\infty {\rm d}\ell \; h^2(f,z,\ell) \, \frac{\partial^2 R(z,\ell)}{\partial z \partial \ell} \,, \tag{2.5}$$

where z is the redshift, $h(f,z,\ell)$ is the amplitude of the Fourier transform of the trace of the metric perturbation generated by each event, and $\partial^2 R(z,\ell)/\partial z \partial \ell$ denotes the event rate per unit loop length and per unit redshift. This rate is directly proportional to $\mathbf{n}(\ell,t)$, and therefore one must know the number density of loops. This approach has been considered in Refs. [211, 212, 131, 215, 90, 91, 219].

2.2.3 Cosmology

Finally, one must provide the details of the expansion history of the Universe. Unless specified otherwise, we assume a standard flat Λ-CDM model. The Hubble rate reads

$$H(z) = H_0 \mathcal{H}(z), \tag{2.6}$$

where

$$\mathcal{H}(z) = \sqrt{\Omega_\Lambda + \Omega_{\rm mat}(1+z)^3 + \Omega_{\rm rad}\mathcal{G}(z)(1+z)^4} \,, \tag{2.7}$$

and we use Planck-2018 fiducial parameters [25],

$$\begin{aligned} H_0 &= 100h \ \ \mathrm{km/s/Mpc}\,, \\ h &= 0.678\,, \\ \Omega_{\mathrm{mat}} &= 0.308\,, \\ \Omega_{\mathrm{rad}} &= 9.1476 \times 10^{-5}\,, \\ \Omega_{\Lambda} &= 1 - \Omega_{\mathrm{mat}} - \Omega_{\mathrm{rad}}\,. \end{aligned} \tag{2.8}$$

The function $\mathcal{G}(z)$, which takes into account the effective number of degrees of freedom $g_*(z)$ and the effective number of entropic degrees of freedom $g_S(z)$, is given by [48]

$$\mathcal{G}(z) = \frac{g_*(z) g_{\mathrm{S}}^{4/3}(0)}{g_*(0) g_{\mathrm{S}}^{4/3}(z)}\,. \tag{2.9}$$

Unless explicitly stated otherwise, we use the Standard Model numbers of degrees of freedom as given by `microMEGAS` [220]. We also make use of the following functions to describe proper distance

$$\varphi_r(z) = \int_0^z \frac{\mathrm{d}z'}{\mathcal{H}(z')}\,\mathrm{d}z \tag{2.10}$$

and proper volume

$$\varphi_v(z) = \frac{4\pi\varphi_r^2(z)}{(1+z)^3\mathcal{H}(z)}\,. \tag{2.11}$$

We describe the imprint of the expansion history on the SGWB from cosmic string loops in Section 2.5.3. There we also discuss the effect of possible departures from this picture, including the impact of increasing the effective number of degrees of freedom in the early Universe as well as the impact of an equation-of-state different from that during radiation domination.

The following sections describe in detail the different ingredients which enter into the calculation of the spectrum of gravitational waves.

2.3 String network modelling

We have mentioned earlier that one of the most important aspects of a cosmic string network is its ability to reach a scaling solution. Analytical modelling as well as early cosmic strings simulations demonstrated the approach of the long string network to this attractor regime [221, 93, 101]. Loops, however, reach scaling over a longer time scale and therefore larger simulations are need to attain this regime. It is only more recently that Nambu-Goto simulations performed by two independent groups [99, 95] have shown the existence of a population of scaling loops.

As outlined in Section 2.2, in order to calculate the spectrum of GWs expected today, a crucial input is the loop number density $\mathbf{n}(\ell, t)$ at all times t, since GWs are generated throughout the history of the cosmic string network. In order to extrapolate results from simulations, which run only over a finite time interval, to any moment in the history of the network, the scaling of loops is crucial since it implies that

$$\mathbf{n}(\ell, t) = t^{-4}\mathcal{N}(\gamma)\,, \tag{2.12}$$

where $\gamma = \ell/t$ is the ratio of the size of the loop to roughly the horizon scale.

In order to obtain $\mathbf{n}(\ell, t)$, one approach is to determine the loop production function $\mathcal{P}(\ell, t)\,\mathrm{d}\ell$, namely the number density of non-self-intersecting loops of lengths between ℓ and $\ell + \mathrm{d}\ell$ produced per unit time, per unit volume, which in scaling satisfies

$$\mathcal{P}(\ell, t) = t^{-5}\mathcal{P}(\gamma)\,. \tag{2.13}$$

The number density of non-self-intersecting loops is then obtained by solving the Boltzmann equation for loops: loops are diluted with the expansion of the Universe, lose energy through GWs, and are sourced by loops being chopped off the infinite string network as described by $\mathcal{P}(\ell, t)\,\mathrm{d}\ell$.[2] The loop number density can thus be computed by integrating the loop production function

$$\mathbf{n}(\ell, t) = \int_{t_i}^{t} \mathrm{d}t'\,\mathcal{P}(\ell', t')\left(\frac{a(t')}{a(t)}\right)^3\,, \tag{2.14}$$

where the effect of the expansion is explicitly seen through the dependence of the scale factor $a(t)$, and ℓ' (which is given below) contains information on the evolution of the length of the loop due to its gravitational decay from the time of formation t' to the observation time t. More explicitly, assuming that, on average, the total power emitted by a loop is given by $\Gamma G\mu^2$, where Γ is a dimensionless constant (independent of the size and shape of a loop), then

$$\ell = \ell' + \Gamma G\mu\,(t' - t)\,. \tag{2.15}$$

(Namely, a loop with length ℓ' at time t' has length ℓ at time $t > t'$.) As we discuss in more detail in later sections, the value of Γ is given by the sum of the GW power radiated at all frequencies, and therefore generally one would expect it to depend on the shape of the loop. However, following the estimates from simple loops [117, 224, 225] as well as the results obtained from recent simulations [114], in this paper we take $\Gamma = 50$.

The scaling loop number density for a power law cosmology parametrized by $a(t) \sim t^{\nu}$ can be obtained by combining Eqs. (2.12)-(2.15). Changing variables from t' to $\gamma' = \ell/t'$ one finds [103]

$$\mathcal{N}(\gamma) = \left[\frac{1}{(\gamma + \Gamma G\mu)^{3(1-\nu)+1}}\right]\int_{\gamma}^{\infty} (\gamma' + \Gamma G\mu)^{3(1-\nu)}\mathcal{P}(\gamma')\;\mathrm{d}\gamma'\,, \tag{2.16}$$

which can be easily computed once $\mathcal{P}(\gamma)$ is given.[3]

Finally, we now relate $\mathcal{P}(\ell, t)$ — the loop production function for non-self-intersecting loops — to the long string network with energy density ρ_∞. If we assume that the production of loops is the dominant energy loss mechanism of the long string network, then [64]

$$\frac{\mathrm{d}\rho_\infty}{\mathrm{d}t} = -2H(1 + \bar{v}^2)\rho_\infty - \mu\int_0^\infty \ell\mathcal{P}(\ell, t)\,\mathrm{d}\ell\,, \tag{2.17}$$

where $H = \dot{a}/a$ is the Hubble parameter and $\bar{v} = \sqrt{\langle 0|v^2|0\rangle}$ is the root-mean-squared (RMS) velocity of the long strings. The first term in this equation describes the dilution of the long string

[2] In principle loops could also collide with each other (to create larger, possibly self-intersecting, loops), leading to a more involved Boltzmann equation, see [96]. Loops could also rejoin the infinite string network, see [222, 223]. However, in Ref. [95], this effect was shown not to be significant for non-self-intersecting loops, and we will neglect it here.

[3] In Eq. (2.14) we have assumed that $t \gg t_i$, meaning that the contribution from the loop distribution at the initial time t_i can be neglected, and this is also the reason for the infinite upper limit in (2.16). Note that the Boltzmann equation may not always allow a scaling solution (see the analysis of [52], valid for all $t \geq t_i$).

energy density in an expanding Universe, while the second, proportional to the loop production function, takes into account the energy lost into loops. Loop production is essential to achieve the linear scaling of long strings, see *e.g.* [64].

In remainder of this section, we review three expressions for the loop number density $\mathbf{n}(\ell, t)$ which have been proposed in the literature for Nambu-Goto strings. Then, in Section 2.3.4, we discuss the case of Abelian-Higgs string networks.

2.3.1 Model I: analytic approach

In the case of NG strings, the first expression for $\mathbf{n}(\ell, t)$ we consider is based on an analytic approach, which was initially developed by Kibble in Ref. [63] and later extended in Refs. [128, 129, 213, 216]. Here, the basic idea is that the loops produced by the long string network are described by a single free parameter (essentially the size of loops at formation), while Eq. (2.17) is used to determine the normalization of the loop production function.

As a first step in the determination of $\mathbf{n}(\ell, t)$, it is therefore necessary to have an analytical handle on the evolution of the long string energy density ρ_∞, and hence also of the RMS velocity $\bar{v}$ appearing in Eq. (2.17). To do so, following [216], we use the successful Velocity-dependent One-Scale (VOS) model [97, 98] since this not only describes the scaling evolution of the long string network, but also its non-scaling evolution through the radiation-matter transition.[4]

The VOS model is a quantitative thermodynamical description of the cosmological evolution of the network, in terms of two variables: In terms of the characteristic length $L \equiv (\mu/\rho_\infty)^{1/2}$ — which measures the average distance between long strings — and $\bar{v}$, the VOS equations of motion are [97, 98]

$$\frac{\mathrm{d}\bar{v}}{\mathrm{d}t} = \left(1-\bar{v}^2\right)\left[\frac{k(\bar{v})}{L} - 2H\bar{v}\right], \tag{2.18}$$

$$\frac{\mathrm{d}L}{\mathrm{d}t} = \left(1+\bar{v}^2\right)HL + \frac{c_\mathrm{c}}{2}\bar{v}\,, \tag{2.19}$$

where the constant phenomenological parameter c_c quantifies the efficiency of the loop-chopping mechanism. Indeed, since Eq. (2.19) is simply Eq. (2.17) rewritten in terms of L, it follows that

$$c_\mathrm{c}\bar{v}\frac{\rho_\infty}{L} = \mu\int_0^\infty \ell\mathcal{P}(\ell,t)\,\mathrm{d}\ell\,. \tag{2.20}$$

In Eq. (2.18), the function $k(\bar{v})$ phenomenologically accounts for the effects of small-scale structure (namely, multiple kinks) on long strings, and we use the ansatz proposed in [98]

$$k(\bar{v}) = \frac{2\sqrt{2}}{\pi}\left(1-\bar{v}^2\right)\left(1+2\sqrt{2}\bar{v}^3\right)\frac{1-8\bar{v}^6}{1+8\bar{v}^6}\,, \tag{2.21}$$

which reproduces the expected asymptotic behaviour of $k(\bar{v})$ both in the relativistic and non-relativistic limits. The linear scaling of the long string network in the radiation- and matter-dominated backgrounds follows directly from Eqs. (2.18)-(2.19) since the particular solutions

$$\frac{L}{t} = \sqrt{\frac{k(\bar{v})(k(\bar{v})+c_\mathrm{c})}{4\nu(1-\nu)}} \equiv \xi_s \qquad \text{with} \qquad \bar{v} = \sqrt{\left(\frac{k(\bar{v})}{k(\bar{v})+c_\mathrm{c}}\right)\left(\frac{1-\nu}{\nu}\right)} \equiv \bar{v}_s\,, \tag{2.22}$$

[4] Here we reformulate the results presented in the original papers, in an attempt to unify our notation across the present paper.

where the subscript s stands for "scaling", are attractor solutions of these equations for $a \propto t^\nu$ and $0 < \nu < 1$. More generally, Eqs. (2.18)-(2.19) can be solved throughout any cosmological era, including the radiation-to-matter and matter-to-dark-energy transitions, and hence one can trace the evolution of cosmic string networks in a realistic cosmological background [216]. We note that although the VOS model only treats small-scale structure phenomenologically through $k(\bar{v})$, Eqs. (2.18,2.19) were shown to provide an accurate description of the long string network evolution in both Nambu-Goto [226] and Abelian-Higgs [227] simulations.[5] In the NG case, taking $c_{\rm c} = 0.23 \pm 0.04$ fits both radiation and matter era simulations [98]. (Note that $c_{\rm c}$ is the only free parameter in the VOS model.)

The second step is to relate the loop production function to the long string network as described by the VOS model. Let us define $\xi \equiv \frac{L(t)}{t}$ and, as before, $\gamma \equiv \frac{\ell}{t}$. Then, in terms of these variables, it follows from Eq. (2.17) (or alternatively Eqs. (2.19) and (2.20)) that the loop production function satisfies

$$\int_0^\infty \gamma \mathcal{P}(\gamma)\, {\rm d}\gamma = \frac{2}{\xi^2}\big[1 - \nu(1+\bar{v}^2)\big] = c_{\rm c}\frac{\bar{v}}{\xi^3}\,. \tag{2.23}$$

We now make the following assumption, characteristic of this model I: *throughout cosmic history, all loops are assumed to be created with a length ℓ that is a fixed fraction of the characteristic length of the long string network*, namely $\ell = \alpha_L L$, with $\alpha_L < 1$. Thus

$$\mathcal{P}(\gamma) = \tilde{C}\delta_{\rm D}(\gamma - \alpha_L \xi)\,, \tag{2.24}$$

where from Eq. (2.23)

$$\tilde{C} = \frac{c_{\rm c}}{\alpha_L}\frac{\bar{v}}{\xi^4} \tag{2.25}$$

with $\bar{v}$ and $\xi = L/t$ being the solutions of the VOS equations (2.18)-(2.19). In fact, for reasons we now explain, we will consider a slightly modified form of $\mathcal{P}(\gamma)$, see (2.26) below. Indeed, note that the value of $\tilde{C}$ given in (2.25) is in fact an upper limit, since Eq. (2.23) does not capture the fact that some of the energy from the long string network goes into redshifting of the peculiar velocities of loops: we account for this by introducing a reduction of the energy of loops by a factor of $f_r \sim \sqrt{2}$ [64]. Furthermore, the assumption that all loops are created with exactly the same size is not expected to capture the true distribution of loop lengths at formation. The effect of relaxing this assumption was studied in Ref. [213], where it was found that considering a distribution of lengths generally leads to a decrease of the amplitude of the SGWB. To account for this effect, we introduce a second factor, $\mathcal{F}$, which in Ref. [103] was estimated to be $\mathcal{O}(0.1)$ for Nambu-Goto strings. Taking these correction factors into account, we rewrite the loop production function in (2.24) as

$$\mathcal{P}(\gamma) = \left(\frac{\mathcal{F}}{f_r}\right)\tilde{C}\delta(\gamma - \alpha_L\xi) \equiv A\ \delta_{\rm D}(\gamma - \alpha_L\xi)\,. \tag{2.26}$$

We stress that this expression is valid throughout cosmic history, even when the cosmic string

[5] Several other analytical models, using more than one length scale, have been developed in an attempt to provide a description of a cosmic string network including small scales [228, 229, 94, 230]. These models can describe, in particular, the effects of gravitational radiation and gravitational backreaction. They generally contain a larger number of phenomenological parameters, and clearly the one describing the strength of gravitational backreaction cannot be calibrated with simulations (since simulations do not include gravitational backreaction). For an impact of the effect of gravitational backreaction on cosmic string dynamics, see Ref. [231].

network is not in a linear scaling regime (in this case γ and $\tilde{C}$ will be time-dependent). [6] Note also that since the length of a loop decreases with time due to gravitational radiation, see (2.15), the maximum size of loops in this model is $\ell/t = \alpha_L \xi$.

The third and final step is to substitute Eq. (2.26) into Eq. (2.14) in order to obtain the loop number density $\mathbf{n}(\ell, t)$ for all times, including during the radiation-to-matter and matter-to-dark-energy transitions. Note that this in general requires solving the VOS equations (2.19) and (2.20). However, deep in the *radiation era* ($\nu = 1/2$), the long string network is scaling and described by the VOS solutions (2.22), namely $\xi_r = 0.271$ and $v_r = 0.662$, hence it follows that the loop distribution is given by

$$\mathbf{n}_r(\gamma) = \frac{A_r}{\alpha} \frac{(\alpha + \Gamma G\mu)^{3/2}}{(\gamma + \Gamma G\mu)^{5/2}}, \tag{2.27}$$

with $A_r = 0.54$ (we fix $\mathcal{F} = 0.1$, $f_r = \sqrt{2}$), and where we have defined $\alpha = \alpha_L \xi_r$. As noted above, this expression is only valid for $x \leq \alpha$. In a matter-only universe ($\nu = 2/3$), the VOS scaling solutions (2.22) give $\xi_m = 0.625$ and $v_m = 0.583$ and the loop distribution is

$$\mathbf{n}_m(\gamma) = \frac{A_m}{\alpha_m} \frac{\alpha_m + \Gamma G\mu}{(\gamma + \Gamma G\mu)^2}, \tag{2.28}$$

where $\alpha_m = \alpha_L \xi_m$, $A_m = 0.039$ and $x \leq \alpha_m$.

In Section 2.5.2, we use this analytical approach to estimate the effect of the radiation-to-matter transition on the GW spectrum in the LISA frequency band. In order to ease comparison with other loop distributions — to which we now turn — our results will be expressed in terms of $\alpha = \alpha_L \xi_r$ (and not the more natural parameter of this model, namely α_L). Furthermore, we also explore the effect of changing the loop size at formation, through α, in Section 2.6.2.

2.3.2 Model II: simulation-inferred model of Blanco-Pillado, Olum, Shlaer (BOS)

The second loop number density distribution $\mathbf{n}(\ell, t)$ we consider was discussed in Refs. [95, 103]. There the authors performed NG simulations of cosmic string networks in the radiation and matter eras, and obtained the loop production functions for non-self-intersecting loops directly from these simulations. We now review these results and present the corresponding loop number density distributions in different cosmological eras.

Radiation era

In the radiation era, the results of Ref. [103] together with Eq. (2.16), lead to the following scaling number density of loops

$$\mathbf{n}_r(\gamma) = \frac{0.18}{(\gamma + \Gamma G\mu)^{5/2}}, \tag{2.29}$$

[6] Note that in the radiation era, the choice $\ell = \alpha_L L$ is equivalent to assuming that $\ell = \alpha t$, with $\alpha = \alpha_L \xi_r$ (where ξ_r is given in Eq. (2.22) with $\nu = 1/2$). In Ref. [95] the length of the loops produced in radiation and matter era simulations is estimated to be, respectively, $\ell_r = 0.1t \simeq 0.33 L_r$ and $\ell_m = 0.18t \simeq 0.35 L_m$. These values are well-described by a single value of α_L (more so than by a single value of ℓ/t).

with a cutoff at the maximum size of a loop, $x \equiv \ell/t = 0.1$. It then follows from (2.12) that the number density of loops in physical units reads

$$\mathbf{n}_r(\ell, t) = \frac{0.18}{t^{3/2}(\ell + \Gamma G\mu t)^{5/2}}\,, \tag{2.30}$$

with $\ell \leq 0.1t$. In Ref. [103], the form of the loop production function was found numerically. It is not exactly a $\delta_{\rm D}$-function, as assumed in Model I, however, in Ref. [103] the precise form of the loop production function was argued not to be important, since for any function that respects the equation of energy balance given by Eq. (2.23), the final form of the number density is universal. Hence, one may argue that the most important piece of information from the simulation is the normalization factor of the loop number density in (2.29).

Comparing Eq. (2.29) with Eq. (2.27) shows the same power-law behaviour in the denominator, and furthermore fixing $\alpha = 0.1$ (the maximum size of loops in these radiation-era numerical simulations), the normalization of Eq. (2.27) yields 0.17 in the numerator, which is in good agreement with Eq. (2.29).

Matter era

The scaling distribution of loops from the radiation era survive past radiation-matter equality. The resulting number density of loops can be written in terms of the radiation density, $\Omega_{\rm rad}$, and redshift z as

$$\mathbf{n}_{\rm r,m}(\ell, t) = \frac{0.18\big(2{\rm H}_0\sqrt{\Omega_{\rm rad}}\big)^{3/2}}{(\ell + \Gamma G\mu t)^{5/2}}(1+z)^3\,, \tag{2.31}$$

where $t(z)$. This matches the previous expression (2.30) deep in the radiation era, and has the correct redshifting behaviour in the matter era.

Finally, loops are also produced once the network reaches scaling in the matter era. Following the results in Ref. [103], the corresponding loop distribution is given by

$$\mathbf{n}_{\rm m}(\ell, t) = \frac{0.27 - 0.45(\ell/t)^{0.31}}{t^2(\ell + \Gamma G\mu t)^2} \tag{2.32}$$

for $\ell/t < 0.18$. However, as we shall see in Section 2.5, for the values of the string tension $G\mu \lesssim 10^{-10}$ of relevance to LISA, the contribution of this population of loops to the SGWB is in fact negligible relative to (2.30) and (2.31).

To summarize, in order to calculate the SGWB generated by cosmic string loops described by model II, Eqs. (2.29-2.32) contain all the necessary information on the number density of loops at all times, from the formation of the cosmic string network until now.

2.3.3 Model III: simulation-inferred model of Lorenz, Ringeval, Sakellariadou (LRS)

The final loop distribution we consider is that developed in Ref. [123] and based on a different NG string simulation to model II, namely [99]. Furthermore, as opposed to Ref. [103], the loop production function is not the quantity inferred from the simulation: rather, the authors [99]

extract directly the distribution of non-self-intersecting scaling loops from their simulation. On scales $\gamma \gg \Gamma G\mu$ they find[7]

$$\mathcal{N}(\gamma) = \frac{C_0}{\gamma^p} \qquad \text{for} \qquad \gamma \gg \Gamma G\mu\,, \tag{2.33}$$

where the values of the two constants C_0 and p in the radiation and matter eras are

$$p = 2.60^{+0.21}_{-0.15}\big|_{\rm r}\,, \qquad p = 2.41^{+0.08}_{-0.07}\big|_{\rm m}\,, \tag{2.34}$$

$$C_0 = 0.21^{-0.12}_{+0.13}\big|_{\rm r}\,, \qquad C_0 = 0.09^{-0.03}_{+0.03}\big|_{\rm m}\,. \tag{2.35}$$

Compared with Eq. (2.29), the radiation era solution has a similar amplitude but the power p appears somewhat greater that 5/2, with the indicated error bars. The power in the matter era differs from the one of Model II.

In order to extend the loop distribution (2.33) down to smaller scales, the authors of [123] solve the Boltzmann equation described in sec. 2.3, using a loop production function which itself is theoretically derived. Indeed, following the analytical work of Polchinski, Rocha and collaborators [137, 232, 138], it is modelled by a power law $\mathcal{P}(\gamma) \propto \gamma^{2\chi-3}$ for $\gamma > \gamma_{\rm c}$. Here $\gamma_{\rm c} \ll \Gamma G\mu$ is a scale characteristic of gravitational backreaction, and was estimated in Ref. [232] to be given by

$$\gamma_{\rm c} \equiv 20(G\mu)^{1+2\chi}. \tag{2.36}$$

The scaling loop distribution $\mathcal{N}(\gamma)\ \forall\gamma$ is then obtained[8] by substituting $\mathcal{P}(\gamma) \propto \gamma^{2\chi-3}$ into equation (2.16), and finally the constant χ is fixed by comparing the resulting distribution on scales $\gamma \gg \Gamma G\mu$ to the numerically obtained distribution Eq. (2.33). One finds [123][9]

$$\chi_{\rm r} = 0.200^{+0.07}_{-0.10}\,, \qquad \chi_{\rm m} = 0.295^{+0.03}_{-0.04}\,. \tag{2.37}$$

These values, together with Eq. (2.35), fix all the parameters in the loop distribution $\forall\gamma$.

The resulting distribution is given in Ref. [123]. In our analysis below, we have worked with the exact distribution given in that reference, but it is useful to present its approximate analytic form in the different regimes of loop length assuming scaling:

- For loops with length scale large compared to $\gamma_{\rm d} \equiv \Gamma G\mu$:

$$\mathcal{N}(x \gg \gamma_{\rm d}) \simeq \frac{C}{(\gamma+\gamma_{\rm d})^{3-2\chi}}\,, \tag{2.38}$$

- For loops with length scale smaller than $\gamma_{\rm d}$, but larger than $\gamma_{\rm c}$:

$$\mathcal{N}(\gamma_{\rm c} < \gamma \ll \gamma_{\rm d}) \simeq \frac{C(3\nu-2\chi-1)}{2-2\chi}\frac{1}{\gamma_{\rm d}}\frac{1}{\gamma^{2(1-\chi)}}\,, \tag{2.39}$$

- For loops with length scale smaller than $\gamma_{\rm c}$, the distribution is flat:

$$\mathcal{N}(\gamma \ll \gamma_{\rm c} \ll \gamma_{\rm d}) \simeq \frac{C(3\nu-2\chi-1)}{2-2\chi}\frac{1}{\gamma_{\rm c}^{2(1-\chi)}}\frac{1}{\gamma_{\rm d}}\,. \tag{2.40}$$

[7] NG simulations do not include gravitational radiation, for which the characteristic scale is $\Gamma G\mu$

[8] As shown in Ref. [123], the form of the loop production function on smaller scales than $\gamma_{\rm c}$ is essentially unimportant to the final loop distribution.

[9] In Ref. [123], it is assumed that $\chi < (3\nu-1)/2$; see Ref. [52] for an analysis in the case $\chi \geq (3\nu-1)/2$.

In the above,

$$C = C_0(1-\nu)^{2-p}\,. \tag{2.41}$$

Relative to the BOS distribution, notice that the distribution in Eq. (2.40) contains many more small loops (due to the inverse power of γ_c which is itself very small). In fact, these small loops dominate the stochastic GW spectrum at high frequencies, as was already discussed in Ref. [91], and hence can lead to very different constraints on $G\mu$ to that of the BOS model in the high frequency regime. Indeed, the energy density in these small loops is very large, so the question of energy balance between the long string network and the loop distribution — at least as described by Eq. (2.17) (with caveats mentioned in footnote 3) — remains to be fully understood.

2.3.4 Abelian-Higgs field theory simulations

So far we have focused on Nambu-Goto strings which are infinitely thin. However, as mentioned in the introduction, cosmic strings are solitonic solutions of classical field theory models [60] which means that, in principle, they can decay not only by releasing energy into gravitational waves but also directly into excitations of their elementary constituents. For this reason, a number of authors have simulated cosmic strings in different field theories. In this short section we review this work and the implications it may have for the loop-distribution $\mathbf{n}(\ell, t)$.

In Ref. [233] global (axionic) strings were studied and it was shown that decay into elementary constituents indeed takes place, in this case due to the coupling with the massless Goldstone mode present in the vacuum of the theory. For local strings with no long-range interactions (and which, in the infinitely thin limit, are expected to be described by the NG action), the excitations in the vacuum are massive, and hence the expectation is that this radiation will be suppressed for long wavelength modes of the strings. This expectation is supported by simulations of individual oscillating strings [226] and standing waves [234], which observe that massive particle radiation originates in high curvature regions of the string, *e.g.*, in cusp-like regions where the string doubles back on itself [141]. These simulations also support the fact that, except for the short bursts of energy, the strings evolve according to the Nambu-Goto equations of motion. Furthermore, recent simulations of individual loops in the Abelian-Higgs model [139] report that, for loops smaller than a critical length scale, the lifetimes of loops scale with the square of their lengths. Extrapolating their results to large loops, these authors conclude that for loops larger than the critical length scale, GW emission is expected to dominate over particle emission [139].

In contrast, large-scale field theory (FT) simulations of the whole network of strings [110, 112, 235, 113] observe that the network of infinite strings reaches a scaling regime, thanks to energy loss into classical radiation of the scalar and gauge fields of the Abelian-Higgs model. These large-scale simulations of cosmic string networks are therefore in disagreement with the above massive radiation arguments: they show the presence of extensive massive radiation being emitted, and so loops formed in these simulations decay within a Hubble time. This intriguing discrepancy has been under debate for the last ~ 20 years, but the origin of this radiation is not currently understood.

The similarities and differences between FT and NG simulations of string networks can then be summarized as follows: the infinite strings are rather similar in curvature radius and length density, but loops decay into field modes in the FT simulations. In FT simulations the strings' energy density goes into massive modes of the fields, which are not part of the string network any more. As a consequence, the string loops decay within a Hubble time, and hence do not contribute as a source of GWs all through cosmic history. In the Nambu-Goto picture, this channel does not exist,

and instead the energy of the infinite strings goes into loops, which then decay into gravitational radiation.

Our analysis in this paper is based on the NG classical evolution of strings. Hence, we assume, as supported by NG simulations, that loops are formed throughout cosmic history, and they decay into GWs, as we describe in Section 2.4. Our conclusions about the ability of LISA to measure a GW background from cosmic strings is therefore based on this fundamental assumption.

2.4 Gravitational wave emission from strings

As outlined in Section 2.2, a crucial input into the calculation of the SGWB from cosmic strings is the loop power spectrum $P_{\rm gw}(f,\ell)$ (see Method I of Section 2.2.1). Alternatively (for method II, Section 2.2.2), one requires both $h(f,z,\ell)$ and $\partial^2 R(z,\ell)/\partial z\partial l$. Our purpose in this section is to determine these crucial quantities. We also discuss the possibility of detecting individual burst events from loops, as well the contribution of long strings to the SGWB.

2.4.1 GW loop power spectrum

The power lost into gravitational radiation by an isolated loop of length ℓ can be calculated using the standard formulae in the weak gravity regime [236]. As a first approximation, we assume that the loop evolves in flat space, meaning that its evolution is periodic and radiation is only emitted at discrete frequencies, $\omega_n = 2\pi n/T$, where $T = l/2$ is the period of the loop, and $n = 1, 2, \ldots$. Then the power emitted at frequency ω_n per solid angle is given by [224, 118]

$$\frac{\mathrm{d}P_n}{\mathrm{d}\Omega} = 8\pi G\mu^2 n^2 \left(|A_+|^2 + |A_\times|^2\right), \tag{2.42}$$

where $A_{+,\times}$ are the amplitudes of the two gravitational wave polarizations. In a coordinate system in which $\hat{\mathbf{\Omega}} = \hat{\mathbf{z}}$, they are given by

$$A_+ = I_x^+ I_x^- - I_y^+ I_y^- , \tag{2.43a}$$

$$A_\times = I_x^+ I_y^- + I_y^+ I_x^- \tag{2.43b}$$

where the $I^\pm$'s are functions of the mode number n, and are related to the Fourier transform of the stress-energy tensor of the string. (The $\pm$ refer to the fact that the solutions of the NG equations in flat space are a superposition of left and right-moving waves, see appendix 2.A, where we also give the explicit expressions of $I^\pm$ in terms of these solutions.) These $I^\pm$ functions therefore encode the information about the geometric shape of the loop over its entire oscillation. Integration of Eq. (2.42) over the sphere around the loop yields the power, P_n, emitted in each mode for a particular loop. If the loop contains cusps, kinks, and kink-kink collisions, then one can show generically that for large n, P_n scales as $n^{-4/3}$, $n^{-5/3}$, and n^{-2} respectively [117, 108]. It is important to stress that the gravitational radiation from loops is quite anisotropic: for cusps, most of the radiation at high frequencies is localized within a small solid angle surrounding the cusp direction; for kinks, the radiation is emitted in a narrow strip on the celestial sphere around the loop (see Section 2.4.2 below).

The procedure outlined above has been used to calculate the power spectrum of certain simple analytic solutions of loops with a small number of harmonics [117, 224, 225]. The results are in general agreement with the analytic estimates from cusps and kinks given above. However, in order

to calculate the stochastic gravitational wave spectrum from the whole network of loops, we need to estimate an *averaged loop power spectrum*, since different loops of different shapes (but same ℓ) may have quite distinct power spectra. One approach is to consider realistic loops obtained from a simulation. Furthermore, one could aim to go beyond the first approximation mentioned above (namely that the loop evolves in flat space), and consider how the shape of a loop changes due to the emission of gravitational radiation: that is, gravitational backreaction may be important to determine an accurate average power spectrum of loops.

The effect of gravitational backreaction on the average loop power spectrum was first considered in Ref. [114]. Starting from a representative group of ~ 1000 non-self-intersecting loops from a population of scaling loops in a large scale simulation, a simple toy model for backreaction was applied (the loops were smoothed at different scales), and finally the average power spectrum of the full family of loops was computed. The resulting spectrum — which we denote as the *BOS spectrum* — was found to be quite smooth, with a long tail well-described by $n^{-4/3}$, namely the high frequency region was dominated by cusps present on the smooth loops. Furthermore, the distribution of results for the total power, $\Gamma = \sum_{n=1}^{\infty} P_n$, for those loops was found to be highly peaked at $\Gamma \approx 50$. It is clear, however, that there is still some uncertainty in the accuracy of this power spectrum, since the smoothing procedure used in Ref. [237] only shares some of the key ingredients found in the results of recent studies of the gravitational backreaction [119, 120, 121, 238]. These latter results indicate that some parts of the power spectrum could be affected differently by more realistic backreaction.

In the following, we also consider the simple averaged loop power spectra that are determined exclusively from the frequency dependence of specific events (cusp, kinks and kink-kink collisions), namely

$$P_n = \frac{\Gamma}{\zeta(q)} n^{-q}\,, \tag{2.44}$$

where $\zeta(q)$ is the Riemann zeta function, introduced as a normalization factor to enforce the total power of the loop to be equal to $\Gamma = \sum_n P_n$. The parameter q takes the values 4/3, 5/3, or 2 depending on whether the emission is dominated by cusps, kinks or kink-kink collision respectively.[10] The sensitivity of the final SGWB to the value of q will give us an indication of the robustness of our results relative to the uncertainty on P_n.

In terms of this average power spectrum P_n, Method I of Section 2.2.1 yields the stochastic gravitational wave background as [114]

$$\Omega_{\rm GW}(\ln f) = \frac{8\pi G^2 \mu^2 f}{3H_0^2} \sum_{n=1}^{\infty} C_n(f) P_n\,, \tag{2.45}$$

where

$$C_n(f) = \frac{2n}{f^2} \int_0^{\infty} \frac{{\rm d}z}{H(z)(1+z)^6}\, \mathbf{n}\!\left(\frac{2n}{(1+z)f}, t(z)\right), \tag{2.46}$$

which depends on the loop distribution through $\mathbf{n}\!\left(\frac{2n}{(1+z)f}, t(z)\right)$, and on the assumed cosmological background through $H(z)$ and $t(z)$. As seen in Section 2.3, the number density of loops depends on the total power Γ, and hence for consistency it is important to ensure that the average loop power spectrum is properly normalized.

[10] This power spectrum should be understood as a discrete set of numbers that represent the power at each mode. We take this spectrum as it is, but we should bear in mind that this may not be a good approximation at low harmonics, where the structure of the entire loop becomes important.

2.4.2 GW waveforms from bursts

As described in Section 2.2.2, an alternative method to compute the SGWB from strings is to consider the incoherent superposition of many bursts from cusps, kinks and kink-kink collisions. The logarithmic Fourier transform of the corresponding waveforms from these individual events was calculated in Ref. [105, 106, 108]:

$$h(\ell, z, f) = A_q(\ell, z) f^{-q}\,, \tag{2.47}$$

where

$$A_q(\ell, z) = g_1^{(q)} \frac{G\mu H_0 \ell^{2-q}}{(1+z)^{q-1}\varphi_r(z)}\,. \tag{2.48}$$

Here ℓ is the length of the loop at redshift z at which this particular event takes place, $\varphi_r(z)$ is a measure of the proper distance from the observer to the source (cf. (2.10) in Section 2.2.3), and as before $q = 4/3, 5/3$ and 2, for cusps, kinks and kink-kink collisions, respectively. The numerical constant $g_1^{(q)}$ accounts for the fact that not all cusps and kinks are identical (different cusps/kinks will have different geometry/sharpness), and this modulates the strength of the GW burst.

As mentioned above, cusps and kinks radiate non-isotropically meaning that the above waveform is only valid for directions near the cusp or kink direction, and it should be cutoff on angles larger than [106, 105]

$$\theta_{\rm cutoff}(\ell, z, f) = \left(\frac{1}{g_2 f(1+z)\ell}\right)^{1/3}, \tag{2.49}$$

where $g_2 = \frac{\sqrt{3}}{4}$. On taking into account the geometry of this beaming effect, the fraction $\Delta(\ell, z, f)$ of observable bursts from cusps, kinks and kink-kink collisions is given by [212]

$$\Delta(\ell, z, f) = \left(\frac{\theta_{\rm cutoff}(\ell, z, f)}{2}\right)^{3(2-q)} \Theta(1 - \theta_{\rm cutoff}(\ell, z, f))\,. \tag{2.50}$$

The rate of bursts, which is required for the calculation of the SGWB with method II (see Eq.(2.5)), is then given by [212]

$$\frac{\partial^2 R(z,\ell)}{\partial z \partial \ell} = 2\varphi_v(z)\; H_0^{-3} \left(\frac{\mathbf{n}(\ell, t(z))}{\ell(1+z)}\right) \Delta(\ell, z, f)\,, \tag{2.51}$$

where $\varphi_v(z)$ given in Eq. (2.11).

Finally, we can collect these results together, and insert Eqs. (2.47) and (2.51) into Eq. (2.5) to find that the SGWB from Method II for a given type of burst to be given by

$$\Omega_{\rm GW}(\ln f) = \frac{\left(g_1^{(q)}\right)^2 g_2^{-2+q}}{2^{5-3q}} \frac{2N_q (G\mu)^2 (2\pi f)^3}{3H_0^3} \int_0^\infty {\rm d}\gamma \int_{z_{min}(\gamma,f)}^\infty {\rm d}z\, \frac{(f t(z))^{-2-q}}{(1+z)^{4+q}} \gamma^{1-q} \frac{H_0}{H(z)}\, \mathcal{N}(\gamma)\,, \tag{2.52}$$

where N_q is the average number of bursts per oscillation in a loop, and $z_{min}(\gamma, f)$ is the solution to $\theta_{\rm cutoff}(\ell, z_{min}, f) = 1$.

Determining the average number of cusps and kinks for the loop network is a very non-trivial task and the subject of ongoing work, and given this uncertainty it is common to take $N_c = N_k = \mathcal{O}(1)$. However, one can also consider a situation in which there will be contributions from all these types

of events [90, 91, 219], namely N_c number of cusps, N_k kinks and N_{kk} number of kink-kink collisions (with $N_{kk} = N_k^2/4$, on assuming that there are equal numbers of left- and right-going kinks). We then impose that the sum of all these events to the averaged total power of the loop, Γ, is equal to the value used in the expression for the loop number density[11]. The resulting constraint between the set of parameters $g_1^{(q)}, g_2, N_c, N_k$ and Γ is given in appendix 2.A.

Before presenting the results of the SGWB for the three loop distributions of Section 2.5, we finish this section by commenting on two important issues: the separation of strong infrequent bursts from the SGWB; and the potential contribution (which we have not discussed until now) of GWs being emitted by the long string network.

2.4.3 Strong infrequent bursts

The superposition of GW bursts from many cusps and/or kinks, as calculated in Section 2.4.2, leads to a Gaussian stochastic background of GWs [29]. However, strong infrequent bursts observed with a time interval greater than the period of GWs $\sim 1/f$ ($\sim 10^2 - 10^3$ s for LISA) exhibit a non-Gaussian discontinuous signal, often referred to as "popcorn-like" [130]. Typically, these are bursts from low redshift, $z \ll 1$. If a burst occurs in our neighbourhood and the amplitude is strong enough, then the signal can be identified individually by the burst detection pipeline.

The non-Gaussian background from infrequent bursts is typically expected to be above the Gaussian background when strings have large tension and small initial loop size (*e.g.*, $G\mu \sim 10^{-6}$ and $\alpha \sim 10^{-11}$ for LISA [130]). Infrequent bursts are negligible for strings satisfying the current pulsar timing limit $G\mu < 10^{-11}$. We should therefore supplement, in principle, the expression for the SGWB calculation with a correction that suppresses the contribution from infrequent bursts. However, in practice, we have found that for large initial loop sizes, removing the rare burst has practically no effect on the present-day SGWB spectrum (see also [211, 212, 48, 114]), at least when the number of cusps and kinks per loop oscillation period is $\mathcal{O}(1)$.

An interesting possibility is that the number of infrequent strong bursts could be greatly enhanced if we consider clustering of loops inside the dark-matter halo of our galaxy. This would mean that the loop number density could be enhanced by several orders of magnitude at the Sun's position greatly improving the detectability of single-burst events in LISA for $G\mu < 10^{-11}$ [239]. It has also been shown recently using numerical relativity simulations that, for certain configurations, very small loops can emit GW bursts by collapsing to form black holes [116]. These are interesting proposals, but we do not discuss them further here, as they go beyond the scope of this paper, where we focus on the SGWB from a string network.

2.4.4 Gravitational wave emission from long strings

So far we have exclusively focused on the GW signal emitted from sub-horizon string loops. However, long strings (infinite and super-horizon loops) also emit GWs. One contribution to this signal is characterized by GWs emitted around the horizon scale at each time t, sourced by the anisotropic stress of the network [240, 241, 242, 206]. This background is actually expected to be emitted by any network of cosmic defects in scaling, independently of the topology and origin of the defects [206], and hence represents an irreducible background generated by any type of viable defect network that has reached scaling. However, in the case of NG cosmic string networks, this background

[11] This is basically the same type of condition used to impose the normalization of the loop power spectrum in Eq. (2.44).

represents a sub-dominant signal compared to the GW background emitted from the loops. In the case of field-theory strings (for which simulations to date indicate the absence of "stable" loops), it is instead the only GW signal (and hence the dominant one) emitted by the network.

The GW energy density spectrum of this secondary background produced by long strings is predicted to be exactly scale-invariant for the modes emitted during radiation domination [206]. At the level of the power spectrum, this background mimics therefore the spectral shape of the dominant signal from the loop decay (see discussion in Section 2.5.1), except with a much smaller amplitude. Even though the shape of the power spectrum of this irreducible GW background is well understood theoretically, its ultimate amplitude depends on the fine details of the so called *unequal-time-correlator* of the network's energy-momentum tensor. Unfortunately, this correlator can only be obtained accurately from sufficiently fine lattice simulations of defect networks. It is therefore difficult to assess at this point whether this background can be detectable with LISA. In the case of global defects, the scale-invariant GW power spectrum has been estimated in Ref. [241, 242]. The amplitude of the spectral plateau has been calibrated in lattice field theory simulations for global strings[12] as [206]

$$h^2\Omega_{\rm GW} \simeq 4\times 10^4\, h^2\Omega_{\rm rad}(G\mu)^2\,. \tag{2.53}$$

Even though the numerical prefactor is much larger than unity, the quadratic scaling proportional to $(G\mu)^2$ suppresses significantly this background (see *e.g.* [243] for a comparison of this signal and that emitted from the decay of string loops). This amplitude is clearly subdominant when compared to the amplitude of the dominant GW signal from the loops, which scales as $(G\mu)^{1/2}$ (see Eq. (2.56) and the discussion in Section 2.5.1). A proper assessment of the ability of LISA to detect the power spectrum of this stochastic background requires further results not available yet; namely, lattice simulations of cosmic networks with a larger dynamical range.

One can also consider the contribution to the GW spectrum coming from the accumulation of small-scale structure on long strings. These kinks are the product of the multiple intercommutations that infinite strings suffer over the course of their cosmological evolution, and were noticed early on in numerical simulation of cosmic networks [221, 135]. The emission of GW from individual infinite strings modulated by kinks has been calculated in Refs. [204, 244]. Using these results, one can also compute the spectrum produced by these kinks on a network assuming the simple model in which their characteristic scale is given by αt. At high frequencies one can then estimate that the radiation-era plateau of this contribution should be [64]

$$h^2\Omega_{\rm GW} \simeq \frac{128\pi^2}{3\xi^2\alpha}\, h^2\Omega_{\rm rad}(G\mu)^2\,, \tag{2.54}$$

which for $\alpha \approx 0.1$ and $\xi_{\rm r} = 0.271$ shows a rough agreement with the value obtained from field theory simulations. On the other hand, recently, Ref. [245] has calculated the GW spectrum produced by kink-kink collisions on long strings, and found that the amplitude is larger than in previous estimates. This is because the characteristic scale α turns out to be much smaller than 0.1 according to their semi-analytic estimation of the kink number distribution.

As all these backgrounds are clearly sub-dominant against the SGWB from loops, we will not consider them in the following analysis of the paper (except for a brief discussion of the bispectrum in Section 2.6.3).

[12] In the more interesting case of Abelian-Higgs lattice field theory simulations, there is unfortunately no quantification of the amplitude of this background.

2.5 Spectrum of the SGWB from cosmic string loops

As discussed above, a string network evolves towards a scaling solution in which its energy density is simply proportional to the total background energy density $\Omega_\infty \propto G\mu\, \Omega_{\rm tot}$. The string network constantly produces loops which then emit GWs, and follow the background expansion instead of simply redshifting (which would correspond to $\Omega_\infty \propto a^{-2}$ for static infinite strings). This continuous emission and tracking with expansion makes cosmic strings a perfect source for probing the expansion history of the Universe. In fact, in this section we show that all features visible in a stochastic GW frequency spectrum can be traced to a corresponding characteristic period in the evolution of the Universe.

We start our analysis by determining the basic shape of the SGWB spectrum over many decades in frequency, once a given loop number density distribution is chosen. We then study the impact of loops created relatively recently, that is, during the radiation-to-matter transition. Finally, we characterize the impact of extra degrees of freedom and other possible modifications of the equation of state in the very early Universe.

2.5.1 Basic spectral shape

The expressions given in Eqs. (2.45) and (2.52) can be used to compute the SGWB. In the following, we set $\Gamma = 50$ and we use Method I (Eq. (2.45)) to generate several SGWB spectra for different values of $G\mu$. To illustrate our main points, we first take the loop number density from Model II and the loop power spectrum denoted by BOS in Section 2.4.1: the results are shown in Fig. 2.1. In Fig. 2.2 on the other hand, we use the loop number density from Model III and a monochromatic spectrum of cusps only ($q = 4/3$). The difference between these results for the same value of $G\mu$ comes almost entirely from the different loop number density of small loops in these models, as discussed in Section 2.3.3.

These figures plot the SGWB for a set of representative values of $G\mu$ together with the current sensitivity curves for EPTA pulsar timing collaboration [246], as well as the projected curves for the SKA [47] and LISA [207] collaborations. In particular, we show the spectrum of $G\mu = 10^{-10}$ as being the order of the bound on the string tension coming from current observations of pulsar timing arrays (PTAs). This bound should be improved in the next few years. However, as the limit on $\Omega_{\rm GW}$ becomes stronger and one probes lower values of the tension, one can see that the peak of the SGWB moves towards high frequencies and outside of the PTA frequency bands. This makes future bounds less strong than one would have thought because the PTA frequency band will then be at the steep section of the SGWB curve. Eventually, the SKA collaboration will become more competitive, potentially setting a bound of $G\mu = 2 \times 10^{-13}$, three orders of magnitude stronger than current PTA constraints.

An important point to make here is that if any of these observations detect a SGWB, one will probably have to wait for LISA before one can elucidate the origin of such background. It is therefore interesting to see that if $G\mu$ is in the range of values accessible by PTA experiments, the higher-frequency part of the SGWB signal will be well within LISA's sensitivity curve. The spectrum for $G\mu = 10^{-13}$ in Fig. 2.1 shows how such a curve might appear in LISA.

Looking at the curves for $G\mu = 10^{-15}$ and 10^{-17} in Fig. 2.1, it is clear that for lower string tensions, PTA-type experiments become irrelevant for detecting a background and at this level LISA becomes the right instrument to probe these light strings [89]. The "bump" of the SGWB will pass directly through the LISA sensitivity band, as shown for $G\mu = 10^{-15}$, and $G\mu = 10^{-17}$ is

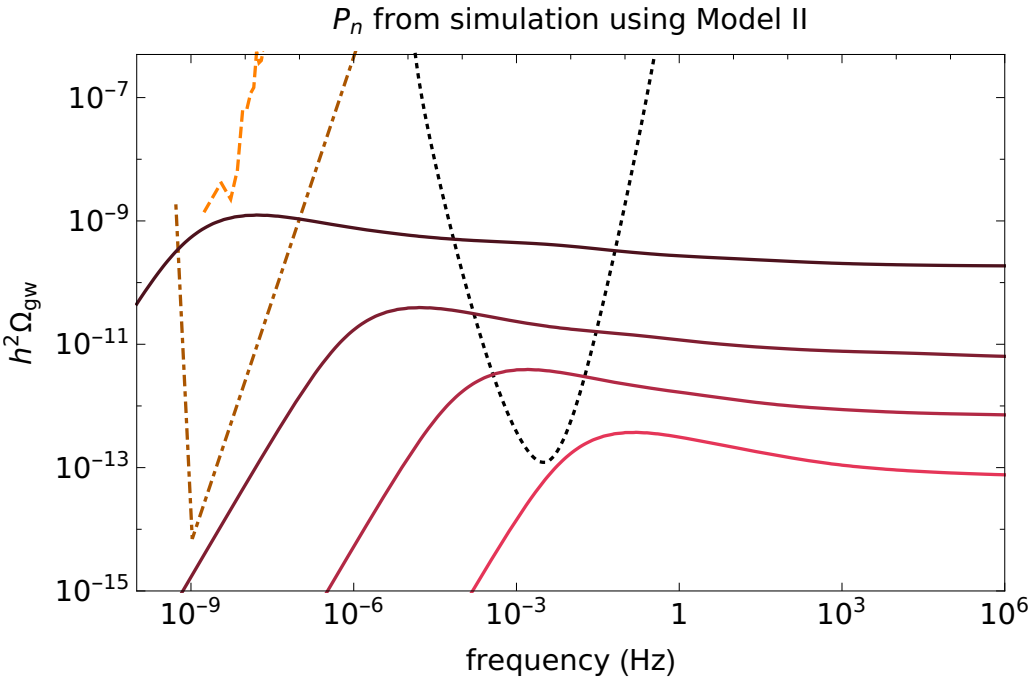

Figure 2.1: Cosmic string SGWB curves (all in red) near various relevant values of $G\mu$. The dashed orange curve is the EPTA sensitivity, and the darkest red curve just below is for $G\mu = 10^{-10}$. The dash-dotted dark orange curve is the (projected) SKA sensitivity, and the dark red curve just below is for $G\mu = 10^{-13}$. The dotted black curve is the LISA PLS; the red curve whose peak passes through it, and the light red curve just below, are for $G\mu = 10^{-15}$ and 10^{-17} respectively. The P_n are inferred from simulation [114], and the loop number density is from Model II.

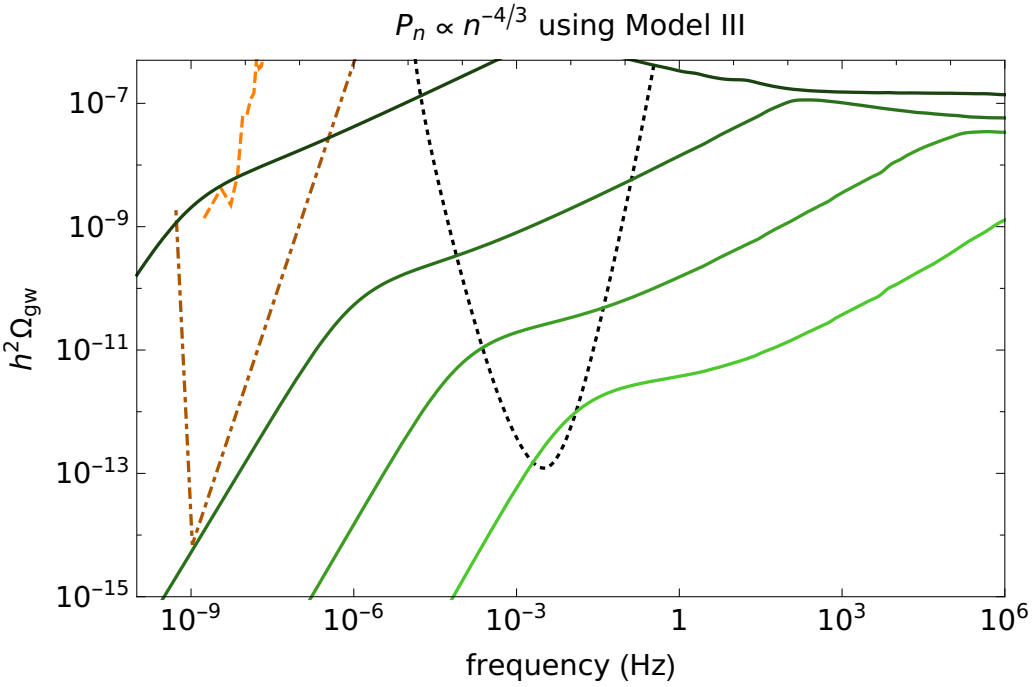

Figure 2.2: Idem as Fig. 2.1, but with $P_n \propto n^{-4/3}$ and using the loop number density from Model III [123].

the order of the lower bound on tension that LISA will set.

The high frequency regime

As we can see from the SGWB curves shown in Fig. 2.1, the spectrum becomes flat at very high frequencies. This can be understood analytically using a scaling number density of loops as well as a simplified cosmological background that describes the evolution of the Universe deep in the radiation era. The combination of these two facts allows us to find an expression (following Method I) for the spectrum of the form

$$\Omega_{\rm GW}^{\rm plateau}(\ln f)_I = \frac{64\pi G^2\mu^2\Omega_{\rm rad}}{3}\left(\sum_{n=1}^{\infty} P_n\right)\left(\int \mathrm{d}\gamma\ \mathcal{N}_r(\gamma)\right). \tag{2.55}$$

This shows that indeed the SGWB is flat in this regime, but also that it only depends on two properties of the network of strings: the averaged total power emitted by a loop, and the total number of loops. Applying this to Model II, we find

$$\Omega_{\rm GW}^{\rm plateau}(\ln f)_I \approx 8.04\Omega_{\rm rad}\sqrt{\frac{G\mu}{\Gamma}}\,. \tag{2.56}$$

This is a relevant result as it tells us that the value of the high-frequency plateau only depends on $G\mu$ and the total Γ. In particular, it does not depend on the exact form of the loop's power spectrum, nor on if the GW emission is dominated by cusps or kinks, but rather depends only on the total radiation emitted by the loops.

Similarly, we can perform the same kind of computation using Method II. Starting with Eq. (2.52), and taking the cosmological background to be in the radiation era, we find [13] a good agreement for the plateau with the expression found in Eq. (2.56). This is expected, given that the plateau only depends on quantities that must be identical in both methods. However, given the different nature of the calculations performed in both methods, this is a good consistency check.

2.5.2 Radiation-to-matter transition

Numerical simulations studying the strings scaling have typically been performed in fixed backgrounds: pure radiation domination and pure matter domination [103, 114, 123, 90]. The usual simplified approach would be to just switch between the two loop distributions at radiation–matter equality; however, in reality we expect the network to smoothly evolve between the two regimes. In fact, the string network evolves rather slowly and, as pointed out in [216], does not reach scaling regime with matter background up until the current accelerated expansion starts. This may have a significant impact on the number density of loops in the matter era.

We can study the impact of more careful modelling of the transition using the analytical model discussed in Section 2.3.1. In Fig. 2.3 we compare results coming from the full evolution of the loop density, Eq. (2.16), with the simplified spectrum obtained performing an instantaneous switch between the scaling results in matter domination (Eq. (2.28)), and radiation domination (Eq. (2.27)). Fig. 2.3 shows examples of spectra for several values of $G\mu$ and $\alpha = 0.1$ using both prescriptions. As we can see, the inclusion of a smooth radiation-to-matter transition only modifies

[13] Note that in order to make this comparison, one should express the result in terms of the total power emitted Γ. We give in appendix 2.A the calculation of Γ in terms of the parameters N_q, g_1, g_2.

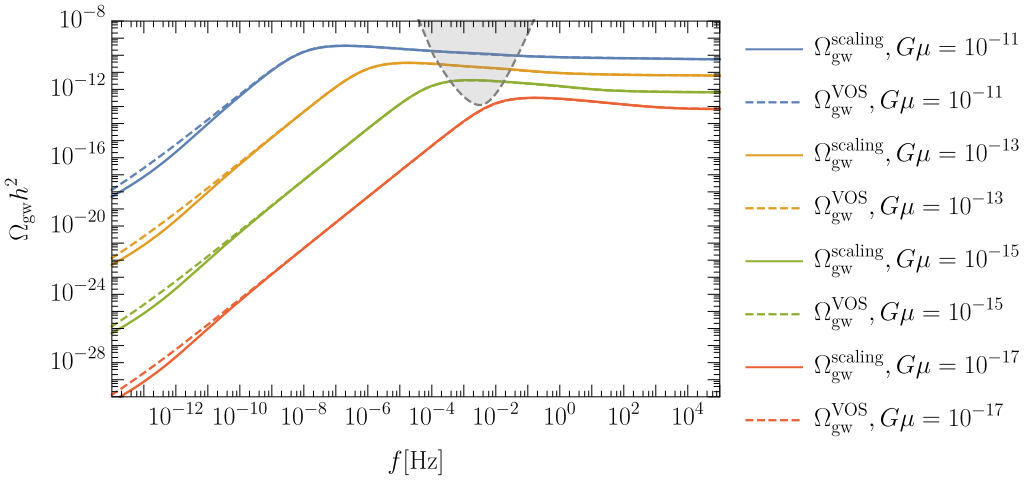

Figure 2.3: Examples of spectra for several values of $G\mu$ and $\alpha = 10^{-1}$ using both the full VOS solution (with *VOS* superscript) and assuming the network is always in scaling through Eqs. (2.27,2.28) (with *scaling* superscript). The gray area indicates LISA sensitivity.

the spectrum significantly at very low frequencies $f \lesssim 10^{-10}$ Hz, outside of the LISA band. The reason is that it is only at these very low frequencies that the signal is dominated by loops created in the matter era [114].

Even though the peak in the spectrum always appears due to matter domination, for low $G\mu \lesssim 10^{-11}$ it is only created by redshifting of GWs and the loop density in the matter background, while the loops dominantly contributing are formed much earlier, deep in the radiation era. With this we can safely conclude that for large loops $\alpha = 0.1$ suggested by recent simulations, the modelling of the radiation-to-matter transition is irrelevant in the LISA sensitivity window. In Section 2.6.2 we discuss how this situation may change if we assumed smaller loop sizes.

2.5.3 Variation of the relativistic degrees of freedom

Another feature in the expansion rate of the Universe that would leave a clear signature in the stochastic GW spectrum of a cosmic string network is a modification in the number of relativistic degrees of freedom [222]. Whenever the temperature of the plasma forming our radiation background drops below the mass of a certain particle, that species will annihilate, injecting energy into the plasma and temporarily reducing its rate of cooling. This effect is automatically included in our calculation by solving the Friedman equation, Eq. (2.7), which includes the impact of changes in the number of degrees of freedom on the expansion rate through Eq. (2.9).

We show the impact of including this variation in Fig. 2.4, which shows both the result obtained using the Standard Model number of degrees of freedom and just a constant value. As we can see, the modification of number of degrees of freedom produces smooth variations in the spectrum at the frequency corresponding to the temperature of the modification. The most prominent of these variations in the spectrum correspond to electron-positron annihilation at $T \approx 200\,\text{KeV}$ where the lines first separate, the QCD phase transition at $f \approx 10^{-2}$ Hz ($T \approx 100\,\text{GeV}$), and the electroweak

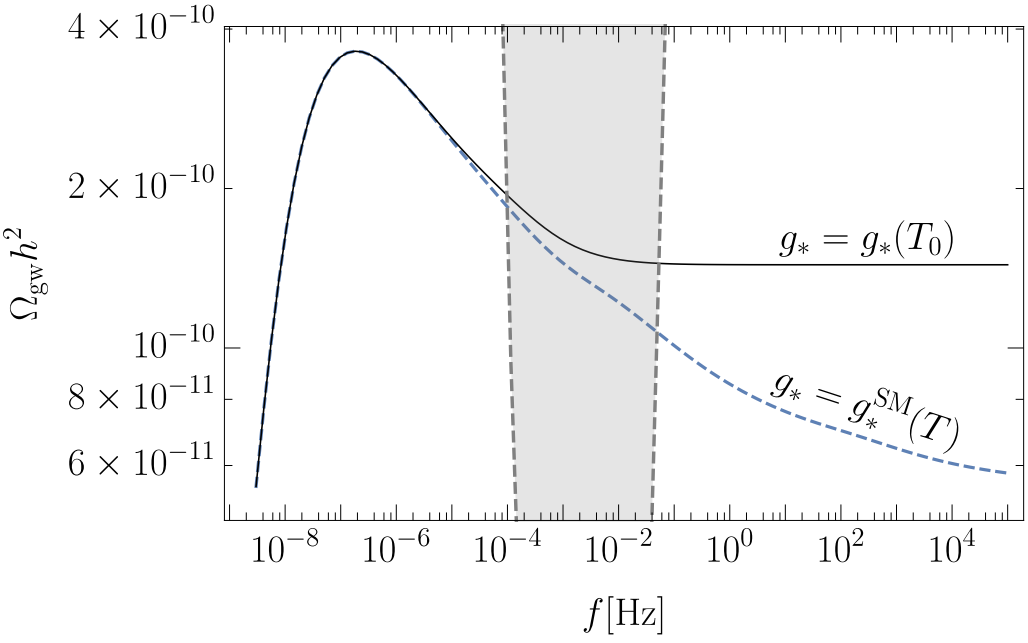

Figure 2.4: Examples of spectra with $G\mu = 10^{-11}$ assuming a constant number of degrees of freedom (black solid line) and standard cosmology with SM particle content (blue dashed line). The gray area indicates LISA sensitivity.

scale at $f \gtrsim 10^2$ Hz. This means LISA could probe the QCD equation of state and other SM processes through their impact on the stochastic background from cosmic strings [247].

Crucially, this effect would also potentially allow us to observe extra degrees of freedom (DOF) from beyond the standard model [218, 248, 114, 249]. Had the number of DOF increased by a factor of Δg_*, that would have created another smooth step, changing the value of the plateau at the corresponding frequency by

$$\frac{\Omega_{\rm GW}}{\Omega_{\rm GW}^{\rm SM}} \approx \left(\frac{g_*^{\rm SM}}{g_*^{\rm SM}+\Delta g_*}\right)^{1/3}, \tag{2.57}$$

where $g_*^{\rm SM}$ and $g_{*S}^{\rm SM}$ are the number of degrees of freedom and the number of entropy degrees of freedom, both calculated in the standard model.

We can numerically check that the frequency corresponding to a modification of the expansion rate occurring at a temperature T_Δ is given by [218]

$$f_\Delta = (8.67\times10^{-3}\,{\rm Hz})\left(\frac{T_\Delta}{\rm GeV}\right)\left(\frac{0.1\times50\times10^{-11}}{\alpha\,\Gamma\,G\mu}\right)^{1/2}\left(\frac{g_*^{\rm SM}(T_\Delta)}{g_*^{\rm SM}(T_0)}\right)^{\frac{8}{6}}\left(\frac{g_{*S}^{\rm SM}(T_0)}{g_{*S}^{\rm SM}(T_\Delta)}\right)^{\frac{7}{6}}. \tag{2.58}$$

Using this estimate, we can see that LISA frequency band corresponds to probing temperatures of the order of a few GeV. It is important to point out this could lead to a significant improvement over the current probes of the expansion rate, which can reach only to the BBN temperature of a few MeV, which is still 3 orders of magnitude lower than the potential of a cosmic string signal at LISA. In Fig. 2.5, we show examples of a cosmic string stochastic background in standard cosmology with $G\mu = 10^{-11}$ and several modifications with $\Delta g_* = 100$ new degrees of freedom dropping out of equilibrium at the range of temperatures of interest in LISA.

2.5.4 Probing the cosmological equation of state at early times

The reasoning used in the last subsection also clearly applies to more dramatic modifications of cosmology in which the expansion at early times is dominated by something other than primordial radiation. A typical example here would be an early period of matter domination [250] after which the matter decays and the Universe resumes the standard radiation dominated expansion. Another example, so-called *kination* [251, 179, 180, 252, 253, 254, 255, 182, 256, 183], is a period of domination of a new constituent of energy that redshifts faster than radiation and eventually becomes subdominant, avoiding any conflict with late time experiments.

Observation of the plateau of GW spectrum from a cosmic string network would indeed verify radiation domination up to T_Δ from Eq. (2.58). If any non-standard behaviour is observed, it can be traced back to the underlying modification. Simply expanding Eq. (2.45) at high frequencies, we can check that the impact of modified redshifting in a background $H^2 \propto a^{-\beta}$ would simply lead to

$$\Omega_{\rm GW}(f > f_\Delta) \propto \begin{cases} f^{(8-2\beta)/(2-\beta)} & \beta \geq \frac{10}{3}, \\ f^{-1} & \beta < \frac{10}{3}, \end{cases} \tag{2.59}$$

behaviour above T_Δ. An early period of matter domination corresponds to $\beta = 3$. However, for expansion in the early Universe with any $\beta < \frac{10}{3}$, the emission from the string network is in fact subdominant to the tail of the distribution produced at later times. This leads to some degeneracy, and in fact if the network simply achieved scaling only at that time after their production [64], or if

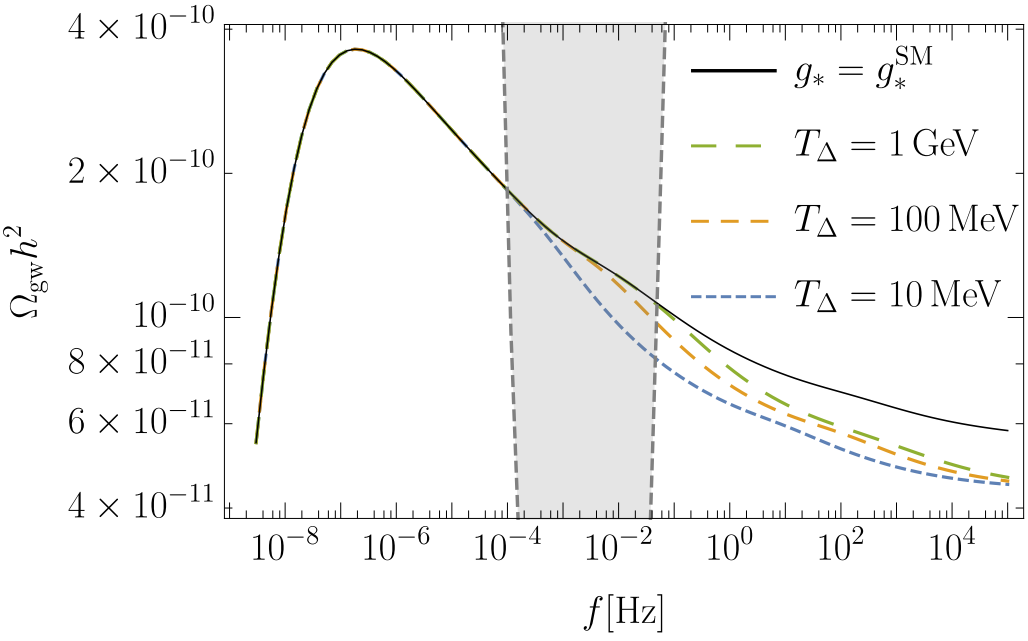

Figure 2.5: Examples of spectra with $G\mu = 10^{-11}$ in standard cosmology (black solid line) and several spectra in cosmological evolution with $\Delta g_* = 100$ new degrees of freedom annihilating at at the range of temperatures of interest in LISA. The gray area indicates LISA sensitivity.

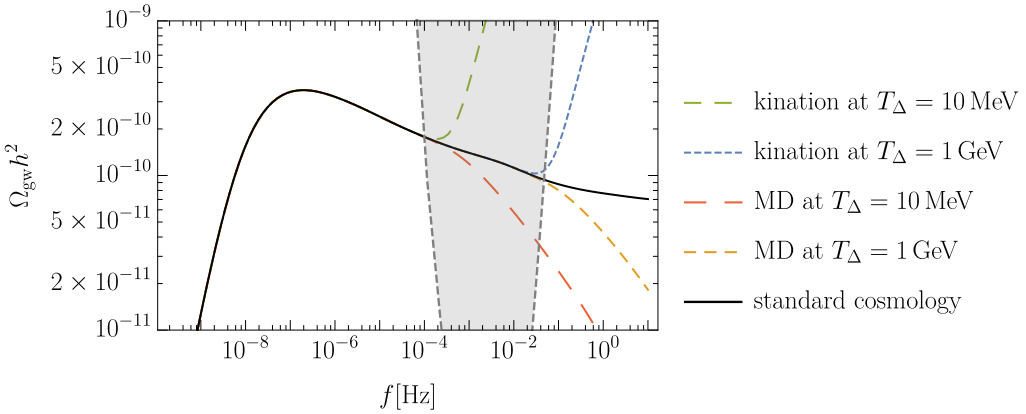

Figure 2.6: Examples of spectra with $G\mu = 10^{-11}$ in standard cosmology (black solid line) and several spectra in cosmological evolution with a period of early matter domination as well as kination ending in the range of temperatures of interest in LISA. The black dashed line indicates LISA sensitivity.

scaling was delayed due to the network having been diluted by inflation [257], it would also amount to the lower case in Eq. (2.59). For scenarios with a new energy constituent redshifting faster than radiation (that is, $\beta > 4$), the spectrum rises after T_Δ, which generically gives better observational prospects.[14] We show examples of the resulting spectra with the range of T_Δ of interest for LISA in various modified cosmologies in Fig 2.6. It would significantly modify predictions of any other process relying on the standard expansion rate, for instance modifying predictions for dark matter relics [] and electroweak Baryogenesis both in terms of its possible GW signal [] and yield of baryons [].

2.6 Probing the SGWB from a string network with LISA

The *Laser Interferometer Space Antenna* (LISA) [207], approved by the European Space Agency (ESA) in 2017, will be the first GW observatory in space. The final configuration adopted by the collaboration has been fixed to six links, 2.5 million km–length arms, and 4 years nominal duration, possibly extensible to 10 years. LISA will have the ability to search for GWs around the currently unexplored millihertz regime.

To characterize the detectability of a SGWB with a spectrum described by a single power law (fully characterized by an amplitude and slope), Ref. [258] introduced a very useful concept: the power law sensitivity curve (PLS) of a detector. This is a method that exploits the fact that the sensitivity of a detector increases when integrating a SGWB signal over frequency, in addition to integrating over time. The PLS curve is a spectral representation that graphically quantifies, for a given signal-to-noise ratio, the ability of a detector to measure a SGWB with a power law (PL) spectrum. Searches by current GW experiments (by LIGO/VIRGO and PTAs) on power spectra

[14] Note, however, that the current Planck data puts a constraint on the total energy density of gravitational waves [132] $\int \Omega_{\rm GW}\, h^2 d(\ln f) < 3.8\times10^{-6}$. Consequently, any deviations from radiation domination with $\beta > 4$ should have had a limited duration to avoid overproduction of GWs.

of the form $\Omega_{\rm GW}(f) = Af^n$ have not succeeded in a detection, and hence they only provide upper bounds on the amplitude A for different fixed values of the spectral index n [32, 259, 34].

Recently, the LISA collaboration has presented a new technique for a systematic reconstruction of a SGWB signal without assuming a power-law spectrum [35]. The idea is to first separate the entire LISA band into smaller frequency bins, and then to reconstruct a given arbitrary signal within each bin, where it can be well-approximated in terms of a power law. The method can reconstruct, in this way, signals with arbitrary spectral shapes, taking into due account instrumental noise at each frequency bin. Such analysis would be particularly appropriate for our case, as the spectral shape of the SGWB from cosmic string loops is not a simple plateau (and hence not a simple power law) for the lowest $G\mu$ values that LISA can probe. Furthermore, the spectrum can also exhibit scale-dependent features within the LISA frequency band, such as whenever there are changes in the number of relativistic degrees of freedom and/or the early Universe equation-of-state.

As this multi-band analysis technique has only very recently become available ($\sim 1-2$ weeks before the completion of this draft), in the present paper we will simply continue using as a criterion for detection that the spectrum of the SGWB from the string loops must be equal or above the PLS curve. We will use the LISA PLS as introduced by Ref. [258], but using the most updated LISA sensitivity curves based on the final configuration of LISA and new knowledge on its noise (see Ref. [260] for all relevant LISA documents up to date, and in particular Ref. [261] for a direct download of the *Science Requirements Document*). The details of the updated LISA PLS curve used in this work can be found in Ref. [35]. Whenever we claim detection of a given spectrum of the SGWB from cosmic string loops, if the spectrum is a power-law within the LISA sensitivity band, this can be interpreted as a detection of a SGWB after 3 years of collecting data (which corresponds to 4 years of LISA operation), with a signal-to-noise (S/N) ratio ≥ 10. If the shape is more complicated than a simple power law, a more elaborated analysis following Ref. [35] is required to assess the S/N for a given detection, see also [262]. In the present work, we simply quantify the parameter space compatible with a detection, but do not quantify the S/N associated to such detection, neither we reconstruct such parameter space with appropriate statistical techniques. We leave these aspects for future work.

2.6.1 Projected constraints on the string tension

The LISA PLS band is well-positioned to set strong constraints on the string tension, due to how the "bump" in the SGWB shifts as $G\mu$ decreases. This effect can be seen *e.g.* in Fig. 2.1, where we show how the SGWB curve for a network shifts through the LISA band for varying tension.

This shows us that it is the trailing edge of the SGWB bump which will be the last part of that curve to pass through the LISA sensitivity band. By varying the string tension, it is possible to find the lowest $G\mu$ for which this intersection still takes place. While the exact bound depends on our choice of model and P_n, in the regime LISA will probe, all three models predict a string tension bound of $\mathcal{O}\big(10^{-17}\big)$. This is shown in Fig. 2.7, where we chose $P_n \propto n^{-4/3}$ for purposes of comparison, as this is the chromatic index of pure cusps, which are expected to dominate at high frequencies. Other choices include $P_n \propto n^{-5/3}$ (for kinks), $P_n \propto n^{-2}$ (for kink-kink collisions), or an averaged spectrum of loops taken from simulation (cf. Fig. 2.1). However, these changes have at most $\mathcal{O}(1)$ effects on the bounds set by LISA.

By comparing Eq. (2.27) to Eq. (2.29), we see that with our choice of α and A_r, these two expressions converge when $\alpha \gg \Gamma G\mu$. As this is the case here, the curves for Model I and Model II in Fig. 2.7 are effectively identical.

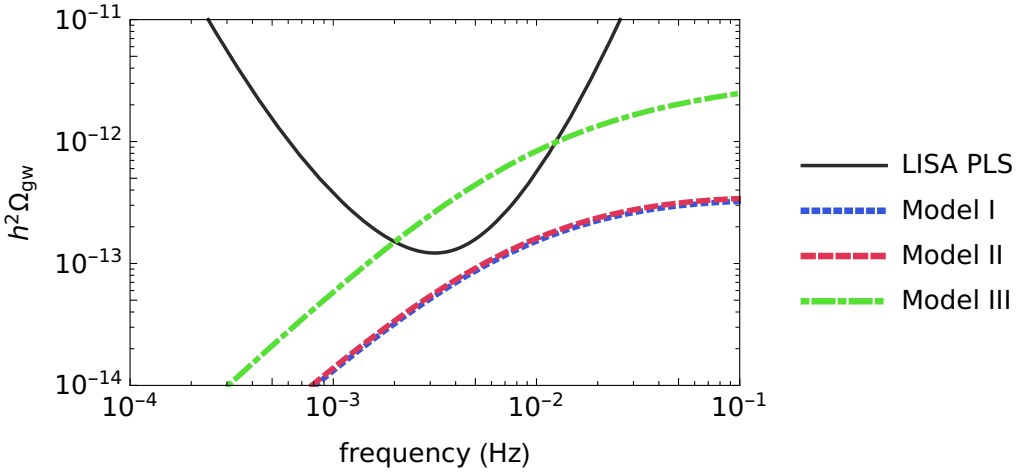

Figure 2.7: A comparison of the LISA sensitivity curve to the SGWB predicted by all three models using $G\mu = 10^{-17}$, $P_n \propto n^{-4/3}$. Models I and II are effectively identical in this regime, due to $\alpha \gg \Gamma G\mu$. We therefore see that we expect that LISA could only constrain string tensions higher than $G\mu \approx 10^{-17}$.

While we are primarily concerned with setting bounds on string tension, it is worth noting here that for string tensions larger than the lower bounds, particularly those of an order of magnitude or larger, LISA will probe the high-frequency side of the SGWB bump. The particular shape of this region depends on how the degrees of freedom change across the Universe's history. This is additionally important because while the three models all predict roughly equal bounds for the LISA window at this particular tension, Models I and II disagree with Model III at high frequencies. *E.g.*, when $G\mu = 10^{-17}$, the plateau for Models I and II happens at $h^2\Omega_{\rm GW} \approx 6.04 \times 10^{-14}$, while Model III's plateau is at $h^2\Omega_{\rm GW} \approx 9.98 \times 10^{-9}$. Thus, if strings with a tension much greater than $\mathcal{O}(10^{-17})$ exist, these discrepant regions will pass through the LISA band.

2.6.2 Agnostic approach to loop size and intercommutation probability

In previous sections, we discussed the results obtained from the largest and more recent Nambu-Goto simulations. In this section, we take a different approach: an "agnostic" approach that extends our analysis further by studying the capability of LISA to probe scenarios characterized by different loop sizes α parametrically using Model I. This not only allows us to fully characterize the parameter space available for exploration with LISA, but also to understand LISA's ability to detect string models that deviate from the standard Nambu-Goto scenario. Throughout this section, we will take the normalizing parameter introduced in Section 2.3.1, $\mathcal{F} = 1$ and $f_r = \sqrt{2}$.

Loop size

Although the typical shape of the SGWB generated by cosmic string networks is roughly independent of α, the amplitude of the radiation-era plateau and the height, broadness and location of the peak of the spectrum are determined by the size of the loops that are created (as well as by

cosmic string tension). In reality, the amplitude of the spectra generally decreases with decreasing α and, therefore, one would expect LISA to be less sensitive in general to scenarios in which loops are created with a smaller size. In fact, one finds, using Eq. (2.2), Eq. (2.4) and Eq. (2.27), that the amplitude of the radiation era plateau is given by

$$\Omega_{\rm GW}^{\rm plateau}\,h^2 = \frac{128}{9}\pi A_r \Omega_{\rm rad}\,h^2 \frac{G\mu}{\epsilon}\Big[(\epsilon+1)^{3/2}-1\Big] \simeq 1.02\times 10^{-2}\frac{G\mu}{\epsilon}\Big[(\epsilon+1)^{3/2}-1\Big]\,, \tag{2.60}$$

where $\epsilon = \alpha/(\Gamma G\mu)$.

To analyse the capability of LISA to probe scenarios with different loop sizes, we consider two different regimes. Let us first consider the case in which the physical length of loops is, at the time of production, significantly larger than the gravitational backreaction scale, with $\epsilon \gg 1$ (which we shall refer to as large loops, for simplicity). In this case (particularly in the frequency range probed by LISA) the dominant contribution to the SGWB comes, in general, from loops created in the radiation era. As a result, we have roughly $\Omega_{\rm GW} \propto \alpha^{1/2}$ for $\alpha \gg \Gamma G\mu$ and fixed $G\mu$ (as Eq. (2.27) shows). Indeed, we see by using Eq. (2.60), that for $\epsilon \gg 1$ the amplitude of the radiation era plateau[15] is given by

$$\Omega_{\rm GW}^{\rm plateau}\,h^2 \simeq 1.02\times 10^{-2}\sqrt{\frac{G\mu\alpha}{\Gamma}}\,. \tag{2.61}$$

This effect is seen in Fig. 2.8, where the SGWB spectra generated by cosmic string networks with $G\mu = 10^{-10}$ and different values of α are plotted. Note however that one does not have a mere overall decrease of the amplitude of the spectrum as α decreases. As this figure illustrates, the broadness of the peak of the spectra also decreases as a result of the decrease of the size of loops, since for smaller α loops survive (and emit gravitational waves) for a shorter period of time. We also note that although the relation in Eq. (2.61) is exact for the radiation-era plateau while $\alpha \gg \Gamma G\mu$, the decrease in the height of the peak starts to slow down as we decrease α. This happens due to the fact that, as α decreases and the lifetime of loops is shortened, the number of loops created in the radiation era that decay during the matter era also diminishes. Thus, for sufficiently small α, the dominant contribution to the peak of the spectrum are loops produced in the matter era (during which $n(\ell,t)$ is roughly independent of α for $\alpha \gg \Gamma G\mu$, as Eq. (2.28) shows). As a result, the relative height of the peak of the spectrum in relation to the radiation-era flat region increases as loop size decreases. This also means that, as α is lowered, the effect of the radiation-to-matter transition on the shape and amplitude of the spectra becomes increasingly relevant. As a matter of fact, assuming that cosmic string networks remain in a linear scaling regime after the onset of the radiation-matter transition leads to a significant underestimation of the size and number density of loops produced during the matter era [216]. On the other hand, as we have seen in Section 2.5.2, for $\alpha = 10^{-1}$ the effect of this assumption of linear scaling is only observed at frequencies that are outside of the LISA sensitivity window. As we consider smaller loops the effect of the radiation-to-matter transition becomes relevant for the LISA mission. For this reason, we take this effect into consideration in this agnostic forecast of the LISA projected constraints.

Another effect that we have to take into consideration when analysing the sensitivity of LISA to scenarios with different loop sizes is the change of the location of the peak of the spectrum with

[15] Note that this has the same dependence on Γ and $G\mu$ as Eq. (2.56) and, by setting $\alpha = 0.1$ and $\mathcal{F} = 0.1$, one approximately recovers the result therein.

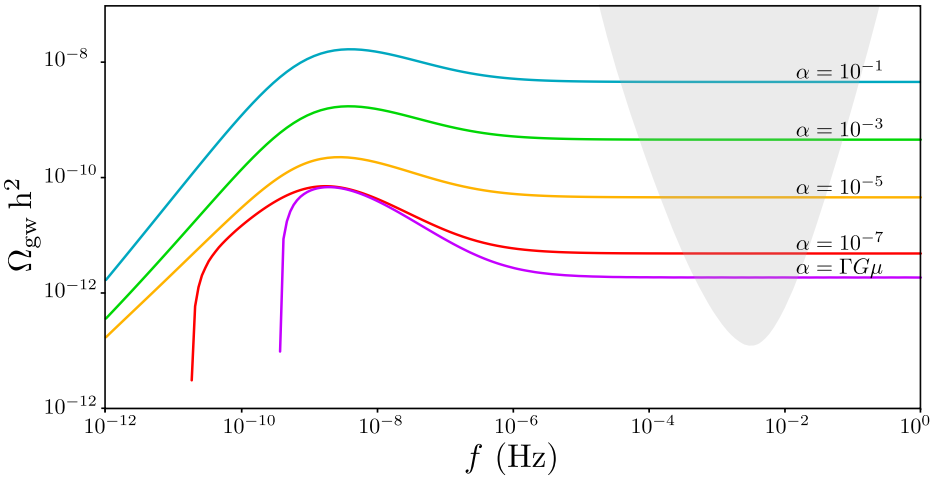

Figure 2.8: The stochastic gravitational wave background generated by cosmic string networks with $G\mu = 10^{-10}$ and different values of the loop-size parameter α. The shaded area represents the LISA sensitivity window. In these plots, we consider only the fundamental mode of emission and we did not include the change in the effective number of degrees of freedom.

the variation of $G\mu$. The peak frequency scales approximately as [213][16]

$$f_{\rm peak} \sim \frac{1}{\alpha}\left(2 + \frac{\alpha}{\Gamma G\mu}\right)^{10/9}, \tag{2.62}$$

which gives

$$f_{\rm peak} \propto \alpha^{1/9}(\Gamma G\mu)^{-10/9} \tag{2.63}$$

in the large loop regime. For fixed $G\mu$, the dependence on α is weak and the peak appears at approximately the same frequency as shown in Fig. 2.8 (wherein one can also see that the slight shift towards higher frequencies predicted in Eq. (2.62) is present). However, the frequency in which the peak appears depends more strongly on cosmic string tension and, as a result, the peak of the spectrum, which has a significantly higher amplitude, is expected to shift towards higher frequencies — and into the LISA window — as $G\mu$ is lowered. This effect may be seen in Fig. 2.9, where we plot the SGWB spectra generated by cosmic string networks with two different values of loop-size parameter α for different values of $G\mu$.

In the small loop regime — in which the physical length of loops is significantly smaller than the gravitational backreaction scale, with $\alpha \ll \Gamma G\mu$ — the shape of the SGWB spectrum is not affected by varying α or $G\mu$. As matter of fact, in this regime, loops survive significantly less than a Hubble time and may, therefore, be regarded as decaying effectively immediately (on cosmological timescales) once they are formed [217]. Thus, a decrease in the size of loops in this regime merely results in a linear shift of the spectrum towards higher frequencies, without any impact on its overall shape. For the same reason, decreasing the value of cosmic string tension merely causes a decrease

[16] Although this relation was fitted using a framework based on the one-scale model (in which cosmic strings are assumed to be in the linear scaling regime throughout their evolution), we have verified that it still provides a reasonably good approximation, with only small deviations, within the framework we use here.

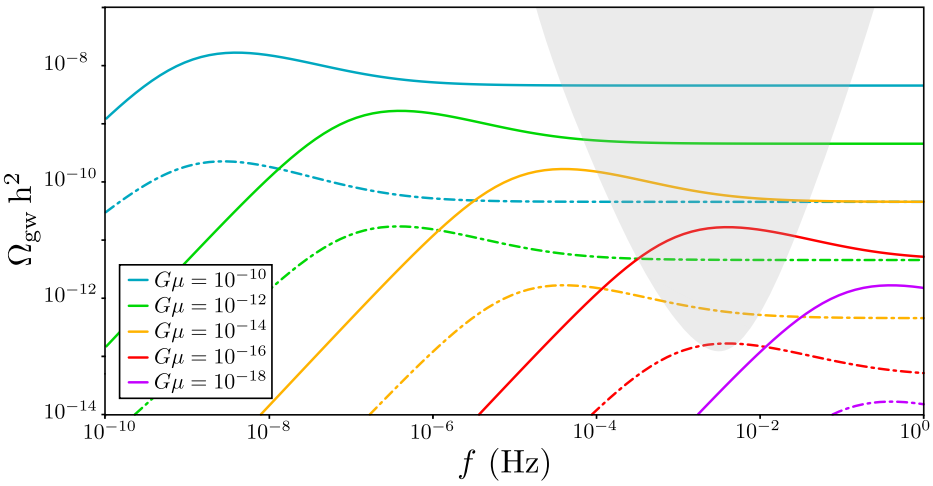

Figure 2.9: The stochastic gravitational wave background generated by cosmic string networks with $\alpha = 10^{-1}$ (solid lines) and $\alpha = 10^{-5}$ (dash-dotted lines) for different values of $G\mu$. The shaded area represents the LISA sensitivity window. In these plots, we consider only the fundamental mode of emission and we did not include the change in the effective number of degrees of freedom.

of the amplitude of the spectrum: $\Omega_{\rm GW} \propto G\mu$, for fixed α. In fact, using Eq. (2.60), one finds that for $\epsilon \ll 1$ the amplitude of the radiation era plateau is, in this case,

$$\Omega_{\rm gw}^{\rm plateau} h^2 = \frac{64}{3}\pi A_r h^2 \Omega_{\rm rad} G\mu \simeq 1.52 \times 10^{-2} G\mu\,. \tag{2.64}$$

This does not depend on the size of loops α and on Γ and it may, therefore, be regarded as the "minimal" amplitude of the radiation era plateau for fixed $G\mu$. This is illustrated in Fig. 2.10, where the spectra generated by small cosmic string loops is plotted for different values of α and $G\mu$.

The combination of all these different effects makes it non-trivial to extend the forecasts computed for a single value of α to significantly different loop sizes. For instance, as Fig. 2.9 shows, LISA may probe cosmic string networks with $\alpha = 10^{-1}$ up to tensions just above $G\mu = 10^{-18}$. In the case of networks with $\alpha = 10^{-5}$, however, the maximum tension that LISA will be able to detect is below $G\mu = 10^{-16}$, which is significantly lower than one would naively expect from Eq. (2.61). Moreover, Fig. 2.10 demonstrates that there is a range of α in the small loop regime for which the peak of the spectrum — which is quite prominent in this regime — coincides with the LISA window (for some values of $G\mu$) and, therefore, such scenarios may be more strongly constrained with LISA than other scenarios in which α is larger. To take these effects into account, we have performed a numerical computation of the $(\alpha, G\mu)$ parameter space available for exploration with LISA. The results are plotted in Fig. 2.11, and they show us the capability of LISA to probe different cosmic string scenarios characterized by the production of loops with different sizes. Here, we follow the approach introduced in Ref. [213] and present constraints for $n_* = 1$ (dashed line) and $n_* = 10^5$ (dash-dotted line), where n_* represents the maximum mode of emission included in the simple gravitational wave power spectrum from loops with $q = 4/3$. These curves represent the lowest possible values of the string tension that LISA will be able to probe for each value of α, in

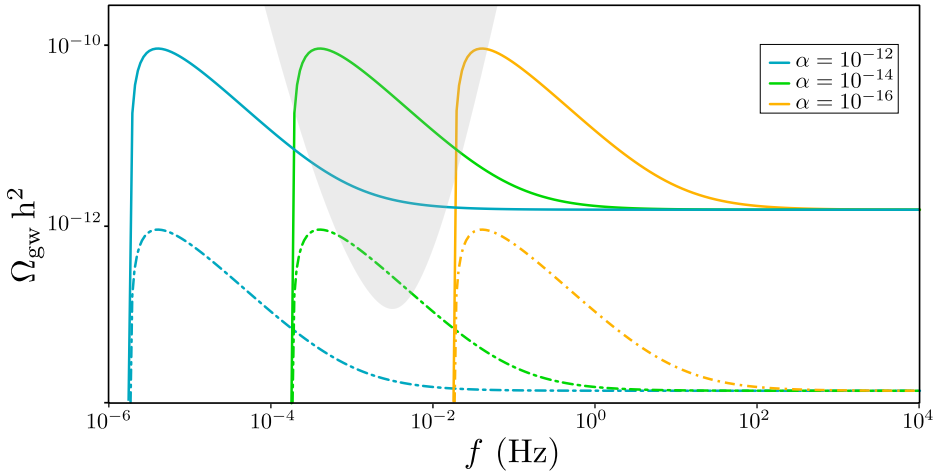

Figure 2.10: The stochastic gravitational wave background generated by cosmic string networks with $G\mu = 10^{-10}$ (solid lines) and $G\mu = 10^{-12}$ (dash-dotted lines) for different values of the loop-size parameter α in the small-loop regime. The shaded area represents the LISA sensitivity window. In these plots, we consider only the fundamental mode of emission and we did not include the change in the effective number of degrees of freedom.

these two scenarios.

To analyse these results, let us start by considering the small-loop regime. LISA cannot probe the SGWB generated by cosmic string loops to arbitrarily small α. This is a mere consequence of the fact that LISA shall only probe a finite frequency window and of the fact that, as we have seen, lowering α in the small-loop regime moves the spectrum towards higher frequencies. As a matter of fact, the minimum frequency emitted by a cosmic string network is that of loops created at the present time, $f_{\rm min} \sim 2/(\alpha t_0)$, and therefore the minimum loop-size parameter that can be probed with LISA is given by

$$\alpha_{min} = 6.8 \times 10^{-18}\,, \tag{2.65}$$

independently of $G\mu$. As a result, scenarios in which the networks produce tiny loops will be beyond the reach of LISA.[17] In any case, this shows us that, in principle, LISA shall be able to probe cosmic string scenarios spanning about 17 orders of magnitude in loop size.[18] In the small-loop regime, the amplitude of the peak of the spectrum — located at $f_{\rm peak} = 2\times 10^{-17}/\alpha$ (Hz) — is given by [217][19]

$$\Omega_{\rm GW}^{\rm peak} h^2 \simeq 60 \Omega_{\rm GW}^{\rm plateau} h^2 \simeq 9.1 \times 10^{-1} G\mu\,. \tag{2.66}$$

One then finds that LISA will not be able to probe small-loop models for $G\mu < 1.3 \times 10^{-13}$. This is, thus, the most stringent bound that LISA may put on the cosmic string tension in scenarios in

[17] These scenarios are not particularly well physically motivated, since one generally expects smoothing to occur on scales smaller than the gravitational backreaction scale. Nevertheless, several works have reported the existence of such tiny loops [263, 110].

[18] Note however that, for tensions compatible with current CMB bounds, the SGWB spectrum "leaves" the LISA window for larger values of α, around $\alpha \sim 10^{-16}$ (cf. Fig. 2.11).

[19] Here, we have included the effect of the redshifting of the peculiar velocities of loops that was not taken into account in the analytical approximation for the SGWB spectrum generated by small loops in Ref. [217].

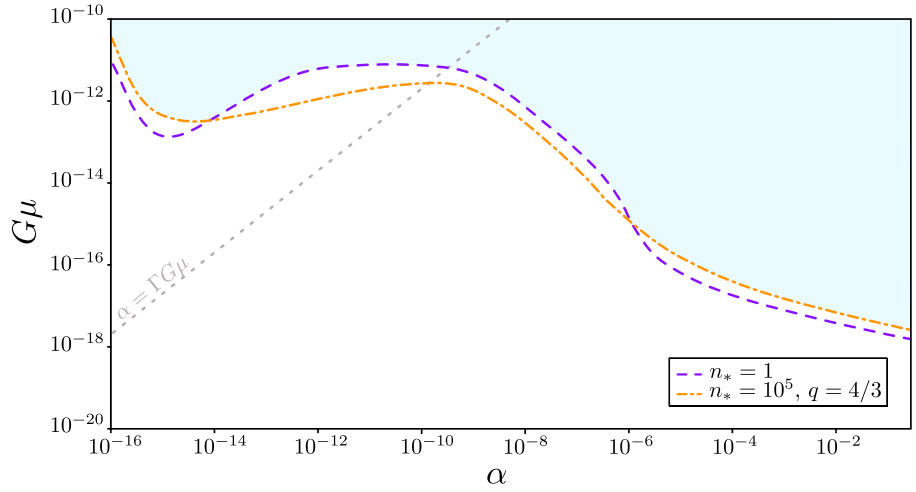

Figure 2.11: Projected constraints on $G\mu$ of the LISA mission for cosmic string scenarios characterized by different loop-size parameter α for $n_* = 1$ (dashed line) and $n_* = 10^5$, with $q = 4/3$ (dash-dotted line). The shaded area corresponds to the region of the $(\alpha, G\mu)$ parameter space that will be fully available for exploration with LISA. The dotted line corresponds to scenarios for which $\alpha = \Gamma G\mu$, so that the region above this line corresponds to cosmic string models in which loops are small, while the region bellow corresponds to the large loop regime.

which loops are created with small size. This value corresponds to the case in which $\alpha \sim 10^{-15}$ and $n_* = 1$, as Fig. 2.11 shows, for which the peak of the spectrum coincides with the maximum sensitivity of the LISA window (cf. Fig. 2.10).

In the large-loop regime, as we have seen, the amplitude of the spectra is highly dependent on the size of loops and, for this reason, so is the strength of the constraints that LISA may put on cosmic string tension. The amplitude of the radiation era plateau of spectrum for small loops in Eq. (2.64) may be regarded as the "minimal" amplitude of this plateau. Thus, one may use it to derive the value of cosmic string tension above which all cosmic string scenarios in which loop production is significant (with $\alpha > 10^{-16}$) are excluded:

$$G\mu < 8.0 \times 10^{-12}\,. \tag{2.67}$$

This provides us with the safest (yet most conservative) model-independent LISA bound on cosmic string tension, which corresponds to the value of the plateau observed at the mid-α range in Fig. 2.11. Note however that LISA shall be able to establish significantly more stringent constraints for the largest possible α. Indeed, LISA may go seven orders of magnitude beyond the bound in Eq. (2.67) for $\alpha = 10^{-1}$:

$$G\mu(\alpha = 10^{-1}) < 3.4 \times 10^{-18}\,. \tag{2.68}$$

As we have seen in Section 2.6.1, this corresponds approximately to the case of Nambu-Goto strings, apart from a factor of ~ 0.1 (since in that case only about 10% of the energy lost by the network goes into gravitational radiation). Apart from this factor, these results are in agreement with those presented in Section 2.6.1.

Intercommutation probability

In this paper, we have assumed that the intercommutation probability P is equal to 1. In effect, this amounts to stating that when two strings collide, they exchange partners every time. Indeed, in the Abelian-Higgs model (in the BPS and "type II" regime), the collision of two straight strings with velocities $\pm v$ and relative orientation given by an angle θ essentially always (that is, in nearly all of the (θ, v) parameter space) leads to the strings exchanging partners during the collision (see Ref. [65, 66]). Setting $P = 1$ is then equivalent to this statement. For other field theory strings, such as Abelian-Higgs strings in the type I regime, the collision may lead to other outcomes, such as the formation of a junction [67, 68]. We do not consider these more complicated cases here.

Recent development in String Theory suggest that fundamental strings (or F-strings) and 1-dimensional Dirichlet branes (or D-strings) may be stretched to macroscopic sizes and play the cosmological role of cosmic superstrings. The copious production of these cosmic superstrings is, in fact, predicted to occur at the end of several brane-inflationary scenarios (see, *e.g.*, Refs. [264, 265, 71]).

Cosmic superstrings may have an intercommutation probability P significantly smaller than unity, as a result of their quantum nature: in fact it has been shown [266] that $10^{-3} \lesssim P \lesssim 1$ in collisions between F-strings and $10^{-1} \lesssim P \lesssim 1$ for D-string collisions. When a FF- or DD-string collision occurs, the strings may then — unlike ordinary strings — pass through each other without intercommutation. For this reason, cosmic superstring networks are expected to lose energy less efficiently. Their energy density, and consequently the amplitude of the SGWB they generate, may therefore be expected to be larger than that of ordinary strings. Hence, the constraints derived on $G\mu$ in this paper are conservative: with $P < 1$, the bounds on $G\mu$ will be tighter (see, *e.g.*, Ref. [107] for a discussion of this effect at LIGO frequencies). In general, one expects the loop-chopping parameter of these networks to be such that

$$c_{\rm c}(P) = c_{\rm c}(1) P^{\gamma} \,, \tag{2.69}$$

where $c_{\rm c}(1) = c_{\rm c} = 0.23$ is the loop-chopping parameter of ordinary strings (which have $P = 1$). Although one may naively expect, within the one-scale framework, $\gamma = 1$ [265], numerical simulations indicate that this effect is less dramatic due to an accumulation of small-scale structure on cosmic strings with reduced intercommutation probability. It has been observed that $\gamma = 1/2$ in Nambu-Goto simulations in Minkowski space [267] and $\gamma = 1/3$ in both radiation- and matter-era simulations [268]. Since the exact value of γ is still a matter for debate, here we restrict ourselves to a (mostly) qualitative discussion of the effects of P.

Weakly interacting networks, with $c_{\rm c} \ll 1$, scale in the radiation era according to $\xi = \sqrt{2} c_{\rm c}$ and $\bar{v}^2 \approx 1/2$ [269]. Therefore, one may, in general, expect the amplitude of the radiation era plateau of the SGWB to scale as [133]

$$\Omega_{\rm GW}^{\rm plateau} \propto c_{\rm c}^{-2} \propto P^{-2\gamma} \,. \tag{2.70}$$

Note however that, in this case, the length of the loops created is not known. There is some evidence that the reduction of the intercommuting probability is more efficient in suppressing the production of large loops than of small loops [268], which seems to indicate that smaller α ($\sim \Gamma G\mu$) may be favoured for these networks. However, the precise number density of loops has not been determined using numerical simulations yet. Nevertheless, one may obtain, using Eqs. (2.67,2.70), a conservative α-independent constraint on the cosmic string tension of networks with $P \ll 1$. This bound — corresponding to the lowest $G\mu$ for which the SGWB is within the reach of LISA for all values of α — is presented in Table 2.1 for $P = 10^{-1}, 10^{-2}, 10^{-3}$.

	Conservative		Stringent	
P	$\gamma = 1/2$	$\gamma = 1/3$	$\gamma = 1/2$	$\gamma = 1/3$
10^{-1}	8.0×10^{-13}	1.7×10^{-12}	3.4×10^{-19}	5.6×10^{-19}
10^{-2}	8.0×10^{-14}	3.7×10^{-13}	2.9×10^{-20}	1.2×10^{-19}
10^{-3}	8.0×10^{-15}	8.0×10^{-14}	8.5×10^{-21}	2.9×10^{-20}

Table 2.1: Projected constraints of the LISA mission for cosmic string scenarios with reduced intercommutation probability P. Here, "Conservative" refer to the safe (α-independent) bounds obtained using the minimal amplitude of the radiation-era plateau, while the constraints labeled as "Stringent" correspond to those of scenarios with the largest possible α.

Naturally, as with ordinary strings, LISA will impose tighter constraints for scenarios in which α is large. The most stringent constraint on $G\mu$ will necessarily be those of scenarios characterized by the largest possible α, with $\alpha_{\rm max} \sim 0.3P^{\gamma}$ (corresponding to the characteristic length of the network which may, in this case, be significantly smaller than the horizon). These constraints are also recorded in Table 2.1 for the same values of P. These two constraints are then indicative of the ability of LISA to detect cosmic string scenarios with a reduced intercommutation probability.

However, we note that there are relevant aspects of cosmic superstring dynamics that were not taken into account when deriving these constraints. In particular, when superstrings of different types collide, they are expected to bind together to create a third type of string, which has a higher tension than its two constituents. This is expected to lead to networks with junctions and a hierarchy of tensions [71]. The creation of junctions is expected to have an impact on the large scale dynamics of cosmic string networks [270, 271, 272, 273, 274, 275, 276, 277] and therefore to affect the shape and amplitude of the SGWB generated by cosmic superstrings [278, 133]. Moreover, there are several other important aspects regarding the gravitational wave emission by cosmic superstrings that need to be clarified — most notably the number and strength of the cusps [279] as well as the possible coupling of superstrings to other fields — before a detailed study of the parameter space available to LISA can be performed.

2.6.3 Gravitational wave bispectrum from long strings

The GW signal due to the gravitational decay of loops that we have analysed in this paper cannot be resolved beyond its stochastic nature, and it is expected to be Gaussian.[20] The irreducible emission of GWs from a defect network (described in Section 2.3.4) is however expected to be highly non-Gaussian. This is simply due to the fact that the source of the GWs is bilinear in the amplitude (modulo derivatives) of the fields of which the cosmic strings are made. This implies that any correlator of an odd number of tensor perturbations will be characterized by the correlation of an even product of fields, which is non-vanishing even if the fields were Gaussian. We therefore expect that any non-Gaussianity in the continuous stochastic background sourced by a cosmic string network is due to the irreducible GW emission, even if this signal is sub-dominant in terms

[20] In reality, on top of the continuous stochastic Gaussian background from cosmic strings, there can be individual bursts emitted by nearby strings or a "popcorn" discontinuous noise [130]; recall the discussion in Section 2.4.3. These signals due to bursts represent, in a sense, a temporal deviation from Gaussianity, that can be measured from the two-point function. However, they do not correspond to the type of non-Gaussianity that we are referring to in this subsection, as they do not form a continuous stochastic background.

of amplitude of power spectra.

The capability of LISA to detect 3-point correlations of SGWB has been recently analysed in detail in Ref. [280]. At present, the 3-point GW function of this background can be estimated analytically only in a simplified case, namely in the large-N limit of a global phase transition due to the spontaneous symmetry breaking of $O(N)$ into $O(N-1)$. The GW background due to the dynamics of such global defects has been estimated in the limit $N \gg 1$ (see Section 2.4.4 and in particular Eq. (2.53)). The 3-point function (in the equilateral configuration) has been presented in Ref. [281]. Order of magnitude calculations in the large-N limit leads to a GW bispectrum peaked in the equilateral configuration as [281]

$$k^6 \mathcal{B}(k,k,k) \sim C_{\rm NL}(k^{3/2} P_h(k))^2 \qquad \text{with} \qquad C_{\rm NL} \sim \frac{3.6}{\sqrt{N}}\,, \tag{2.71}$$

where P_h is the total power spectrum (summing over the two polarizations) and $N \gg 1$ is the number of components of the symmetry-breaking field. This is of course a very rough estimate for global strings, for which $N = 2$, and we certainly do not know how this relation is modified in the case of Abelian-Higgs strings. However, Eq. (2.71) suggests very clearly that, in general, that we should expect a large departure from Gaussianity for the irreducible GW background from any defect network.

Let us note that even though Ref. [280] has provided a formalism to characterize a potential detection by LISA of the bispectrum of a SGWB, Refs. [282, 283] have recently pointed out that propagation effects of GWs across a perturbed universe like ours — from the generation point to the LISA detector — will suppress the bispectrum to unobservable levels. This suppression is expected to be present for any non-Gaussian SGWB, as long as the signal consists of GWs that have travelled across cosmological scales. If this claim is finally sustained, it will essentially imply that independently of the level of (intrinsic) non-Gaussianity of a given SGWB, the 3-point function of GWs will never be measured by direct detection detectors[21].

2.7 Discussion and conclusion

In this paper we have analysed the ability of LISA to detect and characterize a SGWB produced by a network of cosmic strings. Our key finding is that LISA will be able to probe cosmic string with tensions $G\mu \gtrsim \mathcal{O}(10^{-17})$, under a "standard" set of assumptions: namely, that the string dynamics are accurately described by the Nambu-Goto action, that colliding strings always intercommute, and that the average loop size at formation (in units of cosmic time t) is $\alpha \approx 0.1$. This presents an improvement of ~ 6 orders of magnitude over current constraints from pulsar timing arrays (PTA), and potentially in ~ 3 orders of magnitude over estimated future constraints from next generation of PTA experiments[22]. We have also explored scenarios in which the latter two assumptions are relaxed. Decreasing the loop size at formation α generically leads to weaker constraints on the string tension. Decreasing the intercommutation probability P leads to a range of possible constraints, due to the uncertainty about α in these scenarios; however, for larger values of α, networks with a small intercommutation probability are very strongly constrained, with LISA being able to reach tensions as small as $G\mu \approx 10^{-20}$.

[21] Note that measurements of a 3-point function of perturbations in the CMB evade this problem.

[22] The reason for this is that the spectrum of the SGWB from cosmic strings, shifts towards larger frequencies for small tensions, and hence "leaves behind" the frequency window accessible to PTA experiments, no matter how precise these may become. See Figs. 2.1 and 2.2.

In addition, we have shown the difference in shape of the GW spectra accessible to LISA, between model II and model III. In particular, we observe that the high-frequency plateau for model II is visible in the LISA band, whereas this is never the case for model III. Therefore, LISA could be actually used to discriminate between these two models[23]. Furthermore, we have discussed how a detection of the string SGWB (for a given model) could be used to probe fundamental physics, such as changes in the number of relativistic degrees of freedom, or the inclusion of transient epochs prior of radiation domination, characterized by a non-standard equation of state. Such studies are of particular interest in LISA, because its detection window is well-positioned to measure the segment of the string SGWB which contains information about these processes (in the event that $G\mu$ is at least an order of magnitude above the lower bound). Thus, a detection of cosmic strings is of use and interest to the cosmology and particle physics communities at large.

Note that in our assessment of detection we have assumed an ideal case in which the stream data to be measured by LISA is perfectly cleaned from all resolvable sources, glitches, and any impurities in general. In particular, we assume that the presence of the foreground of galactic binaries can be subtracted exploiting its yearly modulation [286]. We consider the only signal on top of LISA's intrinsic noise to be that of the homogeneous and isotropic stochastic GW background from the sub-horizon loops of a string network. Future work will quantify the ability of LISA to reconstruct the spectral shape of the SGWB for the lowest tensions that can be probed, as well as possible spectral features due to changes in the number of degrees of freedom. For this we plan to use the recent technique for systematic reconstruction SGWB signals without assuming any specific spectral template [35].

Finally, we remark that we have not discussed the GW signal from Abelian-Higgs simulations, nor considered how the dynamics of cosmic superstring networks would alter LISA's detection prospects. Most importantly, no simulation to date has included the real effect of back-reaction on the string network[24] (*i.e.*, gravitational self-interaction), and therefore the best that can be done is to model back-reaction with some ansatz. Our results are therefore predicated on such ansatz representing good approximations to how true back-reaction would affect the SGWB from a string network.

2.A Nambu-Goto dynamics

The dynamics of relativistic zero-thickness strings can be obtained from the Nambu-Goto action (see for example [64] and references therein),

$$S_{\rm NG} = -\mu \int \mathrm{d}^2\xi \, \sqrt{-\gamma}, \tag{2.72}$$

where μ parametrizes the tension of the string, and the integral describes the area of the string worldsheet, whose induced metric is given by γ.

The equations of motion from this action can be solved in flat space in the gauge where the most generic solution can be shown to be of the form

$$X^\mu(\sigma, t) = \frac{1}{2}\big[X^\mu_-(\sigma_-) + X^\mu_+(\sigma_+)\big], \tag{2.73}$$

[23] For a critical discussion about the details behind each model, we refer the reader to the recent references [52] and [284, 285].

[24] See however Refs. [115, 119, 120, 121, 238, 116] for work along this direction.

where σ and t are spacelike and timelike coordinates, respectively, on the worldsheet, and we have introduced $\sigma_\pm = t \pm \sigma$. Furthermore we fix the gauge to $X^0_\pm = \sigma_\pm$, and the spatial part of these functions are normalized so that $|\mathbf{X}'_\pm| = 1$.

2.A.1 Loop dynamics

Using the solutions found earlier, one can describe the evolution of a loop in its rest frame with the periodic functions $\mathbf{X}_\pm(\sigma_\pm) = \mathbf{X}_\pm(\sigma_\pm + \ell)$. This implies that

$$\int_0^\ell \mathbf{X'}_\pm(\sigma_\pm)\,\mathrm{d}\sigma_\pm = 0\,, \tag{2.74}$$

where ℓ is the length of the loop. This, together with the unit normalization, means that the functions $\mathbf{X'}_\pm(\sigma_\pm)$ would trace out a loop on the Kibble-Turok sphere whose centre of mass is at the centre of the sphere. These trajectories will therefore generically cross at points where

$$\mathbf{X'}_-(\sigma^c_-) = \mathbf{X'}_+(\sigma^c_+)\,. \tag{2.75}$$

These special points in the string evolution are called cusps, and it is easy to check that they represent instants during the string's periodic motion when the string doubles back onto itself, $\mathrm{d}\mathbf{X}/\mathrm{d}\sigma = 0$, and therefore moves at the speed of light, $|\,\mathrm{d}\mathbf{X}/\mathrm{d}t\,| = 1$. On the other hand, string intersections can lead to intercommutations, which lead to kinks on both the previously-existing string and the newly-formed loop. Kinks are discontinuities of either of $\mathbf{X'}_\pm(\sigma_\pm)$.

The consequences for GW emission of these two type of features are discussed in 2.A.2.

2.A.2 Gravitational wave power from cusps and kinks

Solving the linearized Einstein equation for a single Nambu-Goto cosmic string loop, one can write the GW strain in the local wave zone as a mode sum [106]

$$\bar{h}_{\mu\nu}(t,\mathbf{x}) \approx \frac{4G\mu\ell}{r}\sum_n \exp\left[-\frac{4\pi\mathrm{i}n}{l}(t-r)\right] I^{(\mu}_{n,+} I^{\nu)}_{n,-}\,, \tag{2.76}$$

where $r \equiv |\mathbf{x}|$ is the distance to the source, and ℓ is the invariant loop length. The motion of the loop worldsheet is parametrized by the functions $X^\mu_\pm(\sigma_\pm)$ and contributes to the GW signal through the integrals

$$I^\mu_{n,\pm} \equiv \frac{1}{\ell}\int_0^\ell \mathrm{d}\sigma_\pm \exp\left[-\frac{2\pi\mathrm{i}n}{\ell}X^\mu_\pm k_\mu\right]\partial_\pm X^\mu_\pm\,, \tag{2.77}$$

where $k^\mu = (1,\mathbf{x}/r)$ is a null wavevector and $\partial_\pm = \partial/\partial\sigma_\pm$.[25] The $n = \pm 1$ frequencies correspond to the fundamental mode of the loop (set by the period of loop oscillation $T = \ell/2$),

$$f_1 \approx \frac{d_\mathrm{h}}{\ell} \times 10^{-18}\ \mathrm{Hz}, \tag{2.78}$$

which for many loops is far below the LISA frequency window of 10^{-4}–10^{-2} Hz (unless there were loops of size ℓ many orders of magnitude smaller than the present-day Hubble length d_H). We are

[25] In the calculation of the GW loop power spectrum, we define the analogous function in a coordinate system whose z axis is in the $vb\hat{\Omega}$ direction. In this case we can write $\mathbf{I}^\pm_n = \frac{1}{\ell}\int_0^\ell \mathrm{d}\sigma_\pm \exp\left[-\frac{2\pi\mathrm{i}n}{\ell}(\sigma_\pm - X_z(\sigma_\pm))\right]\mathbf{X'}_\pm(\sigma_\pm)$.

therefore typically concerned with much higher frequencies $f \gg f_1$, *i.e.* very high-order harmonics of the loop, $|n| \gg 1$. In this limit, the integrals in Eq. (2.77) are *generically* exponentially suppressed for large n, and there is little contribution to the GW signal at high frequencies.

There are two important exceptions where the integrals in Eq. (2.77) are *not* exponentially suppressed, and have a much weaker power-law decay with frequency: (i) when there is a saddle point in the phase, $k_\mu \partial_\pm X^\mu_\pm = 0$; (ii) when the function $\partial_\pm X^\mu_\pm$ is discontinuous.

In order to obtain a GW strain that is not exponentially suppressed, one or the other of these conditions must hold for both sets of integrals $I^\mu_{n,+}$ and $I^\mu_{n,-}$. This gives rise to three possibilities [106, 64, 90]:

1. Both sets of integrals have a saddle point in the phase, *i.e.* there are points $X^{\mu *}_\pm$ such that $k_\mu \partial_\pm X^{\mu *}_\pm = 0$. These points are then necessarily the same, $X^{\mu *}_+ = X^{\mu *}_-$. Physically, we interpret this as an event where part of the loop moves at the speed of light, forming a sharp, transient feature; this is what we referred to as a *cusp* earlier. The cusp emits a GW burst, which is beamed along the spatial direction corresponding to $X^{\mu *}_\pm$, with an opening angle $\theta_\mathrm{b} = [1/(g_2 f \ell)]^{1/3} \approx [2/(\sqrt{3} n)]^{1/3}$.

2. One of the sets of integrals has a saddle point, while the other has a discontinuity in the integrand, which is interpreted as a discontinuity in the shape of the loop; this is what we called a *kink* before. In this case, the power-law scaling for $\bar{h}_{\mu\nu}$ occurs not just centred on a single direction (as for a cusp), but around a one-dimensional, "fan-like" set of directions. We interpret this as the kink propagating around the loop, beaming GWs as it does so, with the beam opening angle being given again by $\theta_\mathrm{b} = [1/(g_2 f \ell)]^{1/3} \approx [2/(\sqrt{3} n)]^{1/3}$.

3. Both sets of integrals have a discontinuity at the same point on the worldsheet. This case corresponds to two kinks, one left-moving and one right-moving, meeting each other. We call this a *kink-kink collision*. In this case, there is no saddle point condition to determine a preferred direction, so the GW emission is isotropic rather than beamed.

In each of these three cases, one can calculate the asymptotic $|n| \gg 1$, $f \gg f_1$ GW waveform, and take the Fourier transform of this to get the strain spectrum $\tilde{h}(f)$. This gives

$$\tilde{h}_\mathrm{c}(f, \mathbf{r}) = g_1^c \frac{G\mu\ell^{2/3}}{r f^{4/3}}, \qquad \tilde{h}_\mathrm{k}(f, \mathbf{r}) = g_1^k \frac{G\mu\ell^{1/3}}{r f^{5/3}}, \qquad \tilde{h}_\mathrm{kk}(f, \mathbf{r}) = g_1^{kk} \frac{G\mu}{r f^2}, \tag{2.79}$$

for the cusp, kink, and kink-kink collision cases, respectively, taking care to account for the beaming angle in the cusp and kink cases.

Using these expressions, one can obtain the total power emitted for these events by performing the following integral:

$$P = \frac{1}{T} \int_0^\infty \mathrm{d}f \, \frac{\pi f^2}{2G} \int_{S^2} \mathrm{d}^2 r \;\; r^2 \tilde{h}_i^2(f, \mathbf{r}) \,. \tag{2.80}$$

For example, in the case of cusps, one can estimate the power to be

$$P = \frac{3\pi^2 g_1^2}{2^{1/3} g_2^{2/3}} \left(G\mu^2\right), \tag{2.81}$$

so we can say that a typical loop with N_c cusps will have a power of order of

$$\Gamma = N_c \frac{3\pi^2 g_1^2}{2^{1/3} g_2^{2/3}} \,. \tag{2.82}$$

This expression allows us to relate the parameters of the cusp waveform g_1 and g_2 to the total power emitted from this loop when the loop is assumed to emit only in the form of cusps. This relation is important in order to make a consistent calculation of the total SGWB and compare Methods I and II.

Chapter 3

Cosmic string loop production functions

This chapter is a reproduction of Ref. [52] in collaboration with Christophe Ringeval, Mairi Sakellariadou and Danièle Steer. Our aim in this paper was to study the loop production function (LPF) of Polchinski and collaborators Refs. [137, 287, 232]. Relative to the delta-function LPF which is the simplest to study analytically, this LPF takes into account the small-scale structure on strings and gravitational radiation, effects which cannot be considered in numerical simulations. This LPF has a power-law shape allowing loops to be formed at different scales. The resulting loop distribution, obtained by solving the Boltzmann equation, had already been studied in Ref. [123] but in a particular regime of parameter space which we wanted here to extend in order to compare it with numerical results of other groups for large loops. I contributed to all the sections of this paper.

Abstract

Numerical simulations of Nambu-Goto cosmic strings in an expanding universe show that the loop distribution relaxes to a universal configuration, the so-called scaling regime, which is of power law shape on large scales. Precise estimations of the power law exponent are, however, still matter of debate while numerical simulations do not incorporate all the radiation and backreaction effects expected to affect the network dynamics at small scales. By using a Boltzmann approach, we show that the steepness of the loop production function with respect to loops size is associated with drastic changes in the cosmological loop distribution. For a scale factor varying as $a(t) \propto t^{\nu}$, we find that sub-critical loop production functions, having a Polchinski-Rocha exponent $\chi < (3\nu - 1)/2$, yield scaling loop distributions which are mostly insensitive to infrared (IR) and ultra-violet (UV) assumptions about the cosmic string network. For those, cosmological predictions are expected to be relatively robust, in accordance with previous results. On the contrary, critical and super-critical loop production functions, having $\chi \geq (3\nu - 1)/2$, are shown to be IR-physics dependent and this generically prevents the loop distribution to relax towards scaling. In the latter situation, we discuss the additional regularizations needed for convergence and show that, although a scaling regime can still be reached, the shape of the cosmological loop distribution is modified compared to the naive expectation. Finally, we discuss the implications of our findings.

3.1 Introduction

The advent of gravitational wave astronomy provides an unprecedented opportunity to search for topological defects, and in particular cosmic strings [288, 61, 143, 289]. In an expanding and decelerating universe, a cosmic string network relaxes towards an attractor configuration exhibiting universal properties — known as a scaling solution — and it subsequently remains self-similar with the Hubble radius [69, 64, 290, 291, 292, 293, 294, 75, 88]. Hence, if cosmic strings were formed in phase transitions early in the history of the universe, scaling implies that they should be present all over the sky with a surface density growing with redshift z. Strings induce anisotropies in the Cosmic Microwave Background (CMB) and they have been searched for in the Planck data [72, 295, 74, 296, 297, 298]. The current CMB constraints give an upper bound for the string energy per unit length μ of $G\mu < \mathcal{O}\big(10^{-7}\big)$, where G is the Newton's constant. However, CMB photons come from the highest observable redshift set by their last scattering surface, namely $z_{\rm lss} \simeq 1088$. For gravitons, z is only bounded by our understanding of the Friedmann-Lemaître model, or more probably by the redshift at which cosmic inflation ended. For this reason, the stochastic gravitational wave background (SGWB) is an observable particularly sensitive to cosmic strings and could provide the opportunity for a first detection.

Current constraints on $G\mu$ from the SGWB are already much stronger than those from the CMB, of order $G\mu < \mathcal{O}\big(10^{-11}\big)$ [90, 89, 91] (the actual value depends on some yet unknown microphysical parameters). However, as opposed to the CMB constraints, bounds from GW crucially depend on the loop distribution. Indeed, through their production by the string network, oscillating closed cosmic string loops constitute the main source of the SGWB. Although loop production is observed and measured in Nambu-Goto cosmic string simulations [99, 100, 109], it is still a matter of debate if it plays the same role in a field theoretical model [110, 111, 112, 113]. Clearly the detailed shape of the scaling loop distribution function is important to determine the properties of the SGWB at different frequencies. Nambu-Goto simulations from two independent groups have shown that, on *large scales* (see discussion below), where these simulations can be trusted, it is a power-law, namely

$$t^4 \mathbf{n}(\gamma, t) \propto \gamma^p . \tag{3.1}$$

Here we have defined

$$\gamma(\ell, t) \equiv \frac{\ell}{t} , \qquad \mathbf{n}(\gamma, t) \equiv \frac{\mathrm{d}n}{\mathrm{d}\ell} , \tag{3.2}$$

where $n(\ell, t)$ is the number density distribution of loops of size ℓ at cosmic time t, and the time-independence of the combination $t^4\mathbf{n}$ is precisely the scaling regime. The simulations of Ref. [99] give

$$p = -2.60^{-0.21}_{+0.15}\big|_{\rm rad} , \qquad p = -2.41^{-0.08}_{+0.07}\big|_{\rm mat} . \tag{3.3}$$

Analysis of the simulations of Refs. [103, 114] favours slightly different values, namely $p = -5/2$ in the radiation and $p = -2$ in the matter era. It is, however, important to stress that the approach taken in the numerical simulations of Refs. [103, 114] is quite different to that of Ref. [99]. In the latter reference, the shape of the scaling loop distribution $t^4\mathbf{n}(\gamma)$ is estimated from simulations whereas in the former references this is the shape of the scaling loop production function which is inferred from numerical results.

Let us also notice that, due to the huge disparity of scales in the problem (ranging from, for instance, the distance between kinks formed by string intercommutations, to the horizon size), numerical simulations of cosmic string networks cannot incorporate all physical effects. In Nambu-Goto simulations, in particular, effects from GW emission and backreaction onto the string dynamics

are ignored[1]. This is why Eq. (3.1) can only be trusted for loops large enough that these effects remain negligible. GW emission means that loops loose energy and hence become smaller, with an average emitted GW power $P_{\rm gw} = \Gamma G\mu^2$ where Γ is a numerical constant estimated to be $\Gamma = \mathcal{O}(50)$ [117, 118, 114]. Hence, loops decoupled from the Hubble flow shrink at an average rate given by

$$\gamma_{\rm d} \equiv \Gamma G\mu. \tag{3.4}$$

One therefore expects Eq. (3.1) to hold for loops of length $\ell \gtrsim \ell_{\rm d} = \gamma_{\rm d} t$ (numeric-wise, this is a quite small number already for $G\mu < 10^{-7}$). Emitted GWs will also backreact onto the string thereby affecting its dynamics. The consequences of this process for the network and the loops are still unknown and being studied [119]. However, one expects that loop production should be cut-off below some length scale $\ell_{\rm c} \equiv \gamma_{\rm c} t$, with presumably $\gamma_{\rm c} \leq \gamma_{\rm d}$, which we discuss below.

As was realized very early on. [64], in practise, to include these physical effects one needs to combine results of simulations with analytical modelling. A powerful framework for this is to use a Boltzmann approach to estimate the loop distribution on cosmological time and length scales [96, 122, 123, 124, 125, 126, 127]. At this stage it is remarkable to notice that *radically different* assumptions about the loop production function can lead to *similar* powers p on large scales (where the results should be fitted against simulations). Indeed, on one hand, motivated by the one-scale model of cosmic string evolution [61, 64], an often studied case is one in which [128, 105, 129, 130, 48, 131, 107, 132, 133]

$$\mathcal{P}(\gamma, t) \propto \delta_{\rm D}(\gamma - \alpha), \tag{3.5}$$

namely all stable loops are formed with size $\ell = \alpha t$ at time t (for constant α). It is then straightforward to extract the loop density distribution [64] (see Section 3.2.2) and show that in the radiation era $p = -5/2$ while in the matter era $p = -2$. On the other hand, all cosmic string simulations show that a lot of small-scale structure, namely kinks generated from string intercommutation, build up on the strings (see Refs. [134, 102, 101, 93, 135, 136, 94] for a discussion of small-scale structure on strings). As a result, one expects loops to be formed on a wide range of scales at any given time. The most recent analytical work along these lines is by Polchinski-Rocha and collaborators [137, 138, 122], who proposed a model of loop production from long strings. It is given by

$$t^5 \mathcal{P}(\gamma > \gamma_{\rm c}, t) \propto \gamma^{2\chi - 3}, \tag{3.6}$$

where the parameter χ will be referred to as the Polchinski-Rocha (PR) exponent[2]. This is clearly very different from a Dirac distribution as a loop production function. In Ref. [123], the authors have included backreaction effects to the PR model and extended Eq. (3.6) to the domains $\gamma < \gamma_{\rm c}$, but, motivated by the numerical results of Ref. [99], have considered only the cases $\chi < \chi_{\rm crit}$ where

$$\chi_{\rm crit} = \frac{3\nu - 1}{2}\,. \tag{3.7}$$

Here, we have assumed that the scale factor behaves as $a \propto t^\nu$ so that $\chi_{\rm crit} = 0.25$ and $\chi_{\rm crit} = 0.5$ for the radiation and matter era, respectively. Under the condition $\chi < \chi_{\rm crit}$, Refs. [122, 123] have shown that the loop distribution behaves as a power law on large scales, with the power p in Eq. (3.1) given by

$$p = 2\chi - 3. \tag{3.8}$$

[1] See, however, Ref. [115] and more recently Ref. [116] for an isolated loop.

[2] The PR exponent is related to the two-point correlation function of tangent vectors along cosmic strings.

From Eqs. (3.3) and (3.8), the Nambu-Goto simulations of Ref. [99] therefore give

$$\chi_{\rm r} = 0.200^{+0.07}_{-0.10}\,, \qquad \chi_{\rm m} = 0.295^{+0.03}_{-0.04}, \tag{3.9}$$

for the radiation and matter era, respectively. We also note that χ has been estimated from the two-point correlators of tangent vectors along the long strings using an average over multiple Abelian Higgs simulations in Ref. [112] where it was found that $\chi_{\rm r} = 0.22$ and $\chi_{\rm m} = 0.35$. At this stage it is intriguing to notice that the powers $p = -5/2$ in the radiation era, and $p = -2$ in the matter era, correspond precisely to $\chi = \chi_{\rm crit}$ where the analysis of Ref. [123] breaks down. One of the aims of this paper is precisely to extend the analysis of Ref. [123] to the "critical case" $\chi = \chi_{\rm crit}$ and to the "super-critical case" $\chi > \chi_{\rm crit}$.

Before doing so, however, it is important to comment that while the two loop production functions of Eqs. (3.5) and (3.6) lead to similar loop distributions on large scales, they lead to very important differences for small loops, namely for $\gamma < \gamma_{\rm d}$. Until recently, these differences on small scales were of no great concern for observable predictions. For instance, predictions for the CMB power spectrum and induced non-Gaussianities are essentially blind to cosmic string loops[3] (see Ref. [75] for a review). However, the situation is not the same for gravitational waves. The Polchinski-Rocha (PR) loop production function induces a larger population of small loops. Small loops oscillate faster, and being more numerous, they can potentially dominate the GW emission within some frequency range.

In this paper, we show that the value of $\chi = \chi_{\rm crit}$ is a separatrix between two different behaviours. For values $\chi < \chi_{\rm crit}$, we recover the results presented in Refs. [123, 90] and confirm the weak dependence of the scaling loop distribution on the details of the backreaction cut-off at small scales. We will refer to this property as being ultra-violet (UV) insensitive. We also show that the predicted loop number density is not affected by assumptions made for the distribution of the largest loops, and this property will be referred to as infrared (IR) insensitive. On the contrary, values of $\chi \geq \chi_{\rm crit}$, including the equality, exhibit a very strong sensitivity to the IR. In fact, under the simplest assumptions, we show that the loop distribution cannot even reach a scaling regime and diverges in time. Scaling solutions can still be reached provided additional assumptions are made to regularize the IR behaviour, the validity of which still remains to be assessed in the cosmological context. For all these possible regularized scaling solutions, we show that the loop distribution shape is modified compared to the naive expectation.

The paper is organized as follows. In the next section, we recap the hypothesis and solutions of the Boltzmann equation presented in Ref. [123]. We then show in Section 3.2.4 that the solutions can be readily extended to the super-critical cases $\chi > \chi_{\rm crit}$ and that the loop distribution never reaches scaling in that case. In Section 3.2.5, we solve the Boltzmann equation for the critical value $\chi = \chi_{\rm crit}$ and show again that the loop distribution diverges with time. In Section 3.3, we discuss the extra-assumptions needed in the IR to produce a scaling loop distribution with $\chi \geq \chi_{\rm crit}$. For those, we derive the new scaling loop distributions and critically compare the results in all three cases, sub-critical, critical and super-critical. We finally conclude by briefly discussing the implications of our findings.

3.2 Cosmic string loop evolution

[3] The tri-spectrum depends however on χ due to its sensitivity to tangent vector correlators [299, 300].

3.2.1 Boltzmann equation and loop production function

The number density $n(\ell, t)$ of cosmic string loops of size ℓ at cosmic time t is assumed to follow a conservation equation

$$\frac{\mathrm{d}}{\mathrm{d}t}\left(a^3\frac{\mathrm{d}n}{\mathrm{d}\ell}\right) = a^3\mathcal{P}(\ell, t), \tag{3.10}$$

where $\mathcal{P}(\ell, t)$ is a loop production function (LPF) giving the number density distribution of loops of size ℓ produced per unit of time at t and $a(t)$ is the scale factor[4]. For an individual loop, gravitational wave emission induces energy loss through

$$\frac{\mathrm{d}\ell}{\mathrm{d}t} = -\gamma_{\mathrm{d}}. \tag{3.11}$$

Combining Eqs. (3.10) and (3.11), and working in terms of the variables (γ, t) and $\mathbf{n} \equiv \mathrm{d}n/\mathrm{d}\ell$ given in Eq. (3.2), one obtains the two-dimensional Boltzmann equation

$$t\frac{\partial(a^3\mathbf{n})}{\partial t} - (\gamma + \gamma_{\mathrm{d}})\frac{\partial(a^3\mathbf{n})}{\partial\gamma} = a^3 t\mathcal{P}(\gamma, t). \tag{3.12}$$

Its general solution can be obtained by changing variables to (t, v) where $v = t(\gamma + \gamma_{\mathrm{d}})$. Then Eq. (3.12) becomes

$$\left.\frac{\partial[a^3\mathbf{n}(t, v)]}{\partial t}\right|_v = a^3\mathcal{P}(t, v). \tag{3.13}$$

Assuming the infinite (super-horizon) string network is in scaling, the t-dependence of the LPF is of the form

$$t^5\mathcal{P}(\gamma, t) = \mathcal{S}(\gamma) = \mathcal{S}\Big(\frac{v}{t} - \gamma_{\mathrm{d}}\Big), \tag{3.14}$$

and it is straightforward to integrate Eq.(3.13) from some initial time t_{ini} and find its general solution. In terms of the variables (γ, t) it reads

$$\mathbf{n}(\gamma, t) - \mathbf{n}_{\mathrm{ini}}(\gamma, t) = \int_{t_{\mathrm{ini}}}^{t}\left[\frac{a(t')}{a(t)}\right]^3\mathcal{S}\Big[\frac{(\gamma + \gamma_{\mathrm{d}})t}{t'} - \gamma_{\mathrm{d}}\Big]\frac{\mathrm{d}t'}{t'^5}, \tag{3.15}$$

where

$$\mathbf{n}_{\mathrm{ini}}(\gamma, t) = \left[\frac{a(t_{\mathrm{ini}})}{a(t)}\right]^3\mathcal{N}_{\mathrm{ini}}\left[(\gamma + \gamma_{\mathrm{d}})t - \gamma_{\mathrm{d}}t_{\mathrm{ini}}\right], \tag{3.16}$$

with $\mathcal{N}_{\mathrm{ini}}(\ell)$ the initial loop distribution at $t = t_{\mathrm{ini}}$. Notice that the time dependence appears because $\mathbf{n}_{\mathrm{ini}}(\gamma, t)$ is evaluated at $t' = t_{\mathrm{ini}}$ and physically encodes the fact that, at time t, a loop of length γt corresponds to an initial loop of size $\ell = \gamma t + \gamma_{\mathrm{d}}(t - t_{\mathrm{ini}})$. Hence, once the loop production function $\mathcal{S}(\gamma)$ is specified over its entire domain of definition, the loop distribution is uniquely given by Eq. (3.15). As mentioned in the Introduction, physically very different LPF can give similar loop distributions for large loops. We now discuss the LPF.

[4]This equation can be generalized to include collision terms describing loop fragmentation as well as loop collisions, see Ref. [96].

3.2.2 Dirac distribution for the loop production function

In order to compare with results in the literature, let us solve explicitly the Boltzmann equation with a delta function LPF, motivated by the one-scale model, given in Eq. (3.5), namely $t^5\mathcal{P}(\gamma,t) = c\delta(\gamma-\alpha)$. From Eq. (3.15),

$$t^4\mathbf{n}(\gamma<\alpha,t) - t^4\mathbf{n}_{\rm ini}(\gamma,t) = c\left[\frac{a\left(t\dfrac{\gamma+\gamma_{\rm d}}{\alpha+\gamma_{\rm d}}\right)}{a(t)}\right]^3 \frac{(\alpha+\gamma_{\rm d})^3}{(\gamma+\gamma_{\rm d})^4}\Theta\left[\gamma+\gamma_{\rm d}-\frac{t_{\rm ini}}{t}(\alpha+\gamma_{\rm d})\right]. \qquad (3.17)$$

The left-hand side of Eq. (3.17) contains $\mathbf{n}_{\rm ini}$, which is determined from the initial loop distribution $\mathcal{N}_{\rm ini}$ through Eq. (3.16). This term is usually a transient for initial loop distribution converging fast enough to zero at large ℓ. However, if (as in numerical simulations) $\mathcal{N}_{\rm ini}$ is assumed to be the Vachaspati-Vilenkin (VV) distribution [301] one has $t_{\rm ini}^4\mathcal{N}_{\rm ini}(\ell) \propto (t_{\rm ini}/\ell)^{5/2}$ and because the argument of $\mathcal{N}_{\rm ini}$ in Eq. (3.16) grows with t we see that, in the particular case of the radiation era ($\nu = 1/2$), the whole term becomes time-independent and "scales". In a realistic situation, the VV distribution is valid up to some size, typically the initial horizon size $\ell < d_{\rm h}(t_{\rm ini})$, where $d_{\rm h}(t) = t/(1-\nu)$ with $\nu = 1/2$ or $2/3$ in the radiation or matter era, respectively. Above $d_{\rm h}(t_{\rm ini})$, loops are of super-horizon length and should actually be considered as long (dubbed "infinite") strings from a dynamical point of view. Once the argument of $\mathcal{N}_{\rm ini}$ (through $\mathbf{n}_{\rm ini}$) in Eq. (3.17) becomes larger than this cut-off, the corresponding term in the left-hand side of Eq. (3.17) disappears.

Neglecting therefore the effects from initial distribution $\mathbf{n}_{\rm ini}(\gamma,t)$, we find the loop distribution in the radiation era:

$$t^4\mathbf{n}(\gamma,t) = c\,\frac{(\alpha+\gamma_{\rm d})^{3/2}}{(\gamma+\gamma_{\rm d})^{5/2}}\Theta(\alpha-\gamma)\,. \qquad (3.18)$$

This expression corresponds to a scaling solution with a $p = -5/2$ power-law for $\gamma \gg \gamma_{\rm d}$, as stated in the Introduction. For loops formed during matter era one has

$$t^4\mathbf{n}(\gamma,t) = c\,\frac{(\alpha+\gamma_{\rm d})}{(\gamma+\gamma_{\rm d})^{2}}\Theta(\alpha-\gamma)\,, \qquad (3.19)$$

and this corresponds to a scaling solution with a $p = -2$ power-law for $\gamma \gg \gamma_{\rm d}$. Notice that, in both cases, the distributions are flat for values of $\gamma < \gamma_{\rm d}$.

3.2.3 Polchinski-Rocha loop production function

In the remainder of this paper we focus on the PR loop production function, which exhibits a power-law dependence in γ. For large loops, it is given by

$$t^5\mathcal{P}(\gamma \geq \gamma_{\rm c}, t) = c\,\gamma^{2\chi-3}. \qquad (3.20)$$

The "backreaction scale" $\gamma_{\rm c}$ was calculated in Ref. [232] and is given by[5]

$$\gamma_{\rm c} \equiv \Upsilon(G\mu)^{1+2\chi}, \qquad (3.21)$$

[5]The dependence on $G\mu$ is to be expected given that this scale is fixed by gravitational physics.

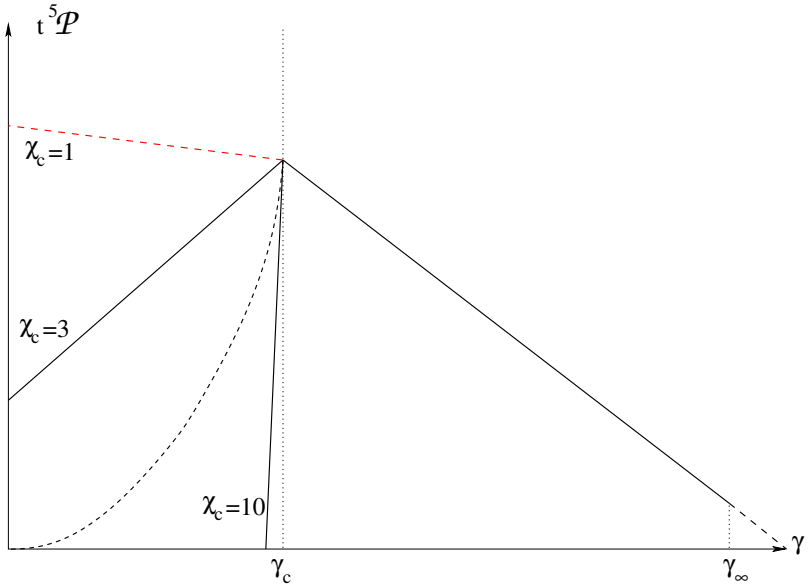

Figure 3.1: Sketch of possible loop production function shapes under the gravitational backreaction length scale $\gamma_c \equiv \ell_c/t$ (logarithmic units), namely $\mathcal{P}(\gamma \leq \gamma_c, t) = c_c\,\gamma^{2\chi_c-3}$ where the constant c_c is chosen such that $\mathcal{P}$ is continuous at $\gamma = \gamma_c$. According to Ref. [232], minimal gravitational backreaction effects correspond to $\chi_c = 1$ and we take this value as a motivated lower bound. The larger the value of χ_c, the sharper the cut is.

where $\Upsilon = \mathcal{O}(20)$. This suggests that the very small scales on a string network can potentially be strongly dependent on the value of χ. On scales $\gamma < \gamma_{\rm c}$, the actual shape of the LPF is unknown, but, surely, loop production has to be cut-off. A phenomenologically motivated expression has been proposed in Ref. [123], namely

$$t^5 \mathcal{P}(\gamma < \gamma_{\rm c}, t) = c_{\rm c}\, \gamma^{2\chi_{\rm c}-3}, \tag{3.22}$$

with $\chi_{\rm c} > 1$. Continuity of the loop production function at $\gamma = \gamma_{\rm c}$ imposes

$$c_{\rm c} = c\, \gamma_{\rm c}^{2(\chi-\chi_{\rm c})}. \tag{3.23}$$

The scaling function $\mathcal{S}(\gamma)$ is completely determined by Eqs. (3.20) and (3.22) and reads

$$\mathcal{S}(\gamma) = c\, \gamma^{2\chi-3}\Theta(\gamma-\gamma_{\rm c}) + c_{\rm c}\, \gamma^{2\chi_{\rm c}-3}\Theta(\gamma_{\rm c}-\gamma)\,. \tag{3.24}$$

Before giving explicit solutions of the Boltzmann equation for the PR based LPF, let us remark that the original PR model applies to loops produced by long (dubbed "infinite") strings, whereas in numerical simulations loops are also created from other loops and can potentially reconnect. Hence, the fit to numerical simulations can be viewed as a renormalization procedure that allows us to extend the properties of loops chopped off from long strings to those produced by other loops. In particular, the fit completely fixes the normalization constant c in the loop distribution. Unless specified otherwise, we have used the values reported in Ref. [99]. Simulations show that the largest loops created in a cosmological network are as large as the largest correlation length scale, which is a fraction of the Hubble radius. This typical correlation length allows us to define

$$\gamma_\infty = \left(\frac{\mu}{\rho_\infty t^2}\right)^{1/2}, \tag{3.25}$$

where ρ_∞ is the energy density of super-horizon sized (infinite) strings in scaling [134, 102, 101, 99]. One gets $\gamma_\infty \simeq 0.32$ in the radiation era and $\gamma_\infty \simeq 0.56$ in the matter era. The PR model with values of c consistent with those of simulations predicts a fractional number of loops having $\gamma \geq \gamma_\infty$. However, and as sketched in Fig. 3.1, the IR behaviour of $\mathcal{P}(\gamma, t)$ (at large γ) could a priori be different than for $\gamma < \gamma_\infty$ and we will explore this possibility in Section 3.3.

3.2.4 Non-critical loop production function

In this section, we present the solution of the Boltzmann equation obtained for the non-critical cases, *i.e.*, $\chi \neq \chi_{\rm crit}$. As shown in Ref. [123], substituting Eq. (3.24) into Eq. (3.15) gives the unique solution. In the domain $\gamma \geq \gamma_{\rm c}$ it reads

$$t^4\mathbf{n}(\gamma \geq \gamma_{\rm c}, t) = t^4\mathbf{n}_{\rm ini}(\gamma, t) + \frac{c}{\epsilon}(\gamma+\gamma_{\rm d})^{2\chi-3}\left[f\!\left(\frac{\gamma_{\rm d}}{\gamma+\gamma_{\rm d}}\right) - \left(\frac{t}{t_{\rm ini}}\right)^{-\epsilon} f\!\left(\frac{\gamma_{\rm d}}{\gamma+\gamma_{\rm d}}\frac{t_{\rm ini}}{t}\right)\right], \tag{3.26}$$

and, in the domain $\gamma < \gamma_{\rm c}$,

$$\begin{aligned} t^4\mathbf{n}(\gamma < \gamma_{\rm c}, t) = {} & t^4\mathbf{n}_{\rm ini}(\gamma, t) + \frac{c}{\epsilon}(\gamma+\gamma_{\rm d})^{3\nu-4}\,(\gamma_{\rm c}+\gamma_{\rm d})^{-\epsilon}\, f\!\left(\frac{\gamma_{\rm d}}{\gamma_{\rm c}+\gamma_{\rm d}}\right) \\ & - \frac{c}{\epsilon}(\gamma+\gamma_{\rm d})^{2\chi-3}\left(\frac{t}{t_{\rm ini}}\right)^{-\epsilon} f\!\left(\frac{\gamma_{\rm d}}{\gamma+\gamma_{\rm d}}\frac{t_{\rm ini}}{t}\right) \\ & + \frac{c_{\rm c}}{\epsilon_{\rm c}}(\gamma+\gamma_{\rm d})^{2\chi_{\rm c}-3}\left[f_{\rm c}\!\left(\frac{\gamma_{\rm d}}{\gamma+\gamma_{\rm d}}\right) - \left(\frac{\gamma+\gamma_{\rm d}}{\gamma_{\rm c}+\gamma_{\rm d}}\right)^{\epsilon_{\rm c}} f_{\rm c}\!\left(\frac{\gamma_{\rm d}}{\gamma_{\rm c}+\gamma_{\rm d}}\right)\right]. \end{aligned} \tag{3.27}$$

In these equations, we have defined

$$f(x) \equiv {}_2\mathrm{F}_1(3-2\chi,\epsilon;\epsilon+1;x)\,, \qquad f_\mathrm{c}(x) \equiv {}_2\mathrm{F}_1(3-2\chi_\mathrm{c},\epsilon_\mathrm{c};\epsilon_\mathrm{c}+1;x)\,. \tag{3.28}$$

with ${}_2\mathrm{F}_1(a,b;c;x)$ being the Gauss hypergeometric function, and

$$\epsilon \equiv 3\nu - 2\chi - 1, \qquad \epsilon_\mathrm{c} \equiv 3\nu - 2\chi_\mathrm{c} - 1. \tag{3.29}$$

The above solution is valid provided one waits long enough for some transient domains to disappear[6]. For completeness, the full solution including the transients is presented in the Appendix 3.A. Let us stress that these equations become singular for $\epsilon = 0$, which corresponds to $\chi = \chi_\mathrm{crit}$, and that case must be treated separately, see Section 3.2.5.

The behaviour of the solution given by Eqs. (3.27) and (3.26) depends on whether $\chi < \chi_\mathrm{crit}$, which we refer to as the sub-critical case, or whether $\chi > \chi_\mathrm{crit}$, the super-critical one.

Sub-critical loop production function

As discussed in Section 3.2.2, the first term in the right-hand side of Eq. (3.26), which is determined from the initial loop distribution, vanishes if one waits long enough. For all positive values of ϵ, namely $\chi < \chi_\mathrm{crit}$, the last term in Eq. (3.26) is also a transient that asymptotically vanishes for $t \gg t_\mathrm{ini}$. At vanishing argument, the hypergeometric function converges to unity and the time dependence of this term indeed scales as $(t/t_\mathrm{ini})^{-\epsilon}$.

Hence, the Boltzmann equation for $\epsilon > 0$ predicts a scaling loop distribution for $\gamma \geq \gamma_\mathrm{c}$ given by

$$t^4\mathbf{n}(\gamma \geq \gamma_\mathrm{c}, t) = \frac{c}{\epsilon}\,(\gamma+\gamma_\mathrm{d})^{2\chi-3}\, f\!\left(\frac{\gamma_\mathrm{d}}{\gamma+\gamma_\mathrm{d}}\right). \tag{3.30}$$

For $\gamma \gg \gamma_\mathrm{d}$ the hypergeometric function tends to 1, and we recover the power-law distribution given in Eq. (3.8); it matches numerical simulations where gravitational effects are absent:

$$t^4\mathbf{n}(\gamma \gg \gamma_\mathrm{d}, t) \simeq \frac{c}{\epsilon}\,\gamma^{2\chi-3}. \tag{3.31}$$

Furthermore we can now predict the effects associated with *gravitational wave emission*. Taking the limit $\gamma \ll \gamma_\mathrm{d}$ (but still $\gamma > \gamma_\mathrm{c}$), one gets[7]

$$t^4\mathbf{n}(\gamma_\mathrm{c} < \gamma \ll \gamma_\mathrm{d}, t) \simeq \frac{c}{2-2\chi}\frac{\gamma^{2\chi-2}}{\gamma_\mathrm{d}}\,. \tag{3.33}$$

Notice that since we are in the regime $\chi < \chi_\mathrm{crit}$ we necessarily have $\chi < 1$. The only effect of gravitational wave emission onto the scaling loop distribution is to reduce the power law exponent by one unit in the domain $\gamma_\mathrm{c} < \gamma \ll \gamma_\mathrm{d}$ [122].

To see what are the effects of *gravitational wave backreaction* on the loop distribution, let us consider Eq. (3.27). As before, the first and third terms in the right-hand side of Eq. (3.27) are

[6] In the matter era, the hypergeometric function simplifies to a polynomial expression, see Eq. (55) in Ref. [123].

[7] To derive this expression, we have expanded the hypergeometric function around unity [302]

$$f(x) \underset{1}{\sim} \frac{\Gamma(3\nu-2\chi)\Gamma(2\chi-2)}{\Gamma(3\nu-3)}x^{-\epsilon} + \frac{\epsilon}{2-2\chi}\,(1-x)^{2\chi-2}\,. \tag{3.32}$$

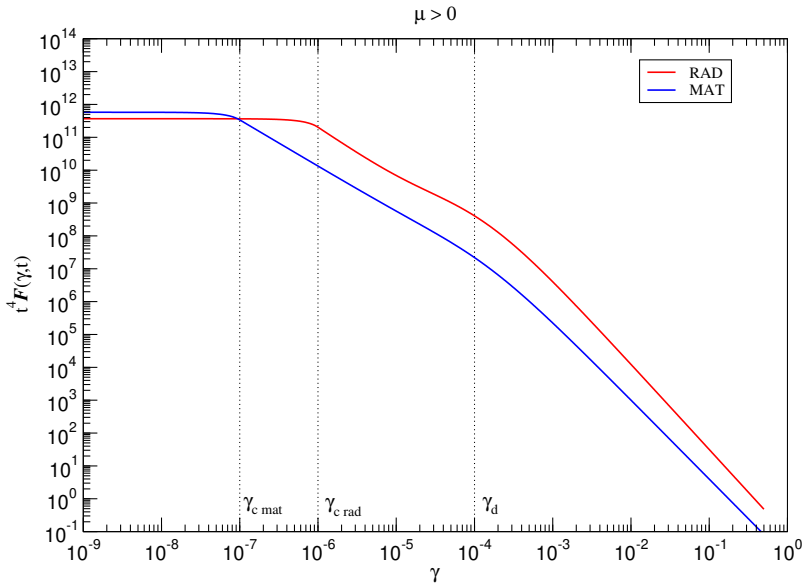

Figure 3.2: Scaling loop distribution in the radiation and matter era for $\epsilon > 0$, which corresponds to $\chi < (3\nu - 1)/2$. The values for $\gamma_{\rm d}$ and $\gamma_{\rm c}$ are illustrative only.

transient and only the second term and the fourth one survive. They are explicitly time-independent showing that this part of the loop distribution also reaches scaling. Using the expansion (3.32), the matching condition (3.23), and taking the limit $\gamma \ll \gamma_{\rm c}$ gives

$$\begin{aligned} t^4 \mathbf{n}(\gamma \ll \gamma_{\rm c}, t) &= c \left(\frac{1}{2-2\chi} + \frac{1}{2\chi_{\rm c} - 2} \right) \frac{\gamma_{\rm c}^{2\chi-2}}{\gamma_{\rm d}} + \mathcal{O}\left(\gamma_{\rm d}^{2\chi-3}\right) \\ &\simeq \frac{c}{2-2\chi} \frac{\gamma_{\rm c}^{2\chi-2}}{\gamma_{\rm d}} \,, \end{aligned} \tag{3.34}$$

where in the last step we have taken the limit for $\chi_{\rm c} \gg \chi$ and $\gamma_{\rm c} \ll \gamma_{\rm d}$. This expression makes clear that the details of the backreaction process, namely the values of $\chi_{\rm c}$, have only a weak effect on the final loop distribution [123]. Therefore, in the domain $\gamma < \gamma_{\rm c}$, the scaling loop distribution is flat.

The exact form for the scaling loop distribution is plotted in Fig. 3.2 for both the radiation and matter era, see also Eqs. (3.67) to (3.69). Notice that the value of $\gamma_{\rm c}$ is χ-dependent, and thus, even at constant $G\mu$, $\gamma_{\rm c}$ changes between radiation and matter.

Super-critical loop production function

As discussed in the Introduction, we now consider shallower loop production functions having $\epsilon < 0$, *i.e.* super-critical values of $\chi > \chi_{\rm crit}$. All solutions derived in Section 3.2.4 are regular in this limit, and we can straightforwardly use Eqs. (3.26) and (3.27).

In the domain $\gamma \geq \gamma_{\rm c}$, neglecting the first term in the right-hand side of Eq. (3.26) for the aforementioned reasons, we see that the third term (which was a transient for $\epsilon > 0$) is now becoming

a growing function of time as it scales as $(t/t_{\rm ini})^{-\epsilon}$. Therefore, for $t \gg t_{\rm ini}$, and for all values of $\gamma \geq \gamma_{\rm c}$, the hypergeometric function that multiplies $(t/t_{\rm ini})^{-\epsilon}$ in Eq. (3.26) approaches unity and one gets

$$t^4\mathbf{n}(\gamma \geq \gamma_{\rm c}, t) \simeq -\frac{c}{\epsilon}\left(\gamma+\gamma_{\rm d}\right)^{2\chi-3}\left[-f\left(\frac{\gamma_{\rm d}}{\gamma+\gamma_{\rm d}}\right)+\left(\frac{t}{t_{\rm ini}}\right)^{-\epsilon}\right], \tag{3.35}$$

which is not scaling! Another feature of this solution is that, taking the limit $\gamma_{\rm c} \leq \gamma \ll \gamma_{\rm d}$, one has

$$t^4\mathbf{n}(\gamma_{\rm c} \leq \gamma \ll \gamma_{\rm d}, t) \simeq -\frac{c}{\epsilon}\gamma_{\rm d}^{2\chi-3}\left[-\frac{\epsilon}{2-2\chi}\left(\frac{\gamma}{\gamma_{\rm d}}\right)^{2\chi-2}+\left(\frac{t}{t_{\rm ini}}\right)^{-\epsilon}\right]. \tag{3.36}$$

The solution only exhibits the $\gamma^{2\chi-2}$ power-law transiently. As soon as the growing term $(t/t_{\rm ini})^{-\epsilon}$ takes over, the loop distribution becomes flat and incessantly grows with time. Notice that because $\epsilon < 0$, positiveness of the loop distribution still implies that $c > 0$ because it is now dominated by the terms $(t/t_{\rm ini})^{-\epsilon}$. Equation (3.23) implies $c_{\rm c} > 0$ as well.

The solution in the domain $\gamma < \gamma_{\rm c}$ presents the same pathology, namely, the fourth term of Eq. (3.27), which is a transient for $\epsilon > 0$, now becomes dominant and one gets for $\gamma \ll \gamma_{\rm c}$

$$t^4\mathbf{n}(\gamma \ll \gamma_{\rm c}, t) \simeq -\frac{c}{\epsilon}\gamma_{\rm d}^{2\chi-3}\left[-\left(\frac{\epsilon}{2-2\chi}+\frac{\epsilon}{2\chi_{\rm c}-2}\right)\left(\frac{\gamma_{\rm c}}{\gamma_{\rm d}}\right)^{2\chi-2}+\left(\frac{t}{t_{\rm ini}}\right)^{-\epsilon}\right], \tag{3.37}$$

which is flat and smoothly connects to the solution (3.36) at $\gamma = \gamma_{\rm c}$.

In Fig. 3.3, we have plotted the exact solutions at various successive redshifts showing the non-scaling behaviour of the super-critical cases, $\chi > \chi_{\rm crit}$. The time divergence ends up washing out the change in slope of the loop distribution between $\gamma_{\rm c}$ and $\gamma_{\rm d}$. But scaling is lost, and we have an incessantly growing number density of loops at all scales.

Because Eq. (3.35) is actually valid in the regime probed by numerical simulations, this behaviour not being observed, we conclude that deeply super-critical loop production functions are unlikely to be physical. Of course, one cannot exclude the possibility that $\epsilon < 0$ but very close to zero (hence χ close to its critical value $\chi_{\rm c}$), since the time-dependence of Eq. (3.35) would hardly remain visible in time-limited numerical simulations while being relevant on cosmological time-scales. We now turn to the critical case itself, $\epsilon = 0$.

3.2.5 Critical loop production function

None of the solutions of Section 3.2.4 are valid for $\epsilon = 0$. Hence, we return to the general solution (3.15) where, using Eq. (3.20) with $\chi = \chi_{\rm crit}$ given in Eq. (3.7), one has

$$\mathcal{S}(\gamma) = c\,\gamma^{3\nu-4}\Theta(\gamma-\gamma_{\rm c}) + c_{\rm c}\,\gamma^{2\chi_{\rm c}-3}\Theta(\gamma_{\rm c}-\gamma)\,. \tag{3.38}$$

Here we have used the equality $2\chi_{\rm crit} - 3 = 3\nu - 4$. As before, the initial condition at $t = t_{\rm ini}$ and continuity of the solution at $\gamma = \gamma_{\rm c}$, which is enforced by Eq. (3.38), completely fix the solution of Eq. (3.15). We still find a complete integral (see Ref. [302]) that is presented, in full, in the Appendix 3.A.2. Below, we report only the parts relevant for our discussion. In the domain $\gamma \geq \gamma_{\rm c}$, one has

$$t^4\mathbf{n}(\gamma \geq \gamma_{\rm c}, t) = t^4\mathbf{n}_{\rm ini}(\gamma, t) + c(\gamma+\gamma_{\rm d})^{3\nu-4}\left[g\left(\frac{\gamma_{\rm d}}{\gamma+\gamma_{\rm d}}\right)-g\left(\frac{\gamma_{\rm d}}{\gamma+\gamma_{\rm d}}\frac{t_{\rm ini}}{t}\right)\right], \tag{3.39}$$

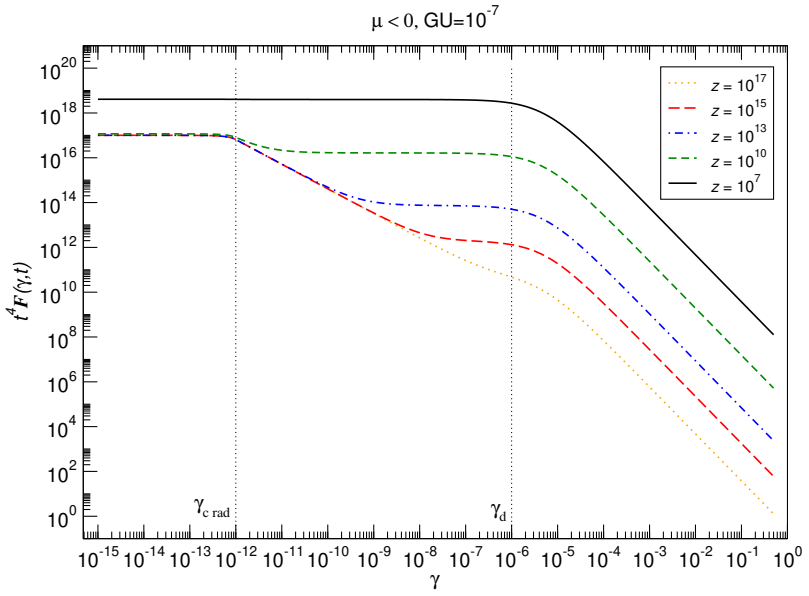

Figure 3.3: Growing loop distribution generated by a super-critical loop production function having $\chi = 0.45$ during the radiation era. The string tension has been set to $G\mu = 10^{-7}$ and the initial conditions are arbitrarily set at $z_{\rm ini} = 10^{18}$ with $\mathcal{N}_{\rm ini}(\ell) = 0$ and $c = 0.14$. At redshift $z = 10^7$, the change of shape associated with gravitational wave backreaction becomes washed out by the number loops which diverges with time.

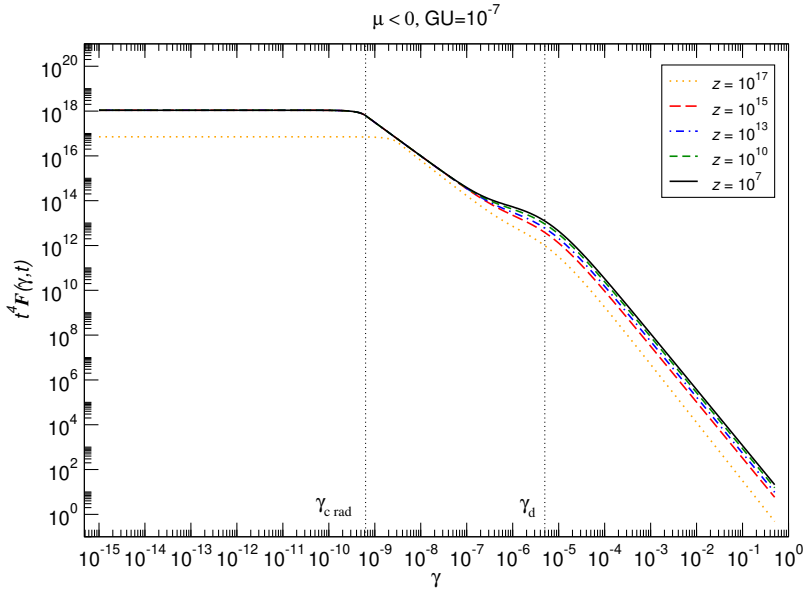

Figure 3.4: Loop number density distribution at various redshifts for a critical loop production function having $\chi_{\rm r} = \chi_{\rm crit} = 0.25$. The network is assumed to be formed at $z_{\rm ini} = 10^{18}$ and $c = 0.03$. At redshift $z = 10^{17}$, the loop distribution is not yet fully relaxed from the initial conditions. For later redshifts, $z < 10^{15}$, the non-scaling logarithmic divergence becomes clearly visible for all loops larger than the gravitational wave emission scale, $\gamma \geq \gamma_{\rm d}$. The smaller ones, having $\gamma < \gamma_{\rm d}$, remain in a transient scaling for most of the cosmological evolution, until the non-scaling behaviour takes over (see text).

and in the domain $\gamma < \gamma_{\rm c}$, the solution reads

$$\begin{aligned} t^4\mathbf{n}(\gamma<\gamma_{\rm c},t) &= t^4\mathbf{n}_{\rm ini}(\gamma,t) \\ &+ \frac{c_{\rm c}}{\epsilon_{\rm c}}(\gamma+\gamma_{\rm d})^{2\chi_{\rm c}-3}\left[f_{\rm c}\left(\frac{\gamma_{\rm d}}{\gamma+\gamma_{\rm d}}\right)-\left(\frac{\gamma+\gamma_{\rm d}}{\gamma_{\rm c}+\gamma_{\rm d}}\right)^{\epsilon_{\rm c}}f_{\rm c}\left(\frac{\gamma_{\rm d}}{\gamma_{\rm c}+\gamma_{\rm d}}\right)\right] \\ &+ c(\gamma+\gamma_{\rm d})^{3\nu-4}\left[g\left(\frac{\gamma_{\rm d}}{\gamma_{\rm c}+\gamma_{\rm d}}\right)-g\left(\frac{\gamma_{\rm d}}{\gamma+\gamma_{\rm d}}\frac{t_{\rm ini}}{t}\right)\right]. \end{aligned} \tag{3.40}$$

The function $g(x)$ is ν-dependent. In the radiation era, for $\nu = 1/2$, it reads

$$g_{\rm rad}(x) \equiv \ln\left(\frac{1-\sqrt{1-x}}{1+\sqrt{1-x}}\right)+\frac{2}{3}\frac{4-3x}{(1-x)^{3/2}}\,, \tag{3.41}$$

while in the matter era, for $\nu = 2/3$,

$$g_{\rm mat}(x) \equiv \frac{1}{1-x}\ln\left(\frac{1-x}{x}\right). \tag{3.42}$$

As before, neglecting the terms associated with $\mathcal{N}_{\rm ini}$, and taking the limit $t \gg t_{\rm ini}$, Eq. (3.39) can be further expanded for $\gamma \gg \gamma_{\rm d}$ as

$$t^4\mathbf{n}(\gamma\gg\gamma_{\rm d},t) \simeq c\,\gamma^{3\nu-4}\ln\left(\frac{t}{t_{\rm ini}}\right), \tag{3.43}$$

for both the radiation and matter eras. As a result, the critical case $\chi = \chi_{\rm crit}$ suffers from the same problems as the super-critical ones: the loop number distribution never reaches a scaling regime. For $\epsilon = 0$, the power-law exponent is $3\nu - 4 = 2\chi_{\rm crit} - 3$ and smoothly connects to its sub- and super-critical values. Let us notice however that the time divergence is logarithmic, and therefore, could very well remain undetected in numerical simulations while being quite relevant on cosmological time-scales. The limit $\gamma_{\rm c} \leq \gamma \ll \gamma_{\rm d}$ gives

$$t^4\mathbf{n}(\gamma_{\rm c}\leq\gamma\ll\gamma_{\rm d},t) \simeq c\,\gamma_{\rm d}^{3\nu-4}\left[\frac{1}{3-3\nu}\left(\frac{\gamma}{\gamma_{\rm d}}\right)^{3\nu-3}+\ln\left(\frac{t}{t_{\rm ini}}\right)\right], \tag{3.44}$$

which, up to the logarithmic divergence, is in all points similar to Eq. (3.36). As for the super-critical case, in the future infinity limit $t/t_{\rm ini} \to \infty$, the dependence in γ disappears, the loop distribution becomes flat, grows, and never reaches scaling. However, because the divergence is only logarithmic in time, even on cosmological time scales, the first term can remain dominant. In this situation, we are in presence of a very long transient scaling in the domain $\gamma \ll \gamma_{\rm d}$.

Finally, for the small loops $\gamma \ll \gamma_{\rm c}$, and assuming $\gamma_{\rm c} \ll \gamma_{\rm d}$, we can expand Eq. (3.40) at large times $t \gg t_{\rm ini}$. We get

$$\begin{aligned} t^4\mathbf{n}(\gamma\ll\gamma_{\rm c},t) &\simeq \frac{c_{\rm c}}{2\chi_{\rm c}-2}\frac{\gamma_{\rm c}^{2\chi_{\rm c}-2}}{\gamma_{\rm d}}+c\gamma_{\rm d}^{3\nu-4}\left[\frac{1}{3-3\nu}\left(\frac{\gamma_{\rm c}}{\gamma_{\rm d}}\right)^{3\nu-3}+\ln\left(\frac{t}{t_{\rm ini}}\right)\right] \\ &= c\,\gamma_{\rm d}^{3\nu-4}\left[\left(\frac{1}{3-3\nu}+\frac{1}{2\chi_{\rm c}-2}\right)\left(\frac{\gamma_{\rm c}}{\gamma_{\rm d}}\right)^{3\nu-3}+\ln\left(\frac{t}{t_{\rm ini}}\right)\right], \end{aligned} \tag{3.45}$$

Type	$\gamma < \gamma_{\rm c}$	$\gamma_{\rm c} < \gamma < \gamma_{\rm d}$	$\gamma > \gamma_{\rm d}$
Sub-critical $\epsilon > 0$	$\dfrac{c}{2-2\chi}\gamma_{\rm c}^{2\chi-2}\gamma_{\rm d}^{-1}$	$\dfrac{c}{2-2\chi}\gamma^{2\chi-2}\gamma_{\rm d}^{-1}$	$\dfrac{c}{\epsilon}\gamma^{2\chi-3}$
Critical $\epsilon = 0$	$c\,\gamma_{\rm d}^{3\nu-4}\ln\left(\dfrac{t}{t_{\rm ini}}\right)$	$c\,\gamma_{\rm d}^{3\nu-4}\ln\left(\dfrac{t}{t_{\rm ini}}\right)$	$c\,\gamma^{3\nu-4}\ln\left(\dfrac{t}{t_{\rm ini}}\right)$
Super-critical $\epsilon < 0$	$-\dfrac{c}{\epsilon}\gamma_{\rm d}^{2\chi-3}\left(\dfrac{t}{t_{\rm ini}}\right)^{-\epsilon}$	$-\dfrac{c}{\epsilon}\gamma_{\rm d}^{2\chi-3}\left(\dfrac{t}{t_{\rm ini}}\right)^{-\epsilon}$	$-\dfrac{c}{\epsilon}\gamma^{2\chi-3}\left(\dfrac{t}{t_{\rm ini}}\right)^{-\epsilon}$

Table 3.1: Asymptotic contributions to the loop number density assuming no infrared regularization. At late times, the critical and super-critical cases are non-scaling and the loop number density diverges. For the critical case, notice however that a transient scaling can take place in the domains $\gamma < \gamma_{\rm d}$ for most of the cosmological evolution (see text).

where the last step is obtained from Eq. (3.23), which ensures the continuity of the loop production function. Again, this is in all point similar to the super-critical case of Eq. (3.37) and smoothly connects to the domain $\gamma \geq \gamma_{\rm c}$. The logarithmic divergence will ultimately make the small loop number density grow, although the presence of the first term will strongly delay this process and one should expect a very long transient scaling.

Figure 3.4 shows the loop number density distribution in the radiation era as derived from the exact expression, Eqs. (3.73) to (3.75), for $G\mu = 10^{-7}$, and at various redshifts. Here again, $\mathcal{N}_{\rm ini} = 0$ has been assumed to clearly show the effects coming from the production function. The network is arbitrarily assumed to be formed at $z_{\rm ini} = 10^{18}$ and relaxation from the initial conditions takes place down to redshift $z = 10^{17}$. For redshifts $z \leq 10^{15}$, the domain $\gamma \geq \gamma_{\rm d}$ clearly exhibits the logarithmic divergence. The loops having $\gamma < \gamma_{\rm d}$ remain, however, in the transient scaling for essentially all the cosmological evolution.

3.2.6 Discussion

Critical and super-critical loop production functions, having $\chi \geq \chi_{\rm crit} = (3\nu - 1)/2$, yield a non-scaling and growing population of cosmic string loops. This results from the combination of various non-trivial effects acting together. For $\chi \geq \chi_{\rm crit}$, the loop production functions are shallower with respect to loop sizes than the sub-critical ones. Therefore, they produce, on site, relatively larger loops compared to the smaller ones. These larger loops will contribute to the final population of loops of given size since they incessantly shrink by gravitational wave emission. Similarly, at all times, loops of given size disappear by the same effect. The detailed balance of loops disappearing, being created on site, and being populated by shrunk larger loops is obviously χ-dependent and the overall result is precisely given by the solution of the Boltzmann equation (3.12). Taking shallower loop production functions clearly enhances the feeding by larger loops, at all scales. The critical value $\chi_{\rm crit}$ is the precise power-law exponent above which such an effect produces a non-stationary solution. We summarize our results in Table 3.1.

In striking contrast with the sub-critical case, we see that the critical and super-critical loop production functions induce non-scaling loop distributions. This is quite dramatic in the super-critical case as the number density of loops grows, on all scales, as $(t/t_{\rm ini})^{-\epsilon}$, with $\epsilon < 0$. The

situation for the critical case $\chi = \chi_{\rm crit}$ is, somehow, less catastrophic, as the divergence is only logarithmic in time. In particular, for most of the cosmologically relevant situations, we find that the loop number density remains in a transient scaling regime at small scales, for all $\gamma \ll \gamma_{\rm d}$. The number density of larger loops, having $\gamma \geq \gamma_{\rm d}$, is however logarithmically growing with time and never scales.

3.3 Possible infrared regularizations

In view of the previous discussion, a way to regularize (super-) critical loop production functions is to change their shape in some domains. As discussed in the Introduction, the PR model does not necessarily apply to super-horizon loops, the ones having $\gamma > \gamma_\infty$, and these seem to be precisely responsible for the time divergence. A possible regularization is therefore making a hard cut in the IR, namely postulating that the loop production function is exactly vanishing above some new IR scale, say $\gamma > \gamma_\infty$. Other regulator shapes are considered in Section 3.3.3.

We now consider the same PR loop production function as in Section 3.2 for $\gamma \leq \gamma_\infty$ but we now require that $t^4\mathcal{P}(\gamma > \gamma_\infty, t) = 0$ at all times. As a result, there is a new domain of solution for Eq. (3.12) in which one trivially finds

$$\mathbf{n}(\gamma \geq \gamma_\infty, t) = \mathbf{n}_{\rm ini}(\gamma, t). \tag{3.46}$$

The calculations are slightly longer than in Section 3.2 but do not present new difficulties. They are detailed in the Appendix 3.B. The introduction of a new scale at γ_∞ introduces various new transient domains in which the loop distribution $t^4\mathbf{n}$ grows for a while before becoming stationary. Ignoring these domains, the main changes can be summarized as follows.

The asymptotic solutions are given by those of the previous section *provided* we make the formal replacement

$$\frac{t}{t_{\rm ini}} \longrightarrow \frac{\gamma_\infty + \gamma_{\rm d}}{\gamma + \gamma_{\rm d}}\,. \tag{3.47}$$

This expression makes clear that all terms that were explicitly depending on $t/t_{\rm ini}$ are regularized to γ-dependent terms. As a result, the IR-regularized critical loop distribution reaches scaling, but it does no longer exhibit the same shape on large scales. In the following, we explicitly derive the induced distortions for the critical and super-critical case and discuss the impact of forcing an unneeded IR-regularization to the sub-critical loop production functions.

3.3.1 Critical loop production function

For critical loop production function $\chi = \chi_{\rm crit}$, after the disappearance of the transient domains (see Appendix 3.B), the loop distribution in the domain $\gamma \geq \gamma_{\rm c}$ (and $\gamma < \gamma_\infty$) reads

$$\begin{aligned} t^4\mathbf{n}(\gamma_{\rm c} \leq \gamma < \gamma_\infty, t) = {} & t^4\mathbf{n}_{\rm ini}(\gamma, t) \\ & + c(\gamma + \gamma_{\rm d})^{3\nu-4}\left[g\left(\frac{\gamma_{\rm d}}{\gamma + \gamma_{\rm d}}\right) - g\left(\frac{\gamma_{\rm d}}{\gamma_\infty + \gamma_{\rm d}}\right)\right], \end{aligned} \tag{3.48}$$

and in the domain $\gamma < \gamma_c$, one gets

$$\begin{aligned} t^4\mathbf{n}(\gamma<\gamma_c,t) &= t^4\mathbf{n}_{\rm ini}(\gamma,t) \\ &+ \frac{c_c}{\epsilon_c}(\gamma+\gamma_d)^{2\chi_c-3}\left[f_c\left(\frac{\gamma_d}{\gamma+\gamma_d}\right)-\left(\frac{\gamma+\gamma_d}{\gamma_c+\gamma_d}\right)^{\epsilon_c} f_c\left(\frac{\gamma_d}{\gamma_c+\gamma_d}\right)\right] \\ &+ c(\gamma+\gamma_d)^{3\nu-4}\left[g\left(\frac{\gamma_d}{\gamma_c+\gamma_d}\right)-g\left(\frac{\gamma_d}{\gamma_\infty+\gamma_d}\right)\right]. \end{aligned}$$

The logarithmic growth in time has disappeared, and the solutions are now scaling. Taking Eq. (3.48) in the limit $\gamma \gg \gamma_d$ and neglecting all terms associated with the initial conditions, one gets

$$t^4\mathbf{n}(\gamma\gg\gamma_d,t) \simeq c\,\gamma^{3\nu-4}\ln\left(\frac{\gamma_\infty}{\gamma}\right). \tag{3.49}$$

The limit $\gamma_c < \gamma \ll \gamma_d$ consistently gives

$$t^4\mathbf{n}(\gamma_c<\gamma\ll\gamma_d,t) = c\,\gamma_d^{3\nu-4}\left[\frac{1}{3-3\nu}\left(\frac{\gamma}{\gamma_d}\right)^{3\nu-3}+\ln\left(\frac{\gamma_d}{\gamma_\infty}\right)\right], \tag{3.50}$$

and the distribution is back to the scaling power law $\gamma^{3\nu-3}$.
Finally, small loops with $\gamma \ll \gamma_c \ll \gamma_d$ also scale with a flat distribution as

$$t^4\mathbf{n}(\gamma\ll\gamma_c,t) = c\,\gamma_d^{3\nu-4}\left[\left(\frac{1}{3-3\nu}+\frac{1}{2\chi_c-2}\right)\left(\frac{\gamma_c}{\gamma_d}\right)^{3\nu-3}+\ln\left(\frac{\gamma_d}{\gamma_\infty}\right)\right]. \tag{3.51}$$

In conclusion, the IR-regularization we have used solves the logarithmic time divergence of the loop distribution which now reaches scaling on all length scales. For $\gamma \ll \gamma_d$, Eqs. (3.50) and (3.51) compared to Eqs. (3.44) and (3.45) show that the regularization is neat, the dependence of the loop distribution with respect to γ is not affected. However, for $\gamma > \gamma_d$, the power law behaviour now receives a logarithmic correction. We therefore conclude that the critical loop production function, even regularized, exhibits an IR sensitivity.

3.3.2 Non-critical loop production function

The calculation follows in all points the one of Section 3.3.1 and applies to both sub- and super-critical cases, $\epsilon > 0$ and $\epsilon < 0$. The full solution is presented in the Appendix 3.B, and we focus below on the asymptotic behaviour only. For the purely IR domain, $\gamma > \gamma_\infty$, the solution is still given by Eq. (3.46), our IR-regulator assuming an exactly vanishing production function there. Again neglecting all transients, the solution in the domain $\gamma_c \le \gamma < \gamma_\infty$ reads

$$\begin{aligned} t^4\mathbf{n}(\gamma_c\le\gamma<\gamma_\infty,t) &= t^4\mathbf{n}_{\rm ini}(\gamma,t)+\frac{c}{\epsilon}(\gamma+\gamma_d)^{2\chi-3}f\left(\frac{\gamma_d}{\gamma+\gamma_d}\right) \\ &- \frac{c}{\epsilon}(\gamma+\gamma_d)^{3\nu-4}\left(\gamma_\infty+\gamma_d\right)^{-\epsilon} f\left(\frac{\gamma_d}{\gamma_\infty+\gamma_d}\right), \end{aligned} \tag{3.52}$$

while for $\gamma < \gamma_{\rm c}$ one obtains

$$\begin{aligned} t^4\mathbf{n}(\gamma_+ \leq \gamma < \gamma_{\rm c}, t) = t^4\mathbf{n}_{\rm ini}(\gamma, t) \\ + \frac{c_{\rm c}}{\epsilon_{\rm c}}(\gamma+\gamma_{\rm d})^{2\chi_{\rm c}-3}\left[f_{\rm c}\left(\frac{\gamma_{\rm d}}{\gamma+\gamma_{\rm d}}\right) - \left(\frac{\gamma+\gamma_{\rm d}}{\gamma_{\rm c}+\gamma_{\rm d}}\right)^{\epsilon_{\rm c}} f_{\rm c}\left(\frac{\gamma_{\rm d}}{\gamma_{\rm c}+\gamma_{\rm d}}\right)\right] \\ + \frac{c}{\epsilon}(\gamma+\gamma_{\rm d})^{3\nu-4}\left(\gamma_{\rm c}+\gamma_{\rm d}\right)^{-\epsilon} f\left(\frac{\gamma_{\rm d}}{\gamma_{\rm c}+\gamma_{\rm d}}\right) \\ - \frac{c}{\epsilon}(\gamma+\gamma_{\rm d})^{3\nu-4}\left(\gamma_{\rm d}+\gamma_\infty\right)^{-\epsilon} f\left(\frac{\gamma_{\rm d}}{\gamma_\infty+\gamma_{\rm d}}\right). \end{aligned} \tag{3.53}$$

Here again, the IR cut in the loop production functions can be viewed as the same formal replacement as (3.47). Let us now discuss separately the physical consequences for the sub- and super-critical loop production functions, and we start by the simplest case which is the sub-critical one.

Sub-critical case

Even if sub-critical loop production functions produce a scaling loop distribution without any regularization, one may wonder whether forcing the (unnecessary, for scaling!) cut at $\gamma > \gamma_\infty$ can significantly change the shape of the scaling loop distribution.

At late times, and for sub-critical production functions, $\epsilon > 0$, we can take the limit $\gamma \gg \gamma_{\rm d}$ of (3.52)

$$t^4\mathbf{n}(\gamma_{\rm d} \ll \gamma < \gamma_\infty, t) \simeq \frac{c}{\epsilon}\gamma^{2\chi-3}\left[1 - \left(\frac{\gamma}{\gamma_\infty}\right)^{\epsilon}\right]. \tag{3.54}$$

Compared to Eq. (3.31), we see that the correction term $(\gamma/\gamma_\infty)^\epsilon$ induced by the IR-regularization has an effect only for $\gamma \simeq \gamma_\infty$ and becomes rapidly negligible as soon as $\gamma < \gamma_\infty$. For loops having $\gamma \ll \gamma_{\rm d}$, we get

$$t^4\mathbf{n}(\gamma_{\rm c} \leq \gamma \ll \gamma_{\rm d}, t \geq t_{\rm c}) \simeq \frac{c}{2-2\chi}\frac{\gamma^{2\chi-2}}{\gamma_{\rm d}}, \tag{3.55}$$

the correction $(\gamma_{\rm d}/\gamma_\infty)^\epsilon$ can always be safely ignored. Finally, for loops smaller than the GW backreaction length, $\gamma \ll \gamma_{\rm c}$, we recover Eq. (3.34). The IR-correction added corresponds to the fourth term of Eq. (3.53) and remains again always negligible for $\epsilon > 0$.

We therefore conclude that sub-critical loop production functions yield scaling loop distributions that are immune to the IR behaviour of the network.

Super-critical case

For super-critical values of $\chi > \chi_{\rm crit}$, we have $\epsilon < 0$ and most of the arguments applying for $\epsilon > 0$ are now reversed. For instance, the limit $\gamma_{\rm d} \ll \gamma < \gamma_\infty$ becomes

$$t^4\mathbf{n}(\gamma_{\rm d} \ll \gamma < \gamma_\infty, t) \simeq -\frac{c}{\epsilon}\gamma^{2\chi-3}\left[\left(\frac{\gamma_\infty}{\gamma}\right)^{-\epsilon} - 1\right] \simeq -\frac{c}{\epsilon}\gamma_\infty^{-\epsilon}\,\gamma^{3\nu-4}. \tag{3.56}$$

The time divergence of the loop distribution is solved but the power-law exponent has been changed from $2\chi - 3$ to $3\nu - 4$, see Eq. (3.35). For smaller loops, we get

$$t^4\mathbf{n}(\gamma_\mathrm{c} \leq \gamma \ll \gamma_\mathrm{d}, t) \simeq -\frac{c}{\epsilon}\gamma_\mathrm{d}^{2\chi-3}\left[-\frac{\epsilon}{2-2\chi}\left(\frac{\gamma}{\gamma_\mathrm{d}}\right)^{2\chi-2} + \left(\frac{\gamma_\infty}{\gamma_\mathrm{d}}\right)^{-\epsilon}\right]. \tag{3.57}$$

Since $\gamma_\infty/\gamma_\mathrm{d} \gg 1$, the IR cut is adversely introducing a new length scale! Thus, let us define γ_ir by

$$\gamma_\mathrm{ir} \equiv \left[\frac{-\epsilon}{(2-2\chi)\gamma_\infty^{-\epsilon}}\right]^{\frac{1}{2-2\chi}} \gamma_\mathrm{d}^{\frac{3-3\nu}{2-2\chi}}. \tag{3.58}$$

For $\gamma > \gamma_\mathrm{ir}$, Eq. (3.57) shows that the loop distribution is flat, the dependence in γ remains negligible compared to the constant term introduced by the regularization. On the contrary, for $\gamma < \gamma_\mathrm{ir}$, we recover a power-law behaviour as $\gamma^{2\chi-2}$. This new IR scale is relevant only if $\gamma_\mathrm{ir} > \gamma_\mathrm{c}$, which is model- and regularization-dependent. Nonetheless, if we assume the dependency in $G\mu$ for γ_d given in Eq. (3.4),

$$\gamma_\mathrm{ir} \propto (G\mu)^{\frac{3-3\nu}{2-2\chi}}, \tag{3.59}$$

and using Eq. (3.21)

$$\frac{\gamma_\mathrm{ir}}{\gamma_\mathrm{c}} \propto (G\mu)^{\frac{4\chi^2-2\chi+1-3\nu}{2-2\chi}}. \tag{3.60}$$

This defines a particular value for χ, namely

$$\chi_\mathrm{IR} \equiv \frac{1+\sqrt{12\nu-3}}{4}, \tag{3.61}$$

whose numerical value in the radiation era is $\chi_\mathrm{IR} \simeq 0.683$ and $\chi_\mathrm{IR} \simeq 0.809$ for the matter era. For all values $\chi_\mathrm{crit} < \chi < \chi_\mathrm{IR}$, the exponent of Eq. (3.60) is negative. For $G\mu$ small enough, we generically have $\gamma_\mathrm{ir} > \gamma_\mathrm{c}$. As a result, the regularized loop distribution is now scaling but exhibits a new plateau for $\gamma_\mathrm{ir} < \gamma < \gamma_\mathrm{d}$, which smoothly connects to the $\gamma^{2\chi-2}$ behaviour in the domain $\gamma_\mathrm{c} \leq \gamma < \gamma_\mathrm{ir}$. For larger values of $\chi > \chi_\mathrm{IR}$ (and deeper negative values of ϵ), only the plateau exists in the whole domain $\gamma_\mathrm{c} \leq \gamma < \gamma_\mathrm{d}$, the amplitude of the constant term $(\gamma_\infty/\gamma_\mathrm{d})^{-\epsilon}$ is so large that it erases any features that could be associated with the scale of gravitational wave emission. This situation is actually reminiscent with the time-divergent behaviour discussed in Section 3.2.4.

Finally, for the very small loops, $\gamma \ll \gamma_\mathrm{c}$, with $\gamma_\mathrm{c} \ll \gamma_\mathrm{d}$, the loop distribution reads

$$t^4\mathbf{n}(\gamma \ll \gamma_\mathrm{c}, t \geq t_\mathrm{c}) \simeq c\left(\frac{1}{2-2\chi} + \frac{1}{2\chi_\mathrm{c}-2}\right)\frac{\gamma_\mathrm{c}^{2\chi-2}}{\gamma_\mathrm{d}} - \frac{c}{\epsilon}\gamma_\infty^{-\epsilon}\gamma_\mathrm{d}^{3\nu-4} + \mathcal{O}\Big(\gamma_\mathrm{d}^{2\chi-3}\Big). \tag{3.62}$$

It is scaling with a plateau behaviour. The amplitude of the plateau is either given by the first term, the one varying as $\gamma_\mathrm{c}^{2\chi-2}/\gamma_\mathrm{d}$, or the second term which is proportional to $\gamma_\infty^{-\epsilon}\gamma_\mathrm{d}^{3\nu-4}$. That depends on their relative amplitude. Neglecting the terms in χ_c, which are sub-dominant, the ratio $\mathcal{R}$ of the first to second term in the right-hand side of Eq. (3.62) simplifies to

$$\mathcal{R} = \left(\frac{\gamma_\mathrm{ir}}{\gamma_\mathrm{c}}\right)^{2-2\chi}. \tag{3.63}$$

Consistently with the behaviour in the $\gamma > \gamma_\mathrm{c}$ domains, for $\chi_\mathrm{crit} < \chi < \chi_\mathrm{IR}$, one always has $\mathcal{R} \gg 1$ and the regularization effects are small. Only for $\chi > \chi_\mathrm{IR}$, the plateau at $\gamma < \gamma_\mathrm{c}$ is dominated by the regulator and continuously matches the one at $\gamma > \gamma_\mathrm{c}$.

We conclude that IR-regularization of super-critical loop production functions solves their time-divergence, but this has the consequence of significantly modifying the shape of the actual scaling distribution. The results are therefore strongly IR-sensitive.

3.3.3 Influence of a power-law IR-regularization

Considering the strong dependence of the loop number density on the parameter γ_∞, one might ask whether the shape of the IR-cutoff has an additional influence on the results. To perform this analysis, we introduce an additional source term $c_\infty \gamma^{2\chi_\infty - 3}\Theta(\gamma - \gamma_\infty)$ to the collision term of the Boltzmann equation (3.20) and, neglecting all possible transients, compute its contribution, say $t^4\mathbf{n}_\infty$, to the asymptotic loop number density. For this source term to be a well-behaved IR-regulator, it has to fulfil two conditions. First $\epsilon_\infty > 0$ otherwise we expect this term to present the same time-divergent behaviour as the critical and super-critical distributions. Then, we should have $c_\infty = c\gamma_\infty^{2(\chi-\chi_\infty)}$ for the loop production function to be continuous in γ_∞. Then the contribution of such a power-law cutoff is

$$\begin{aligned} t^4\mathbf{n}_\infty(\gamma < \gamma_\infty) = &\frac{c_\infty}{\epsilon_\infty}\frac{(\gamma+\gamma_\mathrm{d})^{3\nu-4}}{(\gamma_\infty+\gamma_\mathrm{d})^{\epsilon_\infty}} f_\infty\left(\frac{\gamma_\mathrm{d}}{\gamma_\infty+\gamma_\mathrm{d}}\right) \\ &- \frac{c_\infty}{\epsilon_\infty}(\gamma+\gamma_\mathrm{d})^{2\chi_\infty-3}\left(\frac{t_\mathrm{ini}}{t}\right)^{\epsilon_\infty} f_\infty\left(\frac{\gamma_\mathrm{d}}{\gamma+\gamma_\mathrm{d}}\frac{t_\mathrm{ini}}{t}\right), \end{aligned} \tag{3.64}$$

where

$$f_\infty(x) \equiv {}_2\mathrm{F}_1\left(3-2\chi_\infty, \epsilon_\infty; \epsilon_\infty+1; x\right). \tag{3.65}$$

The condition $\epsilon_\infty > 0$ ensures that all time-dependent contributions are suppressed at late-times. Under the assumption that $\gamma_\mathrm{d} \ll \gamma_\infty$, the contribution to the scaling loop number density coming from the power-law cutoff is

$$t^4\mathbf{n}_\infty(\gamma < \gamma_\infty) = c_\infty \frac{(\gamma+\gamma_\mathrm{d})^{3\nu-4}}{\epsilon_\infty \gamma_\infty^{\epsilon_\infty}} = c\frac{(\gamma+\gamma_\mathrm{d})^{3\nu-4}}{\epsilon_\infty \gamma_\infty^{\epsilon}}. \tag{3.66}$$

This additional part generically contributes and can modify the shape of the loop distribution, as for instance it would modify the value of γ_ir for the super-critical case in Eq. (3.58). However, for large enough values of ϵ_∞, namely for $\epsilon_\infty \gg |\epsilon|$, it can safely be neglected with respect to the one computed earlier. As a result, the IR-regularization effects we have found in the previous section are relatively generic in the sense that they are not simply induced by the choice of an infinitely sharp cut in the LPF but rather by suppressing the production of large loops.

3.4 Conclusions

The aim of this paper has been to carry out an exhaustive study of the effect of the loop production function on the cosmological distribution of loops. As explained in the Introduction, numerical simulations of Nambu-Goto cosmic string networks are not currently able to capture some important physical effects at very small scales, for instance GW emission and its backreaction effects. Hence, determining the loop distribution, by construction, requires an interplay between numerical results (valid for larger loops where the extra physics should be negligible) and analytical modelling.

Type	$\gamma < \gamma_{\rm c}$	$\gamma_{\rm c} < \gamma < \gamma_{\rm ir}$	$\gamma_{\rm ir} < \gamma < \gamma_{\rm d}$	$\gamma > \gamma_{\rm d}$
Sub-critical	$\frac{c}{2-2\chi}\gamma_{\rm c}^{2\chi-2}\gamma_{\rm d}^{-1}$	$\frac{c}{2-2\chi}\gamma^{2\chi-2}\gamma_{\rm d}^{-1}$	–	$\frac{c}{\epsilon}\gamma^{2\chi-3}$
IR Critical	$\frac{c}{3-3\nu}\gamma_{\rm c}^{3\nu-3}\gamma_{\rm d}^{-1}$	$\frac{c}{3-3\nu}\gamma^{3\nu-3}\gamma_{\rm d}^{-1}$	–	$c\gamma^{3\nu-4}\ln\left(\frac{\gamma_\infty}{\gamma}\right)$
IR Super-critical with $\chi < \chi_{\rm IR}$	$\frac{c}{2-2\chi}\gamma_{\rm c}^{2\chi-2}\gamma_{\rm d}^{-1}$	$\frac{c}{2-2\chi}\gamma^{2\chi-2}\gamma_{\rm d}^{-1}$	$-\frac{c}{\epsilon}\gamma_\infty^{-\epsilon}\gamma_{\rm d}^{3\nu-4}$	$-\frac{c}{\epsilon}\gamma_\infty^{-\epsilon}\gamma^{3\nu-4}$
IR Super-critical with $\chi > \chi_{\rm IR}$	$-\frac{c}{\epsilon}\gamma_\infty^{-\epsilon}\gamma_{\rm d}^{3\nu-4}$	$-\frac{c}{\epsilon}\gamma_\infty^{-\epsilon}\gamma_{\rm d}^{3\nu-4}$	$-\frac{c}{\epsilon}\gamma_\infty^{-\epsilon}\gamma_{\rm d}^{3\nu-4}$	$-\frac{c}{\epsilon}\gamma_\infty^{-\epsilon}\gamma^{3\nu-4}$

Table 3.2: Asymptotic contributions to the loop number density assuming a "strong" enough infrared cutoff. With this assumption, both critical and super-critical loop number densities scale with time but their shape is modified compared to the unregularized ones (see Table 3.1).

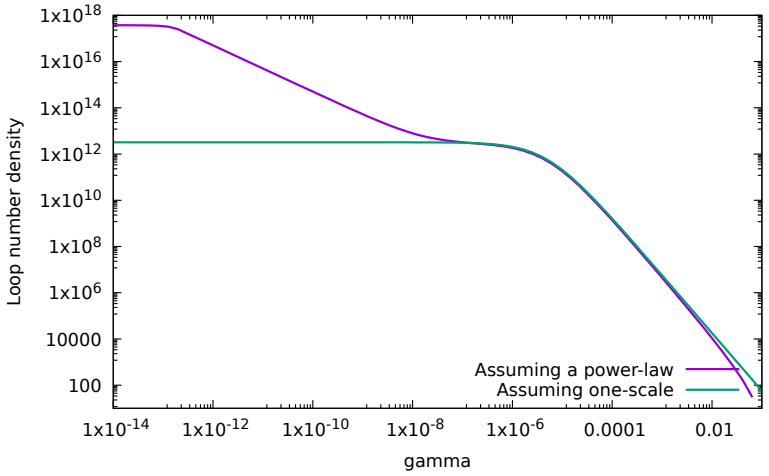

Figure 3.5: Difference between loop distributions in the radiation era generated by a Dirac distribution LPF (green lower curve) and a super-critical, IR-regularized, Polchinski-Rocha one (purple top curve). Given a super-critical power-law loop production function, one can reproduce the large scale behaviour of the loop distribution with a Dirac distribution for the loop production function (see Section 3.2.2). Doing so, one loses the small-scale behaviour of the loop distribution. For illustration purposes, we have chosen $G\mu = 10^{-7}$, $c \simeq 0.25$ and $\gamma_\infty = 0.1$ for the super-critical LPF and $c \simeq 5.7$ for the Dirac distribution.

The analytical tool used to solve for the loop distribution is the Boltzmann equation (3.20). On the one hand, we have shown that very different LPF, namely, a Dirac distribution motivated by the one-scale model, and a sub-critical Polchinski-Rocha power-law distribution ($\chi < \chi_{\rm crit}$) taking into account the small-scale structure built up on the strings, can give rise to a scaling, power-law, distribution on large scales, albeit with different power-law exponents. On the other hand, we have found that the actual value of the power-law exponent, *i.e.*, the value of χ with respect to $\chi_{\rm crit} = (3\nu - 1)/2$, produces very different behaviours. Critical and super-critical LPFs ($\chi \geq \chi_{\rm crit}$) lead to time-divergent loop distributions, which do not scale. The critical case however exhibits only a logarithmic growth for large loops, $\gamma \geq \gamma_{\rm d}$, and a very long transient scaling for the smaller ones, $\gamma < \gamma_{\rm d}$, that can last longer than the age of the universe.

The divergent behaviour of the critical and super-critical cases has been traced back to a relative over-production of large loops with respect to small loops, and we have shown that it can be regularized by arbitrarily assuming that the PR loop production function vanishes above some length scale γ_∞. We find, however, that although such an IR regularization fixes the time divergence, it is also changing the shape of the loop distribution. For this reason, we conclude that both the critical and super-critical LPF are genuinely IR-sensitive. For the critical case, we find that the large loop distribution acquires a new logarithmic dependence in γ (again for $\gamma \geq \gamma_{\rm d}$). On the small scales $\gamma < \gamma_{\rm d}$, the predictions are all very different and depend on both the PR exponent χ and on the IR regulator. The results of our study are summarized in Tables 3.1 and 3.2, where we give the asymptotic contributions to the loop number density on all scales γ depending on the value of the parameter $\epsilon \equiv 3\nu - 2\chi - 1$ (it vanishes for $\chi = \chi_{\rm crit}$). Let us notice that for extreme values of $G\mu$, and times close to the transition from the radiation to the matter era, these results may not apply and one should rely on the complete solutions given in the appendices.

It is interesting to observe from the last row of Table 3.2, that in the super-critical case only and assuming an IR cutoff, the obtained distribution for large $\gamma \geq \gamma_{\rm d}$ is essentially identical to that obtained from assuming a Dirac distribution for the LPF. In particular, for large γ there is a $-5/2$ power-law in the radiation era and -2 power-law in the matter era, which are the values for the exponents that we have obtained in Section 3.2.2. At the same time, both distributions are completely different on smaller scales. This is illustrated in Fig. 3.5.

In this paper, following Ref. [123], we have also introduced a small distance scale $\gamma_{\rm c}$ below which gravitational backreaction is expected to be important. Generically, for $\gamma_{\rm c} \ll \gamma_{\rm d}$, and for all values of χ, the amplitude of the loop distribution at small $\gamma < \gamma_{\rm c}$ is enhanced relative to the Dirac distribution LPF, and, as discussed in Ref. [90], this leads to observational consequences on the SGWB. Another interesting feature we have not discussed in the main text concern the various transient domains associated with the IR regularization. They are excited soon after the network is created, but also during the transition from the radiation to matter era. As such, they may also lead to interesting phenomenological consequences, in particular regarding a gravitational wave signature.

3.A Complete solutions

In this appendix, we give the explicit expressions of the solution of the Boltzmann equation (3.12). Details of the calculation can be found in Refs. [123, 125] and we here simply report the results.

3.A.1 Non-critical loop production function

For the piecewise PR loop production function given in Eqs. (3.20) and (3.22), assuming $\chi \neq \chi_{\rm crit}$, one gets

$$\begin{aligned}
t^4\mathbf{n}(\gamma \geq \gamma_{\rm c}, t) = &\left(\frac{t}{t_{\rm ini}}\right)^4 \left(\frac{a_{\rm ini}}{a}\right)^3 t_{\rm ini}^4 \mathcal{N}_{\rm ini}\left\{\left[\gamma + \gamma_{\rm d}\left(1 - \frac{t_{\rm ini}}{t}\right)\right] t\right\} \\
&+ \frac{c}{\epsilon}(\gamma+\gamma_{\rm d})^{2\chi-3} f\!\left(\frac{\gamma_{\rm d}}{\gamma+\gamma_{\rm d}}\right) \\
&- \frac{c}{\epsilon}(\gamma+\gamma_{\rm d})^{2\chi-3}\left(\frac{t}{t_{\rm ini}}\right)^{-\epsilon} f\!\left(\frac{\gamma_{\rm d}}{\gamma+\gamma_{\rm d}}\frac{t_{\rm ini}}{t}\right), \qquad (3.67)\\
t^4\mathbf{n}(\gamma_\tau \leq \gamma < \gamma_{\rm c}, t) = &\left(\frac{t}{t_{\rm ini}}\right)^4 \left(\frac{a_{\rm ini}}{a}\right)^3 t_{\rm ini}^4 \mathcal{N}_{\rm ini}\left\{\left[\gamma + \gamma_{\rm d}\left(1 - \frac{t_{\rm ini}}{t}\right)\right] t\right\} \\
&+ \frac{c_{\rm c}}{\epsilon_{\rm c}}(\gamma+\gamma_{\rm d})^{2\chi_{\rm c}-3}\left[f_{\rm c}\!\left(\frac{\gamma_{\rm d}}{\gamma+\gamma_{\rm d}}\right) - \left(\frac{\gamma+\gamma_{\rm d}}{\gamma_{\rm c}+\gamma_{\rm d}}\right)^{\epsilon_{\rm c}} f_{\rm c}\!\left(\frac{\gamma_{\rm d}}{\gamma_{\rm c}+\gamma_{\rm d}}\right)\right] \\
&+ \frac{c}{\epsilon}(\gamma+\gamma_{\rm d})^{3\nu-4}(\gamma_{\rm c}+\gamma_{\rm d})^{-\epsilon} f\!\left(\frac{\gamma_{\rm d}}{\gamma_{\rm c}+\gamma_{\rm d}}\right) \\
&- \frac{c}{\epsilon}(\gamma+\gamma_{\rm d})^{2\chi-3}\left(\frac{t}{t_{\rm ini}}\right)^{-\epsilon} f\!\left(\frac{\gamma_{\rm d}}{\gamma+\gamma_{\rm d}}\frac{t_{\rm ini}}{t}\right), \qquad (3.68)\\
t^4\mathbf{n}(0 < \gamma < \gamma_\tau, t) = &\left(\frac{t}{t_{\rm ini}}\right)^4 \left(\frac{a_{\rm ini}}{a}\right)^3 t_{\rm ini}^4 \mathcal{N}_{\rm ini}\left\{\left[\gamma + \gamma_{\rm d}\left(1 - \frac{t_{\rm ini}}{t}\right)\right] t\right\} \\
&+ \frac{c_{\rm c}}{\epsilon_{\rm c}}(\gamma+\gamma_{\rm d})^{2\chi_{\rm c}-3} f_{\rm c}\!\left(\frac{\gamma_{\rm d}}{\gamma+\gamma_{\rm d}}\right) \\
&- \frac{c_{\rm c}}{\epsilon_{\rm c}}(\gamma+\gamma_{\rm d})^{2\chi_{\rm c}-3}\left(\frac{t}{t_{\rm ini}}\right)^{-\epsilon_{\rm c}} f_{\rm c}\!\left(\frac{\gamma_{\rm d}}{\gamma+\gamma_{\rm d}}\frac{t_{\rm ini}}{t}\right). \qquad (3.69)
\end{aligned}$$

where we recap that

$$f(x) \equiv {}_2\mathrm{F}_1(3-2\chi, \epsilon; \epsilon+1; x)\,, \qquad f_{\rm c}(x) \equiv {}_2\mathrm{F}_1(3-2\chi_{\rm c}, \epsilon_{\rm c}; \epsilon_{\rm c}+1; x)\,. \qquad (3.70)$$

and

$$\epsilon \equiv 3\nu - 2\chi - 1, \qquad \epsilon_{\rm c} \equiv 3\nu - 2\chi_{\rm c} - 1. \qquad (3.71)$$

There is a transient domain for loops having γ smaller than

$$\gamma_\tau(t) \equiv (\gamma_{\rm c}+\gamma_{\rm d})\frac{t_{\rm ini}}{t} - \gamma_{\rm d}, \qquad (3.72)$$

which describes a virgin population of loops that started their evolution with a $\gamma < \gamma_{\rm c}$ and which have never been contaminated by shrunk loops produced at $\gamma > \gamma_{\rm c}$. This population of loops cannot exist forever and the domain disappears for times $t \geq t_\tau$ where $\gamma_\tau(t_\tau) = 0$.

3.A.2 Critical loop production function

In the critical case, the piecewise loop production function is given by Eq. (3.20) in the domain $\gamma \geq \gamma_{\rm c}$ with $\chi = \chi_{\rm crit}$, and Eq. (3.22) for $\gamma < \gamma_{\rm c}$ which is unchanged. The solution reads

$$\begin{aligned} t^4\mathbf{n}(\gamma \geq \gamma_{\rm c}, t) &= \left(\frac{t}{t_{\rm ini}}\right)^4 \left(\frac{a_{\rm ini}}{a}\right)^3 t_{\rm ini}^4 \mathcal{N}_{\rm ini}\left\{\left[\gamma + \gamma_{\rm d}\left(1 - \frac{t_{\rm ini}}{t}\right)\right] t\right\} \\ &\quad + c(\gamma+\gamma_{\rm d})^{3\nu-4}\left[g\left(\frac{\gamma_{\rm d}}{\gamma+\gamma_{\rm d}}\right) - g\left(\frac{\gamma_{\rm d}}{\gamma+\gamma_{\rm d}}\frac{t_{\rm ini}}{t}\right)\right], \qquad (3.73) \\ t^4\mathbf{n}(\gamma_\tau \leq \gamma < \gamma_{\rm c}, t) &= \left(\frac{t}{t_{\rm ini}}\right)^4 \left(\frac{a_{\rm ini}}{a}\right)^3 t_{\rm ini}^4 \mathcal{N}_{\rm ini}\left\{\left[\gamma + \gamma_{\rm d}\left(1 - \frac{t_{\rm ini}}{t}\right)\right] t\right\} \\ &\quad + \frac{c_{\rm c}}{\epsilon_{\rm c}}(\gamma+\gamma_{\rm d})^{2\chi_{\rm c}-3}\left[f_{\rm c}\left(\frac{\gamma_{\rm d}}{\gamma+\gamma_{\rm d}}\right) - \left(\frac{\gamma+\gamma_{\rm d}}{\gamma_{\rm c}+\gamma_{\rm d}}\right)^{\epsilon_{\rm c}} f_{\rm c}\left(\frac{\gamma_{\rm d}}{\gamma_{\rm c}+\gamma_{\rm d}}\right)\right] \\ &\quad + c(\gamma+\gamma_{\rm d})^{3\nu-4}\left[g\left(\frac{\gamma_{\rm d}}{\gamma_{\rm c}+\gamma_{\rm d}}\right) - g\left(\frac{\gamma_{\rm d}}{\gamma+\gamma_{\rm d}}\frac{t_{\rm ini}}{t}\right)\right], \qquad (3.74) \\ t^4\mathbf{n}(0 < \gamma < \gamma_\tau, t) &= \left(\frac{t}{t_{\rm ini}}\right)^4 \left(\frac{a_{\rm ini}}{a}\right)^3 t_{\rm ini}^4 \mathcal{N}_{\rm ini}\left\{\left[\gamma + \gamma_{\rm d}\left(1 - \frac{t_{\rm ini}}{t}\right)\right] t\right\} \\ &\quad + \frac{c_{\rm c}}{\epsilon_{\rm c}}(\gamma+\gamma_{\rm d})^{2\chi_{\rm c}-3} f_{\rm c}\left(\frac{\gamma_{\rm d}}{\gamma+\gamma_{\rm d}}\right) \\ &\quad - \frac{c_{\rm c}}{\epsilon_{\rm c}}(\gamma+\gamma_{\rm d})^{2\chi_{\rm c}-3}\left(\frac{t}{t_{\rm ini}}\right)^{-\epsilon_{\rm c}} f_{\rm c}\left(\frac{\gamma_{\rm d}}{\gamma+\gamma_{\rm d}}\frac{t_{\rm ini}}{t}\right), \qquad (3.75) \end{aligned}$$

where we recap that the first integral $g(x)$ is given by

$$g_{\rm rad}(x) \equiv \ln\left(\frac{1-\sqrt{1-x}}{1+\sqrt{1-x}}\right) + \frac{2}{3}\frac{4-3x}{(1-x)^{3/2}}, \qquad g_{\rm mat}(x) \equiv \frac{1}{1-x}\ln\left(\frac{1-x}{x}\right), \qquad (3.76)$$

in the radiation and matter era, respectively. Notice that the small scales transient, Eq. (3.75), is identical to Eq. (3.69). To ease comparison with the non-critical case, let us stress that for $\chi = \chi_{\rm crit}$, one has $\epsilon = 0$ and $2\chi_{\rm c} - 3 = 3\nu - 4$ such that the critical functional shape is smoothly interpolating between the sub- and super-critical solutions presented in Section 3.A.1.

3.B Sharp infrared regularization

The sharp IR-regularization consists in cutting the loop production function above some length scale γ_∞. Therefore, it is a piecewise function over three domains: for $\gamma < \gamma_{\rm c}$ it is given by Eq. (3.22), for $\gamma_{\rm c} \leq \gamma < \gamma_\infty$ by Eq. (3.20) and for $\gamma \geq \gamma_\infty$ it is vanishing. The new length scale γ_∞ introduces a new, time-dependent, length scale defined by

$$\gamma_+(t) \equiv (\gamma_{\rm d} + \gamma_\infty)\frac{t_{\rm ini}}{t} - \gamma_{\rm d}. \qquad (3.77)$$

Physically its meaning is the following: if we consider a loop which was created at time $t_{\rm ini}$ with the maximal possible size $\gamma_\infty t_{\rm ini}$, then at time t its length is $\ell_+ = \gamma_+ t$. Therefore, at time t, loops having $\gamma < \gamma_+(t)$ are not affected by the IR cutoff and the non-regularized solutions are still valid.

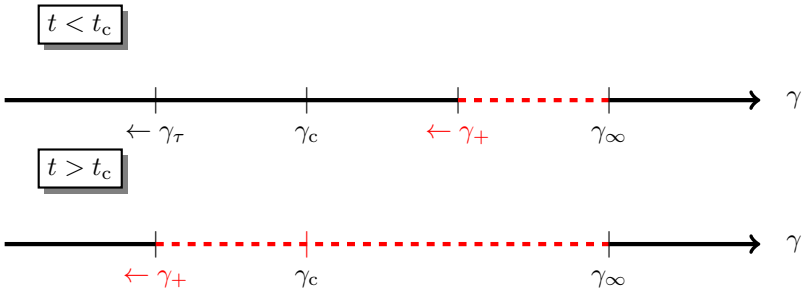

Figure 3.6: Schematic representation of the different domains of γ for $t < t_c$ and for $t > t_c$. The black regions are causally disconnected from the cutoff at γ_∞ such that the solutions are exactly the same as the non-regularized ones. On the contrary, this is not the case in the red dotted regions and one has to use the modified expression for $t^4\mathbf{n}(\gamma \geq \gamma_+, t)$ (see text).

On the contrary, the loop distribution for $\gamma > \gamma_+(t)$ has to be re-derived by solving the Boltzmann equation and satisfying the two continuity conditions at $\gamma = \gamma_c$ and $\gamma = \gamma_\infty$. In doing so, we must distinguish the cases for which $\gamma_+(t) > \gamma_c$ from those having $\gamma_+(t) < \gamma_c$. To this end, we define $t = t_c$ through $\gamma_+(t_c) = \gamma_c$ from which

$$t_c \equiv \frac{\gamma_\infty + \gamma_d}{\gamma_d + \gamma_c} t_{ini}. \tag{3.78}$$

If we compare Eqs. (3.72) and (3.77), we have $\gamma_\tau(t_{ini}) = \gamma_c$ and $\gamma_+(t_{ini}) = \gamma_\infty$; the domains never collide: $\gamma_+(t) - \gamma_\tau(t) = (\gamma_\infty - \gamma_c)(t_{ini}/t) > 0$. At last, the domain $\gamma < \gamma_+(t)$ disappears completely for $t > t_+$ where

$$t_+ \equiv \left(1 + \frac{\gamma_\infty}{\gamma_d}\right) t_{ini}, \tag{3.79}$$

which is defined by $\gamma_+(t_+) = 0$. The different transient domains thus defined are summarized in Fig. 3.6. In practice, the solution is affected by the IR cutoff only within the red dashed zones appearing in this figure, but for completeness, we give, and repeat, the solutions in all contiguous domains.

3.B.1 Non-critical loop production function

We distinguish the two cases, $t \leq t_c$ and $t > t_c$. During the relaxation period $t \leq t_c$, the solution reads

$$t^4\mathbf{n}(\gamma \geq \gamma_\infty, t < t_c) = \left(\frac{t}{t_{ini}}\right)^4 \left(\frac{a_{ini}}{a}\right)^3 t_{ini}^4 \mathcal{N}_{ini}\left\{\left[\gamma + \gamma_d\left(1 - \frac{t_{ini}}{t}\right)\right] t\right\}, \tag{3.80}$$

$$\begin{aligned} t^4\mathbf{n}(\gamma_+ \leq \gamma < \gamma_\infty, t < t_c) = {} & \left(\frac{t}{t_{ini}}\right)^4 \left(\frac{a_{ini}}{a}\right)^3 t_{ini}^4 \mathcal{N}_{ini}\left\{\left[\gamma + \gamma_d\left(1 - \frac{t_{ini}}{t}\right)\right] t\right\} \\ & + \frac{c}{\epsilon}(\gamma + \gamma_d)^{2\chi-3} f\left(\frac{\gamma_d}{\gamma + \gamma_d}\right) \\ & - \frac{c}{\epsilon}(\gamma + \gamma_d)^{3\nu-4} (\gamma_\infty + \gamma_d)^{-\epsilon} f\left(\frac{\gamma_d}{\gamma_\infty + \gamma_d}\right), \end{aligned} \tag{3.81}$$

$$t^4\mathbf{n}(\gamma_{\rm c} \le \gamma < \gamma_+, t < t_{\rm c}) = \left(\frac{t}{t_{\rm ini}}\right)^4 \left(\frac{a_{\rm ini}}{a}\right)^3 t_{\rm ini}^4 \mathcal{N}_{\rm ini}\left\{\left[\gamma + \gamma_{\rm d}\left(1 - \frac{t_{\rm ini}}{t}\right)\right] t\right\} + \frac{c}{\epsilon}(\gamma+\gamma_{\rm d})^{2\chi-3} f\left(\frac{\gamma_{\rm d}}{\gamma+\gamma_{\rm d}}\right) - \frac{c}{\epsilon}(\gamma+\gamma_{\rm d})^{2\chi-3}\left(\frac{t}{t_{\rm ini}}\right)^{-\epsilon} f\left(\frac{\gamma_{\rm d}}{\gamma+\gamma_{\rm d}}\frac{t_{\rm ini}}{t}\right), \tag{3.82}$$

$$t^4\mathbf{n}(\gamma_\tau \le \gamma < \gamma_{\rm c}, t < t_{\rm c}) = \left(\frac{t}{t_{\rm ini}}\right)^4 \left(\frac{a_{\rm ini}}{a}\right)^3 t_{\rm ini}^4 \mathcal{N}_{\rm ini}\left\{\left[\gamma + \gamma_{\rm d}\left(1 - \frac{t_{\rm ini}}{t}\right)\right] t\right\} + \frac{c_{\rm c}}{\epsilon_{\rm c}}(\gamma+\gamma_{\rm d})^{2\chi_{\rm c}-3}\left[f_{\rm c}\left(\frac{\gamma_{\rm d}}{\gamma+\gamma_{\rm d}}\right) - \left(\frac{\gamma+\gamma_{\rm d}}{\gamma_{\rm c}+\gamma_{\rm d}}\right)^{\epsilon_{\rm c}} f_{\rm c}\left(\frac{\gamma_{\rm d}}{\gamma_{\rm c}+\gamma_{\rm d}}\right)\right] + \frac{c}{\epsilon}(\gamma+\gamma_{\rm d})^{3\nu-4}(\gamma_{\rm c}+\gamma_{\rm d})^{-\epsilon} f\left(\frac{\gamma_{\rm d}}{\gamma_{\rm c}+\gamma_{\rm d}}\right) - \frac{c}{\epsilon}(\gamma+\gamma_{\rm d})^{2\chi-3}\left(\frac{t}{t_{\rm ini}}\right)^{-\epsilon} f\left(\frac{\gamma_{\rm d}}{\gamma+\gamma_{\rm d}}\frac{t_{\rm ini}}{t}\right), \tag{3.83}$$

$$t^4\mathbf{n}(0 < \gamma < \gamma_\tau, t < t_{\rm c}) = \left(\frac{t}{t_{\rm ini}}\right)^4 \left(\frac{a_{\rm ini}}{a}\right)^3 t_{\rm ini}^4 \mathcal{N}_{\rm ini}\left\{\left[\gamma + \gamma_{\rm d}\left(1 - \frac{t_{\rm ini}}{t}\right)\right] t\right\} + \frac{c_{\rm c}}{\epsilon_{\rm c}}(\gamma+\gamma_{\rm d})^{2\chi_{\rm c}-3} f_{\rm c}\left(\frac{\gamma_{\rm d}}{\gamma+\gamma_{\rm d}}\right) - \frac{c_{\rm c}}{\epsilon_{\rm c}}(\gamma+\gamma_{\rm d})^{2\chi_{\rm c}-3}\left(\frac{t}{t_{\rm ini}}\right)^{-\epsilon_{\rm c}} f_{\rm c}\left(\frac{\gamma_{\rm d}}{\gamma+\gamma_{\rm d}}\frac{t_{\rm ini}}{t}\right). \tag{3.84}$$

For later times, $t \ge t_{\rm c}$, we get the solution

$$t^4\mathbf{n}(\gamma \ge \gamma_\infty, t \ge t_{\rm c}) = \left(\frac{t}{t_{\rm ini}}\right)^4 \left(\frac{a_{\rm ini}}{a}\right)^3 t_{\rm ini}^4 \mathcal{N}_{\rm ini}\left\{\left[\gamma + \gamma_{\rm d}\left(1 - \frac{t_{\rm ini}}{t}\right)\right] t\right\}, \tag{3.85}$$

$$t^4\mathbf{n}(\gamma_{\rm c} \le \gamma < \gamma_\infty, t \ge t_{\rm c}) = \left(\frac{t}{t_{\rm ini}}\right)^4 \left(\frac{a_{\rm ini}}{a}\right)^3 t_{\rm ini}^4 \mathcal{N}_{\rm ini}\left\{\left[\gamma + \gamma_{\rm d}\left(1 - \frac{t_{\rm ini}}{t}\right)\right] t\right\} + \frac{c}{\epsilon}(\gamma+\gamma_{\rm d})^{2\chi-3} f\left(\frac{\gamma_{\rm d}}{\gamma+\gamma_{\rm d}}\right) - \frac{c}{\epsilon}(\gamma+\gamma_{\rm d})^{3\nu-4}(\gamma_\infty+\gamma_{\rm d})^{-\epsilon} f\left(\frac{\gamma_{\rm d}}{\gamma_\infty+\gamma_{\rm d}}\right), \tag{3.86}$$

$$t^4\mathbf{n}(\gamma_+ \le \gamma < \gamma_{\rm c}, t \ge t_{\rm c}) = \left(\frac{t}{t_{\rm ini}}\right)^4 \left(\frac{a_{\rm ini}}{a}\right)^3 t_{\rm ini}^4 \mathcal{N}_{\rm ini}\left\{\left[\gamma + \gamma_{\rm d}\left(1 - \frac{t_{\rm ini}}{t}\right)\right] t\right\} + \frac{c_{\rm c}}{\epsilon_{\rm c}}(\gamma+\gamma_{\rm d})^{2\chi_{\rm c}-3}\left[f_{\rm c}\left(\frac{\gamma_{\rm d}}{\gamma+\gamma_{\rm d}}\right) - \left(\frac{\gamma+\gamma_{\rm d}}{\gamma_{\rm c}+\gamma_{\rm d}}\right)^{\epsilon_{\rm c}} f_{\rm c}\left(\frac{\gamma_{\rm d}}{\gamma_{\rm c}+\gamma_{\rm d}}\right)\right] + \frac{c}{\epsilon}(\gamma+\gamma_{\rm d})^{3\nu-4}(\gamma_{\rm c}+\gamma_{\rm d})^{-\epsilon} f\left(\frac{\gamma_{\rm d}}{\gamma_{\rm c}+\gamma_{\rm d}}\right) - \frac{c}{\epsilon}(\gamma+\gamma_{\rm d})^{3\nu-4}(\gamma_{\rm d}+\gamma_\infty)^{-\epsilon} f\left(\frac{\gamma_{\rm d}}{\gamma_\infty+\gamma_{\rm d}}\right), \tag{3.87}$$

$$
\begin{aligned}
t^4\mathbf{n}(\gamma_\tau \leq \gamma < \gamma_+, t \geq t_\mathrm{c}) &= \left(\frac{t}{t_\mathrm{ini}}\right)^4 \left(\frac{a_\mathrm{ini}}{a}\right)^3 t_\mathrm{ini}^4\, \mathcal{N}_\mathrm{ini}\left\{\left[\gamma + \gamma_\mathrm{d}\left(1 - \frac{t_\mathrm{ini}}{t}\right)\right] t\right\} \\
&+ \frac{c_\mathrm{c}}{\epsilon_\mathrm{c}} (\gamma + \gamma_\mathrm{d})^{2\chi_\mathrm{c}-3} \left[f_\mathrm{c}\left(\frac{\gamma_\mathrm{d}}{\gamma + \gamma_\mathrm{d}}\right) - \left(\frac{\gamma + \gamma_\mathrm{d}}{\gamma_\mathrm{c} + \gamma_\mathrm{d}}\right)^{\epsilon_\mathrm{c}} f_\mathrm{c}\left(\frac{\gamma_\mathrm{d}}{\gamma_\mathrm{c} + \gamma_\mathrm{d}}\right)\right] \\
&+ \frac{c}{\epsilon} (\gamma + \gamma_\mathrm{d})^{3\nu-4} (\gamma_\mathrm{c} + \gamma_\mathrm{d})^{-\epsilon} f\left(\frac{\gamma_\mathrm{d}}{\gamma_\mathrm{c} + \gamma_\mathrm{d}}\right) \\
&- \frac{c}{\epsilon} (\gamma + \gamma_\mathrm{d})^{2\chi-3} \left(\frac{t}{t_\mathrm{ini}}\right)^{-\epsilon} f\left(\frac{\gamma_\mathrm{d}}{\gamma + \gamma_\mathrm{d}} \frac{t_\mathrm{ini}}{t}\right), \qquad (3.88)
\end{aligned}
$$

$$
\begin{aligned}
t^4\mathbf{n}(0 < \gamma < \gamma_\tau, t \geq t_\mathrm{c}) &= \left(\frac{t}{t_\mathrm{ini}}\right)^4 \left(\frac{a_\mathrm{ini}}{a}\right)^3 t_\mathrm{ini}^4\, \mathcal{N}_\mathrm{ini}\left\{\left[\gamma + \gamma_\mathrm{d}\left(1 - \frac{t_\mathrm{ini}}{t}\right)\right] t\right\} \\
&+ \frac{c_\mathrm{c}}{\epsilon_\mathrm{c}} (\gamma + \gamma_\mathrm{d})^{2\chi_\mathrm{c}-3} f_\mathrm{c}\left(\frac{\gamma_\mathrm{d}}{\gamma + \gamma_\mathrm{d}}\right) \\
&- \frac{c_\mathrm{c}}{\epsilon_\mathrm{c}} (\gamma + \gamma_\mathrm{d})^{2\chi_\mathrm{c}-3} \left(\frac{t}{t_\mathrm{ini}}\right)^{-\epsilon_\mathrm{c}} f_\mathrm{c}\left(\frac{\gamma_\mathrm{d}}{\gamma + \gamma_\mathrm{d}} \frac{t_\mathrm{ini}}{t}\right). \qquad (3.89)
\end{aligned}
$$

Neglecting all transients and initial condition effects, these equations show that the IR cut can be viewed as the formal replacement written in Eq. (3.47).

3.B.2 Critical loop production function

For the critical case $\chi = \chi_\mathrm{crit}$ and the sharp IR cut at γ_∞, one gets during the relaxation times $t < t_\mathrm{c}$

$$
\begin{aligned}
t^4\mathbf{n}(\gamma \geq \gamma_\infty, t < t_\mathrm{c}) &= \left(\frac{t}{t_\mathrm{ini}}\right)^4 \left(\frac{a_\mathrm{ini}}{a}\right)^3 t_\mathrm{ini}^4\, \mathcal{N}_\mathrm{ini}\left\{\left[\gamma + \gamma_\mathrm{d}\left(1 - \frac{t_\mathrm{ini}}{t}\right)\right] t\right\}, \qquad (3.90) \\
t^4\mathbf{n}(\gamma_+ \leq \gamma < \gamma_\infty, t < t_\mathrm{c}) &= \left(\frac{t}{t_\mathrm{ini}}\right)^4 \left(\frac{a_\mathrm{ini}}{a}\right)^3 t_\mathrm{ini}^4\, \mathcal{N}_\mathrm{ini}\left\{\left[\gamma + \gamma_\mathrm{d}\left(1 - \frac{t_\mathrm{ini}}{t}\right)\right] t\right\} \\
&+ c(\gamma + \gamma_\mathrm{d})^{3\nu-4} \left[g\left(\frac{\gamma_\mathrm{d}}{\gamma + \gamma_\mathrm{d}}\right) - g\left(\frac{\gamma_\mathrm{d}}{\gamma_\infty + \gamma_\mathrm{d}}\right)\right], \qquad (3.91) \\
t^4\mathbf{n}(\gamma_\mathrm{c} \leq \gamma < \gamma_+, t < t_\mathrm{c}) &= \left(\frac{t}{t_\mathrm{ini}}\right)^4 \left(\frac{a_\mathrm{ini}}{a}\right)^3 t_\mathrm{ini}^4\, \mathcal{N}_\mathrm{ini}\left\{\left[\gamma + \gamma_\mathrm{d}\left(1 - \frac{t_\mathrm{ini}}{t}\right)\right] t\right\} \\
&+ c(\gamma + \gamma_\mathrm{d})^{3\nu-4} \left[g\left(\frac{\gamma_\mathrm{d}}{\gamma + \gamma_\mathrm{d}}\right) - g\left(\frac{\gamma_\mathrm{d}}{\gamma + \gamma_\mathrm{d}} \frac{t_\mathrm{ini}}{t}\right)\right], \qquad (3.92) \\
t^4\mathbf{n}(\gamma_\tau \leq \gamma < \gamma_\mathrm{c}, t < t_\mathrm{c}) &= \left(\frac{t}{t_\mathrm{ini}}\right)^4 \left(\frac{a_\mathrm{ini}}{a}\right)^3 t_\mathrm{ini}^4\, \mathcal{N}_\mathrm{ini}\left\{\left[\gamma + \gamma_\mathrm{d}\left(1 - \frac{t_\mathrm{ini}}{t}\right)\right] t\right\} \\
&+ \frac{c_\mathrm{c}}{\epsilon_\mathrm{c}} (\gamma + \gamma_\mathrm{d})^{2\chi_\mathrm{c}-3} \left[f_\mathrm{c}\left(\frac{\gamma_\mathrm{d}}{\gamma + \gamma_\mathrm{d}}\right) - \left(\frac{\gamma + \gamma_\mathrm{d}}{\gamma_\mathrm{c} + \gamma_\mathrm{d}}\right)^{\epsilon_\mathrm{c}} f_\mathrm{c}\left(\frac{\gamma_\mathrm{d}}{\gamma_\mathrm{c} + \gamma_\mathrm{d}}\right)\right] \\
&+ c(\gamma + \gamma_\mathrm{d})^{3\nu-4} \left[g\left(\frac{\gamma_\mathrm{d}}{\gamma_\mathrm{c} + \gamma_\mathrm{d}}\right) - g\left(\frac{\gamma_\mathrm{d}}{\gamma + \gamma_\mathrm{d}} \frac{t_\mathrm{ini}}{t}\right)\right], \qquad (3.93) \\
t^4\mathbf{n}(0 < \gamma < \gamma_\tau, t < t_\mathrm{c}) &= \left(\frac{t}{t_\mathrm{ini}}\right)^4 \left(\frac{a_\mathrm{ini}}{a}\right)^3 t_\mathrm{ini}^4\, \mathcal{N}_\mathrm{ini}\left\{\left[\gamma + \gamma_\mathrm{d}\left(1 - \frac{t_\mathrm{ini}}{t}\right)\right] t\right\}
\end{aligned}
$$

$$+\frac{c_{\rm c}}{\epsilon_{\rm c}}(\gamma+\gamma_{\rm d})^{2\chi_{\rm c}-3}f_{\rm c}\left(\frac{\gamma_{\rm d}}{\gamma+\gamma_{\rm d}}\right)$$
$$-\frac{c_{\rm c}}{\epsilon_{\rm c}}(\gamma+\gamma_{\rm d})^{2\chi_{\rm c}-3}\left(\frac{t}{t_{\rm ini}}\right)^{-\epsilon_{\rm c}}f_{\rm c}\left(\frac{\gamma_{\rm d}}{\gamma+\gamma_{\rm d}}\frac{t_{\rm ini}}{t}\right). \tag{3.94}$$

Finally, for times $t\geq t_{\rm c}$, $\gamma_+(t)$ becomes smaller than $\gamma_{\rm c}$ and the complete critical IR-regularized loop distribution reads

$$t^4\mathbf{n}(\gamma\geq\gamma_\infty,t\geq t_{\rm c})=\left(\frac{t}{t_{\rm ini}}\right)^4\left(\frac{a_{\rm ini}}{a}\right)^3 t_{\rm ini}^4\,\mathcal{N}_{\rm ini}\left\{\left[\gamma+\gamma_{\rm d}\left(1-\frac{t_{\rm ini}}{t}\right)\right]t\right\}, \tag{3.95}$$

$$t^4\mathbf{n}(\gamma_{\rm c}\leq\gamma<\gamma_\infty,t\geq t_{\rm c})=\left(\frac{t}{t_{\rm ini}}\right)^4\left(\frac{a_{\rm ini}}{a}\right)^3 t_{\rm ini}^4\,\mathcal{N}_{\rm ini}\left\{\left[\gamma+\gamma_{\rm d}\left(1-\frac{t_{\rm ini}}{t}\right)\right]t\right\}$$
$$+c(\gamma+\gamma_{\rm d})^{3\nu-4}\left[g\left(\frac{\gamma_{\rm d}}{\gamma+\gamma_{\rm d}}\right)-g\left(\frac{\gamma_{\rm d}}{\gamma_\infty+\gamma_{\rm d}}\right)\right], \tag{3.96}$$

$$t^4\mathbf{n}(\gamma_+\leq\gamma<\gamma_{\rm c},t\geq t_{\rm c})=\left(\frac{t}{t_{\rm ini}}\right)^4\left(\frac{a_{\rm ini}}{a}\right)^3 t_{\rm ini}^4\,\mathcal{N}_{\rm ini}\left\{\left[\gamma+\gamma_{\rm d}\left(1-\frac{t_{\rm ini}}{t}\right)\right]t\right\}$$
$$+\frac{c_{\rm c}}{\epsilon_{\rm c}}(\gamma+\gamma_{\rm d})^{2\chi_{\rm c}-3}\left[f_{\rm c}\left(\frac{\gamma_{\rm d}}{\gamma+\gamma_{\rm d}}\right)-\left(\frac{\gamma+\gamma_{\rm d}}{\gamma_{\rm c}+\gamma_{\rm d}}\right)^{\epsilon_{\rm c}}f_{\rm c}\left(\frac{\gamma_{\rm d}}{\gamma_{\rm c}+\gamma_{\rm d}}\right)\right]$$
$$+c(\gamma+\gamma_{\rm d})^{3\nu-4}\left[g\left(\frac{\gamma_{\rm d}}{\gamma_{\rm c}+\gamma_{\rm d}}\right)-g\left(\frac{\gamma_{\rm d}}{\gamma_\infty+\gamma_{\rm d}}\right)\right], \tag{3.97}$$

$$t^4\mathbf{n}(\gamma_\tau\leq\gamma<\gamma_+,t\geq t_{\rm c})=\left(\frac{t}{t_{\rm ini}}\right)^4\left(\frac{a_{\rm ini}}{a}\right)^3 t_{\rm ini}^4\,\mathcal{N}_{\rm ini}\left\{\left[\gamma+\gamma_{\rm d}\left(1-\frac{t_{\rm ini}}{t}\right)\right]t\right\}$$
$$+\frac{c_{\rm c}}{\epsilon_{\rm c}}(\gamma+\gamma_{\rm d})^{2\chi_{\rm c}-3}\left[f_{\rm c}\left(\frac{\gamma_{\rm d}}{\gamma+\gamma_{\rm d}}\right)-\left(\frac{\gamma+\gamma_{\rm d}}{\gamma_{\rm c}+\gamma_{\rm d}}\right)^{\epsilon_{\rm c}}f_{\rm c}\left(\frac{\gamma_{\rm d}}{\gamma_{\rm c}+\gamma_{\rm d}}\right)\right]$$
$$+c(\gamma+\gamma_{\rm d})^{3\nu-4}\left[g\left(\frac{\gamma_{\rm d}}{\gamma_{\rm c}+\gamma_{\rm d}}\right)-g\left(\frac{\gamma_{\rm d}}{\gamma+\gamma_{\rm d}}\frac{t_{\rm ini}}{t}\right)\right], \tag{3.98}$$

$$t^4\mathbf{n}(0<\gamma<\gamma_\tau,t\geq t_{\rm c})=\left(\frac{t}{t_{\rm ini}}\right)^4\left(\frac{a_{\rm ini}}{a}\right)^3 t_{\rm ini}^4\,\mathcal{N}_{\rm ini}\left\{\left[\gamma+\gamma_{\rm d}\left(1-\frac{t_{\rm ini}}{t}\right)\right]t\right\}$$
$$+\frac{c_{\rm c}}{\epsilon_{\rm c}}(\gamma+\gamma_{\rm d})^{2\chi_{\rm c}-3}f_{\rm c}\left(\frac{\gamma_{\rm d}}{\gamma+\gamma_{\rm d}}\right)$$
$$-\frac{c_{\rm c}}{\epsilon_{\rm c}}(\gamma+\gamma_{\rm d})^{2\chi_{\rm c}-3}\left(\frac{t}{t_{\rm ini}}\right)^{-\epsilon_{\rm c}}f_{\rm c}\left(\frac{\gamma_{\rm d}}{\gamma+\gamma_{\rm d}}\frac{t_{\rm ini}}{t}\right). \tag{3.99}$$

Chapter 4

Impact of the small-scale structure on the Stochastic Background of Gravitational Waves from cosmic strings

This chapter is a reproduction of Ref. [56] of which I am the sole author. This paper is the direct continuation of Chapter 3 and my aim was to study the stochastic background of GW with the loop distributions of the previous chapter. The power-law loop production function (LPF) of Polchinski and collaborators has been known to enhance the number of very small loop in the form of an *extra population of small loops*. The question addressed in this chapter is whether this enhancement modifies the shape of the GW background and the bounds on the string tension $G\mu$. I calculate analytical templates for the evaluation of the stochastic background of GW adapted to these loop number densities and use them to identify four classes of stochastic background signals.

Abstract

Numerical simulations and analytical models suggest that infinite cosmic strings produce cosmic string loops of all sizes with a given power-law. Precise estimations of the power-law exponent are still matter of debate while numerical simulations do not incorporate all the radiation and back-reaction effects expected to affect the network at small scales. Previously it has been shown, using a Boltzmann approach, that depending on the steepness of the loop production function and the gravitational back-reaction scale, a so-called EPSL can be generated in the loop number density. We propose a framework to study the influence of this extra population of small loops on the SGWB. We show that this extra population can have a significant signature at frequencies higher than $H_0(\Gamma G\mu)^{-1}$ where Γ is of order 50 and H_0 is the Hubble constant. We propose a complete classification of the GW power spectra expected from cosmic strings into four classes, including the model of Blanco-Pillado, Olum and Shlaer and the model of Lorenz, Ringeval and Sakellariadou. Finally, we show that given the uncertainties on the Polchinski-Rocha exponents, two hybrid classes of GW power spectrum can be considered giving very different predictions for the SGWB.

4.1 Introduction

The first direct observation of Gravitational Waves (GW) coming from the merger of two black holes [18] was both a wonderful check of the theory of General Relativity and the onset of GW astronomy. Since GW propagate freely throughout the Universe, they are not limited by the last scattering surface, and give us an unprecedented opportunity to look for topological defects, and in particular cosmic strings.

Cosmic strings are one-dimensional topological defects that may have formed during a symmetry-breaking phase transition in the early Universe [61, 69, 64, 88]. Nambu-Goto strings are a powerful one-dimensional approximation to study these solitonic solutions on cosmological scales. The evolution of a Nambu-Goto string network in an expanding background has been studied both analytically [61, 301, 63, 303, 304, 94, 137, 287, 232, 123, 103, 230, 305, 52] and through numerical simulations [102, 93, 102, 101, 95, 109, 99] in the last decades, and is still subject of intense research.

A general result is that the network relaxes to an attractor solution known as the scaling solution and remains self-similar with the Hubble radius. If cosmic strings were formed, scaling means they survive during the whole history of the Universe and are present all over the sky. Strings can induce anisotropies on the Cosmic Microwave Background and have been searched for in the Planck data. The current CMB constraints give an upper bound for the string tension μ of $G\mu < 1.5 \times 10^{-7}$ for Nambu-Goto strings and $G\mu < 2 \times 10^{-7}$ for Abelian-Higgs strings, where G is Newton's constant [306, 75, 72, 74].

These bounds are calculated assuming a given scenario for the evolution of the loop number density throughout the history of the Universe (see below), and can depend a lot on those assumptions. Furthermore, each closed cosmic string loop radiates GW and the superposition of them produces a Stochastic Background of Gravitational Waves (SGWB) [117, 244, 118, 106, 307, 308] which could be detected by gravitational wave detectors. This background has been looked for in LIGO/Virgo for O1 and O2 and gives already a tighter upper bound for $G\mu$ which is, however, very dependent on the cosmic string model used, ranging from $G\mu < 1.1 \times 10^{-6}$ to $G\mu < 2.1 \times 10^{-14}$ [91, 32]. In Section 4.4.3 we will explain the origin of the orders of magnitude difference between these two constraints. The most stringent and stable constraint today comes from pulsar timing experiment giving $G\mu \lesssim 10^{-10}$ [213].

Building a model for the evolution of the cosmic string network is challenging, and involves both analytical modelling and numerical simulations. Nambu-Goto simulations are necessary to determine the large-scale behaviour of the loop number density, but are unable to provide a description of the smallest scales as they do not include gravitational radiation nor the back-reaction that dominates on these scales [120, 238, 121]. One of the difficulties is the proliferation of kinks – which are discontinuities in the tangent vector of the string. Kinks are formed every time two strings intersect each other, are removed by outgoing loops and are smoothed by gravitational back-reaction. If the scaling of the large scales is today well-supported by numerical simulations, the build-up of a population of kinks has raised some doubts on the scaling properties of the small-scales [137, 94, 136, 303, 304, 305, 230, 309, 109] and this situation cannot be settled with simulations available today. A first attempt to model analytically the number of kinks using the one-scale model was performed in Refs. [303, 304], and showed that kinks accumulate until the number of kinks reaches a scaling regime introducing another scale to the system [136]. Models were later introduced to take into account this small-scale structure, these include the three-scale model [94], a renormalized velocity-dependent one-scale model [305, 230] and the Polchinski-Rocha model based on fractal dimensions [137, 138, 307, 287] which we will use in the following. It introduces a positive exponent

χ defined later in the equation (4.1), and one of its particular prediction is that the gravitational back-reaction scale is not $\Gamma G\mu t$ as in Refs. [307, 309], but rather the smaller scale $\Upsilon(G\mu)^{1+2\chi}t$ where Υ is of order 20.

The goal of this article is to provide a unified framework which can continuously describe, with a limited set of parameters, different cosmic string loop models from the literature and give predictions for the SGWB. It is built using the analytical model of Polchinski and Rocha [137, 287, 232] and later developments [52, 123], and therefore includes the parameter χ. With this framework, we aim at gaining a deeper understanding of the SGWB and why constraints on the string tension from LIGO/Virgo are so model-dependent. We also expect to use this framework to give model-independent constraints on the string tension.

Using our unified framework, we can furthermore focus on two particular models, the BOS [103] and the LRS [123] models. The BOS model is based on the simulations conducted in Refs. [103, 95] and makes the assumption that the production of loops with sizes smaller than the gravitational radiation scale $t\Gamma G\mu$, where $\Gamma \approx 50$, is suppressed. On the other hand, the LRS model is based on the simulations conducted in Ref. [99] and based on the analytical studies of Refs. [137, 287] which assume that small loops are produced down to the gravitational back-reaction scale, which is smaller than the gravitational radiation scale by several orders of magnitude. As a result the two models give very different predictions for the loop number density. Relative to the first one, the second gives rise to an Extra Population of Small Loops (EPSL). The smaller back-reaction scale *à la* Polchinski-Rocha can be introduced in the BOS model producing also an additional population of small loops [52]. It is therefore interesting to understand its effect on the SGWB.

This paper is set up as follows. Section 4.2 describes the theoretical framework used to unify several cosmic string models found in the literature. In particular, we show that the loop number density is naturally composed of two distinct population, a SLND which is very similar to the prediction of the one-scale model, and an EPSL. Section 4.3 shows how to calculate analytically an estimate to the SGWB from cosmic strings and discusses the validity of the approximations made. Section 4.4 then combines the results to obtain the dependence of several types of GW experiments to the uncertainties on the cosmic string parameters. Finally, Section 4.5 presents our conclusions.

4.2 Theoretical framework

4.2.1 The network of infinite strings

A standard way to model the evolution of cosmic strings is to study *infinite strings* and *closed loops* as two distinct populations in interaction. These infinite strings of cosmological sizes are stretched by the expansion of the universe characterized by the scale factor $a(t)$ which evolves as t^ν where $\nu = 1/2$ in the radiation-dominated era and $\nu = 2/3$ in the matter-dominated era. At the same time, they lose energy by forming loops. Closed loops are formed when two infinite strings intersect each other or when one self-intersects. In principle these loops can rejoin the infinite strings or fragment into smaller loops. At the end of the fragmentation, one is left with smaller non-self intersecting long-lived loops. It is this population of long-lived non self-intersecting loops that dominates the SGWB and that we model.

In this article, we assume the inter-commutation probability to be equal to one, although some types of cosmic strings may have it strictly smaller than one [310]. Based on analytical models [64] and numerical simulations [99, 103, 95] we expect the network of infinite strings to *scale* in radiation-dominated or in matter-dominated era. Scaling is an attractor solution of the network in which all

the relevant length scales are proportional to the horizon size $d_{\rm h}$ which itself is proportional to the cosmic time t. During scaling the energy density contained in cosmic strings evolves as $\rho_\infty \propto t^{-2}$.

The loop production function $\mathcal{P}(\ell, t)$ is the number of long-lived non self-intersecting loops of invariant length ℓ per unit volume per unit time formed at cosmic time t. In scaling, $t^5\mathcal{P}(\ell, t)$ is expected to be only a function of the scaling variable $\gamma = \ell/t$. There exist different calculations in the literature concerning the shape of this loop production function. In the one-scale model introduced in Ref. [63], all loops are assumed to be formed with the same size, meaning the loop production function is a Dirac-delta distribution. This typical size is then inferred from numerical simulations. In the work of [137, 287], it has been argued that the loop production function is a power-law, something which was found in the simulations of [109] and is compatible with the simulations of [99]. In such a case the loop production function is parameterized by a parameter χ and a multiplicative constant c

$$t^5\mathcal{P}(\ell, t) = c\gamma^{2\chi-3} \text{ for } \gamma_{\rm c} < \gamma \tag{4.1}$$

where the analytical study of the small-scale structure of [137] suggested the introduction of a *gravitational back-reaction scale* $\gamma_{\rm c}$ below which the production of loops by the network is suppressed

$$\gamma_{\rm c} = \Upsilon(G\mu)^{1+2\chi} \tag{4.2}$$

where Υ is of order 20. This loop production function was developed in an attempt to take into account the small-scale structure of the network. The exponent χ controls the rate at which the fractal dimension d_f of the infinite strings approaches to 1 on the smallest scales [137]

$$d_f - 1 \propto \frac{\chi(\ell/t)^{2\chi}}{(2\chi+1)(2\chi+2)} \tag{4.3}$$

It was shown in Ref. [123] that the precise shape of the loop production function below $\gamma_{\rm c}$ has only a small impact on the LND. It has been used in Refs. [90, 123] to calculate the loop number density and leads to a significant EPSL with respect to the one-scale scenario. To fit the numerical simulations of [99], their analysis assumed the network to be *sub-critical* meaning $\chi < \chi_{\rm crit}$ where

$$\chi_{\rm crit} = \frac{3\nu - 1}{2} = \begin{cases} 1/4 & \text{in radiation era} \\ 1/2 & \text{in matter era} \end{cases} \tag{4.4}$$

They were able to infer the slope of the loop production function from the loop number density and obtained $\chi_{\rm r} = 0.2$ and $\chi_{\rm m} = 0.295$ [123]. Critical $\chi = \chi_{\rm crit}$ and super-critical $\chi > \chi_{\rm crit}$ networks were finally studied in Chapter 3. This super-critical regime is supported by the Nambu-Goto simulations of [103] in which they measured the loop production function and obtained $\chi_{\rm r} = 0.5$ and $\chi_{\rm m} = 0.655$. It is therefore important to include super-critical regimes in our framework for future applications.

4.2.2 Loop number density

Once the loop production function is known, it can be injected into the Boltzmann equation for the LND $\mathbf{n}(\ell, t)$

$$\frac{\mathrm{d}}{\mathrm{d}t}\left(a^3\mathbf{n}\right) = a^3\mathcal{P}(\ell, t), \tag{4.5}$$

where the effect of the expansion of the universe is taken into account by introducing the scale factor a. The loops radiate GW with a rate we assume to be constant and given by Refs. [114, 118]

$$\frac{\mathrm{d}\ell}{\mathrm{d}t} = -\Gamma G\mu \equiv -\gamma_{\mathrm{d}} \tag{4.6}$$

where Γ is of order 50 [117, 114]. This Boltzmann equation can be solved if one assumes either radiation or matter domination and that the network of infinite strings is scaling so that the loop production function scales and is given by equation (4.1). The complete set of solutions can be found in Chapter 3. The loop number density no longer necessarily scales, unless one assumes that the loop production function is cutoff for $\gamma \geq \gamma_\infty$, where γ_∞ is expected to be of the order of the Hubble horizon. The authors suggest the inclusion of a sharp infrared cutoff to regularize those new solutions and showed that the precise shape of the cutoff only has a small effect on the loop distribution. We neglect it in the remainder of this paper. Even in these critical and super-critical regimes, one can observe a large population of small loops in the LND up to a new value of $\chi = \chi_{\mathrm{IR}}$

$$\chi_{\mathrm{IR}} = \frac{1+\sqrt{12\nu-3}}{4} = \begin{cases} \approx 0.68 \text{ in radiation era} \\ \approx 0.8 \text{ in matter era} \end{cases} > \chi_{\mathrm{crit}} \tag{4.7}$$

introducing an additional knee in the LND at

$$\gamma_{\mathrm{IR}} = \left(\frac{-\epsilon\gamma_\infty^{\epsilon}}{2-2\chi}\right)^{1/(2-2\chi)} \gamma_{\mathrm{d}}^{(3-3\nu)/(2-2\chi)} \tag{4.8}$$

in which ϵ is given by[1]

$$\epsilon \equiv 3\nu - 2\chi - 1 \tag{4.9}$$

The fact that critical and super-critical models present an extra population of small loops motivates us to study the impact of this population on the SGWB

4.2.3 Normalization of the loop production function

Currently, there is a debate on how to normalize the loop production function, that is the constant c in (2.1) based on measurements from numerical simulations. In this section, we will review two different approaches followed in the community.

The first approach — explicitly stated in Refs. [95, 284], and implicitly used in the one-scale model [64] — is to use an energy conservation equation to put an upper bound on the energy lost by the network of infinite strings into loops. Assuming that the energy density of the infinite string network ρ_∞ is lost through the expansion of the Universe, redshifting and by the formation of non-self-intersecting loops [64]

$$\frac{\mathrm{d}\rho_\infty}{\mathrm{d}t} = -2H(1+\langle v_\infty^2\rangle)\rho_\infty - \mu\int \ell\mathcal{P}(\ell,t)\,\mathrm{d}\ell \tag{4.10}$$

where H is the Hubble parameter and $\langle v_\infty^2\rangle$ is the average velocity of the infinite strings and has been measured to be 0.45 (resp. 0.40,0.35) in a flat space-time (resp. radiation dominated, matter-dominated) [95]. On assuming that the scale factor $a \propto t^\nu$ and inserting (4.1) into (4.10), the

[1] This parameter is noted μ in Refs. [52, 123, 90]. We change the notation to avoid confusion with the string tension.

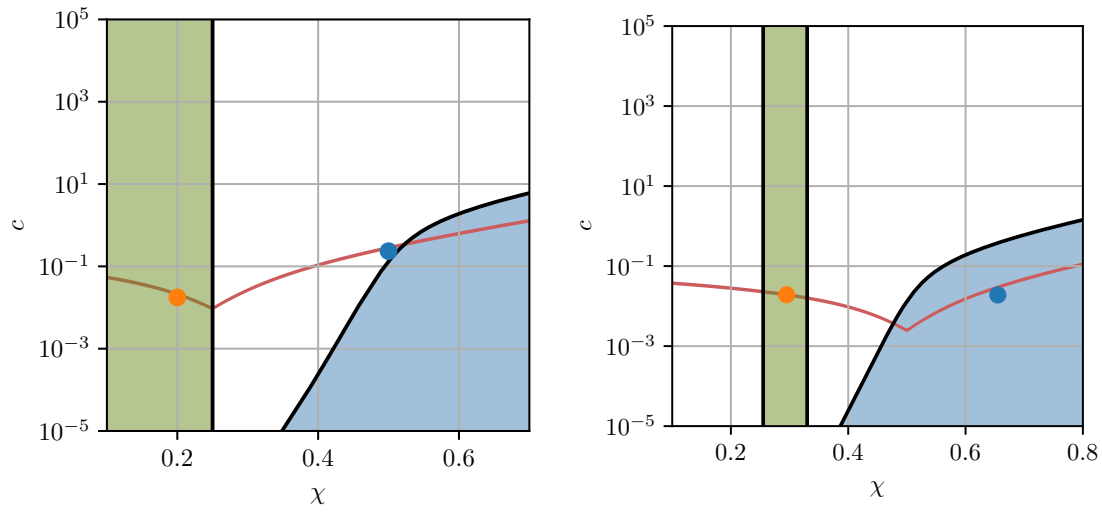

(a) Radiation era.

(b) Matter era.

Figure 4.1: Normalization of the loop production function. The boundary of the blue region is given by the "one-scale energy balance". The green region is given by measurements in Ref. [99]. The red line shows the set of parameters giving order unity loops per Hubble radius, see Section 4.2.4. The blue dot corresponds to the parameters of the BOS model, and the orange dot to those of the LRS model.

energy density of the infinite strings

$$\rho_\infty(t) = \frac{c\mu t^{-2}}{2[1-\nu(1+\langle v_\infty^2\rangle)]}\int_{\gamma_c}^{\gamma_\infty}\gamma^{2\chi-2}\,\mathrm{d}\gamma \tag{4.11}$$

is the well-known attractor scaling solution $\rho_\infty \propto \mu t^{-2}$. This can be compared to the values found for each era in numerical simulations and used to give an upper bound for the parameter c once χ, γ_c and γ_∞ are fixed. The corresponding allowed parameter space for (c,χ) is denoted as "one-scale energy balance" in Fig. 4.1. It should be noted that numerical simulations do not include any gravitational radiation nor back-reaction, meaning that there the only equivalent to a lower cutoff in the integral of equation (4.11) is determined by the smallest length-scale set at the initialization of the simulation. If $\chi \leq 1/2$, the integral is dominated by this non-physical lower bound, and one expect $t^2\rho_\infty$ to diverge if the simulation is long enough [284].

Another approach advocated in Ref. [123] is to consider only the large scale LND determined in simulations as trustworthy. It can be parameterized as a power-law on large-scales $\gamma > \gamma_d$ and fitted to the analytical predictions [52]

$$t^4\mathbf{n} = A\gamma^{-p}. \tag{4.12}$$

In the numerical simulations of [99], they obtain a value of A which is compatible with other numerical simulations. As shown in Section 4.2.4, the value of A is related to the parameters of the loop production function (c,χ). Hence a given value of A determines a curve in the (c,χ) which is the red line of Fig. 4.1.

While there seems to be a general agreement for the parameter A, there is a strong tension on the parameter p. Even though the uncertainty interval given for p in Ref. [99] does not exclude the degenerate value $5/2$ in the radiation era, their best fit systematically points to a higher value than $5/2$ and the authors have used the best fit value $p = 2.6$ since then, thus selecting the green region of parameter space denoted in Fig. 4.1.

One can see that these two interpretations of two different numerical simulations do not agree on the values for the different parameters. It should be noted that the loop production function has been measured directly in Ref. [95] giving values for (c,χ) compatible with the energy-balance argument. The group of Ringeval and al. is currently working to improve the measurement of the loop production function in their own simulations to see whether an agreement can be met and results of [285] can be reproduced or not.

For the remainder of this paper, for a given value for χ, we will determine the normalization factor c as to fit the parameter A of the large scale LND. This assumption allows us to study both models on the same footing and is more likely to remain valid once an agreement will be found.

4.2.4 Decomposition of the contributions in the different eras

The aim of this study is to determine whether the EPSL described in Ref. [123] and Chapter 3 are observable features of the SGWB. To this end, we propose a natural decomposition of the loop number density into two parts, as Fig. 4.2 illustrates. The first contribution, which we called the SLND, is of the form

$$t^4\mathbf{n}(\gamma) = C(\gamma+\gamma_d)^{-p}\Theta(\gamma_\infty-\gamma) \tag{4.13}$$

where γ_∞ is a cutoff on the sizes of the loops. It is, for instance, the result of a Dirac loop production $t^5\mathcal{P} = c\delta(\gamma_\infty-\gamma)$ [64]. In this particular case $C = c(\gamma_\infty+\gamma_d)^{3-3\nu}$ and $p = 4-3\nu$. It also describes

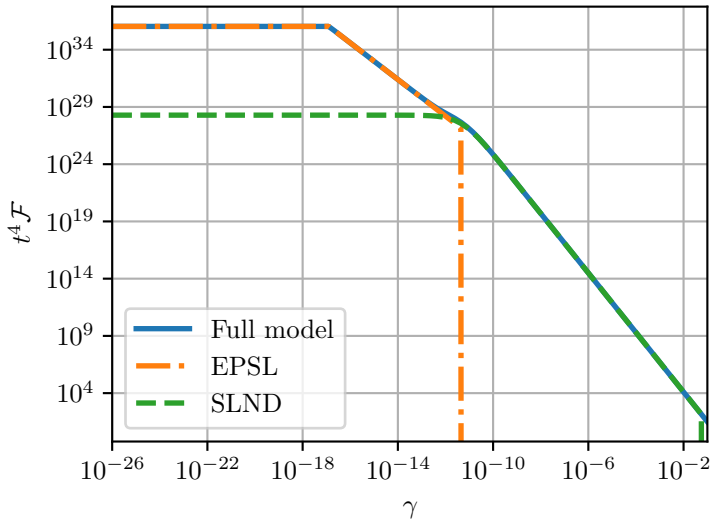

Figure 4.2: The decomposition of the LND into two populations, the SLND and the EPSL for $\chi = 0.2$ and $G\mu = 10^{-13}$ in the radiation era. The infrared cutoff is set to $\gamma_\infty = 0.1$.

well the large scale behaviour if the loop production function is the power-law of equation (4.1) [52]. Then the constants are fixed by

- in the sub-critical regime $\chi < \chi_{\rm crit}$, $C = \dfrac{c}{\epsilon}$ and $p = 3 - 2\chi$
- in the super-critical regime $\chi > \chi_{\rm crit}$, $C = -\dfrac{c\gamma_\infty^{-\epsilon}}{\epsilon}$ and $p = 4 - 3\nu$

where ϵ is given in equation (4.9) and c is fixed by the normalization of the loop production function, as discussed in Section 4.2.3. These approximations break down near $\chi_{\rm crit}$ and one should add regularization terms coming directly from the analytical expression of Chapter 3. For clarity, we omit these terms here and put the details in Appendix 4.C.

On top of the SLND, we superimpose an EPSL described as a piece-wise function, motivated by the work of Chapter 3 [2]

$$t^4\mathbf{n}(\gamma) = \begin{cases} \dfrac{c\gamma_{\rm d}^{-1}}{2-2\chi}\gamma_{\rm c}^{2\chi-2} & \text{if } \gamma < \gamma_{\rm c} \\ \dfrac{c\gamma_{\rm d}^{-1}}{2-2\chi}\gamma^{2\chi-2} & \text{if } \gamma_{\rm c} < \gamma < \gamma_{\rm d} \\ 0 & \text{if } \gamma_{\rm d} < \gamma \end{cases} \tag{4.14}$$

This definition comes directly from the fact that we assumed a sharp cutoff at the *back-reaction scale* $\gamma_{\rm c}$. The analytic formulae would be a little more complicated with a power-law cutoff, but the result would not be qualitatively modified.

[2] Based only on the asymptotic description provided in Table 3.2 this decomposition might seem artificial and one could be concerned that loops smaller than $\gamma_{\rm d}$ are counted twice. In fact, it is just the opposite and this decomposition is well motivated when we refer to the full solutions. See Appendix 4.B for more details.

In the following, the analysis focuses on the impact of these two populations either in radiation-dominated era, or in matter-dominated era. One should note that large loops produced during the radiation era can survive long enough to be an important source of GW in the matter era. They are a non-scaling population of loops and some models (see [114]) predict they dominate during the matter-dominated era. Their contribution to the SGWB is calculated in Appendix 4.E.3 and taken into account in our analysis. On the contrary loops of size smaller than $\gamma_{\rm d}$ during radiation era, which is the case of the EPSL, do not survive long enough in the matter era to be a significant contribution to the SGWB.

4.3 The Stochastic Background of Gravitational Waves

4.3.1 Emission of gravitational waves

Cosmic string loops oscillate and emit GW. The incoherent sum of their gravitational radiation forms a SGWB which was first calculated in Ref. [117]. The oscillation of the loops is not the only channel of gravitational radiation and burst-like events, from cusps, kinks and kink-kink collisions are also sources of gravitational radiation whose wave-forms were calculated in Refs. [105, 106, 90].

There exists two main methods to calculate the SGWB. The first consists in introducing an effective decomposition into harmonics $\mathrm{P_m}, \mathrm{m} \in \mathbb{N}$ where the lowest modes are dominated by the oscillatory movement of the loop with typical frequency $2/\ell$, where ℓ is the invariant length of the loop, and the higher modes are dominated by burst-like events [114]. Typically, $\mathrm{P_m} \propto m^{-q}$ with $q = 4/3$ (respectively $5/3, 2$) for cusps (respectively kinks and kink-kink collisions). The energy density carried by the GW per unit logarithmic interval of frequency is given by Ref. [114]

$$\rho_{\rm gw}(t, f) = G\mu^2 \sum_{m=1}^{\infty} C_m(f)\mathrm{P_m} \tag{4.15}$$

$$C_m(f) = \frac{2m}{f^2} \int_0^{z_*} \frac{\mathrm{d}z}{H(z)(1+z)^6} \mathbf{n}\left[\frac{2m}{(1+z)f}, t(z)\right] \tag{4.16}$$

in which $H(z)$ is the Hubble parameter, $t(z)$ is the cosmic time, and f is the frequency of the wave in the detector. Details on the cosmological parameters used in this paper are summarized in Appendix 4.A. The redshift at which cosmic strings where formed is denoted by z_*, and it depends on the energy scale of the phase transition determined by the string tension. Considering the phase transition happened during the radiation era and that the temperature today is T_0, the redshift z_* is given by

$$1 + z_* \propto \frac{10^{39/2}\ \mathrm{GeV}}{T_0} \sqrt{G\mu} \tag{4.17}$$

which we will fix to be infinity in the following.

The other method to calculate the SGWB consists in considering the sum of all burst-like events which are typically not isotropic [106, 308, 212]. This approach allows one to remove events resolved inside a detector from the SGWB, as they are not part of the background any more. A detailed discussion of the differences of the two approaches can be found in Chapter 3.

In this paper we will use the first method. To keep the following analysis simple, we make the simplifying assumption that cosmic string loops emit only in their fundamental mode. The modes $m > 1$ are only a small modification of its qualitative properties [213, 311] and we discuss briefly

their impact Section 4.3.3. Introducing $\mathrm{Q} = 16\pi/(3\Gamma)$, the fraction of the critical density given by the energy of GW is

$$\Omega_{\mathrm{GW}}(\ln f) = \frac{\mathrm{Q}}{f H_0^2}\gamma_{\mathrm{d}}^2 \int_0^\infty \frac{\mathrm{d}z}{H(z)(1+z)^6}\mathbf{n}\left[\frac{2}{(1+z)f}, t(z)\right]. \tag{4.18}$$

4.3.2 Asymptotic description of the stochastic background of GW

With the assumptions made in this framework, one can calculate the energy density power spectrum for each contribution individually, namely the contribution from SLND on one side and the contribution from the EPSL on the other side. Consider for instance the SGWB produced by the SLND in the radiation era.

In the radiation era, we can make the following approximations for the Hubble parameter and the cosmic time

$$H(z) = (1+z)^2 H_{\mathrm{r}} \tag{4.19}$$

$$t(z) = \frac{1}{2(1+z)^2 H_{\mathrm{r}}} \tag{4.20}$$

where $H_{\mathrm{r}} = H_0\sqrt{\Omega_{\mathrm{rad}}}$. This allows us to simplify equation (4.18) into

$$\Omega_{\mathrm{GW}}(\ln f) = \frac{64\mathrm{Q}H_{\mathrm{r}}\Omega_{\mathrm{rad}}}{f}\gamma_{\mathrm{d}}^2 \int_{z_{\mathrm{eq}}}^\infty \mathrm{d}z\, t^4 \mathbf{n}\left[\frac{4(1+z)H_{\mathrm{r}}}{f}\right]. \tag{4.21}$$

Inserting the SLND contribution from equation (4.13) and noticing that $p > 1$

$$\Omega_{\mathrm{GW}}(\ln f) = \frac{4\mathrm{Q}C\Omega_{\mathrm{rad}}}{(p-1)}\gamma_{\mathrm{d}}^{3-p}\left[\left(1+\frac{4H_{\mathrm{r}}(1+z_{\mathrm{eq}})}{f\gamma_{\mathrm{d}}}\right)^{1-p} - \left(1+\frac{\gamma_\infty}{\gamma_{\mathrm{d}}}\right)^{1-p}\right] \tag{4.22}$$

We can make several remarks on this particular result that can be extended to the other contributions. The power spectrum has of two characteristic frequency scales. In particular $f = 4H_{\mathrm{r}}(1+z_{\mathrm{eq}})\gamma_\infty^{-1}$ is a low frequency cutoff for the energy density. This frequency is so low with respect to the frequency range of the GW detectors that we omit it in the following. The frequency $f = 4H_{\mathrm{r}}(1+z_{\mathrm{eq}})\gamma_{\mathrm{d}}^{-1}$ is a knee in the SGWB. These two scales are well separated and the power spectrum can be approximated by power-laws far from these frequencies.

We performed the same calculations for the other contributions, the SLND and EPSL during the radiation and the matter era in the Appendices 4.D and 4.E and summed up the asymptotic behaviour in Tables 4.1, 4.2 and 4.3. We can make the general remarks:

- a typical frequency scale at which the power spectrum presents a knee, roughly $H_0\gamma_{\mathrm{d}}^{-1}$ for the SLND and $H_0\gamma_{\mathrm{c}}^{-1}$ for the EPSL. Those two frequencies are very well separated.
- at low and high frequencies, the power spectrum behaves as a power law
- the width of the knees can be estimated from the complete calculations but is essentially small compared to the separation between $H_0\gamma_{\mathrm{d}}^{-1}$ and $H_0\gamma_{\mathrm{c}}^{-1}$ for $G\mu \ll 1$
- the power spectrum is cutoff at low frequencies, roughly $H_0\gamma_\infty^{-1}$ for the SLND and $H_0\gamma_{\mathrm{d}}^{-1}$ for the EPSL

Frequency range	$f \ll H_0\gamma_{\rm d}^{-1}$	$H_0\gamma_{\rm d}^{-1} \ll f$
Radiation era	$\mathrm{Q_r}\gamma_{\rm d}^2\left[\dfrac{f}{4(1+z_{\rm eq})H_{\rm r}}\right]^{2-2\chi_{\rm r}}$	$\mathrm{Q_r}\gamma_{\rm d}^{2\chi_{\rm r}}$
Matter era	$\dfrac{\mathrm{Q_m}}{2(2-\chi_{\rm m})}\gamma_{\rm d}^2\left(\dfrac{f}{3H_{\rm m}}\right)^{2-2\chi_{\rm m}}$	$3H_{\rm m}\mathrm{Q_m}\gamma_{\rm d}^{2\chi_{\rm m}-1}f^{-1}$
Decaying into matter era	$\dfrac{2\mathrm{Q_{rm}}(1+z_{\rm eq})^{2\chi_{\rm r}}}{(4\chi_{\rm r}+1)}\gamma_{\rm d}^2\left(\dfrac{f}{3\sqrt{1+z_{\rm eq}}H_{\rm m}}\right)^{2-2\chi_{\rm r}}$	$\dfrac{3\mathrm{Q_{rm}}H_{\rm m}}{(1-3\chi_{\rm r})}\gamma_{\rm d}^{2\chi_{\rm r}-1}f^{-1}$

Table 4.1: SLND – sub-critical case. For clarity, we have introduced $\mathrm{Q_r} = \dfrac{4c_{\rm r}\Omega_{\rm rad}\mathrm{Q}}{(1-\chi_{\rm r})(1-4\chi_{\rm r})}$, $\mathrm{Q_m} = \dfrac{27c_{\rm m}\Omega_{\rm mat}\mathrm{Q}}{8(1-2\chi_{\rm m})}$ and $\mathrm{Q_{rm}} = \dfrac{27c_{\rm r}\Omega_{\rm mat}\mathrm{Q}}{8(1-4\chi_{\rm r})\sqrt{1+z_{\rm eq}}}$.

Frequency range	$f \ll H_0\gamma_{\rm d}^{-1}$	$H_0\gamma_{\rm d}^{-1} \ll f$
Radiation era	$\tilde{\mathrm{Q}}_{\rm r}\gamma_{\rm d}^2\left(\dfrac{f}{4(1+z_{\rm eq})H_{\rm r}}\right)^{3/2}$	$\tilde{\mathrm{Q}}_{\rm r}\gamma_{\rm d}^{1/2}$
Matter era	$\dfrac{\tilde{\mathrm{Q}}_{\rm m}}{H_{\rm m}}\gamma_{\rm d}^2 f$	$3H_{\rm m}\tilde{\mathrm{Q}}_{\rm m}f^{-1}$
Decaying into matter era	$\tilde{\mathrm{Q}}_{\rm rm}\gamma_{\rm d}^2\left(\dfrac{f}{3\sqrt{1+z_{\rm eq}}H_{\rm m}}\right)^{3/2}$	$\dfrac{12H_{\rm m}\tilde{\mathrm{Q}}_{\rm rm}}{\sqrt{1+z_{\rm eq}}}\gamma_{\rm d}^{-1/2}f^{-1}$

Table 4.2: SLND – super-critical case. For clarity, $\tilde{\mathrm{Q}}_{\rm r} = \dfrac{16c_{\rm r}\gamma_\infty^{-\epsilon_{\rm r}}\Omega_{\rm rad}\mathrm{Q}}{3(4\chi_{\rm r}-1)}$, $\tilde{\mathrm{Q}}_{\rm m} = \dfrac{3c_{\rm m}\Omega_{\rm mat}\gamma_\infty^{-\epsilon_{\rm m}}\mathrm{Q}}{8(2\chi_{\rm m}-1)}$ and $\tilde{\mathrm{Q}}_{\rm rm} = \dfrac{27c_{\rm r}\Omega_{\rm mat}\gamma_\infty^{-\epsilon_{\rm m}}\mathrm{Q}}{8(4\chi_{\rm r}-1)}$.

From these tables, one recovers that the loops produced during the radiation-dominated era give a plateau at high frequencies while all the other contributions decay as f^{-1} meaning that at high enough frequencies, the SGWB is a plateau where the dominant contribution comes from the radiation era. On the contrary, the low frequency region is usually dominated by GW produced during the matter-dominated era. Indeed, the contributions from radiation era and from the loops produced in radiation era and decaying into matter era have similar shapes in the low frequency range, but as $\Omega_{\rm mat} \gg \Omega_{\rm rad}$, the latter contribution dominates.

Another feature one can see is that in the sub-critical case (Table 4.1), the slopes of the SGWB from the large loop population is dependent on the values of $\chi_{\rm r}$ and $\chi_{\rm m}$ where the r index denotes radiation-domination and m matter-domination. Whereas in the super-critical regime Table 4.2, the frequency dependence of the spectrum is completely frozen.

For the EPSL, the spectrum presents a knee at the frequency scale $H_0\gamma_{\rm c}^{-1}$ and is completely suppressed on frequencies below $H_0\gamma_{\rm d}^{-1}$. Therefore, any impact on the SGWB happens on frequencies higher than $H_0\gamma_{\rm d}^{-1}$. In this frequency range, the dominant contribution coming for SLND is the radiation-domination one.

Frequency range	$f \ll H_0\gamma_\mathrm{c}^{-1}$	$H_0\gamma_\mathrm{c}^{-1} \ll f$
Radiation era $\chi_\mathrm{r} < 1/2$	$\dfrac{\hat{\mathrm{Q}}_\mathrm{r}}{(1-2\chi_\mathrm{r})(1-\chi_\mathrm{r})}\gamma_\mathrm{d}\left[\dfrac{f}{4(1+z_\mathrm{eq})H_\mathrm{r}}\right]^{1-2\chi_\mathrm{r}}$	$\dfrac{2\hat{\mathrm{Q}}_\mathrm{r}}{(1-2\chi_\mathrm{r})}\gamma_\mathrm{d}\gamma_\mathrm{c}^{2\chi_\mathrm{r}-1}$
Radiation era $\chi_\mathrm{r} = 1/2$	$2\hat{\mathrm{Q}}_\mathrm{r}\gamma_\mathrm{d}\ln\left(\dfrac{\gamma_\mathrm{d} f}{4H_\mathrm{r}(1+z_\mathrm{eq})}\right)$	$2\hat{\mathrm{Q}}_\mathrm{r}\left[1+\ln\left(\dfrac{\gamma_\mathrm{d}}{\gamma_\mathrm{c}}\right)\right]\gamma_\mathrm{d}$
Radiation era $\chi_\mathrm{r} > 1/2$	$\dfrac{\hat{\mathrm{Q}}_\mathrm{r}}{(2\chi_\mathrm{r}-1)(1-\chi_\mathrm{r})}\gamma_\mathrm{d}^{2\chi_\mathrm{r}}$	$\dfrac{\hat{\mathrm{Q}}_\mathrm{r}}{(2\chi_\mathrm{r}-1)(1-\chi_\mathrm{r})}\gamma_\mathrm{d}^{2\chi_\mathrm{r}}$
Matter era	$\dfrac{\hat{\mathrm{Q}}_\mathrm{m}}{3-2\chi_\mathrm{m}}\gamma_\mathrm{d}\left(\dfrac{f}{3H_\mathrm{m}}\right)^{1-2\chi_\mathrm{m}}$	$3H_\mathrm{m}\hat{\mathrm{Q}}_\mathrm{m}\gamma_\mathrm{d}\gamma_\mathrm{c}^{2\chi_\mathrm{m}-2}f^{-1}$

Table 4.3: EPSL. For clarity, $\hat{\mathrm{Q}}_\mathrm{r} = 2c_\mathrm{r}\Omega_\mathrm{rad}\mathrm{Q}$ and $\hat{\mathrm{Q}}_\mathrm{m} = \dfrac{27c_\mathrm{m}\Omega_\mathrm{mat}Q}{16(1-\chi_\mathrm{m})}$.

4.3.3 Beyond the fundamental mode

In Subsection 4.3.2 we have made the assumption that a loop emits GW in its fundamental mode, but this is not generally the case, especially if cusps or kinks are present on the loop [106, 308]. If cusps or kinks are present, the higher modes of the spectral power P_m are not zero but behave as m^{-q} where $q = 4/3$ for cusps, $5/3$ for kinks and 2 for kink-kink collisions. Even though there have been attempts to calculate the spectral power for all values of m [118], some even taking into account the gravitational back-reaction [120], we will make the following Ansatz for P_m

$$\mathrm{P}_\mathrm{m} = \Gamma\frac{m^{-q}}{\zeta(q)} \tag{4.23}$$

where ζ is the Riemann zeta function to ensure the normalization of P_m. Starting from equation (4.15) during the radiation era and injecting this spectral power P_m gives

$$\Omega_\mathrm{GW}(\ln f) = \frac{16\mathrm{Q}H_\mathrm{r}\Omega_\mathrm{rad}}{f}\gamma_\mathrm{d}^2\sum_1^\infty\frac{m^{-q}}{\zeta(q)}m\int_{z_\mathrm{eq}}^\infty \mathrm{d}z\, t^4\mathbf{n}\left[\frac{4(1+z)mH_\mathrm{r}}{f}\right]. \tag{4.24}$$

For the SLND from equation (4.13)

$$\Omega_\mathrm{GW}(\ln f) = \frac{4\mathrm{Q}C\Omega_\mathrm{rad}}{(p-1)}\gamma_\mathrm{d}^2\sum_1^\infty\frac{m^{-q}}{\zeta(q)}\left[\left(\frac{4H_\mathrm{r}m(1+z_\mathrm{eq})}{f}+\gamma_\mathrm{d}\right)^{1-p} - (\gamma_\infty+\gamma_\mathrm{d})^{1-p}\right]. \tag{4.25}$$

At high frequency and under the assumption that $\gamma_\infty \gg \gamma_\mathrm{d}$, the spectral power is factorized and one recovers the result assuming only the fundamental mode

$$\Omega_\mathrm{GW}(\ln f) = \frac{4\mathrm{Q}C\Omega_\mathrm{rad}}{(p-1)}\gamma_\mathrm{d}^{3-p}. \tag{4.26}$$

At low frequency the picture is slightly different and

$$\Omega_\mathrm{GW}(\ln f) = \frac{4\mathrm{Q}C\Omega_\mathrm{rad}}{(p-1)}\gamma_\mathrm{d}^2\left[\frac{4H_\mathrm{r}(1+z_\mathrm{eq})}{f}\right]^{1-p}\frac{\zeta(p+q-1)}{\zeta(q)}. \tag{4.27}$$

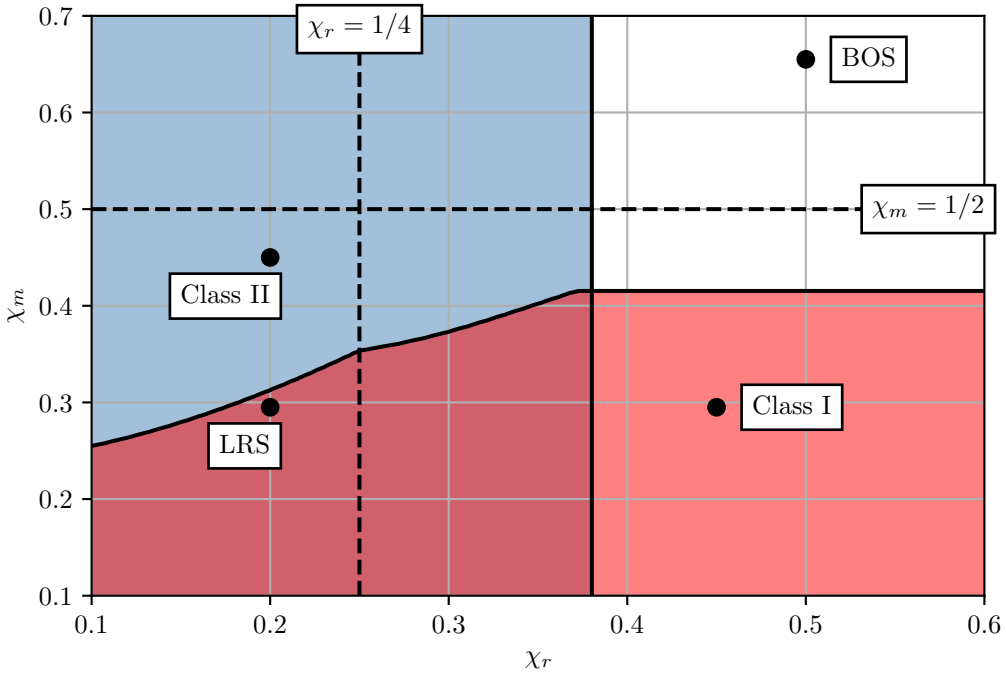

Figure 4.3: Impact of the extra population of small loops onto the SGWB in the parameter space $\chi_\mathrm{r}, \chi_\mathrm{m}$ for $G\mu = 10^{-13}$. In the blue region, the high frequency plateau for Ω_GW is dominated by the extra population of small loops produced during radiation era. In the red region, the spectrum presents a peak around $H_0 {\gamma_\mathrm{c}^{(m)}}^{-1}$ produced by the EPSL during the matter era. Outside those regions, the population of small loops can be neglected.

Even though we have only included the effects of the spectral power $\mathrm{P_m}$ on this single case, a simple calculation shows that this result can be generalized to the other types of loops distribution we discussed so far. At high frequencies, the SGWB of GW is insensitive to the decomposition into harmonics, while at low frequencies it is multiplied by a factor

$$\frac{\zeta(p+q-1)}{\zeta(q)}. \tag{4.28}$$

4.4 Results

The aim of this section is to characterize the shape of the SGWB, as a function of the loop production function exponents χ_r and χ_m. In particular, we assess the influence of the EPSL on the SGWB and divide the parameter space $(\chi_\mathrm{r}, \chi_\mathrm{m})$ into four classes with specific features.

4.4.1 Influence of the Extra Population of Small Loops on the SGWB

We can split the parameter space $(\chi_{\rm r}, \chi_{\rm m})$ in different regions depending on whether the EPSL from radiation or matter era has a significant imprint on the SGWB.

Loops from the radiation era produce a plateau at high frequency in the SGWB. The extra population of small loops introduces new features in the spectrum if its plateau is higher than the plateau of SLND, meaning

$$\frac{3(2\chi_{\rm r}-1/2)}{2(1-2\chi_{\rm r})}\left(\frac{\Upsilon}{\gamma_\infty}\right)^{2\chi_{\rm r}-1}\sqrt{\frac{\Gamma}{\gamma_\infty}}(G\mu)^{4\chi_{\rm r}^2-1/2}>1. \tag{4.29}$$

This is shown as the blue region of Fig. 4.3. In this figure we have used the regularized formulae of Appendix 4.C around $\chi_{\rm crit}$. We provide an analytical expansion in terms of $1/\ln(G\mu)$ in Appendix 4.F for the position of the blue region. It should be noted that the EPSL produced during radiation era can be dominant at high frequencies even if the network is super-critical. This sets a new scale for $\chi_{\rm r}$, between $\chi_{\rm crit}$ and $\chi_{\rm IR}$.

For loops produced during matter era, we assume that the extra population of small loops is visible if its peak at frequency $3H_{\rm m}\gamma_{\rm c}^{-1}$ with amplitude

$$\frac{27{\rm Q}c_{\rm m}\Omega_{\rm mat}}{8(3-2\chi_{\rm m})(2-2\chi_{\rm m})}\gamma_{\rm d}\gamma_{\rm c}^{2\chi_{\rm m}-1} \tag{4.30}$$

is bigger than all the other contributions at this frequency. This is represented as the red region in Fig. 4.3. Contrary to the loops produced during the radiation era, only a subset of the sub-critical models during matter era produce detectable features for the SGWB.

From Fig. 4.3, one can see that the BOS model can be safely replaced by an effective Dirac distribution loop production function for two reasons. First, the network is super-critical during both matter and radiation era meaning the SLND is universal with slope $-5/2$ during the radiation era and -2 during matter era [52]. Secondly, Fig. 4.3 shows that the extra population of small loops has a negligible impact on the SGWB.

4.4.2 Hybrid models

Fig. 4.3 can be used to build a classification of the various SGWB in the parameter space $(\chi_{\rm r}, \chi_{\rm m})$. Including the separation between sub-critical and super-critical regimes, there are nine different classes of spectra one can expect. For simplicity let us neglect the separation between sub-critical and super-critical and present four classes having distinctive features in terms of the SGWB.

The two first classes are represented by the well-known BOS model in Fig. 4.4a and the LRS model in Fig. 4.4b whose properties have been summed up on the figure. As we showed in the previous section, the BOS model can effectively neglect entirely the EPSL. On the contrary, it EPSL is a dominant source of GW in both the radiation and the matter era for the LRS model.

We can add to this list two new hybrid classes of models. In Fig. 4.4c, the EPSL of the radiation era can be neglected but not during the matter era, leading to peak around the frequency $3H_{\rm m}\gamma_{\rm c}^{-1}$. As we explain in the following section, this peak leads to interesting features when we consider the detection by GW detectors. Fig. 4.4d shows the opposite class in which the EPSL of the matter era can be neglected but not in the radiation era, producing a small valley in the SGWB.

As we attempted to make apparent in Fig. 4.4, each of those classes have different shapes on which one can read the parameters of the cosmic string network, apart from models like the BOS models, for which the shape of the SGWB does not depend on $(\chi_{\rm r}, \chi_{\rm m})$.

(a) $G\mu = 10^{-13}$, $\chi_{\rm r} = 0.5$, $\chi_{\rm m} = 0.655$.

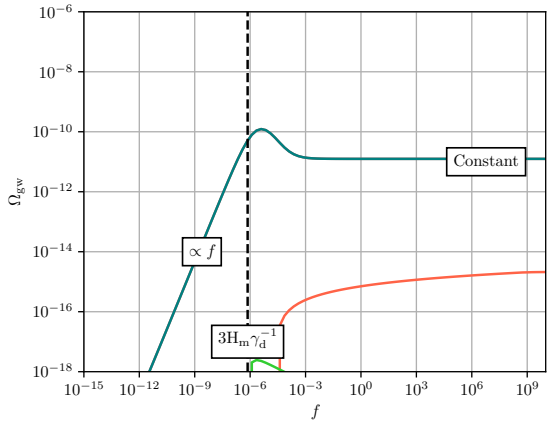

(b) $G\mu = 10^{-13}$, $\chi_{\rm r} = 0.2$, $\chi_{\rm m} = 0.295$.

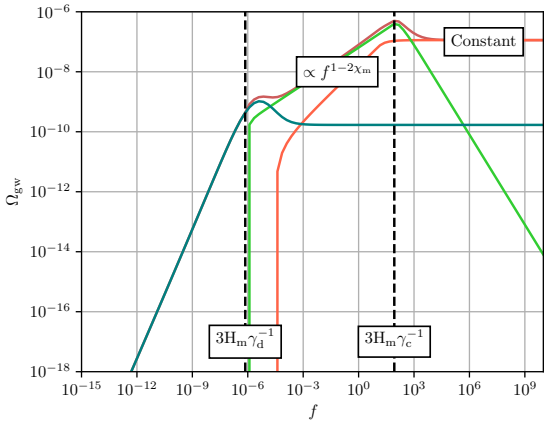

(c) $G\mu = 10^{-13}$, $\chi_{\rm r} = 0.45$, $\chi_{\rm m} = 0.295$.

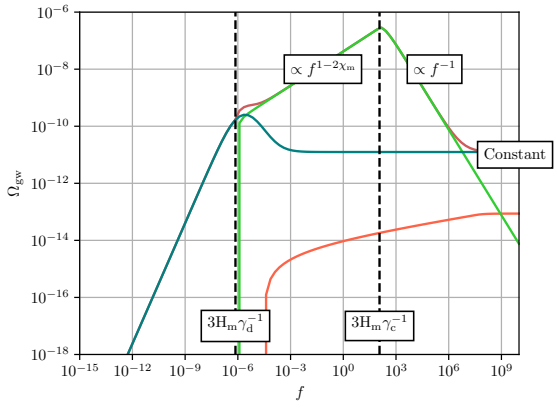

(d) $G\mu = 10^{-13}$, $\chi_{\rm r} = 0.2$, $\chi_{\rm m} = 0.45$.

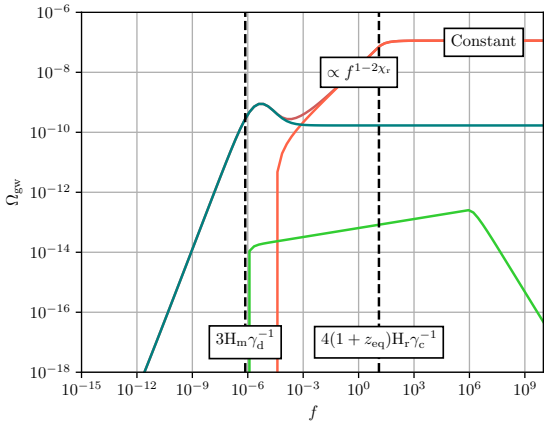

Figure 4.4: Four different classes of SGWB.

4.4.3 Constraints on the string tension from GW experiments

We have not yet been able to detect any SGWB in the European Pulsar Timing Array [213] nor in the first two LIGO/Virgo runs [91, 32], giving only upper bounds on the cosmic string tension. New data analysis techniques are being devised for the next generation of GW detectors such as LISA [35]. If ongoing and future GW experiments could potentially detect the SGWB coming from cosmic strings, it is a challenging data analysis problem to characterize the observed spectrum and distinguish between the variety of expected astrophysical and cosmological sources.

In this section, we do not pretend to tackle any of the technical difficulties of the detection of a SGWB. In particular, we will assume that we are able to separate the astrophysical foreground from the cosmological source of GW. The theoretical GW detector is modelled as having a given sensitivity curve, function of the frequency. We will make the assumption that the bandwidth of the detector is infinitely thin around a typical frequency and a given sensitivity $\Omega_{\rm GW}$. This is of course a brutal assumption, however we expect that progress in the data analysis techniques can be effectively taken into account by changing the sensitivity of the instrument. As we possess analytic expressions for the stochastic background of gravitational waves within our framework, we can easily explore the parameter space $(G\mu, \chi_{\rm r}, \chi_{\rm m})$. The result are summarized in Fig. 4.5.

As was shown in previous sections, the extra population of small loops modifies the GW spectrum at frequencies higher than $3H_{\rm m}\gamma_{\rm d}^{-1}$, hence we expect it to have an impact on high frequency instruments such as LIGO/Virgo. It turns out the effect of the EPSL is quite dramatic for ground-based telescopes as illustrated in Fig. 4.5a. Not only does the constraint on $G\mu$ spans over nearly 10 orders of magnitude on the parameter space, it also presents a folding for small values of $\chi_{\rm m} \lesssim 0.3$ and $\chi_{\rm r} \gtrsim 0.3$. The folding is illustrated by a slice at constant $\chi_{\rm m}$ in Fig. 4.5b. This peculiar feature means that the constraint on $G\mu$ for these models is not an upper bound on $G\mu$ but rather that a set of intervals for $G\mu$ being excluded. This can be understood by looking at Fig. 4.4c. The peak at $f = 3H_{\rm m}\gamma_{\rm d}^{-1}$ caused by the EPSL produced during matter era enters within the bandwidth of the detectors for a given set of $G\mu$ excluding another interval for $G\mu$.

On the contrary, experiments at lower frequencies, are not affected by the extra population of small loops and are only sensitive to the slopes of the SLND. As the shape of the SLND is universal for super-critical models we expect the detection surface to be flat in the upper-right corner for low frequency experiments. For sub-critical networks however, the shape of the spectrum is modified, and we expect the detection surface to be dependent on the values of $\chi_{\rm r}$ and $\chi_{\rm m}$ as can be seen in Figs. 4.5c and 4.5d.

4.5 Conclusion

Our framework allowed us to produce analytic formulae for the SGWB for cosmic strings including its small-scale structure. In particular, the introduction of a back-reaction scale $\gamma_{\rm c} \ll \gamma_{\rm d}$ produces an EPSL which can have an important effect on the SGWB for the LRS model [123]. We proposed a parametrization, using variables $\chi_{\rm r}$ and $\chi_{\rm m}$, of the uncertainty on the dynamics of the infinite string network [123, 52]. We showed that the predictions of BOS [114] are stable if one introduces this back-reaction scale, and that the extra population of loops is subdominant in terms of GW production in this particular model. We are also in agreement with LRS [123].

We showed the small-scale structure of cosmic strings can have a significant impact on the SGWB even *outside the super-critical regime* and calculated the region of the parameter space where its effect cannot be neglected. We classified the GW power spectra coming from cosmic strings into

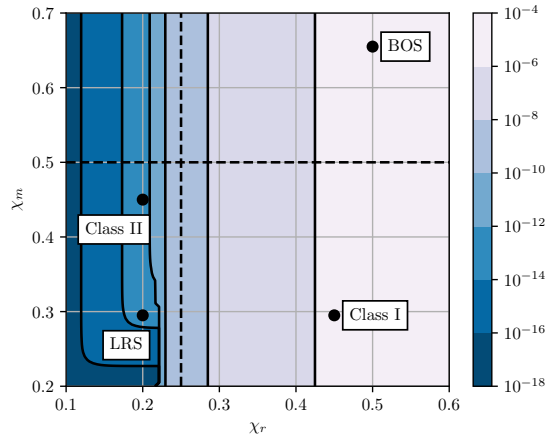

(a) LIGO/Virgo, sensitivity of $\Omega_{\rm GW} = 10^{-7}$ taken at $f = 20$ Hz.

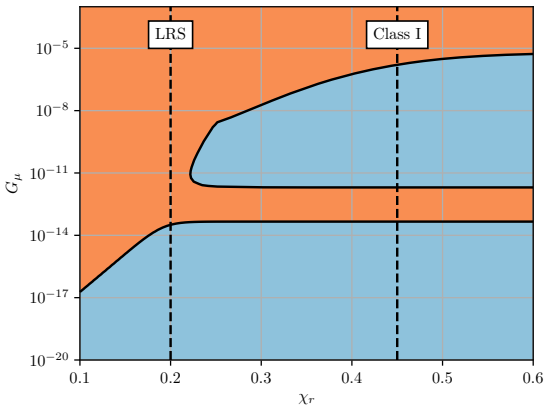

(b) LIGO/Virgo constraints on $G\mu$ at $\chi_{\rm m} = 0.295$. The orange region is excluded giving non-convex constraints on $G\mu$ for a given model.

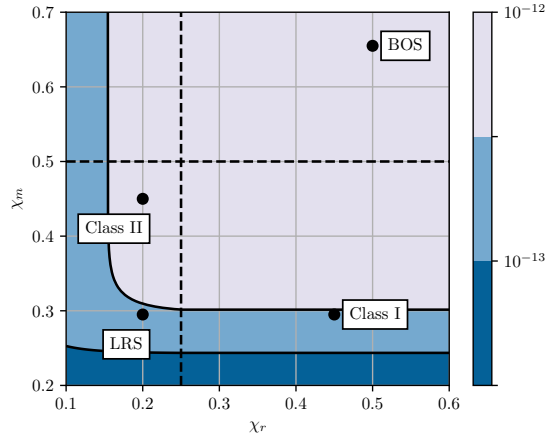

(c) PTA, sensitivity of $\Omega_{\rm GW} = 10^{-12}$ taken at $f = 2 \times 10^{-9}$ Hz.

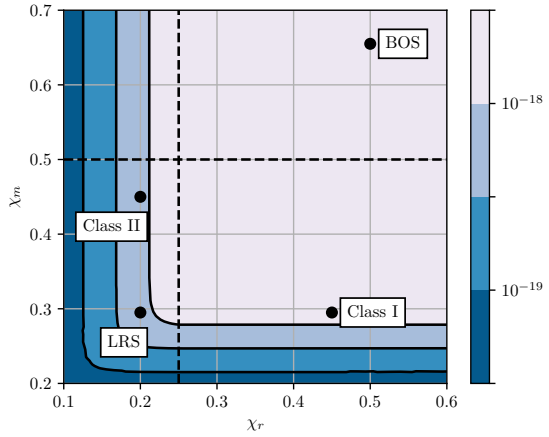

(d) LISA, sensitivity of $\Omega_{\rm GW} = 10^{-13}$ taken at $f = 10^{-2}$ Hz.

Figure 4.5: Detection surface for the three types of GW detectors in the $(\chi_{\rm r}, \chi_{\rm m})$ parameter space. The color scale gives the upper bound on $G\mu$. Note that the detection surface is folded for LIGO/Virgo explaining why constraints on $G\mu$ jump several orders of magnitude in the lower left corner. Fig. 4.5b is a slice at constant $\chi_{\rm m}$.

four different classes, for which we have shown two new and called *hybrid models*. The values of the parameters $\chi_{\rm r}$ and $\chi_{\rm m}$ for these two hybrid models are not supported by any numerical simulation, however the uncertainty on $\chi_{\rm r}$ and $\chi_{\rm m}$ motivates us to consider them.

We have also estimated systematically the constraints on the string tension $G\mu$ of different types of GW detectors and showed that low-frequency experiments will provide more stable and model-independent bounds while ground-based detectors will be very sensitive to the details of the small-scale structure of the cosmic string network.

4.A Cosmological parameters

We assumed the Λ-CDM cosmology with the parameters in Table 4.4. For the sake of simplicity, we neglected the impact of the late-time acceleration of the Universe. We also neglected the changes in the relativistic degrees of freedom, something which would decrease slightly the high frequency plateau. The Hubble parameter is

$$H(z) = H_0\sqrt{\Omega_{\rm rad}(1+z)^4 + \Omega_{\rm mat}(1+z)^3} \tag{4.31}$$

and the cosmic time is given by

$$t(z) = \int_z^\infty \frac{{\rm d}z'}{H(z')(1+z')} \tag{4.32}$$

Parameter	Value
h	0.678
H_0	$100h{\rm km.s^{-1}Mpc^{-1}}$
$\Omega_{\rm rad}$	9.1476×10^{-5}
$\Omega_{\rm mat}$	0.308
$H_{\rm r}$	$H_0\sqrt{\Omega_{\rm rad}}$
$H_{\rm m}$	$H_0\sqrt{\Omega_{\rm mat}}$

Table 4.4: Cosmological parameters from Ref. [312].

4.B Note on the decomposition of the loop number density

In the sub-critical regime, the scaling LND is given by

$$t^4\mathbf{n}(\gamma_{\rm c}\leq\gamma) = \frac{c}{\epsilon}(\gamma+\gamma_{\rm d})^{2\chi-3} f\left(\frac{\gamma_{\rm d}}{\gamma+\gamma_{\rm d}}\right) \tag{4.33}$$

In this equation the function f is defined by

$$f(x) \equiv {}_2{\rm F}_1(3-2\chi,\epsilon;\epsilon+1;x) \underset{1}{\sim} \frac{\Gamma(3\nu-2\chi)\Gamma(2\chi-2)}{\Gamma(3\nu-3)}x^{-\epsilon} + \frac{\epsilon}{2-2\chi}(1-x)^{2\chi-2} \tag{4.34}$$

where we have expanded the hypergeometric function around unity using Gamma functions [313]. Taking the limit $\gamma_{\rm c}\leq\gamma\ll\gamma_{\rm d}$

$$t^4\mathbf{n}(\gamma_{\rm c}\leq\gamma\ll\gamma_{\rm d}) \sim \frac{\Gamma(3\nu-2\chi)\Gamma(2\chi-2)}{\Gamma(3\nu-3)}\frac{c}{\epsilon}\gamma_{\rm d}^{2\chi-3} + \frac{c\gamma_{\rm d}^{-1}}{2-2\chi}\gamma^{2\chi-2} \tag{4.35}$$

where the Gamma function factor is 1 for $\chi = \chi_{\rm crit}$, of order unity for $0.1 < \chi$ and eventually diverges for $\chi = 0$. A similar approach in the super-critical regime $\epsilon < 0$ leads to Eq. (3.57)

$$t^4\mathbf{n}(\gamma_{\rm c} \leq \gamma \ll \gamma_{\rm d}) \simeq \frac{c\gamma_{\rm d}^{-1}}{2-2\chi}\gamma^{2\chi-2} - \frac{c\gamma_\infty^{-\epsilon}}{\epsilon}\gamma_{\rm d}^{-4+3\nu} \tag{4.36}$$

The scale $\gamma_{\rm IR}$ giving a knee in the LND is precisely set by the competition between these two contributions. It should be noted that the EPSL *can be described uniformly in the three regimes* sub-critical, critical and super-critical. This property makes it easier for us to conduct our analysis and makes this decomposition very natural.

4.C Regularization around $\chi_{\rm crit}$ for the standard loop number density

The decomposition for the SLND of Section 4.2.4 fails around $\chi_{\rm crit}$ and needs regularization terms to remain consistent. Introducing $\gamma_{\rm d}$, we suggest the following scheme

- for sub-critical regimes, $C = \frac{\rm c}{\epsilon}\left[1 - \left(\frac{\gamma_{\rm d}}{\gamma_\infty}\right)^\epsilon\right]$
- for super-critical regimes, $C = -\frac{\rm c}{\epsilon}\left(\gamma_\infty^{-\epsilon} - \gamma_{\rm d}^{-\epsilon}\right)$

leading to the limit when $\epsilon \to 0$

$$C = {\rm c}\ln\left(\frac{\gamma_{\rm d}}{\gamma_\infty}\right) \tag{4.37}$$

This regularization scheme gives a good approximation around $\chi_{\rm crit}$ at the expanse of underestimating the LND for large γ. We can use this approximation to calculate the stochastic background for which we give the asymptotic behaviour in Table 4.5.

Frequency range	$f \ll H_0\gamma_{\rm d}^{-1}$	$H_0\gamma_{\rm d}^{-1} \ll f$
Radiation era	$\mathrm{Q_r}\gamma_{\rm d}^2\left(\frac{f}{4(1+z_{\rm eq})H_{\rm r}}\right)^{3/2}$	$\mathrm{Q_r}\sqrt{\gamma_{\rm d}}$
Matter era	$\frac{\mathrm{Q_m}}{H_{\rm m}}\gamma_{\rm d}^2 f$	$27H_{\rm m}\mathrm{Q_m}f^{-1}$
Decaying into matter era	$\frac{\mathrm{Q_{rm}}}{4}\gamma_{\rm d}^2\left(\frac{f}{3\sqrt{1+z_{\rm eq}}H_{\rm m}}\right)^{3/2}$	$\frac{3H_{\rm m}\mathrm{Q_{rm}}}{\sqrt{1+z_{\rm eq}}}\gamma_{\rm d}^{-1/2}f^{-1}$

Table 4.5: SLND – critical case. For simplicity $\mathrm{Q_r} = \frac{8c_{\rm r}\Omega_{\rm rad}}{3}\ln\left(\frac{\gamma_\infty}{\gamma_{\rm d}}\right)$, $\mathrm{Q_m} = \frac{3c_{\rm m}\Omega_{\rm mat}}{8}\ln\left(\frac{\gamma_\infty}{\gamma_{\rm d}}\right)$, $\mathrm{Q_{rm}} = \frac{27c_{\rm r}\Omega_{\rm mat}}{4}\ln\left(\frac{\gamma_\infty}{\gamma_{\rm d}}\right)$.

4.D Contributions in the radiation era

In the radiation era, we can make the following approximations:

$$H(z) = (1+z)^2 H_{\rm r} \tag{4.38}$$

$$t(z) = \frac{1}{2(1+z)^2 H_{\rm r}} \tag{4.39}$$

where $H_{\rm r} = H_0\sqrt{\Omega_{\rm rad}}$. In this case,

$$\Omega_{\rm GW}(\ln f) = \frac{64 {\rm Q} H_{\rm r}\Omega_{\rm rad}}{f}\gamma_{\rm d}^2 \int_{z_{\rm eq}}^{\infty} {\rm d}z\, t^4 \mathbf{n}\left[\frac{4(1+z)H_{\rm r}}{f}\right]. \tag{4.40}$$

4.D.1 Standard loop distribution

If we consider in the radiation era a loop distribution function

$$t^4\mathbf{n}(\gamma) = C(\gamma+\gamma_{\rm d})^{-p}\Theta(\gamma_\infty - \gamma), \tag{4.41}$$

we can evaluate analytically $\Omega_{\rm GW}$. In particular there is a typical frequency $f_b = 4(1+z_{\rm eq})H_{\rm r}\gamma_{\rm d}^{-1}$ which corresponds to a knee in the power spectrum which can be used to rewrite the GW power spectrum.

$$\Omega_{\rm GW}(\ln f) = \frac{4{\rm Q}C\Omega_{\rm rad}}{(p-1)}\gamma_{\rm d}^{3-p}\left[\left(1+\frac{4H_{\rm r}(1+z_{\rm eq})}{f\gamma_{\rm d}}\right)^{1-p} - \left(1+\frac{\gamma_\infty}{\gamma_{\rm d}}\right)^{1-p}\right] \tag{4.42}$$

4.D.2 Extra population of small loops

We perform the same analysis but with the distribution defined in equation (4.14). Due to the piece-wise nature of the LND, we have to distinguish two cases. In this case, $f_a = 4(1+z_{\rm eq})H_{\rm r}\gamma_{\rm d}^{-1}$ and $f_b = 4(1+z_{\rm eq})H_{\rm r}\gamma_{\rm c}^{-1}$

$$\Omega_{\rm GW}(\ln f < \ln f_b) = \frac{4{\rm Q}c_{\rm r}\Omega_{\rm rad}}{(1-2\chi_{\rm r})(2-2\chi_{\rm r})}\gamma_{\rm d}\gamma_{\rm c}^{2\chi_{\rm r}-1}\left[\left(\frac{f_b}{f}\right)^{2\chi_{\rm r}-1} - \left(\frac{\gamma_{\rm d}}{\gamma_{\rm c}}\right)^{2\chi_{\rm r}-1}\right] \tag{4.43}$$

$$\Omega_{\rm GW}(\ln f > \ln f_b) = \frac{4{\rm Q}c_{\rm r}\Omega_{\rm rad}}{(1-2\chi_{\rm r})(2-2\chi_{\rm r})}\gamma_{\rm d}\gamma_{\rm c}^{2\chi_{\rm r}-1}\left[(2-2\chi_{\rm r}) - \frac{f_b}{f}(1-2\chi_{\rm r}) - \left(\frac{\gamma_{\rm d}}{\gamma_{\rm c}}\right)^{2\chi_{\rm r}-1}\right] \tag{4.44}$$

One can remark several things

- when $\chi_{\rm r} < 1/2$ the value of the plateau at high frequencies is given by the scale $\gamma_{\rm c}$
- when $\chi_{\rm r} > 1/2$ the plateau is given by the scale $\gamma_{\rm d}$ in a way very similar to the SLND

In the special case where $\chi_{\rm r} = 1/2$, the cutoff is of primordial importance

$$\Omega_{\rm GW}(\ln f < \ln f_b) = 4{\rm Q}c_{\rm r}\Omega_{\rm rad}\gamma_{\rm d}\ln\left(\frac{f}{f_a}\right) \tag{4.45}$$

$$\Omega_{\rm GW}(\ln f > \ln f_b) = 4{\rm Q}c_{\rm r}\Omega_{\rm rad}\gamma_{\rm d}\left[1 - \frac{f_b}{f} + \ln\left(\frac{\gamma_{\rm d}}{\gamma_{\rm c}}\right)\right] \tag{4.46}$$

4.E Contributions during matter era

In the matter era, we can make the following approximations:

$$H(z) = (1+z)^{3/2} H_{\rm m} \tag{4.47}$$

$$t(z) = \frac{2}{3(1+z)^{3/2} H_{\rm m}} \tag{4.48}$$

where $H_{\rm m} = H_0\sqrt{\Omega_{\rm mat}}$. In this case,

$$\Omega_{\rm GW}(f) = \frac{81 Q H_{\rm m} \Omega_{\rm mat}}{16 f} \gamma_{\rm d}^2 \int_0^{z_{\rm eq}} {\rm d}z\, (1+z)^{-3/2} t^4 \mathbf{n}\left[\frac{3\sqrt{1+z} H_{\rm m}}{f}\right] \tag{4.49}$$

We expect two types of sources in the matter era, scaling loops formed during the matter era and remnants from the radiation era which decay with time.

4.E.1 Scaling loops during matter era – Standard loop distribution

Assuming a scaling large-loop distribution

$$t^4 \mathbf{n}(\gamma) = C(\gamma + \gamma_{\rm d})^{-p} \Theta(\gamma_\infty - \gamma) \tag{4.50}$$

Changing variables from z to $x = \dfrac{3\sqrt{1+z} H_{\rm m}}{f \gamma_{\rm d}}$ we obtain

$$\Omega_{\rm GW}(f) = \frac{3^5 Q C H_{\rm m}^2 \Omega_{\rm mat}}{8 f^2} \gamma_{\rm d}^{1-p} \int_{\frac{3H_{\rm m}}{f\gamma_{\rm d}}}^{\frac{3\sqrt{1+z_{\rm eq}} H_{\rm m}}{f\gamma_{\rm d}}} {\rm d}x\, (1+x)^{-p} x^{-2} \Theta\left(\frac{\gamma_\infty}{\gamma_{\rm d}} - x\right) \tag{4.51}$$

Approximate solution

One can introduce the typical frequency

$$f_c = (p+1)^{1/p} \frac{3 H_{\rm m}}{\gamma_{\rm d}} \tag{4.52}$$

and use it to interpolate the GW power spectrum between the two solvable regimes of low and high frequency

$$\Omega_{\rm GW}(\ln f) = \frac{81 Q C H_{\rm m} \Omega_{\rm mat}}{8 f} \gamma_{\rm d}^{2-p} \left(\frac{f}{f_c + f}\right)^p \tag{4.53}$$

Exact solution

There exists a well-defined exact primitive to this integral we can use to obtain an exact solution even around the peak.

$$- \frac{{}_2{\rm F}_1\left(p, 1+p; 2+p; -\dfrac{1}{x}\right)}{(1+p) x^{p+1}} \tag{4.54}$$

Indeed, even though the Gauss hypergeometric function has a radius of convergence of 1, it turns out it converges for $\frac{1}{x} < 0$.

This primitive can be used but is not very practical. However, we can use it to perform a simple comparison. We know that the region where the approximation will be the worse is around f_c, we can calculate the precision of this approximation there.

In the case of the approximate solution

$$\Omega_{\rm GW}(f_c) = \frac{3^4 {\rm Q} C H_{\rm m} \Omega_{\rm mat}}{f_c 2^{p+3}} \gamma_{\rm d}^{2-p} \tag{4.55}$$

While for the exact solution, if $f = f_c$

$$\Omega_{\rm GW}(f_c) = \frac{3^4 {\rm Q} C H_{\rm m} \Omega_{\rm mat}}{8 f_c} \gamma_{\rm d}^{2-p} \left[{}_2{\rm F}_1\left(p, 1+p; 2+p; -(p+1)^{1/p}\right) - \frac{{}_2{\rm F}_1\left(p, 1+p; 2+p; -\frac{(p+1)^{1/p}}{\sqrt{1+z_{\rm eq}}}\right)}{\sqrt{1+z_{\rm eq}}^{p+1}} \right] \tag{4.56}$$

Then the ratio between the exact value divided by the approximate one in the limit $z_{\rm eq} \to \infty$ is

$$2^p {}_2{\rm F}_1\left(p, 1+p; 2+p; -(p+1)^{1/p}\right) \underset{p=2}{=} 0.82 \tag{4.57}$$

We see that the approximate solution overestimate the value of the peak.

4.E.2 Scaling loops during matter era – extra population of small loops

Assuming the EPSL distribution. Five cases happen depending on the frequencies:

$$f_1 = \frac{3 H_{\rm m}}{\gamma_{\rm d}}, f_2 = \frac{3 H_{\rm m} \sqrt{1+z_{\rm eq}}}{\gamma_{\rm d}} \tag{4.58}$$

$$f_3 = \frac{3 H_{\rm m}}{\gamma_{\rm c}}, f_4 = \frac{3 H_{\rm m} \sqrt{1+z_{\rm eq}}}{\gamma_{\rm c}} \tag{4.59}$$

$\Omega_{\rm GW}(f < f_1) = 0$. The other results come straightforwardly

$$\Omega_{\rm GW}(f_1 < f < f_2) = \frac{81 {\rm Q} c_{\rm m} H_{\rm m} \Omega_{\rm mat}}{8(3-2\chi_{\rm m})(2-2\chi_{\rm m}) f} \gamma_{\rm d} \gamma_{\rm c}^{2\chi_{\rm m}-2} \left(\frac{f_3}{f}\right)^{2\chi_{\rm m}-2} \left[1 - \left(\frac{f_1}{f}\right)^{3-2\chi_{\rm m}}\right] \tag{4.60}$$

we can check the continuity in f_1. The next region gives

$$\Omega_{\rm GW}(f_2 < f < f_3) = \frac{81 {\rm Q} c_{\rm m} H_{\rm m} \Omega_{\rm mat}}{8(3-2\chi_{\rm m})(2-2\chi_{\rm m}) f} \gamma_{\rm d} \gamma_{\rm c}^{2\chi_{\rm m}-2} \left(\frac{f_3}{f}\right)^{2\chi_{\rm m}-2} \left[1 - \left(\frac{f_3}{f_4}\right)^{3-2\chi_{\rm m}}\right] \tag{4.61}$$

One can check easily the continuity in f_2 and f_3.

$$\Omega_{\rm GW}(f_3 < f < f_4) = \frac{81 Q c_{\rm m} H_{\rm m} \Omega_{\rm mat}}{8(3-2\chi_{\rm m})(2-2\chi_{\rm m}) f} \gamma_{\rm d} \gamma_{\rm c}^{2\chi_{\rm m}-2} \frac{f_3}{f} \left[(3-2\chi_{\rm m}) \frac{f}{f_3} + (2\chi_{\rm m}-2) - \left(\frac{f}{f_4}\right)^{3-2\chi_{\rm m}} \right] \tag{4.62}$$

$$= \frac{81 Q c_{\rm m} H_{\rm m} \Omega_{\rm mat}}{8(2-2\chi_{\rm m}) f} \gamma_{\rm d} \gamma_{\rm c}^{2\chi_{\rm m}-2} () \{ 1 - \frac{f_3}{f} \frac{1}{3-2\chi_{\rm m}} \left[(2-2\chi_{\rm m}) + \left(\frac{f}{f_4}\right)^{3-2\chi_{\rm m}} \right] \} \tag{4.63}$$

here are again two formulae for the continuity in f_3 and f_4. The last region gives

$$\Omega_{\rm GW}(f_4 < f) = \frac{81 Q c_{\rm m} H_{\rm m} \Omega_{\rm mat}}{8(2-2\chi_{\rm m}) f} \gamma_{\rm d} \gamma_{\rm c}^{2\chi_{\rm m}-2} \left(1 - \frac{f_3}{f_4}\right) \tag{4.64}$$

4.E.3 Decaying loops from radiation era

For loops created during radiation era, the relaxation term in matter era is

$$t^4 \mathbf{n}(\gamma) = C \left(\frac{t}{t_{\rm eq}}\right)^4 \left(\frac{1+z}{1+z_{\rm eq}}\right)^3 \left(\frac{t_{\rm eq}}{t}\right)^p (\gamma+\gamma_{\rm d})^{-p} \Theta \left[\gamma_\infty + \gamma_{\rm d} - (\gamma+\gamma_{\rm d}) \frac{t}{t_{\rm eq}} \right] \tag{4.65}$$

$$= c \left(\frac{1+z_{\rm eq}}{1+z}\right)^{3-3p/2} (\gamma+\gamma_{\rm d})^{-p} \Theta \left[\gamma_\infty + \gamma_{\rm d} - (\gamma+\gamma_{\rm d}) \left(\frac{1+z_{\rm eq}}{1+z}\right)^{3/2} \right] \tag{4.66}$$

Loops smaller than $\gamma_{\rm d}$ decay very rapidly. Changing variables from z to $x = \dfrac{3\sqrt{1+z} H_{\rm m}}{f \gamma_{\rm d}}$

$$\Omega_{\rm GW}(f) = \frac{81 Q C H_{\rm m} \Omega_{\rm mat}}{8f} (1+z_{\rm eq})^{3/2(2-p)} \gamma_{\rm d}^{2-p} \left(\frac{f\gamma_{\rm d}}{3H_{\rm m}}\right)^{3p-7} \int x^{3p-8} (1+x)^{-p} \, {\rm d}x \tag{4.67}$$

Approximate solution

Using the same idea as in the previous section, we introduce a new frequency f_d that separates the different regimes.

$$f_d = \frac{3H_{\rm m}}{\gamma_{\rm d}} \left[\frac{2p-7}{3p-7} \frac{(1+z_{\rm eq})^{-1/2} - (1+z_{\rm eq})^{3/2(2-p)}}{(1+z_{\rm eq})^{-(p+1)/2} - (1+z_{\rm eq})^{3/2(2-p)}} \right]^{1/p} \tag{4.68}$$

One can use to find an interpolating formula for the GW power spectrum

$$\Omega_{\rm GW}(\ln f) = \frac{81 Q C H_{\rm m} \Omega_{\rm mat}}{8f} \gamma_{\rm d}^{2-p} \left(\frac{f}{f+f_d}\right)^p \frac{(1+z_{\rm eq})^{-1/2} - (1+z_{\rm eq})^{3/2(2-p)}}{3p-7} \tag{4.69}$$

This expression starts to be much more complicated because we need to keep track of the two boundary terms of the integral. Different behaviour appear:

- $p < 7/3 \approx 2.33$, a very soft slope, all the integrals are dominated by the lower bound

- $7/3 < p < 7/2 = 3.5$, the large f bound is dominated by the lower bound and the low f is dominated by the higher bound.
- $7/2 < p$, a very steep slope, all the integrals are dominated by the higher bound

In practice, we will only consider $p \in [2, 3]$

There is also a well-defined primitive for this integral

$$\frac{x^{-7+3p}\,{}_2\mathrm{F}_1(p, -7+3p; -6+3p; -x)}{-7+3p} \tag{4.70}$$

but it is not very practical to use.

4.F Analytic estimation for the boundary in χ_r

The question is to find for which values of χ_r does the EPSL leave a signature in the SGWB. This boils down to finding the value for χ_r at which the two contributions are equal. $G\mu$ being an infinitesimal quantity, one can perform an expansion as:

$$\chi_\mathrm{r}(G\mu) = \chi_\star + \frac{A}{\ln(G\mu)} + \frac{B}{\ln^2(G\mu)} \tag{4.71}$$

. Where $\chi_\star = \sqrt{3\nu - 1}/2 = \dfrac{1}{2\sqrt{2}}$. One obtains

$$A = \frac{1}{8\chi_\star} \ln\left(\frac{(1-2\chi_\star)}{(2\chi_\star + 1 - 3\nu)(3-3\nu)} \left(\frac{\Gamma}{\gamma_\infty}\right)^{3\nu-2} \left(\frac{\Upsilon}{\gamma_\infty}\right)^{1-2\chi_\star} \right) \tag{4.72}$$

$$B = \frac{-A}{4\chi_\star}\left[2A + \frac{1}{2\chi_\star + 1 - 3\nu} + \frac{1}{2-2\chi_\star} + \frac{1}{1-2\chi_\star} + \ln\left(\frac{\Upsilon}{\gamma_\infty}\right)\right] \tag{4.73}$$

Chapter 5

Constraints on cosmic strings using data from the third Advanced LIGO-Virgo observing run

This chapter is a reproduction of [59] written by the LIGO/Virgo/KAGRA collaboration. The aim of this work was to use the data from the third observing run (O3) to put constraints on cosmic strings. I was asked to be part of the paper writing team, together with five other colleagues, and of the analysis team. Therefore, I contributed fully to writing the paper. Regarding calculations, I was responsible for the burst analysis, and I cross-checked all the results from the stochastic analysis. The code I developed for the LISA collaboration was very useful in this context, and was the basis of the new analysis (it underwent review within the collaboration). Relative to previous publications by the LVK collaboration on cosmic strings, the novelties in this paper were:

- The addition of a new class of models dubbed Models **C**, developed in the Chapters 3 and 4.
- The addition of the waveforms for kink-kink collisions, something relevant for very wiggly strings.
- The update of certain numerical factors in the waveforms for cusps, kinks and kink-kink collisions.

Abstract

We search for gravitational-wave signals produced by cosmic strings in the Advanced LIGO and Virgo full O3 data set. Search results are presented for gravitational waves produced by cosmic string loop features such as cusps, kinks and, for the first time, kink-kink collisions. A template-based search for short-duration transient signals does not yield a detection. We also use the stochastic gravitational-wave background energy density upper limits derived from the O3 data to constrain the cosmic string tension, $G\mu$, as a function of the number of kinks, or the number of cusps, for two cosmic string loop distribution models. Additionally, we develop and test a third model which interpolates between these two models. Our results improve upon

the previous LIGO-Virgo constraints on $G\mu$ by one to two orders of magnitude depending on the model which is tested. In particular, for the one-loop distribution model, we set the most competitive constraints to date, $G\mu \lesssim 4\times10^{-15}$. In the case of cosmic strings formed at the end of inflation in the context of Grand Unified Theories, these results challenge simple inflationary models.

5.1 Introduction

The Advanced LIGO [314] and Advanced Virgo [315] detectors have opened a new channel to observe the Universe through the detection of gravitational waves. In their first three observing runs (O1, O2, and the first half of O3) the LIGO Scientific Collaboration and the Virgo Collaboration have reported the detection of 50 candidate gravitational-wave events from compact binary coalescences [19]. These detections have yielded important information on the population properties of these compact binary sources [316]. In the future, ground-based detectors may discover new sources of gravitational waves [317], some of which could probe the physics of the early Universe. Cosmic strings [61] belong to this category of sources. The third observing run (O3) started on April 1, 2019, and ended on March 27, 2020, and we use the data from the LIGO-Hanford (H1), LIGO-Livingston (L1) and Virgo (V1) interferometers to place constraints on cosmic strings. These constraints are reported in this letter.

Cosmic strings are line-like topological defects — analogues of vortices in different condensed matter systems — which are formed from spontaneous symmetry breaking phase transitions (with the additional condition that the vacuum manifold has non-contractible closed curves [61, 64, 69, 88]). In cosmology, such phase transitions may have occurred at grand unification [62], corresponding to an energy scale of about 10^{16} GeV, and more generally at lower energy scales. Thus cosmic strings, through their different observational predictions, offer a tool to probe particle physics beyond the Standard Model at energy scales much above the ones reached by accelerators. In particular, the production of gravitational waves by cosmic strings [117, 204] is one of the most promising observational signatures that can be accessed by ground-based detectors.

The width of the string, of the order of the energy scale of the transition, is generally negligible compared to the cosmological scales over which it extends. This limit is well described by the Nambu-Goto action. Nambu-Goto strings [64] are parametrized by a dimensionless quantity: the string tension $G\mu$ related to the energy scale η at which cosmic strings are formed, $G\mu \sim (\eta/M_{\rm Pl})^2$, where G stands for Newton's constant, $M_{\rm Pl}$ is the Planck mass, μ denotes the string linear mass density[1], and we set the speed of light $c = 1$. In an expanding background, such as a radiation or dominated era, a cosmic string network relaxes towards a scaling solution — a self-similar, attractor solution in which all typical loop lengths are proportional to cosmic time, or equivalently they scale with the Hubble radius. Super-horizon (also called infinite) strings reach this scaling solution [221, 101, 135] being stretched by the expansion of the Universe and by losing energy through the formation of sub-horizon (loop) strings, which consequently lead to a cascade of smaller loops eventually decaying through emission of gravitational waves [92, 208, 204]. In this chapter we focus on the gravitational waves emitted by the network of loops. The length distribution of loops

[1]Cosmic superstrings [318], the analogues of cosmic strings arising from string theory, are characterized also by the intercommutation probability which can take values between 10^{-3} and 1 for fundamental superstrings (F-strings) and between 10^{-1} and 1 for D-branes extended in one macroscopic dimension (D-strings). In our present study we concentrate on field theoretical objects [294], and in particular Nambu-Goto strings with intercommutation probability of order one.

will therefore be crucial in determining the gravitational-wave signatures from cosmic strings. We consider different models for the loop distribution, each of which has been studied in the literature, and whose differences arise from different modelling of the production and cascade of loops from the infinite string network.

Cosmic string loops oscillate periodically in time, emitting gravitational waves with power [117] $P_{\rm gw} = \Gamma_{\rm d} G\mu^2$ and decay in a lifetime $\ell/\gamma_{\rm d}$, where $\Gamma_{\rm d}$ is a numerical factor ($\Gamma_{\rm d} \sim 50$ [118]), ℓ is the invariant loop length and $\gamma_{\rm d} = \Gamma_d G\mu$ is the gravitational-wave length scale measured in units of time[2]. The high-frequency ($f\ell \gg 1$, where f denotes frequency) gravitational-wave spectrum of an oscillating loop is dominated by bursts emitted by string features called cusps and kinks [105, 106, 205]. Cusps[3] are points on the string that briefly travel at the speed of light; they are generic features for smooth loops. Kinks are discontinuities in the tangent vector of the string that propagate at the speed of light. They appear in pairs as the result of collisions between two cosmic strings and are chopped off when a loop forms, hence a loop can contain any integer number of kinks. Numerical simulations of Nambu-Goto strings have shown that kinks accumulate over the cosmological evolution [221, 101, 135], while the number of cusps per loop is yet undetermined.

Cusps are short-lived and produce beamed gravitational waves in the forward direction of the cusp, while left-moving (right-moving) kinks propagate around the string, creating gravitational waves with a fan-like emission (like a lighthouse) in the directions generated by right-moving (left-moving) waves. Additionally, the collision of two kinks is expected to radiate gravitational waves isotropically. In this chapter, we report on searches for gravitational waves produced by cusps, kinks and kink-kink collisions, using O3 LIGO-Virgo data. In addition to distinct individual bursts, the incoherent superposition of weaker gravitational-wave bursts from cosmic strings produced over the history of the Universe would create a stochastic gravitational-wave background [211, 205].

Cosmic strings emit gravitational waves with a wide range of frequencies that can be searched by other means, including the cosmic microwave background [321], Big Bang nucleosynthesis [322] and pulsar timing arrays [323, 324, 36], see also *e.g.*, [38, 37, 43].

The gravitational-wave emission from cosmic string loops is introduced in Section 5.2. We consider two simulation-based models [103, 123] (labelled **A** and **B**) for the distribution of cosmic string loops. In addition, we develop a third model (labelled **C**) which interpolates between the other two models. From these, we derive gravitational-wave burst rates and the dimensionless energy density spectra in Section 5.2. Individual gravitational-wave bursts are searched in O3 data with a dedicated analysis presented in Section 5.3. The incoherent superposition of bursts from cusps, kinks and kink-kink collisions, produces a stationary and nearly Gaussian stochastic background of gravitational waves. We search O3 data for this background and the results, detailed in [325], are summarized in Section 5.4. Both the burst and stochastic background searches yield no detection. Combining their sensitivities, we constrain two cosmic string parameters in Section 5.5: the string tension $G\mu$ and the number of kinks per loop. We provide a table listing the meanings of symbols used in this study in Appendix 5.A.

[2]Super-horizon cosmic strings also emit gravitational waves, due to their small-scale structure resulting from string intercommutations [204, 244, 319].

[3]We also include the so-called pseudocusps [320], defined as cuspy features moving with a velocity close to the speed of light.

5.2 Gravitational waves from cosmic string loops

Gravitational waves are produced by cusps, kinks and kink-kink collisions on cosmic string loops. The strain waveforms are linearly polarized and have been calculated in [106, 205, 105]. For a loop of length ℓ at redshift z, they are power-law functions in the frequency domain for the strain [91]:

$$h_i(\ell, z, f) = A_i(\ell, z) f^{-q_i}, \tag{5.1}$$

where $i = \{\mathrm{c}, \mathrm{k}, \mathrm{kk}\}$ identifies the cusp, kink, and kink-kink collision cases. The power-law indices are $q_\mathrm{c} = 4/3$, $q_\mathrm{k} = 5/3$, and $q_\mathrm{kk} = 2$ and the signal amplitude A_i is given by [106]

$$A_i(\ell, z) = g_{1,i} \frac{G\mu\ \ell^{2-q_i}}{(1+z)^{q_i-1} r(z)}, \tag{5.2}$$

where $r(z)$ is the comoving distance to the loop. In the following we adopt the cosmological model used in [91]; it is encoded in three functions $\varphi_r(z)$, $\varphi_V(z)$, and $\varphi_t(z)$ (see Appendix A of [91]). The proper distance, the proper volume element and the proper time are given by $r(z) = \varphi_r(z)/H_0$, $\mathrm{d}V(z) = \varphi_V(z)/H_0^3\,\mathrm{d}z$, and $t(z) = \varphi_t(z)/H_0$ respectively, where $H_0 = 67.9$ km s^{-1} Mpc^{-1} [312] is the present value of the Hubble constant. The prefactor $g_{1,i}$ takes three different numerical values [219]: $g_{1,\mathrm{c}} = 8/\Gamma^2(1/3) \times (2/3)^{2/3} \approx 0.85$, $g_{1,\mathrm{k}} = 2\sqrt{2}/\pi/\Gamma(1/3) \times (2/3)^{2/3} \approx 0.29$, and $g_{1,\mathrm{kk}} = 1/\pi^2 \approx 0.10$, where Γ is the Gamma function [313].

Cusps and kinks emit gravitational waves in highly concentrated beams. Cusps are transient and produce a beam along a single direction, while kinks propagate around the loop, beaming over a fan-like range of directions. The beam opening angle is

$$\theta_m = (g_2 f (1+z)\ell)^{-1/3}, \tag{5.3}$$

where $g_2 = \sqrt{3}/4$ [219] is a numerical factor. To guarantee self-consistency (validity of the waveform), we require that $\theta_m < 1$rad, which is equivalent to setting a lower limit on the frequency for a fixed loop length. For kink-kink collisions the gravitational-wave emission is isotropic [108].

The burst rate of type i, per unit loop size and per unit volume, can be decomposed into four factors:

$$\frac{\partial^2 R_i}{\partial \ell V^2} = \frac{2}{\ell} N_i \times \frac{\partial^2 \mathcal{N}}{\partial \ell \partial V} \times \Delta_i \times (1+z)^{-1}. \tag{5.4}$$

The first factor accounts for an average of N_i gravitational-wave burst events of type i produced per loop oscillation time periodicity $\ell/2$. The second factor stands for the number of loops per unit loop size and per unit volume at cosmic time t

$$\mathbf{n}(\ell, t) = \frac{\partial^2 \mathcal{N}}{\partial \ell \partial V}. \tag{5.5}$$

The third factor, Δ_i, reflects that only a fraction of burst events can be effectively detected due to the beamed emission of gravitational waves with respect to the 4π solid angle. The gravitational-wave emission within a cone for cusps, a fan-like range of directions for kinks and all directions for kink-kink collisions can be conveniently absorbed into a single beaming fraction expression: $\Delta_i = (\theta_m/2)^{3(2-q_i)}$. Finally the last factor shows that the burst emission rate is red-shifted by $(1+z)^{-1}$.

The burst rate at redshift z is then obtained by integrating over all loop sizes,

$$\frac{\mathrm{d}R_i}{\mathrm{d}z} = f\frac{\varphi_V(z)}{H_0^3(1+z)}\int_{\ell_{\min}}^{\ell_{\max}} \mathrm{d}\ell\, \frac{2N_i}{\ell}\mathbf{n}(\ell,t)\Delta_i. \tag{5.6}$$

Introducing the dimensionless loop size parameter $\gamma \equiv \ell/t$, Eq. (5.6) reads:

$$\begin{aligned}\frac{\mathrm{d}R_i}{\mathrm{d}z} &= \frac{\phi_V(z)}{H_0^3(1+z)} \\ &\quad\times \int_{\gamma_{\min}(z,f)}^{\gamma_{\max}(z)} \mathrm{d}\gamma\, \frac{2N_i}{\gamma}\mathbf{n}(\gamma,z)\Delta_i(\gamma,z,f).\end{aligned} \tag{5.7}$$

The upper bound of the integral, $\gamma_{\max}(z)$, is derived by requiring the loop size to be smaller than the horizon size, *i.e.*, $\gamma_{\max} = 2$ and 3 for radiation and matter dominated universes, respectively [91]. The lower bound, $\gamma_{\min}$, corresponds to the fundamental frequency of a loop, *i.e.*, $2/\ell$, leading to $\gamma_{\min}(z,f) = 2/[f(1+z)\varphi_t(z)/H_0]$.

We consider two analytical models, labelled **A** [103] and **B** [123], to describe the distribution of cosmic string loops, $\mathbf{n}(\gamma,z)$, in a scaling regime, within a Friedmann-Lemaître-Robertson-Walker metric. These models were respectively dubbed M=2 and M=3 in [91]. In model **A** the number of long-lived non-self-intersecting loops of invariant length ℓ per unit volume per unit time formed at cosmic time t, is directly inferred from Nambu-Goto simulations of cosmic string networks in the radiation and matter eras. Model **B** is based on a different Nambu-Goto string simulation [99]. In this model the distribution of non-self-intersecting scaling loops is the extracted quantity. Within model **B**, loops are formed at all sizes following a power-law specified by a parameter taking different values in the radiation and matter eras, while the scaling loop distribution is cut-off on small scales by the gravitational back-reaction scale. There is a qualitative difference between these two models, since in the latter, tiny loops are produced in a much larger amount than in the former. In addition, we will use a new model, based on [52] and labelled **C**, which extends and encompasses both models **A** and **B**. Similarly to model **B**, model **C** assumes that the scaling loop distribution is a power-law, but leaves its slope unspecified. Given the wide parameter space opened by model **C**, we will select two samples: models **C-1** and **C-2**. Model **C-1** (respectively **C-2**) reproduces qualitatively the loop production function of model **A** (resp. **B**) in the radiation era and the loop production of model **B** (resp. **A**) in the matter era. We expect the addition of these two models to showcase intermediate situations in between the two simulation-inferred models **A** and **B**. The loop distribution functions $\mathbf{n}(\gamma,z)$ for the three models are given in the Appendix[4].

For models **A**, **B** and **C**, the contributions from cusps, kinks and kink-kink collisions to the gravitational-wave emission must be considered altogether. Indeed, the dimensionless decay constant Γ_d of a cosmic string, driving the loop size evolution, can be decomposed into three contributions:

$$\begin{aligned}\Gamma_\mathrm{d} &\equiv \frac{P_\mathrm{gw}}{G\mu^2} = \sum_i \frac{P_{\mathrm{gw},i}}{G\mu^2} \\ &= N_\mathrm{c}\frac{3\pi^2 g_{1,\mathrm{c}}^2}{(2\delta)^{1/3}g_2^{2/3}} + N_\mathrm{k}\frac{3\pi^2 g_{1,\mathrm{k}}^2}{(2\delta)^{2/3}g_2^{1/3}} + N_\mathrm{kk}2\pi^2 g_{1,\mathrm{kk}}^2,\end{aligned} \tag{5.8}$$

[4]See Appendix for more descriptions on the cosmic string loop distributions, and the burst analysis pipeline

where $\delta = \max(1, 1/(2g_2))$, since the gravitational-wave frequency cannot be smaller than the fundamental frequency of the loop, $2/\ell$, while the condition $\theta_m < 1$ for cusps and kinks imposes $f > 1/(\ell g_2)$. Parameters $N_{\rm c}, N_{\rm k}$ are respectively the average number of cusps and kinks per oscillation. The number of kink-kink collisions per oscillation $N_{\rm kk}$ is $N_{\rm kk} \approx N_{\rm k}^2/4$ in the limit of large $N_{\rm k}$. While this equation is only an approximation when $N_{\rm k}$ is order unity, the kink-kink contribution is very small in this case and the error would hardly affect our results. On the other hand, it is clear that the kink-kink collision quickly dominates the gravitational-wave production when the number of kinks increases, as it was also shown in Ref. [90]. In this analysis we fix $N_{\rm c}$ to be 1; we comment later on the effects of increasing the number of cusps. The only free parameter is the number of kinks $N_{\rm k}$; we consider $N_{\rm k} = 1, \ldots, 200$, with the upper limit being motivated by numerical simulations of string loops that favour $\Gamma_{\rm d} \sim 50$ [118].

The incoherent superposition of bursts from loops with all possible sizes through the history of the Universe produces a stochastic gravitational wave background [326]. The normalized energy density of which is defined as

$$\Omega_{\rm GW}(f) = \frac{f}{\rho_c}\frac{{\rm d}\rho_{\rm GW}}{{\rm d}f} \ , \tag{5.9}$$

where $\rho_{\rm c} = 3H_0^2c^2/(8\pi G)$. The spectrum of the stochastic gravitational wave background is [212]

$$\Omega_{\rm GW}(f) = \frac{4\pi^2}{3H_0^2} f^3 \sum_i \int {\rm d}z \int {\rm d}\ell \ h_i^2 \times \frac{\partial^2 R_i}{\partial z \partial \ell}. \tag{5.10}$$

The integration range is restricted by two requirements. First, the size of a loop is limited to a fraction of the Hubble radius, or equivalently of the cosmic time $\ell < \alpha t(z)$. Second, the frequency has to be larger than the low-frequency cutoff $f\ell(1+z) > \delta$. In Fig. 5.1 we show examples of gravitational-wave spectra calculated with Eq. (5.10). The two plots at the top are derived from model **A** and **B** with $N_k \gg 1$. The dominant contribution comes from kink-kink collisions. The lower plots show gravitational-wave spectra taking $N_k = 1$ (left) and $N_k = 100$ (right) and are derived from model **C** with a given set of parameters (see Appendix), *i.e.*, $\chi_{\rm rad} = 0.45$, $\chi_{\rm mat} = 0.295$, $c_{\rm rad} = 0.15$, and $c_{\rm mat} = 0.019$; the subscripts refer to matter and radiation eras, respectively. When $N_{\rm k}$ is large, the dominant contribution to the spectrum depends on the frequency band, which is a unique feature in this model. In this study, we ignore the suppression of the gravitational waves from cusps due to the primordial black hole production as pointed out in [327]. Including such an effect leads to lower spectrum amplitudes when $N_{\rm k}$ is small and consequently reduces the sensitivity to cosmic string signals. In Fig. 5.1 we also show the 2σ power-law integrated (PI) curves [258] indicating the integrated sensitivity of the O3 search [325], along with projections for 2 years of the Advanced LIGO-Virgo network at design sensitivity, and the envisioned upgrade of Advanced LIGO, A+ [328], sensitivity after 2 years, assuming a 50% duty cycle.

5.3 Burst Search

The O3 data set is analysed with a dedicated burst search algorithm previously used to produce LIGO-Virgo results [329, 91, 107]. The burst analysis pipeline, as well as its O3 configuration, is described in the Appendix. The search can be summarized into three analysis steps. First, we carry out a matched-filter search using the cosmic string waveform in Eq. (5.1). Then, resulting candidates are filtered to retain only those detected in more than one detector within a time window accounting for the difference in the gravitational-wave arrival time between detectors. Finally,

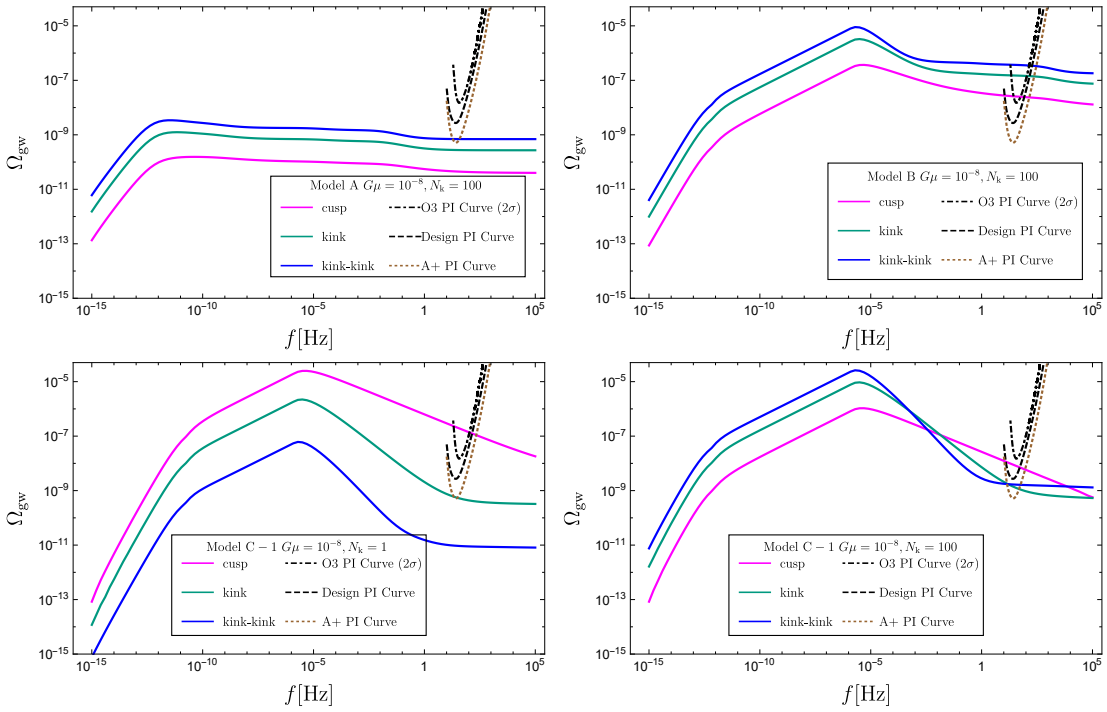

Figure 5.1: Predictions of the gravitational-wave energy density spectra using different models for the loop distribution function $\mathbf{n}(\gamma, z)$ and for two values of the number of kinks per loop oscillation N_k, 1 and 100. The string tension $G\mu$ is fixed to 10^{-8}. Top-left: model **A**, $N_k = 100$. Top-right: model **B**, $N_k = 100$. Bottom-left: model **C-1**, $N_k = 1$. Bottom-right: model **C-1**, $N_k = 100$. For model **C-1**, we use the following model parameters (see Appendix): $\chi_{rad} = 0.45$, $\chi_{mat} = 0.295$, $c_{rad} = 0.15$, $c_{mat} = 0.019$; the subscripts refer to the radiation and matter eras, respectively. We also show the energy density spectra of the three different components and 2-σ power-law integrated (PI) curves [258] for the O3 isotropic stochastic search [325], and projections for the HLV network at design sensitivity, and the A+ detectors [328].

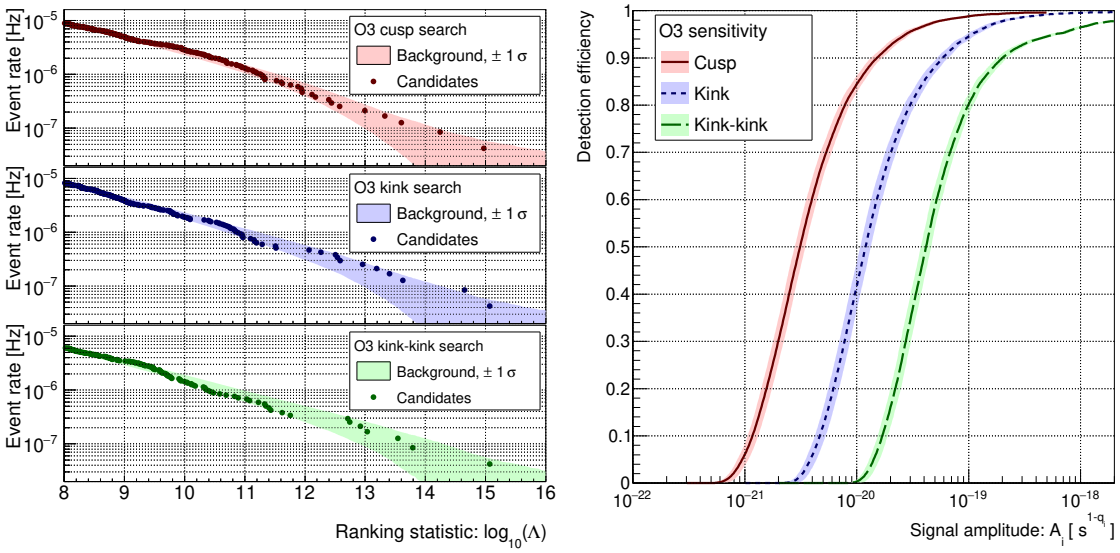

Figure 5.2: Left panel: cumulative distribution of cosmic string burst candidate events produced by cusps (top), kinks (middle) and kink-kink collisions (bottom). The expected distributions from background noise are represented by $\pm 1\sigma$ shaded areas. Right panel: the detection efficiency is measured using simulated signals, as a function of the signal amplitude for cusps, kinks and kink-kink collisions. Note that the horizontal axis measures different amplitude quantities, A_i, for the three types of signals, parametrized by the waveform frequency power law q_i.

double- and triple-coincident events are ranked using an approximated likelihood ratio $\Lambda(x)$, where x is a set of parameters used to discriminate true cosmic string signals from noise [330]. The burst search is performed separately for cusps, kinks and kink-kink collision waveforms, integrating $T_{\rm obs} = 273.5$ days of data when at least two detectors are operating simultaneously.

The left panel of Fig. 5.2 presents the cumulative distribution of coincident O3 burst events as a function of the likelihood ratio Λ for the cusp, kink and kink-kink collision searches. To estimate the background noise associated with each search, time shifts are applied to each detector strain data such that no real gravitational-wave event can be found in coincidence. For this study, we use 300 time-shifts, totalling $T_{\rm bkg} = 225$ years of data containing only noise coincident events, the distribution of which is represented in the left panel of Fig. 5.2 with a $\pm 1\sigma$ shaded band. The candidate events, obtained with no time shift, are all compatible with the noise distribution within $\pm 2\sigma$. The cusp, kink and kink-kink collision waveforms are very similar, resulting in the loudest events being the same for the three searches. The ten loudest events were carefully scrutinized. They all originate from a well-known category of transient noise affecting all detectors, that are broadband and very short-duration noise events of unknown instrumental origin [331, 332].

From the non-detection result, we measure our search sensitivity to cosmic string signals by performing the burst search analysis over O3 data with injections of simulated cusp, kink and kink-collision waveforms. The amplitudes of injected signals comfortably cover the range where none to almost all the signals are detected. Other parameters (sky location, polarization angle, high-frequency cutoff) are randomly distributed. To recover injected signals, we use the loudest-event

method described in [333], where the detection threshold is set to the level of the highest-ranked event found in the search: $\log_{10}(\Lambda) \simeq 15.0$, 15.1, and 15.1 for cusps, kinks, and kink-kink collisions, respectively. The resulting efficiencies $\varepsilon_i(A_i)$ as a function of the signal amplitude are presented in the right panel of Fig. 5.2. Cusp events directed at Earth with $A_{\rm c} > 2 \times 10^{-20}{\rm s}^{-1/3}$ would have produced a result more significant than any of the ones obtained by our search, with $\sim 90\%$ confidence. In terms of loop proper lengths, this corresponds, for example, to loops larger than $1.7 \times 10^6 (G\mu/10^{-10})^{-3/2}$ light years at redshift 100. The expected detection burst rate is calculated from the detection efficiency:

$$R_i = \int \frac{{\rm d}R_i}{{\rm d}A_i} \varepsilon_i(A_i)\ {\rm d}A_i\,. \tag{5.11}$$

The detectable burst rate $\frac{{\rm d}R_i}{{\rm d}A_i}$ is obtained from Eq. (5.7), which can be expressed in terms of amplitude using Eq. (5.2) and calculated for the lowest value of the high-frequency cutoff f_* which can be most abundantly observed (see Appendix for details).

We assume that the occurrence of a detectable burst of gravitational waves follows a Poisson distribution with mean given by the estimated detection rate. For a set of parameters $(G\mu, N_{\rm k})$, models which predict a detection rate larger than $2.996/T_{\rm obs}$ are excluded at 95%, *i.e.*, we exclude models that predict a $> 95\%$ confidence level detection.

5.4 Stochastic Search

A search for a stochastic gravitational wave background [326] is carried out using the LIGO and Virgo O3 data [325] in which a correlated background in different interferometer pairs is sought. These results are combined with those from the previous two observing runs, O1 and O2 [31, 91, 32]. The results reported in [325] assume the normalized energy density of the stochastic background, Eq. (5.9), to be a power-law α of the frequency:

$$\Omega_{\rm GW}(f) = \Omega_{\rm ref} \left(\frac{f}{f_{\rm ref}}\right)^{\alpha}, \tag{5.12}$$

where $f_{\rm ref}$ denotes a reference frequency, fixed to 25 Hz, a convenient choice in the sensitive part of the frequency band. The search reported in Ref. [325] does not detect a stochastic background, and so sets upper limits depending on the value of α. The stochastic background from cosmic strings in the LIGO-Virgo frequency band is predicted to be approximately flat, setting the upper bound $\Omega_{\rm GW} \leq 5.8 \times 10^{-9}$ at the 95% credible level for a flat $\alpha = 0$ background and using a log-uniform prior in $\Omega_{\rm GW}$; the 20-76.6 Hz band is responsible for 99% of this sensitivity.

In the present study, we perform a Bayesian analysis taking into account the precise shape of the background (see Fig. 5.1) instead of a power-law and use it to derive upper limits on the cosmic string parameters. We first calculate the log-likelihood function assuming a Gaussian distributed noise, which up to a constant is

$$\ln \mathcal{L}(\hat{C}_a^{IJ} | G\mu, N_k) = -\frac{1}{2} \sum_{IJ,a} \frac{(\hat{C}_a^{IJ} - \Omega_{\rm GW}^{(M)}(f_a; G\mu, N_k))^2}{\sigma_{IJ}^2(f_a)}. \tag{5.13}$$

Here $\hat{C}_a^{IJ} \equiv \hat{C}^{IJ}(f_a)$, and IJ are detector pairs L1-H1, L1-V1, and H1-V1. $\hat{C}^{IJ}(f_a)$ and $\sigma^2(f_a)$ are, respectively, a cross-correlation estimator for the IJ detector pair and its variance at frequency

f_a as detailed in [334]. Following the same approach as in the O1 stochastic analysis we use the frequency bins ranging from 20 to 86 Hz [91]; higher frequencies do not contribute to the sensitivity. The gravitational-wave energy density, $\Omega_{\rm GW}^{(M)}(f_a; G\mu, N_k)$, is predicted by the cosmic string model $M = \{\mathbf{A}, \mathbf{B}, \mathbf{C}\}$ and computed with Eq. (5.10) at frequency f_a.

For our Bayesian analysis, we specify priors for the parameters in the cosmic string model, *i.e.*, $p(G\mu|I_{G\mu})$ and $p(N_{\rm k}|I_{N_{\rm k}})$. The variables $I_{G\mu}$ and $I_{N_{\rm k}}$ denote the information on the distributions of $G\mu$ and N_k, which are determined by theory predictions. For $p(G\mu|I_{G\mu})$, we choose a log-uniform prior for $10^{-18} \leq G\mu \leq 10^{-6}$. Here the upper bound is set by the cosmic microwave background measurements [72, 74, 132, 295]. The lower bound is arbitrary, chosen for consistency with the study in Ref. [54]; we note, however, that our results remain almost unchanged if we choose a smaller value for the lower bound on $G\mu$. For $p(N_{\rm k}|I_{N_{\rm k}})$, we aim at constraining $G\mu$ for each choice of $N_{\rm k}$. Therefore the prior $p(N_{\rm k}|I_{N_{\rm k}})$ is taken to be a δ-function for each value of $N_{\rm k}$. The number of kinks per loop oscillation $N_{\rm k}$ being fixed, the posterior for the parameter $G\mu$ is calculated according to Bayes' theorem:

$$p(G\mu|N_{\rm k}) \propto \mathcal{L}(\hat{C}_a^{IJ}|G\mu, N_{\rm k}) p(G\mu|I_{G\mu}) p(N_{\rm k}|I_{N_{\rm k}}). \tag{5.14}$$

We calculate 95% credible intervals for $G\mu$.

5.5 Constraints

We show in Fig. 5.3 the region of the $G\mu$ and N_k parameter space excluded at the 95% confidence level by the burst and stochastic searches; the number of cusps $N_{\rm c}$ being fixed to 1. For the stochastic search (Section 5.4) we present constraints from the combined O1+O2+O3 data; for the burst search (Section 5.3) we derive constraints from the non-detection result using O3 data. We consider three models for the Nambu-Goto cosmic string loop distributions, dubbed **A**, **B** and **C**. For the latter we choose two sets of benchmark numbers: for model **C**-1 we set $(\chi_{\rm r}, \chi_{\rm m}) = (0.45, 0.295)$ and for model **C**-2 $(\chi_{\rm r}, \chi_{\rm m}) = (0.2, 0.45)$ (see the Appendix).

Using model **A**, the derived gravitational-wave power spectrum is much weaker than in the other models, leading to weaker constraints. Model **C**-2 mimics the loop production function of model **A** in the matter era and of model **B** in the radiation era. In the frequency band of LIGO-Virgo, the stochastic background is dominated by the contribution from loops in the radiation era, hence models **B** and **C**-2 give similar results. Conversely, the gravitational-wave power spectrum obtained from model **C**-1, which mimics the loop production function of model **A** in the radiation era and of model **B** in the matter era, presents more subtle features. Larger values of $G\mu$ do not necessarily produce larger signal amplitudes, creating structures in the constraint plot. For an analytical understanding of these findings, we refer the reader to [56]. For a better understanding of the loop visibility domain in terms of redshift, we refer to the Fig. 2 of [90].

The stochastic analysis leads to the following constraints on $G\mu$. For model **A**, we rule out the range $G\mu \gtrsim (9.6 \times 10^{-9} - 10^{-6})$, depending on the number of kinks per oscillation $N_{\rm k}$. For model **B**, we rule out: $G\mu \gtrsim (4.0 - 6.3) \times 10^{-15}$. For model **C**-1, we rule out $G\mu \gtrsim (2.1 - 4.5) \times 10^{-15}$, aside from a small region where $N_{\rm k} \gtrsim 180$. Finally, for model **C**-2, we rule out: $G\mu \gtrsim (4.2 - 7.0) \times 10^{-15}$.

The burst search upper limits are not as stringent as the ones derived from the stochastic search. In particular, the constraints on the string tension for model **A** are too weak to be represented in the figure. The only case where the burst analysis leads to tighter constraints, is for model **C**-1 and for $N_{\rm k} > 70$.

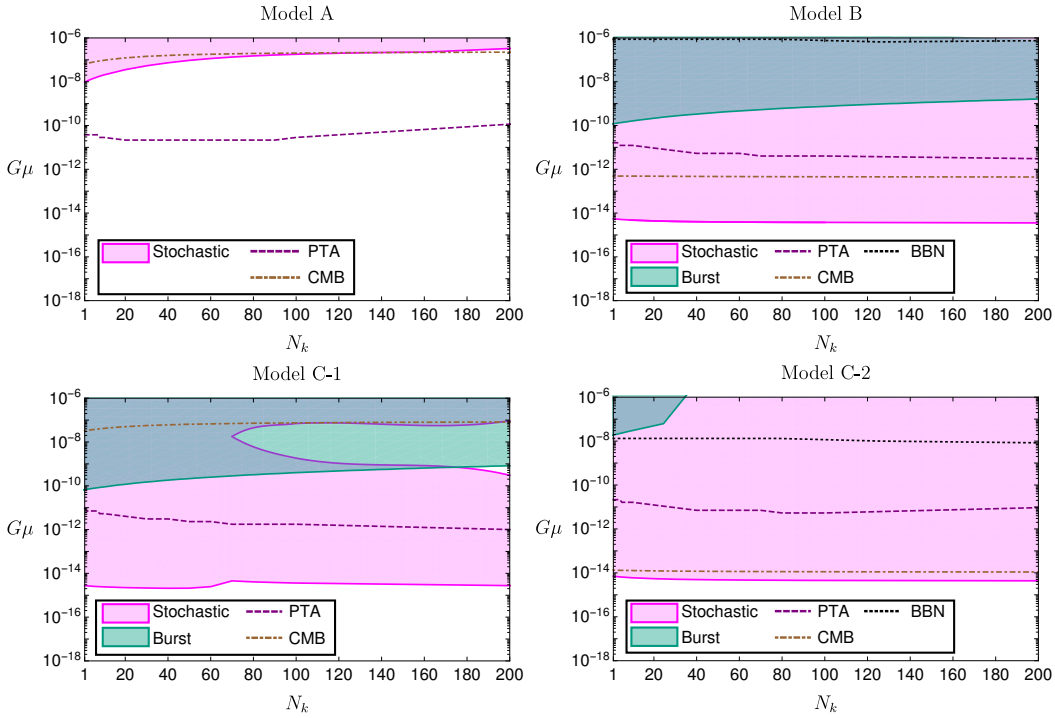

Figure 5.3: Exclusion regions at 95% C.L. on the cosmic string parameter space, $(N_{\rm k}, G\mu)$, derived from the stochastc search (pink), the burst search (turquoise) and both searches. Four models are considered to describe the distribution of cosmic string loops: model **A** (top-left), model **B** (top-right), model **C**-1 (bottom-left) and model **C**-2 (bottom-right). Note that the stochastic result combines the data of O1, O2 and O3 while the burst search only includes O3 data. We also report limits from other experiments: pulsar timing arrays (PTA) [323, 324], cosmic microwave background (CMB) [321] and Big Bang nucleosynthesis [322]. The notch in the SWGB constraint for Model **C-1** is explained in Appendix 5.D.

In the present analysis, the average number of cusps per oscillation on a loop has been set to 1. It has been shown that the number of cusps per period of string oscillation scales with the number of harmonics on the loop [335]. Note that with many cusps on the string, the decay constant $\Gamma_{\rm d}$ is enhanced and the lifetime of the loop is hence greatly reduced. Consequently, a high number of cusps on the loops gives qualitatively the same result as increasing the number of kinks: for model **A**, the constraints are weakened, whereas for models **B** and **C** the bounds are insensitive to $N_{\rm c}$; this has been confirmed by our numerical study.

One can also compare these results with limits obtained from pulsar timing array measurements, and indirect limits from Big Bang nucleosynthesis and cosmic microwave background data [323]. Note that in our analysis we do not investigate non-standard thermal history; see however, *e.g.* [336, 337]. Repeating the analysis done in Ref. [91] with $N_{\rm k}$ up to 200, we find that for model **A**, the strongest limit comes from pulsar timing measurements, excluding string tensions $G\mu \gtrsim 10^{-10}$. For model **B**, **C**-1 and **C**-2 the strongest upper limits are derived from this search. The next observing run, O4, will give us a new opportunity to detect signals from cosmic strings.

5.6 Conclusions

Using data from the third observing run of Advanced LIGO and Virgo, we have performed a burst and a stochastic gravitational wave background search to constrain the tension of Nambu-Goto strings, as a function of the number of kinks per oscillation, for four loop distributions. We have tested models **A** and **B** already considered in the O1 and O2 analyses [32]. The current constraints on $G\mu$ are stronger by two and one orders of magnitude for models **A** and **B**, respectively, when fixing $N_{\rm k} = 1$. In addition, we have used two variants of a new model, dubbed model **C**, that interpolates between models **A** and **B**. For the first time, we have studied the effect of kink-kink interactions, which is relevant for large numbers of kinks, and investigated the effect of a large number of cusps, as both effects are favoured by cosmic string simulations. In the context of cosmic strings formed at the end of an inflationary era, these results raise questions about the validity of simple inflationary models (occurred between $10^{16} - 10^{11}$ GeV) in the context of Grand Unified Theories [62], unless one invokes extra fields in order to avoid cosmic string formation [338].

Given the current experimental results, it would seem important to intensify numerical and theoretical studies on cosmic strings. From a numerical point of view, the number of kinks and cusps should be determined. Concerning phenomenological aspects, new models, like model **C** that interpolates between model **A** and **B**, should be further explored as well as models including particle physics leading to cosmic string formation in the early Universe. On the experimental side, the sensitivity of Advanced LIGO and Virgo detectors will continue to improve [328] and a fourth interferometer, KAGRA [339], will join the network.

5.A Table of quantities appearing in the chapter

The main quantities used in this analysis and their meaning are listed in Table 5.1.

G	Gravitational constant
z	redshift
μ	string tension
$N_{\rm c}$	average number of cusps per loop oscillation
$N_{\rm k}$	number of kinks
$\Gamma_{\rm d}$	dimensionless decay constant of cosmic strings
g_1, g_2	dimensionless prefactors for the GW amplitude and beaming angle
ℓ	cosmic string loop length
$\gamma \equiv \ell/t$	loop size parameter
θ_m	beaming angle for GW emission
$P_{\rm gw}$	power of GW emission of cosmic strings
R_i	GW burst rate
$\mathbf{n}(\ell, t)$	number density of cosmic string loops with length ℓ at t
$\Omega_{\rm GW}(f)$	present fractional GW energy density spectrum
$\mathcal{L}$	likelihood used in the Bayesian analysis
$p(\text{parameters}\|I)$	probability density distribution of "parameters" given prior information "I"

Table 5.1: Table of quantities appearing in the chapter.

5.B Loop distributions

For model **A**, the loop distribution is given by the sum of

$$t^4 \mathbf{n}_{\rm rad} = \frac{0.18 \times 2\sqrt{H_0}\Omega_{\rm rad}^{3/4}}{(\gamma+\gamma_{\rm d})^{5/2}} t^{3/2}(1+z)^3 \begin{cases} \Theta\left(0.18t - \ell\right) & t < t_{\rm eq} \\ \Theta\left[0.18t_{\rm eq} - \ell + \gamma_{\rm d}(t - t_{\rm eq})\right] & t > t_{\rm eq} \end{cases} \tag{5.15}$$

for loops produced during the radiation era, and

$$t^4 \mathbf{n}_{\rm mat} = \frac{0.27 - 0.45\gamma^{0.31}}{(\gamma+\gamma_{\rm d})^2} \Theta(0.18-\gamma)\Theta\left[\ell + \gamma_{\rm d}(t - t_{\rm eq}) - 0.18 t_{\rm eq}\right] \tag{5.16}$$

for loops produced during the matter era. Note that $t_{\rm eq}$ is the time of the radiation to matter transition and that $\gamma_{\rm d} = \Gamma_{\rm d} G\mu$.

Models **B** and **C** rely on the assumption that loops are produced at all sizes with a given power-law. The loop production $\mathcal{P}$ is parametrized by two additional parameters (c, χ)

$$t^5 \mathcal{P} = c \left(\frac{\ell}{t}\right)^{2\chi-3}, \tag{5.17}$$

and is cutoff on scales smaller than the gravitational backreaction scale $\gamma_{\rm c} \approx 20(G\mu)^{1+2\chi}$. The parameter χ controls the *tilt* of the loop production function, low values of χ favour the production of very small loops whereas high values of χ can be approximated by a Dirac delta loop production function on the large scales, *i.e.*, to the one-scale model. For model **B**, the loop distribution is the

sum of

$$t^4\mathbf{n}_{\rm rad} = \begin{cases} \dfrac{0.08}{(\gamma+\gamma_{\rm d})^{3-2\chi_{\rm r}}} & \gamma_{\rm d} < \gamma \\ \dfrac{0.08(1/2-2\chi_{\rm r})}{(2-2\chi_{\rm r})\gamma_{\rm d}\gamma^{2-2\chi_{\rm r}}} & \gamma_{\rm c} < \gamma < \gamma_{\rm d} \\ \dfrac{0.08(1/2-2\chi_{\rm r})}{(2-2\chi_{\rm r})\gamma_{\rm d}\gamma_{\rm c}^{2-2\chi_{\rm r}}} & \gamma < \gamma_{\rm c} \end{cases} \tag{5.18}$$

for loops produced during the radiation era,

$$t^4\mathbf{n}_{\rm mat} = \begin{cases} \dfrac{0.015}{(\gamma+\gamma_{\rm d})^{3-2\chi_{\rm m}}} & \gamma_{\rm d} < \gamma \\ \dfrac{0.015(1-2\chi_{\rm m})}{(2-2\chi_{\rm m})\gamma_{\rm d}\gamma^{2-2\chi_{\rm m}}} & \gamma_{\rm c} < \gamma < \gamma_{\rm d} \\ \dfrac{0.015(1-2\chi_{\rm m})}{(2-2\chi_{\rm m})\gamma_{\rm d}\gamma_{\rm c}^{2-2\chi_{\rm m}}} & \gamma < \gamma_{\rm c} \end{cases} \tag{5.19}$$

for loops produced during the matter era, and

$$t^4\mathbf{n}_{\rm rad-mat} = \left(\frac{t}{t_{\rm eq}}\right)^3 \left(\frac{1+z}{1+z_{\rm eq}}\right)^3 t_{\rm eq}^4 \mathbf{n}_{\rm rad}^{(3)}\left[\frac{\gamma t + \gamma_{\rm d}(t-t_{\rm eq})}{t_{\rm eq}}\right] \tag{5.20}$$

for loops produced during the radiation era and decaying during the matter era. The subscripts $_{\rm rad}$ and $_{\rm mat}$ refer to the radiation- and matter-dominated eras, respectively, and $\gamma_{\rm c}$ is the gravitational back-reaction scale.

For model **C**, the loop distribution can be approximated in the radiation era as

$$t^4\mathbf{n}_{\rm rad} = \frac{c_{\rm rad}}{1/2-2\chi_{\rm r}} \begin{cases} (\gamma+\gamma_{\rm d})^{2\chi_{\rm r}-3} - \dfrac{\gamma_\infty^{2\chi_{\rm r}-1/2}}{(\gamma+\gamma_{\rm d})^{5/2}} & \gamma_{\rm d} < \gamma \\ \dfrac{\gamma^{2\chi_{\rm r}-2}}{(2-2\chi_{\rm r})\gamma_{\rm d}} - \dfrac{\gamma_\infty^{2\chi_{\rm r}-1/2}}{(\gamma+\gamma_{\rm d})^{5/2}} & \gamma_{\rm c} < \gamma < \gamma_{\rm d} \\ \dfrac{\gamma_{\rm c}^{2\chi_{\rm r}-2}}{(2-2\chi_{\rm r})\gamma_{\rm d}} - \dfrac{\gamma_\infty^{2\chi_{\rm r}-1/2}}{(\gamma+\gamma_{\rm d})^{5/2}} & \gamma < \gamma_{\rm c} \end{cases} \tag{5.21}$$

and in the matter era as

$$t^4\mathbf{n}_{\rm mat} = \frac{c_{\rm mat}}{1-2\chi_{\rm m}} \begin{cases} (\gamma+\gamma_{\rm d})^{2\chi_{\rm m}-3} - \dfrac{\gamma_\infty^{2\chi_{\rm m}-1}}{(\gamma+\gamma_{\rm d})^{2}} & \gamma_{\rm d} < \gamma \\ \dfrac{\gamma^{2\chi_{\rm m}-2}}{(2-2\chi_{\rm m})\gamma_{\rm d}} - \dfrac{\gamma_\infty^{2\chi_{\rm m}-1}}{(\gamma+\gamma_{\rm d})^{2}} & \gamma_{\rm c} < \gamma < \gamma_{\rm d} \\ \dfrac{\gamma_{\rm c}^{2\chi_{\rm m}-2}}{(2-2\chi_{\rm m})\gamma_{\rm d}} - \dfrac{\gamma_\infty^{2\chi_{\rm m}-1}}{(\gamma+\gamma_{\rm d})^{2}} & \gamma < \gamma_{\rm c} \end{cases} \tag{5.22}$$

where γ_∞ is the size of the largest loops in scaling units.

5.C The burst analysis pipeline

The cosmic string burst search pipeline is divided into three main analysis steps. First, the cosmic string gravitational waveform is searched in LIGO and Virgo data using match-filtering techniques.

A bank of waveform templates is chosen to match the expected signal in the frequency domain:

$$\tau_{i,j}(f) = Af^{-q_i}\Theta(f_j - f)\Theta(f - f_l). \tag{5.23}$$

The spectral index q_i is taken from Eq. (5.1) for cusps, kinks or kink-kink collisions. The waveform frequency f is limited in range using the Heaviside function Θ. The low-frequency cut-off f_l, resulting from the size of the feature producing the gravitational waves, takes values well below the sensitive band of the LIGO and Virgo detectors. We take $f_l = 16\,\mathrm{Hz}$. The high-frequency cutoff f_j is a consequence of the gravitational-wave emission being observable only within a (frequency-dependent) viewing angle θ_m, given in Eq. (5.3). The angle between the line of sight and the gravitational-wave direction, θ, must be smaller than $\theta_m/2$, yielding $f < [2g_2\ell(1+z)\theta^3]^{-1}$. This high-frequency cutoff is unknown and is considered as a free parameter, taking discrete values indexed by j. When searching for gravitational waves produced by cusps and kinks, we use 31 templates with high-frequency cutoff values distributed between 30 Hz and 4096 Hz and spaced in such a way that we guarantee less than 0.1 % loss in the signal-to-noise ratio due to template mismatch. The cutoffs f_j are sparser at higher frequencies, with 17 templates below 100 Hz. For kink-kink collisions, the gravitational-wave radiation is isotropic and a single template covering the entire frequency band is used.

The standard matched filter output for template $\tau_{i,j}$ on the gravitational wave data h_{det} is

$$\rho_{i,j,\mathrm{det}}(t) = 4\,\mathrm{Re}\int_0^\infty \frac{\tau^*_{i,j}(f)h_{\mathrm{det}}(f)}{S_n(f)}\exp\bigl(2\sqrt{-1}\pi f t\bigr)\,\mathrm{d}f. \tag{5.24}$$

Here, $S_n(f)$ is the single-sided noise power spectral density of the detector. It is estimated locally over a few minutes of detector data. The normalization parameter A in each template is determined by [308]

$$4\,\mathrm{Re}\int_0^\infty \frac{\tau^*_{i,j}(f)\tau_{i,j}(f)}{S_n(f)}\exp\bigl(2\sqrt{-1}\pi f t\bigr)\,\mathrm{d}f = 1. \tag{5.25}$$

The O3 LIGO-Virgo dataset is analysed in five consecutive chunks of data to account for the detectors' noise evolution over the entire run. This is because the statistic we use to rank events better separates the signal from noise when the characteristics of the noise are relatively unchanged. The chunk boundaries are defined by sudden changes of sensitivity of one detector and by commissioning interventions, including the 1-month commissioning break in October 2019. The signal-to-noise ratio time-series $\rho_{i,j,\mathrm{det}}(t)$ is computed for each detector, accumulating a total of 245 days, 252 days and 250 days for the L1, H1 and V1 detectors respectively. The signal-to-noise ratio time-series are required to be above 3.75 and are clustered among templates. If multiple templates trigger within a 0.1 second window, we cluster the event as a single trigger, the parameters of which are derived from the highest signal-to-noise ratio template in the cluster.

After the match-filtering step, a time coincidence is performed pair-wise between the triggers of each detector using a time window wide enough to account for the maximum light-travel time between detectors and calibration time uncertainties of 8ms. A resulting set of double- and triple-coincident events is obtained when at least two detectors are taking data in nominal conditions, yielding a total observation time of $T_{\mathrm{obs}} = 273.5$ days.

Finally, to discriminate astrophysical signals from background noise, we apply the multivariate method described in [330], which uses a set of simulated cosmic string events and typical noise events to statistically infer the probability for a coincident event to be signal or noise. Hence, a likelihood ratio, Λ, is constructed with parameters characterizing the event [107]. For the O3

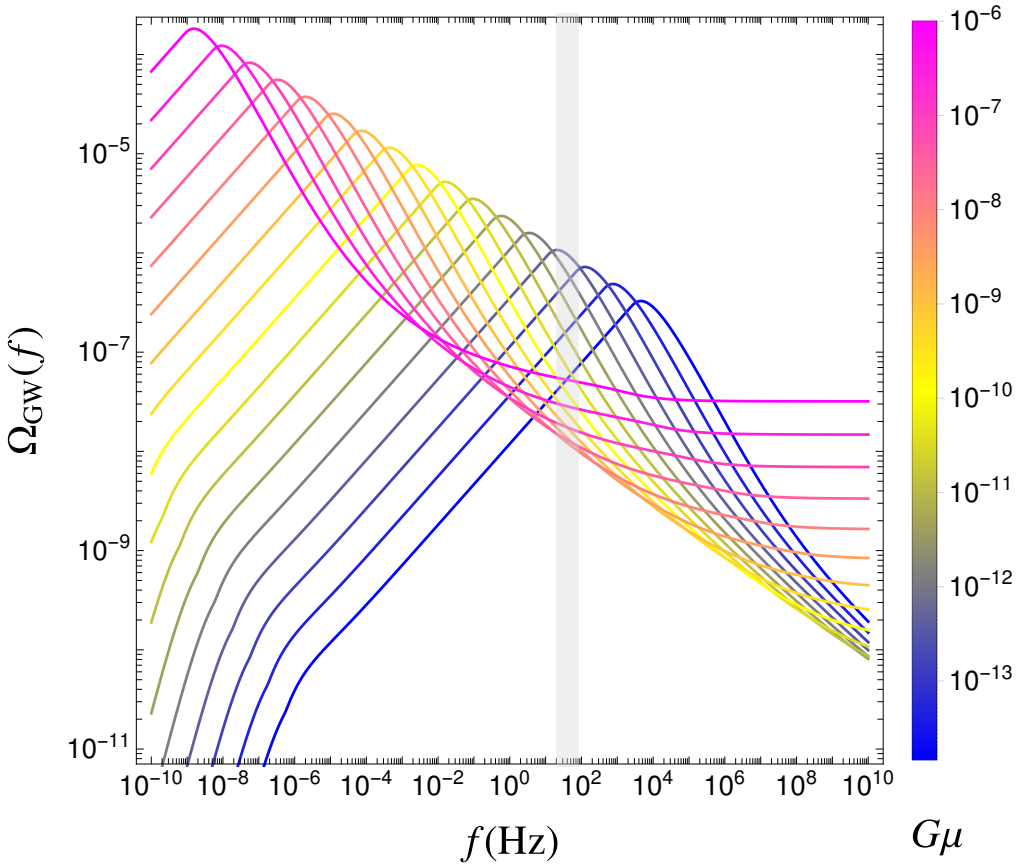

Figure 5.4: The gravitational-wave spectra for model **C-1** for different choices of $G\mu$ where N_k is fixed to be 90. The gray band corresponds to the frequency range $(20-86)$ Hz used in the analysis.

analysis, we introduce for the first time the event duration as a new discriminating variable. The event duration is defined as the duration for which $\rho_{i,j,\rm det}(t)$ remains above threshold considering all templates j and using a tolerance of 100 ms. Using this parameter, coupled to the signal-to-noise ratio, allows us to reject a large population of long-duration and low signal-to-noise ratio transient noise events contributing to the search background.

5.D Feature in SGWB constraint for Model C-1

The stochastic gravitational-wave constraint for model **C-1** has a special feature, shown in Fig. 5.3. The appearance of this notch, when $N_{\rm k} > 70$, is induced by the unique behaviour of the gravitational-wave spectrum in this model. In Fig. 5.4 we compare the corresponding spectrum for different choices of $G\mu$ with $N_{\rm k}$ fixed to be 90. The cosmic string network produces a stochastic background

in a wide frequency range, while LIGO/Virgo is only sensitive to a very narrow frequency window labelled by the grey band. As $G\mu$ increases, the stochastic power spectrum within the LIGO/Virgo window does not change monotonically. This leads to a non-exclusion in a small range of $G\mu$ when $N_{\rm k} > 70$. The exact location of the notch is determined through a detailed Bayesian analysis presented in the main text.

Chapter 6

Particle emission and gravitational radiation from cosmic strings: observational constraints

This chapter is a reproduction of Ref. [53] written in collaboration with Danièle Steer and Tanmay Vachaspati. The discrepancies between the Nambu-Goto (NG) description of cosmic strings – which predicts long-lived loops – and the numerical simulations of field theory strings – in which loop decay rapidly into particles– has been a matter of debate for a long time in the community. Our aim for this work was to bridge the gap between these two descriptions using a Boltzmann approach and modifying the evolution laws for isolated loops. Our main assumption is that isolated loops on large scales behave according to the NG equations of motion, but decay rapidly below a certain scale due to particle emission from cusps and kink-kink collisions. This point of view was motivated by a series of numerical simulations in Ref. [139] of which Tanmay Vachaspati was an author. This paper takes advantage of the experience with manipulating the Boltzmann equation I gained when working on Chapter 3. This is also the first chapter of my PhD interested in different signatures than the GW signatures. I have contributed to all the sections of this chapter.

Abstract

We account for particle emission and gravitational radiation from cosmic string loops to determine their effect on the loop distribution and observational signatures of strings. The effect of particle emission is that the number density of loops no longer scales. This results in a high frequency cutoff on the stochastic gravitational wave background, but we show that the expected cutoff is outside the range of current and planned detectors. Particle emission from string loops also produces a diffuse gamma ray background that is sensitive to the presence of kinks and cusps on the loops. However, both for kinks and cusps, and with mild assumptions about particle physics interactions, current diffuse gamma-ray background observations do not constrain $G\mu$.

6.1 Introduction

Most often the dynamics of local cosmic strings formed in a phase transition in the early universe (see [64, 88, 69] for reviews) is described by the Nambu-Goto (NG) action. This approximation is valid when the microscopic width of the string

$$w \sim \mu^{-1/2} \sim 1/\eta \tag{6.1}$$

(with μ the string tension and η the energy scale of the phase transition), is very small relative to its characteristic macroscopic size ℓ — a situation which is well satisfied in the early universe. Closed loops of NG strings loose energy slowly by radiating gravitational waves, and as a result NG string networks contain numerous loops whose decay generate a stochastic gravitational wave background (SGWB) ranging over a wide range of frequencies [64]. Depending on the details of the particular cosmic string model, the corresponding constraints on the dimensionless string tension $G\mu$ from the SGWB are $G\mu \lesssim 10^{-7}$ at LIGO-Virgo frequencies [91], $G\mu \lesssim 10^{-11}$ at Pulsar frequencies [89], whereas at LISA frequencies one expects to reach $G\mu \lesssim 10^{-17}$ (see Chapter 2).

On the other hand, at a more fundamental level, cosmic strings are topological solutions of field theories. Their dynamics can therefore also be studied by solving the field theory equations of motions. In studies of large scale field theory string networks [110, 112, 74, 113], loops are observed to decay directly into particles and gauge boson radiation on a short time scale of order of the loop length. Hence, field theory string network simulations predict very different observational consequences — in particular no SGWB from loops.

Since field theory and Nambu-Goto strings in principle describe the same physics, and hence lead to the same observational consequences, this is an unhappy situation. Based on high resolution field theory simulations, a possible answer to this long-standing conundrum was proposed in Ref. [139]. In particular, for a loop of length ℓ containing *kinks*, a new characteristic length scale $\ell_0 = \ell_{\rm k}$ was identified, and it was shown that if $\ell \gtrsim \ell_{\rm k}$ gravitational wave emission is the dominant decay mode, whereas for smaller loops $\ell \lesssim \ell_{\rm k}$ particle radiation is the primary channel for energy loss. That is,

$$\frac{{\rm d}\ell}{{\rm d}t} = \begin{cases} -\gamma_{\rm d}, & \ell \gg \ell_{\rm k} \\ -\gamma_{\rm d}\dfrac{\ell_{\rm k}}{\ell}, & \ell \ll \ell_{\rm k}, \end{cases} \tag{6.2}$$

where

$$\gamma_{\rm d} \equiv \Gamma G\mu$$

with $\Gamma \sim 50$ the standard constant describing gravitational radiation from cosmic string loops [117, 224, 225, 114]. Notice that Nambu-Goto strings correspond to $\ell_{\rm k} \to 0$; and if particle radiation is dominant for all loops, $\ell_{\rm k} \to \infty$. In practise $\ell_{\rm k}$ is neither of these two limiting values, and in Ref. [139] was estimated (for a given class of loops with kinks) to be given by

$$\ell_{\rm k} \sim \beta_{\rm k}\frac{w}{\Gamma G\mu} \tag{6.3}$$

where w is the width of the string, Eq. (6.1), and the constant $\beta_{\rm k} \sim \mathcal{O}(1)$. Note that the simulations of [139] consider the oscillations of loops with kinks over their entire lifetime. The results show episodic emission, with the *net* result of all the dynamics being the $1/\ell$ behaviour of Eq. (6.2).

If a loop contains *cusps*, then one expects the above to be modified to [140, 141]

$$\frac{\mathrm{d}\ell}{\mathrm{d}t} = \begin{cases} -\gamma_{\mathrm{d}}, & \ell \gg \ell_{\mathrm{c}} \\ -\gamma_{\mathrm{d}}\sqrt{\dfrac{\ell_{\mathrm{c}}}{\ell}}, & \ell \ll \ell_{\mathrm{c}} \end{cases} \tag{6.4}$$

where

$$\ell_{\mathrm{c}} \sim \beta_{\mathrm{c}} \frac{w}{(\Gamma G\mu)^2} \tag{6.5}$$

with $\beta_{\mathrm{c}} \sim \mathcal{O}(1)$. We note that this $1/\sqrt{\ell}$ dependence is less certain since, to the best of our knowledge, no field theory simulations of loops with cusps over their entire lifetime exist. [1]

The aim of this paper is to determine the observational effects — and corresponding constraints on $G\mu$ — of a finite, fixed, value of ℓ_{k} or ℓ_{c}. A first immediate consequence of the presence of the fixed scale is that the distribution of loops $\mathbf{n}(\ell, t)$, with $\mathbf{n}(\ell, t)\,\mathrm{d}\ell$ the number density of loops with length between ℓ and $\ell + d\ell$ at time t, will no longer be scaling. That is, contrary to the situation for NG strings, the loop distribution will depend explicitly on t as well as the dimensionless variable $\gamma = \ell/t$. We determine this non-scaling loop distribution $\mathcal{N}(\gamma, t)$ in Section 6.2, taking into account exactly (and for the first time) the back-reaction of particle emission on the loop distribution.

We then study the consequence of the non-scaling distribution of non-self intersecting loops on the stochastic GW background, determining the fraction of the critical density in GWs per logarithmic interval of frequency,

$$\Omega_{\mathrm{GW}}(t_0, f) = \frac{8\pi G}{3H_0^2}\, f\, \frac{\mathrm{d}\rho_{\mathrm{gw}}}{\mathrm{d}f}\,, \tag{6.6}$$

where H_0 is the Hubble parameter, and the $\mathrm{d}\rho_{\mathrm{gw}}/\mathrm{d}f$ factor is the energy density in gravitational waves per unit frequency f observed today (at $t = t_0$). A scaling distribution of NG loops gives a spectrum which is flat at high frequencies [64]; we will show below that a consequence of the non-scaling of the loop distribution is the introduction of a characteristic frequency f_*, with $\Omega_{\mathrm{GW}}(f > f_*) \to 0$. The precise value of f_* depends on ℓ_{k} or ℓ_{c}, as well as $G\mu$. For cusps and kinks with ℓ_{c} and ℓ_{k} given respectively by Eqs. (6.2) and (6.4), the characteristic frequency f_* is outside the LIGO and LISA band provided $G\mu \gtrsim 10^{-17}$, and so in this case the new cutoff will only be relevant for very light strings but for which the amplitude of the signal is below the observational thresholds of planned gravitational wave detectors.

In Section 6.5 we turn to particle physics signatures. At lower string tensions $G\mu$, the gravitational signatures of strings weaken, while the particle physics ones are expected to increase. Following [340], we focus on so-called "top down" models for production of ultra-high energy cosmic rays in which heavy particles, namely the quanta of massive gauge and Higgs field of the underlying (local) field theory trapped inside the string, decay to give ultra-high energy protons and gamma rays. We focus on the diffuse gamma ray flux which at GeV scales is constrained by Fermi-LAT [341]. However, taking into account back-reaction of the emitted particles on the loop distribution we find that current gamma ray observations do not lead to significant constraints. (Early studies on the production of cosmic rays assumed NG strings and particle emission rates

[1] Ref. [141] studies a single cusp on a field-theory string, and gives the energy emitted per cusp, from which one deduces the $1/\sqrt{\ell}$ behaviour. It shows that the shape of the string is modified after the cusp event, and argues that further smaller cusps will be formed in future loop oscillations. What we assume above is that the net result is an $1/\sqrt{l}$ dependence.

that were based on dynamics without taking back-reaction into account. See Refs. [340, 342, 343, 344, 345] and [340] for a review. Other work has focused on strings with condensates, *e.g.* [346, 85, 125], or strings coupled to other fields such as Kaluza-Klein or dilaton fields [347, 81].)

This paper is organized as follows. In Section 6.2 we determine the effect of an ℓ-dependent energy loss

$$\frac{\mathrm{d}\ell}{\mathrm{d}t} = -\gamma_{\mathrm{d}}\mathcal{J}(\ell), \tag{6.7}$$

on the loop distribution $\mathbf{n}(\ell, t)$. The function $\mathcal{J}(\ell)$ will initially be left arbitrary. Specific cases corresponding to (i) NG loops with $\mathcal{J} = 1$; (ii) loops with kinks, see Eq. (6.2), and (iii) loops with cusps, see Eq. (6.4) are studied in subsections 6.3.1-6.3.3. Given the loop distribution, we then use it to calculate the SGWB in Section 6.4, and the predicted diffuse gamma ray flux in 6.5. We conclude in Section 6.6 by discussing the resulting experimental constraints on $G\mu$.

6.2 The loop distribution

All observational consequences of string loops depend on $\mathbf{n}(t, \ell)\,\mathrm{d}\ell$, the number density of non self-intersecting loops with length between ℓ and $\ell + \mathrm{d}\ell$ at time t. In this section we calculate $\mathbf{n}(t, \ell)$ given (6.7), that is we take into account the back-reaction of the emitted particles on the loop distribution. As noted in the introduction, the existence of the fixed scale ℓ_{k} or ℓ_{c} means that the loop distribution will no longer scale, that it will no longer be a function of the dimensionless variable $\gamma \equiv \ell/t$.

6.2.1 Boltzmann equation and general solution

The loop distribution satisfies a Boltzmann equation which, taking into account the ℓ-dependence of $\dot{\ell}$ (that is the flux of loops in ℓ-space), is given by Ref. [96]

$$\left.\frac{\partial}{\partial t}\right|_{\ell}\left(a^3\mathbf{n}\right) + \left.\frac{\partial}{\partial \ell}\right|_{t}\left(\frac{\mathrm{d}\ell}{\mathrm{d}t}a^3\mathbf{n}\right) = a^3\mathcal{P} \tag{6.8}$$

where $a(t)$ is the cosmic scale-factor, and the loop production function (LPF) $\mathcal{P}(t, \ell)$ is the rate at which loops of length ℓ are formed at time t by being chopped of the infinite string network. On substituting (6.7) into Eq. (6.8) and multiplying each side of the equation by $\mathcal{J}(\ell)$, one obtains

$$\frac{1}{\gamma_{\mathrm{d}}}\left.\frac{\partial}{\partial t}\right|_{\ell} g(t, \ell) - \mathcal{J}(\ell)\left.\frac{\partial}{\partial \ell}\right|_{t} g(t, \ell) = a^3\mathcal{J}(\ell)\mathcal{P}(t, \ell), \tag{6.9}$$

where

$$g(t, \ell) \equiv \gamma_{\mathrm{d}}\mathcal{J}(\ell)a^3(t)\mathbf{n}(t, \ell). \tag{6.10}$$

In order to solve (6.9), we first change variables from (t, ℓ) to

$$\tau \equiv \gamma_{\mathrm{d}}t\ , \qquad \xi \equiv \int \frac{\mathrm{d}\ell}{\mathcal{J}(\ell)}. \tag{6.11}$$

Notice from (6.7) and (6.11) that for a loop formed at time t_i with length ℓ_i, its length at time t satisfies

$$\xi(\ell) + \gamma_{\mathrm{d}}t = \xi(\ell_i) + \gamma_{\mathrm{d}}t_i. \tag{6.12}$$

In terms of these variables Eq. (6.9) reduces to a wave equation with a source term

$$\left.\frac{\partial}{\partial\tau}\right|_{\xi} g(\tau,\xi) - \left.\frac{\partial}{\partial\xi}\right|_{\tau} g(\tau,\xi) = \mathcal{S}(\tau,\xi), \tag{6.13}$$

where

$$\mathcal{S}(\tau,\xi) = a^3(\tau)\mathcal{J}(\xi)\mathcal{P}(\tau,\xi).$$

We now introduce the light-cone variables

$$2u \equiv \tau - \xi \ , \qquad 2v \equiv \tau + \xi, \tag{6.14}$$

so that the evolution equation simply becomes

$$\left.\frac{\partial}{\partial u}\right|_{v} g(u,v) = \mathcal{S}(u,v), \tag{6.15}$$

which is straightforward to integrate. In the following we neglect any initial loop distribution at initial time $t_{\rm ini}$ (since this is rapidly diluted by the expansion of the universe), so that the general solution of (6.15), and hence the original Boltzmann equation Eq. (6.8), is

$$g(u,v) = \int_{-v}^{u} \mathrm{d}u'\, S(u',v). \tag{6.16}$$

Finally one can convert back to the original variables $\mathbf{n}(\ell,t)$ using (6.10) to find

$$\mathbf{n}(t,\ell) = \frac{1}{\gamma_{\rm d}\mathcal{J}(\ell)a^3(t)} \int_{-v(t,\ell)}^{u(t,\ell)} \mathrm{d}u' \ a^3\big(u',v(t,\ell)\big)\mathcal{J}(u',v(t,\ell))\mathcal{P}(u',v(t,\ell)) \tag{6.17}$$

where $v(t,\ell)$ is obtained from Eqs. (6.11) and (6.14). Notice that $\mathcal{J}$ appears in two places: as an overall factor in the denominator, as well as in the integrand.

6.2.2 Solution for a δ-function loop production function

We now assume that all loops are chopped off the infinite string network with length αt at time t. This assumption, which has often been used in the literature, will lead to analytic expressions. The value $\alpha \sim 0.1$ is suggested by the NG simulations of [95, 103], particularly in the radiation era. However, one should note that other simulations [99] are consistent with power-law loop productions functions [52, 123], which have also been predicted analytically [137, 232, 138]. These will be considered elsewhere. Since $\alpha t \gg (\ell_{\rm k}, \ell_{\rm c})$ for $\alpha \sim 0.1$, we expect that particle radiation from infinite strings will not affect the (horizon-size) production of loops from the scaling infinite string network, and hence we consider a loop production function of the form

$$\mathcal{P}(t,\ell) = \mathrm{C}t^{-5}\delta\left(\frac{\ell}{t} - \alpha\right) \tag{6.18}$$

where the constant C, which takes different values in the radiation and matter eras, will be specified below. Substituting into (6.16), assuming $a \propto t^{\nu}$, (with $\nu = 1/2$ in the radiation era, and $\nu = 2/3$ in the matter era) gives

$$g(u,v) = \mathrm{C}\int_{-v}^{u} \mathrm{d}u' \ \mathcal{J}[\ell(u',v)]t(u',v)^{-5}a[t(u',v)]^3\delta\left[\frac{\ell(u',v)}{t(u',v)} - \alpha\right].$$

In order to evaluate this integral, in which $v = v(t, \ell)$ is *fixed*, let us denote the argument of the δ-function by

$$y \equiv \frac{\ell(u', v)}{t(u', v)} - \alpha.$$

For the given v, the argument vanishes ($y = 0$) for some $u'(v)$, that we will denote $u_\star(v)$ and which therefore satisfies

$$\ell(u_\star, v) = \alpha t(u_\star, v). \tag{6.19}$$

Let us rewrite this more simply as $\ell_\star = \alpha t_\star$ where $\ell_\star \equiv \ell(u_\star, v) = \ell_\star(v)$ and $t_\star \equiv t(u_\star, v) = t_\star(v)$. Now, from the v equation in (6.14), one has $2v = \gamma_{\rm d} t_\star(v) + \xi(\ell_\star(v))$. Furthermore — since our final goal is to write the loop distribution in terms of (t, ℓ) (rather than v) — we note from the same equation that v is related to (t, ℓ) by $2v = \gamma_{\rm d} t + \xi(\ell)$. Thus $t_\star(t, \ell)$, which will be required below, is the solution of

$$\gamma_{\rm d} t_\star + \xi(\alpha t_\star) = \gamma_{\rm d} t + \xi(\ell), \tag{6.20}$$

which physically is simply relating the length of the loop $\alpha t_\star$ at its formation time $t_\star$, with its length ℓ at time t, see Eq. (6.12).

The final step needed to evaluate the integral in Eq. (6.2.2) is the Jacobian of the transformation from u' to y which, on using (6.14), is given by

$$\left.\frac{\partial}{\partial u'}\right|_v (y(u', v)) = -\frac{\gamma_{\rm d}\mathcal{J}(\ell(u', v))t(u', v) + \ell(u', v)}{\gamma_{\rm d} t(u', v)^2}.$$

Evaluating this at $u' = u_\star$ and using $\ell_\star = \alpha t_\star$ gives

$$\left.\frac{\partial}{\partial u}\right|_v (y(u_\star, v)) = -\frac{\gamma_{\rm d}\mathcal{J}[\alpha t_\star(t, \ell)] + \alpha}{\gamma_{\rm d} t_\star(t, \ell)}.$$

Having now expressed all the relevant quantities in terms of (t, ℓ), one can combine the above results and use the definition of g in terms of $\mathbf{n}(t, \ell)$ in Eq. (6.10) to find

$$t^4 \mathbf{n} = \mathrm{C} \frac{1}{\mathcal{J}(\ell)} \frac{\mathcal{J}(\alpha t_\star)}{\alpha + \gamma_{\rm d}\mathcal{J}(\alpha t_\star)} \left(\frac{t_\star}{t}\right)^{-4} \left(\frac{a(t_\star)}{a(t)}\right)^3. \tag{6.21}$$

This equation, which is exact, is the central result of this section and gives the loop distribution for any form of energy loss $\mathrm{d}\ell/\mathrm{d}t = -\gamma_{\rm d}\mathcal{J}(\ell)$, provided the loop production function is a δ-function. It generalizes and extends other approximate results which may be found in the literature.

For loops that are formed in a given era (either radiation or matter domination) and decay in the *same* era, the above solution reduces to

$$t^4 \mathbf{n} = \mathrm{C} \frac{1}{\mathcal{J}(\ell)} \frac{\mathcal{J}(\alpha t_\star)}{\alpha + \gamma_{\rm d}\mathcal{J}(\alpha t_\star)} \left(\frac{t_\star}{t}\right)^{3\nu - 4}. \tag{6.22}$$

In the matter era, however, there also exists a population of loops which were *formed* in the radiation era, where $\mathrm{C} = c_{\rm rad}$, and decay in the matter era. Indeed, this population generally dominates over loops formed in the matter era. From (6.21) one can find a general expression for the distribution at any redshift z, provided the loops were formed in the radiation era ($\nu = 1/2$): it is given by

$$t^4 \mathbf{n}(t, \ell) = c_{\rm rad} \frac{1}{\mathcal{J}(\ell)} \frac{\mathcal{J}(\alpha t_\star)}{\alpha + \gamma_{\rm d}\mathcal{J}(\alpha t_\star)} \left(\frac{t_\star}{t}\right)^{-5/2} (1 + z(t))^3 \left(2\sqrt{\Omega_{\rm rad}} H_0 t\right)^{3/2} \tag{6.23}$$

This reduces to (6.21) in the radiation era, and has the correct scaling in the matter era.

In the following we use standard Planck cosmology with Hubble constant $H_0 = 100h$km/s/Mpc, $h = 0.678$, $\Omega_{\rm mat} = 0.308$, $\Omega_{\rm rad} = 9.1476 \times 10^{-5}$ and $\Omega_\Lambda = 1 - \Omega_{\rm mat} - \Omega_{\rm rad}$ [25]. We model the varying number of effective degrees of freedom in the radiation era through $H(z) = H_0\mathcal{H}(z)$ with $\mathcal{H}(z) = \sqrt{\Omega_\Lambda + \Omega_{\rm mat}(1+z)^3 + \Omega_R\mathcal{G}(z)(1+z)^4}$ where $\mathcal{G}(z)$ is directly related to the effective number of degrees of freedom $g_*(z)$ and the effective number of entropic degrees of freedom $g_S(z)$ by Ref. [48]

$$\mathcal{G}(z) = \frac{g_*(z)g_S^{4/3}(0)}{g_*(0)g_S^{4/3}(z)}. \tag{6.24}$$

We model this by a piecewise constant function whose value changes at the QCD phase transition ($T = 200$MeV), and at electron-positron annihilation ($T = 200$KeV):

$$\mathcal{G}(z) = \begin{cases} 1 & \text{for } z < 10^9, \\ 0.83 & \text{for } 10^9 < z < 2 \times 10^{12}. \\ 0.39 & \text{for } z > 2 \times 10^{12} \end{cases} \tag{6.25}$$

6.3 Loop distributions for particle radiation from cusps and kinks

Given a specific form of $\mathcal{J}(\ell)$, the loop distribution $\mathbf{n}(\ell, t)$ is given by (6.21), where $t_\star(t, \ell)$ is obtained by solving (6.20). The existence or not of an *analytical* solution depends on the form of $\mathcal{J}(\ell)$. In this section we consider three cases:

1. *Nambu-Goto loops*: here $\dot{\ell} = -\gamma_{\rm d}$ so that $\mathcal{J} = 1$;

2. *Loops with kinks*: The asymptotic behaviour of $\mathcal{J}(\ell)$ is given in Eq. (6.2). This can be captured, for instance, by $\mathcal{J}_1 = 1 + \ell_{\rm k}/\ell$ or alternatively by

$$\mathcal{J}_{\rm k} = \sqrt{1 + \left(\frac{\ell_{\rm k}}{\ell}\right)^2}. \tag{6.26}$$

   This second form gives a simpler analytic expression for $t_\star$, and we work with it below. (We have checked that the differences in predictions arising from the choice of $\mathcal{J}_1$ or $\mathcal{J}_{\rm k}$ are negligible.)

3. *Loops with cusps*: Following Eq. (6.4), we take

$$\mathcal{J}_c = \left[1 + \left(\frac{\ell_{\rm c}}{\ell}\right)^{3/2}\right]^{1/3}, \tag{6.27}$$

   which has the correct asymptotic behaviour and also leads to analytical expressions. An alternative and seemingly simpler, form $\mathcal{J} = 1 + \sqrt{\ell_{\rm c}/\ell}$ does not give analytical expressions for $\mathbf{n}(t, \ell)$.

We now determine the corresponding loop distribution in scaling units, namely in terms of the variables

$$\gamma \equiv \frac{\ell}{t}, \qquad \gamma_{\rm k}(t) \equiv \frac{\ell_{\rm k}}{t}, \qquad \gamma_{\rm c}(t) \equiv \frac{\ell_{\rm c}}{t}, \tag{6.28}$$

and determine

$$\mathcal{N}(t,\gamma) \equiv t^4 \mathbf{n}(t,\gamma). \tag{6.29}$$

6.3.1 NG strings

A first check is that the above formalism yields the well-known, standard, loop distribution for NG strings ($\mathcal{J} = 1$). Eq. (6.11) yields $\xi = \ell$, and from Eq. (6.20) it follows that

$$\frac{t_\star}{t} = \frac{\gamma + \gamma_{\rm d}}{\alpha + \gamma_{\rm d}}.$$

Hence, from Eq. (6.22)

$$\mathcal{N}_{NG}(t,\gamma) = {\rm C}\frac{(\alpha+\gamma_{\rm d})^{3(1-\nu)}}{(\gamma+\gamma_{\rm d})^{4-3\nu}}, \tag{6.30}$$

which is the standard scaling NG loop distribution for a delta-function loop production function [64]. In the radiation/matter eras, and on the scales $\alpha \gg \gamma_{\rm d}$ observed in simulations, comparison with the numerical results of [95, 103, 99] sets the value of C to respectively

$$\begin{aligned} c_{\rm rad}\alpha^{3/2} &\simeq 0.18 \qquad \text{(radiation era)} \\ c_{\rm mat}\alpha &\simeq 0.27 \qquad \text{(matter era)} \end{aligned}$$

The scaling distribution Eq. (6.30) is shown in the black (solid) curve in Fig 6.1, where we have taken $\alpha = 0.1$, $\gamma_{\rm d} = 10^{-6}$ and $\nu = 1/2$ (radiation era).

6.3.2 Loops with kinks

From Eq. (6.11), with $\mathcal{J}_k$ given Eq. (6.26), we now have $\xi(\ell) = \sqrt{\ell^2 + \ell_{\rm k}^2}$. Thus, from Eq. (6.20), $t_\star$ satisfies a quadratic equation with solution

$$\frac{t_\star}{t} = \frac{-\bar\gamma\left(\frac{\gamma_{\rm d}}{\alpha}\right) + \sqrt{\bar\gamma^2 - \gamma_{\rm k}^2\left(1 - \left(\frac{\gamma_{\rm d}}{\alpha}\right)^2\right)}}{\alpha\left(1 - \left(\frac{\gamma_{\rm d}}{\alpha}\right)\right)} \tag{6.31}$$

where $\gamma_{\rm k}(t)$ is given in (6.28) and

$$\bar\gamma(t,\gamma) \equiv \gamma_{\rm d} + \sqrt{\gamma_{\rm k}^2(t) + \gamma^2} \tag{6.32}$$

Since $\alpha \sim 0.1$ and $\gamma_{\rm d} \equiv \Gamma G\mu \lesssim 10^{-6}$ (from cosmic microwave background constraints on cosmic strings [72]) in our analytical expressions below we ignore terms in $\gamma_{\rm d}/\alpha$ so that $(\alpha t_\star/t)^2 = \bar\gamma^2 - \gamma_{\rm k}^2(t)$. (This approximation was not used in our numerical calculations.) Thus, from Eq. (6.21) we find, assuming $\alpha \gg \gamma_{\rm d}$,

$$\mathcal{N}(t,\gamma) = {\rm C}\alpha^{3(1-\nu)}\left(\frac{\bar\gamma^2(t,\gamma)}{1+\gamma_{\rm k}^2(t)/\gamma^2}\right)^{1/2}\left(\bar\gamma^2(t,\gamma) - \gamma_{\rm k}^2(t)\right)^{\frac{3\nu-5}{2}} \qquad \text{where } \gamma \le \alpha, \tag{6.33}$$

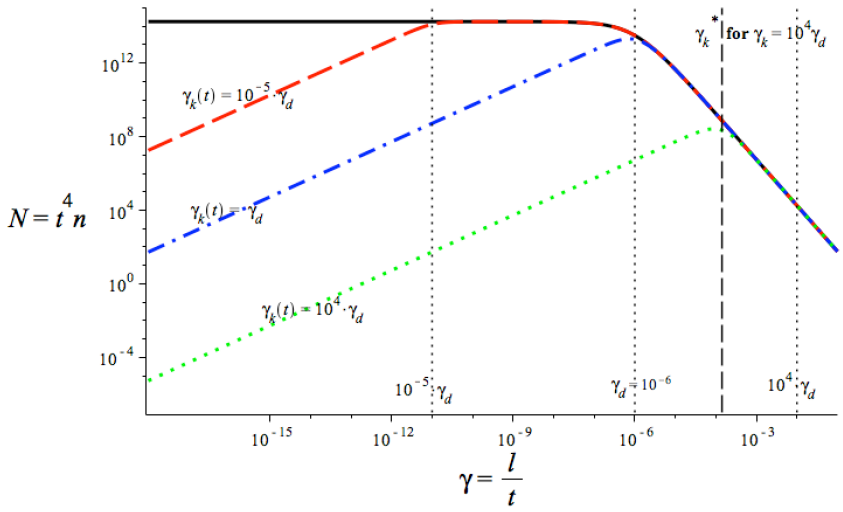

Figure 6.1: Loop distribution for kinks in the radiation era, with $\alpha = 0.1$ and $\gamma_{\rm d} = 10^{-6}$, and at several different epochs. Black solid line: $\gamma_{\rm k} = 0$ ($t \to \infty$), the NG loop distribution. Red dash line: $\gamma_{\rm k}(t) = 10^{-5}\gamma_{\rm d}$ (corresponding to $t = 10^5 t_k$). Blue dot-dash line $\gamma_{\rm k}(t) = \gamma_{\rm d}$ (corresponding to $t = t_k$). Green dotted line $\gamma_{\rm k}(t) = 10^4\gamma_{\rm d}$ (corresponding $t = 10^{-4}t_k$).

This distribution, in the radiation era, is plotted in Fig. 6.1 for illustrative values of $\gamma_{\rm k}(t)$, with $\gamma_{\rm d} = 10^{-6}$, $\alpha = 0.1$.

The important qualitative and quantitative features to notice are the following:

- The existence of the fixed scale $\ell_{\rm k}$ gives rise to a non-scaling distribution: $\mathcal{N}$ is explicitly t-dependent.
- When $\gamma_{\rm k} \to 0$, namely when $t \to \infty$, Eq. (6.33) reduces to the standard scaling NG loop distribution given in Eq. (6.30) (in the limit $\alpha \gg \gamma_d$).
- For $\gamma \gg \gamma_{\rm k}(t)$, the loop distribution is scaling since $\bar{\gamma} \sim \gamma + \gamma_{\rm d}$, so that
$$\mathcal{N}(t,\gamma) \simeq {\rm C}\alpha^{3(1-\nu)}(\gamma + \gamma_{\rm d})^{3\nu-4}. \tag{6.34}$$
This behaviour is clear in Fig. 6.1 where for $\gamma \gg \gamma_{\rm k}(t)$ the various curves coincide with the NG curve. Hence, for loops of these lengths, gravitational radiation is important but particle radiation plays no role. Furthermore
  - when $\gamma_{\rm d} \gg \gamma \gg \gamma_{\rm k}$, the distribution is *flat*, see Fig 6.1 dashed-red curve.
  - when $\gamma \gg (\gamma_{\rm d}, \gamma_{\rm k})$ $\mathcal{N}$ drops off as $\gamma^{3\nu-4}$, as for NG loops, a dependence which is simply due to the expansion of the universe.
- For $\gamma \ll \gamma_{\rm k}(t)$, the distribution no-longer scales because of particle radiation. Indeed, $\bar{\gamma} \sim \gamma_{\rm k}(t) + \gamma_{\rm d}$ so that
$$\mathcal{N} \simeq {\rm C}\alpha^{3(1-\nu)}\gamma_{\rm d}^{\frac{3\nu-5}{2}}\left(\frac{\gamma}{\gamma_{\rm k}(t)}\right)(2\gamma_{\rm k}(t) + \gamma_{\rm d})^{\frac{3\nu-5}{2}}(\gamma_{\rm k}(t) + \gamma_{\rm d}). \tag{6.35}$$

This linear dependence on γ for $\gamma \ll \gamma_k$ is visible in Fig. 6.1. Notice that

– when $\gamma_{\rm d} \ll \gamma_{\rm k}$, there is no plateau in the distribution, which goes from the linear behaviour Eq.(6.35) to the scaling behaviour Eq. (6.34), at a value of γ obtained by equating these two equations, namely

$$\gamma^*_{\rm k}(t) \simeq \sqrt{2\gamma_{\rm k}\gamma_{\rm d}}.$$

This is clearly visible in the green-dotted curve in Fig. 6.1.

When $\gamma_{\rm k}(t) \ll \gamma_{\rm d}$, an excellent approximation to the distribution is

$$\mathcal{N}(\gamma,t) \simeq {\rm C}\alpha^{3(1-\nu)}\frac{1}{\mathcal{J}(\gamma,t)}(\gamma+\gamma_{\rm d})^{3\nu-4}. \tag{6.36}$$

where, for the kinks considered here,

$$\mathcal{J}(\gamma,t) = \sqrt{1+\left(\frac{\gamma_{\rm k}(t)}{\gamma}\right)^2}.$$

On the other hand, when $\gamma_{\rm k}(t) \geq \gamma_{\rm d}$ the distribution changes behaviour, and for $\gamma_{\rm k}(t) \gg \gamma_{\rm d}$ *its amplitude is significantly suppressed due to particle emission.* Indeed, when $\gamma = \gamma^*_{\rm k}(t)$, which is at the maximum of $\mathcal{N}$ (see green curve, Fig 6.1), $\mathcal{N}$ scales as $\gamma_{\rm k}^{-(4-3\nu)/2}$ which decreases with increasing $\gamma_{\rm k}$. The equality $\gamma_{\rm d} = \gamma_{\rm k}(t)$ defines a *characteristic time* t_k by

$$t_k \equiv \frac{\ell_{\rm k}}{\gamma_{\rm d}}. \tag{6.37}$$

For $t \ll t_k$, particle emission is dominant, $\gamma_{\rm k}(t) \geq \gamma_{\rm d}$, and the distribution is suppressed. Using $\ell_{\rm k}$ given by Eq. (6.3),

$$t_k = \beta_k \frac{t_{pl}}{\Gamma^2(G\mu)^{5/2}} \simeq \beta_k t_{eq}\left(\frac{2.5\times10^{-24}}{G\mu}\right)^{5/2}$$

or in terms of redshift

$$z_k \simeq z_{eq}\left(\frac{G\mu}{2.5\times10^{-24}}\right)^{5/4}\frac{1}{\sqrt{\beta_k}} \tag{6.38}$$

where $z_{eq} \simeq \Omega_{\rm mat}/\Omega_{\rm rad} \sim 3367$. The LH panel of Fig. 6.2 shows the loop distribution for different redshifts for $\ell_{\rm k}$ given in Eq. (6.3) and $\beta_k = 1$. The effect of the suppression of the loop distribution at $z \gg z_k$ on the SGWB will be discussed in Section 6.4.

6.3.3 Loops with cusps

For loops with cusps, where $\mathcal{J} = \mathcal{J}_{\rm c}$ given in Eq. (6.27), the analysis is very similar. We only give the salient features. As for kinks (see Eq. 6.37), one can define a characteristic time through $\gamma_{\rm d} = \gamma_{\rm c}(t)$, namely

$$t_c \equiv \frac{\ell_{\rm c}}{\gamma_{\rm d}}, \tag{6.39}$$

and again, as for kinks, when $t \ll t_c$ the effects of particle radiation are more important and the loop distribution is suppressed. For $\ell_{\rm c}$ given in Eq. (6.5), we have

$$t_c = \beta_c \frac{t_{pl}}{\Gamma^3 (G\mu)^{7/2}} \simeq \beta_c t_{eq} \left(\frac{4.6 \times 10^{-18}}{G\mu} \right)^{7/2} \tag{6.40}$$

or in terms of redshift

$$z_c \simeq z_{eq} \left(\frac{G\mu}{4.6 \times 10^{-18}} \right)^{7/4} \frac{1}{\sqrt{\beta_c}}. \tag{6.41}$$

For the relevant range, namely $G\mu < 10^{-6}$, we have $z_c < z_k$ and hence the observational consequences of cusps, both on the SGWB and the diffuse Gamma-ray background, are expected to be more significant than those of kinks — since, as discussed above, the loop distribution is suppressed when $z < (z_c, z_k)$, see Fig. 6.2.

The explicit γ-dependence of the distribution is the following. First, substituting $\mathcal{J}_{\rm c}$ in the definition of $\xi(\gamma)$ and t_*, Eqs.(6.11) and (6.20) respectively, we find

$$\xi(\ell) = \left(\ell^{3/2} + \ell_{\rm c}^{3/2} \right)^{2/3},$$
$$\left(\frac{\alpha t_\star}{t} \right)^{3/2} = \left[\gamma_{\rm d} + \left(\gamma^{3/2} + \gamma_{\rm c}^{3/2} \right)^{2/3} \right]^{3/2} - \gamma_{\rm c}^{3/2} \qquad \text{for } \alpha \gg \gamma_{\rm d}.$$

It then follows from Eq. (6.22) that the resulting distribution again scales for $\gamma \gg \gamma_{\rm c}$ where it is given by Eq. (6.34); and for $\gamma \ll \gamma_{\rm d}$, $\mathcal{N} \propto \sqrt{\gamma}$. When $\gamma_{\rm c} \gg \gamma_{\rm d}$, we find

$$\mathcal{N} \propto \begin{cases} \gamma^{3\nu-4} & (\gamma \gg \gamma_{\rm c}^*) \\ \sqrt{\gamma} & (\gamma \ll \gamma_{\rm c}^*) \end{cases}$$

where

$$\gamma_{\rm c}^* \simeq (\gamma_{\rm d} \sqrt{\gamma_{\rm c}})^{2/3}.$$

6.4 The Stochastic Gravitational Wave Background

The stochastic GW background $\Omega_{\rm GW}(t_0, f)$ given in (6.6) is obtained by adding up the GW emission from all the loops throughout the whole history of the Universe which have contributed to frequency f. Following the approach developed in Refs. [128, 64, 114]

$$\Omega_{\rm GW}(\ln f) = \frac{8\pi G^2 \mu^2 f}{3H_0^2} \sum_{j=1}^{\infty} C_j(f) P_j \,, \tag{6.42}$$

where

$$C_j(f) = \frac{2j}{f^2} \int_0^{z_{\rm friction}} \frac{{\rm d}z}{H(z)(1+z)^6} \; n\left(\frac{2j}{(1+z)f}, t(z) \right), \tag{6.43}$$

and $z_{\rm friction}$ is the redshift below which friction effects on the string dynamics become negligible [64]

$$z_{\rm friction} \simeq z_{\rm eq} \, (4.4 \times 10^{16}) \left(\frac{G\mu}{10^{-11}} \right). \tag{6.44}$$

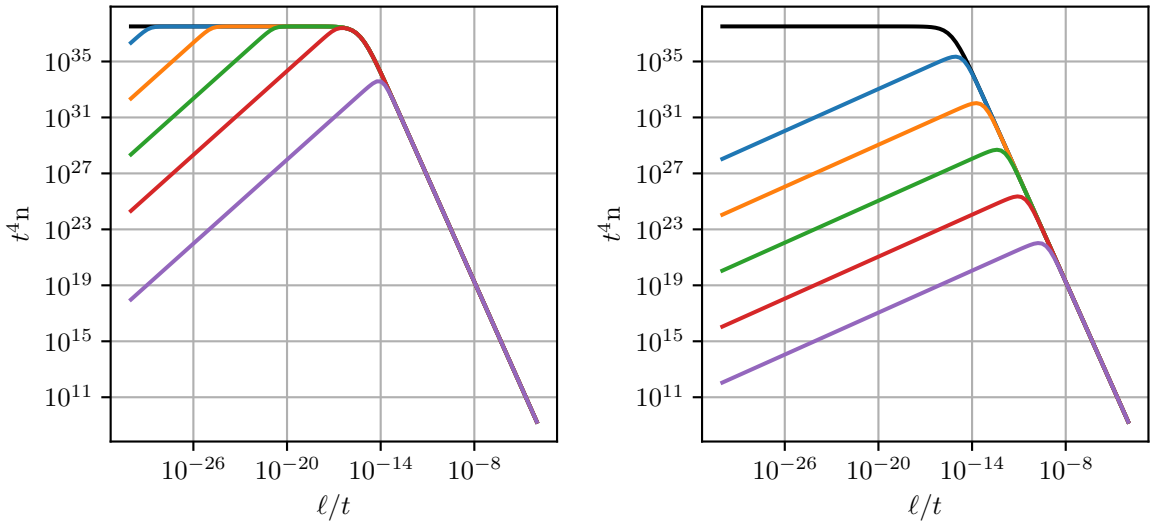

Figure 6.2: Loop number density $\mathcal{N} = t^4 n$ for kinks [LH panel] and cusps [RH panel], for $G\mu = 10^{-17}$. Thus $z_k \sim 10^{12}$ and $z_c \sim 10^4$. From bottom to top, the curves show snapshots of the loop distribution at redshifts $z = 10^{13}, 10^{11}, 10^9, 10^7, 10^5$, and the black curve is the scaling loop distribution at $z \to 0$. The loop distributions are suppressed for $z \gg z_k$ or $z \gg z_c$.

The C_j depend on the loop distribution $\mathbf{n}(\ell, t)$ through $\mathbf{n}(2j/((1+z)f), t(z))$, whilst the P_j are the "average loop gravitational wave power-spectrum", namely the power emitted in gravitational waves in the jth harmonic of the loop. By definition of Γ, these must be normalized to

$$\Gamma = \sum_{j=1}^{\infty} P_j.$$

For loops with kinks, $P_j \propto j^{-5/3}$, whereas for loops with cusps $P_j \propto j^{-4/3}$ [117, 108, 64].

As explained above, the effect of $\gamma_{\rm k}$ and $\gamma_{\rm c}$ on the loop distribution is particularly important at large redshifts $z > (z_c, z_k)$, and hence in the radiation era. Therefore, we expect the effect of particle radiation to be visible in the high-frequency part of the spectrum. This is indeed observed in Fig. 6.3, where the LH panel is for kinks with $\ell_{\rm k}$ given in Eq. (6.3) and $P_j \propto j^{-5/3}$; whereas the RH panel is for cusps with $\ell_{\rm c}$ given in Eq. (6.5) and $P_j \propto j^{-4/3}$. As a result of the non-scaling loop distribution, the spectrum is no longer flat at high frequencies and, as expected, the effect is more significant for cusps than for kinks since $z_c < z_k$.

We can estimate the frequency above which the spectrum decays as follows. In the radiation era

$$H(z) = (1+z)^2 \sqrt{\Omega_{\rm rad}} H_0 \tag{6.45}$$

$$t(z) = \frac{1}{2(1+z)^2} \frac{1}{\sqrt{\Omega_{\rm rad}} H_0} \tag{6.46}$$

At high frequency, the lowest harmonic $j = 1$ is expected to dominate [64], so we set $P_j = \Gamma \delta_{j,1}$.

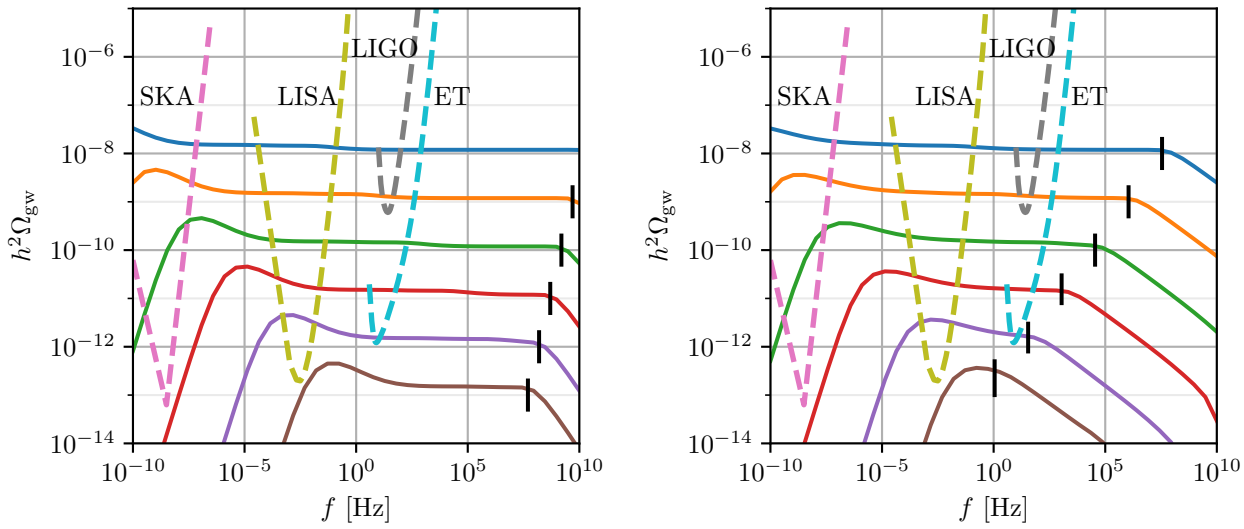

Figure 6.3: SGWB including the backreaction of particle emission on the loop distribution. LH panel: kinks on loops, RH panel: cusps on loop. The spectra are cutoff at high frequency, as indicated by the black vertical lines. $G\mu$ ranges from 10^{-17} (lower curve), through 10^{-15}, 10^{-13},10^{-11}, 10^{-9} and 10^{-7} (upper curve). Also plotted are the power-law integrated sensitivity curves from SKA (pink dashed) [47], LISA (yellow dashed) [35], adv-LIGO (grey dashed) [31] and Einstein Telescope (blue dashed) [348, 349].

Then using (6.45) and (6.46), Eq. (6.42) simplifies to

$$\begin{aligned}\Omega_{\rm GW}(\ln f) = & \quad 2^4\frac{16\pi(\Gamma G\mu)^2}{3\Gamma}\frac{H_0}{f}\Omega_{\rm rad}^{3/2}\int_{z_{\rm eq}}^{z_{\rm friction}}{\rm d}z\ \mathcal{N}\Big(\frac{2}{(1+z)f},t(z)\Big)\\ \propto & \quad \frac{H_0}{f}\left[\int_{z_{\rm eq}}^{z_{c,k}}{\rm d}z\ \mathcal{N}\Big(\frac{2}{(1+z)f},t(z)\Big)+\int_{z_{c,k}}^{z_{\rm friction}}{\rm d}z\ \mathcal{N}\Big(\frac{2}{(1+z)f},t(z)\Big)\right].\\ \simeq & \quad \frac{H_0}{f}\int_{z_{\rm eq}}^{z_{c,k}}{\rm d}z\ \mathcal{N}\Big(\frac{2}{(1+z)f},t(z)\Big). \qquad (6.47)\end{aligned}$$

Here, in going from the second to the third equality, we have used the fact that (i) for $G\mu \gtrsim 10^{-18}$, which is relevant range for current and future GW detectors, $z_{\rm eq} < (z_c, z_k) \ll z_{\rm friction}$ (see Eqs. (6.38), (6.41) and (6.44)), and (ii) that the loop distribution above $z_{(c,k)}$ is subdominant, see *e.g.* discussion above equation (6.37) in Section 6.3.2. Using Eq.(6.46) as well as the approximation for the loop distribution for $z < z_k$ given in Eq. (6.36), it follows that for kinks

$$[\Omega_{\rm GW}(\ln f)]_k \propto \int_{x_{\rm eq}}^{x_k}\left[1+\left(\frac{\ell_{\rm k}xf^2}{8H_0\sqrt{\Omega_{\rm rad}}}\right)^2\right]^{-1/2}(\gamma_{\rm d}+x)^{-5/2}\,{\rm d}x \qquad (6.48)$$

where we have changed variable from z to

$$x = \frac{4}{f}(1+z)H_0\sqrt{\Omega_{\rm rad}}$$

so that

$$x_{\rm eq} = \frac{4}{f}(1+z_{\rm eq})H_0\sqrt{\Omega_{\rm rad}}\,, \qquad x_k = \frac{4}{f}(1+z_k)H_0\sqrt{\Omega_{\rm rad}}\,.$$

In order to understand the frequency dependence of $\Omega_{\rm GW}$, let us initially focus on the standard NG case, namely $\ell_k = 0$. (Here, the same change of variable starting from the first line of Eq. (6.47) again yields Eq. (6.48) but with upper bound replaced by $x_{\rm friction} = 4(1+z_{\rm friction})H_0\sqrt{\Omega_{\rm rad}}/f$). Then Eq. (6.48) gives

$$[\Omega_{\rm GW}(\ln f)]_{NG} \propto \frac{1}{\left(\frac{f_{\rm eq}}{f}+1\right)^{3/2}} - \frac{1}{\left(\frac{f_{\rm friction}}{f}+1\right)^{3/2}},$$

where

$$f_{\rm eq} = \frac{4H_0\sqrt{\Omega_{\rm rad}}(1+z_{\rm eq})}{\gamma_{\rm d}} \sim \frac{10^{-18}}{G\mu}{\rm s}^{-1}\,, \qquad f_{\rm friction} = \frac{4H_0\sqrt{\Omega_{\rm rad}}(1+z_{\rm friction})}{\gamma_{\rm d}} \sim 10^{10}{\rm s}^{-1},$$

and where in the last equality we have used Eq. (6.44). At frequencies f for which $f_{\rm friction} \gg f \gg f_{\rm eq}$ it follows that $[\Omega_{\rm GW}(\ln f)]_{NG} \to$ constant meaning that the spectrum is flat, which is the well-known result for NG strings [64].

For $\ell_{\rm k} \neq 0$, the argument is altered because of the frequency dependence of the term in square brackets in Eq. (6.48). A further characteristic frequency now enters: this is can be obtained by combining the typical scales of the two terms in Eq. (6.48). Namely, on one hand, from the first

term (in square brackets) we have $\ell_{\rm k} f^2 \sim 8H_0\sqrt{\Omega_{\rm rad}}x^{-1}$; and on the other hand from the second (standard NG) term we have $x \sim \gamma_{\rm d}$. Combining these yields the characteristic frequency

$$f_k \sim \left(\frac{8H_0\sqrt{\Omega_{\rm rad}}}{\ell_{\rm k}\gamma_{\rm d}}\right)^{1/2}. \tag{6.49}$$

For $f_k > f > f_{eq}$ the spectrum is still flat, as in the NG case. However, for $f > f_k$ it decays since the first term in square brackets in Eq. (6.48) dominates. With $\ell_{\rm k}$ given in Eq. (6.3), $f_k \propto (G\mu)^{1/4}\beta_{\rm k}^{-1/2}$, and this behaviour is clearly shown in Fig. 6.3 where f_k is shown with a vertical black line for each value of $G\mu$, and we have assumed $\beta_{\rm k} = 1$.

For cusps the analysis proceeds identically with

$$f_c = \left(\frac{8H_0\sqrt{\Omega_{\rm rad}}}{\ell_{\rm c}\gamma_{\rm d}}\right)^{1/2}. \tag{6.50}$$

Now, on using $\ell_{\rm c}$ defined in Eq. (6.5), we have $f_c \propto (G\mu)^{3/4}\beta_{\rm c}^{-1/2}$. The spectrum of SGWB in this case is shown in the RH panel of Fig. 6.3 where f_c is shown with a vertical black line for each value of $G\mu$, and we have taken $\beta_{\rm c} = 1$.

As the figure shows, with $\beta_{\rm c} = 1$ and in the range of $G\mu$ of interest for GW detectors, the decay of $\Omega_{\rm GW}$ for $f > f_c$ is *outside* the observational window of the LIGO, LISA (and future ET) detectors. In order to have $f_c \sim f_{\rm LIGO}$, one would require large values of $\beta_{\rm c}$ which are not expected.

6.5 Emission of particles

The loops we consider radiate not only GW but also particles. Indeed, for loops with kinks, from Eq. (6.2)

$$\dot{\ell}\Big|_{\rm particle} = -\gamma_{\rm d}\frac{\ell_{\rm k}}{\ell} \tag{6.51}$$

The emitted particles are heavy and in the dark particle physics sector corresponding to the fields that make up the string. We assume that there is some interaction of the dark sector with the standard model sector. Then the emitted particle radiation will eventually decay, and a significant fraction of the energy $f_{\rm eff} \sim 1$ will cascade down into γ-rays. Hence, the string network will be constrained by the Diffuse Gamma-Ray bound measured at GeV scales by Fermi-LAT [341]. This bound is

$$\omega_{\rm DGRB}^{\rm obs} \lesssim 5.8 \times 10^{-7}\ {\rm eVcm}^{-3}, \tag{6.52}$$

where $\omega_{\rm DGRB}$ is the total electromagnetic energy injected since the universe became transparent to GeV γ-rays at $t_\gamma \simeq 10^{15}$s, see *e.g.* [346].

The rate per unit volume at which string loops lose energy into particles can be obtained by integrating (6.51) over the loop distribution $\mathbf{n}(\ell, t) = t^{-4}\mathcal{N}(\gamma, t)$, namely

$$\Phi_{\rm H}(t) = \mu\gamma_{\rm d}\ell_{\rm k}\int_0^{\alpha t}\mathbf{n}(\ell,t)\frac{{\rm d}\ell}{\ell} = \mu t^{-3}\gamma_{\rm d}\gamma_{\rm k}\int_0^{\alpha}\frac{\mathcal{N}(\gamma',t)}{\gamma'}\,{\rm d}\gamma' \tag{6.53}$$

The Diffuse Gamma Ray Background (DGRB) contribution is then given by (see *e.g.* [346])

$$\begin{aligned}\omega_{\rm DGRB} &= f_{\rm eff}\int_{t_\gamma}^{t_0}\frac{\Phi_{\rm H}(t)}{(1+z)^4}\,{\rm d}t\\ &= f_{\rm eff}\mu\gamma_{\rm d}\int_{t_\gamma}^{t_0}\frac{\gamma_{\rm k}(t)}{t^3(1+z(t))^4}\left[\int_0^\alpha\frac{\mathcal{N}(\gamma',t)}{\gamma'}\,{\rm d}\gamma'\right]{\rm d}t\\ &= \Gamma(8.4\times10^{39})f_{\rm eff}\left(\frac{G\mu}{c^4}\right)^2\int_{t_\gamma}^{t_0}\frac{\gamma_{\rm k}(t)}{t^3(1+z(t))^4}\left[\int_0^\alpha\frac{\mathcal{N}(\gamma',t)}{\gamma'}\,{\rm d}\gamma'\right]{\rm d}t \qquad {\rm eVcm}^{-3}\end{aligned} \tag{6.54}$$

where in the last line we have explicitly put in factors of c converted to physical units of eV/cm^3. For cusps, one finds

$$\omega_{\rm DGRB} = \Gamma(8.4\times10^{39})f_{\rm eff}\left(\frac{G\mu}{c^4}\right)^2\int_{t_\gamma}^{t_0}\frac{\sqrt{\gamma_{\rm c}(t)}}{t^3(1+z(t))^4}\left[\int_0^\alpha\frac{\mathcal{N}(\gamma',t)}{\sqrt{\gamma'}}\,{\rm d}\gamma'\right]{\rm d}t \qquad {\rm eVcm}^{-3} \tag{6.55}$$

In the matter dominated era, the loop distribution is dominated by those loops produced in the radiation era but decay in the matter era: its general expression is given in Eq. (6.23), and can be deduced straightforwardly from the results of subsections 6.3.2 and 6.3.3 for kinks and cusps respectively. We have calculated (6.54) and (6.55) numerically, and the results are shown in Fig. 6.4 for kinks [LH panel] and cusps [RH panel], together with the Fermi-LAT bound. It is clear from this figure that particle radiation from loops containing kinks and/or cusps, with $\ell_{\rm k}$ and $\ell_{\rm c}$ given in (6.3) and (6.5), are not constrained by the Fermi-LAT data.

The general shape of the spectra in Fig. 6.4 can be understood from the results of Section 6.2. Let us focus on the case of cusps (for kinks the analysis is similar). First, we can determine the range of $G\mu$ for which the characteristic time t_c defined in Eq. (6.39) falls within the range of integration of (6.55), namely

$$t_\gamma \le t_c \le t_0 \qquad \Longleftrightarrow \qquad 10^{-19} \lesssim G\mu \lesssim 10^{-18}$$

(we have assumed $\beta_{\rm c}=1$ and, from Eq. (6.40), $t=t_c$ implies $G\mu\sim 4.6\times10^{-18}(t_{\rm eq}/t)^{2/7}$). This range of $G\mu$ defines the position of the maximum of the DGRB in the RH panel of Fig. 6.4. For lower $G\mu$, all times in the integration range are *smaller* than t_c. As we have discussed in Section 6.3.3, in this case the loop distributions are *suppressed* due to particle radiation: there are fewer loops, and hence fewer particles are emitted leading to a decrease in the DGRB. This is shown in Fig. 6.4, and using the results of Section 6.3.3, one can show that for $G\mu \ll 10^{-19}$, $\Phi_{\rm H}(t)\propto\mu^{2/3}\ell_{\rm c}^{-1/6}(1+z)^3t^{-4/3}$ leading to

$$\omega_{\rm DGRB}\propto\mu^{2/3}\ell_{\rm c}^{-1/6}\propto(G\mu)^{13/12} \qquad (G\mu\ll10^{-19}).$$

On the other hand, for $G\mu \gg 10^{-18}$, all times in the integration range are *larger* than t_c. There is no suppression of the loop distribution, since GR dominates over particle emission (see Section 6.2). But precisely because GR dominates, fewer particles are emitted, and hence we also have a decrease in the DGRB. We now find that $\Phi_{\rm H}(t)\propto\gamma_{\rm d}^{-1}\mu\sqrt{\ell_{\rm c}}(1+z)^3t^{-2}$ so that

$$\omega_{\rm DGRB}\propto\sqrt{\ell_{\rm c}}\propto(G\mu)^{-5/4}$$

which is the slope seen in Fig. 6.4. For kinks the discussion is very similar, and the slopes are given in the caption of the figure. However, each kink event emits fewer particles, leading to a lower overall DGRB.

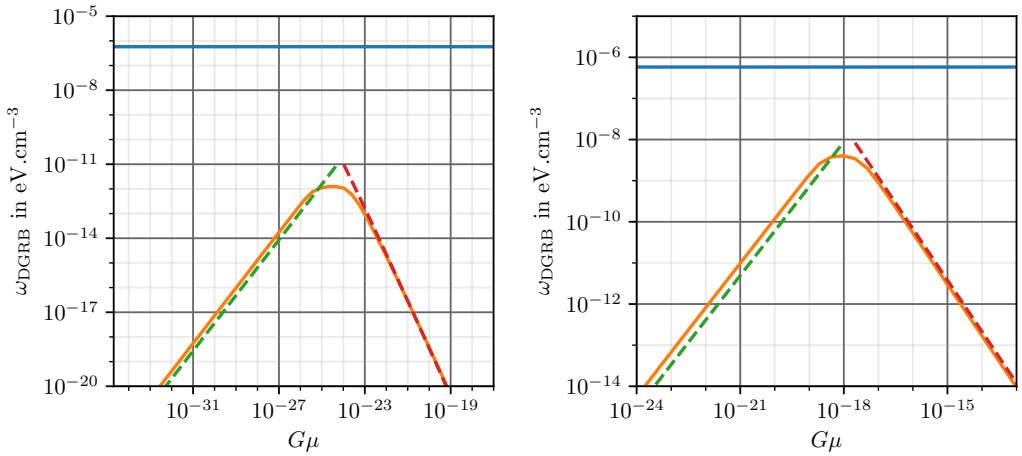

Figure 6.4: Contribution of cosmic strings to the Diffuse Gamma-Ray Background. The (blue) horizontal line is the experimental constraint from Fermi-LAT, while the (orange) line is the exact numerical calculation for kinks (LH panel) and cusps (RH panel). On either side of the maxima, the slope and amplitude can be estimated using the results of previous sections. Kinks: for low $G\mu$ the slope is 9/8 (dashed-green line), and for high $G\mu$ it depends on $\mu^{-2}\log(\mu)$ (dashed-red line). Cusps: For low $G\mu$ the slope is 13/12 (dashed-green line), and for high $G\mu$ it is $-5/4$ (dashed-red line). The slightly different amplitude between the numerical calculation and the analytical one is because the latter assumes a matter dominated universe, and hence neglects effects of late time acceleration.

6.6 Conclusion

Cosmic string loops emit both particle and gravitational radiation. Particle emission is more important for small loops, while gravitational emission dominates for large loops. In this work, we have accounted for both types of radiation in the number density of loops and calculated the expected stochastic gravitational wave background and the diffuse gamma ray background from strings. Our results show that the number density of loops gets cutoff at small lengths due to particle radiation. The strength of the cutoff depends on the detailed particle emission mechanism from strings – if only kinks are prevalent on strings, small loops are suppressed but not as much as in the case when cusps are prevalent (see Fig. 6.2). The cutoff in loop sizes implies that the stochastic gravitational wave background will get cut off at high frequencies (see Fig. 6.3). The high frequency cutoff does not affect current gravitational wave detection efforts but may become important for future experiments.

Particle emission from strings can provide an important alternate observational signature in the form of cosmic rays. Assuming that the particles emitted from strings decay into standard model Higgs particles that then eventually cascade into gamma rays, we can calculate the gamma ray background from strings. This background is below current constraints in the case of both kinks and cusps.

It is important to evaluate more carefully the prevalence of kinks versus cusps on cosmological string loops. In Ref. [139], particle radiation from a loop of a specific shape was studied where the shape was dictated by general expectations for the behaviour of the cosmological string network. That particular loop only contained kinks. It would be of interest to study other loop shapes that are likely to be produced from the network and that contain cusps and to assess if the $1/\sqrt{\ell}$ dependence in (6.4) (and assumed throughout this paper) is an accurate characterization of such loops over their lifetimes. In practice one might expect that if kinks are smoothed out by particle emission, then cusps (perhaps minicusps) must be produced, and if cusps (or minicusps) annihilate then kinks must be produced. Hence, in reality the situation might be a combination of both cases. Finally, it would also be interesting to study other loop production functions, particularly those of [137, 232, 138] which predict a larger number of small loops relative to the situation studied in Section 6.2.2; hence one might expect a larger gamma ray background from strings in this case [2].

[2] Work in progress

Chapter 7

Irreducible cosmic production of relic vortons

This chapter is a reproduction of Ref. [58] written in collaboration with Patrick Peter, Christophe Ringeval and Danièle Steer. The aim of this paper was to quantify the abundance of *vortons*, stable configuration of loops, in networks of current-carrying cosmic strings. These vortons can be candidates for Dark Matter and their predicted abundance can therefore be constrained by observations since $\Omega_{\rm mat} \lesssim 0.3$. In Ref. [125], Patrick Peter and Christophe Ringeval had used a Boltzmann equation to calculate the accumulation of vortons from an initial distribution of cosmic string loops. In this paper, we build upon the solution Eq. (6.21) found in Chapter 6 for the continuity equation, but in this chapter loops have a charge in addition to a length. With this framework, we were able to calculate the abundance of vortons formed from the loop production function, something which is new and had not been calculated before. I contributed to all the sections of this chapter.

Abstract

The existence of a scaling network of current-carrying cosmic strings in our Universe is expected to continuously create loops endowed with a conserved current during the cosmological expansion. These loops radiate gravitational waves and may stabilize into centrifugally supported configurations. We show that this process generates an irreducible population of vortons which has not been considered so far. In particular, we expect vortons to be massively present today even if no loops are created at the time of string formation. We determine their cosmological distribution, and estimate their relic abundance today as a function of both the string tension and the current energy scale. This allows us to rule out new domains of this parameter space. At the same time, given some conditions on the string current, vortons are shown to provide a viable and original dark matter candidate, possibly for all values of the string tension. Their mass, spin and charge spectrum being broad, vortons would have an unusual phenomenology in dark matter searches.

7.1 Introduction

Cosmic strings are expected to be formed in most extensions of the standard particle physics model as stable line-like topological defects formed during high temperature, $T_{\rm ini}$ say, symmetry breaking

phase transitions in the early Universe [61]. This occurs whenever a symmetry $\mathcal{G}$ is broken down to a smaller one $\mathcal{H}$ provided the first homotopy group of the quotient group $\mathcal{G}/\mathcal{H}$ (vacuum manifold) is non-trivial, producing similarly non-trivial topological solutions for the symmetry-breaking Higgs field. The scaling evolution of cosmic string networks (see *e.g.* Ref. [123] and references therein) means that they are present throughout the evolution of the Universe, possibly giving rise to numerous observational signatures, such as line-like discontinuities in temperature in the Cosmic Microwave Background (CMB), or bursts of gravitational waves [106, 114, 90]. These very much sought-for signatures in turn lead to strong constraints on the string tension $G\mu$.

Most studies of cosmic strings suppose they are structureless, with equal energy per unit length and tension, and therefore they are expected to be well described by a no-scale 2-dimensional worldsheet action, *i.e.* the Nambu-Goto action. This is no longer the case if, as first realized by Witten [143, 144], particles coupled to the string-forming Higgs field can condense in the string core and subsequently propagate along the worldsheet. The resulting strings thus behave like current carrying wires and are endowed with a much richer structure [145, 146].

One of the simplest examples of current-carrying strings is that of a $\mathrm{U}(1)_R\times\mathrm{U}(1)_Q$ gauge theory with an unbroken gauge symmetry Q (which might be electromagnetism, but not necessarily) and a broken symmetry R [143]. This model generalizes the prototypical Abelian-Higgs model of cosmic strings behind much of the existing work on cosmic strings. At a temperature $T_{\rm ini}$, and a cosmic time $t_{\rm ini}$, the Higgs field ϕ with $Q=0$ and $R=1$ acquires a non-zero vacuum expectation value $|\langle\phi\rangle|\neq 0$, thereby breaking the first component $\mathrm{U}(1)_R$ of the total invariance group; this leads to the formation of vortex lines. The field ϕ vanishes at the core of the string and its phase varies by an integer times 2π along any closed path around the vortex: this is the standard Kibble mechanism. If the theory contains fermions obtaining their masses from the $\mathrm{U}(1)_Q$ broken symmetry, those form zero modes in the string core where the symmetry is restored, thereby forming a superconducting current.

The model also comprises a second scalar field σ with $Q=1$ and $R=0$, the coupling potential between ϕ and σ being chosen such that $\langle\sigma\rangle=0$ in vacuum (where $|\langle\phi\rangle|\neq 0$). Under certain conditions, it is energetically favourable to have $\langle\sigma\rangle\neq 0$ at the core of the string where $\langle\phi\rangle=0$. At a temperature $T_{\rm cur}<T_{\rm ini}$, and cosmic time $t_{\rm cur}>t_{\rm ini}$, the charged scalar field σ thus condenses on the string and acts as a bosonic charge carrier making the string current-carrying (and in fact actually superconducting). In the present paper, we assume that the current sets in long after the string formation scale. In the language of Refs. [350, 149], this means we assume the current is formed long after the friction damping regime has finished, *i.e.* during the radiation era. In practice, it means that we consider $T_{\rm ini}$ (and $t_{\rm ini}$) to be the end of the friction dominated regime.

Cosmic strings can also be produced [351, 352] in superstring theory, also forming, under specific conditions, a network similar to a Nambu-Goto network [353]. Whether these so-called cosmic superstrings can carry a current deserves more investigation since they have been shown to not be able to hold fermionic zero modes so that only bosonic condensates can source such a current [318]. It should, however, be mentioned that because cosmic superstrings live in a higher dimensional manifold, their motion in the extra dimensions projected into the ordinary 3 dimensional space should be describable by means of a phenomenological non-trivial equation of state [354, 355] mimicking that of a current-carrying string; this can be interpreted as moduli field condensates.

The presence of currents flowing along the strings affects the dynamics of the network, and in this paper we particularly focus on vortons [147, 148, 149, 150, 151, 152, 153, 154], namely closed loops of string which are stabilized by the angular momentum carried by the current. Vortons do not radiate classically, and here we make the assumption that they are classically stable as well (see

for instance [155, 156, 157] for numerical studies of their stability). On cosmological scales, they appear as point particles having different quantized charges and angular momenta.

In this work, we extend the derivation of the vorton abundance of Ref. [149] by not only considering vortons produced from pre-existing loops *at* $t_{\rm ini}$, but also those vortons that may form from the loops chopped off the network at all subsequent times. In particular, we extend the work of Ref. [125], in which a Boltzmann equation governing the vorton density has been derived and integrated for any loop production function (LPF), but not explicitly solved to get cosmological constraints. Let us notice that some of these new produced vortons, when created from the network, may be highly boosted. However, extrapolating the mean equation of state obtained for Nambu-Goto cosmic string loops, their momentum gets redshifted away and, on average, they behave as non-relativistic matter [99]. For this reason, the produced vortons are, as those originally considered in Ref. [149], potential dark matter and cosmic rays candidates [148, 356].

The total abundance of vortons today is expected to depend on $t_{\rm cur}$ as well as $t_{\rm ini}$, and hence on the underlying particle physics model. Determining their density parameter today, say $\Omega_{\rm tot}$, and using the current constraints on $\Omega_{\rm DM}h^2 \simeq 0.12$ will allow us to place constraints on the physics at work in the early Universe [25].

The formation and build-up of a population of vortons can be studied using a Boltzmann Eq. [125]. In this paper, we extend this work by applying the framework introduced in Chapter 6 to estimate quantitatively the density of vortons today. In Section 7.2 below, we review the necessary physics underlying vorton properties, then in Section 7.3, we evaluate the distribution of loops and vortons, in order to be able to calculate, in Section 7.4, the actual vorton distribution and, finally, their relic abundance in Section 7.5. We end this work by some concluding remarks.

7.2 Assumptions on the physics of vortons

As discussed in the introduction, we focus in this paper on cosmic strings that emerged at a temperature $T_{\rm ini}$ and later became current carrying at a temperature $T_{\rm cur}$.

For non-conducting strings, the boost invariance along the string implies that the string tension $\mathcal{T}$ and its energy per unit length μ are equal and, in order of magnitude, given by $\mu = \mathcal{T} = m_\phi^2$, where $m_\phi \propto |\langle\phi\rangle|$ is the mass of the string-forming Higgs field ϕ. As soon as a current flows along the string, the worldsheet Lorentz invariance is broken and so is the degeneracy between the stress-energy tensor eigenvalues μ and $\mathcal{T}$ [357, 358, 146], the tension being reduced and the energy per unit length increased by the current in such a way that

$$\mathcal{T} < m_\phi^2 < \mu. \tag{7.1}$$

The equation of state of current-carrying strings [359, 360, 355, 361, 362, 363] provides us with a saturation condition

$$\mu - \mathcal{T} \leq m_\sigma^2 \implies 0 < \frac{\mu - \mathcal{T}}{m_\phi^2} \leq \frac{m_\sigma^2}{m_\phi^2}\,, \tag{7.2}$$

according to which there exists a maximal spacelike current, above which it becomes energetically favoured for the condensate to flow out of the string. For a timelike current [360, 364], *i.e.* a charge, there exists a phase frequency threshold allowing, in principle, for arbitrary large values of the charge. However, vacuum polarization effectively reduces the integrated charge [365] so that saturation holds for all possible situations.

Denoting by λ the Compton wavelength of the current carrier ($\lambda \simeq m_\sigma^{-1}$), we define the parameter $\mathcal{R}$ by

$$\mathcal{R} \equiv \lambda\sqrt{\mu}\,. \tag{7.3}$$

Because $\mu \simeq m_\phi^2$, this quantity is approximately the ratio between the Compton wavelengths of the current carrier and the one of the string forming Higgs field, or, equivalently, $\mathcal{R} \simeq m_\phi/m_\sigma$ which we assume to be greater than unity. Given (7.2), it is safe to assume that, at least for $\mathcal{R} \gg 1$, the string tension and the energy per unit length are numerically so similar that distinguishing between them is irrelevant in the forthcoming cosmological context; we will thus denote them both by the notation μ.

A current-carrying closed string loop is characterized by two classically conserved integral quantum numbers N and Z, generally non-zero, which prevent the loop from disappearing completely [366]. As the loop loses energy through friction or radiation, it reaches a classically stable state called a *vorton* [147]. However, this state can decay through quantum tunnelling if the size of the loop is comparable with the Compton wavelength of the current carrier, λ. Hence, a vorton can only be stable if the current flowing along the string loop can prevent its collapse and if its proper length is much larger than λ.

Although the values of N and Z are initially randomly distributed, it is expected that the majority of closed loops are of nearly *chiral* [367, 151, 361, 368] type with almost identical quantum numbers [366]. Besides, the loop rotation velocity $v_{\rm vort} = \sqrt{\mathcal{T}/\mu} \simeq 1$ is roughly approximated by that of light and

$$|Z| \approx N. \tag{7.4}$$

In the rest of the paper, we focus on such nearly chiral vortons. Using of the central limit theorem, we estimate that the value of N at the formation of a loop is given by

$$N_\star = \sqrt{\frac{\ell_\star}{\lambda}}. \tag{7.5}$$

In (7.5) and in the rest of this paper, a subscript $\star$ on a quantity denotes the value it had at the time of formation of the corresponding loop. Since the charge N is conserved, we can, in what follows, omit the index $\star$ and simply write $N_\star = N$.

To estimate the size of the vortons ℓ_0, we first have to note that they have been shown to approach circularity [155]. Moreover, large vortons would also tend to circularize through either gravitational or gauge field radiation, on time scales much smaller than the Hubble time. It thus seems reasonable to consider mostly circular loops, therefore described by one parameter only, namely their radius $r_0 = \ell_0/2\pi$. Vortons are also characterized by their angular momentum quantum number $J = NZ \approx N^2$. Equivalently, it is also given in terms of the energy per unit length and tension by [148] $J = 2\pi r_0^2\sqrt{\mathcal{T}\mu}$, *i.e.* $J^2 = \mu\mathcal{T}\ell_0^4/(4\pi^2)$. Hence, for chiral vortons with $\mathcal{R} \gg 1$

$$\ell_0 = \sqrt{\frac{2\pi}{\mu}}N = \sqrt{\frac{2\pi\ell_\star}{\lambda\mu}} \approx \sqrt{\frac{\ell_\star}{\lambda\mu}}, \tag{7.6}$$

provided $\ell_0 > \lambda$. The length $\ell_0(N)$ being itself a function of the charge N, this is equivalent to imposing that $N > \mathcal{R}$. Therefore, $\mathcal{R}$ gives also the minimal possible charge of a vorton.

Following the same procedure as in Chapter 6, we model the physics of the vortons using an

arbitrary function $\mathcal{J}$ which describes how the current-carrying loops lose energy

$$\frac{\mathrm{d}\ell}{\mathrm{d}t} = -\Gamma G\mu \mathcal{J}(\ell, N), \tag{7.7}$$

$$\frac{\mathrm{d}N}{\mathrm{d}t} = 0, \tag{7.8}$$

in which $\Gamma \approx 50$ is a numerical factor for the emission of gravitational waves (GW) [118]. In order to model string networks with vortons, we impose the following properties on $\mathcal{J}$:

- $\mathcal{J}(\ell \gg \ell_0, N) \approx 1$, meaning that on scales much larger than the vorton size, the effect of the current is mostly negligible so that the dynamics of the current-carrying string is well approximated by that of a Nambu-Goto string; gravitational wave radiation is the dominant energy-loss mechanism, and we neglect other such mechanisms.
- $\mathcal{J}(\ell \ll \ell_0, N) \approx 0$ if $\ell_0 > \lambda$, meaning that the angular momentum carried by the current prevents the loop from shrinking, provided the loop is large enough to prevent quantum tunnelling.

We will consider a smooth form of $\mathcal{J}$, regulated by a parameter σ, in particular

$$\mathcal{J}(\ell, N) = \frac{1}{2}\left\{1 + \tanh\left[\frac{\ell - \ell_0(N)}{\sigma}\right]\right\}. \tag{7.9}$$

We call *vortons* all the loops with sizes $\ell \leq \ell_0(N)$ and $N > \mathcal{R}$. In the limit $\sigma \to 0$, $\mathcal{J}(\ell, N)$ reduces to $\Theta[\ell - \ell_0(N)]$, and the vortons accumulate around $\ell_0(N)$.

Let us mention that our approach, and results, differ from the vorton abundances derived in Refs. [151, 150]. These latter references were concerned with the extreme limit in which the current carrier condensation and string forming times are similar ($\mathcal{R} \simeq 1$ in our notation). For this reason, they were not concerned with the emission of gravitational waves. Indeed, in the limit $\mathcal{R} \to 1$, strong currents have been shown to dampen the loop oscillations and this allows for a population of vortons to be rapidly created (soon after the string forming phase transition). The vortons considered in Refs. [151, 150] are of this kind only. Let us recall that the current-carrier particles are trapped on the string worldsheet by means of a binding potential. As such, when there are strong currents, there is always the possibility that they tunnel out [360]. Such an instability could drastically affect the current, and hence the mechanism by which the vortons considered in Refs. [151, 150] are formed. On the contrary, the vortons we are considering here carry weak currents and our results are only valid in the domains for which $\mathcal{R} > 1$. The damping mechanism by which the weak current-carrying loops become vortons is the emission of gravitational waves (as in Ref. [149]).

Having recalled the basic properties of vortons and their dynamics, we now turn to the expected distributions of loops of various kinds, including those ending up as vortons.

7.3 Distribution of loops and vortons

In the following sections, we extend a statistical method originally based on the Boltzmann Eq. [96, 123, 122, 125] to study current carrying strings. Our aim is to find the number density of vortons, marginalized over their charge N, with length ℓ at time $t > t_{\mathrm{cur}}$, given some initial loop distribution at time t_{ini} and some assumptions about the loop production function (see Fig. 7.1).

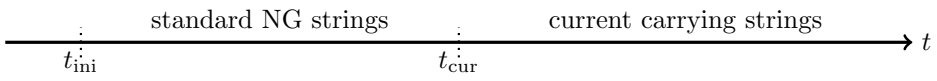

Figure 7.1: At time $t_{\rm ini}$ and temperature $T_{\rm ini}$ a network of strings forms with an initial distribution. At the later time $t_{\rm cur}$ the strings become current-carrying, and vortons can form. At all times, loop can be produced from long strings and larger loops with a given loop production function.

7.3.1 Continuity equation for the flow of loops in phase space

Let $\partial^2/\partial\mathcal{N}(\ell,t,N)^2\ /\ell N$ be the number density of loops with length ℓ and charge N at time t. In an expanding universe with scale factor $a(t)$, and taking into account the fact that loops lose length at a rate which depends on their length as expressed through Eq. (7.7), the continuity equation for the number density of loops is given by [96, 53]

$$\frac{\partial}{\partial t}\left[a^3\frac{\partial^2\mathcal{N}}{\partial\ell\partial N}\right]-\Gamma G\mu\frac{\partial}{\partial\ell}\left[a^3\mathcal{J}(\ell,N)\frac{\partial^2\mathcal{N}}{\partial\ell\partial N}\right]=a^3\mathcal{P}(\ell,t,N). \tag{7.10}$$

Here $\mathcal{P}(\ell,t,N)$ is the charged loop production function (LPF), namely the rate at which loops of length ℓ and charge N are formed at time t by being chopped off the string network, and we will specify it below. Note that this equation is exactly equivalent to that of Ref. [125], as we explain in details in Appendix 7.A.

The solution to Eq. (7.10) can be obtained in integral form following a similar procedure to that explained in Chapter 6, though one must take into account the new independent variable N. Upon multiplying by $\mathcal{J}(\ell,N)$, Eq. (7.10) becomes

$$\frac{\partial g}{\partial t}-\Gamma G\mu\mathcal{J}(\ell,N)\frac{\partial g}{\partial\ell}=a^3(t)\mathcal{J}(\ell,N)\mathcal{P}(\ell,t,N), \tag{7.11}$$

where we have defined

$$g(\ell,t,N)\equiv a^3\mathcal{J}(\ell,N)\frac{\partial^2\mathcal{N}}{\partial\ell\partial N}\,. \tag{7.12}$$

The change of variables $()\{\ell,t,N\}\to()\{\xi,\tau,N\}$, with

$$\xi\equiv\int\frac{\mathrm{d}\ell}{\mathcal{J}(\ell,N)}\qquad\text{and}\qquad\tau\equiv\Gamma G\mu t, \tag{7.13}$$

enables Eq. (7.11) to be written in the simpler form

$$\frac{\partial g(\xi,\tau,N)}{\partial\tau}-\frac{\partial g(\xi,\tau,N)}{\partial\xi}=\frac{a^3(\tau)}{\Gamma G\mu}\mathcal{J}(\xi,N)\mathcal{P}(\xi,\tau,N). \tag{7.14}$$

Upon using *light cone* type coordinates

$$u\equiv\frac{1}{2}(\tau-\xi)\qquad\text{and}\qquad v\equiv\frac{1}{2}(\tau+\xi), \tag{7.15}$$

it follows that Eq. (7.10) reduces to

$$\frac{\partial g(u,v,N)}{\partial u}=\frac{a^3(u,v)}{\Gamma G\mu}\mathcal{J}(u,v,N)\mathcal{P}(u,v,N), \tag{7.16}$$

which can be integrated between $t_{\rm cur}$ and t, or in terms of the variable $u = -v + \tau = -v + \Gamma G\mu t$, between $u_{\rm cur} = -v + \tau_{\rm cur} = -v + \Gamma G\mu t_{\rm cur}$ to u,

$$g(u, v, N) - g(-v + \Gamma G\mu t_{\rm cur}, v, N) = \int_{-v+\Gamma G\mu t_{\rm cur}}^{u} \frac{a^3(u', v)}{\Gamma G\mu} \mathcal{J}(u', v, N)\mathcal{P}(u', v, N)\ {\rm d}u' \,, \qquad (7.17)$$

the integral in Eq. (7.17) being calculated with v constant. Rewritten in terms of $\partial^2\mathcal{N}/\partial\ell\partial N$ using Eq. (7.12) finally gives

$$\begin{aligned} a^3(t)\mathcal{J}(\ell, N)\frac{\partial^2\mathcal{N}}{\partial\ell\partial N} &= a^3(t_{\rm cur})\mathcal{J}(\ell_{\rm cur}, N)\frac{\partial^2\mathcal{N}}{\partial\ell\partial N}(\ell_{\rm cur}, t_{\rm cur}, N) \\ &\quad + \int_{-v+\Gamma G\mu t_{\rm cur}}^{u} \frac{a^3(u', v)}{\Gamma G\mu} \mathcal{J}(u', v, N)\mathcal{P}(u', v, N)\ {\rm d}u' \,. \end{aligned} \qquad (7.18)$$

Here $\ell_{\rm cur}$ is the size of the loops at condensation and is a function $\ell_{\rm cur}(\ell, t, N)$. It is found using the variable $v = \tau + \xi$ of Eq. (7.15) which is a constant along the flow, namely $\ell_{\rm cur}$ is a solution of

$$\xi(\ell_{\rm cur}, N) = \xi(\ell, N) + \Gamma G\mu(t - t_{\rm cur}). \qquad (7.19)$$

The solution of the continuity Eq. (7.10) is therefore given by Eq. (7.18). On the right-hand-side, we recognize two terms. The first are the loops left over from the pre-existing loop distribution at the time of condensation, $t = t_{\rm cur}$. The second term contains those loops which are produced from the string network at time $t > t_{\rm cur}$. As we will see in more detail in Section 7.4, each of these distributions contain three kinds of loops [149]:

1. *Doomed loops*: these loops have an initial size which is too small to support a current, and hence they decay through gravitational radiation never becoming vortons. They are characterized by quantum numbers $N < \mathcal{R}$.

2. *Proto-vortons*: these are loops which are initially large enough to be stabilized by a current (thus $N > \mathcal{R}$), but have not yet reached the vorton size ℓ_0.

3. *Vortons*: these are all those proto-vortons which have decayed by gravitational radiation to become vortons. Hence, vortons have $N > \mathcal{R}$, and in the limit $\sigma \to 0$, they accumulate with length $\ell_0(N)$.

Our aim in the following is to extract these different distributions. Each will contain two contributions: those formed from the initial distribution *i.e.* coming from the first term in Eq. (7.18), and those produced at later times from being chopped off the string network, *i.e.* coming from the second term in Eq. (7.18). In the case of vortons, we call these two families "relaxed vortons" and "produced vortons", respectively. In Section 7.5, we will use these to determine their relic density and put constraints on $G\mu$ and $\mathcal{R}$.

7.3.2 The loop distribution at condensation

A first step is to specify the loop distribution at $t_{\rm cur}$. The strings are assumed to form at a temperature $T_{\rm ini}$ corresponding to a time $t_{\rm ini}$ in the early Universe. At all times $t_{\rm ini} < t < t_{\rm cur}$, that is before condensation, they behave as standard Nambu-Goto strings, see Fig. 7.1. Hence, the

loop distribution is the canonical one, *i.e.* contains a population of loops formed at $t_{\rm ini}$ and another population of scaling loops created from the long strings and larger loops [52].

The main simplifying assumption of our work is to assume a Dirac distribution for the loop production function, namely

$$\mathcal{P}(\ell,t) = Ct^{-5}\delta\!\left(\frac{\ell}{t}-\alpha\right), \tag{7.20}$$

with $C=1$ and $\alpha = 0.1$ as to match the Kibble, or one scale, model [61]. Hence, all the produced loops that are chopped off the network are assumed to be of the same size, given by the fraction α of t, which is, up to a constant of order unity, the horizon size. This assumption allows us to analytically solve for the produced vorton distribution later on. However, we stress that more realistic loop production functions, such as the Polchinski-Rocha one [137, 138, 122, 123, 56], produce smaller loops while matching in amplitude with the Dirac LPF for $\ell/t = \alpha$ [99, 52]. Therefore, when gravitational wave emission from loops is accounted for (which is the case here), the resulting scaling loop distributions end up being quite similar over the length scales $\ell > \gamma_{\rm d} t$. They may, however, differ significantly on smaller length scales, namely for $\gamma_{\rm c} t < \ell < \gamma_{\rm d} t$, where $\gamma_{\rm c}$ stands for the length scale at which gravitational backreaction damps the LPF [123]. For Nambu-Goto strings, this length scale is expected to verify $\gamma_{\rm c} \ll \gamma_{\rm d}$ [309, 232]. Therefore, our results derived here from a Dirac LPF should provide a robust lower bound for all the others LPF, and may also be directly applicable to the Polchinski-Rocha ones but only in the limit in which $\gamma_{\rm c} \simeq \gamma_{\rm d}$.

Under these assumptions, the resulting distribution of cosmic string loops at time $t_{\rm cur}$ is given by [52]

$$\begin{aligned}\frac{{\rm d}\mathcal{N}}{{\rm d}\ell}(\ell,t_{\rm cur}) = {} & C\,t_{\rm cur}^{-3/2}\frac{(\alpha+\Gamma G\mu)^{3/2}}{(\ell+\Gamma G\mu t_{\rm cur})^{5/2}}\Theta(\alpha t_{\rm cur}-\ell)\Theta[\ell+\Gamma G\mu t_{\rm cur}-t_{\rm ini}(\alpha+\Gamma G\mu)] \\ & + C_{\rm ini}\left(\frac{t_{\rm ini}}{\ell}\right)^{5/2} t_{\rm ini}^{-4}\Theta[(\alpha+\Gamma G\mu)t_{\rm ini}-\ell-\Gamma G\mu t_{\rm cur}].\end{aligned} \tag{7.21}$$

The first term is the scaling loop distribution associated with the Dirac LPF of Eq. (7.20). The second term is the initial distribution of loops at $t_{\rm ini}$ associated with the random walk model of Vachaspati-Vilenkin [301]. Assuming the random walk to be correlated over a length scale $\ell_{\rm corr}$, one has [301]

$$C_{\rm ini} \simeq 0.4\left(\frac{t_{\rm ini}}{\ell_{\rm corr}}\right)^{3/2}. \tag{7.22}$$

A natural value for $\ell_{\rm corr}$ is obtained by assuming that it is given by the thermal process forming the strings, namely $\ell_{\rm corr} = 1/T_{\rm ini}$. We will, however, discuss various other possible choices in Section 7.5.

At the time of condensation $t_{\rm cur}$, the loops acquire quantum numbers N, and we assume again a Dirac distribution for the generated charge:

$$\frac{\partial^2\mathcal{N}}{\partial\ell\partial N} = \frac{{\rm d}\mathcal{N}}{{\rm d}\ell}\,\delta\!\left(N-\sqrt{\frac{\ell}{\lambda}}\right). \tag{7.23}$$

This is in agreement with Refs. [149, 125] and motivated by the fact that, if a thermal process of temperature $T_{\rm cur} = 1/\lambda$ is at work during current condensation, the conserved number N laid down along the string should be given by a stochastic process of root mean squared value close to $\sqrt{\ell/\lambda}$.

String formation at $t_{\rm ini}$ and current condensation at $t_{\rm cur}$ are assumed to occur in the radiation era. In the following we will use as model parameters $G\mu$ and $\mathcal{R}$. The current condensation redshift can be determined using entropy conservation:

$$1+z_{\rm cur}=\left(\frac{q_{\rm cur}}{q_0}\right)^{1/3}\frac{T_{\rm cur}}{T_{\rm cmb}}\,, \tag{7.24}$$

where $q_{\rm cur}=q(z_{\rm cur})$, and $q_0=q(z=0)$, denotes the number of entropic relativistic degrees of freedom at the time of current condensation, and today, respectively. In the following, we consider $T_{\rm cur}$ to be given by

$$T_{\rm cur}=\frac{1}{\lambda}=\frac{\sqrt{\mu}}{\mathcal{R}}\,, \tag{7.25}$$

and we take $T_{\rm cmb}=2.725\,{\rm K}$. In order to solve Eq. (7.24) for $z_{\rm cur}$, we have used the tabulated values of $q(z)$ associated with the thermal history in the Standard Model and computed in Ref. [369]. Still, from entropy conservation, the redshift associated with the formation of the string network (at the temperature $T_{\rm ini}$) is given by

$$1+z_{\rm ini}=\left(\frac{q_{\rm ini}}{q_0}\right)^{1/3}\frac{T_{\rm ini}}{T_{\rm cmb}}\,, \tag{7.26}$$

where

$$T_{\rm ini}=\sqrt{\mu}=\mathcal{R}T_{\rm cur}\,. \tag{7.27}$$

7.4 Cosmological distribution of vortons

From Eq. (7.18), we can determine the distribution $\frac{{\rm d}\mathcal{N}}{{\rm d}\ell}$ of relaxed vortons and produced vortons. Both of these being stable, they will contribute to the relic content of the universe.

Regarding the distributions of doomed loops and proto-vortons, these could be important for some observational effects of strings, for instance the stochastic gravitational wave background, but they cannot contribute significantly to the dark matter content of the Universe [123]. Their distributions are determined from Eq. (7.18) through

$$\left.\frac{{\rm d}\mathcal{N}}{{\rm d}\ell}\right|_{\rm doom}(\ell,t) \equiv \int {\rm d}N\,\frac{\partial^2\mathcal{N}}{\partial\ell\partial N}\Theta(\mathcal{R}-N), \tag{7.28}$$

$$\left.\frac{{\rm d}\mathcal{N}}{{\rm d}\ell}\right|_{\rm proto}(\ell,t) \equiv \int {\rm d}N\,\Theta(N-\mathcal{R})\frac{\partial^2\mathcal{N}}{\partial\ell\partial N}\Theta[\ell-\ell_0(N)], \tag{7.29}$$

and are given in Appendix 7.B.

In order to determine the vorton distribution, we recall that a vorton is a loop with topological number $N>\mathcal{R}$ and size $\ell\leq\ell_0(N)$ if $\sigma>0$. In the limit $\sigma\to 0$, the charge N of the vorton is proportional to its length $\ell_0(N)=N/\sqrt{\mu}$. In order to deal correctly with the singular behaviour in the limit $\sigma\to 0$, we firstly express the vorton distribution in terms of the charge N, namely calculate $\frac{{\rm d}\mathcal{N}}{{\rm d}N}$, then take the limit $\sigma\to 0$, and finally determine $\frac{{\rm d}\mathcal{N}}{{\rm d}\ell}$ through a simple change of variables since $\ell=\ell_0=N/\sqrt{\mu}$.

Our starting point is therefore

$$\left.\frac{{\rm d}\mathcal{N}}{{\rm d}N}\right|_{\rm vort}(t,N)\equiv\Theta(N-\mathcal{R})\int{\rm d}\ell\,\frac{\partial^2\mathcal{N}}{\partial\ell\partial N}\Theta[\ell_0(N)-\ell], \tag{7.30}$$

which we calculate for both relaxed and produced vortons below.

7.4.1 Relaxation term

The distribution of the vortons coming from the initial conditions at the condensation is determined from (7.30), substituting the first term of Eq. (7.18), together with the initial distribution of loops in Eq. (7.23). This gives

$$\left.\frac{\mathrm{d}\mathcal{N}}{\mathrm{d}N}\right|_{\rm vort,rel} = \Theta(N-\mathcal{R})\int_{-\infty}^{\ell_0(N)}\left[\frac{a(t_{\rm cur})}{a(t)}\right]^3\frac{\mathcal{J}(\ell_{\rm cur},N)}{\mathcal{J}(\ell,N)}\frac{\mathrm{d}\mathcal{N}}{\mathrm{d}\ell}(\ell_{\rm cur},t_{\rm cur})\delta\!\left(N-\sqrt{\frac{\ell_{\rm cur}}{\lambda}}\right)\mathrm{d}\ell\,, \quad (7.31)$$

in which $\ell_{\rm cur}(\ell,t,N)$, given in Eq. (7.19), is the size of the loop at condensation. In order to integrate over the Dirac delta distribution, we change integration variable from ℓ to

$$y = N-\sqrt{\frac{\ell_{\rm cur}}{\lambda}}\,, \quad (7.32)$$

with corresponding Jacobian

$$\frac{\mathrm{d}y}{\mathrm{d}\ell} = -\frac{1}{2\sqrt{\lambda\ell_{\rm cur}}}\left.\frac{\partial\ell_{\rm cur}}{\partial\ell}\right|_{t,N} = -\frac{1}{2\sqrt{\lambda\ell_{\rm cur}}}\frac{\mathcal{J}(\ell_{\rm cur},N)}{\mathcal{J}(\ell,N)}\,, \quad (7.33)$$

where we have used Eq. (7.19). As a result, the $\mathcal{J}$ terms cancel, and we obtain

$$\left.\frac{\mathrm{d}\mathcal{N}}{\mathrm{d}N}\right|_{\rm vort,rel} = 2\lambda N\Theta(N-\mathcal{R})\left[\frac{a(t_{\rm cur})}{a(t)}\right]^3\frac{\mathrm{d}\mathcal{N}}{\mathrm{d}\ell}\big(\lambda N^2,t_{\rm cur}\big)\Theta()\{\ell_{\rm cur}[\ell_0(N),t,N]-\lambda N^2\}. \quad (7.34)$$

In the limit $\sigma\to 0$, the size of a vorton is $\ell=\ell_0(N)=N/\sqrt{\mu}$, and Eq. (7.19) simplifies to

$$\ell_{\rm cur}[\ell_0(N),t,N] = \Gamma G\mu(t-t_{\rm cur})+\ell_0(N). \quad (7.35)$$

Finally, using $\mathrm{d}\mathcal{N}/\mathrm{d}\ell = \sqrt{\mu}\ \mathrm{d}\mathcal{N}/\mathrm{d}N$, the vorton distribution generated from the initial loop distribution at $t_{\rm cur}$ is given by

$$\left.\frac{\mathrm{d}\mathcal{N}}{\mathrm{d}\ell}\right|_{\rm vort,rel}(\ell,t) = 2\lambda\mu\ell\left[\frac{a^3(t_{\rm cur})}{a^3(t)}\right]\frac{\mathrm{d}\mathcal{N}}{\mathrm{d}\ell}\big(\lambda\mu\ell^2,t_{\rm cur}\big)\Theta\big[\Gamma G\mu(t-t_{\rm cur})+\ell-\lambda\mu\ell^2\big]\Theta(\ell-\lambda). \quad (7.36)$$

This distribution scales like matter (modulo the time-dependence in the Θ-functions). This term was already derived in Ref. [125], and our results agree though the approach is different.

We now turn to the vorton population sourced by loops chopped off from the network, namely from the second term in Eq. (7.18).

7.4.2 Production term

After the condensation, all the strings and loops carry a current, which implies that all new loops formed from the network will inherit the charge density carried by their mother strings. As a result, the charged loop production function is still given by Eq. (7.20), modulated by the charge density distribution, *i.e.*

$$\mathcal{P}(\ell,t,N) = Ct^{-5}\delta\!\left(\frac{\ell}{t}-\alpha\right)\delta\!\left(N-\sqrt{\frac{\ell}{\lambda}}\right)\Theta(t-t_{\rm cur}). \quad (7.37)$$

Substituting into the last term of Eq. (7.18) (see Chapter 6) gives the number density

$$\frac{\partial^2\mathcal{N}}{\partial\ell\partial N}=\frac{C}{\mathcal{J}(\ell,N)}\left[\frac{a(t_\star)}{a(t)}\right]^3 t_\star^{-4}\frac{\mathcal{J}(\alpha t_\star,N)}{\alpha+\Gamma G\mu\mathcal{J}(\alpha t_\star,N)}\delta\!\left(N-\sqrt{\frac{\alpha t_\star}{\lambda}}\right)\Theta(t_\star-t_{\rm cur}). \tag{7.38}$$

where $t_\star(\ell,t,N)$ is the time of loop formation, obtained by solving

$$\Gamma G\mu t_\star+\xi(\alpha t_\star,N)=\Gamma G\mu t+\xi(\ell,N), \tag{7.39}$$

which again follows from the fact that $2v=\Gamma G\mu t+\xi(\ell,N)$ is a conserved quantity during the lifetime of the loops. The definition in Eq. (7.30) then gives

$$\begin{aligned}\left.\frac{\mathrm{d}\mathcal{N}}{\mathrm{d}N}\right|_{\rm vort,prod}&=\Theta(N-\lambda\sqrt{\mu})\\&\times\int_{-\infty}^{\ell_0(N)}\mathrm{d}\ell\,\frac{C}{\mathcal{J}(\ell,N)}\left[\frac{a(t_\star)}{a(t)}\right]^3 t_\star^{-4}\frac{\mathcal{J}(\alpha t_\star,N)}{\alpha+\Gamma G\mu\mathcal{J}(\alpha t_\star,N)}\delta\!\left(N-\sqrt{\frac{\alpha t_\star}{\lambda}}\right)\Theta(t_\star-t_{\rm cur}).\end{aligned} \tag{7.40}$$

We again integrate the Dirac delta distribution by means of the change of variable

$$\tilde{y}=N-\sqrt{\frac{\alpha t_\star}{\lambda}}\,, \tag{7.41}$$

with corresponding Jacobian

$$\frac{\mathrm{d}\tilde{y}}{\mathrm{d}\ell}=-\sqrt{\frac{\alpha}{\lambda}}\frac{1}{2\sqrt{t_\star}}\left.\frac{\partial t_\star}{\partial\ell}\right|_{t,N}=-\sqrt{\frac{\alpha}{\lambda}}\frac{1}{2\sqrt{t_\star}}\frac{\mathcal{J}(\alpha t_\star,N)}{\mathcal{J}(\ell,N)[\alpha+\Gamma G\mu\mathcal{J}(\alpha t_\star)]}\,. \tag{7.42}$$

Thus Eq. (7.40) gives

$$\begin{aligned}\left.\frac{\mathrm{d}\mathcal{N}}{\mathrm{d}N}\right|_{\rm vort,prod}&=\Theta(N-\lambda\sqrt{\mu})\\&\times\frac{2\lambda N}{\alpha}C\left[\frac{a\big(\lambda N^2/\alpha\big)}{a(t)}\right]^3\left(\frac{\lambda N^2}{\alpha}\right)^{-4}\Theta(\lambda N^2-\alpha t_{\rm cur})\Theta\left[t_\star(\ell_0(N),t,N)-\frac{\lambda N^2}{\alpha}\right].\end{aligned} \tag{7.43}$$

In the limit $\sigma\to 0$, Eq. (7.39) reduces to

$$(\alpha+\Gamma G\mu)t_\star=\ell_0(N)+\Gamma G\mu t, \tag{7.44}$$

and, using the fact that vortons have size $\ell=\ell_0(N)=N/\sqrt{\mu}$, it follows that the produced vorton distribution is given by

$$\begin{aligned}\left.\frac{\mathrm{d}\mathcal{N}}{\mathrm{d}\ell}\right|_{\rm vort,prod}&=\frac{2\lambda\mu\ell}{\alpha}C\left[\frac{a\big(\lambda\mu\ell^2/\alpha\big)}{a(t)}\right]^3\\&\times\left(\frac{\lambda\mu\ell^2}{\alpha}\right)^{-4}\Theta(\lambda\mu\ell^2-\alpha t_{\rm cur})\Theta\!\left(\frac{\Gamma G\mu t+\ell}{\alpha+\Gamma G\mu}-\frac{\lambda\mu\ell^2}{\alpha}\right)\Theta(\ell-\lambda),\end{aligned} \tag{7.45}$$

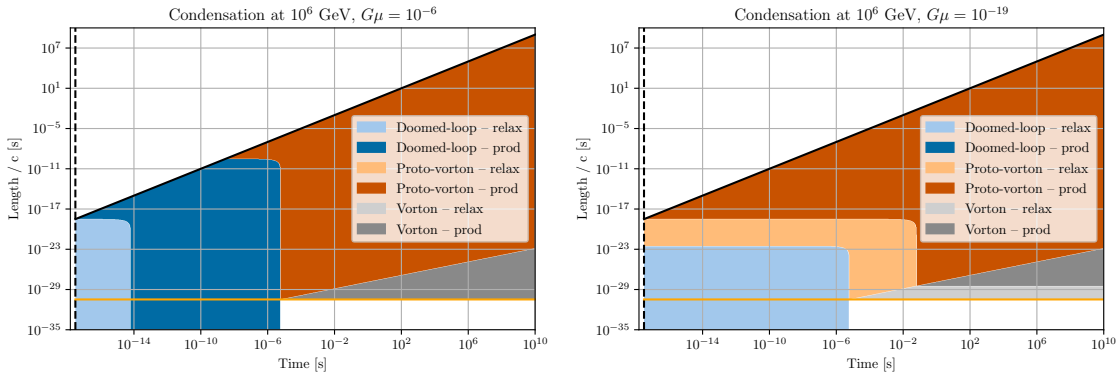

Figure 7.2: Diagram (ℓ, t) for the different types loops/vortons. The left panel is for $G\mu = 10^{-16}$ and the right panel for $G\mu = 10^{-19}$. The dark-dashed vertical line is the time of condensation, when strings become superconducting. The diagonal dark line represents $\ell = \alpha t$ (with $\alpha = 0.1$) the size at which loops are produced. The orange horizontal line shows the value of λ.

which again scales as matter.

In Fig. 7.2 we show the different regions of (ℓ, t)-space which are populated by either relaxed or produced vortons, and also proto-vortons and doomed loops (see Appendix 7.B). Essentially, for vortons, these are fixed by the Θ-functions in Eq. (7.45) and Eq. (7.36). In particular, we observe that for

$$G\mu > \frac{\alpha G t_{\rm cur}}{\lambda^3} \iff \mathcal{R} > \frac{\alpha t_{\rm cur}}{\lambda}\,, \tag{7.46}$$

there are no relaxed vortons produced, explaining the differences between the two panels of Fig. 7.2.

A consequence of the different Θ-functions in Eq. (7.45) is that when evaluating $t_\star$, the formation time of loops, it turns out that all vortons were produced initially during radiation era. If one imposes that the loop production function of Eq. (7.37) is only valid for $t < t_{\rm eq}$, one finds that Eq. (7.45) is multiplied by the Heaviside function $\Theta(\alpha t_{\rm eq} - \lambda\mu\ell^2)$.

7.5 Relic abundance

In the previous sections we have established that the number density of vortons produced during the radiation era contains two components, namely the relaxed vortons with length distribution given in Eq. (7.36), and the produced vortons with length distribution given in Eq. (7.45).

7.5.1 Analytic estimates

In order to estimate the density parameter associated with the relic vortons today, we can use the results of the previous section evaluated at present time $t = t_0$. The density parameter for each population is defined by

$$\Omega \equiv \frac{8\pi G\mu}{3H_0^2}\int_0^\infty \ell \frac{{\rm d}\mathcal{N}}{{\rm d}\ell}\,{\rm d}\ell\,. \tag{7.47}$$

Starting with the contribution of the relaxed vortons, from Eq. (7.36), estimated today, the dimensionless loop distribution reads

$$t_0{}^4 \left.\frac{\mathrm{d}\mathcal{N}}{\mathrm{d}\ell}\right|_{\rm vort,rel} = \frac{2\mathcal{R}^2}{(1+z_{\rm cur})^3}\frac{\ell}{\lambda}\left(\frac{t_0}{t_{\rm cur}}\right)^4 t_{\rm cur}^4 \frac{\mathrm{d}\mathcal{N}}{\mathrm{d}\ell}\Theta(\ell-\lambda)\,\Theta[\ell_{\rm T}(t_0)-\ell]\,, \tag{7.48}$$

where we have introduced the typical length [125]

$$\ell_{\rm T}(t_0) \equiv \frac{\lambda}{2\mathcal{R}^2}\left[1+\sqrt{1+4\mathcal{R}^2\frac{\gamma_{\rm d}(t_0-t_{\rm cur})}{\lambda}}\right], \tag{7.49}$$

solution of the quadratic equation appearing in the argument of the first Heaviside function in Eq. (7.36). As explicit in the above expression, this is the maximal possible length of a relaxed vorton today, larger loops belonging to the (relaxed) proto-vorton distribution, see also Fig. 7.2. In this expression, the loop distribution at $t_{\rm cur}$ is given by Eq. (7.21). The vorton distribution of Eq. (7.48) obtained by taking, in Eq. (7.21), $C=0$ and $C_{\rm ini}$ given by Eq. (7.22) is the one originally considered and derived in Ref. [149]. We see that by considering $C\neq 0$, *i.e.* by including all the Nambu-Goto loops produced between $t_{\rm ini}$ and $t_{\rm cur}$, we are adding a new population, not considered so far, to the relaxed vorton abundance.

It is actually possible to derive an analytical expression for the density parameter of these new relaxed vortons only. Let us consider a loop distribution at $t_{\rm cur}$ given by Eq. (7.21) with $C\neq 0$ and $C_{\rm ini}=0$. In other words, we take the extreme situation in which at $t=t_{\rm ini}$, there is no loop at all. All loops present at $t_{\rm cur}$ are therefore created from the network between $t_{\rm ini}$ and $t_{\rm cur}$. Plugging Eq. (7.48) into Eq. (7.47), one gets after some algebra

$$\begin{aligned}\Omega_{\rm rel}^{\rm min} = {}& \frac{2\mathcal{R}^2 C}{9(1+z_{\rm cur})^3(H_0 t_{\rm cur})^2}\frac{(\alpha+\gamma_{\rm d})^{3/2}}{(M_{\rm pl}t_{\rm cur})^2\gamma_{\rm d}} \\ & \times ()\{\frac{x_{\rm max}^3}{\left[\gamma_{\rm d}+\left(\lambda x_{\rm max}/\bar{\ell}_{\rm cur}\right)^2\right]^{3/2}} - \frac{x_{\rm min}^3}{\left[\gamma_{\rm d}+\left(\lambda x_{\rm min}/\bar{\ell}_{\rm cur}\right)^2\right]^{3/2}}\},\end{aligned} \tag{7.50}$$

with the dimensionless numbers

$$x_{\rm max} \equiv \min\left(\frac{\ell_{\rm T}}{\lambda},\frac{\bar{\ell}_{\rm cur}}{\lambda}\right), \qquad x_{\rm min} = \max\left[1,\frac{1}{\mathcal{R}}\sqrt{\frac{\bar{\ell}_{\rm ini}(t_{\rm cur})}{\lambda}}\right], \tag{7.51}$$

and where we have introduced the new length scales

$$\bar{\ell}_{\rm cur} \equiv \frac{\sqrt{\alpha\lambda t_{\rm cur}}}{\mathcal{R}}\,, \qquad \bar{\ell}_{\rm ini}(t_{\rm cur}) \equiv t_{\rm ini}(\alpha+\gamma_{\rm d}) - \gamma_{\rm d}t_{\rm cur}\,. \tag{7.52}$$

From the fact that we started with no loop at all at the string forming time $t_{\rm ini}$, Eq. (7.50) is necessarily a robust lower bound for the relaxed vorton abundance today. These objects will be referred to as the "irreducible relaxed vortons".

Similarly, the produced vorton density distribution today is given by Eq. (7.45) evaluated at $t=t_0$. The dimensionless distribution today reads

$$t_0{}^4 \left.\frac{\mathrm{d}\mathcal{N}}{\mathrm{d}\ell}\right|_{\rm vort,prod} = \frac{2C}{\left[1+z(t_\ell)\right]^3}\left(\frac{\alpha}{\mathcal{R}}\frac{\lambda}{t_0}\right)^3\left(\frac{t_0}{\ell}\right)^7\Theta\big(\ell-\bar{\ell}_{\rm cur}\big)\,\Theta\big[\bar{\ell}_{\rm T}(t_0)-\ell\big]\,\Theta(\ell-\lambda)\,, \tag{7.53}$$

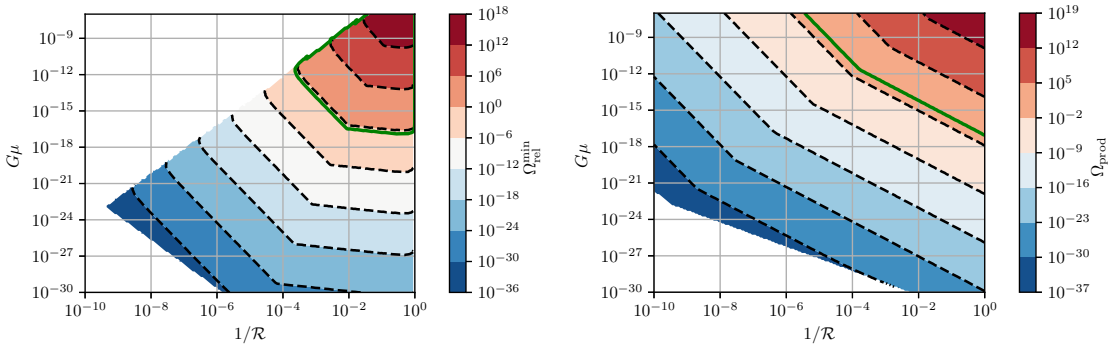

Figure 7.3: The left panel shows the density parameter $\Omega_{\rm rel}^{\rm min}$ (today) from the population of *irreducible relaxed* vortons, *i.e.* we have assumed that there is no loop at the string forming time ($C_{\rm ini} = 0$). The right panel shows the density parameter $\Omega_{\rm prod}$ of *produced* vortons derived analytically in Eq. (7.58). The thick green line shows the value $\Omega_{\rm DM} = 0.3$, typical of the current dark matter density parameter. The white patches on these figures correspond to regions of the parameter space where no vortons are present: all loops there are either doomed or proto-vortons. Abundances of these two populations of vortons have not been derived before and constitute an irreducible contribution.

where we have made explicit the new length scale

$$\bar{\ell}_{\rm T}(t_0) \equiv \frac{\lambda}{2\mathcal{R}^2}\frac{\alpha}{\alpha+\gamma_{\rm d}}\left[1+\sqrt{1+4\mathcal{R}^2\frac{\alpha+\gamma_{\rm d}}{\alpha}\frac{\gamma_{\rm d}t_0}{\lambda}}\right], \tag{7.54}$$

which is the analogue of $\ell_{\rm T}(t_0)$ but for the produced vortons, see Eq. (7.49). This is the maximal possible size of a produced vorton today. Let us notice the appearance of the redshift $z(t_\ell)$, evaluated at some (past) ℓ-dependent cosmic time

$$t_\ell \equiv \frac{\mathcal{R}^2}{\alpha}\frac{\ell^2}{\lambda}\,. \tag{7.55}$$

Plugging Eq. (7.53) into (7.47), one gets

$$\Omega_{\rm prod} = \frac{16\pi G\mu}{3(H_0t_0)^2}C\left(\frac{\alpha}{\mathcal{R}^2}\right)^3\left(\frac{t_0}{\lambda}\right)^2\int_{y_{\rm min}}^{y_{\rm max}}\frac{[1+z(t_{\lambda t})]^3}{y^6}\,{\rm d}y\,, \tag{7.56}$$

with

$$y_{\rm min} \equiv \max\left(1,\frac{\bar{\ell}_{\rm cur}}{\lambda}\right), \qquad y_{\rm max} \equiv \frac{\bar{\ell}_{\rm T}(t_0)}{\lambda}\,. \tag{7.57}$$

Equation (7.56) shows that the knowledge of the whole thermal history of the Universe through $z(t_{\lambda t})$ is a priori required to accurately determine $\Omega_{\rm prod}$. This is expected as the "time of flight" of a proto-vorton between its creation and stabilization as a vorton depends on its size at formation. Therefore, at any given time, the population of produced vortons keeps a memory of the past history of the Universe.

The integral (7.56) can be analytically performed with some simplifying assumptions. One can consider an exact power-law expansion for the radiation and matter era together with an instantaneous transition at $t_{\rm eq}$. Taking $a(t) \propto t^{\nu}$, with $\nu = \nu_{\rm rad} \equiv 1/2$ and $\nu = \nu_{\rm mat} \equiv 2/3$ in the radiation and matter era, respectively, one gets

$$\begin{aligned}\Omega_{\rm prod} = {} & \frac{16\pi G\mu}{3(H_0 t_0)^2} C \Big(\frac{\alpha}{\mathcal{R}^2}\Big)^3 \left(\frac{t_0}{\lambda}\right)^{2-3\nu_{\rm mat}} \\ & \times \left\{ \left(\frac{\mathcal{R}^2}{\alpha}\right)^{3\nu_{\rm rad}} \frac{[\min(y_{\rm max}, y_{\rm eq})]^{6\nu_{\rm rad}-5} - y_{\rm min}^{6\nu_{\rm rad}-5}}{5-6\nu_{\rm rad}} \left(\frac{t_{\rm eq}}{\lambda}\right)^{3(\nu_{\rm mat}-\nu_{\rm rad})} \right. \\ & \left. + \left(\frac{\mathcal{R}^2}{\alpha}\right)^{3\nu_{\rm mat}} \frac{y_{\rm max}^{6\nu_{\rm mat}-5} - [\max(1, y_{\rm eq})]^{6\nu_{\rm mat}-5}}{5-6\nu_{\rm mat}} \right\},\end{aligned} \tag{7.58}$$

where

$$y_{\rm eq} \equiv \frac{\bar{\ell}_{\rm eq}}{\lambda}\,, \quad \text{with} \quad \bar{\ell}_{\rm eq} \equiv \frac{\sqrt{\alpha\lambda t_{\rm eq}}}{\mathcal{R}}\,. \tag{7.59}$$

Unsurprisingly, the particular cosmic time $t_{\rm eq}$ imprints a new length scale $\bar{\ell}_{\rm eq}$ in the distribution.

We have represented in Fig. 7.3 both $\Omega_{\rm rel}^{\rm min}$ and $\Omega_{\rm prod}$ as a function of $(G\mu, 1/\mathcal{R})$ given by the Eqs. (7.50) and (7.58). The thick green line shows the contour matching the value $\Omega_{\rm DM} = 0.3$. For the irreducible relaxed vortons, the only additional parameter entering Eq. (7.50) is $z_{\rm cur}$, which has been determined using $a(t) \propto t^{\nu_{\rm rad}}$ for the radiation era together with the thermal initial conditions of Eq. (7.24) (using $q_{\rm cur} = 104$). As already discussed, these two populations of vortons are an unavoidable consequence of the loop production associated with a scaling cosmic string network and have not been considered before. For instance, taking $\mathcal{R} \lesssim 10^2$, these figures show that all values of $G\mu$ greater than 10^{-15} are overclosing the Universe with vortons, even though no loops at all are present at $t_{\rm ini}$ when the strings are formed. Although not very visible on the figure, there is a small region around $\mathcal{R} = 1$ in which $\Omega_{\rm rel}^{\rm min} = 0$. Indeed, if $t_{\rm ini} = t_{\rm cur}$ and $C_{\rm ini} = 0$, there is no time at all to produce loops before the current appears. However, this region is actually ruled out as filled with vortons produced afterwards (see right panel of Fig. 7.3).

Returning to Eqs. (7.48) and (7.21), the most general situation for the relaxed vortons is to start with a mixture of loops created at the string forming time and loops created from the network between $t_{\rm ini}$ and $t_{\rm cur}$, *i.e.* one has both $C \neq 0$ and $C_{\rm ini} \neq 0$. Moreover, from Eq. (7.56), the accurate expression for $\Omega_{\rm prod}$ requires specifying the whole thermal history of the Universe and the integral has to be performed numerically. In the next section, we numerically integrate both $\Omega_{\rm rel}$ and $\Omega_{\rm prod}$ and discuss their sensitivity to the initial conditions.

7.5.2 Numerical integration and initial conditions

Compared to the previous section, we now numerically integrate both $\Omega_{\rm rel}$ and $\Omega_{\rm prod}$ starting from the general initial loop distribution described in Section 7.3.2. Thermal initial conditions are taken assuming that the number of relativistic degrees of freedom is given by the Standard Model as derived in Ref. [369].

Figures 7.4 and 7.5 show the density parameters today of all the relaxed vortons, the produced vortons and the sum of the two contributions when the string forming network at $t = t_{\rm ini}$ is given by the Vachaspati-Vilenkin initial condition (see Section 7.3.2). This implies that the typical size of loops at $t_{\rm ini}$ is given by thermal fluctuations of the Higgs field and $\ell_{\rm corr} = 1/\sqrt{\mu}$.

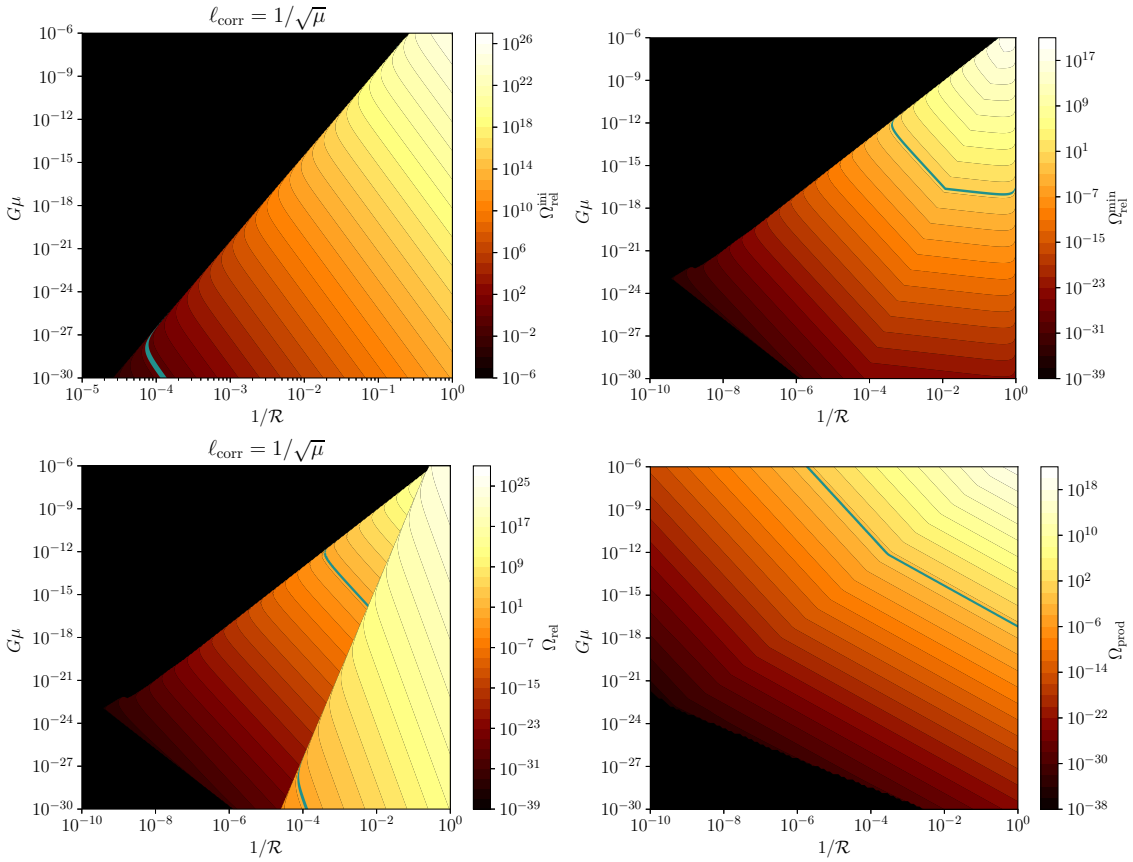

Figure 7.4: The upper left-hand panel shows the density parameter of relaxed vortons coming only from loops present at the string-forming phase transition, when starting from a Vachaspati-Vilenkin distribution at $t = t_{\rm ini}$. This is the population derived in Ref. [149], that we recover by setting $C = 0$ in our equations. The upper right-hand panel shows the numerically evaluated density parameter of the irreducible relaxed vortons $\Omega_{\rm rel}^{\rm min}$ (to be compared to our analytic estimation in the left panel of Fig. 7.3). The lower left-hand panel shows the density parameter $\Omega_{\rm rel}$ (today) from the population of all *relaxed* vortons (the sum of the upper left and right panels). Thermal history effects are visible on the upper boundary towards the minimum possible values of $1/\mathcal{R}$ and $G\mu$. The lower right-hand panel shows the density parameter $\Omega_{\rm prod}$ today of *produced* vortons derived numerically, and is indistinguishable from our analytic estimation of Eq. (7.58) (see right-hand panel of Fig. 7.3). The thick green line corresponds to all density parameter values in the range $[0.2, 0.4]$.

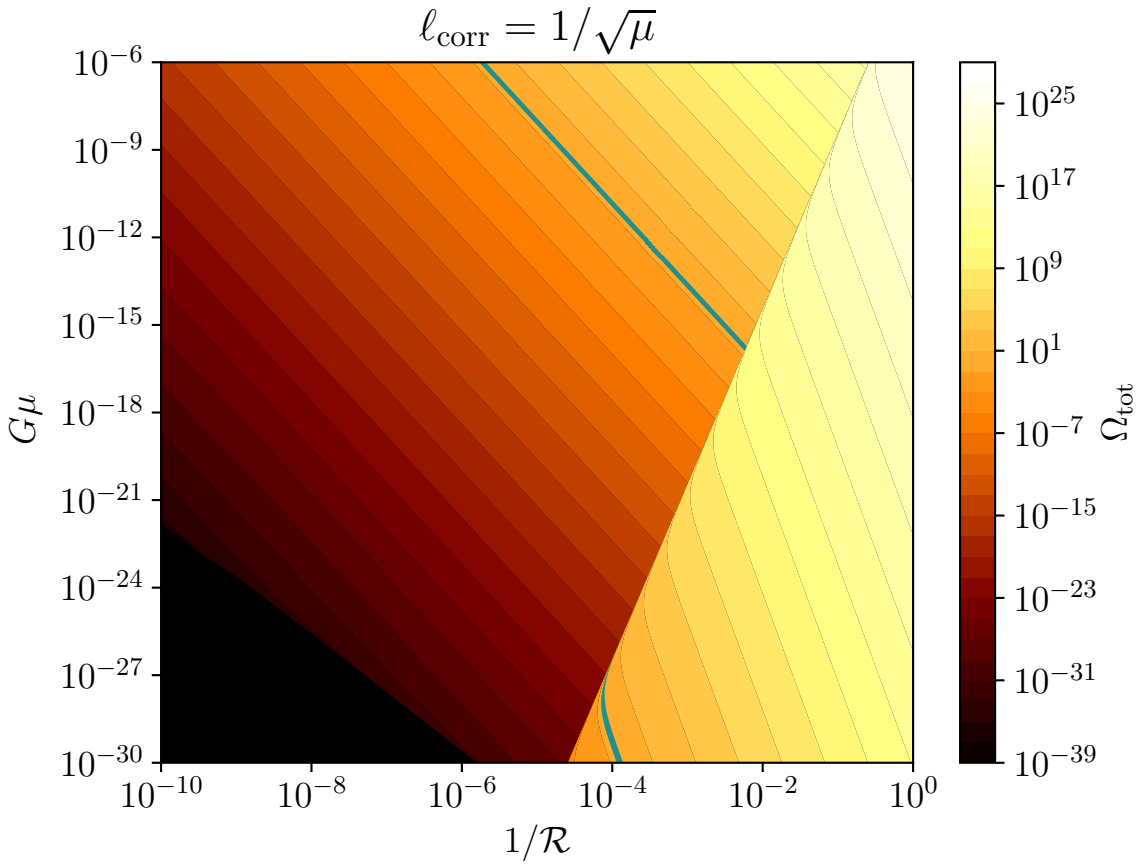

Figure 7.5: The total relic abundance of all vortons starting from a Vachaspati-Vilenkin initial loop distribution, with an initial thermal correlation length cur$orr = 1/\sqrt{\mu}$, and a one-scale loop production function with $\alpha = 0.1$. The green line corresponds to the range of values $[0.2, 0.4]$. The different populations contribution is represented in Fig. 7.4.

The lower right panel of Fig. 7.4, compared to the right panel of Fig. 7.3, shows that our approximated formula (7.58) is relatively accurate. The lower left panel of Fig. 7.4 exhibits a triangle-like region which is not visible on the left panel of Fig. 7.3. This region, with a high density of relaxed vortons, is precisely the one associated with the relaxed vortons created from the loops initially present at the string forming time and which were studied in Ref. [149]. This contribution is represented alone in the upper left panel of Fig. 7.4. In this corner of parameter space, we recover the results already presented in Ref. [149]: essentially all values of $G\mu$ are ruled out, only values of $G\mu = \mathcal{O}\big(10^{-30}\big)$ and $\mathcal{R} = \mathcal{O}\big(10^{4}\big)$ remain compatible with the cosmological bounds.

When all contributions are combined, as shown in Fig. 7.5, one can see that for all $G\mu$ there are values of $\mathcal{R}$ which make the vortons either an acceptable candidate for dark matter (green line) or a subdominant component today (left of the green line). However, this figure also shows that there is an absolute lower bound for $\mathcal{R}$ below which vortons would overclose the universe, independently of the value of $G\mu$ (which is also given by the green line). For instance, there are no acceptable regions for which $\mathcal{R} < 10^2$, implying that stable vortons in our Universe can only be created if the temperature of current condensation is *at least* two orders of magnitude lower than the one of the formation of strings. This result is the consequence of the irreducible relaxed and produced vorton contributions closing the parameter space up to the maximum admissible values of $G\mu$. It may have some implications on the particle physics models creating strings and currents [62, 370].

Despite the fact that Vachaspati-Vilenkin initial conditions are quite motivated from the point of view of a thermal process, loops could be created from other processes [371, 372]. Therefore, instead of assuming $\ell_{\rm corr} = 1/\sqrt{\mu}$, one could use the Kibble argument [61, 350] and take $\ell_{\rm corr} = d_{\rm h}t_{\rm ini}$, where $d_{\rm h}t_{\rm ini} = 2t_{\rm ini}$ denotes the distance to the would-be particle horizon at the string forming time. Doing so leads to the same overall relic abundance of vortons as in Section 7.5.1 where we were assuming $C_{\rm ini} = 0$. There are simply not enough loops initially, compared to the one produced later on, to significantly change the final density parameter.

In order to quantitatively study the dependence of $\Omega_{\rm tot}$ with respect to the loop distribution at $t_{\rm ini}$, we have represented in Fig. 7.6 the values of $\Omega_{\rm tot} = 0.3$ in the plane $(G\mu, 1/\mathcal{R})$ for various choices of $\ell_{\rm corr}$. They range from the thermal value $\ell_{\rm corr} = 1/\sqrt{\mu}$ to the causal one $\ell_{\rm corr} = d_{\rm h}t_{\rm ini}$, and even above, a situation that could appear if loops have been formed during cosmic inflation [373]. Everything on the right of the lines represented in this figure would lead to an overclosure of the Universe, while everything on the left is compatible with current measurements. The hatched region in this figure shows the robust bound discussed earlier, where there are only irreducible relaxed vortons and produced vortons.

In all our analysis and equations, we have left the parameter α arbitrary, fixing only $\alpha = 0.1$ for the figures for well motivated reasons. Changing α to smaller values, while keeping everything else fixed, increases the population of doomed loops, and thus decreases the vortons abundance. The explicit dependence in α can be read off from Eqs. (7.50) and (7.58).

7.5.3 Other observables

A network of cosmic strings can let imprints in various cosmological observables, such as the stochastic background of gravitational waves and the Cosmic Microwave Background (CMB). In the present case, the stabilization of vortons is expected to prevent a part of the energy to be converted into gravitational waves. We have therefore estimated the gravitational wave power spectrum generated from proto-vortons and doomed loops only. Their loop number densities are clarified in the Ap-

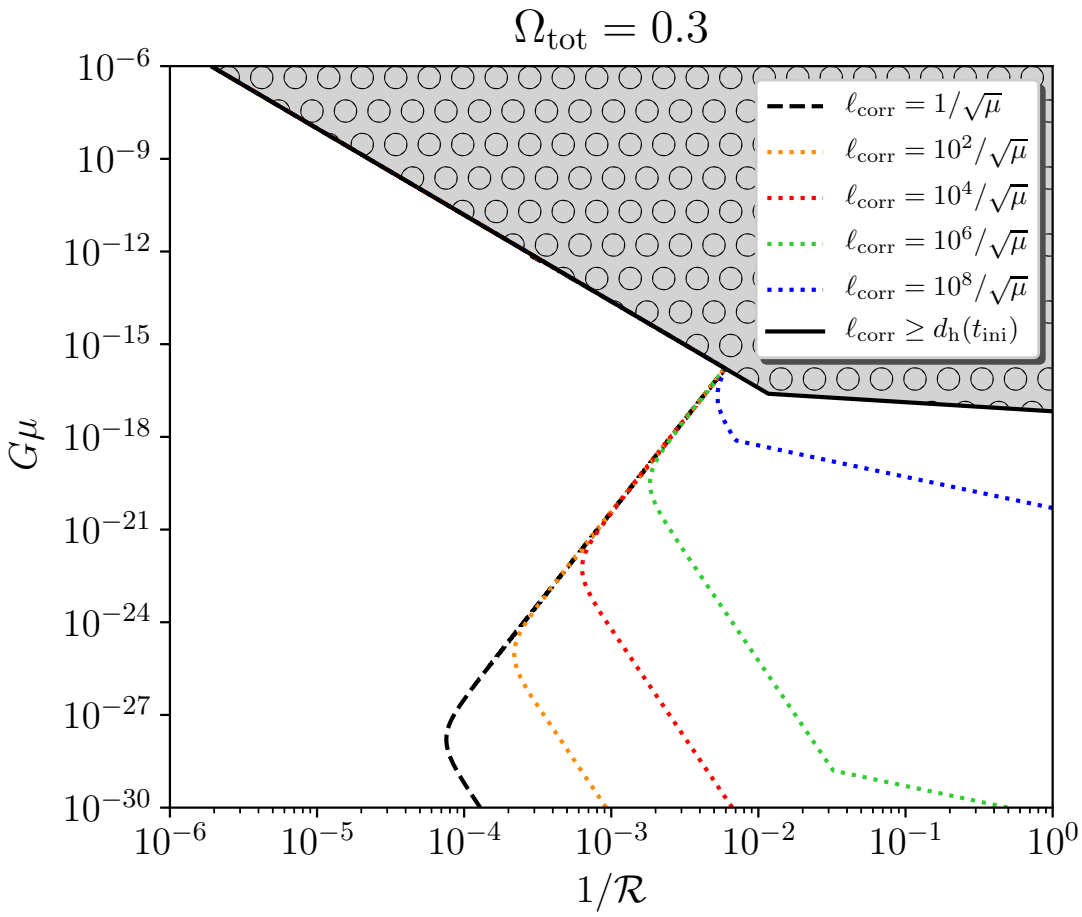

Figure 7.6: The total relic abundance of all vortons starting from a Vachaspati-Vilenkin initial loop distribution with various correlation length $\ell_{\rm corr}$ ranging from the thermal one $1/\sqrt{\mu}$ to the Kibble one $d_{\rm h}t_{\rm ini}$. Each curve represents the value $\Omega_{\rm tot} = 0.3$. Domains right of this curve lead to vortons overclosing the Universe, domains on the left are compatible with current cosmological constraints. The upper hatched region corresponds to the irreducible relaxed and produced vortons not affected by the initial conditions.

pendix 7.B. Due to the very small size of the vortons, the lack of energy in terms of gravitational waves ends up being negligible and the predictions for the stochastic background of gravitational waves remain unchanged compared to Nambu-Goto strings with a one-scale loop production function (see Chapter 4). For the one-scale LPF, the current Laser Interferometer Gravitational-Wave Observatory (LIGO) bound on the string tension is $G\mu < \mathcal{O}(10^{-11})$ [89, 90, 91] but depends on some assumptions on the string microstructure. Concerning the CMB, detectable distortions induced by cosmic strings are mostly due to the long strings in scaling such that they are not sensitive to the loop distribution and provide a robust upper bound $G\mu < \mathcal{O}(10^{-7})$ for all types of strings [374, 72, 375, 295, 376]. Both of these bounds therefore apply to current-carrying strings with vortons. Let us also remark that current-carrying strings may lead to other observational signatures, for instance gamma ray or radio bursts [377, 378] (see also Chapter 6).

7.6 Conclusion

The main result of this work is the derivation of the relic abundance of an irreducible population of vortons not considered so far. These vortons are continuously created by the scaling string network at all times during the cosmological expansion and allow us to probe new regions of the parameter space $(G\mu, 1/\mathcal{R})$, namely energy scales that spawn the entire spectrum from TeV scales to the Planck scale. In particular, vortons are a viable dark matter candidate for all possible value of $G\mu$ (with, however, some quite tuned values of $\mathcal{R}$). We have derived their number density distribution at all times, which is the quantity of interest for dark matter direct detection searches [356, 379, 380], and derived the relevant cosmological constraints, summarized in figures 7.5 and 7.6.

Throughout this work, we have, however, assumed that all the scaling loops are produced at the same size αt. A more complete analysis would take into account the fact that the loop production function is *a priori* more complicated. Due to the proliferation of kinks on the infinite string network and the fragmentation of large loops, we expect scaling loops to be produced at all sizes with a power-law LPF

$$\mathcal{P}(\ell, t, N) = Ct^{-5}\left(\frac{\ell}{t}\right)^{2\chi-3}\delta\left(N - \sqrt{\frac{\ell}{\lambda}}\right)\Theta(t - t_{\rm cur})\Theta(\ell - \gamma_{\rm c} t), \tag{7.60}$$

where χ is the so-called Polchinski-Rocha exponent and $\gamma_{\rm c}$ is the gravitational backreaction scale. Under this assumption, many more small loops are produced, and one can expect some boost to the density of vortons [54, 56]. Solving for the vorton distribution by using a Polchinski-Rocha LPF is, however, mathematically challenging, and we have not taken this route in the present paper.

Let us also mention that, in the present work, we have solved a continuity equation to derive the vorton number density. This approach is strictly equivalent to the one presented in Ref. [125], which is based on solving a Boltzmann equation. As a matter of fact, all the results presented have been cross-checked using the two methods. For completeness, we give in Appendix 7.A a proof of the equivalence between the two formalisms and how to pass from one evolution equation to the other.

Finally, concerning the influence of the initial conditions, let us remark that in the most generic situation, one cannot exclude that the redshift $z_{\rm ini}$ at which strings are formed and the redshift $z_{\rm cur}$ at which the current appears are independent of the value of $G\mu$ and $\mathcal{R}$ (or λ). Although such a situation would be difficult to envisage for cosmic strings interpreted as topological defects, it could be very well the case for cosmic superstrings. For instance, $z_{\rm ini}$ could be very large,

close to the Planck energy scales while the warped observed value of $G\mu$ can remain very low. In this case, our assumptions of Section 7.3.2 do no longer apply and this could change the relaxed vorton contribution. However, this would not change the produced vorton abundance, these being generated by the network at all subsequent times. A complete model-independent treatment would require to consider a four-dimensional parameter space made of $(G\mu, \mathcal{R}, z_{\rm ini}, z_{\rm cur})$, which could be explored using Monte-Carlo-Markov-Chain methods, but we leave such a study for a future work.

7.A Connection between the Boltzmann and continuity equations

We clarify in this Appendix the equivalence between Eq. (2.7) of Ref. [125] and our Eq. (7.10) to show that the difference merely comes from the use of either lagrangian or eulerian coordinates. In Ref. [125], one has $\ell = \ell(\ell_{\rm ini}, t)$, *i.e.*, one follows the evolution of a given loop size ℓ that begun with an initial value $\ell_{\rm ini}$; somehow, the relevant variable is $\ell_{\rm ini}$, and the flow is lagrangian. In the present work, the size of the loop ℓ is just what it is at the time one is concerned with, with no mention of the individual loop; this is the eulerian version.

Going from the eulerian set $\{\ell, t\}$ to the lagrangian one $\{\ell_{\rm ini}, t\}$ means that for any quantity $X(\ell, t) = X[\ell(\ell_{\rm ini}, t)]$, one has

$$\mathrm{d}X = \left(\frac{\partial X}{\partial t}\right)_{\ell} \mathrm{d}t + \left(\frac{\partial X}{\partial \ell}\right)_{t} \mathrm{d}\ell = \left(\frac{\partial X}{\partial t}\right)_{\ell_{\rm ini}} \mathrm{d}t + \left(\frac{\partial X}{\partial \ell_{\rm ini}}\right)_{t} \mathrm{d}\ell_{\rm ini}\,,$$

with the subscript on the brackets for the partial derivatives indicating the quantity left constant for the evaluation of the derivative. Similarly expanding the differential $\mathrm{d}\ell$ and identifying the partial derivatives, one finds

$$\left(\frac{\partial X}{\partial t}\right)_{\ell_{\rm ini}} = \left(\frac{\partial X}{\partial t}\right)_{\ell} + \left(\frac{\partial X}{\partial \ell}\right)_{t}\left(\frac{\partial \ell}{\partial t}\right)_{\ell_{\rm ini}} \quad \text{and} \quad \left(\frac{\partial X}{\partial \ell_{\rm ini}}\right)_{t} = \left(\frac{\partial X}{\partial \ell}\right)_{t}\left(\frac{\partial \ell}{\partial \ell_{\rm ini}}\right)_{t}. \tag{7.61}$$

One also notes that

$$j \equiv \frac{\mathrm{d}\ell}{\mathrm{d}t} = \left(\frac{\partial \ell}{\partial \ell_{\rm ini}}\right)_{t}\frac{\mathrm{d}\ell_{\rm ini}}{\mathrm{d}t} + \left(\frac{\partial \ell}{\partial t}\right)_{\ell_{\rm ini}} = \left(\frac{\partial \ell}{\partial t}\right)_{\ell_{\rm ini}}, \tag{7.62}$$

the final step being a consequence of the fact that in lagrangian coordinates, $\ell_{\rm ini}$ does not depend on time. Combining (7.62) and (7.61), one immediately gets that

$$\left(\frac{\partial X}{\partial t}\right)_{\ell} + j(\mathcal{P}X\ell)_t = \left(\frac{\partial X}{\partial t}\right)_{\ell_{\rm ini}}. \tag{7.63}$$

We are now in position to compare Eq. (2.7) of Ref. [125] and our Eq. (7.10). The former indeed reads

$$\frac{\partial}{\partial t}\big(a^3 F \mathcal{J}_{\rm PSD}\big) + j\frac{\partial}{\partial \ell}\big(a^3 F \mathcal{J}_{\rm PSD}\big) = a^3 \mathcal{P}\mathcal{J}_{\rm PSD}, \tag{7.64}$$

where $\mathcal{J}_{\rm PSD} = \partial\ell/\partial\ell_{\rm ini}$ accounts for phase space distortion, and we have set $F \equiv \frac{\partial^2 \mathcal{N}}{\partial \ell \partial N}$ for convenience. Expanding the partial derivatives of (7.64) and simplifying by $\mathcal{J}_{\rm PSD}$ (assumed non vanishing), one gets

$$\frac{\partial}{\partial t}\big(a^3 F\big) + j\frac{\partial}{\partial \ell}\big(a^3 F\big) + \frac{a^3 f}{\mathcal{J}_{\rm PSD}}\left[\left(\frac{\partial \mathcal{J}_{\rm PSD}}{\partial t}\right)_{\ell} + j\left(\frac{\partial \mathcal{J}_{\rm PSD}}{\partial \ell}\right)_{t}\right] = a^3\mathcal{P}, \tag{7.65}$$

the term in square brackets being, by virtue of (7.61) and (7.62), simply $\left(\partial\mathcal{J}_{\rm PSD}/\partial t\right)_{\ell_{\rm ini}}$. Given the definition of $\mathcal{J}_{\rm PSD}$ and swapping partial derivatives, it turns out that

$$\left(\frac{\partial\mathcal{J}_{\rm PSD}}{\partial t}\right)_{\ell_{\rm ini}} = \left(\frac{\partial j}{\partial\ell}\right)_t \frac{\partial\ell}{\partial\ell_{\rm ini}} = \mathcal{J}_{\rm PSD}\left(\frac{\partial j}{\partial\ell}\right)_t,$$

so that Eq. (7.65) now becomes

$$\frac{\partial}{\partial t}\left(a^3F\right) + j\frac{\partial}{\partial\ell}\left(a^3F\right) + \left(a^3F\right)\frac{\partial j}{\partial\ell} = a^3\mathcal{P}, \tag{7.66}$$

which is, as announced, Eq. (7.10) after grouping the $\ell-$derivative terms and making j explicit as in Eq. (7.7).

To conclude this appendix, we give in Table 7.1, a dictionary between the different notations used in Refs. [149, 125] and the present work.

Present work	Ref. [125]
μ	U
ℓ_0	$\ell_{\rm v}$
$\mathcal{R}$	N_*
$\gamma_{\rm d}$	$\gamma_{\rm d}$
$\sigma \to 0$	$\gamma_{\rm v} \to 0$
$\ell_\star = \lambda^3\mu$	ℓ_+
$\ell_{\rm T}(t)$	$\ell_{\rm T}(t)$

Table 7.1: Dictionary of notations between the present work and Refs. [149, 125].

7.B Distribution of proto-vortons and doomed loops

In this Appendix, we give the distributions of proto-vortons and doomed loops, both of which contribute to the stochastic gravitational wave background. Proto-vortons and doomed loops decay through gravitational wave radiation and their collapse is not prevented by the current: indeed for both, $\mathcal{J} = 1$ (in the limit $\sigma \to 0$). Hence, for these distributions, and without loss of generality, we set $\mathcal{J} = 1$ in this Appendix.

7.B.1 Doomed loops

Doomed loops are the loops which do not have enough current to prevent their final collapse, hence $N < \mathcal{R}$. From Eqs. (7.28), (7.18) and (7.23), the relaxed doomed loop distribution, that is to say the doomed loops which are produced from the initial conditions at condensation, reads

$$\left.\frac{{\rm d}\mathcal{N}}{{\rm d}\ell}\right|_{\rm doom,rel} = \left[\frac{a(t_{\rm cur})}{a(t)}\right]^3 \int {\rm d}N\, \frac{{\rm d}\mathcal{N}}{{\rm d}\ell}(\ell_{\rm cur}, t_{\rm cur})\delta\left(N - \sqrt{\frac{\ell_{\rm cur}}{\lambda}}\right)\Theta(\mathcal{R} - N), \tag{7.67}$$

in which $\ell_{\rm cur}$, the size of the loop during condensation at $t_{\rm cur}$, is given by

$$\ell_{\rm cur}(\ell, t) = \Gamma G\mu(t - t_{\rm cur}) + \ell. \tag{7.68}$$

Integrating over the charge N and replacing $\ell_{\rm cur}$, one obtains the number density of doomed loops in relaxation

$$\left.\frac{\mathrm{d}\mathcal{N}}{\mathrm{d}\ell}\right|_{\rm doom,rel} = \left[\frac{a(t_{\rm cur})}{a(t)}\right]^3 \frac{\mathrm{d}\mathcal{N}}{\mathrm{d}\ell}[\Gamma G\mu(t-t_{\rm cur})+\ell, t_{\rm cur}]\Theta\left[\mathcal{R}-\sqrt{\frac{\Gamma G\mu(t-t_{\rm cur})+\ell}{\lambda}}\right]. \tag{7.69}$$

Concerning the doomed loops produced after condensation, from Eqs. (7.28) and (7.38), their number density is given by

$$\left.\frac{\mathrm{d}\mathcal{N}}{\mathrm{d}\ell}\right|_{\rm doom,prod} = C\int \mathrm{d}N\,\Theta(\mathcal{R}-N)\left[\frac{a(t_\star)}{a(t)}\right]^3 t_\star^{-4}\frac{1}{\alpha+\Gamma G\mu}\delta\left(N-\sqrt{\frac{\alpha t_\star}{\lambda}}\right)\Theta(t_\star - t_{\rm cur}), \tag{7.70}$$

in which $t_\star$ is the loop formation time. Assuming, as we have done throughout this paper, that loops are produced at a given size $\ell = \alpha t$ at time t, the formation time satisfies

$$t_\star(\ell, t) = \frac{\ell+\Gamma G\mu t}{\alpha+\Gamma G\mu}. \tag{7.71}$$

Finally, integrating over the charge N and replacing the formation time by the above equation, one obtains the number density of doomed loops produced after condensation:

$$\begin{aligned}\left.\frac{\mathrm{d}\mathcal{N}}{\mathrm{d}\ell}\right|_{\rm doom,prod} &= C\left[\frac{a\left(\frac{\ell+\Gamma G\mu t}{\alpha+\Gamma G\mu}\right)}{a(t)}\right]^3 \frac{(\alpha+\Gamma G\mu)^3}{(\ell+\Gamma G\mu t)^4} \\ &\quad\times\Theta\left(\frac{\ell+\Gamma G\mu t}{\alpha+\Gamma G\mu}-t_{\rm cur}\right)\Theta\left[\mathcal{R}-\sqrt{\frac{\alpha(\ell+\Gamma G\mu t)}{\lambda(\alpha+\Gamma G\mu)}}\right].\end{aligned} \tag{7.72}$$

7.B.2 Proto-vortons

Proto-vortons are loops which will eventually become vortons after a certain time, but which are still large enough to behave like Nambu-Goto strings. From Eq. (7.29), (7.18) and (7.23), the distribution of "relaxed proto-vortons" is given by

$$\left.\frac{\mathrm{d}\mathcal{N}}{\mathrm{d}\ell}\right|_{\rm proto,relax} = \int \mathrm{d}N\,\Theta(N-\mathcal{R})\left[\frac{a(t_{\rm cur})}{a(t)}\right]^3 \frac{\mathrm{d}\mathcal{N}}{\mathrm{d}\ell}(\ell_{\rm cur}, t_{\rm cur})\delta\left(N-\sqrt{\frac{\ell_{\rm cur}}{\lambda}}\right)\Theta[\ell-\ell_0(N)], \tag{7.73}$$

where $\ell_0(N) = N/\sqrt{\mu}$ and, again, the size of the loop at formation is given by

$$\ell_{\rm cur}(\ell, t) = \Gamma G\mu(t-t_{\rm cur})+\ell. \tag{7.74}$$

On carrying out the integral over the charge N in equation (7.73), the number density of proto-vortons produced at condensation is

$$\begin{aligned}\left.\frac{\mathrm{d}\mathcal{N}}{\mathrm{d}\ell}\right|_{\rm proto,relax} &= \left[\frac{a(t_{\rm cur})}{a(t)}\right]^3 \frac{\mathrm{d}\mathcal{N}}{\mathrm{d}\ell}[\Gamma G\mu(t-t_{\rm cur})+\ell, t_{\rm cur}] \\ &\quad\times\Theta\left[\ell-\sqrt{\frac{\Gamma G\mu(t-t_{\rm cur})+\ell}{\lambda\mu}}\right]\Theta\left[\sqrt{\frac{\Gamma G\mu(t-t_{\rm cur})+\ell}{\lambda}}-\mathcal{R}\right].\end{aligned} \tag{7.75}$$

Proto-vortons can also be produced after condensation, in which case their distribution is obtained from Eqs. (7.29) and (7.38)

$$\left.\frac{\mathrm{d}\mathcal{N}}{\mathrm{d}N}\right|_{\mathrm{proto,prod}} = C\int \mathrm{d}N \left[\frac{a(t_\star)}{a(t)}\right]^3 t_\star^{-4}\frac{\Theta(N-\mathcal{R})}{\alpha+\Gamma G\mu}\delta\!\left(N-\sqrt{\frac{\alpha t_\star}{\lambda}}\right)\Theta(t_\star - t_{\mathrm{cur}})\Theta[\ell-\ell_0(N)]. \tag{7.76}$$

Similarly, the loop formation time $t_\star$ is given by

$$t_\star(\ell,t) = \frac{\ell+\Gamma G\mu t}{\alpha+\Gamma G\mu}, \qquad \ell_0(N) = \frac{N}{\sqrt{\mu}}\,. \tag{7.77}$$

The distribution of proto-vortons produced after the condensation now reads

$$\begin{aligned}\left.\frac{\mathrm{d}\mathcal{N}}{\mathrm{d}N}\right|_{\mathrm{proto,prod}} &= C\left[\frac{a\left(\frac{\ell+\Gamma G\mu t}{\alpha+\Gamma G\mu}\right)}{a(t)}\right]^3 \frac{(\alpha+\Gamma G\mu)^3}{(\ell+\Gamma G\mu t)^4} \\ &\quad\times\Theta\!\left(\frac{\ell+\Gamma G\mu t}{\alpha+\Gamma G\mu}-t_{\mathrm{cur}}\right)\Theta\!\left[\ell-\sqrt{\frac{\alpha(\ell+\Gamma G\mu t)}{\lambda\mu(\alpha+\Gamma G\mu)}}\right]\Theta\!\left[\sqrt{\frac{\alpha(\ell+\Gamma G\mu t)}{\lambda\mu(\alpha+\Gamma G\mu)}}-\mathcal{R}\right].\end{aligned} \tag{7.78}$$

Part II

Primordial Black Holes

Chapter 8

Introduction to primordial black holes

Since Primordial Black Holes (PBHs) were proposed almost 50 years ago [381, 382, 383], it has been realized that they can be relevant in various aspects of cosmology, ranging from dark matter [384] and the generation of large-scale structures through Poisson fluctuations [385, 386] to the seeding of supermassive black holes in galactic nuclei [387, 388]. More recently, they have attracted even more attention as it was pointed out that they may account for the black-holes observed to merge by the LIGO/Virgo collaboration [389] through their gravitational wave emission, see *e.g.* Refs. [390, 391]. The aim of this introduction is to give a very generic overview of PBH formation and the constraints that have been established on their abundance (for reviews, see Refs. [392, 393, 394, 395] that were the inspiration for this introduction). Then in Section 8.4, I introduce the Mathieu equation and its parametric instabilities which are crucial for the next chapter.

8.1 PBH masses and Hawking evaporation

The most commonly considered PBH formation mechanism is the collapse of large over-densities during radiation era. At the re-entry of time, the Hubble horizon $d_{\rm h} = 2ct$ turns out to be the Schwarzschild radius $R_S = 2GM/c^2$ of a black hole with mass

$$M \approx \frac{\gamma c^3 t}{G} \approx \gamma 10^{15} \left(\frac{t}{10^{-23}\mathrm{s}} \right) \mathrm{g}, \tag{8.1}$$

where γ is a numerical factor smaller than 1 denoting the fraction of the Hubble horizon collapsing into the black hole. Hence, PBH masses may range from $\sim 10^{-5}$g if produced at the Planck time (10^{-43}s) to $\sim 10^5$ solar masses for those formed one second after the big bang. In Chapter 9, we study PBHs formed through a different mechanism called the *preheating instability*. The order of magnitude is nonetheless similar, and we show that these PBHs may have masses ranging from 10g to a solar mass.

Hawking famously discovered in Ref. [396] that black holes radiate particles through quantum

effects with a black-body spectrum of temperature

$$T_{\rm BH} = \frac{\hbar c^3}{8\pi G k_{\rm B} M}, \tag{8.2}$$

the subscript BH meaning either Black Hole or Bekenstein-Hawking. *Hawking radiation* is therefore more important, the lower the mass of the black hole. I should mention at this point that there is a profound analogy between the properties of black holes (mass, area and surface gravity) and thermodynamics (energy, entropy and temperature) also known as *black hole thermodynamics* [397] but this is out of the scope of this manuscript.

The radiation of a black-hole is that of a black body and its luminosity can be approximated by the *Bekenstein-Hawking luminosity*

$$L = A\sigma T_{\rm BH}^4 = \frac{\hbar c^6}{15360\pi G^2 M^2} \tag{8.3}$$

in which $A = 4\pi R_S^2$ is the area of the horizon and σ the Stefan-Boltzmann constant. The underlying assumption behind this equation is that of pure photon emission by a black hole with no charge nor spin. The lifetime of a black hole with initial mass M_0 can be estimated by integrating this equation with $L = (\,{\rm d}M/{\rm d}t\,)c^2$, to find

$$\tau = \frac{5120\pi G^2}{\hbar c^4} M_0^3 \approx 3 \times 10^{11} \left(\frac{M_0}{5 \times 10^{14}{\rm g}} \right)^3 \text{ years}. \tag{8.4}$$

A more precise analysis would take into account that the actual Hawking radiation is not exactly that of a black body and depends on the spin and the charge of the black hole [398]. Additionally, black holes do not only emit photons but also neutrinos, gravitons and subsequently electrons, muons and even hadrons as the mass drops, *i.e.* the Hawking temperature rises [399]. Taking these into account, the critical mass $M_\star$ for which the lifetime equals the age of the Universe of 13.8Gyr is [400]

$$M_\star = 5.0 \times 10^{14}{\rm g}. \tag{8.5}$$

In the next sections, I will briefly review some constraints on the fraction of Dark Matter (DM) in the form of PBHs

$$f_{\rm PBH} = \frac{\Omega_{\rm PBH}}{\Omega_{\rm DM}}. \tag{8.6}$$

PBHs with masses below $M_\star$ have all completely evaporated by the present day and cannot account for the DM content of the Universe. However, they may still be relevant for other aspects in cosmology. The constraints on PBH abundance are generally divided between *evaporation constraints* that apply to PBHs with masses $M \lesssim 10^{17}$g, and *constraints on non-evaporating black holes*.

8.2 Evaporation constraints

PBHs with masses around $10^9 - 10^{13}$g would evaporate during or shortly after Big Bang Nucleosynthesis. The injection of high-energy neutrinos and antineutrinos [401], of high-energy nucleons and anti-nucleons [402] and of photons [403] have a strong impact on the abundance of light elements which allows us to place constraints on their numbers. This bound is not shown in Fig. 8.1 since it concerns PBHs that have evaporated today and therefore cannot account for the DM content

of the Universe today. It is, however, important to constrain the production of PBHs during the preheating instability with masses ranging from 10g to a solar mass.

PBHs with masses slightly above the critical mass $M_\star$ are strongly constrained by observations of the extragalactic γ-ray background (EGB) [404]. Measurements of the diffuse EGB constrain the average number density of PBHs at the present epoch. This bound has subsequently been updated by refining the description of the PBH emission [405] and by taking into account new generations of detectors.

It has also been suggested that the positrons produced by PBHs of masses $10^{16} - 10^{17}$g would annihilate and contribute to the flux of the 511 KeV annihilation line radiation from the Galactic Centre (GC) [406]. Measurements of this line by SPI/INTEGRAL now exclude models in which PBHs of this mass range constitute all the DM [407].

There are other evaporation constraints in this mass range. Constraints on the electron-positron flux from Voyager 1 limit the contribution if PBHs to the local DM density [408]. PBHs of masses around $M_\star$ clustering inside our Galaxy would produce an anisotropic Galactic γ-ray background. The ratio of the anisotropic to isotropic intensity in EGRET observations between 30MeV and 120MeV has been used by Ref. [409] to claim the detection PBH clustering in our galaxy. However, more detailed analyses by Refs. [410, 411] used these observations to constrain the PBH abundance. It should be noted that this limit is sensitive to the width of the PBH mass function.

These bounds depend crucially on whether Hawking evaporation is realized in nature. If not, such light PBHs would be stable and viable as DM.

8.3 Constraints on non-evaporating PBHs

Contrary to the bounds presented in the previous section, the constraints on non-evaporating PBHs do not rely on the assumption that Hawking evaporation is realized in nature, but on the gravitational interaction of PBHs with their environment.

Gravitational lensing is a very powerful method to constrain or detect PBHs at it is solely based on gravitational physics and does not suffer from the uncertainties that exist in the studies of the radiation of black holes and their interaction with the surrounding matter. There are different types of gravitational lensing events. *Microlensing* events are lensed objects in which the angular separation of the images is too small to be resolved by observations [412]. The observer sees the unresolved superposition of two images which is brighter than the original source. Microlensing observations of the Large and Small Magellanic clouds by the EROS collaboration, the MACHO project and the OGLE experiment probe the fraction of DM halo in black holes in the mass range $10^{-8} - 1$ solar mass. More recently, the high-cadence observations (one observation every two minutes) of more than tens of million stars in M31 by the Subaru Hyper Suprime-Cam (HSC) placed stringent upper limits on the abundance of PBHs with masses $10^{-13} - 10^{-5}$ solar mass [413]. Microlensing may also affect the magnification distribution of type 1a supernovae (SN1a). If the DM is concentrated in compact object, then a few of the SN1a would be significantly magnified [414]. These constraints are represented in Fig. 8.1. On the other side, *femtolensing* refers to lensing events in which the wavelength of light is comparable or larger than the Schwarzschild radius of the lens

$$R_S \equiv \frac{2GM}{c^2} = 0.3 \times \left(\frac{M}{10^{-13} M_\odot}\right) \text{nm}. \tag{8.7}$$

This technique probes PBHs with masses between $10^{-16} - 10^{-13}$ solar masses. Due to diffraction,

it was proposed that femtolensing of γ-ray bursts would induce oscillatory features in their spectrum [415]. However, it was later demonstrated that most γ-ray bursts are too large to be modelled as point-like sources [416] relaxing the limits from femtolensing.

A slightly more controversial type of constraint come from *dynamical effects*: PBHs affecting or even disrupting astrophysical systems through their gravitational interactions. Indeed, it was pointed out that the passage of a PBH through a white dwarf could ignite the thermonuclear reaction at the origin of type 1a supernovae and that we can constrain the abundance of PBHs by observing the mass distribution of white dwarfs [417]. Similarly, a high abundance of PBHs with $M = 10^{-14} - 10^{-8} M_\odot$ would disrupt neutron stars [418]. Wide halo binaries in the galactic halo– binaries of stars with large separations of order one parsec and very weak binding energy – are also vulnerable to disruption from the passing of PBHs. It is a challenging task to distinguish wide halo binaries from the purely coincident position in the sky of two stars, but it still places upper bounds for $M \sim 100 M_\odot$ [419]. At higher mass scales, PBHs moving randomly in the Galactic disks would increase the variance of the stars' velocity, a mechanism called *disk heating* [420]. A relatively similar mechanism in nature, but on larger scales constrain the existence of massive intergalactic black holes with $M > 10^{15} M_\odot$ which would increase the peculiar velocity of galaxies. As we have measured the peculiar velocity of our galaxy with the CMB dipole anisotropy, this places a bound on the very large end of the mass spectrum [421].

Massive PBHs distributed randomly in space with Poisson fluctuations may generate primordial density perturbations and enhance the matter power spectrum at small scales: this is called the *large scale structure* constraint [385]. Observations of the Lyman-α absorption lines in the spectra of distant galaxies and quasars are used to estimate the inhomogeneous distribution of baryonic matter along the line of sight and allow to probe the DM perturbations on small scales. In Fig. 8.2, this constraint is decomposed into its individual components from Clusters (Cl), Milky Way galaxies (Gal) and dwarf galaxies (dG), as they originate from different redshifts.

At early times, PBHs could have had a large luminosity due to the *accretion* of background gas [422]. A complete analysis of the phenomenon is however very challenging and require numerical simulations, as the luminosity of the black hole backreacts on its environment thereby reducing accretion. Accretion by PBHs may have an impact in the early Universe on the power spectrum of the CMB temperature and the polarization anisotropies [423]; and in the present day they would contribute to the observed number density of compact X-ray objects in galaxies [424].

Finally, the detection of gravitational waves from coalescing black holes by the LIGO / Virgo / KAGRA (LVK) collaboration opens a new window to look for PBHs [18]. Black holes and neutron stars formed by standard stellar evolution can only have masses larger than $\sim 1 M_\odot$, hence a compact object with a mass lower than $1 M_\odot$ would be necessarily of primordial origin. However, no such objects were found in the different LVK searches [316, 19]. Even if the black holes detected by the LVK are not necessarily of primordial origin, the observations place important constraints on the number of PBHs in our neighbourhood. A different type of constraint comes from the gravitational wave background produced by a population of massive PBHs [425], or by large second-order tensor perturbations generated by the scalar perturbations which produce them [426].

8.4 Mathieu instability with the method of multiple scales

The primordial black holes studied later in Chapter 9 are produced after inflation, during a phase called the *preheating instability* [427, 428]. The oscillations of the inflaton at the bottom of its potential act as a forcing term in the equation of motion for the Mukhanov-Sasaki variable, leading

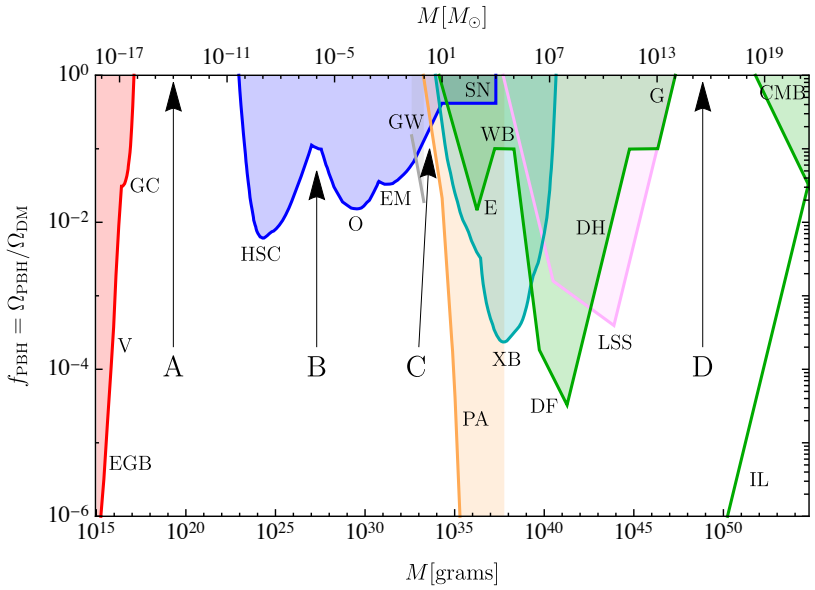

Figure 8.1: Constraints on $f(M)$ for a monochromatic mass function. Evaporation constraints (red) excludes PBHs slightly above the critical mass $M_\star = 5 \times 10^{14}$. Its enveloppe is determined by bounds from the diffuse Extra Galactic Background (EGB), Voyager positron flux (V) and the 511KeV annihilation line in the Galactic Centre (GC). Constraints on the Galactic γ-ray background have not been included in the figure as it is very sensitive to the width of the PBH mass function. Constraints from lensing (blue) include the microlensing of M31 by the high-cadence Subaru HSC experiment (HSC), of the Magellanic clouds by EROS and MACHO (EM) and of the galactic bulge by OGLE (O). Microlensing of type 1a supernovae (SN) is also reported on the figure. Dynamical effects (green) include limits from the existence of wide binaries (WB), disk heating (DH) and the CMB dipole (CMB). Accretion limits include – in the early Universe – the observations of the CMB distortions (orange, PA) and –in the present day – of X-ray compact objects in the galaxy (light blue, XB). Constraints from gravitational waves (gray, GW) are also reported. Figure taken from Ref. [394].

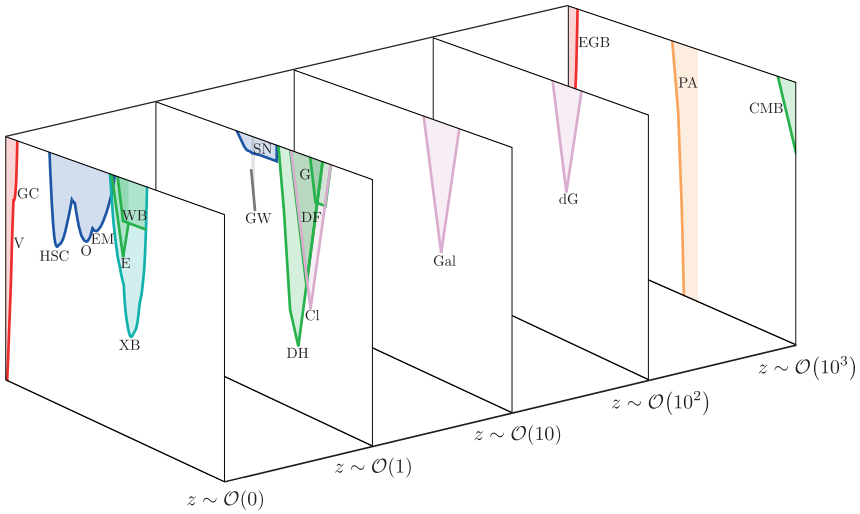

Figure 8.2: The limits on the PBH abundance of Fig. 8.1 for different redshifts. The large scale structure limit has been broken down into its individual components from clusters (Cl), Milky Way galaxies (Gal) and dwarf galaxies (dG). This figure is taken from Ref. [394].

to an enhancement in the production of primordial black holes. Before diving into the details of the preheating phase, let me review the key properties of the Mathieu equation (9.2) used in the next chapter.

The Mathieu equation is a second-order ordinary differential equation

$$\frac{\mathrm{d}^2 x}{\mathrm{d}t^2} + (A + 2q\cos 2t)x = 0 \tag{8.8}$$

in which A and q are constant. This equation describes a parametrically forced linear oscillator whose frequency changes sinusoidally in time as in Fig. 8.3. In Section 9.2, the variable playing the role of x will be the Mukhanov-Sasaki variable, and Eq. (8.8) will be used to determine the evolution of this variable through preheating. As is well-known and as is discussed in detail below, the solutions of Eq. (8.8) are unstable if the resonant frequency $\sqrt{A} \sim 1$ and if the amplitude of the forcing $q \ll 1$. One can understand this instability by performing an expansion for $q \ll 1$ using the method of multiple scales [429]. We also assume that

$$A = 1 + q\delta, \tag{8.9}$$

where $\delta = \mathcal{O}(1)$ as $q \to 0$. The method of multiple scales is a technique to construct uniformly valid approximations to the solutions of perturbative problems by introducing fast scale and slow scale variables, and treating them as if they were independent. This additional degree of freedom introduced by the new variables is then used to remove secular terms in the expansion.

In the case of the Mathieu equation, the idea of the method of multiple scales is to describe the evolution over long-time scales of the order q^{-1} by introducing the "slow" variable

$$\eta = qt. \tag{8.10}$$

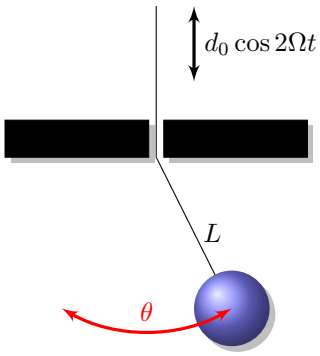

Figure 8.3: This parametrically forced linear oscillator is described by the Mathieu equation (8.8) in the limit of small angles.

We then look for a solution of the form

$$x(t, q) = \tilde{x}(t, \eta, q)$$

where $\tilde{x}(t, \eta, q)$ is a function of two time variables (t, η) that gives x when $\eta = qt$. The derivatives of x are written as partial derivatives of $\tilde{x}$

$$\frac{\mathrm{d}x}{\mathrm{d}t} = \frac{\partial \tilde{x}}{\partial t} + q\frac{\partial \tilde{x}}{\partial \eta}, \tag{8.11}$$

$$\frac{\mathrm{d}^2x}{\mathrm{d}t^2} = \frac{\partial^2 \tilde{x}}{\partial t^2} + 2q\frac{\partial^2 \tilde{x}}{\partial \eta \partial t} + q^2\frac{\partial^2 \tilde{x}}{\partial \eta^2}. \tag{8.12}$$

Substituting into the original Mathieu equation (8.8), we find that $\tilde{x}$ satisfies

$$\frac{\partial^2 \tilde{x}}{\partial t^2} + 2q\frac{\partial^2 \tilde{x}}{\partial \eta \partial t} + q^2\frac{\partial^2 \tilde{x}}{\partial \eta^2} + (1 + q\delta + 2q\cos 2t)\tilde{x} = 0. \tag{8.13}$$

Actually, $\tilde{x}(t, \eta, q)$ only has to satisfy this equation when $\eta = qt$, but we require that Eq. (8.13) remains satisfied for all values of (t, η). In particular, this requirement implies that x satisfies Eq. (8.8).

With the method of multiple scales, we have replaced an ordinary differential equation for x by a partial differential equation for $\tilde{x}$, which may seem like an even more difficult problem. But thanks to the extra degree of freedom provided by the independence of the short and long scales, we will below require that $\tilde{x}(t, \eta, q)$ is a *periodic function* of the "fast" variable t.

We perform an expansion for $\tilde{x}$ for small values of the amplitude $q \ll 1$

$$\tilde{x}(t, \eta, q) = x_0(t, \eta) + qx_1(t, \eta) + \mathcal{O}(q^2),$$

and insert it in Eq. (8.13). The leading and next-to-leading order equations in are

$$\frac{\partial^2 x_0}{\partial t^2} + x_0 = 0 \tag{8.14}$$

$$\frac{\partial^2 x_1}{\partial t^2} + x_1 = -2\frac{\partial^2 x_0}{\partial t \partial \eta} - (\delta + 2\cos 2t)x_0. \tag{8.15}$$

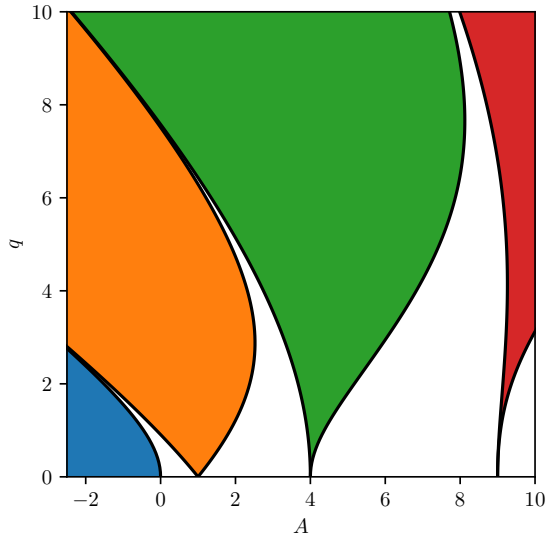

Figure 8.4: Stability diagram for the Mathieu equation (8.8). The periodic solutions $\mu = 0$ (black solid lines) delimit the different instability bands starting at $A = 1, 4$ and 9; each with a different color. In the empty/white regions, the solutions are stable. The multi-scale analysis of Section 8.4 concerns the bottom of the orange region at $A \sim 1$. The rest of the diagram has been determined numerically.

The solution of Eq. (8.14) of course

$$x_0(t, \eta) = C(\eta) \exp(it) + \text{complex conjugate},$$

in which $C(\eta)$ is an arbitrary complex valued function of η. Substituting into Eq. (8.15) gives

$$\frac{\partial^2 x_1}{\partial t^2} + x_1 = -C(\eta)\, \mathrm{e}^{3it} - \left(2i \frac{\mathrm{d}C}{\mathrm{d}\eta} + C^*(\eta) + \delta C(\eta) \right) \mathrm{e}^{it} + \text{c.c.} \tag{8.16}$$

Whose solution for x_1 is periodic in t and does not contain secular terms in t if and only if the coefficient of the term $\exp(it)$ is zero[1]. This implies that the function $C(\eta)$ satisfies the ordinary differential equation

$$2i \frac{\mathrm{d}C}{\mathrm{d}\eta} + C^* + \delta C = 0. \tag{8.17}$$

Finally, by separating the real and imaginary parts of $C(\eta) = a + ib$, we find that it satisfies the system

$$\frac{\mathrm{d}}{\mathrm{d}\eta} \begin{pmatrix} a \\ b \end{pmatrix} = \frac{1}{2} \begin{pmatrix} 0 & 1 - \delta \\ 1 + \delta & 0 \end{pmatrix} \begin{pmatrix} a \\ b \end{pmatrix}. \tag{8.18}$$

[1]Take the linear second-order ODE $\ddot{y} + y = \exp(ait)$ with $a \in \mathbb{R}$. The solutions of the homogeneous equation are a superposition of a sine and a cosine. A particular solution when $a \neq \pm 1$ is a periodic $y(t) = \exp(ait)/(1 - a^2)$, whereas when $a = \pm 1$, a particular solution $y(t) = \exp(it)(1 - 2it)/4$ always contain a secular term, and is therefore non-periodic. The purpose of the multi-scale analysis is precisely to remove this secular term from the expansion.

The eigenvalues of this matrix equation are $\lambda = \pm\sqrt{1-\delta^2}/2$, and the function $C(\eta)$ governing the long-time evolution is proportional to $\exp(\pm\lambda\eta) = \exp(\pm\mu t)$ in which

$$\mu = \frac{q}{2}\sqrt{1-\delta^2} \tag{8.19}$$

is also known as the *Floquet coefficient*. This result implies that at leading order in $q \ll 1$, the solution is

- periodic if $\mu = 0$, hence when $|\delta| = 1$ or equivalently when $A = 1 + q$
- stable if μ is imaginary, hence when $|\delta| > 1$ or equivalently when $A > 1 + q$
- unstable if μ is real, hence when $|\delta| < 1$ or equivalently when $A < 1 + q$

In Chapter 9, I am interested in the unstable solution, when $A \approx 1$, in which case the coefficient μ is proportional to q

$$\mu = \frac{q}{2}. \tag{8.20}$$

Chapter 9

Primordial black holes from metric preheating

This chapter is a reproduction of Ref. [57] written in collaboration with Vincent Vennin. The aim of this article was to extend the calculation of the PBH mass function during the preheating instability in Ref. [430], of which Vincent Vennin was one of the authors. Indeed, the analysis carried out in Ref. [430] showed that the production of ultra-light PBHs from this instability is so efficient that they can quickly come to dominate the universe content, finding that the fraction of the total energy budget that is comprised inside PBHs, is larger than one. This clearly signals an inconsistency and the authors of the article had to include renormalization procedures to cope with this issue. In the present article, we show that this issue is due to the technique used to calculate the mass fraction, limited to narrow distributions; and use the *excursion-set* formalism to calculate the mass fraction. This work makes use of much of the experience I gained during my research internship in 2017 with Gilles Chabrier at the University of Exeter on the *excursion-set* formalism but applied to the formation of stars and clouds in the galaxy.

Abstract

We calculate the mass distribution of Primordial Black Holes (PBHs) produced during metric preheating. After inflation, the oscillations of the inflaton at the bottom of its potential source a parametric resonant instability for small-scale scalar perturbations, that may collapse into black holes. After reviewing pedagogically different techniques that have been developed in the literature to compute mass distributions of PBHs, we focus on the excursion-set approach. We derive a Volterra integral equation that is free of a singularity sometimes encountered, and apply it to the case of metric preheating. We find that if the energy density at which the instability stops, ρ_Γ, is sufficiently smaller than the one at which inflation ends, $\rho_{\rm end}$, namely if $\rho_\Gamma^{1/4}/\rho_{\rm end}^{1/4} < 10^{-5}(\rho_{\rm end}^{1/4}/10^{16}{\rm GeV})^{3/2}$, then PBHs dominate the universe content at the end of the oscillatory phase. This confirms the previous analysis of Ref. [430]. By properly accounting for the "cloud-in-cloud" mechanism, we find that the mass distribution is more suppressed at low masses than previously thought, and peaks several orders of magnitude above the Hubble mass at the end of inflation. The peak mass ranges from 10 g to stellar masses, giving rise to different possible cosmological effects that we discuss.

9.1 Introduction

Since Primordial Black Holes (PBHs) were proposed almost 50 years ago [382, 383], it has been realized that they can be relevant in various aspects of cosmology, ranging from dark matter [384] and the generation of large-scale structures through Poisson fluctuations [385, 386] to the seeding of supermassive black holes in galactic nuclei [387, 388]. More recently, they have attracted even more attention as it was pointed out that they may account for the progenitors of the black-hole merging events detected by the LIGO/Virgo collaboration [389] through their gravitational wave emission, see *e.g.* Refs. [390, 391]. There are several observational bounds that constrain the abundance of PBHs in various mass ranges (for a recent review, see *e.g.* Ref. [393]).

PBHs are expected to form when large density fluctuations re-enter the Hubble radius and collapse into black holes. Their abundance is usually computed by assuming that they are rare objects that are formed at around a single scale, and the probability that a given region of the universe ends up in a black hole can be inferred from the knowledge of the primordial curvature power spectrum at that scale. Such an approach may however fail in cases where PBHs are abundantly produced, and/or if they arise over a wide range of masses. This could notably be the case for PBHs with masses smaller than 10^9 g, which Hawking evaporate before big-bang nucleosynthesis and are therefore not limited by observational constraints.

A prototypical example of a mechanism leading to such ultra-light, yet extremely abundant, PBHs, is the parametric instability of single-field metric preheating [427, 428] (see Ref. [431] for multiple-field setups). After inflation, the oscillations of the inflaton at the bottom of its potential source a parametric instability in the equation of motion of scalar perturbations, that are enhanced on small scales. In Ref. [430], it was shown that the production of ultra-light PBHs from this instability is so efficient that they can quickly come to dominate the universe content, such that reheating no longer occurs because of the inflaton decay, but rather through PBHs evaporation.

Although these conclusions lead to a substantial change in the cosmological scenario, they were however reached by employing the usual estimate for PBH abundance, whose usage is questionable in contexts in which PBHs are abundant. The goal of this paper is to re-examine this calculation, in the light of more refined techniques that were originally proposed for large-scale structures but that can (and have) also be applied to PBHs. This will allow us to investigate generic properties of the expected mass distribution of ultra-light black holes, in regimes in which they densely populate the primordial universe.

This could have important consequences for various physical phenomena associated to those black holes. For instance, it was recently shown [432] that gravitational waves induced at second order by the gravitational potential underlain by ultra-light PBHs lead to a stochastic background that might be detected in future gravitational-wave experiments, and that is even already excluded in some regimes. Since the amplitude and frequency coverage of this background strongly depend on the details of the mass distribution of PBHs, it seems important to derive robust predictions for the scenarios in which they are produced.

The rest of this paper is organized as follows. In Section 9.2, we briefly describe the mechanism of metric preheating and the production of PBHs that is associated to it. In Section 9.3, we review the different techniques that have been proposed to compute the abundance of objects formed from gravitational collapse. Our main goal is to identify those that are best suited to the problem at hand, but we also designed this section as a pedagogical introduction to the calculation of the mass fraction, trying to highlight some aspects that are often left implicit. This section may however be skipped by readers already familiar with the topic. In Section 9.4, we apply one of the methods

introduced in Section 9.3, namely the excursion-set approach, to the calculation of the mass fraction of PBHs arising from metric preheating. We finally present our conclusions in Section 9.5, and the paper ends with several appendices where various technical aspects of the calculation are deferred.

9.2 Metric preheating

In this section, we briefly review the physics of metric preheating. More details can be found in Refs. [427, 433, 430, 434]. If a homogeneous and isotropic universe, described by the Friedmann-Lemaître-Robertson-Walker metric $\mathrm{d}s^2 = -\mathrm{d}t^2 + a^2(t)\mathrm{d}x^2$ where a is the scale factor, is dominated by a single scalar field ϕ, scalar perturbations are described by a single gauge-invariant combination of fluctuations in the scalar field and in the metric components, the so-called Mukhanov-Sasaki variable [435, 436]. Its equation of motion in Fourier space is given by [437]

$$v_{\boldsymbol{k}}'' + \left[k^2 - \frac{\left(a\sqrt{\epsilon_1}\right)''}{a\sqrt{\epsilon_1}}\right] v_{\boldsymbol{k}} = 0\,. \tag{9.1}$$

In this expression, a prime denotes derivative with respect to conformal time η (related to cosmic time via $\mathrm{d}t = a\mathrm{d}\eta$), and $\epsilon_1 = -\dot{H}/H^2$ is the first slow-roll parameter, where $H = \dot{a}/a$ is the Hubble parameter. If the inflaton ϕ oscillates at the bottom of a quadratic potential $V(\phi) = m^2\phi^2/2$,[1] the scale factor undergoes oscillations too (superimposed to an average matter-like behaviour), and Eq. (9.1) can be put in the form [427]

$$\frac{\mathrm{d}^2}{\mathrm{d}z^2}\left(\sqrt{a}v_{\boldsymbol{k}}\right) + \left[A_{\boldsymbol{k}} - 2q\cos(2z)\right]\left(\sqrt{a}v_{\boldsymbol{k}}\right) = 0\,, \tag{9.2}$$

with

$$A_{\boldsymbol{k}} = 1 + \frac{k^2}{m^2a^2}, \quad q = \frac{\sqrt{6}}{2}\frac{\phi_{\mathrm{end}}}{M_{\mathrm{pl}}}\left(\frac{a_{\mathrm{end}}}{a}\right)^{3/2}\,. \tag{9.3}$$

In those expressions, a_{end} and ϕ_{end} are the values of a and ϕ at the onset of the oscillating phase, *i.e.* at the end of inflation, M_{pl} is the reduced Planck mass, and $z \equiv mt + \pi/4$.

If $A_{\boldsymbol{k}}$ and q were constant, this equation would be of the Mathieu type, and it would feature parametric resonant instabilities when $A_{\boldsymbol{k}}$ and q fall into the instability bands. In Ref. [427] (see also Ref. [434] where the perturbative decay of the inflaton is included in the analysis), the time dependence of $A_{\boldsymbol{k}}$ and q is shown to be sufficiently slow to be considered as adiabatic, and the resonant instability takes place when $A_{\boldsymbol{k}}$ and q cross the instability bands. At the end of inflation, the displacement of the field away from the minimum of its potential is typically of order the Planck mass, so Eq. (9.3) indicates that q starts out being of order one and quickly decreases afterwards. This means that one falls into the regime of "narrow resonance", $q \ll 1$, in which the boundaries of the first instability band are given by $1 - q < A_{\boldsymbol{k}} < 1 + q$, which here translates into

$$k < a\sqrt{3Hm}. \tag{9.4}$$

Since the universe behaves as matter-dominated during the oscillatory phase, $a\sqrt{H} \propto a^{1/4}$, the upper bound (9.4) increases with time, and the range of modes subject to the instability widens as

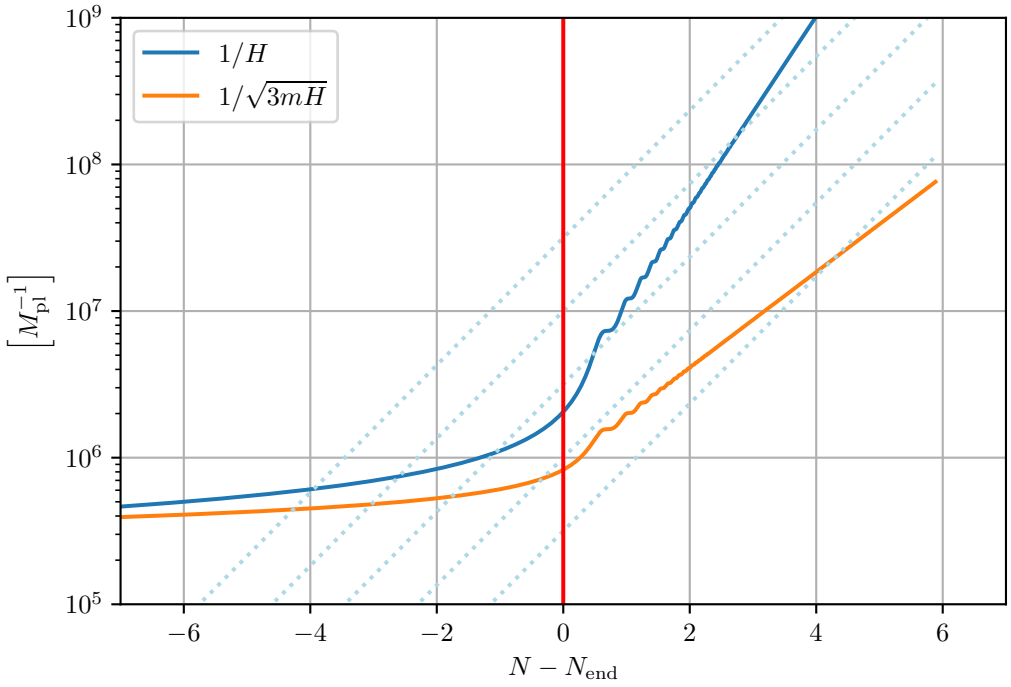

Figure 9.1: Evolution of the physical scales appearing in Eq. (9.6), with time parametrised by the number of e-fold $N = \ln a$ (counted from the end of inflation). The blue line represents the Hubble radius $1/H$, the orange line the new length scale $1/\sqrt{3Hm}$ and the dotted lines the physical wavelengths of modes of interest, which may enter the instability band after inflation, during the oscillatory phase. Here the Klein-Gordon equation for the inflaton field has been solved for the quadratic potential $V(\phi) = m^2\phi^2/2$, where $m = 10^{-6}M_{\rm pl}$.

time proceeds. Inside the first instability band, the Floquet index of the unstable mode is given by $\mu_{\boldsymbol{k}} \simeq q/2$, so $v_{\boldsymbol{k}} \propto a^{-1/2}\exp\left(\int \mu_{\boldsymbol{k}} \mathrm{d}z\right) \propto a$ [438, 427].

Note that during the oscillatory phase, $H \ll m$, so the upper bound in Eq. (9.4) corresponds to a sub-Hubble scale. As a consequence, the modes subject to the instability are (i) all super-Hubble modes and (ii) those sub-Hubble modes such that $aH < k < a\sqrt{3Hm}$. For super-Hubble modes, the fact that $v \propto a$ implies that the curvature perturbation is simply conserved, which is a well-know result [435, 436], and the dynamics of super-Hubble scales is therefore not affected by the oscillations. For sub-Hubble scales however, in a matter-dominated background, the overdensity $\delta = \delta\rho/\bar{\rho}$ (where $\bar{\rho}$ is the energy density of the background) is related to the Mukhanov-Sasaki variable via $\delta_{\boldsymbol{k}} \propto [k/(aH)]^2 v_{\boldsymbol{k}}/(aM_{\rm pl})$ (notice that, at sub-Hubble scales, there is no gauge ambiguity in the

[1] As the amplitude of the oscillations get damped, the leading order in a Taylor expansion of the function $V(\phi)$ around its minimum quickly dominates, which yields a quadratic potential unless there is an exact cancellation at that order.

definition of the density contrast, see Section 9.3.7 for further details), so the fact $v_{\boldsymbol{k}} \propto a$ implies that

$$\delta_{\boldsymbol{k}} \propto a\,, \tag{9.5}$$

and the density contrast grows inside the band

$$aH < k < a\sqrt{3Hm}. \tag{9.6}$$

The scales appearing in this relation are displayed in Fig. 9.1. An instability is triggered if the physical wavelength of a mode (dotted line) is smaller than the Hubble radius (blue line) during the oscillatory phase and larger than the new scale $1/\sqrt{3Hm}$ (orange line). Let us note that this implies that the instability only concerns modes that are inside the Hubble radius at the end of the oscillatory phase, which is not the case for the scales probed in the Cosmic Microwave Background (CMB).

The behaviour (9.5) signals that inside the resonance band, scalar-field inhomogeneities behave as pressure-less matter fluctuations in a pressure-less matter universe. As a consequence, an over-density δ_R over the length scale R eventually collapses into a PBH, and in Ref. [439] (see also appendices A and B of Ref. [430]), it is shown that this occurs after a time

$$\Delta t_{\rm collapse} = \frac{\pi}{H\left[t_{\rm bc}(R)\right]\delta_R^{3/2}\left[t_{\rm bc}(R)\right]}, \tag{9.7}$$

where $t_{\rm bc}(R)$ denotes the "band-crossing" time, *i.e.* the time at which the scale R crosses in the instability band (9.6). Assuming that the instability ends when the Hubble scale reaches a certain value that we denote H_Γ,[2] at a time t_Γ, a black hole forms if $t_{\rm end} + \Delta t_{\rm collapse} < t_\Gamma$, which leads to a lower bound on the density contrast, namely

$$\delta_R[t_{\rm bc}(R)] > \left(\frac{3\pi}{2}\right)^{2/3}\left[\frac{H_{\rm bc}(R)}{H_\Gamma} - 1\right]^{-2/3}. \tag{9.8}$$

One then has to assess the probability that the condition (9.8) is fulfilled in a given patch of size R in the universe, in order to compute the abundance of PBHs at every scale. This problem corresponds to the calculation of the mass fraction of PBHs, which we describe in the next section.

9.3 Computation of the mass fraction

The calculation of the mass fraction of gravitationally-formed objects has received much attention over the last decades, and in this section we describe the main tools that have been developed to address it. While our goal is primarily to identify those that are best suited to the problem at hand in this work, we hope to also clarify the main assumptions that these approaches rest on, and how they are connected together. This section is therefore rather independent of the rest of this article (and is not specific to metric preheating), and while it may serve as a pedagogical introduction to calculations of the mass fraction, it can also be skipped by readers already familiar with these techniques.

In general, cosmological fluctuations can be characterized in terms of an over-density field $\delta(\boldsymbol{x})$. In practice, the precise realization of this field is not known, and one can only predict its statistical

[2] This could correspond for instance to the time when H drops below Γ, the decay rate of the inflaton into other degrees of freedom, in the context of perturbative reheating [440, 441, 442] (hence the notation).

properties (for instance, if the field is Gaussian, its is fully characterized by its power spectrum). The problem can thus be divided into two parts. Given a certain realization of the density field in real space, a first question is to identify the regions where the field will collapse into a certain type of astrophysical object. Second, given the statistical properties of the field, one has to work out the probability that such objects form, and the mass distribution associated to them.

The first question is a very delicate one, and little can be learnt about it analytically without resorting to some approximations. The problem can also be tackled numerically, see Section 9.3.6 below. Most of the time, it is assumed that a region where the field collapses is one in which the mean density is larger than some threshold value $\delta_{\rm c}$, that may depend on the size of that region (as well as its shape, the details of its surrounding, etc.). In practice, one coarse-grains the field δ over a spherical region of radius R about the point $\boldsymbol{x}$,

$$\delta_R(\boldsymbol{x}) \equiv \left(\frac{a}{R}\right)^3 \int \mathrm{d}\boldsymbol{y}\delta(\boldsymbol{y}) W\left(\frac{a\left|\boldsymbol{y}-\boldsymbol{x}\right|}{R}\right), \tag{9.9}$$

and the collapse criterion is often assumed to be of the form $\delta_R > \delta_{\rm c}(R)$. In the above expression, W is a window function such that $W(x) \simeq 1$ if $x \ll 1$ and $W(x) \simeq 0$ if $x \gg 1$, and normalized in the sense that $4\pi\int_0^\infty x^2 W(x)\mathrm{d}x = 1$, such that after coarse graining, a constant field remains a constant field of the same value (here $\boldsymbol{x}$ and $\boldsymbol{y}$ are comoving spatial coordinates, while R denotes a physical distance, notations are summarized in Table 9.1 for clarity).

The second question is then a well-posed one, and consists in computing the probability that the collapse criterion is satisfied, and the distribution in sizes R (or in resulting mass M) of the regions where this is the case, knowing the statistics of the random field δ.

9.3.1 The Press-Schechter formalism

A first approach was developed in 1974 by William H. Press and Paul Schechter in Ref. [443] and proceeds as follows. From Eq. (9.9), the Fourier transform of the coarse-grained density perturbation is given by

$$\delta_R(\boldsymbol{k}) = \delta(\boldsymbol{k}) \underbrace{4\pi\left(\frac{a}{kR}\right)^3 \int_0^\infty W\left(\frac{a}{kR}u\right)\sin(u)u\mathrm{d}u}_{\widetilde{W}\left(\frac{kR}{a}\right)}, \tag{9.10}$$

which defines $\widetilde{W}$, that shares similar properties to W. Indeed, when $a/(kR) \gg 1$, the values of u such that $W\left(\frac{a}{kR}u\right)$ is not close to zero are much smaller than one, so one can replace $\sin(u) \simeq u$ in the integral over u, and using the normalization condition stated above, one obtains $\widetilde{W}\left[kR/a\right] \simeq 1$ in that limit. In the opposite limit, when $a/(kR) \ll 1$, since $W \simeq 1$ until $u \sim kR/a$, the integral over u in Eq. (9.10) is of order kR/a, hence $\widetilde{W}\left[kR/a\right] \propto \left[a/(kR)\right]^2 \ll 1$.[3]

[3]The details of $\widetilde{W}$ between these two limits depend on those of W. For instance, if W is a Heaviside step function,

$$W(x) = \frac{3}{4\pi}\theta(1-x), \tag{9.11}$$

where $\theta(x) = 1$ if $x > 0$ and 0 otherwise, and where the pre-factor is set in such a way that the normalization condition is satisfied, Eq. (9.10) gives rise to

$$\widetilde{W}\left(\frac{kR}{a}\right) = 3\left(\frac{a}{kR}\right)^3\left[\sin\left(\frac{kR}{H}\right) - \frac{kR}{H}\cos\left(\frac{kR}{a}\right)\right], \tag{9.12}$$

Notation	Definition
$\delta(\boldsymbol{x})$	Density contrast field on a space slice
$\delta_{\boldsymbol{k}}$	Fourier transform of the density contrast
$\delta_R(\boldsymbol{x})$	Density contrast averaged over a patch of (physical) size R, around (comoving) $\boldsymbol{x}$
$\sigma_R^2 = S = \langle \delta_R^2(\boldsymbol{x}) \rangle$	Variance of $\delta_R(\boldsymbol{x})$ seen as a stochastic variable, also used to label R
$\delta_{\rm c}(R)$ [or $\delta_{\rm c}(S)$]	Collapse criterion over a patch of size R (or with variance S)
$\delta_{\rm D}$	Dirac delta distribution
$P_\delta(k)$	Power spectrum of the density contrast
$\mathcal{P}_\delta(k) = k^3 P_\delta(k)/(2\pi^2)$	Reduced power spectrum of the density contrast

Table 9.1: Definitions and notations.

The power spectrum of δ, P_δ, is defined as

$$\langle \delta(\boldsymbol{k}) \delta^*(\boldsymbol{k}') \rangle = P_\delta(k) \delta_{\rm D}(\boldsymbol{k} - \boldsymbol{k}') = \frac{2\pi^2}{k^3} \mathcal{P}_\delta(k) \delta_{\rm D}(\boldsymbol{k} - \boldsymbol{k}') \,, \tag{9.13}$$

where $\delta_{\rm D}$ is the Dirac distribution, and which also defines the reduced power spectrum $\mathcal{P}_\delta$. The power spectrum of the coarse-grained density field, $P_{\delta_R}(k)$, is defined through a similar relation, and Eq. (9.10) implies that $P_{\delta_R}(k) = P_\delta(k) \widetilde{W}^2(kR/a)$. This allows one to express the coincident two-point function of the coarse-grained density field as

$$\sigma_R^2 \equiv \langle \delta_R^2(\boldsymbol{x}) \rangle = \int_0^\infty \mathcal{P}_\delta(k) \widetilde{W}^2 \left(\frac{kR}{a} \right) \frac{{\rm d}k}{k} \,. \tag{9.14}$$

If δ has Gaussian statistics, so does δ_R since the two are linearly related via Eq. (9.10), hence the probability density function associated to δ_R reads

$$P\left(\delta_R\right) = \frac{e^{-\frac{\delta_R^2}{2\sigma_R^2}}}{\sqrt{2\pi\sigma_R^2}} \,. \tag{9.15}$$

This allows one to express the probability that a given region of size R lies above the threshold,

$$P\left[\delta_R > \delta_{\rm c}(R)\right] = \int_{\delta_{\rm c}(R)}^\infty P(\delta_R) {\rm d}\delta_R = \frac{1}{2} {\rm erfc} \left[\frac{\delta_{\rm c}(R)}{\sqrt{2}\sigma_R} \right] \,. \tag{9.16}$$

An important remark is that when a given region of size R has an average density above the threshold, it ends up inside a structure, the size of which has to be equal *or larger* than R (for instance if δ_R is much larger than $\delta_{\rm c}(R)$, by averaging over a slightly larger distance $R' > R$, one may still find $\delta_{R'} > \delta_{\rm c}(R')$, which indicates that the size of the resulting structure is at least R'). Therefore, the above probability is the one to lie inside structures of size *at least* R.

which verifies the two limits given in the main text. Conversely, one can set W such that $\widetilde{W}$ is a Heaviside step function [*i.e.* W is of a similar form as Eq. (9.12)], and one then has $\delta_R(\boldsymbol{x}) = (2\pi)^{-3/2} \int_{k<a/R} {\rm d}\boldsymbol{k}\, \delta_{\boldsymbol{k}} e^{i\boldsymbol{k}\cdot\boldsymbol{x}}$.

This naturally leads us to the notion of mass fraction $\beta(M)$, defined such as $\beta(M)\mathrm{d}\ln M$ corresponds to the fraction of the universe that is comprised in structures of masses between M and $M+\mathrm{d}M$. By construction, $\int_M^\infty \beta(\tilde{M})\mathrm{d}\ln\tilde{M}$ corresponds to the fraction of the universe made of structures of sizes larger than M. Since there is a one-to-one correspondence between M and R ($M=4\pi\bar{\rho}R^3/3$ at leading order in perturbations), this is nothing but the probability computed in Eq. (9.16). By differentiating both expressions with respect to M, one obtains

$$\beta(M) = -M\frac{\partial R}{\partial M}\frac{\partial}{\partial R}P\left[\delta_R > \delta_\mathrm{c}(R)\right]. \tag{9.17}$$

Making use of Eq. (9.16), this gives rise to

$$\beta(M)\mathrm{d}\ln M = -\left(\frac{1}{2}\frac{\delta_\mathrm{c}}{\sigma_R^2} - \frac{\partial\delta_\mathrm{c}}{\partial\sigma_R^2}\right)\frac{e^{-\frac{\delta_\mathrm{c}^2}{2\sigma_R^2}}}{\sqrt{2\pi\sigma_R^2}}\mathrm{d}\sigma_R^2, \tag{9.18}$$

where we give the result in terms of σ_R^2 for future convenience. In particular, one finds that the abundance of objects is exponentially suppressed when σ_R is smaller than $\delta_\mathrm{c}(R)$.

Although rather straightforward, this approach is however plagued with the following issue. Consider a region of size R centred on a given point $\boldsymbol{x}$, such that the criterion $\delta_R > \delta_\mathrm{c}(R)$ is *not* satisfied. According to the above considerations, that region is not part of any structure, since it is excluded from Eq. (9.16). However, it could happen that if one considers another radius $R' > R$, the criterion $\delta_{R'} > \delta_\mathrm{c}(R')$ is satisfied, hence the region of size R is comprised inside a larger region that does collapse into a structure, which contradicts the fact that it is not part of any. This issue is often referred to as the "cloud-in-cloud problem", and leads to underestimating the number of structures. It can also be seen by considering the limit $\delta_\mathrm{c}(R) \to 0$, in which the entire universe should end up in structures. However, letting $\delta_\mathrm{c} = 0$ in Eq. (9.16) leads to only half of the universe lying in collapsed structures. For this reason, the Press-Schechter result is often simply multiplied by 2. In the following, we will see how to go beyond this approach, and in which cases the Press-Schechter result (with or without the factor 2) provides a good approximation.

9.3.2 The excursion-set approach

In 1990, Peacock and Heavens proposed in Ref. [444] to solve the cloud-in-cloud problem of the Press-Schechter formalism using an excursion set approach. They were soon followed in 1991 by Bower, see Ref. [445], and by Bond, Cole and Efstathiou, see Ref. [446].

The idea is to view δ_R as a random variable. When R is very large, recalling that $\widetilde{W}(x) \simeq 0$ when $x \gg 1$, only a small number of modes contribute to Eq. (9.14) (namely those for which $k < a/R$), hence σ_R is small. In the limit $R \to \infty$, the distribution function (9.15) thus asymptotes a Dirac distribution centred around zero. Starting from $\delta_R = 0$ at $R = \infty$, one can then make R decrease. To be explicit, let us consider the case where $\widetilde{W}$ is a Heaviside function,[4] and

$$\delta_R(\boldsymbol{x}) = (2\pi)^{-3/2}\int_{k<\frac{a}{R}}\mathrm{d}\boldsymbol{k}\,\delta_{\boldsymbol{k}}e^{i\boldsymbol{k}\cdot\boldsymbol{x}}, \tag{9.19}$$

see footnote 3. As R decreases, more and more modes contribute to the above integral. Each of these modes takes a random realization, so δ_R, seen as a function of R, follows a stochastic,

[4] In the case where $\tilde{W}$ is taken as a smooth function of the wavenumber, the random noise appearing in the Langevin equation (9.22) becomes coloured, which makes the analysis more involved [447, 448].

Langevin equation, which can be obtained as follows. Between the "times" R and $R-\Delta R$, the variation in δ_R is given by

$$\delta_{R-\Delta R}(\boldsymbol{x}) - \delta_R(\boldsymbol{x}) = (2\pi)^{-3/2} \int_{\frac{a}{R}<k<\frac{a}{R-\Delta R}} \mathrm{d}\boldsymbol{k}\, \delta_{\boldsymbol{k}} e^{i\boldsymbol{k}\cdot\boldsymbol{x}}\,. \tag{9.20}$$

Given that $\langle\delta(\boldsymbol{k})\rangle$ vanishes, and since the two-point function of $\delta(\boldsymbol{k})$ is given by Eq. (9.13), one finds that $\langle\delta_{R-\Delta R}(\boldsymbol{x}) - \delta_R(\boldsymbol{x})\rangle = 0$ and that $\langle[\delta_{R-\Delta R}(\boldsymbol{x}) - \delta_R(\boldsymbol{x})]^2\rangle = \mathcal{P}_\delta(a/R)\Delta R/R$, at leading order in ΔR. This leads to the Langevin equation

$$\frac{\mathrm{d}\delta_R(\boldsymbol{x})}{\mathrm{d}R} = \sqrt{\frac{\mathcal{P}_\delta(a/R)}{R}}\xi(R)\,, \tag{9.21}$$

where ξ is a white Gaussian noise with vanishing mean and unit variance, *i.e.* $\langle\xi(R)\rangle = 0$ and $\langle\xi(R)\xi(R')\rangle = \delta_{\mathrm{D}}(R-R')$, and one should stress that R is a decreasing variable. Since Eq. (9.14) relates R and σ_R^2 monotonously, the Langevin equation is sometimes written with $S \equiv \sigma_R^2$ as the "time" variable, leading to the particularly simple form

$$\frac{\mathrm{d}\delta_R(\boldsymbol{x})}{\mathrm{d}S} = \xi(S)\,, \tag{9.22}$$

where $\xi(S)$ is a white Gaussian noise normalized with respect to S, and where S is an increasing variable.

Starting from $S=0$ (or equivalently, $R=\infty$), the first "time" (*i.e.* the largest radius R) when δ_R crosses the collapse threshold δ_{c} corresponds to the size of the largest structure surrounding $\boldsymbol{x}$. The calculation thus boils down to solving a first-passage-time problem, for which there are various dedicated techniques in stochastic analysis. Before detailing one of them in Section 9.3.3, let us note that if, along a given realization of the Langevin process (9.22), δ_R crosses $\delta_{\mathrm{c}}(R)$ multiple times, then there are as many substructures, but by considering the first crossing time, *i.e.* the largest structure, one accounts for the "cloud-in-cloud" mechanism described in Section 9.3.1.[5] The distribution of first crossing times, denoted $P_{\mathrm{FPT}}(S)$ hereafter, thus gives the size (hence mass) distribution of structures, according to[6]

$$\beta(M)\mathrm{d}\ln M = -P_{\mathrm{FPT}}(S)\mathrm{d}S\,. \tag{9.24}$$

In this expression, the relationship between $M = 4\pi R^3/3$ and $S = \sigma_R^2$ is given by the link between R and σ_R^2, that is to say by Eq. (9.14), which depends on the initial statistics of the density field.

9.3.3 Volterra integral equations

The first-passage-time problem associated to Eq. (9.22) can be solved by means of a Volterra integral equation, that we derive in this section. We first note that in the absence of any boundary condition,

[5] The distribution of substructures can also be worked out by solving the "two-barrier problem" [449], *i.e.* by deriving the probability that, after upcrossing the threshold $\delta_{\mathrm{c}}(R_1)$ at $R=R_1$, a second upcrossing of $\delta_{\mathrm{c}}(R_2)$ occurs at R_2.

[6] By comparing Eqs. (9.18) and (9.24), one can see that the distribution of first crossing times that would be associated to the Press-Schechter result is given by

$$P_{\mathrm{FPT}}^{\mathrm{PS}}(S) = \left[\frac{1}{2}\frac{\delta_{\mathrm{c}}(S)}{S} - \delta_{\mathrm{c}}'(S)\right]\frac{e^{-\frac{\delta_{\mathrm{c}}^2(S)}{2S}}}{\sqrt{2\pi S}}\,. \tag{9.23}$$

the solution to (the Fokker-Planck equation associated to) Eq. (9.22) is of the Gaussian form

$$P_{\rm free}(\delta_R, S; \delta_{R,\rm in}, S_{\rm in}) = \frac{1}{\sqrt{2\pi\,(S-S_{\rm in})}} \exp\left[-\frac{(\delta_R-\delta_{R,\rm in})^2}{2\,(S-S_{\rm in})}\right], \tag{9.25}$$

which denotes the probability density that the coarse-grained density contrast takes value δ_R at time S, given that at initial "time" $S_{\rm in}$, its value is $\delta_{R,\rm in}$. Since it depends only on $S-S_{\rm in}$ and $\delta_R-\delta_{R,\rm in}$, hereafter it will be noted as $P(\delta_R-\delta_{R,\rm in}, S-S_{\rm in})$ for notation convenience. We also introduce $P(\delta_R, S)$, the solution to Eq. (9.22) when an absorbing boundary at $\delta_R=\delta_{\rm c}(S)$ is enforced, starting from $\delta_R=0$ at $S=0$. It represents realizations of the Langevin equation (9.22) that, at time S, have not yet crossed out the absorbing boundary. Finally, $P_{\rm FPT}(S)$ denotes the probability density associated to the time of first crossing of the boundary $\delta_{\rm c}(R)$, starting from $\delta_R=0$ at $S=0$.

At a given "time" S, any realization of the Langevin equation has either crossed out the absorbing boundary at a previous time $s<S$, or still contributes to the distribution P, so one can write

$$1 = \int_0^S P_{\rm FPT}(s){\rm d}s + \int_{-\infty}^{\delta_{\rm c}(S)} P(\delta_R, S){\rm d}\delta_R\,. \tag{9.26}$$

The link between P and $P_{\rm free}$ can be derived by noting that, at time S, P contains all realizations of $P_{\rm free}$ that have not yet crossed the boundary. In order to get $P(\delta_R)$, one should therefore subtract from $P_{\rm free}$ the probability that a given realization has crossed the boundary at a previous time, and then, from there, has moved to δ_R. In other words,

$$P(\delta_R, S) = P_{\rm free}(\delta_R, S) - \int_0^S P_{\rm FPT}(s) P_{\rm free}\left[\delta_R-\delta_{\rm c}(s), S-s\right]{\rm d}s\,. \tag{9.27}$$

Our goal is to extract $P_{\rm FPT}$ from the above two equations. This can be done by differentiating Eq. (9.26) with respect to S, and by using Eq. (9.27) to express P in terms of $P_{\rm free}$ and $P_{\rm FPT}$ only, leading to

$$\begin{aligned} P_{\rm FPT}(S) =& -\delta_{\rm c}'(S) P_{\rm free}\left[\delta_{\rm c}(S), S\right] + \delta_{\rm c}'(S)\int_0^S {\rm d}s P_{\rm FPT}(s) P_{\rm free}\left[\delta_{\rm c}(S)-\delta_{\rm c}(s), S-s\right] \\ &- \int_{-\infty}^{\delta_{\rm c}(S)} {\rm d}\delta_R \frac{\partial}{\partial S} P_{\rm free}\left(\delta_R, S\right) + \int_{-\infty}^{\delta_{\rm c}(S)} {\rm d}\delta_R P_{\rm FPT}(S) P_{\rm free}\left[\delta_R-\delta_{\rm c}(S), 0\right] \\ &+ \int_{-\infty}^{\delta_{\rm c}(S)} {\rm d}\delta_R \int_0^S {\rm d}s P_{\rm FPT}(s) \frac{\partial}{\partial S} P_{\rm free}\left[\delta_R-\delta_{\rm c}(s), S-s\right]. \end{aligned} \tag{9.28}$$

This expression contains 5 terms. The third term can be computed explicitly by making use of Eq. (9.25), and so can the fifth term (where only the integral over s remains). The fourth term features $P_{\rm free}[\delta_R-\delta_{\rm c}, 0]$, which is nothing but $\delta_{\rm D}[\delta_R-\delta_{\rm c}, 0]$, and the integral over δ_R can also be easily performed. These give rise to

$$\begin{aligned} P_{\rm FPT}(S) =& \left[\frac{\delta_{\rm c}(S)}{S} - 2\delta_{\rm c}'(S)\right] P_{\rm free}\left[\delta_{\rm c}(S), S\right] \\ &+ \int_0^S {\rm d}s \left[2\delta_{\rm c}'(S) - \frac{\delta_{\rm c}(S)-\delta_{\rm c}(s)}{S-s}\right] P_{\rm free}\left[\delta_{\rm c}(S)-\delta_{\rm c}(s), S-s\right] P_{\rm FPT}(s)\,. \end{aligned} \tag{9.29}$$

Although mathematically correct, the above expression is nonetheless flawed with a singularity that appears in the integrand of the second term, close to the upper bound of the integral, where it approaches $\delta_{\rm c}'(S)\delta_{\rm D}(0)$. This leads to numerical issues when trying to solve Eq. (9.29) iteratively, which can be dealt with by introducing an averaging procedure when $s \to S$, as proposed for instance in Ref. [450]. However, Eq. (9.29) is only one version of an infinite set of Volterra equations [451], and it can be generalized as follows. Let us consider the realizations of the Langevin equation which, at time S, lie at the position $\delta_R = \delta_{\rm c}(S)$. At time S, those realizations have necessarily already crossed the boundary, so one can write

$$P_{\rm free}\left[\delta_{\rm c}(S), S\right] = \int_0^S {\rm d}s P_{\rm free}\left[\delta_{\rm c}(S) - \delta_{\rm c}(s), S-s\right] P_{\rm FPT}(s). \tag{9.30}$$

Multiplying both hands of this equation by a generic function $K(S)$, and plugging the result into Eq. (9.29), one obtains

$$\begin{aligned} P_{\rm FPT}(S) = &\left[\frac{\delta_{\rm c}(S)}{S} - 2\delta_{\rm c}'(S) + K(S)\right] P_{\rm free}\left[\delta_{\rm c}(S), S\right] \\ &+ \int_0^S {\rm d}s \left[2\delta_{\rm c}'(S) - \frac{\delta_{\rm c}(S)-\delta_{\rm c}(s)}{S-s} - K(S)\right] P_{\rm free}\left[\delta_{\rm c}(S) - \delta_{\rm c}(s), S-s\right] P_{\rm FPT}(s)\,. \end{aligned} \tag{9.31}$$

Let us stress that this relation is valid for any function $K(S)$. In particular, by setting $K(S) = \delta_{\rm c}'(S)$, one gets rid of the above-mentioned singularity, leading to

$$\begin{aligned} P_{\rm FPT}(S) = &\left[\frac{\delta_{\rm c}(S)}{S} - \delta_{\rm c}'(S)\right] P_{\rm free}\left[\delta_{\rm c}(S), S\right] \\ &+ \int_0^S {\rm d}s \left[\delta_{\rm c}'(S) - \frac{\delta_{\rm c}(S)-\delta_{\rm c}(s)}{S-s}\right] P_{\rm free}\left[\delta_{\rm c}(S) - \delta_{\rm c}(s), S-s\right] P_{\rm FPT}(s)\,. \end{aligned} \tag{9.32}$$

This allows one to compute $P_{\rm FPT}(S)$ iteratively, by discretizing the S variable and starting from $P_{\rm FPT} = 0$ at $S = 0$. See Appendix 9.A for more details. In Eq. (9.32), recall that $P_{\rm free}$ is given by Eq. (9.25), and the function $\delta_{\rm c}(S)$, as well as the link between S and R (the physical scale at which the density contrast is coarse grained), are given by the physical details of the problem under consideration.

9.3.4 Relation between the Press-Schechter and excursion-set formalisms

The excursion-set approach is an extension of the Press-Schechter formalism, that incorporates the cloud-in-cloud mechanism, and allows for multiple crossings of the threshold value. In this section, in order to clarify the link between the two approaches, we discuss two limiting cases where the excursion set yields a result closely related to the one obtained with the Press-Schechter formalism.

Scale-invariant threshold

When the formation threshold, $\delta_{\rm c}(R)$, does not depend on the scale R, the excursion-set approach greatly simplifies. Indeed, in Eq. (9.32), the kernel of the integral term vanishes in that limit, so the Volterra implicit equation becomes an explicit formula for the first-passage-time distribution, namely

$$P_{\rm FPT}(S) = \frac{\delta_{\rm c}}{S} P_{\rm free}\left(\delta_{\rm c}, S\right) = \frac{\delta_{\rm c}}{S} \frac{e^{-\frac{\delta_{\rm c}^2}{2S}}}{\sqrt{2\pi S}}\,, \tag{9.33}$$

where, in the second equality, Eq. (9.25) has been used. One thus recovers Eq. (9.23) exactly, with an additional factor 2. This proves that the Press-Schechter formula, corrected by the factor 2 (the origin of which is left rather heuristic in the Press-Schechter approach, see the discussion at the end of Section 9.3.1), becomes exact in the case of a scale-invariant threshold.

Very red threshold

Another limit of interest is the situation in which the threshold quickly decreases as the scale R decreases. In this case, multiple crossing events become unlikely since after the threshold is crossed for the first time, its value swiftly decays away from the realization of the overdensity. One therefore expects the Press-Schechter formula (without the additional factor 2) to be recovered in this regime.

More precisely, this limit can be studied by introducing the rescaled stochastic variable $\hat{\delta}_R(S) \equiv \delta_R(S)/\delta_{\rm c}(S)$, which follows a Langevin equation with a drift term, $\mathrm{d}\hat{\delta}_R/\mathrm{d}S = -(\delta_{\rm c}'/\delta_{\rm c})\hat{\delta}_R + \xi/\delta_{\rm c}$, but with a time-independent threshold since by construction $\hat{\delta}_{\rm c} = 1$. The "very-red-threshold" limit thus corresponds to the regime in which the drift term dominates over the noise term in this rescaled Langevin equation (conversely, the limit investigated in Section 9.3.4 corresponds to when the noise dominates over the drift).

However, given that, over an infinitesimal time increment ΔS, the drift contribution scales as ΔS while the typical noise contribution scales as $\sqrt{\Delta S}$, the drift term cannot dominate for arbitrarily small time resolutions. In other words, multiple, repeated crossings are inevitable, and one can only require that they happen within a certain finite time interval, below which we do not try to resolve the distribution of first crossing times. Denoting $\epsilon = \Delta \ln R$ the time resolution one requires [since the mass distribution is usually expressed in $\ln(M)$ units, in practice, one imposes a fixed resolution on $\ln(M)$ or equivalently on $\ln(R)$], the very-red limit can thus be mathematically expressed by requiring that

$$\forall R_1, R_2 \text{ such that } \ln\left(\frac{R_1}{R_2}\right) > \epsilon, \delta_{\rm c}(R_1) - \delta_{\rm c}(R_2) \gg \sqrt{S(R_2) - S(R_1)}. \tag{9.34}$$

Notice that for practical purposes, it may be enough to satisfy this criterion at the scales R where the mass function is substantial (unless one wants to resolve the tails properly).

In order to see that Eq. (9.34) leads to the Press-Schechter formula, the integral over $s \in [0, S]$ appearing in Eq. (9.32) can be split into an integral over $[0, S-\eta]$ and an integral over $[S-\eta, S]$, where η is the width of the region where the term $P_{\rm free}$ does not lead to an exponential suppression of the integral. From Eq. (9.25), it is order $(\delta_{\rm c}')^{-2}$, hence it is small in the very-red-threshold limit. It is also related to the ϵ-smoothing scale in S-units [so η is of order $\epsilon \partial S/\partial \ln R = \epsilon \mathcal{P}_\delta(k = a/R)$]. In the first integral, the criterion (9.34) implies that $P_{\rm free}$ exponentially suppresses the integrand, while the second integral is also negligible since the integrand vanishes when $s \to S$ (hence the second integral is of order η^2). Let us now consider the first term in Eq. (9.32). Since $\delta_{\rm c}(S)$ is a decreasing function of S in the regime of interest, the term $P_{\rm free}[\delta_{\rm c}(S), S] \sim e^{-\delta_{\rm c}^2(S)/S}$ does not lead to exponential suppression only for large enough values of S such that $S \gtrsim \delta_{\rm c}^2(S)$, which implies that $\delta_{\rm c}/S \lesssim 1/\sqrt{S}$. Since Eq. (9.34) states that $1/\sqrt{\Delta S} \ll |\delta_{\rm c}'|$, this entails that $\delta_{\rm c}/S \ll |\delta_{\rm c}'|$, hence Eq. (9.32) reduces to $P_{\rm FPT}(S) \simeq -\delta_{\rm c}'(S) P_{\rm free}[\delta_{\rm c}(S), S]$, which matches the Press-Schechter formula (9.23) in the same limit and without the factor 2, as announced above.

Later on in the present work, these considerations will be illustrated by an explicit example in which we will check numerically that when the criterion (9.34) is satisfied, the Press-Schechter result is indeed recovered, see Appendix 9.B.

9.3.5 Other methods

Other approaches to the cloud-in-cloud problem have been proposed, and although, in the present work, we make use of the excursion-set method, for completeness, let briefly mention those alternative techniques.

Supreme statistics

A first approach to the cloud-in-cloud problem was proposed in 1985 by Bhavsar and Barrow in Ref. [452], and is called the "supreme statistics" (or "extreme-value statistics") method. The idea is to consider a region of size R_ℓ, over which the averaged density contrast is above the threshold. This region is made of $\sim (R_\ell/R_\mathrm{s})^3$ subregions of size R_s, and one needs to determine the probability that one of these regions is also above the threshold. On generic grounds, considering n samples, each of size m, all drawn from the same underlying distribution, the distribution of the maxima within each sample, and therefore the most probable maximum value, can be determined using the supreme statistics (see Ref. [453] for a recent example of application to PBHs).

Peak theory

In 1986, Bardeen, Bond, Kaiser and Szalay studied the statistics of peaks of Gaussian random fields in Ref. [454]. Assuming that structures form where the density field locally peaks, this allows one to derive the number density of objects satisfying certain conditions on the size of their peak, the volume enclosed within the peak, the deviation from sphericity of the peak, *etc.* Although the same exponential suppression $\propto e^{-\delta_\mathrm{c}^2(R)/(2\sigma_R^2)}$ as in the Press-Schechter formalism is obtained, see the discussion below Eq. (9.17), the details of the prefactor are found to be different. Ref. [454] also introduced the "peak-background split" approximation, which allows one to compute correlations between peaks belonging to two populations having two different, well-separated scales. The peak-theory and excursion-set approaches can also be combined, see *e.g.* Ref. [455], and a recent comparison between these different techniques can be found in Ref. [456].

Improved Press-Schechter formalism

In 1994, an improved version of the Press-Schechter formalism was proposed by Jedamzik in Ref. [457], in which the number density of isolated overdense regions (defined as overdense regions that are not comprised in larger overdense regions) is computed by making use of Bayes' theorem. The method was improved in Ref. [458] (see also Ref. [459] for further refinements, in particular the implementation of the condition that objects form around peaks), and leads to implicit integral equations, similar to the Volterra equations presented in Section 9.3.3.

9.3.6 Further refinements

The methods presented above assume that structures form when the overdensity δ is above a certain threshold δ_c, but more refined formation criteria have also been studied.

Critical scaling

From studying spherically symmetric collapse of a massless scalar field by numerical means, Choptuik has shown in Ref. [460] that, close to the critical threshold, the mass of the resultant black hole,

M, is proportional to $(\delta - \delta_{\rm c})^\gamma$ where $\gamma \simeq 0.37$ is a universal exponent. This has been generalized to radiation fluids in Refs. [461, 462], and reviews of critical phenomena in gravitational collapse can be found in Refs. [463, 464]. The relation

$$M = K m_H (\delta - \delta_{\rm c})^\gamma, \tag{9.35}$$

where K is a constant and m_H is the mass contained within a Hubble volume at the time the black holes form, has been applied to the calculation of the PBH mass fraction in Ref. [465]. It was then numerically analysed in the context of PBHs in Refs. [466, 467], and further investigations on its applicability can be found in Ref. [468].

Compaction function

Recent numerical works by Musco, see Ref. [469] and subsequent publications, suggest that a more accurate criterion for PBH formation follows from the analysis of the compaction function

$$C(r) = 2\frac{m(r,t) - \bar{m}(r,t)}{R(r,t)}, \tag{9.36}$$

where r is the distance away from the overdensity peak, $m(r,t) - \bar{m}(r,t)$ is the excess mass contained inside a sphere of radius r, and $R(r,t)$ is the areal radius. The scale of the fluctuations relevant for the formation of PBHs is the one that maximizes the compaction function. In other words, a PBH forms at the scale $r_{\rm m}$ where $C(r)$ is maximal, provided $C(r_{\rm m})$ is larger than some threshold $C_{\rm c}$ (which is roughly equivalent to requiring that the overdensity averaged over a sphere of radius $r_{\rm m}$ overcomes the threshold value $\delta_{\rm c}$, see Ref. [470]).

Critical collapse can be implemented with the criterion based on the compaction function (see Appendix A of Ref. [471]), simply by replacing δ by $C(r_{\rm m})$, and $\delta_{\rm c}$ by $C_{\rm c}$ in Eq. (9.35), and by using different values of the constants K and $C_{\rm c}$ (γ is still the same).

Compaction-function based criteria have also been employed within the peak-theory approach in Ref. [471] (see also Refs. [472, 473]). They cannot be directly implemented in the excursion set program since, here, the size of the structure is not determined by the first C-crossing of the threshold, but rather by the "time" (*i.e.* scale) at which C is maximal (and by the value of that maximum through the critical-scaling relation). See also Ref. [470] for a comparison between these different criteria.

9.3.7 Application to primordial black holes

The methods introduced above were originally developed in the context of large-scale structures in general (except for the refinements presented in Section 9.3.6), and their application to the calculation of the mass distributions of PBHs requires some further considerations.

Removing the super-horizon modes

Primordial black holes are expected to form when a large curvature fluctuation re-enters the Hubble radius after inflation, and collapses into a black hole. The relevant smoothing scale R is therefore the Hubble radius at the time the black hole forms. In the coarse-graining procedure (9.9), given the properties of the function $\widetilde{W}$ detailed at the beginning of Section 9.3.1, most modes k that contribute to Eq. (9.14) are such that $k < a/R$, hence they are super Hubble at the time of formation. This

raises two issues (that do not appear in the context of large-scales structures, where all modes that contribute to the overdensity field are far inside the Hubble radius).

First, far super-Hubble curvature perturbations should only lead to a local rescaling of the background metric, and can hardly determine whether an object forms inside a local Hubble patch. Second, in general relativity, there is no unique definition of the energy density (hence of the density contrast), which depends on the space-like hypersurface on which it is computed. All possible choices coincide on sub-Hubble scales (where observations are performed), but they differ on super-Hubble scales. In practice, in most gauges studied in the literature, the density contrast δ and the Bardeen potential Φ are related through a formula of the form [474]

$$\delta_k = -\frac{2}{3}\left(\frac{k}{aH}\right)^2 \Phi_k + \alpha\Phi_k + \beta\frac{\dot{\Phi}_k}{H}\,, \tag{9.37}$$

where α and β are two constants, that possibly depend on the equation-of-state parameter w. For instance, in the Newtonian gauge, $\alpha = \beta = -2$, in the flat gauge, $\alpha = 5 - 3w$ and $\beta = -2$, and in the comoving gauge, $\alpha = \beta = 0$. On sub-Hubble scales, when $k \gg aH$, the first term in Eq. (9.37) dominates, and δ_k does not depend on the choice of slicing as mentioned above. Since the Bardeen potential Φ is related to the curvature perturbation ζ via [475]

$$\zeta_k = \frac{2}{3}\frac{\dot{\Phi}_k/H + \Phi_k}{1+w} + \Phi_k\,, \tag{9.38}$$

on super-Hubble scales, where $\dot{\Phi}_k$ can be neglected since it is proportional to the decaying mode, one has

$$\delta_k \simeq -\frac{2}{5}\left(\frac{k}{aH}\right)^2 \zeta_k + \frac{3\alpha}{5}\zeta_k\,. \tag{9.39}$$

This shows that there are essentially two families of slicings for the density contrast. If $\alpha \neq 0$, as in the Newtonian gauge or in the flat gauge (if $w \neq 5/3$) for instance, on super-Hubble scales, $\delta_k \propto \zeta_k$, so for quasi scale-invariant curvature power spectra (as expected from inflation), super-Hubble modes give a substantial contribution to Eq. (9.14), leading to the problem mentioned above. If, on the contrary, $\alpha = 0$, as in the comoving gauge, then $\delta_k \propto k^2\zeta_k$ on super-Hubble scales, hence it is highly suppressed and far super-Hubble modes do not contribute much to the integral of Eq. (9.10). For this reason, in Ref. [476], it is proposed to work with the comoving density contrast, as a way to effectively remove the contribution from far super-Hubble modes. In principle, a well-defined formation criterion should come with a prescription for which density contrast to use, and in practice, formation criteria derived from numerical investigations are indeed most often formulated in the comoving slicing, see for instance Refs. [477, 469]. This is why we will adopt this choice in what follows, and in Appendix 9.B, we will investigate how the results are modified if one makes a different choice and works with the Newtonian density contrast.

Simplified Press-Schechter estimate

The above considerations lead to a simplified version of the Press-Schechter formalism that is often used to estimate the abundance of PBHs. Indeed, in the integral of Eq. (9.14), modes that lie far below the coarse-graining scale, such that $k \gg a/R$, are cut away by the filter function $\widetilde{W}$, while modes that lie far above the coarse-graining scale, such that $k \ll a/R$, give a negligible contribution since they are suppressed by k^2 as explained in Section 9.3.7. Therefore, the only

modes that give a substantial contribution to Eq. (9.14) are those such that $k \sim aR$, and Eq. (9.14) can be approximated as

$$\sigma_R^2 \sim \mathcal{P}_\delta \left(k = \frac{a}{R} \right) . \tag{9.40}$$

It is then usually assumed that the power spectrum peaks at a single scale. At the time when that scale re-enters the Hubble radius, the fraction of Hubble patches where the density contrast is larger than the critical value is given by Eq. (9.16), so it is common to use directly use Eq. (9.16) as the mass fraction, and to write (see for instance Ref. [478])

$$\beta(M) \sim \mathrm{erfc} \left[\frac{\delta_\mathrm{c}(R)}{\sqrt{2\mathcal{P}_\delta(k)}} \right] \sim \frac{\sqrt{2\mathcal{P}_\delta}}{\sqrt{\pi}\delta_\mathrm{c}} e^{-\frac{\delta_\mathrm{c}^2}{2\mathcal{P}_\delta}} , \tag{9.41}$$

where R is the Hubble radius and M the Hubble mass at the time when $k = aH$, and where in the last expression, we have expanded the error function in the regime where PBHs are rarely produced, *i.e.* when $\delta_\mathrm{c} \gg \sqrt{\mathcal{P}_\delta}$. Let us note that, when comparing Eq. (9.41) to the full Press-Schechter formula (9.17), the same exponential suppression is obtained, but the prefactor is obviously different. However, as noted in Section 9.3.5, that prefactor was also found to differ in other approaches such as peak theory, so one may consider that the details of the prefactor are ultimately dependent on the approach one follows, and that only the exponential suppression is a robust result, in which case Eq. (9.41) may provide a useful estimate. This is why this formula is widely employed, including in Ref. [430] for the calculation of PBHs from metric preheating, in which we are interested in this work.

However, it is pretty clear that this approximation breaks down for broad spectra, *i.e.* when a wide range of scales is involved in the formation of PBHs. As pointed out *e.g.* in Ref. [472], the problem is that Eq. (9.16) is not a differential quantity. So it can happen for instance that the integrated mass fraction,

$$\Omega_\mathrm{PBH} = \int_0^\infty \beta(M) \mathrm{d} \ln M \, , \tag{9.42}$$

which corresponds to the fraction of the total energy budget that is comprised inside PBHs, is found to be larger than one if Eq. (9.41) is used, which clearly signals an inconsistency. This is in fact precisely what happens in Ref. [430], where renormalization procedures had to be introduced to cope with this issue, see Appendix 9.C. In the rest of this paper, we re-examine this problem with the excursion-set formalism, in order to assess more precisely the mass distribution of PBHs produced from the preheating instability.

9.4 Primordial black holes from metric preheating

We are now in a position in which we can apply the excursion-set formalism, presented in Sections 9.3.2 and 9.3.3, to the calculation of the mass fraction of PBHs arising from the preheating instability described in Section 9.2.

9.4.1 Collapse criterion

As explained in Section 9.3.2, one of the two ingredients required by the excursion set approach is the critical value of the density contrast, above which PBHs form. This was derived in the case of metric preheating in Section 9.2, see Eq. (9.8). This formula provides a critical value for the

density contrast evaluated at a time that depends on the scale R (namely at the band-crossing time of R). Below, we rather choose to express all relevant quantities at the same reference time. The reason is that if the time of evaluation depends on the scale R, then, when deriving Eq. (9.20), an additional term, which stands for the time evolution of the mode function, appears. This term acts as a drift term in the Langevin equation (9.22), but it can be absorbed by a change of variables. This amounts to rescaling δ with a transfer function that evolves the density contrast to a fixed time, hence is equivalent to working with fixed-time quantities anyway. In either case, one has to relate the value of the density contrast at the band-crossing time to its value at a fixed, reference time.

Two natural choices for such a reference time are (i) the time at the end of inflation and (ii) the time at the end of the instability phase. The problem with the latter choice is that, since coarse graining δ at a scale R selects modes that are larger than R, see the discussion at the beginning of Section 9.3.7, the scales that contribute to δ_R at the end of the instability are either sub- or super-Hubble, hence they have a priori different behaviours (*i.e.* different transfer functions) between the band-crossing time of R and the end of the instability, which makes it harder to relate $\delta_R[t_{\rm bc}(R)]$ with $\delta_R(t_\Gamma)$. The first option is therefore more convenient, since all scales larger than R are super-Hubble between the end of inflation and the band-crossing time of R.

One thus has to study how δ evolves on super-Hubble scales during the oscillatory phase. In Section 9.3.7, we explained why the comoving density contrast had to be considered. From Eq. (9.37), it is related to the Bardeen potential via $\delta_{\boldsymbol{k}} = -2/3[k/(aH)]^2\Phi_{\boldsymbol{k}}$, while the Bardeen potential is related to the curvature perturbation through Eq. (9.38). As shown in Section 9.2, the curvature perturbation $\zeta_{\boldsymbol{k}}$ is constant on super-Hubble scales during the oscillatory phase. As a consequence, if the equation-of-state parameter w were constant, then Eq. (9.38) seen as a differential equation for $\Phi_{\boldsymbol{k}}$ would show that, up to a quickly decaying mode, $\Phi_{\boldsymbol{k}}$ reaches a constant value, hence $\delta_{\boldsymbol{k}} \propto (aH)^{-2}$.

However, during the oscillatory phase, w is only constant on average, and otherwise undergoes large oscillations. Indeed, at leading order in H/m, the inflaton oscillates according to $\phi \simeq \phi_{\rm end}(a_{\rm end}/a)^3\sin(mt)$, which gives rise to $w = \cos(2mt) + \mathcal{O}(H/m)$. Through Eq. (9.38), these oscillations give rise to oscillations in $\Phi_{\boldsymbol{k}}$ with frequency $\sim m$, hence $\Phi'/(H\Phi)$ is of order $m/H \gg 1$ and can a priori not be neglected in Eq. (9.38). Nonetheless, deep in the oscillatory phase, when $H \ll m$, these oscillations can be averaged out, and one has

$$\Phi_{\boldsymbol{k}} \simeq \frac{3}{5}\zeta_{\boldsymbol{k}}\,. \tag{9.43}$$

In order to verify the validity of this statement, in Fig. 9.2, we display the numerical solution of Eq. (9.38) in the same situation as the one shown in Fig. 9.1 (namely, from the numerical solution of the Klein-Gordon equation, we extract $w(t)$ and $H(t)$, and solve Eq. (9.38) for $\Phi_{\boldsymbol{k}}(t)$ while assuming that $\zeta_{\boldsymbol{k}}$ is constant). We also superimpose the approximation (9.43). One can see that, after a few oscillations, it provides an excellent fit to the full numerical solution. Therefore, on average, the Bardeen potential is indeed constant, and $\delta_{\boldsymbol{k}} \propto (aH)^{-2}$.

As stressed above, all scales contributing to δ_R are super-Hubble between the end of inflation and the band-crossing time, hence they all evolve according to $\delta_{\boldsymbol{k}} \propto (aH)^{-2} \propto a$ in a matter-dominated era. Therefore, δ_R itself evolves in the same way, and

$$\delta_R\left(t_{\rm end}\right) = \delta_R\left[t_{\rm bc}(R)\right]\frac{a_{\rm end}}{a\left[t_{\rm bc}(R)\right]}\,. \tag{9.44}$$

Combining this result with Eq. (9.8), and denoting by $R_{\rm end}$ the value of R at the end of inflation, one obtains for the critical value of the density contrast at the end of inflation

$$\delta_{\rm c}(R,t_{\rm end}) = \left(\frac{3\pi}{2}\right)^{2/3}\left[\frac{H_{\rm end}}{H_\Gamma} - \left(R_{\rm end}H_{\rm end}\right)^3\right]^{-2/3}. \tag{9.45}$$

9.4.2 Overdensity variance

The second ingredient required by the excursion-set approach is the expected variance of δ_R, σ_R^2, and how it relates to R. If one sets the function $\widetilde{W}$ to a Heaviside function in Eq. (9.14), see footnote 3, one has

$$\sigma_R^2(t_{\rm end}) = \int_0^{a/R}\mathcal{P}_\delta\left(k,t_{\rm end}\right)\frac{{\rm d}k}{k}. \tag{9.46}$$

As explained in Section 9.4.1, in the comoving gauge, the density contrast is related to the Bardeen potential via $\delta_{\boldsymbol{k}} = -2/3[k/(aH)]^2\Phi_{\boldsymbol{k}}$, and the link between the Bardeen potential and the curvature perturbation is given by Eq. (9.43). This gives rise to

$$\sigma_R^2(t_{\rm end}) = \left(\frac{2}{5}\right)^2\int_0^{a/R}\left(\frac{k}{a_{\rm end}H_{\rm end}}\right)^4\mathcal{P}_\zeta\left(k,t_{\rm end}\right)\frac{{\rm d}k}{k}. \tag{9.47}$$

In this expression, the curvature power spectrum $\mathcal{P}_\zeta\left(k,t_{\rm end}\right)$ depends on the details of the inflationary phase that precedes metric preheating. Hereafter, we will assume that the inflationary potential can still be assumed as being almost quadratic at the time the scales of interest cross out the Hubble radius during inflation, where the mass of the inflaton is related to $H_{\rm end}$, and the power spectrum is obtained by solving the Mukhanov-Sasaki equation (9.1) numerically during inflation, starting from the Bunch-Davies vacuum.

9.4.3 Numerical results

As explained in Section 9.3.2, in the excursion-set approach, the mass fraction of PBHs is directly related to the first-crossing-time distribution of realizations of the Langevin equation (9.22), see Eq. (9.24). This distribution can be estimated using a Monte-Carlo sampling. In Fig. 9.3, we show a few realizations of the Langevin equation (9.22), for the density contrast δ_R evaluated on comoving slices at the end of inflation. The collapse threshold obtained in Eq. (9.45) is displayed with the (quasi) horizontal black dashed line, and in the right panel, the time of first crossing is shown with the vertical black dashed line.

This gives rise to the mass fraction displayed in Fig. 9.4 with the vertical black bars and where the size of the bars corresponds to a 5σ estimate of the statistical error using jackknife resampling. We report a good convergence in estimating the mass fraction for a sample of 10^6 trajectories with 1000 logarithmically spaced values of R.

This method is, however, computationally expensive, especially in the tails of the distribution where one needs to simulate a very large number of Langevin realizations to compensate for the sparse statistics. Instead, as explained in Section 9.3.3, one can solve the Volterra equation (9.32), making use of the numerical procedure outlined in Appendix 9.A. For $n_{\rm points}$ values of R, this algorithm requires to invert a $n_{\rm points}\times n_{\rm points}$ lower triangular matrix, which is far more efficient

than having to solve Langevin realizations.[7] In practice, we find good convergence for $n_{\rm points} \geq 500$. The result is displayed in Fig. 9.4 with the red line, where one can check that the two methods give compatible results.

The total fraction of the universe made of PBHs, $\Omega_{\rm PBH}$, is obtained by integrating the mass fraction, see Eq. (9.42). The result is shown in Fig. 9.5 as a function of $\rho_{\rm end}$, the energy density at the end of inflation, and ρ_Γ, the energy density at the end of the instability phase. It is obtained from numerically solving the Volterra equation. One can see that the transition from small values of $\Omega_{\rm PBH}$ to values of order one is very sharp, and that there exist a region in parameter space, corresponding to the dark red region in the right panel of Fig. 9.5, where the universe is dominated by a gas of PBHs already at the end of the oscillatory phase.

Another quantity of interest is the typical mass of the resulting black holes, which is displayed across parameter space in Fig. 9.6. In the left panel, the average mass is shown, in the form of $\exp(\langle \ln M \rangle)$, and one can see that in the region of parameter space in which PBHs are substantially produced, it spans a large range of values, from 10g to 10^{33}g $\sim M_\odot$, where $M_\odot$ is the mass of the sun. In the right panel, the standard deviation of $\ln(M)$ is displayed, in order to see how many orders of magnitude the mass fraction distribution covers (this standard deviation is also shown with the grey shaded stripe in Fig. 9.4). One can see that $\Delta \ln M < 2$, so the mass distributions never extend over many orders of magnitude.

9.4.4 Analytical approximation

In this section, we try to gain further analytical insight into the numerical results presented in Section 9.4.3 by performing a few approximations. The main simplification comes from the remark that in Eq. (9.45), $H_{\rm end}/H_\Gamma \gg (R_{\rm end} H_{\rm end})^3$ except for the scales that enter the instability band close to the end of the oscillatory phase. Those undergo little amplification anyway, and are therefore mostly irrelevant for PBH production. In that limit, one can approximate Eq. (9.45) as

$$\delta_{\rm c}(R, t_{\rm end}) \simeq \left(\frac{3\pi}{2} \frac{H_\Gamma}{H_{\rm end}} \right)^{2/3} , \tag{9.48}$$

which crucially does not depend on R (hence on S) any more. As explained in Section 9.3.4, in that limit, the first passage-time distribution is given by Eq. (9.33) and one recovers the result from the Press-Schechter formalism, with an additional factor 2. Note that this simplification is rather coincidental in the present case, since when expressed at the band-crossing time, the threshold is strongly scale-dependent, but the behaviour of the comoving density contrast on super-Hubble scale is such that, when re-expressed at the end of inflation, it exactly cancels out that scale dependence (this is no longer true if other density contrasts are used, see Appendix 9.B).

We have not displayed the (two times) Press-Schechter formula (9.33) in Fig. 9.4 since it cannot be distinguished by eye from the red line (*i.e.* the full numerical result), confirming that this is

[7] In terms of numerical performance, when producing Fig. 9.4 we found on our machine that the Volterra approach is more than 1000 times faster than the Monte-Carlo sampling of Langevin realizations. This is a generic result: if $N_{\rm real}$ realizations are simulated, the average number of points per bin is of order $\bar{n} \sim N_{\rm real}/n_{\rm points}$, hence the statistical error is of order $1/\sqrt{\bar{n}} \sim \sqrt{n_{\rm points}/N_{\rm real}}$. Requiring that this is smaller than a target accuracy ϵ leads to $N_{\rm real} > n_{\rm points}/\epsilon^2$. Since each realization requires $n_{\rm points}$ evaluations of the noise, the Langevin approach relies on $\sim n_{\rm points}^2/\epsilon^2$ numerical operations. On the other hand, the Volterra method implies to invert a $n_{\rm points} \times n_{\rm points}$ triangular matrix (see Appendix 9.A), which requires $\sim n_{\rm points}^2$ operations (using the "forward substitution" algorithm), and is thus more efficient by a factor ϵ^2.

indeed an excellent approximation. The (two times) Press-Schechter formula is, however, shown in the left panel of Fig. 9.5 as the dashed green line, where one can check that it reproduces the excursion set result very accurately.

Then, in order to make Eq. (9.33) explicit, one needs to relate the overdensity dispersion $S = \sigma_R^2$ to the mass M, which implies to first derive an approximation for Eq. (9.47). In single-field inflation, in the slow-roll approximation, one has [479, 480]

$$\mathcal{P}_\zeta(k) \simeq \frac{H^2(k)}{8\pi^2 M_{\rm pl}^2 \epsilon_1(k)}\,, \tag{9.49}$$

where $H(k)$ and $\epsilon_1(k)$ are respectively the values of the Hubble parameter and the first slow-roll parameter when the scale k crosses-out the Hubble radius during inflation. As argued before, towards the end of inflation when the inflaton approaches the minimum of its potential, the potential can be approximated as being quadratic, $V(\phi) \simeq m^2\phi^2/2$. In such a potential, the slow-roll trajectory reads [481] $\phi(k) \simeq M_{\rm pl}\sqrt{2-4(N-N_{\rm end})}$. Given that, still at leading order in slow roll, one has $H^2 \simeq V/(3M_{\rm pl}^2)$ and $\epsilon_1 \simeq (V'/V)^2/(2M_{\rm pl}^2)$, this allows one to approximate the power spectrum (9.49) as $\mathcal{P}_\zeta \simeq 3H_{\rm end}^2/(24\pi^2 M_{\rm pl}^2)[1-2\ln(k/a_{\rm end}H_{\rm end})]^2$. Since we have made use of the slow-roll approximation, which breaks down when inflation ends, this formula is in fact accurate only for scales that emerge sufficiently early before the end of inflation, $k \ll a_{\rm end}H_{\rm end}$, and in this regime, Eq. (9.47) gives rise to

$$\sigma_R^2 = \frac{\mathcal{P}_\zeta(k_{\rm end})}{50}\left\{5-\frac{4}{3}\ln\left(\frac{H_{\rm end}M}{4\pi}\right)\left[-3-\frac{2}{3}\ln\left(\frac{H_{\rm end}M}{4\pi}\right)\right]\right\}\left(\frac{H_{\rm end}M}{4\pi}\right)^{-4/3}\,. \tag{9.50}$$

In this expression, we have used that the link between R and M is given by $M = 4\pi\rho R^3/3 = 4\pi H^2 R^3 M_{\rm pl}^2$. By plugging Eqs. (9.48) and (9.50) into Eq. (9.33), one thus obtains an explicit expression for the mass fraction $\beta(M)$, that we do not reproduce here since it is not particularly insightful, but which is nonetheless straightforward.

Note that in general, the mass fraction has to be evolved from the time black holes form (which here depends on the mass) to the time at which β is given, taking into account that PBHs may dilute at a different rate than the background energy density. However, here, given that the universe behaves as matter-dominated during the instability phase, β remains constant so our result does correspond to the mass fraction at the time t_Γ, when the instability stops.

The corresponding formula is displayed in Fig. 9.5 with the solid blue line, and one can check that it gives a reliable approximation to the full result. It can thus be used to assess its overall integral, *i.e.* $\Omega_{\rm PBH}$, and the mass at which it peaks, which we now do.

By integrating Eq. (9.33) over S (and reminding that $\delta_{\rm c}$ does not depend on S), one has

$$\Omega_{\rm PBH} = {\rm erfc}\left[\frac{\delta_{\rm c}}{\sqrt{2S_{\rm max}}}\right], \tag{9.51}$$

where $S_{\rm max}$ is the maximal value of S, *i.e.* the one corresponding to the minimum value of R, or of M. It can thus be obtained by setting $M = 4\pi M_{\rm pl}^2/H_{\rm end}$ in Eq. (9.50), giving rise to $S_{\rm max} = \mathcal{P}_\zeta(k_{\rm end})/10$. Making also use of Eq. (9.48), one obtains

$$\Omega_{\rm PBH} = {\rm erfc}\left[\sqrt{\frac{5}{\mathcal{P}_\zeta(k_{\rm end})}}\left(\frac{3\pi}{2}\frac{H_\Gamma}{H_{\rm end}}\right)^{2/3}\right]. \tag{9.52}$$

This formula is displayed in the left panel of Fig. 9.5 with the dashed blue line, and is found to provide a good fit to the full numerical result. Furthermore, it allows one to identify the region of parameter space in which the universe is dominated by PBHs at the end of the instability phase, $\Omega_{\rm PBH} > 1/2$, which reduces to

$$\frac{\rho_\Gamma^{1/4}}{\rho_{\rm end}^{1/4}} < 8 \times 10^{-6} \left(\frac{\rho_{\rm end}^{1/4}}{10^{16}{\rm GeV}} \right)^{3/2} . \tag{9.53}$$

This upper bound is displayed with the dashed blue line in the right panel of Fig. 9.5, and one can see that it indeed provides an accurate estimate of the boundary between the region in parameter space in which PBHs are very abundantly produced and the region in which they remain subdominant. Up to a prefactor of order one, this also matches Eq. (4.1) of Ref. [430]. Indeed, the bound (9.53) corresponds to requiring that the instability phase be sufficiently long that when the linear theory is extrapolated throughout the oscillatory phase, the most amplified scales, *i.e.* the ones around the Hubble radius at the end of inflation, reach a typical value for the density contrast, $\sqrt{\mathcal{P}_\delta}$, that is of order one when the instability stops. This conclusion seems therefore to be robust to the inclusion of cloud-in-cloud effects, and to the detailed description of the mass distribution of PBHs, which the present, more refined analysis, allows for.

Our analytical approximation can also be used to estimate the typical mass at which the mass fraction peaks. From Eq. (9.33), in the limit of a scale-invariant threshold, the distribution of first-crossing "times" peaks at $S_{\rm peak} = \delta_{\rm c}^2/3$. In practice, this may select a mass that is smaller than the Hubble mass at the end of inflation, which then indicates that the mass fraction is a decreasing function of the mass, and is maximal near the Hubble mass at the end of inflation,

$$M_{\rm end} = \frac{4\pi M_{\rm pl}^2}{H_{\rm end}} \simeq 10{\rm g} \left(\frac{\rho_{\rm end}^{1/4}}{10^{16}{\rm GeV}} \right)^{-2} . \tag{9.54}$$

Otherwise, in the regime where $M \gg M_{\rm end}$, Eq. (9.50) can be approximated by keeping the squared logarithmic term only, and in this limit one obtains

$$\frac{M_{\rm peak}}{\rm g} \simeq 1.22 \times 10^{-9} \frac{\rho_{\rm end}^{1/4}}{10^{16}{\rm GeV}} \left(\frac{\rho_{\rm end}^{1/4}}{\rho_\Gamma^{1/4}} \right)^2 \ln^{3/2} \left[3.62 \times 10^{-7} \left(\frac{\rho_{\rm end}^{1/4}}{10^{16}{\rm GeV}} \right)^2 \left(\frac{\rho_{\rm end}^{1/4}}{\rho_\Gamma^{1/4}} \right)^{4/3} \right] . \tag{9.55}$$

This value is displayed with the dashed green line in Fig. 9.4, where one can check that it provides indeed a reliable estimate. It is interesting to notice that the condition (9.53) for an efficient production of PBHs is (roughly) equivalent to requiring that $M_{\rm peak} > M_{\rm end}$. As a consequence, in the regime where PBHs are abundantly produced, the peak mass is substantially larger than the Hubble mass at the end of inflation, and hence corresponds to scales that emerge from the Hubble radius several e-folds before the end of inflation. This is because, although smaller scales spend more time within the instability band and are thus more amplified, the initial value of their power spectrum is also smaller, and the trade-off selects intermediate scales.

9.5 Discussion and conclusion

In this work, we have made use of the excursion-set approach to accurately compute the mass distribution of primordial black holes that are produced during metric preheating. The parametric

instability of metric preheating occurs in any inflationary model in which the inflaton oscillates around a minimum of its potential after inflation. It is therefore a rather generic, not to say inevitable, phenomenon, for which it is thus important to precisely characterize the properties of the resulting black holes. Since metric preheating leads to the amplification of a wide range of scales, the cloud-in-cloud mechanism, in which small-mass black holes are trapped inside regions later collapsing into larger-mass black holes, plays an important role. This is why one needs to go beyond the simplified, Press-Schechter inspired, common estimate to assess the mass distribution of black holes.

After reviewing the different techniques that have been proposed in the literature to compute mass distributions of PBHs, and highlighting salient aspects of these methods that are most of the time only alluded to, we have studied the problem at hand with the excursion-set formalism, combining different numerical techniques (namely a direct Monte-Carlo sampling of Langevin realizations and numerical solutions of Volterra integral equations) and analytical approximations.

Assuming that the potential of the inflaton is almost quadratic in the last stages of inflation (and during the oscillatory phase), the result only depends on two parameters, namely the energy density at the end of inflation, $\rho_{\rm end}$, and the energy density at the time the inflaton decays into other degrees of freedom and the instability stops [434], ρ_Γ.

We have found that in the region of parameter space corresponding to Eq. (9.53), PBHs are very abundantly produced, in such a way that they even dominate the energy content of the universe at the end of the oscillatory phase. For this to happen, the inflaton needs to be sufficiently weakly coupled, such that more than 5 order of magnitude separate $\rho_{\rm end}^{1/4}$ from $\rho_\Gamma^{1/4}$, but as soon as this is the case, one is led to this rather drastic conclusion that the universe undergoes an early phase of PBH domination.

The typical masses of the black holes range from 10 grams to the mass of the sun. For masses smaller than 10^9 grams, PBHs evaporate before big-bang nucleosynthesis (BBN) and can therefore not be directly constrained. Heavier black holes would, however, survive until and after BBN, and given that the universe is radiation dominated at BBN, this excludes the region with $M > 10^9$g in Fig. 9.6a. In fact, even if $M > 10^9$g, it was recently shown in Ref. [432] that the gravitational potential underlain by a gas of PBHs induces the production of gravitational waves at seconder order in cosmological perturbation theory, and that these gravitational waves may lead to a backreaction problem if $\Omega_{\rm PBH} > 10^{-4}(10^9{\rm g}/M)^{1/4}$ at the time PBHs form. This excludes the value $\Omega_{\rm PBH} \sim 1$ for any $M > 10$g, hence the whole region described by Eq. (9.53), and located above the dashed blue line in Fig. 9.5, may be excluded too.

This region was correctly identified in Ref. [430] already, in which metric preheating was studied with the simplified, Press-Schechter inspired approach described in Section 9.3.7. A detailed comparison between our result and the ones obtained in Ref. [430] is given in Appendix 9.C. The main difference we find concerns the mass at which the mass distributions peak. While in Ref. [430], it was found to correspond to the Hubble mass at the end of inflation, see Eq. (9.54), in the present analysis we find that, in the regime where PBHs are substantially produced, the peak mass is substantially larger, see Eq. (9.55). This is a consequence of the cloud-in-cloud mechanism, which could not be taken into account in Ref. [430], and this has two main consequences. First, since heavier black holes take more time to Hawking evaporate, they survive for a longer period, hence the constraints on the parameters of the model arising from the present result are more stringent than the ones obtained in Ref. [430], which made conservative assumptions as pointed out in that reference. Second, this implies that the bulk of the PBH population comes from modes that exit the Hubble radius several e-folds before the end of inflation, at a stage where it is not clear that the

potential can still be approximated as being quadratic. This means that, in practice, it may be necessary to analyse each potential individually instead of using the generic parametrization employed in this work. We have, however, provided all the relevant formulae and technical considerations for such an exploration to be carried out (the numerical code we have developed to produce the results presented in this article is also publicly available in the arXiv ancillary files).

Let us also highlight that, although a large range of scales is amplified during metric preheating, the mass distributions we have found are rather peaked, and never extend over more than a couple of orders of magnitude. This is in agreement with Ref. [453], where the mass distribution associated to broad spectra was explored, and it was found to be quasi-monochromatic (*i.e.* peaked at a single mass), which corresponds to either the smallest enhanced scale or the largest enhanced scale, depending on the tilt of the spectrum. In the present case, we found that the peak mass arises at rather intermediate scales, but this is because the cloud-in-cloud mechanism plays an important role (such that the mass fraction at small masses is suppressed), while Ref. [453] focused on regimes where the mass fraction remains small and the cloud-in-cloud phenomenon is almost absent.

Another remark of interest is that, as argued in Section 9.3.7, we have evaluated the density contrast in comoving slices in order to apply our PBH formation criterion. In Appendix 9.B, we investigate the consequences of interpreting the formation threshold in a different slicing (namely the Newtonian one). While we find that most conclusions are unchanged, the main difference is that the mass distributions are much wider when working in the Newtonian slicing. This is because, in the Newtonian gauge, the density contrast is not suppressed on super-Hubble scales, hence large-scale fluctuations substantially contribute to the coarse-grained density perturbation inside a Hubble patch. This is precisely the effect we have tried to avoid by using the comoving slicing, since large-scale fluctuations should only lead to a local rescaling of the background, and not determine the fate of overdensities inside the Hubble radius [476].

Let us also note that our analysis was restricted to scales that are larger than the Hubble radius at the end of inflation, and we did not explicitly compute the mass fraction at smaller scales. However, there is a small range of scales that are within the Hubble radius at the end of inflation, but that still enter from below the instability band during the oscillatory phase (see the lowest dotted line in Fig. 9.1). Although the physical status of those scales is unclear (since they remain within the Hubble radius throughout inflation, they behave as Minkowski vacuum fluctuations, and never undergo classical amplification [482, 483, 484, 485]), they can nonetheless be readily incorporated in the excursion-set approach. When doing so, given that the corresponding range of scales is very narrow, and that the initial density contrast is tiny (since those scales are not excited during inflation), we find that this only adds a negligible, low-mass end to the mass distributions we have computed, so these scales can be safely discarded.

A final remark of interest is that the collapse criterion we have employed was derived in Ref. [439] for a universe filled with a scalar field with quadratic potential by assuming a spherically symmetric profile for the overdensity. In the case of a universe filled with a pressure-less perfect fluid, it is well-known that PBH peaks no longer need to be rare and hence may not be close to spherically symmetric, and that corrections arising from spherical asymmetries typically lead to less abundant PBHs (see for instance Ref. [486]). Although those two systems are different, as discussed in detail in Ref. [434], one may expect that a similar effect takes place in the setup under consideration in this work. In order to address it, one would have to generalize the calculation of Ref. [439] to non-spherical geometries, which could be the topic of future work.

In summary, by properly taking into account the cloud-in-cloud mechanism, which plays an important role in the metric preheating instability in which a large range of scales is enhanced,

we have derived accurate predictions for the mass distribution of primordial black holes produced during preheating. Given that those black holes may dominate the universe for a transient period afterwards, reheat the universe by Hawking evaporation, and induce a detectable stochastic gravitational wave background [432], the details of these mass distributions may indeed have important cosmological consequences, some of which remain to be explored.

9.A Numerical solution of the Volterra equation

In Section 9.3.3 we have shown that the first-crossing-time distribution associated to the Langevin equation (9.22) satisfies a family of Volterra integral equation, one of them being of the form

$$\begin{aligned} P_{\rm FPT}(S) = &\left[\frac{\delta_{\rm c}(S)}{S} - \delta_{\rm c}'(S)\right] P_{\rm free}\left[\delta_{\rm c}(S), S\right] \\ &+ \int_0^S {\rm d}s \left[\delta_{\rm c}'(S) - \frac{\delta_{\rm c}(S)-\delta_{\rm c}(s)}{S-s}\right] P_{\rm free}\left[\delta_{\rm c}(S)-\delta_{\rm c}(s), S-s\right] P_{\rm FPT}(s)\,, \end{aligned} \tag{9.56}$$

see Eq. (9.32). Upon discretizing the time variable according to $S = n\Delta s$ and $s = m\Delta s$, where n and m are integer numbers and ΔS is a numerical time step, the Volterra equation can be written as

$$P^n_{\rm FPT} = X^n + M^n{}_m P^m_{\rm FPT}\,, \tag{9.57}$$

where the implicit summation notation is employed. In this formula, $P^n_{\rm FPT}$ and X^n are vectors, and $M^n{}_m$ is a lower triangular matrix, with non-zero cells only if $m \leq n$, defined as

$$P^n_{\rm FPT} = P_{\rm FPT}(n\Delta S) \tag{9.58}$$

$$X^n = \left[\frac{\delta_{\rm c}(n\Delta s)}{n\Delta s} - \delta_{\rm c}'(n\Delta s)\right] P_{\rm free}\left[\delta_{\rm c}(n\Delta s), n\Delta s\right] \tag{9.59}$$

$$M^n{}_m = \left[\delta_{\rm c}'(n\Delta s) - \frac{\delta_{\rm c}(n\Delta s)-\delta_{\rm c}(m\Delta s)}{(n-m)\Delta s}\right] P_{\rm free}\left[\delta_{\rm c}(n\Delta s)-\delta_{\rm c}(m\Delta s), (n-m)\Delta s\right]. \tag{9.60}$$

Note that we chose to solve *the* Volterra equation that is such that the diagonal of the matrix $M^n{}_m$ is 0. If one tries to discretize Eq. (9.31) in general, then one obtains a matrix $M^n{}_m$ with diverging elements on the diagonal, unless the specific choice (9.32) is made, which proves its usefulness.

The solution to Eq. (9.57) is simply given by

$$P_{\rm FPT} = ({\rm Id} - M)^{-1} X. \tag{9.61}$$

Since ${\rm Id} - M$ is a lower triangular matrix, it can be easily inverted with the "forward-substitution" algorithm, the numerical cost of which only scales as the square of the size of the matrix (compared to cubic scaling in general).

9.B Density contrast in the Newtonian slicing

In Section 9.3.7, we motivated the choice of the comoving slicing to evaluate the density contrast on super-Hubble scales, and express our PBH formation criterion. In the present appendix, we explore the consequences of choosing a different slicing, in order to understand how much our conclusions

depend on that choice. In practice, we consider the Newtonian slicing, which consists in setting $\alpha = \beta = -2$ in Eq. (9.37), and Eq. (9.39) reduces to

$$\delta_k \simeq -\frac{2}{5}\left[3 + \left(\frac{k}{aH}\right)^2\right]\zeta_k \,. \tag{9.62}$$

The main difference with the comoving slicing is that, for a curvature perturbation that is scale invariant on super-Hubble scales, the density contrast is not suppressed any more above the Hubble radius. This is why we discarded this choice of slicing in Section 9.3.7, since super-Hubble scales should only lead to a local rescaling of the background field values inside a Hubble patch, and thus not contribute to whether a black hole forms.

In the Newtonian slicing, on super-Hubble scales, $\delta_k \simeq -\frac{6}{5}\zeta_k$, so δ_k is conserved since ζ_k is (and contrary to the comoving slicing where δ_k grows like the scale factor). This means that the variance of the density contrast can equally be evaluated at the end of inflation or at the band-crossing time, namely

$$\sigma_R^2(t_{\rm end}) = \sigma_R^2(t_{\rm bc}) = \left(\frac{6}{5}\right)^2 \int_0^{a/R} \mathcal{P}_\zeta\left(k, t_{\rm end}\right) \frac{{\rm d}k}{k} \,. \tag{9.63}$$

The collapse criterion is given by Eq. (9.8), and it is strongly scale-dependent, contrary to the case of the comoving density contrast. As explained in Section 9.3.4, a good approximation in the case of very red thresholds is given by the Press-Schechter formula without the additional factor of 2. This is explained by the fact that the barrier moves faster than the average trajectories and multiple crossings are unlikely.

We apply the techniques described in Appendix 9.A and present our results in Fig. 9.7. In Fig. 9.7a, one can check that indeed, the (one times) Press-Schechter formula provides a good approximation to the excursion-set result, up until $\Omega_{\rm PBH}$ reaches 1/2. This is because the Press-Schechter formula does not allow for more than half of the universe being collapsed. One can check that the condition (9.34) is indeed verified only when $\Omega_{\rm PBH} < 1/2$. For that purpose we set $\epsilon \approx 1/2$ and, in Fig. 9.7a, we display

$$\max_{\ln(R_1/R_2)>\epsilon}\left[\frac{\sqrt{S(R_2) - S(R_1)}}{\delta_{\rm c}(R_1) - \delta_{\rm c}(R_2)}\right] \tag{9.64}$$

with the solid yellow line. One expects the Press-Schechter formula to provide a good approximation when this quantity is below unity, which is indeed the case. Above $\Omega_{\rm PBH} = 1/2$, the abundance of PBHs continues to slowly increase. This behaviour is rather different from the results obtained with the comoving density contrast in Section 9.4.3, where we found an abrupt transition from $\Omega_{\rm PBH} = 0$ to $\Omega_{\rm PBH} = 1$, see Fig. 9.5.

Beside those differences, by comparing the right panel of Fig. 9.5 with Fig. 9.7b, one can see that the region of parameter space that substantially produces PBHs is roughly the same (in Fig. 9.7b, we have reported the dashed blue line of the right panel of Fig. 9.5 in order to guide the reader's eye). By comparing Fig. 9.6a with Fig. 9.7c, one can see that the typical masses involved are also roughly the same. However, when comparing Figs. 9.6b and 9.7d, one realizes that the mass distributions are much wider in the Newtonian case. This is because, since the density contrast is not suppressed on large scales in the Newtonian slicing, it yields a heavier large-mass tail than in the comoving slicing.

9.C Comparison with Ref. [430]

In Ref. [430], a calculation of the PBH abundance in metric preheating was performed by making use of the simplified, commonly used estimate presented in Section 9.3.7. While this is enough to correctly identify the region in parameter space that leads to substantial PBH production, see the discussion below Eq. (9.53), which is consistent with Eq. (4.1) of Ref. [430], this is a priori not sufficiently accurate to derive detailed predictions about the mass distribution, in particular in regimes where the cloud-in-cloud mechanism plays an important role.

In Ref. [430], it was indeed pointed out that in cases where PBHs are abundantly produced, *i.e.* under the condition (9.53), the simple estimate of Section 9.3.7 predicts $\Omega_{\rm PBH} > 1$, which clearly signals its breaking down. In order to deal with this issue, two solutions were proposed in Ref. [430]: either remove by hand the small-mass end of the distribution, in order to bring $\Omega_{\rm PBH}$ back to one, and to model the possible absorption of small black holes into larger black holes (this was dubbed "renormalization by absorption"); or stop the instability phase prematurely, at the time when $\Omega_{\rm PBH}$ crosses one, since the universe stops being dominated by an oscillating scalar field at that point (this was dubbed "renormalization by premature ending"). Since the later approach effectively removes larger-mass black holes from the distributions (given that heavier black holes come from larger scales, that enter the instability band later), it was assumed in Ref. [430] that these two results would bound the true mass distribution on each side, and that any conclusion that can be drawn in both approaches probably applies to the actual result.

In this appendix, we want to verify these statements, and in Fig. 9.8, we compare the mass fraction obtained in this work (solid red line) with the formulas derived in Ref. [430] when "renormalization" is performed by absorption (olive line) or by premature ending (purple line), starting from the "raw" result (orange line) that leads to the problematic $\Omega_{\rm PBH} > 1$. Although, as expected, neither approach provides a good description of the full result, the order of magnitude of the overall amplitude is correctly reproduced, and the actual mass distribution is indeed approximately bounded by the results from the two renormalization procedures (although it is closer to the "renormalization by absorption" result). This therefore confirms the relevance of Ref. [430].

The main difference in the shape of the mass distribution concerns the location of the peak mass: in Ref. [430], it was found that the mass where most PBHs form is the smallest mass that undergoes parametric amplification, *i.e.* the Hubble mass at the end of inflation, see Eq. (9.54), or the cutoff mass in the case of "renormalization by absorption". Here, we find that the mass distribution peaks several orders of magnitude above that mass, see the discussion following Eq. (9.55).

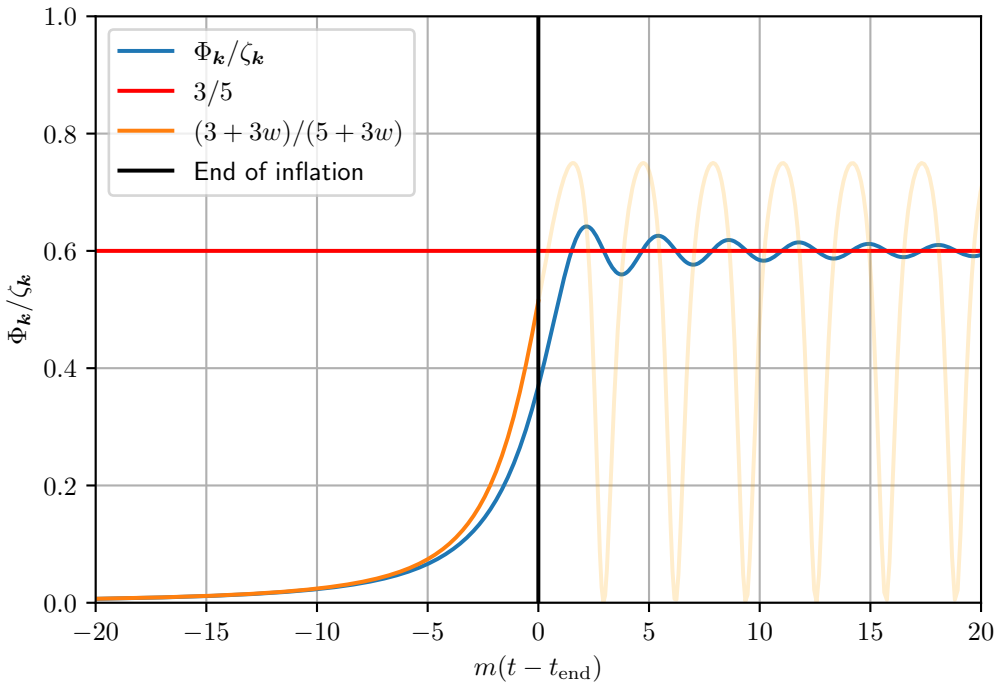

Figure 9.2: Bardeen potential $\Phi_{\boldsymbol{k}}$ rescaled by the curvature perturbation $\zeta_{\boldsymbol{k}}$ during the last e-folds of inflation and the first e-folds of the oscillatory phase, in the same situation as the one displayed in Fig. 9.1, for a scale $\boldsymbol{k}$ that is sufficiently far outside the Hubble radius such that $\zeta_{\boldsymbol{k}}$ can be taken as constant. The blue line stands for the full numerical solution of Eq. (9.38), seen as a differential equation for $\Phi_{\boldsymbol{k}}(t)$, where $w(t)$ and $H(t)$ are extracted from Fig. 9.1. The red line stands for the approximation (9.43), $\Phi_{\boldsymbol{k}}/\zeta_{\boldsymbol{k}} = 3/5$, obtained as the late-time solution of Eq. (9.38) when setting $w = 0$ and $H = 2/(3t)$, and towards which the full numerical result asymptotes after a few oscillations. The orange line stands for Eq. (9.38) where we neglected $\dot{\Phi}_{\boldsymbol{k}}/H$ with respect to $\Phi_{\boldsymbol{k}}$. This approximation is well justified on super-Hubble scales during inflation, since w is almost constant there, but fails during the subsequent oscillatory phase where w vanishes on average but otherwise undergoes large oscillations.

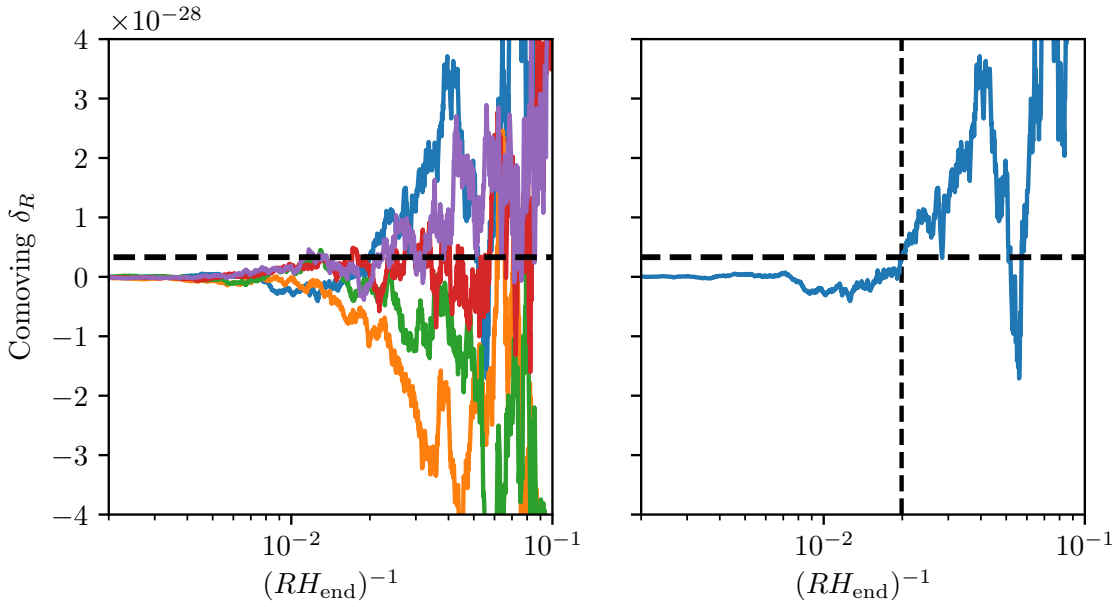

Figure 9.3: Example of Langevin trajectories for the density contrast evaluated on comoving slices at the end of inflation, and coarse-grained at the scale R, for $H_{\rm end} = 10^{-8} M_{\rm pl}$ and $H_\Gamma = 10^{-25} M_{\rm pl}$. The (quasi) horizontal black dashed line shows the collapse criterion (9.45). In the right panel, we isolate one realization and the vertical dashed line denotes the first crossing "time" (*i.e.* scale) of the critical threshold.

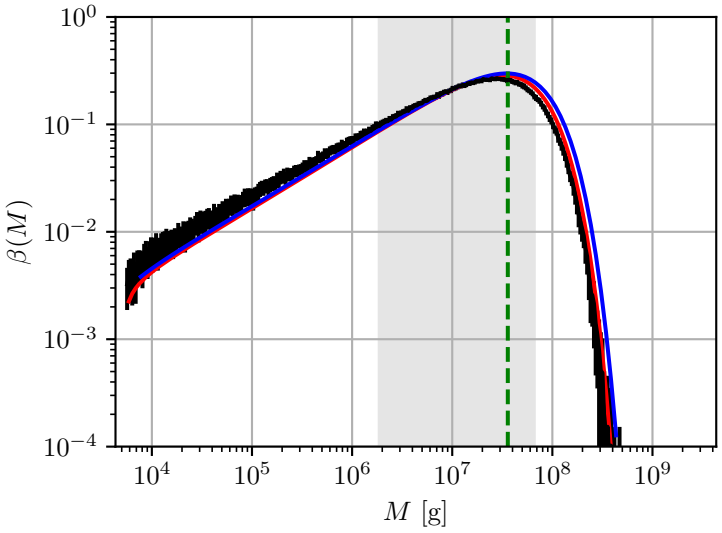

Figure 9.4: Mass fraction β of primordial black holes for $H_{\rm end} = 10^{-8} M_{\rm pl}$ and $H_\Gamma = 10^{-25} M_{\rm pl}$, as a function of the mass M in grams. The vertical black bars stand for the distribution of first crossing times obtained from 10^6 simulated realizations of the Langevin equation (9.22), binned into 1000 logarithmically spaced values of R. The size of the bars correspond to 5σ estimates of the statistical error by jackknife resampling. The red line corresponds to numerically solving the Volterra equation (9.32), using the method described in Appendix 9.A. The blue line displays the analytical approximation developed in Section 9.4.4, which provides a good fit to the full numerical. The vertical green line denotes the mass at which β peaks, as estimated from Eq. (9.55), and the grey shaded area stands for the 1σ deviation of $\ln(M)$ according to the distribution $\beta(M)$, centred on its mean value.

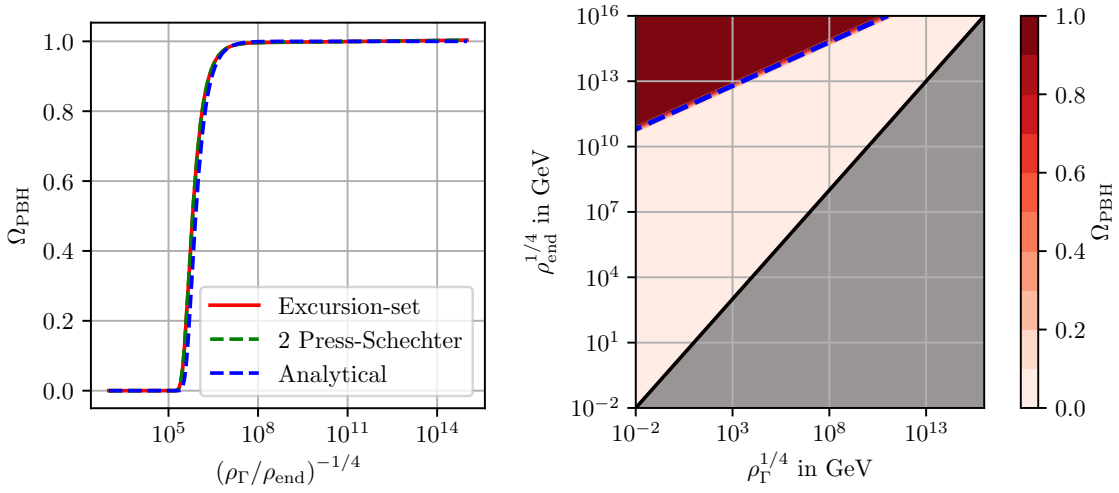

Figure 9.5: Total fraction of the universe comprised in PBHs, $\Omega_{\rm PBH}$, as a function of $\rho_{\rm end}$, the energy density at the end of inflation, and ρ_Γ, the energy density at the end of the instability phase. On the left panel, we fix $\rho_{\rm end} = 10^{-12} M_{\rm pl}^4$ and let ρ_Γ vary. The solid red curve is the full numerical result obtained in the excursion-set approach. The dashed green line corresponds to the Press-Schechter result with the additional factor 2, which becomes exact in the limit of a scale-invariant threshold, see Section 9.3.4. The dashed blue line corresponds to the analytical approximation (9.52). On the right panel, the full parameter space is explored (where $\rho_\Gamma < \rho_{\rm end}$ since the oscillatory phase occurs after inflation). The colour encodes the value of $\Omega_{\rm PBH}$, and the transition from tiny values to values close to one is very abrupt. The dashed blue line stands for the analytical estimate (9.53) for the location of this transition.

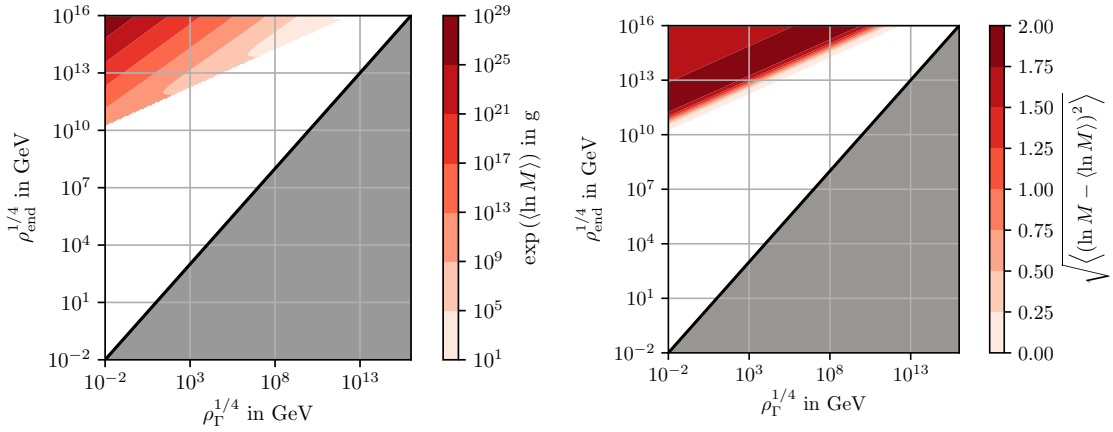

(a) Mean PBH mass.

(b) Dispersion of the PBH masses.

Figure 9.6: Typical masses of the PBHs produced in metric preheating. The left panel shows the average mass, computed from the mass fraction distribution. In the white region the abundance of PBHs is too small to be numerically resolved, hence the average mass cannot be computed. On the right panel, we show the standard deviation of $\ln(M)$, which describes the typical width of the mass fraction distribution.

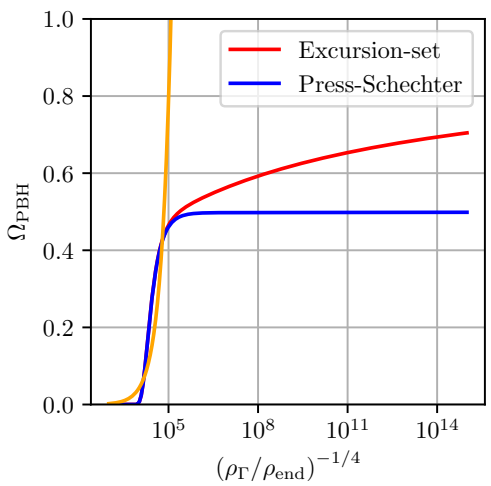

(a) Evolution of Ω_{PBH} at $\rho_{\mathrm{end}} = 10^{-12} M_{\mathrm{pl}}^4$.

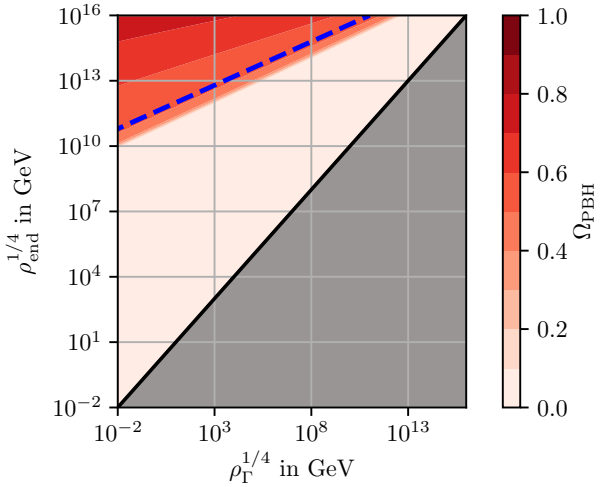

(b) Ω_{PBH} as a function of ρ_{end} and ρ_Γ.

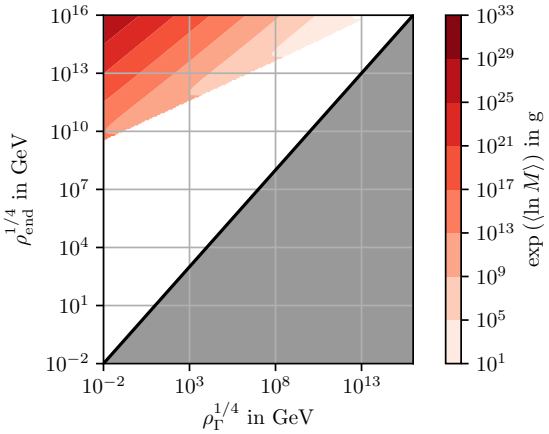

(c) Average mass of PBH.

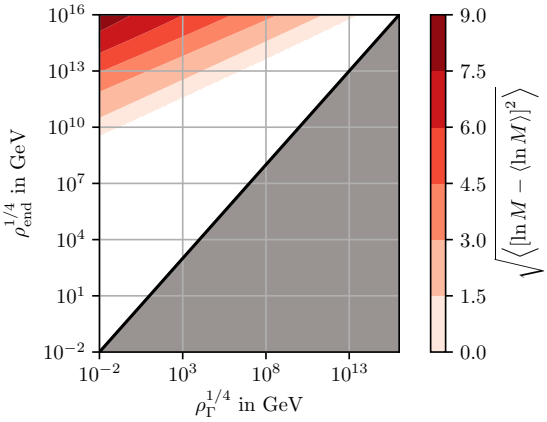

(d) Dispersion of the PBH masses.

Figure 9.7: PBH mass fraction if the formation criterion is interpreted in the Newtonian slicing.

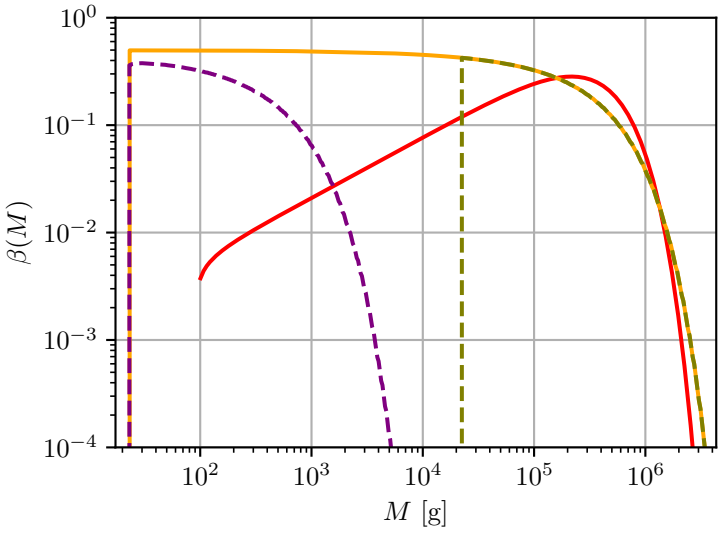

Figure 9.8: Mass fraction β of primordial black holes for $\rho_{\rm end} = 10^{-12} M_{\rm pl}^4$ and $\rho_\Gamma = 10^{-40} M_{\rm pl}$. As in Fig. 9.4, the red line corresponds to numerically solving the Volterra equation (9.32). The olive, orange and purple lines correspond to the results of Ref. [430] and are taken from Fig. 4 of that reference. The orange line displays the "raw" result obtained with the estimate of Section 9.3.7, which leads to the problematic $\Omega_{\rm PBH} > 1$. Then, "renormalization" is either performed by "premature ending" (purple dashed line) or by "absorption" (olive dashed line).

Part III

First order phase transitions

Chapter 10

Generation of gravitational waves from freely decaying turbulence

This chapter is based on an ongoing work with Daniel Cutting, David Weir, Mark Hindmarsh and Kari Rummukainen of the University of Helsinki and my supervisors Chiara Caprini and Danièle Steer. Our collaboration began in November 2018 with an initial visit in Helsinki. Initially, the goal was to study both the formation and the decay of turbulence after a first order phase transition using the numerical simulation code developed by the group in Finland [201]. The project received support from the HPC-Europa3 Transnational Access program, which provided computational resources as well as funding for a one-month visit in May 2019, and by the International Emerging Actions program awarded by the CNRS in February 2020 to fund visits between France and Finland. During the project, we realized that the code was not adapted to study the formation of turbulence and the project refocused on the subsequent phase of free decay. This project is taking a long time to complete as it is at the intersection of many areas of expertise: gravitational waves, turbulence, and massively parallel numerical simulations. Additionally, the Covid pandemic unfortunately put an end to our regular visits between France and Finland which slowed down the completion of the project. I have contributed to all the aspects of this work, including adapting the code of the group at the University of Helsinki to our problem and running the large scale numerical simulations.

Abstract

We calculate the stochastic background of gravitational waves (SGWB) produced by a phase of freely decaying turbulence in the early Universe. Turbulence may be sourced by a first order phase transition at the electroweak scale, in scenarios beyond the Standard Model. In this case, the gravitational wave signal that turbulence generates may fall in the frequency band of the space-based interferometer LISA. We start by reviewing the computation of the SGWB from purely vortical motions in a relativistic fluid to calculate the GW spectrum. We then construct a model for freely decaying turbulence and compare it with direct numerical simulations. In particular, we validate numerically the unequal-time correlations (UETCs) of the velocity field and the evolution laws of the kinetic energy and the integral scale. We stress that any two point correlator must satisfy the *Mercer condition*, and we propose to use the Gibbs kernel for the turbulent UETC: this interpolates well the result of the numerical simulations, and guarantees positivity of the velocity, anisotropic stresses and gravitational wave energy density power spectra. In order to calculate the SGWB spectrum, we directly

perform the four-dimensional integration (on time and wave-vector convolution) using VEGAS: an algorithm based on importance sampling.

10.1 Introduction

Gravitational wave (GW) signals from the early universe have the potential to open a new observational window on high energy physics phenomena. In this context, first-order cosmological phase transitions (FOPTs) provide a compelling source of GWs. This was first proposed many years ago (see Refs. [487, 488, 489, 490, 491, 197]), before it became clear that the electroweak (EW) symmetry breaking proceeds as a cross-over in the Standard Model [492]. However, it has since emerged that many scenarios beyond the Standard Model (BSM) lead to first-order phase transitions at, and beyond, the EW scale, reopening the case for the study of GW production from FOPTs (for a recent, GW-oriented review, see [493]).

This is particularly interesting in the context of the Laser Interferometer Space Antenna (LISA), which has been selected by the European Space Agency in 2017 as the large class mission L3 [207]. LISA is sensitive to a frequency window around the mHz. In the context of primordial GW-sourcing processes that are localized in time, such as a FOPT, the characteristic frequency of the GWs today can be connected to the characteristic time/length scale of the source anisotropic stresses R_*, via

$$f \sim 16.5 \cdot 10^{-3}\,\mathrm{mHz}\,\frac{1}{R_* H_*}\,\frac{T_*}{100\,\mathrm{GeV}}\left(\frac{g_*}{100}\right)^{1/6}. \tag{10.1}$$

Here a subscript $*$ denotes the epoch at which the phase transition occurs. This shows that LISA can potentially detect the GW signal from FOPTs in the window 100 GeV – 1 TeV, if the characteristic time/length scale of the anisotropic stresses is of the order $R_* \sim 10^{-2}$ to 10^{-3} of the Hubble scale H_* at the FOPT time. The latter can be considered as typical values for $R_* H_*$, given that R_* is related to the mean bubble separation (see *i.e.* [202, 493] and references therein). LISA can therefore offer a new way to probe BSM physics, complementary to the Large Hadron Collider.

There are several processes possibly leading to sizable anisotropic stresses in connection with a FOPT. This rich phenomenology renders FOPTs particularly appealing as primordial GW sources. Bubble percolation, with the consequent break of spherical symmetry, is the most direct one [489, 490, 491]. The GW generation by bubble collision has been analysed both with numerical simulations [199, 203, 494, 495] and analytical approaches [198, 496, 497].

The first numerical simulations of the coupled system of a scalar field and a relativistic fluid have shown that sound waves, produced in the fluid by expanding bubbles, are also a promising source of GWs [200, 201, 498, 499]. Refs. [200, 201, 498] showed that they are indeed the dominant GW source, in the case of FOPTs of weak to intermediate strength, *i.e.* $\alpha \lesssim 0.1$, where α is the ratio of the trace anomaly of the energy momentum tensor and the thermal energy.

In stronger FOPTs with $\alpha \sim 1$ or larger, the characteristic time of shock formation $\tau_{\rm sh} \sim R_*/v_{||}$, where $v_{||}$ denotes the root mean squared (rms) velocity of the acoustic motion, can become shorter than the Hubble time $\tau_{\rm sh} H_* \lesssim 1$ [202, 500, 501]. Shocks can therefore develop in the fluid motion, and are expected to convert the acoustic phase into a turbulent one [502]. Vortical flows has also been seen to be generated in the numerical simulations carried out in Ref. [503], by the non-linear interactions of relativistic compressional fluid flows surrounding the colliding bubbles of the stable phase.

In the present work, we study the GW signal generated by a hypothetical turbulent phase in the aftermath of a FOPT. The first analyses of the GW signal from turbulence have relied on analytical

modelling of the turbulent flow, and semi-analytical estimates of the GW signal [197, 504, 505, 506, 507, 508, 509]. Ref. [510] is the most recent one adopting semi-analytical techniques, and evaluates the GW signal from all components (compressional, vortical, magnetic field) of both standard, and helical, freely-decaying magneto-hydrodynamic (MHD) turbulence. Various spectral shapes and scaling of the GW power spectrum have been found, depending on the relative amplitude of the compressional and vortical components, and on the presence of helicity. In Ref. [510], it is also argued that the correct auto-correlation time to be used in the equations describing GW production by turbulence is the Eulerian eddy turnover time $\tau_{\rm e} \sim (k v_{\rm sw})^{-1}$, where $v_{\rm sw}$ is a locally uniform velocity field *sweeping* the vortices in accordance with *Kraichnan Random Sweeping Model* [511], and not the Lagrangian one $\tau_\ell \sim (k v_\ell)^{-1}$, where v_ℓ is the velocity on the scale ℓ (used *e.g.* in Refs. [505, 506, 508]).

Recently, numerical simulations of both non-helical and helical MHD turbulence and the subsequent GW generation have been carried out in Refs. [512, 513, 514, 515]. These works introduce also an initial phase, in which the MHD turbulence develops, starting from a nearly monochromatic electromotive force, or a kinetic forcing. The spectral shape of the GW signal depends on whether magnetic and/or kinetic energy is present in the initial conditions, with a well-established power spectrum, or if it is sourced by the forcing.

In this chapter, we develop a semi-analytical model of GW generation by freely-decaying kinetic, vortical, non-helical turbulence, which is supported by the results of numerical simulations. We rely on the relativistic hydrodynamic code developed by Refs. [200, 201, 498], but we use it to study the evolution of vortical fluid motions, excluding the dynamics of the scalar field undergoing the FOPT (see Section 10.3). We have chosen to over-simplify the turbulence model (no compressional modes, no helicity, no magnetic field, no initial forcing phase) in order to have fully under control the analytical understanding of the GW production. Increase in complexity will be tackled in future works.

The simulation is initialized in Fourier space, assuming Gaussian and vortical velocity fluctuations, following an input power spectrum (see Section 10.3 and Section 10.4.1). We therefore do not simulate the turbulence formation in our numerical simulations, but only the turbulence decay. However, as already pointed out in the analytical evaluations of [516, 508, 509], and found in the numerical simulations of [512, 513, 514, 515], we confirm here that the initial phase, in which the turbulent kinetic energy (*i.e.* the kinetic energy associated with the vortical motion) is sourced and grows, plays an important role in shaping the final GW signal. This is one of our main results, as we shall see. The initial phase of turbulence development is modelled here in three heuristic ways: an instantaneous generation of turbulence, a linear growth of the kinetic energy, as done in Refs. [508, 510], imposing continuity with the free-decay phase; and $\mathcal{C}^1$ growth of the kinetic energy, designed specifically to guarantee that the transition to the decay phase is smooth (see Section 10.4.5). It is difficult to connect these simplified models with the electromotive forcing of Ref. [517, 513], however, they are of help in the analytical interpretation, as we shall see.

Correctly assessing, and implementing, how the GW source decorrelates in time is also of paramount importance for the GW signal evaluation [516, 508, 509]. In the present context, the decorrelation model must be suited to freely-decaying turbulence. This was attempted in Ref. [508], which extended the exponential Kraichnan decorrelation proposed in Ref. [511], and adopted in Refs. [505, 506] in the context of stationary turbulence, to freely-decaying turbulence (erroneously with the Lagrangian eddy turnover time instead of the Eulerian one, as previously mentioned [510]). By doing so, [508] ran into the question of how to define a valid correlation function for a non-stationary process.

The solution of this problem originally proposed in Ref. [508], consisting in modelling the decorrelation directly in the anisotropic stresses with a top-hat Ansatz, rather than in the velocity field, is not satisfactory, since it effectively sets the decorrelation time of the turbulent flow to the light-crossing time $\tau \sim 1/k$, which does not depend on the velocity of the turbulent flow. Here, we consistently address this issue in the context of the theory of positive Kernels, and propose to model the unequal time power spectrum of the turbulent velocity field as a Gibbs Kernel (see Section 10.5). This provides a way to symmetrize the unequal time power spectrum, and it most importantly guarantees that the anisotropic stress two-point function is a valid correlation function, and therefore guarantees that it leads to a positive GW energy density power spectrum (*c.f.* Eq. (10.15)).

Concerning the turbulent velocity decorrelation law, we adopt here the Kraichnan sweeping hypothesis [511], which is supported by numerical works simulating decaying isotropic turbulence [518], and has been used in the context of GW generation in Ref. [510]. The numerical simulations we perform show very good agreement with the Kraichnan Sweeping Model in the inertial range (see Section 10.4.2). Furthermore, we have performed, for the first time to our knowledge, numerical simulations allowing us to measure the unequal time correlations of the velocity field also at large scales, outside the inertial range (see Section 10.4.3). Thanks to these simulations, we can validate the decorrelation model also in the infrared tail of the velocity power spectrum. This might not be of much interest in the study of turbulent evolution, but constitutes a necessary step to calculate GW production by turbulence.

The free-decay of the turbulence can also be extracted from our simulations. We study the evolution of the kinetic energy and of the integral scale of the flow, and link it to the model of Refs. [519, 520] (see Section 3.2). The decay laws inferred from the simulations are broadly consistent with the findings of [520] for the case of purely kinetic, non-helical turbulence. We insert them in the analytical model of the turbulence developed to evaluate the GW production. As we shall see, the exact values of the power-law exponents of the turbulent decay do not play a relevant role in determining the final shape of the GW spectrum, as the bulk of the GW signal is sourced on a characteristic time which is smaller than the typical time it takes for the decay of the kinetic energy and the growth of the integral scale to equilibrate to well-defined power-laws.

Finally, we use the turbulent model developed so far (consisting in the equal time spectral shape, the unequal time symmetrized power spectrum, the time decorrelation at small and large scales, the growth phase of the kinetic energy, the overall free decay and turbulence duration) to evaluate the anisotropic stresses (see Section 10.6.1) and calculate the GW signal (see Section 10.6.2). This is tackled by means of a four-dimensional numerical integration code, which handles the two time integrations arising from the GW time evolution, and the two momentum integrations arising from the velocity power spectrum convolution (*c.f.* Eq. (10.97)).

10.2 Stochastic background of gravitational waves

10.2.1 Generation of gravitational waves

In the cosmological context GWs are described by transverse and traceless tensor perturbations h_{ij} over the background FLRW metric describing the homogeneous and isotropic Universe:

$$\mathrm{d}s^2 = a^2(\eta)\big[-\mathrm{d}\eta^2 + (\delta_{ij} + 2h_{ij})\,\mathrm{d}x^i\,\mathrm{d}x^j\big], \tag{10.2}$$

with $\partial_i h_{ij} = h_{ii} = 0$. It follows from the linearized Einstein equations that

$$\ddot{h}_{ij} + 2\mathcal{H}\dot{h}_{ij} + k^2 h_{ij} = 8\pi G a^2(\eta) T_{ij}^{(TT)}(\mathbf{k}, \eta) \tag{10.3}$$

where $\mathcal{H} = \dot{a}/a$ is the comoving Hubble parameter, $\cdot = \mathrm{d}/\mathrm{d}\eta$, and $T_{ij}^{(TT)}$ is the transverse traceless part of the perturbed fluid stress-energy tensor. We work in the radiation era, and define $T_{ij}^{(TT)} = (4\rho/3)\tilde{\Pi}_{ij}$ so that using Friedmann's equation, Eq. (10.3) can be rewritten as

$$\ddot{h}_{ij} + 2\mathcal{H}\dot{h}_{ij} + k^2 h_{ij} = 4\mathcal{H}^2 \tilde{\Pi}_{ij}(\mathbf{k}, \eta). \tag{10.4}$$

Assuming that there were no changes in the relativistic degrees of freedom, $\mathcal{H} = \eta^{-1}$, and

$$\ddot{h}_{ij} + \frac{2}{\eta}\dot{h}_{ij} + k^2 h_{ij} = \frac{4}{\eta^2}\tilde{\Pi}_{ij}(\mathbf{k}, \eta). \tag{10.5}$$

Changing variable from $h_{ij}(\mathbf{k}, \eta)$ to $\eta\, h_{ij}(\mathbf{k}, \eta)$, Eq (10.5) becomes the equation for a forced harmonic oscillator whose Green's function is known (see Ref. [29] for a review). The solution is

$$h_{ij}(\mathbf{k}, \eta) = 4 \int_{\eta_{\rm ini}}^{\eta} \frac{\sin k(\eta - \zeta)}{k\eta} \tilde{\Pi}_{ij}(\mathbf{k}, \zeta) \frac{\mathrm{d}\zeta}{\zeta}, \tag{10.6}$$

where $\eta_{\rm ini}$ is the conformal time at which the source turns on. Thus,

$$\dot{h}_{ij}(\mathbf{k}, \eta) = 4 \int_{\eta_{\rm ini}}^{\eta} \left[\frac{\cos k(\eta - \zeta)}{\eta} - \frac{\sin k(\eta - \zeta)}{k\eta^2} \right] \tilde{\Pi}_{ij}(\mathbf{k}, \zeta) \frac{\mathrm{d}\zeta}{\zeta}. \tag{10.7}$$

The solution at late times, $\eta \gg \eta_{\rm fin}$ when the source has stopped operating, can be found by matching Eqs. (10.6) and (10.7) with the homogeneous solution [29]. For wavenumbers $k\eta \gg 1$, we can further neglect the sine contribution in Eq (10.7), and obtain

$$\dot{h}_{ij}(\mathbf{k}, \eta > \eta_{\rm fin}) = 4 \int_{\eta_{\rm ini}}^{\eta_{\rm fin}} \frac{\cos k(\eta - \zeta)}{\eta} \tilde{\Pi}_{ij}(\mathbf{k}, \zeta) \frac{\mathrm{d}\zeta}{\zeta}. \tag{10.8}$$

10.2.2 GW energy density power spectrum

The superposition of GW signals, coming from patches in the sky that were causally disconnected at the moment of their emission in the very early universe, can only be studied statistically. Assuming statistical homogeneity and isotropy, the two-point correlation function of the strain tensor can be written

$$\left\langle \dot{h}_{ij}^*(\mathbf{k}, \eta) \dot{h}_{ij}(\mathbf{q}, \eta) \right\rangle = (2\pi)^3 \delta(\mathbf{q} - \mathbf{k}) \left|\dot{h}\right|^2 (k, \eta). \tag{10.9}$$

The fractional GW energy density is (where ρ_c denotes the critical energy density)

$$\frac{\rho_{\rm gw}}{\rho_c} = \frac{\left\langle \dot{h}_{ij}^*(\mathbf{x}, \eta) \dot{h}_{ij}(\mathbf{x}, \eta) \right\rangle}{8\pi G a^2(\eta) \rho_c} \equiv \int \frac{\mathrm{d}k}{k} \frac{\mathrm{d}\Omega_{\rm gw}}{\mathrm{d}\ln k}. \tag{10.10}$$

The fractional GW energy density power spectrum is then

$$\left.\frac{\mathrm{d}\Omega_{\rm gw}}{\mathrm{d}\ln k}\right|_{\eta} = \frac{k^3 \left|\dot{h}\right|^2 (k, \eta)}{2(2\pi)^3 G a^2(\eta) \rho_c}. \tag{10.11}$$

The GW source must also be described statistically: the anisotropic stress two-point correlation function, taken at different times, is defined by

$$\left\langle \tilde{\Pi}_{ij}(\mathbf{k},\zeta), \tilde{\Pi}_{ij}(\mathbf{q},\tau) \right\rangle = (2\pi)^3 \delta(\mathbf{k}-\mathbf{q}) \tilde{\Pi}^2(k,\zeta,\tau). \tag{10.12}$$

From Eq (10.8), one then obtains

$$\left|\dot{h}\right|^2(k,\eta) = \frac{8}{\eta^2} \iint_{\eta_{\rm ini}}^{\eta_{\rm fin}} \cos k(\tau-\zeta) \tilde{\Pi}^2(k,\zeta,\tau) \frac{\mathrm{d}\tau}{\tau} \frac{\mathrm{d}\zeta}{\zeta}, \tag{10.13}$$

where we have used the trigonometric identities and averaged over a long time $\eta \gg k^{-1}$.

Accounting for the fact that the GW signal redshifts as radiation,

$$\left.\frac{\mathrm{d}\Omega_{\rm gw}}{\mathrm{d}\ln k}\right|_{\eta_0} = \left(\frac{a_{\rm fin}}{a_0}\right)^4 \left.\frac{\mathrm{d}\Omega_{\rm gw}}{\mathrm{d}\ln k}\right|_{\eta_{\rm fin}}, \tag{10.14}$$

and combining Eqs. (10.11) and (10.13), one finds

$$\left.\frac{\mathrm{d}\Omega_{\rm gw}}{\mathrm{d}\ln k}\right|_{\eta_0} = \frac{4}{3\pi^2} \Omega_{\rm rad}^0 \frac{g_{\rm fin}}{g_0} \left(\frac{g_{s,0}}{g_{s,\rm fin}}\right)^{4/3} k^3 \iint_{\eta_{\rm ini}}^{\eta_{\rm fin}} \cos k(\tau-\zeta) \tilde{\Pi}^2(k,\zeta,\tau) \frac{\mathrm{d}\tau}{\tau} \frac{\mathrm{d}\zeta}{\zeta}, \tag{10.15}$$

where g and g_s denote respectively the radiation and entropy relativistic degrees of freedom. In Eq. (10.15) we have further used

$$a_{\rm fin} = a_0^2 H_0 \sqrt{\Omega_{\rm rad}^0} \left(\frac{g_{\rm fin}}{g_0}\right)^{1/2} \left(\frac{g_{s,0}}{g_{s,\rm fin}}\right)^{2/3} \eta_{\rm fin} \tag{10.16}$$

to transform the pre-factor ${a_{\rm fin}}^4/(2\pi^3 G {a_0}^4 a_{\rm fin}^2 \eta_{\rm fin}^2 \rho_c)$.

As can be seen from Eq. (10.15), the GW signal is determined by the unequal-time stress energy $\tilde{\Pi}^2(k,\zeta,\tau)$ of the fluid. In the case under analysis, the source of GW is provided by decaying turbulence in a relativistic fluid. In Section 10.4, we model the turbulence power spectrum, and in Section 10.6.1, we derive the connection between the turbulence power spectrum Eq. (10.86) and the anisotropic stress power spectrum: see Eq. (10.95).

As we discuss in Section 10.5, the power spectrum of any random variable must be a positive kernel (see *i.e.* [521]). Consequently, $\tilde{\Pi}^2(k,\zeta,\tau)$ defined in Eq. (10.12), must be a positive kernel, since it describes the random anisotropic stresses arising from the turbulent field. This guarantees that the GW energy density power spectrum is indeed positive, *c.f.* Eq. (10.15). This issue had already been raised in Ref. [508].

10.3 Numerical simulations

We carry out a series of direct numerical simulations in order to study unequal-time correlations (UETCs) during hydrodynamical turbulence in the early Universe. For our numerical simulations we use a modified version of the relativistic hydrodynamics code previously used to study the coupled evolution of the scalar field and the fluid, and the production of gravitational waves during a thermal phase transition [200, 201, 498, 503]. While earlier uses of the code simulated the phase transition itself with the coupled field-fluid model [522], here we are interested in the dynamics of the fluid after the transition has completed. We therefore "turn off" the evolution of the scalar field and are left with the evolution of a relativistic fluid. We now specify the equations of motion of the fluid and then explain how we fix the initial conditions for our simulations.

10.3.1 Evolution laws

The energy momentum tensor of the system is that of a perfect fluid in Minkowski space

$$T^{\mu\nu} = (\epsilon + p)U^\mu U^\nu + g^{\mu\nu}p, \tag{10.17}$$

with ϵ the internal energy density in the fluid, p the pressure, $U^\mu = \gamma(1, \mathbf{v})$ the fluid four-velocity and with Lorentz factor $\gamma = 1/\sqrt{1-v^2}$. We fix the equation of state to be that of a relativistic gas with $p = \epsilon/3$. It has been shown that the hydrodynamic equations of motion in an expanding Universe with zero curvature are the same as the hydrodynamic equations in Minkowski space-time in conformal time, provided the dynamical quantities are replaced by scaled variables [523]. Hence, we do not need to adapt our simulation code to study hydrodynamic turbulence in an expanding background.

The dynamical quantities that we evolve are the fluid energy density $E = \gamma\epsilon$ with equation of motion [201]

$$\dot{E} + \partial_i(Ev^i) + p\left[\dot{\gamma} + \partial_i(\gamma v^i)\right] = 0, \tag{10.18}$$

and the fluid momentum density $Z_i = \gamma^2(\epsilon + p)v_i$, the components of which evolve according to

$$\dot{Z}_i + \partial_j(Z_i v^j) + \partial_i p = 0. \tag{10.19}$$

Our evolution algorithm follows the approach taken in Ref.[524] with a leapfrog method for updating the dynamical quantities. For this chapter we use a van Leer scheme for the advection update, whereas earlier uses of this code used an upward donor cell scheme [525, 526]. We find that using the van Leer scheme the UETCs converge faster with decreasing lattice spacing.

10.3.2 Initial conditions of the numerical simulation

We initialize the velocity field of our simulation in Fourier space

$$\mathbf{v}(\mathbf{x}) = \sum_{\mathbf{k}} \mathbf{v}_\mathbf{k}\, \mathrm{e}^{i\mathbf{k}\cdot\mathbf{x}}, \tag{10.20}$$

where $\mathbf{k}$ takes discrete values in the reciprocal lattice. Each mode $\mathbf{v}_\mathbf{k}$ is randomly distributed and follows Gaussian statistics with mean zero and variance determined by an arbitrary velocity power spectrum serving as initial condition (see Section 10.4.1 for its specification).

The velocity field is then projected onto its vortical component with the projector

$$\mathcal{P}_{ij}(\mathbf{k}) = \delta_{ij} - \hat{\mathbf{k}}_i\hat{\mathbf{k}}_j. \tag{10.21}$$

Since $\mathbf{x} \in \mathbb{R}^3$, we finally impose that

$$\mathbf{v}_\mathbf{k} = \mathbf{v}^*_{-\mathbf{k}}. \tag{10.22}$$

This method allows us to initialize the simulation with an arbitrary choice of velocity power spectrum. Our motivation at the beginning of this project was to start the simulation with sound waves whose power spectrum matched the end state of Ref. [498] This would have allowed us to study the long-term evolution of the thermal phase transition, without having to resolve the thickness of the bubbles on our lattice. We were hoping to observe, for high enough velocities, the formation of shocks and the subsequent development of turbulence. Unfortunately, this idea did not bring significant results, and we adapted this procedure to initialize a purely vortical fluid.

Lattice size	$v_{\mathrm{rms},*}$	$\xi_*/\,\mathrm{d}x$	Duration	τ_0 for UETCs	Label
4096^3	0.1	32	71	–	(A)
2048^3	0.1	79	4.5	0.36	(B)
2048^3	0.1	8.5	92	4.6	(C)

Table 10.1: List of the simulations used in this work. The input values for the initial power spectrum (10.35) are the initial root mean squared turbulent velocity $\sqrt{\langle v^2(\tau_*)\rangle} \sim v_{\mathrm{rms},*}$ and the initial integral scale of the turbulent spectrum ξ_* in units of the lattice spacing $\mathrm{d}x$. The duration of the simulation and the reference time τ_0 at which the UETCs are evaluated are given in units of the eddy turnover time at the integral scale $\tau_\xi = \xi_*/v_{\mathrm{rms},*}$.

10.3.3 Unequal time correlations

We are interested in studying the UETCs of the velocity field in these simulations, in order to calculate $\tilde{\Pi}^2(k,\tau,\zeta)$, see Eq. (10.15). For a field in momentum space, $\mathbf{v}(\mathbf{k},\tau)$, we measure the following correlator

$$\langle \mathbf{v}(\mathbf{k},\tau)\mathbf{v}^*(\mathbf{k}',\zeta)\rangle\,. \tag{10.23}$$

However, evaluating this quantity for many values of τ and ζ is very costly within a numerical simulation, in part because each pair of τ and ζ represents snapshots of the field $\mathbf{v}$ that must be stored concurrently in memory. Instead, we define a reference time τ_0 at which we store in memory the field $\mathbf{v}(\mathbf{k},\tau_0)$, and then compute the UETC at regular intervals with the field on the current timestep, i.e

$$\langle \mathbf{v}(\mathbf{k},\tau_0)\mathbf{v}^*(\mathbf{k}',\tau_0+n\Delta\tau)\rangle\,, \tag{10.24}$$

where here $\Delta\tau$ is the interval between UETC outputs and n is some positive integer.

10.4 Analytical model: freely decaying turbulence

In this section we present the model of freely decaying turbulence used in the present analysis. The model is based on the findings of Refs. [508, 510]: in particular, we correct Ref. [508] by accounting for the Kraichnan sweeping model to describe the time decorrelation of the velocity field, as proposed in Ref. [510] (Section 10.4.2). We extend the results of Ref. [510] by symmetrizing the velocity power spectrum. We adopt a new form of the decorrelation function which is validated by the numerical simulations and describes the decorrelation of the velocity field also at large scales, outside the inertial range (Section 10.4.3). The symmetrization of the velocity power spectrum is chosen to guarantee positivity of the GW energy density power spectrum (10.15). We have also tried to validate the decay laws of the turbulent kinetic energy and correlation scale with the simulation results (Section 10.4.4). With respect to [508] and [510], we propose several forms for the growth phase of the turbulence, which constitutes an important ingredient in order to determine the spectral shape of the GW power spectrum [516, 509, 508] (Section 10.4.5).

10.4.1 Velocity power spectrum

Under the assumption that the velocity field is divergence-free, Gaussian and statistically isotropic and homogeneous, its properties are characterized by the two-point correlation function in real

space [504]

$$b_{ij}(\mathbf{r},\tau,\zeta)=\frac{\langle v_i(\mathbf{x},\tau)v_j(\mathbf{x}+\mathbf{r},\zeta)\rangle}{\langle v^2\rangle}\equiv\Sigma(r,\tau,\zeta)(\delta_{ij}-\hat{\mathbf{r}}_i\hat{\mathbf{r}}_j)+\Gamma(r,\tau,\zeta)\hat{\mathbf{r}}_i\hat{\mathbf{r}}_j. \tag{10.25}$$

The functions Σ and Γ represent respectively the *transverse* and *longitudinal* correlation functions. Since the velocity field is divergence-free, $\partial b_{ij}/\partial r_i=0$ and the correlation functions are related through

$$\Gamma'(r)=\frac{2}{r}[\Sigma(r)-\Gamma(r)]. \tag{10.26}$$

The properties of statistical homogeneity, isotropy and that $\boldsymbol{\nabla}\cdot\mathbf{v}=0$ imply that in Fourier space

$$\left\langle v_i(\mathbf{k},\tau)v_j^*(\mathbf{q},\zeta)\right\rangle\equiv(2\pi)^3\Big(\delta_{ij}-\hat{\mathbf{k}}_i\hat{\mathbf{k}}_j\Big)\delta(\mathbf{k}-\mathbf{q})P_v(k,\tau,\zeta). \tag{10.27}$$

This equation defines for the *velocity spectral density* P_v. It can be expressed in terms of the correlation functions Γ and Σ by matching the Fourier transform of Eq. (10.27) and the trace of Eq. (10.25):

$$P_v(k,\tau,\zeta)=\left\langle v^2\right\rangle\int\mathrm{d}^3r\;e^{i\mathbf{k}\cdot\mathbf{r}}\left[\Sigma(r,\tau,\zeta)+\frac{1}{2}\Gamma(r,\tau,\zeta)\right]. \tag{10.28}$$

One can rewrite the spectral density in terms of spherical coordinates using Eq. (10.26)

$$\begin{aligned}P_v(k,\tau,\zeta)&=4\pi\left\langle v^2\right\rangle\int r^2\,\mathrm{d}r\left[\Sigma(r)+\frac{1}{2}\Gamma(r)\right]\frac{\sin(kr)}{kr}\\&=2\pi\left\langle v^2\right\rangle\int\mathrm{d}r\left[r^3\Gamma'(r)+3r^2\Gamma(r)\right]\frac{\sin(kr)}{kr}.\end{aligned} \tag{10.29}$$

We can understand the large scale behaviour of the spectral density by performing an expansion in $k\ll1$, to find

$$P_v(k,\tau,\zeta)=2\pi\left\langle v^2\right\rangle\int\mathrm{d}r\left[r^3\Gamma'(r)+3r^2\Gamma(r)\right]\left[1-\frac{(kr)^2}{6}+\mathcal{O}\big(k^4\big)\right]. \tag{10.30}$$

It is legitimate to assume that the correlation function (10.25) has a compact support and vanishes outside the horizon, by causality. As a consequence, the leading order of Eq. (10.30) is $r^3\Gamma\big|_0^\infty=0$, and the spectral density on large scales is given by

$$P_v(k\to0)=\frac{2\pi}{3}\left\langle v^2\right\rangle k^2\int_0^\infty\mathrm{d}r\,r^4\,\Gamma(r)+\mathcal{O}\big(k^4\big)\,. \tag{10.31}$$

The integral $\int\mathrm{d}r\,r^4\Gamma(r)$ is also known as the *Loitsyansky integral* and it is a measure of the angular momentum of the system. Therefore, we see that causality in the early universe points to Batchelor turbulence [527], at least at super-horizon scales.

The *power spectrum* $\mathcal{P}_v(k)$ encodes how the kinetic energy is distributed into the different length-scales

$$\left\langle v^2\right\rangle(\tau)\equiv\int\frac{\mathrm{d}k}{k}\mathcal{P}_v(k,\tau,\tau). \tag{10.32}$$

It is related to the spectral density through

$$\mathcal{P}_v(k)=\frac{k^3}{\pi^2}P_v(k). \tag{10.33}$$

To characterize the typical length-scale of the system, we define the *integral scale* ξ in terms of the longitudinal correlation function, or equivalently in terms of the power spectrum

$$\xi(\tau) \equiv \int_0^\infty \mathrm{d}r\, \Gamma(r,\tau,\tau) = \frac{\pi}{4\left\langle v^2\right\rangle} \int k^{-1} \mathcal{P}_v(k,\tau,\tau)\, \mathrm{d}\ln k\,, \tag{10.34}$$

We use the integral scale to define dimensionless, time-dependent wave-numbers $K(\tau) = \mathcal{A}\, k\, \xi(\tau)$, with $\mathcal{A}$ a normalization constant defined later in Eq. (10.36).

Concerning the shape of the velocity power spectrum, we assume that in the inertial range it is determined by the Kolmogorov $K^{-2/3}$ law, and on large scales by the causal K^5 slope, motivated by Eq. (10.31). $\mathcal{P}_v(k)$ is usually approximated by the following formula [508, 510, 528, 527]

$$\mathcal{P}_v(k,\tau,\tau) = \mathcal{B}\left\langle v^2\right\rangle(\tau) \frac{K^5(\tau)}{\left[1+K^2(\tau)\right]^{17/6}}. \tag{10.35}$$

The coefficients $\mathcal{A}$ and $\mathcal{B}$ are chosen to ensure that the definitions of the kinetic energy and the integral scale of Eqs (10.32) and (10.34) are consistent:

$$\mathcal{A} = \frac{55\Gamma(1/3)}{12\sqrt{\pi}\Gamma(17/6)} \approx 4.02, \quad \mathcal{B} = \frac{8\Gamma(17/6)}{3\sqrt{\pi}\Gamma(1/3)} \approx 0.97. \tag{10.36}$$

Note that in Ref. [510], the authors introduce a factor of 5/12 in the denominator of the velocity power spectrum, with the motivation to localize the peak of the spectrum around $K = 1$. We do not follow this convention here.

10.4.2 Kraichnan sweeping model

In order to model the time decorrelation of the velocity field, we adopt the Kraichnan's sweeping scenario [511, 518], as put forward in Ref. [510]. We compare the predictions of this scenario to numerical simulations of a relativistic fluid in the early Universe. We propose a form for the decorrelation function which reduces to the classical sweeping decorrelation scenario in the case of non-decaying turbulence, and in the inertial range. However, in order to perform the calculation of the GW energy density spectrum, we need to model the decorrelation also at large scales: we therefore use a form for the decorrelation function proposed in [529] which appears to be valid also outside the inertial range. As shown in Section 10.4.3, we validate this form with numerical simulation as far as possible. Here we first concentrate on the time decorrelation in the inertial range, and revise the classical sweeping scenario, before extending to large scales in the next section.

Kraichnan's sweeping model is based on the assumption that vortices in the inertial range are advected without deformation by a locally uniform velocity field $\mathbf{V}$, which may be time-dependent [511]:

$$\frac{\partial \mathbf{v}}{\partial t} + i[\mathbf{k}\cdot\mathbf{V}(t)]\mathbf{v} = 0. \tag{10.37}$$

Since $\mathbf{V}$ is locally uniform, the evolution of modes with different wavenumbers $\mathbf{k}$ is decoupled. The turbulent velocity field can be explicitly integrated: from Eq. (10.37) we find

$$\mathbf{v}(\mathbf{k}, t+\Delta t) = \mathbf{v}(\mathbf{k},t) \exp\left(-i\int_t^{t+\Delta t} \mathbf{k}\cdot\mathbf{V}(s)\,\mathrm{d}s\right). \tag{10.38}$$

Under the assumption that the locally uniform velocity field $\mathbf{V}$ is statistically independent of the turbulent velocity field $\mathbf{v}$ at the initial time, the unequal-time correlations of this latter field can be expressed as

$$\langle v_i(\mathbf{k}, t+\Delta t) v_i^*(\mathbf{k}, t)\rangle = \langle v_i(\mathbf{k}, t) v_i^*(\mathbf{k}, t)\rangle \left\langle \exp\left(-i\int_t^{t+\Delta t} \mathbf{k}\cdot\mathbf{V}(s)\,\mathrm{d}s\right)\right\rangle . \tag{10.39}$$

The average of the exponential can be calculated assuming that its argument is a Gaussian random variable [1]. It results that the velocity field decorrelates with a characteristic Gaussian law such as

$$\langle v_i(\mathbf{k}, t+\Delta t) v_i^*(\mathbf{k}, t)\rangle = \langle v_i(\mathbf{k}, t) v_i^*(\mathbf{k}, t)\rangle \exp\big(-\left\langle X^2\right\rangle\big), \tag{10.41}$$

where

$$X^2 \equiv \iint_t^{t+\Delta t} (\mathbf{k}\cdot\mathbf{V}(s))(\mathbf{k}\cdot\mathbf{V}(s'))\,\mathrm{d}s\,\mathrm{d}s' . \tag{10.42}$$

This expression can be further simplified assuming that the locally uniform velocity has on average the same amplitude in the three space directions [511], leading to

$$\langle v_i(\mathbf{k}, t+\Delta t) v_i^*(\mathbf{k}, t)\rangle = \langle v_i(\mathbf{k}, t) v_i^*(\mathbf{k}, t)\rangle \exp\big[-(k\,\Delta t\, v_{\rm sw}(t,\Delta t))^2\big], \tag{10.43}$$

where $v_{\rm sw}(t)$ is the *sweeping velocity* and takes the form [518, 530]

$$v_{\rm sw}^2(t,\Delta t) = \frac{1}{3\Delta t^2}\iint_t^{t+\Delta t} \langle V(s)V(s')\rangle\,\mathrm{d}s\,\mathrm{d}s' . \tag{10.44}$$

The most common assumption for the sweeping velocity is to set it equal to the root-mean-squared velocity of the turbulent field in one direction [511, 531]. Assuming statistical isotropy, this amounts to $v_{\rm sw}^2 \simeq \left\langle v^2\right\rangle/3$. Generalizations for freely decaying turbulence are given for instance in Refs. [518, 530], as $v_{\rm sw}^2(t,\Delta t) = \int_t^{t+\Delta t} \left\langle V^2(s)\right\rangle/\Delta t^2\,\mathrm{d}s \simeq [\left\langle v^2(t)\right\rangle + \left\langle v^2(t+\Delta t)\right\rangle]/2$. In the following, we will adopt a model that reduces to $\left\langle v^2(t)\right\rangle/3$ at equal time and in the inertial range, as presented in the next Section 10.4.3.

10.4.3 Unequal-time correlations outside the inertial range

The Kraichnan sweeping model derived in the previous section only applies to the inertial range. In order to evaluate the GW generation, however, we need to model the time decorrelation of the velocity field on all scales (*c.f.* for example Eq (10.97)).

The decorrelation dynamics at scales larger than the integral scale in freely decaying turbulence has not received a lot of attention in the literature: numerical studies such as those performed in Refs. [518, 530], for example, study decorrelation only in the inertial range. The largest scale analysed in Ref. [532] is $k = 1$, corresponding to the scale of the forcing, *i.e.* of the peak of the energy spectrum: it appears from this analysis that the peak scale already decorrelates slower than scales in the inertial range.

[1] We recall that for a Gaussian random variable,

$$\langle \exp(X)\rangle = \left\langle \sum_{n=0}^{\infty} \frac{X^n}{n!}\right\rangle = \sum_{k=0}^{\infty} \frac{\langle X^2\rangle^k}{2^k k!} = \exp\left(\frac{\langle X^2\rangle}{2}\right) \tag{10.40}$$

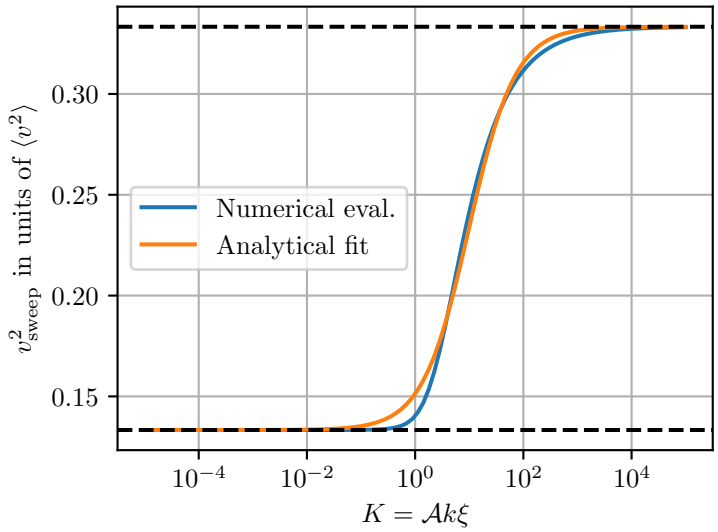

Figure 10.1: Extension of the sweeping velocity at scales larger than the integral scale, following the model given in Eq. (10.45). It interpolates smoothly between $\langle v^2 \rangle /3$ in the inertial range as in Eq. (10.44) and $2\langle v^2 \rangle /15$ on large scales. These limits are shown with the black dashed lines.

In the context of the literature dedicated to GW production by turbulence, this problem has been tackled for instance in Refs. [508, 510], with different approaches. Ref. [508] assumed that the large scales do not decorrelate. The only time dependence of the velocity spectrum outside the inertial range was therefore due to the free decay, and an exponential decorrelation was inserted for wavenumbers in the inertial range by means of a step function. This introduced a non-physical discontinuity (*c.f.* Eq. (57)). Furthermore, as pointed out in Ref. [510], Ref. [508] erroneously used the Lagrangian eddy turnover time as typical decorrelation time.

Ref. [510] was the first to point out that the random sweeping model was the correct one to describe the time decorrelation in the context of GW dedicated studies. This leads to the Eulerian eddy turnover time $\tau_{\rm e}$ as typical decorrelation time [533, 529]

$$v^2_{\rm sw}(k,\tau,\tau) \equiv \frac{1}{k^2\tau^2_{\rm e}(k,\tau)} = \int_0^\infty h\Big(\frac{q}{k}\Big)\mathcal{P}_v(q,\tau,\tau)\,\mathrm{d}\ln q\,, \tag{10.45}$$

in which the function $h(x)$ is given by

$$h(x) = \frac{1}{48}(13 - 8x^2 + 3x^4) + \frac{1}{32}(1-x^2)^3 \ln\frac{1+x}{|1-x|}. \tag{10.46}$$

Note that the function $h(x)$ of Refs. [533, 529] has a factor of 2 difference due to our definition of the power spectrum in Eq. (10.32). As shown in Fig. 10.1, $v_{\rm sw}(k,\tau)$ provides a continuous interpolation from large to small scales, reducing to $\langle v^2(\tau) \rangle /3$ in the inertial range, and going to $2\langle v^2(\tau) \rangle /15$ on large scales. Although we solve the integral (10.45) numerically, we give below an analytical fit

to the sweeping velocity, and compare with the numerical result in Fig. 10.1

$$v_{\rm sw}^2(K,\tau,\tau) \simeq \frac{\left\langle v^2(\tau)\right\rangle}{3}\left(\frac{1+0.2K}{\sqrt{5/2}+0.2K}\right)^2. \tag{10.47}$$

To model decorrelation on all scales, we can therefore use Eq. (10.45) as an extension of the sweeping velocity. Note that, as will be motivated in Section 10.5, we will choose the *geometrical mean* to symmetrize the velocity at unequal times (as opposed *i.e.* to the proposal of Ref. [518]):

$$v_{\rm sw}^2(K,\tau,\zeta) = 2\,\frac{v_{\rm sw}^2(K,\tau,\tau)v_{\rm sw}^2(K,\zeta,\zeta)}{v_{\rm sw}^2(K,\tau,\tau)+v_{\rm sw}^2(K,\zeta,\zeta)}. \tag{10.48}$$

All in all, one can therefore substitute in the exponential of Eq. (10.43) the decorrelation velocity given in Eq. (10.48). From Fig. 10.2, it appears that the decorrelation obtained using the "sweeping" velocity of Eq. (10.48) is qualitatively similar to the step function adopted in Ref. [508], but it is continuous. Furthermore, it provides a slower decorrelation in the infrared than the classical sweeping model, which would amount to fix a constant $v_{\rm sw}^2 \simeq \left\langle v^2\right\rangle/3$ at initial time and at all scales.

The decorrelation model that we adopt interpolates reasonably well the results of numerical simulations, as one can appreciate from Fig. 10.3. There, we plot the unequal time correlation

$$R(k,\tau,\zeta) \equiv \frac{\mathcal{P}_v(k,\tau,\zeta)}{\sqrt{\mathcal{P}_v(k,\tau,\tau)\,\mathcal{P}_v(k,\zeta,\zeta)}}\sqrt{\frac{v_{\rm sw}^2(k,\tau,\tau)+v_{\rm sw}^2(k,\zeta,\zeta)}{2v_{\rm sw}(k,\tau,\tau)v_{\rm sw}(k,\zeta,\zeta)}} \tag{10.49}$$

as a function of $v_{\rm sweep}(k,\tau,\zeta)\,k\,|\tau-\zeta|$ for different values of the wave-number k, both larger and smaller than the wave-number corresponding to the peak of the spectrum at the initial time of the simulation, $k_{\rm peak} \simeq 0.75/\xi(\tau_{\rm ini})$. The second term in the definition of $R(k,\tau,\zeta)$ is motivated in Section 10.5. One of the two times is fixed to a reference time of the order of the eddy turnover time, $\tau_e \sim \xi/\sqrt{\langle v^2\rangle}$, while the other one varies. Because of limitations in the dynamical range of the simulations, it is not possible to analyse very small values of $k/k_{\rm peak}$, but one can appreciate that the model provides a reasonably good fit for the decorrelation of scales $k \geq 0.125\,k_{\rm peak}$.

10.4.4 Evolution of the velocity field in decaying turbulence

Together with the time decorrelation properties of the turbulent field, we also need to model its overall time evolution. From Eq. (10.35), we see that this amounts to describe how the kinetic energy $\left\langle v^2\right\rangle$ and the integral scale ξ evolve with time. For fully developed, freely decaying turbulence, $\left\langle v^2\right\rangle$ and ξ are expected to evolve as power-laws, as we demonstrate in the following. We therefore start by defining the instantaneous scaling exponents

$$p \equiv -\frac{{\rm d}\ln\left\langle v^2\right\rangle}{{\rm d}\ln t}, \quad q \equiv \frac{{\rm d}\ln\xi}{{\rm d}\ln t}. \tag{10.50}$$

In order to analyse the self-similarity properties of the turbulence that ultimately determine its time evolution, in Ref. [519], Olesen starts by noting the invariance of the Navier-Stokes equations upon the rescaling

$$\mathbf{x} \to \ell\mathbf{x}, \quad t \to \ell^{1-h}t, \quad \mathbf{v} \to \ell^h\mathbf{v}, \quad \nu \to \ell^{1+h}\nu, \tag{10.51}$$

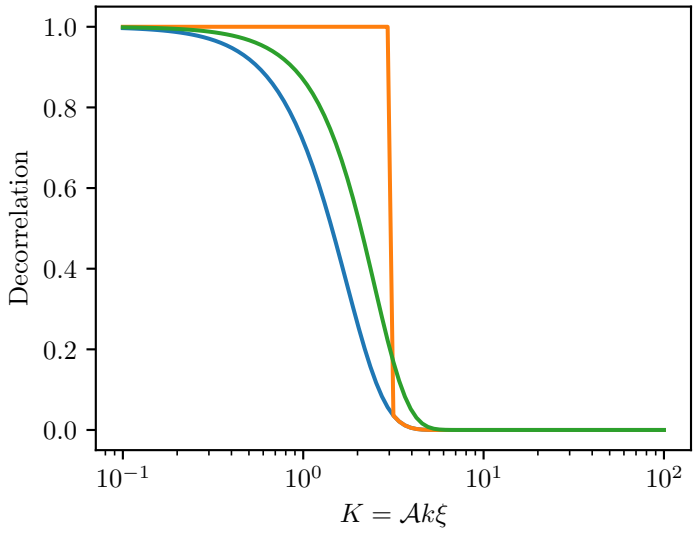

Figure 10.2: Comparison between the outcome of different choices for the velocity field to be inserted in the decorrelation model of Eq. (10.43) (or, more appropriately, Eq. (10.86)). Blue: assuming a constant decorrelation velocity equal to $v_{\rm sw} \simeq \sqrt{\langle v^2 \rangle /3}$ at initial time and at all scales; orange, the step function used in Ref. [508], where the decorrelation is inserted only at $K > K_{\rm peak} \simeq 3$; green: the model proposed here, obtained from Eqs. (10.45) and (10.48).

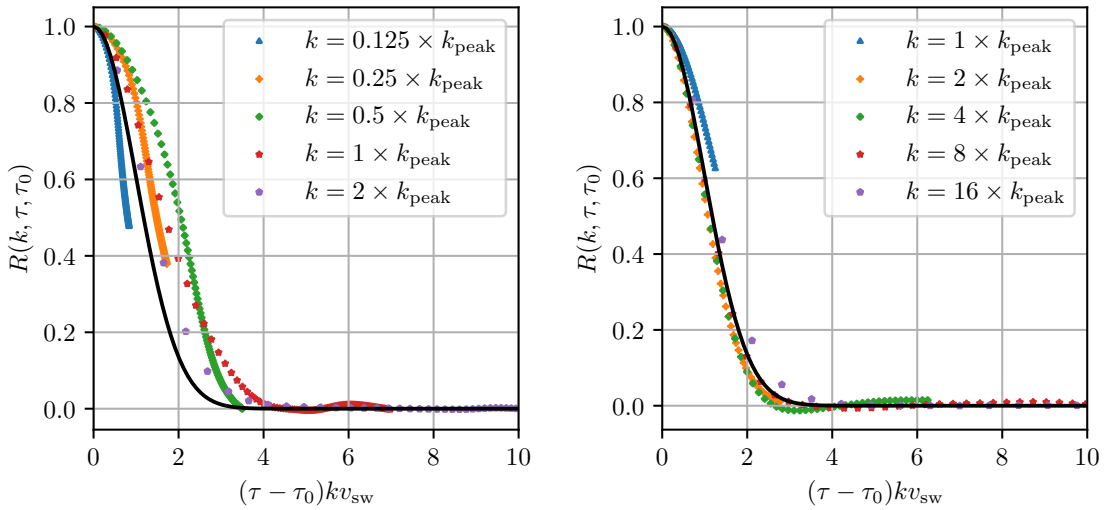

Figure 10.3: Real part of the unequal time correlator measured in simulation (C) on the left panel and simulation (B) on the right panel. The y-axis displays $R(k, \tau_0, \tau)$. The solid dark line is the prediction of our model combining Eqs. (10.43,10.45,10.48).

where ℓ is dimensionless, and the parameter h is *a priori* unknown[2]. In particular, the author shows that in the inertial range – far away from the energy injection scale and the Kolmogorov microscale – the power spectrum follows the scaling

$$\mathcal{P}_v(k,t) = \ell^{-2h}\mathcal{P}_v\left(\frac{k}{\ell}, \ell^{1-h}t\right). \tag{10.52}$$

It is possible to derive, from this equation, the evolution laws for the kinetic energy and the integral scale. Taking $\ell = t^{-1/(1-h)}$, one is left with

$$\mathcal{P}_v(k,t) = t^{2h/(1-h)}\phi\Big(kt^{1/(1-h)}\Big), \tag{10.53}$$

in which $\phi(x) = \mathcal{P}_v(x,1)$ is a function of only one variable. From the argument of ϕ, we see that $t^{1/(1-h)}$ acts as a typical length-scale describing the evolution of the flow. It can therefore be assumed to be proportional, at all times, to the integral scale, so we can write [520]

$$\mathcal{P}_v(k,t) = \xi^{-1-\beta}\phi(k\xi). \tag{10.54}$$

The coefficient β defined in Ref. [520] is directly related to h and can be used to determine the scaling exponent for the integral scale

$$\beta \equiv -1-2h, \quad q = \frac{1}{1-h} = \frac{2}{\beta+3}. \tag{10.55}$$

The evolution of the kinetic energy can be found upon integration

$$\left\langle v^2(t)\right\rangle = \int \mathcal{P}_v(k,t)\,\mathrm{d}\ln k = \xi^{-1-\beta}\int \phi(k\xi)\,\mathrm{d}\ln k \propto \xi^{-1-\beta}, \tag{10.56}$$

meaning that the quantity $\left\langle v^2\right\rangle \xi^{1+\beta}$ is a constant along the evolution, and

$$p = \frac{-2h}{1-h} = 2\frac{1+\beta}{\beta+3}. \tag{10.57}$$

In Ref. [519], it is argued that the parameter h (or equivalently β) should be fixed by the initial conditions. The argument is the following: take $\ell = k^{-1}$, the scaling relation then reads

$$\mathcal{P}_v(k,t) = k^{2h}\psi(k^{h-1}t), \tag{10.58}$$

in which $\psi(x) = \mathcal{P}_v(1,x)$ is a function of only one variable. If, at time $t = 0$, the power spectrum is a power-law $\mathcal{P}_v(k,0) \propto k^{1+\alpha}$, then $\alpha = -1-2h$ thus determining the value of h. However, the argument presented above has a flaw, as noted in Ref. [520]. Indeed, if one calculates the exponent of the power spectrum at any time

$$\frac{\mathrm{d}\ln\mathcal{P}_v}{\mathrm{d}\ln k} = 2h + (h-1)\frac{\mathrm{d}\ln\psi}{\mathrm{d}\ln k}\big(k^{h-1}t\big), \tag{10.59}$$

there is no reason for the second term to vanish when $t \to 0$, and the initial conditions are not sufficient to fix the value of h.

[2] h should not be confused with the function $h(x)$ in Eq. (10.46). We have decided to use the same notation as Ref. [519] for clarity.

Motivated by the work carried out in Ref. [520], we use direct numerical simulations to infer the value of the parameter β and the laws governing freely decaying turbulence. In Fig. 10.4, we show the evolution of the instantaneous exponents p and q in phase space. Combining Eqs (10.55) and (10.57), the scaling exponents satisfy the relationship

$$p = 2(1 - q) \tag{10.60}$$

represented by a dark line in Fig. 10.4. On the other hand, they also have to satisfy

$$p = (1 + \beta)q \tag{10.61}$$

shown for various values of β as dashed lines in Fig. 10.4. The simulation broadly converges to the intersection of Eqs (10.60) and (10.61), thus suggesting that $\beta = 3$. This result is consistent with the findings of Ref. [520] for hydrodynamic simulations.

In Fig. 10.5 we display the evolution of p and q as a function of time and with the predictions for $\beta = 3$:

$$\text{For } \beta = 3, \quad p = \frac{4}{3} \text{ and } q = \frac{1}{3}. \tag{10.62}$$

The simulation relaxes toward the scaling regime after $\sim 30\tau_\xi^*$, where $\tau_\xi^* = \xi_*/v_{\mathrm{rms},*}$ is the *initial eddy turnover time*. As already hinted by Fig. 10.4, the simulation does not reach the exact power-laws corresponding to $\beta = 3$. On the other hand, in Fig. 10.6, the power spectrum remains self-similar with $\beta = 3$ during the scaling regime. We also check in Fig. 10.7 that $\langle v^2 \rangle \xi^{1+\beta}$ remains constant during the scaling regime as shown in Eq. (10.56).

10.4.5 Turbulence sourcing

Refs. [516, 508, 509] have shown the importance of the time continuity of the GW sourcing process in shaping the SGWB signal. Ideally, to properly model the GW source, one would have to simulate the development of the turbulence starting from the PT dynamics. Unfortunately, the simulation code in its present form is not suited for this. However, it is important to ensure time continuity of the GW source, *i.e.* introduce a phase when the turbulence grows. Since we were not able to study the formation of turbulence with our numerical simulations, we model the growth phase heuristically. Starting from an initial time τ_{ini}, we assume that turbulence is sourced on a timescale the order of the eddy turnover time $\tau_\xi^* = \xi_*/v_{\mathrm{rms},*}$. Consequently, turbulence is fully developed at $\tau_{\mathrm{ini}} + \tau_\xi^*$ – we label the corresponding Hubble scale H_* – and then starts decaying (*cf* Fig. 10.8). We consider two heuristic models for the initial growth, occurring in the time interval τ_ξ^*.

First, we suppose that the vortical kinetic energy grows linearly with the conformal time and then starts decaying as a power-law with the coefficients of Eq. (10.50)

$$\left\langle v^2 \right\rangle (\tau) = v_{\mathrm{rms},*}^2 \begin{cases} \dfrac{\tau - \tau_{\mathrm{ini}}}{\tau_\xi^*} & \text{if } \tau < \tau_{\mathrm{ini}} + \tau_\xi^* \\ \left(\dfrac{\tau - \tau_{\mathrm{ini}}}{\tau_\xi^*} \right)^{-p} & \text{if } \tau > \tau_{\mathrm{ini}} + \tau_\xi^*. \end{cases} \tag{10.63}$$

In this first model, we also assume that the integral scale remains constant during the growth phase,

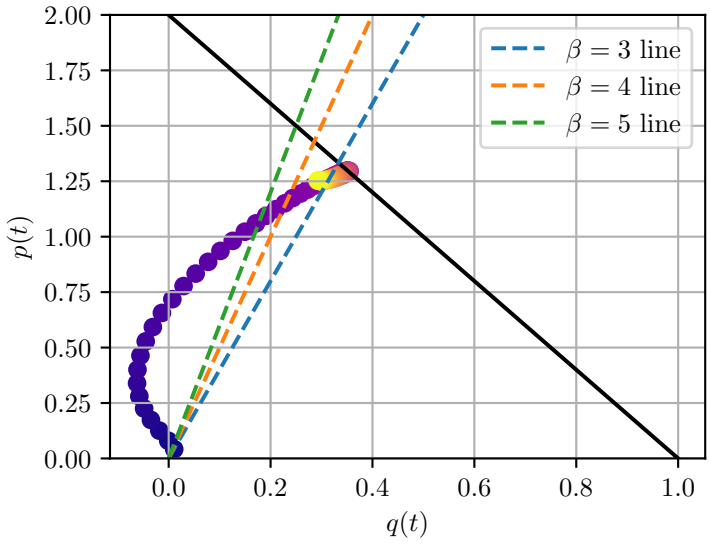

Figure 10.4: Trajectory of the instantaneous exponents (p, q) in simulation (A). Time is represented by the color scheme: early times are shown with darker colors and late times with brighter colors. The dark solid line represents Eq. (10.60). The colored dashed lines show Eq. (10.61) for various choices of β.

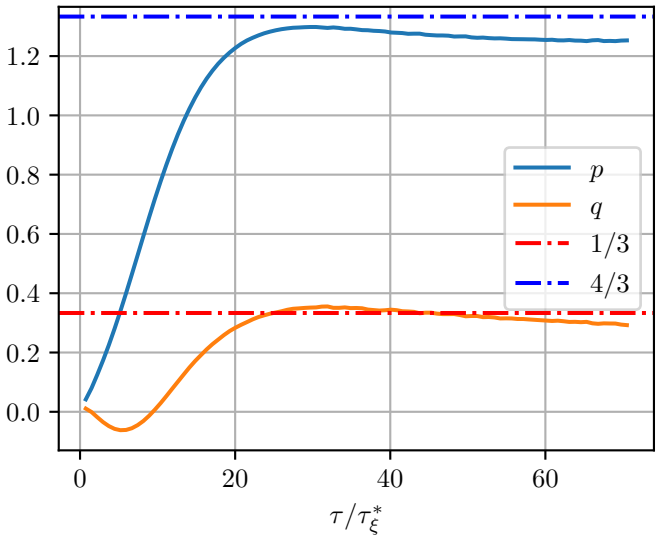

Figure 10.5: Evolution of the instantaneous kinetic energy and integral scale exponents (p, q) as a function of time in simulation (A). The dash-dotted lines show the values expected for p and q if $\beta = 3$.

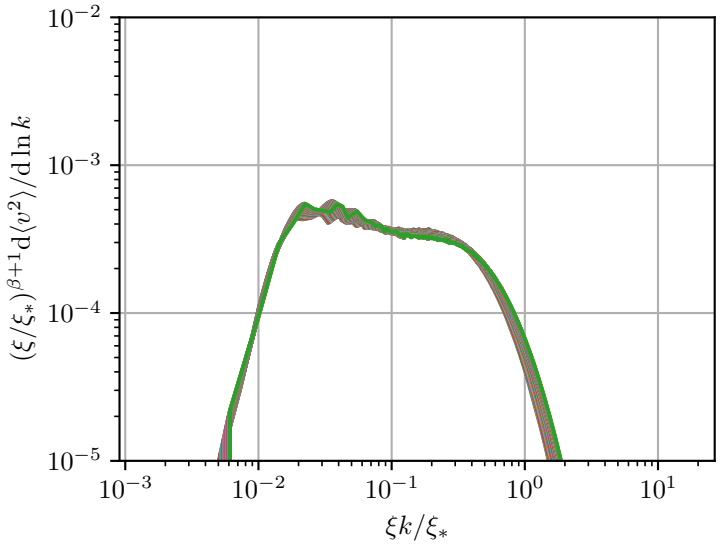

Figure 10.6: Power spectrum of simulation A rescaled with the scaling laws corresponding to $\beta = 3$. We start displaying the power spectra once the scaling regime is reached, after $\sim 30\xi_*/v_{\mathrm{rms},*}$.

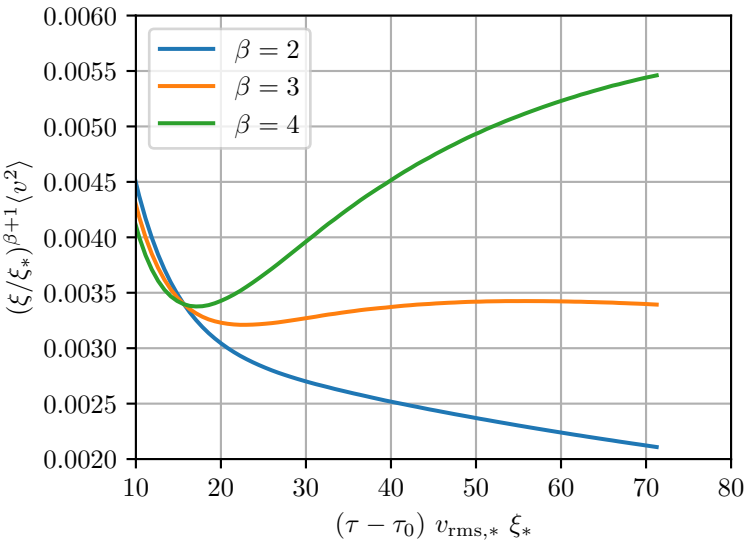

Figure 10.7: Evolution of $\langle v^2\rangle\,\xi^{1+\beta}$ for different values of β in simulation (A). Following Eq. (10.56), this quantity should remain constant in freely decaying turbulence, thus indicating that $\beta \sim 3$.

and starts evolving during the phase of free decay

$$\xi(\tau) = \xi_* \begin{cases} 1 & \text{if } \tau < \tau_{\rm ini} + \tau_\xi^* \\ \left(\dfrac{\tau - \tau_{\rm ini}}{\tau_\xi^*} \right)^q & \text{if } \tau > \tau_{\rm ini} + \tau_\xi^*. \end{cases} \tag{10.64}$$

This is the approach followed by Refs. [508, 510].

Our second model for the growth phase is motivated by the work of Ref. [516]. In this article, the authors propose different forms for the growth phase of the GW source, with increasing regularity: discontinuous, $\mathcal{C}^0$ or $\mathcal{C}^1$. They show that the smoothness of the growth phase has an important impact on the GW spectrum at high frequencies. To test this, let us first define the *smooth step function*

$$\mathrm{SStep}(x) = \begin{cases} 0 & x < 0 \\ 3x^2 - 2x^3 & 0 < x < 1 \\ 1 & 1 < x \end{cases} \tag{10.65}$$

which is both continuous and differentiable at 0 and 1: $\mathrm{SStep}'(0) = \mathrm{SStep}'(1) = 0$. To connect with the decay phase, we define the *smooth power law*

$$\mathrm{SPL}(x, p) = (1 - p)x^p + px^{p-1} \tag{10.66}$$

so that $\mathrm{SPL}'(1, p) = 0$ and $\mathrm{SPL}(1, p) = 1$[3]. With these functions, the vortical kinetic energy

$$\left\langle v^2 \right\rangle(\tau) = v_{\rm rms,*}^2 \begin{cases} \mathrm{SStep}\left(\dfrac{\tau - \tau_{\rm ini}}{\tau_\xi^*} \right) & \text{if } \tau < \tau_{\rm ini} + \tau_\xi^* \\ \mathrm{SPL}\left(\dfrac{\tau - \tau_{\rm ini}}{\tau_\xi^*}, -p \right) & \text{if } \tau > \tau_{\rm ini} + \tau_\xi^*, \end{cases} \tag{10.67}$$

and the integral scale

$$\xi(\tau) = \xi_* \begin{cases} 1 & \text{if } \tau < \tau_{\rm ini} + \tau_\xi^* \\ \mathrm{SPL}\left(\dfrac{\tau - \tau_{\rm ini}}{\tau_\xi^*}, q \right) & \text{if } \tau > \tau_{\rm ini} + \tau_\xi^*. \end{cases} \tag{10.68}$$

are $\mathcal{C}^1$ at the times $\tau_{\rm ini}$ and $\tau_{\rm ini} + \tau_\xi^*$. In both scenarios for the turbulence growth, we assume that the UETCs of Section 10.4.4 hold uniformly during both the growth and the free decay phases, *i.e.* we assume that the velocity field during the growth phase and during the free decay are correlated assuming the model described in Section 10.3.3. If we refer to Fig. 10.8, all four regions contribute to the GW power spectrum. Additionally, we also evaluate the SGWB signal in the case of a scenario of *instantaneous generation*, in which we neglected the growth phase, as in the discontinuous case of Ref. [516].

[3]Note that this function can only be used if $p < 1$

10.5 Mercer condition and consequences

As we have discussed in Section 10.4.4, the kinetic energy and the integral scale are evolving, while the turbulent source decorrelates. GW are therefore generated by a non-stationary, random process, of which we need to model the correlation function. In this section, we would like to take a step back and review some key properties of two-point correlators (see Ref. [521]). Consider an arbitrary stochastic process $\phi(t)$. In our case we are interested in functions defined on one dimension – *i.e.* time – but the discussion can be generalized in higher dimensions. We define the *kernel* of ϕ through the two-point correlation

$$K(t_1, t_2) \equiv \langle \phi(t_1)\phi(t_2) \rangle \,. \tag{10.69}$$

In practice, the kernel K is often defined directly, thus implicitly determining the stochastic function ϕ. This is, for example, what we do in Section 10.4.2: we build the kernel explicitly based on our direct numerical simulations and hints from analytical models. It is therefore important to review the key properties of kernels to ensure that we indeed build a viable one. First, a kernel should be *symmetric* and satisfy the *Cauchy-Schwartz inequality*

$$K(t_1, t_2) = K(t_2, t_1) \tag{10.70}$$

$$K(t_1, t_2) \leq \sqrt{K(t_1, t_1), K(t_2, t_2)}. \tag{10.71}$$

However, these conditions are not sufficient. Indeed, for any well-behaved function f, one can define a stochastic variable

$$X = \int \mathrm{d}t \, f(t)\phi(t), \tag{10.72}$$

whose variance must be positive

$$\left\langle X^2 \right\rangle = \iint \mathrm{d}t_1 \, \mathrm{d}t_2 \, f(t_1) f(t_2) \left\langle \phi(t_1)\phi(t_2) \right\rangle = \iint \mathrm{d}t_1 \, \mathrm{d}t_2 \, f(t_1) f(t_2) K(t_1, t_2) \geq 0. \tag{10.73}$$

This condition is called the *Mercer condition*. It is a necessary and sufficient condition that any symmetric function $K(t_1, t_2)$ should satisfy in order to be a kernel [534]. One can easily show that the linear combination of two kernels and that the multiplication of two kernels yields a kernel

$$K(t_1, t_2) = a_1 K_1(t_1, t_2) + a_2 K(t_1, t_2) \tag{10.74}$$

$$K(t_1, t_2) = K_1(t_1, t_2) \times K_2(t_1, t_2). \tag{10.75}$$

Maybe the simplest example of a positive kernel is the *separable kernel*

$$K(t_1, t_2) = g(t_1) g(t_2) \tag{10.76}$$

since it factorizes the Mercer condition into a square

$$\left\langle h^2 \right\rangle = \iint \mathrm{d}t_1 \, \mathrm{d}t_2 \, f(t_1) f(t_2) K(t_1, t_2) = \left[\int \mathrm{d}t \, f(t) g(t) \right]^2 \geq 0. \tag{10.77}$$

This type of kernel had already been proposed in the context of turbulence during first order phase transition in Ref. [508] where it is referred to as the *coherent approximation*.

Another example of kernels most often used in the literature are *stationary kernels* such that $K(t_1, t_2) = K(t_1 - t_2)$. It has been proven in 1955 that stationary functions are kernels if and only if there exist a positive finite function F such that [535]

$$K(t_1 - t_2) = \int \cos[\omega(t_1 - t_2)] F(\omega)\, \mathrm{d}\omega\,. \tag{10.78}$$

This result is very powerful and provides a demonstration that kernels can be constructed using a Dirac distribution

$$K(t_1, t_2) = \delta(t_1 - t_2). \tag{10.79}$$

A kernel of this form is referred to as *incoherent* in Ref. [508]. Stationary kernels also include the *Gaussian kernel*

$$K(t_1, t_2) = \exp\big[-(t_1 - t_2)^2\big]. \tag{10.80}$$

It is important to note that a top-hat function $\Theta(t_1 - t_2)$ is not a positive kernel, since it is the Fourier transform of a sinus cardinal function. Ref. [508] has used the top-hat function to model time decorrelation of the turbulent anisotropic stresses, but the only reason why the SGWB thereby obtained is positive, is that the authors have manually restricted the function in its regime of positivity ($x_\ell \leq \pi$).

Freely decaying turbulence is, by definition, non-stationary and one may ask if there aren't similar techniques to build well-defined *non-stationary kernels* for the velocity field. Let us mention that a simple departure from the stationary kernels discussed above is provided by *locally stationary kernels* [536]

$$K(t_1, t_2) = K_1\left(\frac{t_1 + t_2}{2}\right) K_2(t_1 - t_2), \tag{10.81}$$

where K_1 is a non-negative function and K_2 a positive stationary kernel. Although locally stationary kernels are very useful, the UETC of Eq. (10.86) is not of this, form since the sweeping velocity depends explicitly on time. We therefore need to go beyond local stationarity, and we do so by introducing *process-convolution* kernels [537]. This specific class of *non-stationary* kernels is defined as such

$$K(t_1, t_2) = \int g(t_1, u) g(t_2, u)\, \mathrm{d}u \tag{10.82}$$

where $g(t, u)$ is a two-valued function. It is easy to show that it satisfies the Mercer condition of Eq (10.73)

$$\begin{aligned} \iint \mathrm{d}t_1\, \mathrm{d}t_2\, f(t_1) f(t_2) K(t_1, t_2) &= \iint \mathrm{d}t_1\, \mathrm{d}t_2\, f(t_1) f(t_2) \int g(t_1, u) g(t_2, u)\, \mathrm{d}u \\ &= \int \mathrm{d}u \left[\int \mathrm{d}t\, f(t) g(t, u)\right]^2 \geq 0. \end{aligned} \tag{10.83}$$

Using this technique, it is possible to build a *non-stationary Gaussian kernel* of the type of Eq. (10.86) using

$$g(t, u) = \frac{1}{[2\pi\Sigma(t)]^{1/4}} \exp\left[-\frac{(t - u)^2}{2\Sigma(t)}\right] \tag{10.84}$$

in which Σ is a variance dependent on time. The kernel then reads

$$K(t_1,t_2) = \int \frac{1}{2\sqrt{\pi}[\Sigma(t_1)\Sigma(t_2)]^{1/4}} \exp\left[-\frac{(t_1-u)^2}{2\Sigma(t_1)} - \frac{(t_2-u)^2}{2\Sigma(t_2)}\right] \mathrm{d}u$$
$$= \sqrt{2}\frac{[\Sigma(t_1)\Sigma(t_2)]^{1/4}}{\sqrt{[\Sigma(t_1)+\Sigma(t_2)]}} \exp\left[-\frac{(t_1-t_2)^2}{2[\Sigma(t_1)+\Sigma(t_2)]}\right]. \tag{10.85}$$

Note that we have designed this kernel so that $K(t,t) = 1$. In terms of our unequal-time velocity power spectrum, this yields

$$\mathcal{P}_v(k,\tau,\eta) = \sqrt{\mathcal{P}_v(k,\tau,\tau)\mathcal{P}_v(k,\eta,\eta)}$$
$$\times \sqrt{\frac{2v_{\rm sw}(k,\tau,\tau)v_{\rm sw}(k,\eta,\eta)}{v^2_{\rm sw}(k,\tau,\tau)+v^2_{\rm sw}(k,\eta,\eta)}} \exp\left[-k^2\frac{(\tau-\eta)^2}{4}v^2_{\rm sw}(k,\tau,\eta)\right] \tag{10.86}$$

in which the unequal-time sweeping velocity is chosen as the harmonic average of the equal-time sweeping velocity as in Eq. (10.48).

10.6 Results

In this section, we evaluate the stochastic background of GWs. We start with reviewing the computation of the unequal time anisotropic stress power spectrum in terms of a purely vortical velocity power spectrum. Equipped with Eq. (10.86), we can avoid modelling the source decorrelation in the anisotropic stresses, as done in Ref. [508]. Furthermore, we have developed a numerical method to perform an exact evaluation of the SGWB, without resorting to approximating the angular dependence in Eq. (10.97) (as done in Ref. [510]). This approach is possible because we use a method of sampling importance to numerically calculate the 4-dimensional integral of Eq. (10.97).

10.6.1 The unequal time anisotropic stress power spectrum

We start with the spatial, off-diagonal part of the energy momentum tensor of the cosmic fluid

$$T_{\ell m}(\mathbf{x},\eta) = (\epsilon+p)u_\ell(\mathbf{x},\eta)u_\ell(\mathbf{x},\eta). \tag{10.87}$$

In order to simplify the computation, we neglect the spatial dependence of the fluid enthalpy density $(\epsilon+p)$ and set the Lorentz factor $\gamma = 1$. We are therefore implicitly assuming that turbulence is non-relativistic. The transverse trace-less projector is

$$\Lambda_{ij\ell m}(\hat{\mathbf{k}}) = \mathcal{P}_{i\ell}(\hat{\mathbf{k}})\mathcal{P}_{jm}(\hat{\mathbf{k}}) - \frac{1}{2}\mathcal{P}_{ij}(\hat{\mathbf{k}})\mathcal{P}_{\ell m}(\hat{\mathbf{k}}), \tag{10.88}$$

with $\mathcal{P}_{ij}$ defined in Eq. (10.21). The two point correlation of the anisotropic stress then reads

$$\left\langle \tilde{\Pi}_{ij}(\mathbf{k},\zeta), \tilde{\Pi}_{ij}(\mathbf{k}',\tau)\right\rangle = \Lambda_{ij\ell m}(\hat{\mathbf{k}})\Lambda_{ijrs}(\hat{\mathbf{k}'})$$
$$\times \int \frac{\mathrm{d}^3p}{(2\pi)^3}\frac{\mathrm{d}^3h}{(2\pi)^3}\left\langle v_\ell(\mathbf{p},\zeta)v_m(\mathbf{k}-\mathbf{p},\zeta)v^*_r(\mathbf{h},\tau)v^*_s(\mathbf{k}'-\mathbf{h},\tau)\right\rangle. \tag{10.89}$$

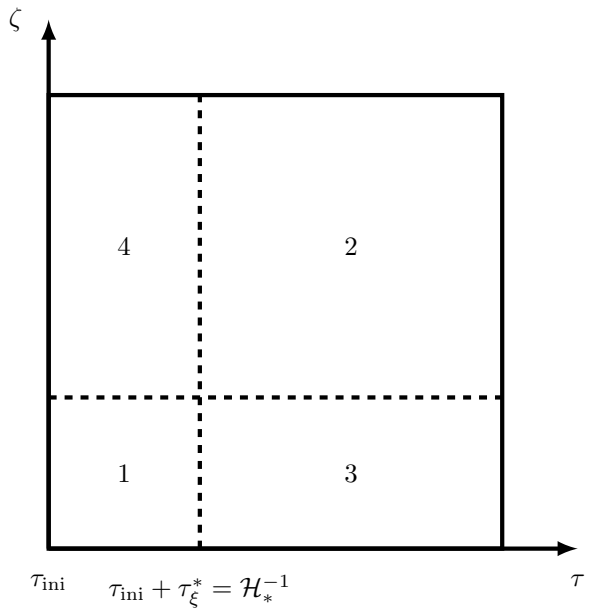

Figure 10.8: Two time diagram for the evolution of turbulence in terms of τ and ζ. The injection of kinetic energy starts at $\tau_{\rm ini}$ and turbulence develops on a timescale given by the eddy turnover time τ_ξ^* in region 1. In region 2, the turbulence is freely decaying. In principle, the growth and free decay phases are correlated: regions 3 and 4 also contribute to the production of GWs.

The four-point velocity correlator can be decomposed into a sum of two-point correlators assuming quasi-normality of the velocity field

$$\begin{aligned}\left\langle \tilde{\Pi}_{ij}(\mathbf{k},\zeta), \tilde{\Pi}_{ij}(\mathbf{k}',\tau)\right\rangle =& \Lambda_{ij\ell m}(\hat{\mathbf{k}})\Lambda_{ijrs}(\hat{\mathbf{k}}') \int \frac{\mathrm{d}^3p}{(2\pi)^3}\frac{\mathrm{d}^3h}{(2\pi)^3} \\ & [\,\langle v_\ell(\mathbf{p},\zeta)v_m(\mathbf{k}-\mathbf{p},\zeta)\rangle \langle v_r^*(\mathbf{h},\tau)v_s^*(\mathbf{k}'-\mathbf{h},\tau)\rangle \\ & + \langle v_\ell(\mathbf{p},\zeta)v_r^*(\mathbf{h},\tau)\rangle \langle v_m(\mathbf{k}-\mathbf{p},\zeta)v_s^*(\mathbf{k}'-\mathbf{h},\tau)\rangle \\ & + \langle v_\ell(\mathbf{p},\zeta)v_s^*(\mathbf{k}'-\mathbf{h},\tau)\rangle \langle v_m(\mathbf{k}-\mathbf{p},\zeta)v_r^*(\mathbf{h},\tau)\rangle]. \end{aligned} \tag{10.90}$$

The first term gives zero, using Eq (10.27) and noting that $\Lambda_{ij\ell m}(\hat{\mathbf{k}})\Lambda_{ijrs}(\hat{\mathbf{k}}) = \Lambda_{\ell mrs}(\hat{\mathbf{k}})$ we obtain

$$\begin{aligned}\left\langle \tilde{\Pi}_{ij}(\mathbf{k},\zeta), \tilde{\Pi}_{ij}(\mathbf{k}',\tau)\right\rangle = \pi^4\Lambda_{\ell mrs}(\hat{\mathbf{k}})\delta(\mathbf{k}-\mathbf{k}') \int \frac{\mathrm{d}^3p}{p^3q^3} P_v(p,\tau,\zeta)P_v(q,\tau,\zeta) \\ \times [(\delta_{\ell r}-\hat{\mathbf{p}}_\ell\hat{\mathbf{p}}_r)(\delta_{ms}-\hat{\mathbf{q}}_m\hat{\mathbf{q}}_s) + (\delta_{\ell s}-\hat{\mathbf{p}}_\ell\hat{\mathbf{p}}_s)(\delta_{mr}-\hat{\mathbf{q}}_m\hat{\mathbf{q}}_r)]. \end{aligned} \tag{10.91}$$

In which $\mathbf{q} = \mathbf{k} - \mathbf{p}$. This calculation has already been done multiple times in the literature [508, 510] with slightly different results. We would like to point out to the reader that the two terms in the contractions of the tensor indices in Eq. (10.91) are not identical as claimed in Ref. [510]. More specifically

$$2\Lambda_{\ell mrs}(\hat{\mathbf{k}})(\delta_{\ell r}-\hat{\mathbf{p}}_\ell\hat{\mathbf{p}}_r)(\delta_{ms}-\hat{\mathbf{q}}_m\hat{\mathbf{q}}_s) = 1 + 2\Big[(\hat{\mathbf{k}}\cdot\hat{\mathbf{p}})^2 + (\hat{\mathbf{k}}\cdot\hat{\mathbf{q}})^2\Big] + (\hat{\mathbf{k}}\cdot\hat{\mathbf{p}})^2.(\hat{\mathbf{k}}\cdot\hat{\mathbf{q}})^2 \tag{10.92}$$

$$2\Lambda_{\ell mrs}(\hat{\mathbf{k}})(\delta_{\ell s}-\hat{\mathbf{p}}_\ell\hat{\mathbf{p}}_s)(\delta_{mr}-\hat{\mathbf{q}}_m\hat{\mathbf{q}}_r) = 1 + (\hat{\mathbf{k}}\cdot\hat{\mathbf{p}})^2.(\hat{\mathbf{k}}\cdot\hat{\mathbf{q}})^2. \tag{10.93}$$

Eq (10.92) is identical to the Eqs (A6) and (A12) of [510], but contrary to their claim, the second term, *i.e.* Eq (10.93), differs. Taking this into account, the stress-energy two point correlation yields [508]

$$\begin{aligned}\left\langle \tilde{\Pi}_{ij}(\mathbf{k},\zeta), \tilde{\Pi}_{ij}(\mathbf{k}',\tau)\right\rangle = \pi^4\delta(\mathbf{k}-\mathbf{k}') \int \frac{\mathrm{d}^3p}{p^3q^3} \mathcal{P}_v(p,\tau,\zeta)\mathcal{P}_v(q,\tau,\zeta) \\ \times \Big[1 + (\hat{\mathbf{k}}\cdot\hat{\mathbf{p}})^2 + (\hat{\mathbf{k}}\cdot\hat{\mathbf{q}})^2 + (\hat{\mathbf{k}}\cdot\hat{\mathbf{p}})^2.(\hat{\mathbf{k}}\cdot\mathbf{q})^2\Big]. \end{aligned} \tag{10.94}$$

We can now extract the kernel of the anisotropic stress defined in Eq. (10.12) and obtain

$$\tilde{\Pi}^2(k,\zeta,\tau) = \frac{\pi^4}{(2\pi)^3}\int \frac{\mathrm{d}^3p}{p^3q^3}\mathcal{P}_v(p,\tau,\zeta)\mathcal{P}_v(q,\tau,\zeta)\Big[1 + (\hat{\mathbf{k}}\cdot\hat{\mathbf{p}})^2\Big]\Big[1 + (\hat{\mathbf{k}}\cdot\hat{\mathbf{q}})^2\Big]. \tag{10.95}$$

The two dot products are often replaced by the coefficients [504]

$$\beta = \hat{\mathbf{k}}\cdot\hat{\mathbf{p}}, \quad \gamma = \hat{\mathbf{k}}\cdot\hat{\mathbf{q}} = \hat{\mathbf{k}}\cdot\widehat{\mathbf{k}-\mathbf{p}} \tag{10.96}$$

10.6.2 The Gravitational wave spectrum

We obtain the stochastic GW spectrum combining Eqs (10.15) and (10.95)

$$\begin{aligned}\left.\frac{\mathrm{d}\Omega_{\rm gw}}{\mathrm{d}\ln k}\right|_{\eta_0} &= \frac{\pi^4k^3}{3\pi^5}\Omega^0_{\rm rad}\frac{g_{\rm fin}}{g_0}\left(\frac{g_{s,0}}{g_{s,\rm fin}}\right)^{4/3} \\ \times \int \frac{\mathrm{d}^3p}{p^3q^3}\Big[1 + (\hat{\mathbf{k}}\cdot\hat{\mathbf{p}})^2\Big]\Big[1 + (\hat{\mathbf{k}}\cdot\hat{\mathbf{q}})^2\Big] &\iint \cos k(\zeta_2-\zeta_1)\mathcal{P}_v(p,\zeta_1,\zeta_2)\mathcal{P}_v(q,\zeta_1,\zeta_2)\frac{\mathrm{d}\zeta_1}{\zeta_1}\frac{\mathrm{d}\zeta_2}{\zeta_2}. \end{aligned} \tag{10.97}$$

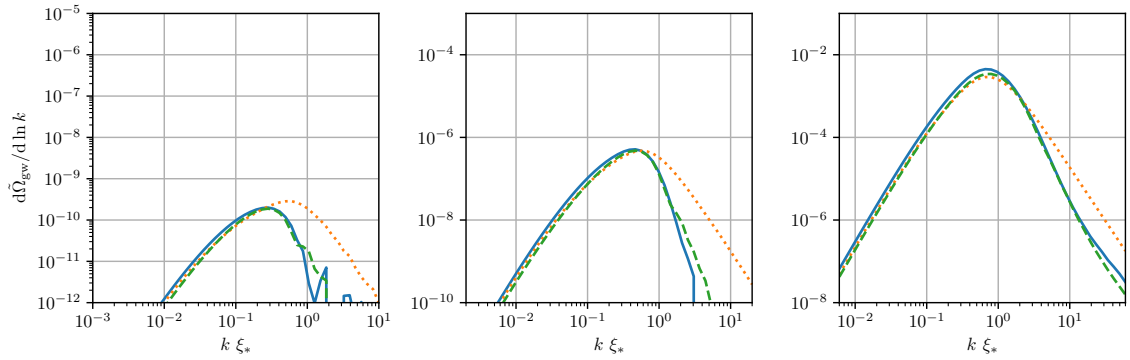

Figure 10.9: Gravitational wave power spectrum in a scenario of an instantaneous generation (dotted lines), a $\mathcal{C}^0$ growth phase (dashed lines) and a $\mathcal{C}^1$ growth phase. The left panel shows $\mathcal{H}_*\xi_* = 10^{-3}$ and $v_{\mathrm{rms},*} = 0.1$, the middle panel $\mathcal{H}_*\xi_* = 10^{-2}$ and $v_{\mathrm{rms},*} = 0.2$ and the right panel $\mathcal{H}_*\xi_* = 10^{-1}$ and $v_{\mathrm{rms},*} = 0.6$.

recalling that $\mathbf{q} = \mathbf{k} - \mathbf{p}$. Rigorously, the computation of the GW background involves performing a four-dimensional integration for each mode k (the integration over the azimuthal angle is trivial). Contrary to previous estimates, we calculate the stochastic background using Eq. (10.97) without any further approximation. We perform this four-dimensional integral using the VEGAS algorithm [538], an iterative and adaptive Monte Carlo scheme. We give more details on the implementation in Appendix 10.A.

More precisely, we factor out the relativistic degrees of freedom and calculate $\mathrm{d}\tilde{\Omega}_{\mathrm{gw}}\big/\mathrm{d}\ln k$ defined as

$$\left.\frac{\mathrm{d}\Omega_{\mathrm{gw}}}{\mathrm{d}\ln k}\right|_{\eta_0} = \Omega_{\mathrm{rad}}^0 \frac{g_{\mathrm{fin}}}{g_0}\left(\frac{g_{s,0}}{g_{s,\mathrm{fin}}}\right)^{4/3}\frac{\mathrm{d}\tilde{\Omega}_{\mathrm{gw}}}{\mathrm{d}\ln k}. \tag{10.98}$$

In our numerical integration, we have assumed that the turbulence is long-lasting, taking the limit η_{fin} to infinity. Since the turbulent source decays in time over a time-scale of the order of the eddy turnover time, this assumption does not influence our result. We have numerically checked that the integration has converged to a fixed result after $\mathcal{O}(10)$ eddy turnover times (for typical values of the parameters in the game, v_{rms} and $\xi\mathcal{H}$, it is expected to last about $300\tau_\xi^*$ – *cf* Ref. [508]). We collect in Figs 10.10 and 10.11 the GW power spectra for different values of the initial root mean squared velocity $v_{\mathrm{rms},*}$ and integral scale ξ_*. As explained in Section 10.4.5, we test three different scenarios for the generation of turbulence: an *instantaneous* generation, a $\mathcal{C}^0$ *growth phase* and a $\mathcal{C}^1$ *growth phase*.

For an *instantaneous generation* of turbulence (see Fig. 10.10), the GW spectrum peaks at a frequency set by the initial integral scale ξ_*^{-1} and presents a $k^{-7/3}$ slope in the ultraviolet. As the initial velocity $v_{\mathrm{rms},*}$ and the initial integral scale ξ_* decrease, the peaks broadens in the infrared and a k^1 region develops. Far in the infrared, the spectrum follows a k^3 slope.

The addition of a growth phase leads to a decrease of GW power and a steeper slope at high frequencies, as predicted by the analytical work of Ref. [516] (see Fig. 10.11). The suppression of the high frequencies shifts the peak to the infrared as the initial velocity decreases, thus the k^1 region of the instantaneous growth phase never develops. It should be noted that, contrary to the findings

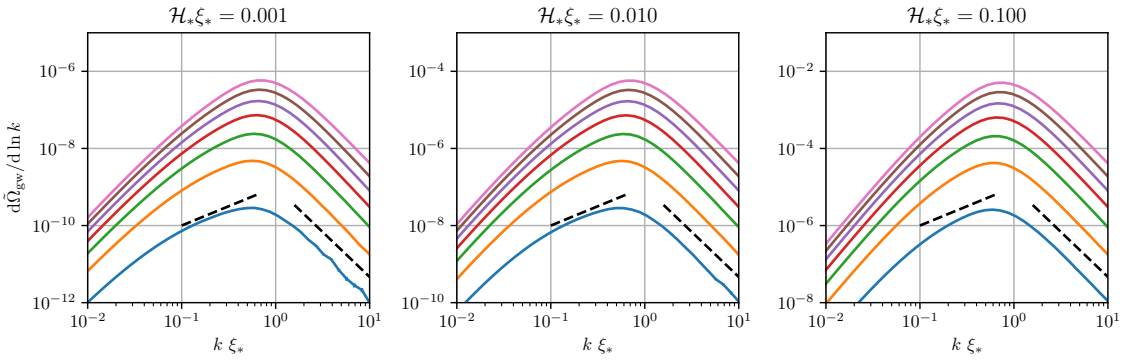

Figure 10.10: Gravitational wave power spectrum for decaying turbulence in a scenario of *instantaneous generation*. Each panel displays a different value for the initial integral scale $\mathcal{H}_*\xi_*$, and $v_{\mathrm{rms},*} = 0.1, 0.2, 0.3, 0.4, 0.5, 0.6$ and 0.7. Dark dashed lines have been added to show a k^1 slope in the intermediate range and a $k^{-7/3}$ in the ultraviolet.

of Ref. [516], the $\mathcal{C}^0$ and $\mathcal{C}^1$ growth phases yield almost identical GW spectrum, as illustrated by Fig. 10.9. This is the reason why we only show the results from the latter. This may be due to the fact that the authors of Ref. [516] were studying short-lasting sources in which they also imposed regularity condition at the end of the source.

At first, it may seem counter-intuitive that the addition of a growth phase decreases the energy in GWs, especially after our discussion on Mercer's condition in Section 10.5. We illustrate this using Fig. 10.8: Mercer's condition of Eq. (10.73) applies to intervals of the form $I \times I$, hence the contributions from the regions 1 and 2 are positive. However, the contributions from the regions 3 and 4 can very well be negative, thus lowering the energy in terms of gravitational waves. This effect depends crucially on the correlations between the growth and the free decay phase, and we leave the study of the growth of turbulence from various initial conditions to a future work.

Finally, we tested the dependence of our results on the duration of the phase transition by varying η_{fin} in our integration algorithm. We found that the GW spectrum develops during the first *eddy turnover times* $\xi_*/v_{\mathrm{rms},*}$ and remains constant when η_{fin} goes to infinity. The generation of GWs is very localized in time and the decay of turbulence cuts it off after a few eddy turnover times.

10.7 Discussion

In this chapter, we studied the GW signal generated by a hypothetical turbulent phase in the aftermath of a FOPT. We have developed a semi-analytical model for the generation of a Stochastic Background of GWs by freely-decaying kinetic, vortical, non-helical turbulence. To do so, we relied on the relativistic hydrodynamic code developed by Refs. [200, 201, 498], and used it to study the evolution of vortical fluid motions. We modified this code to give it a velocity power spectrum as input. The velocity field was initialized in Fourier space, assuming Gaussian and vortical velocity fluctuations, following the given power spectrum.

We adopted the *Kraichnan sweeping hypothesis* to model the turbulent velocity decorrelation.

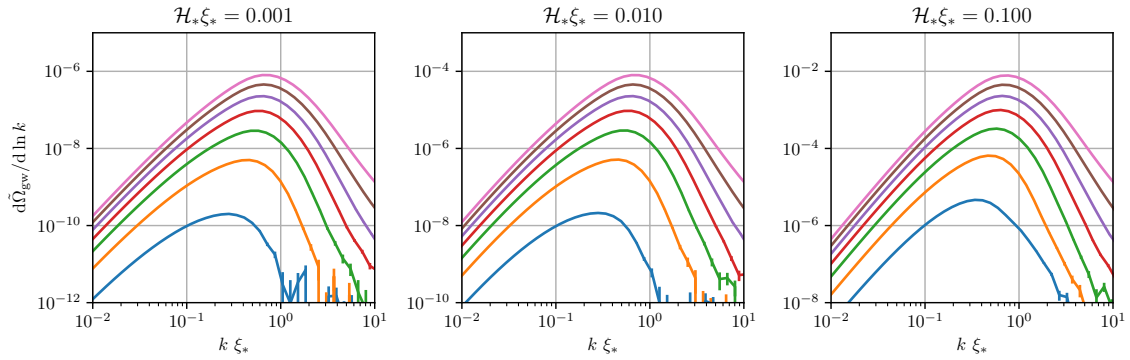

Figure 10.11: Gravitational wave power spectrum for decaying turbulence in a scenario of a $\mathcal{C}^1$ *growth phase*. Each panel displays a different value for the initial integral scale $\mathcal{H}_*\xi_*$, and $v_{\mathrm{rms},*} = 0.1, 0.2, 0.3, 0.4, 0.5, 0.6$ and 0.7.

We consistently addressed issues related to the modelling of decorrelation in the context of the theory of positive Kernels, and proposed to model the unequal time power spectrum of the turbulent velocity field as a *Gibbs Kernel*. This provides a way to symmetrize the unequal time power spectrum, and it most importantly guarantees that the velocity two-point function is a valid correlation function, and therefore guarantees that it leads to a positive GW energy density power spectrum. The numerical simulations we performed showed very good agreement with the Kraichnan Sweeping Model in the inertial range. Furthermore, we have performed numerical simulations allowing us to measure the unequal time correlations of the velocity field also at large scales, outside the inertial range. Thanks to these simulations, we were able to validate the decorrelation model also in the infrared tail of the velocity power spectrum.

We have also used our simulations to extract the free-decay laws of the turbulence. We studied the evolution of the kinetic energy and of the integral scale of the flow. The decay laws inferred from the simulations were broadly consistent with the findings of [520] for the case of purely kinetic, non-helical turbulence. Therefore, we inserted them in the analytical model of the turbulence developed to evaluate the GW production. The exact values of the power-law exponents of the turbulent decay do not play a relevant role in determining the final shape of the GW spectrum, as the bulk of the GW signal is sourced on a characteristic time which is smaller than the typical time it takes for the decay of the kinetic energy and the growth of the integral scale to equilibrate to well-defined power-laws.

One of our main results is the confirmation that the initial phase, in which the turbulent kinetic energy (*i.e.* kinetic energy associated with the vortical motion) is sourced and grows, plays an important role in shaping the final GW signal. The initial phase of turbulence development is modelled here in three heuristic ways: an instantaneous generation of turbulence; a linear growth of the kinetic energy, as done in Refs. [508, 510], imposing continuity with the free-decay phase; and a $\mathcal{C}^1$ growth of the kinetic energy, designed specifically to guarantee that the transition to the decay phase is smooth. More than the regularity of the growth phase, we have shown that correctly assessing, and implementing, how the GW source decorrelates between the growth and the free-decay phases is also of paramount importance for the GW signal evaluation

Finally, we have used the turbulent model developed so far (consisting in the equal time spec-

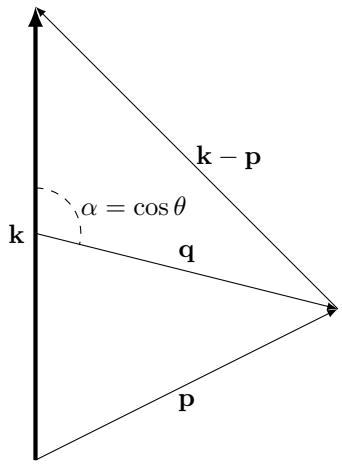

Figure 10.12: Coordinate system consisting of (q, α).

tral shape, the unequal time symmetrized power spectrum, the time decorrelation at small and large scales, the growth phase of the kinetic energy, the overall free decay and turbulence duration) to evaluate the anisotropic stresses (see Section 10.6.1) and calculate the GW signal (see Section 10.6.2). This was tackled by means of a four-dimensional numerical integration code, which handles the two time integrations arising from the GW time evolution, and the two momentum integrations arising from the velocity power spectrum convolution. We leave a detailed analysis of the SGWB signal scaling with the parameters $v_{\mathrm{rms},*}$ and ξ_* to a future analysis.

10.A Tools for the numerical GW power spectrum calculation

We describe here the changes of variable we perform, to tackle numerically the integral of Eq. (10.97). To make the symmetries of the integral apparent, we make the following change of variables $\mathbf{q} = \mathbf{p} - \mathbf{k}/2$ so that

$$\left[1+(\hat{\mathbf{k}}\cdot\hat{\mathbf{p}})^2\right]\left[1+(\hat{\mathbf{k}}\cdot\widehat{\mathbf{k}-\mathbf{p}})^2\right] = 4\frac{\left[k^2/4+q^2(1+(\hat{\mathbf{k}}\cdot\hat{\mathbf{q}})^2/2)\right]^2-(qk\ \hat{\mathbf{k}}\cdot\hat{\mathbf{q}})^2}{|\mathbf{k}/2-\mathbf{q}|^2|\mathbf{k}/2+\mathbf{q}|^2}. \tag{10.99}$$

Expressed in terms of spherical coordinates (q, θ, ϕ), the integrand is invariant by rotations over ϕ and the volume element is

$$\mathrm{d}^3q = q^2\,\mathrm{d}q\,\mathrm{d}\theta\sin(\theta)\,\mathrm{d}\phi = \mathrm{d}\phi\,\mathrm{d}q\sin(\theta)\,\mathrm{d}\theta \tag{10.100}$$

Finally, we change variables from (q, θ) to

$$M \equiv \frac{k^2}{k^2+q^2}, \quad \alpha \equiv \hat{\mathbf{k}}\cdot\hat{\mathbf{q}}. \tag{10.101}$$

Note the symmetry $\alpha \to -\alpha$. The volume element is now

$$\mathrm{d}^3 q = \mathrm{d}\phi \, \frac{k \, \mathrm{d}M}{2\sqrt{1-M} M^{3/2}} \, \mathrm{d}\alpha \tag{10.102}$$

with $M \in]0, 1]$ and $\alpha \in [0, 1]$.

Part IV

Conclusion

Summary and outlook

The main theme of this thesis has been that of constraining early universe cosmology with gravitational waves. The last years have been particularly rich in discoveries in GW physics, following the first direct detection of GWs by the LIGO-Virgo collaboration in 2015. The catalogue GWTC2 resulting from the third observing run of LIGO-Virgo, now contains about 50 observations of compact binary mergers, and PTA observatories such as NANOGRAV have promising data on the SGWB. The next five years will also be of paramount importance for refining our understanding of the science potential of the future LISA mission.

In this context, in this thesis we have focused on *three* possible sources of primordial gravitational waves, each with rather different properties. In Part I, we considered cosmic strings. These are line-like topological defects, which may be formed in phase transitions in the early universe, and are long-lived sources meaning that they may be present in the universe until today. In Part II, we focused on PBHs, which may be formed at the end of inflation, whereas in Part III we discussed GWs formed from turbulence which may be produced in the aftermath of short-lived first order PTs. Our work has tackled theoretical studies of these sources, as well as predictions for LISA, and also constraints from LIGO-Virgo.

Concerning cosmic strings, in Chapter 2, we presented work on the potential of the future LISA mission to constrain these sources. Written in collaboration with members of the LISA Cosmology Working Group, one of the main conclusions of this work is that, with the expected LISA sensitivity, it will be possible constrain strings (or even detect) with tension $G\mu \gtrsim 10^{-17}$. Physically, this corresponds to strings formed at energy scales $\mathcal{O}\big(10^{10}\big)$GeV. The SGWB signal from cosmic string networks is highly model dependent. However, we have found that the signal predictions at LISA frequencies are very similar for the two main cosmic string loop models considered in the literature. The situation is rather different at LIGO/Virgo frequencies: here the SGWB predicted from cosmic strings is more model dependent as discussed in detail in Chapter 5, based on a paper written with the LIGO/Virgo collaboration. In this paper we used the O3-data to constrain cosmic strings at LIGO/Virgo frequencies, for different loop models.

In chapters 3, 4 and 7 we attempted to understand in more detail the loop models, or more exactly the length distribution of cosmic loops. In general, loops can decay through different channels, including gravitational radiation, and hence understanding their distribution is crucial in order to make motivated observational predictions from cosmic strings. Indeed, we have focused on several observables: the SGWB (chapters 2, 4, 5 and 6); GW bursts from cusps and kinks on loops (Chapter 5); and also a diffuse gamma-ray background from cosmic strings (Chapter 6); as well as "vortons" as dark matter (Chapter 7). The loop distribution can be obtained by solving a Boltzmann equation (see Eq. (6.8)), which has two important ingredients: $\dot{\ell}$, namely the rate at which a loop looses energy; and $\mathcal{P}(\ell, t)$, the loop production function (LPF), namely the rate at

which loops of length ℓ are chopped off the infinite string network at time t.

In Chapter 3 we considered different LPFs proposed in the literature, assuming (as done also in Chapter 4) that gravitational radiation is the dominant form of energy loss from loops. These LPFs give the same loop distribution on large scales, where they also agree with different numerical simulations. However, on those scales for which gravitational radiation and gravitational backreaction become important, their predictions differ dramatically. Furthermore, at small scales there are no simulations to compare with. The work presented in Chapter 3 extends results on the loop distribution obtained from the LPF of Polchinski and Rocha.

In Chapter 4, I applied the new models of Chapter 3 to make complete predictions for SGWBs from cosmic strings. These models are part of those constrained by LIGO-Virgo in Chapter 5.

In Chapter 6, we considered the possibility that cosmic strings can also lose energy through other forms of radiation (particle, as well as gravitational). Indeed, during cusps, and kink-kink collisions, parts of the loop may annihilate thus emitting energy in the form of the fundamental fields making up the loop. Motivated by recent work presented in Ref. [139], we modelled these other forms of radiation though a modified expression for $\dot{\ell}$ (see Eq. (6.7)). Feeding this into the Boltzmann equation, and then solving it, determines their effect on the loop distribution, which we calculated for the first time in Chapter 6[4]. We then calculated the γ-ray background emitted by the cosmic string network, and compared it with observations from Fermi-LAT [341].

Finally, in Chapter 7, we considered the possibility that strings may carry a current. This can occur if, for example, the fields forming the string couple to other fields, and fermion zero-modes propagate along the string. The angular momentum due to the current can stabilize a collapsing loop, and form a stationary object called a *vorton* which can act as dark matter. In this chapter we calculated for the first time the population of vortons formed from a current-carrying string network. We used the same approach as in Chapter 6, *i.e.* we solved a Boltzmann equation accounting for a modified $\dot{\ell}$ to model the stabilization of the loops.

In Part II of this thesis we turned our attention to PBHs. Here we have not focused on the possible GW signatures from PBH, but rather we have analysed the production of PBHs during the *preheating instability* at the end of inflation. So far in the literature, *e.g.* in Ref. [430], estimates of the initial mass function considered that the distribution of PBHs was monochromatic, thus leading to an unphysical scenario in which $\Omega_{\rm PBH} > 1$. In Chapter 9 we applied the *excursion-set formalism* to calculate the initial mass function. The advantage of this formalism is that it takes into account a hierarchy of structures, *i.e.* small black holes are likely to be formed in dense regions of space which will eventually collapse into a larger black hole, so that only the largest collapsed structures are accounted for in $\Omega_{\rm PBH}$. We also presented efficient numerical methods to calculate the *distribution of first crossing* using one, among an infinite set of, Volterra integral equations. Accounting for the *cloud-in-cloud* problem with the excursion-set formalism, we found that the abundance of light PBHs is suppressed and that the peak of the initial mass function is shifted to higher masses than previously expected.

Finally, in Part III, we presented some work in progress on the SGWB from freely decaying turbulence following a first order phase transition. The frequency band of the future LISA mission is ideally positioned to probe deviations of the standard model at the electro-weak scale, if they occur in the form of a first order PT associated with the electro-weak symmetry breaking. We have built a semi-analytical model for purely vortical hydrodynamical turbulence, validating our hypothesis on its unequal-time correlations and long-term evolution with massively parallel numerical simulations. We have also reviewed *Mercer's condition*, a property that has to be satisfied by any two-point

[4]Previous work did not take into account the fact that particle radiation could affect the loop distribution.

correlator, and showed how to construct stationary, locally stationary kernels as well as some examples of non-stationary kernels. In particular, we introduced the *Gibbs kernel*, a Gaussian non-stationary kernel. We have shown that the understanding of the initial growth phase of turbulence is of primordial importance to give precise estimates of the SGWB for LISA. We plan to complete our findings by providing analytical fits and scaling laws for the SGWB spectrum, as well as validating them with the predictions on the GW signal from numerical simulations.

Bibliography

[1] Poincaré Henri. "Sur la Dynamique de l'électron". In: *Proc. Acad. Sci.* Vol. 140. 1905, pp. 1504–1508.

[2] Albert Einstein. "On the electrodynamics of moving bodies". In: *Annalen Phys.* 17 (1905), pp. 891–921. DOI: 10.1002/andp.200590006.

[3] Albert Abraham Michelson and Edward Williams Morley. "On the Relative Motion of the Earth and the Luminiferous Ether". In: *Am. J. Sci.* 34 (1887), pp. 333–345. DOI: 10.2475/ajs.s3-34.203.333.

[4] Albert Einstein. "Zur Allgemeinen Relativitätstheorie". In: *Sitzungsber. Preuss. Akad. Wiss. Berlin (Math. Phys.)* 1915 (1915). [Addendum: Sitzungsber.Preuss.Akad.Wiss.Berlin (Math.Phys.) 1915, 799–801 (1915)], pp. 778–786.

[5] Albert Einstein. "Approximative Integration of the Field Equations of Gravitation". In: *Sitzungsber. Preuss. Akad. Wiss. Berlin (Math. Phys.)* 1916 (1916), pp. 688–696.

[6] Albert Einstein. "Über Gravitationswellen". In: *Sitzungsber. Preuss. Akad. Wiss. Berlin (Math. Phys.)* 1918 (1918), pp. 154–167.

[7] Arthur Stanley Eddington. "The propagation of gravitational waves". In: *Proc. Roy. Soc. Lond. A* 102 (1922), pp. 268–282. DOI: 10.1098/rspa.1922.0085.

[8] Jorge L. Cervantes-Cota, S. Galindo-Uribarri, and G-F. Smoot. "A Brief History of Gravitational Waves". In: *Universe* 2.3 (2016), p. 22. DOI: 10.3390/universe2030022. arXiv: 1609.09400 [physics.hist-ph].

[9] F. A. E. Pirani. "Invariant formulation of gravitational radiation theory". In: *Phys. Rev.* 105 (1957), pp. 1089–1099. DOI: 10.1103/PhysRev.105.1089.

[10] Kip S. Thorne. *Black holes and time warps: Einstein's outrageous legacy*. 1994. ISBN: 978-0-393-31276-8.

[11] J. Weber. "Detection and Generation of Gravitational Waves". In: *Phys. Rev.* 117 (1960), pp. 306–313. DOI: 10.1103/PhysRev.117.306.

[12] J. Weber. "Evidence for discovery of gravitational radiation". In: *Phys. Rev. Lett.* 22 (1969), pp. 1320–1324. DOI: 10.1103/PhysRevLett.22.1320.

[13] R. A. Hulse and J. H. Taylor. "Discovery of a pulsar in a binary system". In: *Astrophys. J. Lett.* 195 (1975), pp. L51–L53. DOI: 10.1086/181708.

[14] J. H. Taylor, L. A. Fowler, and P. M. McCulloch. "Measurements of general relativistic effects in the binary pulsar PSR 1913+16". In: *Nature* 277 (1979), pp. 437–440. DOI: 10.1038/277437a0.

[15] M. V. Sazhin. "Opportunities for detecting ultralong gravitational waves". In: Soviet Ast. 22 (Feb. 1978), pp. 36–38.

[16] Steven L. Detweiler. "Pulsar timing measurements and the search for gravitational waves". In: *Astrophys. J.* 234 (1979), pp. 1100–1104. DOI: 10.1086/157593.

[17] J. P. W. Verbiest et al. "The International Pulsar Timing Array: First Data Release". In: *Mon. Not. Roy. Astron. Soc.* 458.2 (2016), pp. 1267–1288. DOI: 10.1093/mnras/stw347. arXiv: 1602.03640 [astro-ph.IM].

[18] B. P. Abbott et al. "Observation of Gravitational Waves from a Binary Black Hole Merger". In: *Phys. Rev. Lett.* 116.LIGO-P150914 (2016), p. 061102. DOI: 10.1103/PhysRevLett.116.061102. arXiv: 1602.03837 [gr-qc].

[19] R. Abbott et al. "GWTC-2: Compact Binary Coalescences Observed by LIGO and Virgo during the First Half of the Third Observing Run". In: P2000061 (Oct. 2020). arXiv: 2010.14527 [gr-qc].

[20] B. P. Abbott et al. "GW170817: Observation of Gravitational Waves from a Binary Neutron Star Inspiral". In: *Phys. Rev. Lett.* 119.LIGO-P170817 (2017), p. 161101. DOI: 10.1103/PhysRevLett.119.161101. arXiv: 1710.05832 [gr-qc].

[21] B. P. Abbott et al. "GW190425: Observation of a Compact Binary Coalescence with Total Mass $\sim 3.4 M_{\odot}$". In: *Astrophys. J. Lett.* 892.1 (2020), p. L3. DOI: 10.3847/2041-8213/ab75f5. arXiv: 2001.01761 [astro-ph.HE].

[22] B. P. Abbott et al. "Gravitational Waves and Gamma-rays from a Binary Neutron Star Merger: GW170817 and GRB 170817A". In: *Astrophys. J. Lett.* 848.2 (2017), p. L13. DOI: 10.3847/2041-8213/aa920c. arXiv: 1710.05834 [astro-ph.HE].

[23] Rosa Poggiani. "Multi-messenger Observations of a Binary Neutron Star Merger". In: *PoS* FRAPWS2018 (2019), p. 013. DOI: 10.22323/1.331.0013.

[24] David W. Hogg. "Distance measures in cosmology". In: (May 1999). arXiv: astro-ph/9905116.

[25] N. Aghanim et al. "Planck 2018 Results. VI. Cosmological Parameters". In: *Astron. Astrophys.* 641 (2020), A6. DOI: 10.1051/0004-6361/201833910. arXiv: 1807.06209 [astro-ph.CO].

[26] Adam G. Riess, William H. Press, and Robert P. Kirshner. "Using SN-Ia light curve shapes to measure the Hubble constant". In: *Astrophys. J. Lett.* 438 (1995), pp. L17–20. DOI: 10.1086/187704. arXiv: astro-ph/9410054.

[27] Adam G. Riess et al. "Cosmic Distances Calibrated to 1% Precision with Gaia EDR3 Parallaxes and Hubble Space Telescope Photometry of 75 Milky Way Cepheids Confirm Tension with ΛCDM". In: *Astrophys. J. Lett.* 908.1 (2021), p. L6. DOI: 10.3847/2041-8213/abdbaf. arXiv: 2012.08534 [astro-ph.CO].

[28] L. Verde, T. Treu, and A. G. Riess. "Tensions between the Early and the Late Universe". In: *Nature Astron.* 3 (July 2019), p. 891. DOI: 10.1038/s41550-019-0902-0. arXiv: 1907.10625 [astro-ph.CO].

[29] Chiara Caprini and Daniel G. Figueroa. "Cosmological Backgrounds of Gravitational Waves". In: *Class. Quant. Grav.* 35.16 (2018), p. 163001. DOI: 10.1088/1361-6382/aac608. arXiv: 1801.04268 [astro-ph.CO].

[30] B.P. Abbott et al. "An Upper Limit on the Stochastic Gravitational-Wave Background of Cosmological Origin". In: *Nature* 460 (2009), p. 990. DOI: 10.1038/nature08278. arXiv: 0910.5772 [astro-ph.CO].

[31] Benjamin P. Abbott et al. "Upper Limits on the Stochastic Gravitational-Wave Background from Advanced LIGO's First Observing Run". In: *Phys. Rev. Lett.* 118.12 (2017), p. 121101. DOI: 10.1103/PhysRevLett.118.121101,10.1103/PhysRevLett.119.029901. arXiv: 1612.02029 [gr-qc].

[32] B.P. Abbott et al. "Search for the Isotropic Stochastic Background Using Data from Advanced LIGO's Second Observing Run". In: *Phys. Rev. D* 100.LIGO-P1800248 (2019), p. 061101. DOI: 10.1103/PhysRevD.100.061101. arXiv: 1903.02886 [gr-qc].

[33] R. Abbott et al. "Upper Limits on the Isotropic Gravitational-Wave Background from Advanced LIGO's and Advanced Virgo's Third Observing Run". In: (Jan. 2021). arXiv: 2101.12130 [gr-qc].

[34] Z. Arzoumanian et al. "The NANOGrav 11-Year Data Set: Pulsar-Timing Constraints on the Stochastic Gravitational-Wave Background". In: *Astrophys. J.* 859.1 (2018), p. 47. DOI: 10.3847/1538-4357/aabd3b. arXiv: 1801.02617 [astro-ph.HE].

[35] Chiara Caprini et al. "Reconstructing the Spectral Shape of a Stochastic Gravitational Wave Background with LISA". In: *JCAP* 11.LISA-CosWG-19-02 (2019), p. 017. DOI: 10.1088/1475-7516/2019/11/017. arXiv: 1906.09244 [astro-ph.CO].

[36] Zaven Arzoumanian et al. "The NANOGrav 12.5 Yr Data Set: Search for an Isotropic Stochastic Gravitational-Wave Background". In: *Astrophys. J. Lett.* 905.2 (2020), p. L34. DOI: 10.3847/2041-8213/abd401. arXiv: 2009.04496 [astro-ph.HE].

[37] Simone Blasi, Vedran Brdar, and Kai Schmitz. "Has NANOGrav Found First Evidence for Cosmic Strings?" In: *Phys. Rev. Lett.* 126.CERN-TH-2020-151 (2021), p. 041305. DOI: 10.1103/PhysRevLett.126.041305. arXiv: 2009.06607 [astro-ph.CO].

[38] John Ellis and Marek Lewicki. "Cosmic String Interpretation of NANOGrav Pulsar Timing Data". In: *Phys. Rev. Lett.* 126.KCL-PH-TH/2020-53, CERN-TH-2020-150 (2021), p. 041304. DOI: 10.1103/PhysRevLett.126.041304. arXiv: 2009.06555 [astro-ph.CO].

[39] Ville Vaskonen and Hardi Veermäe. "Did NANOGrav see a signal from primordial black hole formation?" In: *Phys. Rev. Lett.* 126.5 (2021), p. 051303. DOI: 10.1103/PhysRevLett.126.051303. arXiv: 2009.07832 [astro-ph.CO].

[40] V. De Luca, G. Franciolini, and A. Riotto. "NANOGrav Data Hints at Primordial Black Holes as Dark Matter". In: *Phys. Rev. Lett.* 126.4 (2021), p. 041303. DOI: 10.1103/PhysRevLett.126.041303. arXiv: 2009.08268 [astro-ph.CO].

[41] Yuichiro Nakai et al. "Gravitational Waves and Dark Radiation from Dark Phase Transition: Connecting NANOGrav Pulsar Timing Data and Hubble Tension". In: *Phys. Lett. B* 816 (2021), p. 136238. DOI: 10.1016/j.physletb.2021.136238. arXiv: 2009.09754 [astro-ph.CO].

[42] Andrea Addazi et al. "NANOGrav results and Dark First Order Phase Transitions". In: (Sept. 2020). arXiv: 2009.10327 [hep-ph].

[43] Wilfried Buchmuller, Valerie Domcke, and Kai Schmitz. "From NANOGrav to LIGO with Metastable Cosmic Strings". In: *Phys. Lett. B* 811.CERN-TH-2020-157, DESY 20-154, DESY-20-154 (2020), p. 135914. DOI: 10.1016/j.physletb.2020.135914. arXiv: 2009.10649 [astro-ph.CO].

[44] Kazunori Kohri and Takahiro Terada. "Solar-Mass Primordial Black Holes Explain NANOGrav Hint of Gravitational Waves". In: *Phys. Lett. B* 813 (2021), p. 136040. DOI: 10.1016/j.physletb.2020.136040. arXiv: 2009.11853 [astro-ph.CO].

[45] Jose María Ezquiaga and Daniel E. Holz. "Jumping the Gap: Searching for LIGO's Biggest Black Holes". In: *Astrophys. J. Lett.* 909.2 (2021), p. L23. DOI: 10.3847/2041-8213/abe638. arXiv: 2006.02211 [astro-ph.HE].

[46] B. P. Abbott et al. "Prospects for observing and localizing gravitational-wave transients with Advanced LIGO, Advanced Virgo and KAGRA". In: *Living Rev. Rel.* 23.1 (2020), p. 3. DOI: 10.1007/s41114-020-00026-9.

[47] Gemma Janssen et al. "Gravitational Wave Astronomy with the SKA". In: *Proceedings, Advancing Astrophysics with the Square Kilometre Array (AASKA14): Giardini Naxos, Italy, June 9-13, 2014*. Vol. AASKA14. PoS. 2015, p. 037. DOI: 10.22323/1.215.0037. arXiv: 1501.00127 [astro-ph.IM].

[48] Pierre Binetruy et al. "Cosmological Backgrounds of Gravitational Waves and eLISA/NGO: Phase Transitions, Cosmic Strings and Other Sources". In: *JCAP* 1206 (2012), p. 027. DOI: 10.1088/1475-7516/2012/06/027. arXiv: 1201.0983 [gr-qc].

[49] Pau Amaro-Seoane et al. "eLISA/NGO: Astrophysics and Cosmology in the Gravitational-Wave Millihertz Regime". In: *GW Notes* 6 (2013), pp. 4–110. arXiv: 1201.3621 [astro-ph.CO].

[50] Michele Maggiore et al. "Science Case for the Einstein Telescope". In: *JCAP* 03 (2020), p. 050. DOI: 10.1088/1475-7516/2020/03/050. arXiv: 1912.02622 [astro-ph.CO].

[51] David Reitze et al. "Cosmic Explorer: The U.S. Contribution to Gravitational-Wave Astronomy beyond LIGO". In: *Bull. Am. Astron. Soc.* 51.7 (2019), p. 035. arXiv: 1907.04833 [astro-ph.IM].

[52] Pierre Auclair et al. "Cosmic String Loop Production Functions". In: *JCAP* 06.KCL-PH-TH/2019-19 (2019), p. 015. DOI: 10.1088/1475-7516/2019/06/015. arXiv: 1903.06685 [astro-ph.CO].

[53] Pierre Auclair, Danièle A. Steer, and Tanmay Vachaspati. "Particle Emission and Gravitational Radiation from Cosmic Strings: Observational Constraints". In: *Phys. Rev. D* 101.8 (2020), p. 083511. DOI: 10.1103/PhysRevD.101.083511. arXiv: 1911.12066 [hep-ph].

[54] Pierre Auclair et al. "Probing the Gravitational Wave Background from Cosmic Strings with LISA". In: *JCAP* 04 (2020), p. 034. DOI: 10.1088/1475-7516/2020/04/034. arXiv: 1909.00819 [astro-ph.CO].

[55] Manuel Arca Sedda et al. "The missing link in gravitational-wave astronomy: discoveries waiting in the decihertz range". In: *Class. Quant. Grav.* 37.21 (2020), p. 215011. DOI: 10.1088/1361-6382/abb5c1. arXiv: 1908.11375 [gr-qc].

[56] Pierre G. Auclair. "Impact of the Small-Scale Structure on the Stochastic Background of Gravitational Waves from Cosmic Strings". In: *JCAP* 11 (2020), p. 050. DOI: 10.1088/1475-7516/2020/11/050. arXiv: 2009.00334 [astro-ph.CO].

[57] Pierre Auclair and Vincent Vennin. "Primordial black holes from metric preheating: mass fraction in the excursion-set approach". In: *JCAP* 02 (2021), p. 038. DOI: 10.1088/1475-7516/2021/02/038. arXiv: 2011.05633 [astro-ph.CO].

[58] Pierre Auclair et al. "Irreducible cosmic production of relic vortons". In: *JCAP* 03 (2021), p. 098. DOI: 10.1088/1475-7516/2021/03/098. arXiv: 2010.04620 [astro-ph.CO].

[59] R. Abbott et al. "Constraints on cosmic strings using data from the third Advanced LIGO-Virgo observing run". In: (Jan. 2021). arXiv: 2101.12248 [gr-qc].

[60] H.B. Nielsen and P. Olesen. "Vortex-Line Models for Dual Strings". English. In: *Nuclear Physics B* 61 (Sept. 1973), pp. 45–61. ISSN: 05503213. DOI: 10.1016/0550-3213(73)90350-7.

[61] T.W.B. Kibble. "Topology of Cosmic Domains and Strings". In: *J. Phys. A* 9.ICTP/75/5 (1976), pp. 1387–1398. DOI: 10.1088/0305-4470/9/8/029.

[62] Rachel Jeannerot, Jonathan Rocher, and Mairi Sakellariadou. "How Generic Is Cosmic String Formation in Supersymmetric Grand Unified Theories". In: *Phys. Rev.* D68.10, 103514 (Nov. 2003), p. 103514. DOI: 10.1103/PhysRevD.68.103514. arXiv: hep-ph/0308134.

[63] T.W.B. Kibble. "Evolution of a System of Cosmic Strings". en. In: *Nuclear Physics B* 252 (Jan. 1985), pp. 227–244. ISSN: 05503213. DOI: 10.1016/0550-3213(85)90439-0.

[64] A. Vilenkin and E.P. S. Shellard. *Cosmic Strings and Other Topological Defects*. Cambridge University Press, July 2000. ISBN: 978-0-521-65476-0.

[65] E. P. S. Shellard. "Cosmic String Interactions". In: *Nucl. Phys.* B283 (1987), pp. 624–656. DOI: 10.1016/0550-3213(87)90290-2.

[66] G. J. Verbiest and A. Achucarro. "High Speed Collision and Reconnection of Abelian Higgs Strings in the Deep Type-II Regime". In: *Phys. Rev.* D84 (2011), p. 105036. DOI: 10.1103/PhysRevD.84.105036. arXiv: 1106.4666 [hep-th].

[67] P. Salmi et al. "Kinematic Constraints on Formation of Bound States of Cosmic Strings: Field Theoretical Approach". In: *Phys. Rev.* D77.IMPERIAL-TP-07-TK-01 (2008), p. 041701. DOI: 10.1103/PhysRevD.77.041701. arXiv: 0712.1204 [hep-th].

[68] Neil Bevis et al. "Evolution and Stability of Cosmic String Loops with Y-Junctions". In: *Phys. Rev.* D80 (2009), p. 125030. DOI: 10.1103/PhysRevD.80.125030. arXiv: 0904.2127 [hep-th].

[69] M. B. Hindmarsh and T. W. B. Kibble. "Cosmic Strings". In: *Rept. Prog. Phys.* 58.SUSX-TP-94-74, IMPERIAL-TP-94-95-5, NI-94025 (1995), pp. 477–562. DOI: 10.1088/0034-4885/58/5/001. arXiv: hep-ph/9411342.

[70] Gia Dvali and Alexander Vilenkin. "Formation and Evolution of Cosmic D-Strings". In: *JCAP* 0403 (2004), p. 010. DOI: 10.1088/1475-7516/2004/03/010. arXiv: hep-th/0312007.

[71] Edmund J. Copeland, Robert C. Myers, and Joseph Polchinski. "Cosmic f and d Strings". In: *JHEP* 06 (2004), p. 013. DOI: 10.1088/1126-6708/2004/06/013. arXiv: hep-th/0312067.

[72] P. A. R. Ade et al. "Planck 2013 Results. XXV. Searches for Cosmic Strings and Other Topological Defects". In: *Astron. Astrophys.* 571.CERN-PH-TH-2013-138 (2014), A25. DOI: 10.1051/0004-6361/201321621. arXiv: 1303.5085 [astro-ph.CO].

[73] Tom Charnock et al. "CMB Constraints on Cosmic Strings and Superstrings". In: *Phys. Rev.* D93.12 (2016), p. 123503. DOI: 10.1103/PhysRevD.93.123503. arXiv: 1603.01275 [astro-ph.CO].

[74] Joanes Lizarraga et al. "New CMB Constraints for Abelian Higgs Cosmic Strings". In: *JCAP* 10 (2016), p. 042. DOI: 10.1088/1475-7516/2016/10/042. arXiv: 1609.03386 [astro-ph.CO].

[75] Christophe Ringeval. "Cosmic Strings and Their Induced Non-Gaussianities in the Cosmic Microwave Background". In: *Adv. Astron.* 2010 (2010), p. 380507. DOI: 10.1155/2010/380507. arXiv: 1005.4842 [astro-ph.CO].

[76] Alexander Vilenkin. "Cosmic Strings as Gravitational Lenses". In: *Astrophys. J.* 282.TUTP-84-3 (1984), pp. L51–L53. DOI: 10.1086/184303.

[77] Jolyon K. Bloomfield and David F. Chernoff. "Cosmic String Loop Microlensing". In: *Phys. Rev.* D89.12 (2014), p. 124003. DOI: 10.1103/PhysRevD.89.124003. arXiv: 1311.7132 [astro-ph.CO].

[78] Robert H. Brandenberger. "On the Decay of Cosmic String Loops". In: *Nucl. Phys.* B293.PRINT-86-1356 (CAMBRIDGE) (1987), pp. 812–828. DOI: 10.1016/0550-3213(87)90092-7.

[79] Mark Srednicki and Stefan Theisen. "Nongravitational Decay of Cosmic Strings". In: *Phys. Lett.* B189.PRINT-86-0978-REV.(UC,SANTA-BARBARA), PRINT-86-0978 (UC,SANTA-BARBARA) (1987), p. 397. DOI: 10.1016/0370-2693(87)90648-4.

[80] Pijushpani Bhattacharjee, Christopher T. Hill, and David N. Schramm. "Grand Unified Theories, Topological Defects and Ultrahigh-Energy Cosmic Rays". In: *Phys. Rev. Lett.* 69.FERMILAB-PUB-91-304-A (1992), pp. 567–570. DOI: 10.1103/PhysRevLett.69.567.

[81] Thibault Damour and Alexander Vilenkin. "Cosmic Strings and the String Dilaton". In: *Phys. Rev. Lett.* 78 (1997), pp. 2288–2291. DOI: 10.1103/PhysRevLett.78.2288. arXiv: gr-qc/9610005.

[82] U. F. Wichoski, Jane H. MacGibbon, and Robert H. Brandenberger. "High-Energy Neutrinos, Photons and Cosmic Ray Fluxes from VHS Cosmic Strings". In: *Phys. Rev.* D65.BROWN-HET-1115 (2002), p. 063005. DOI: 10.1103/PhysRevD.65.063005. arXiv: hep-ph/9805419.

[83] Marco Peloso and Lorenzo Sorbo. "Moduli from Cosmic Strings". In: *Nucl. Phys.* B649 (2003), pp. 88–100. DOI: 10.1016/S0550-3213(02)01020-9. arXiv: hep-ph/0205063.

[84] Eray Sabancilar. "Cosmological Constraints on Strongly Coupled Moduli from Cosmic Strings". In: *Phys. Rev.* D81 (2010), p. 123502. DOI: 10.1103/PhysRevD.81.123502. arXiv: 0910.5544 [hep-ph].

[85] Tanmay Vachaspati. "Cosmic Rays from Cosmic Strings with Condensates". In: *Phys. Rev.* D81 (2010), p. 043531. DOI: 10.1103/PhysRevD.81.043531. arXiv: 0911.2655 [astro-ph.CO].

[86] Andrew J. Long, Jeffrey M. Hyde, and Tanmay Vachaspati. "Cosmic Strings in Hidden Sectors: 1. Radiation of Standard Model Particles". In: *JCAP* 1409.09 (2014), p. 030. DOI: 10.1088/1475-7516/2014/09/030. arXiv: 1405.7679 [hep-ph].

[87] Mairi Sakellariadou. "Cosmic Strings". In: *Proceedings, International Workshop on Quantum Simulations via Analogues: Dresden, Germany, July 25-28, 2005*. Vol. 718. Lecture Notes in Physics. 2007, pp. 247–288. DOI: 10.1007/3-540-70859-610. arXiv: hep-th/0602276.

[88] Tanmay Vachaspati, Levon Pogosian, and Daniele Steer. "Cosmic Strings". In: *Scholarpedia* 10.2 (2015), p. 31682. DOI: 10.4249/scholarpedia.31682. arXiv: 1506.04039 [astro-ph.CO].

[89] Jose J. Blanco-Pillado, Ken D. Olum, and Xavier Siemens. "New Limits on Cosmic Strings from Gravitational Wave Observation". In: *Phys. Lett.* B778 (2018), pp. 392–396. DOI: 10.1016/j.physletb.2018.01.050. arXiv: 1709.02434 [astro-ph.CO].

[90] Christophe Ringeval and Teruaki Suyama. "Stochastic Gravitational Waves from Cosmic String Loops in Scaling". In: *JCAP* 12 (2017), p. 027. DOI: 10.1088/1475-7516/2017/12/027. arXiv: 1709.03845 [astro-ph.CO].

[91] B. P. Abbott et al. "Constraints on Cosmic Strings Using Data from the First Advanced LIGO Observing Run". In: *Phys. Rev.* D97.10 (2018), p. 102002. DOI: 10.1103/PhysRevD.97.102002. arXiv: 1712.01168 [gr-qc].

[92] A. Vilenkin. "Gravitational Radiation from Cosmic Strings". In: *Phys. Lett.* 107B (1981), pp. 47–50. DOI: 10.1016/0370-2693(81)91144-8.

[93] Andreas Albrecht and Neil Turok. "Evolution of Cosmic String Networks". In: *Phys. Rev.* D40.PUPT-89-1119, FERMILAB-PUB-89-042-A, FERMILAB-PUB-89-046-A (1989), pp. 973–1001. DOI: 10.1103/PhysRevD.40.973.

[94] Daren Austin, E. J. Copeland, and T. W. B. Kibble. "Evolution of Cosmic String Configurations". English. In: *Physical Review D* 48.SUSSEX-TH-93-3-4, IMPERIAL-TP-92-93-42, NSF-ITP-93-83 (Dec. 1993), pp. 5594–5627. ISSN: 0556-2821. DOI: 10.1103/PhysRevD.48.5594. arXiv: hep-ph/9307325.

[95] Jose J. Blanco-Pillado, Ken D. Olum, and Benjamin Shlaer. "Large Parallel Cosmic String Simulations: New Results on Loop Production". English. In: *Physical Review D* 83.8 (Apr. 2011). ISSN: 1550-7998, 1550-2368. DOI: 10.1103/PhysRevD.83.083514. arXiv: 1101.5173 [astro-ph.CO].

[96] Edmund J. Copeland, T.W.B. Kibble, and Daniele A. Steer. "The Evolution of a Network of Cosmic String Loops". In: *Phys. Rev. D* 58.SUSX-TH-98-005, IMPERIAL-TP-97-98-31, DAMTP-97-152 (1998), p. 043508. DOI: 10.1103/PhysRevD.58.043508. arXiv: hep-ph/9803414.

[97] C. J. A. P. Martins and E. P. S. Shellard. "Quantitative String Evolution". In: *Phys. Rev.* D54.DAMTP-R-96-5 (1996), pp. 2535–2556. DOI: 10.1103/PhysRevD.54.2535. arXiv: hep-ph/9602271.

[98] C. J. A. P. Martins and E. P. S. Shellard. "Extending the Velocity-Dependent One-Scale String Evolution Model". In: *Phys. Rev.* D65 (2002), p. 043514. DOI: 10.1103/PhysRevD.65.043514. arXiv: hep-ph/0003298.

[99] Christophe Ringeval, Mairi Sakellariadou, and Francois Bouchet. "Cosmological Evolution of Cosmic String Loops". In: *JCAP* 0702 (2007), p. 023. DOI: 10.1088/1475-7516/2007/02/023. arXiv: astro-ph/0511646.

[100] Vitaly Vanchurin, Ken D. Olum, and Alexander Vilenkin. "Scaling of Cosmic String Loops". In: *Phys. Rev. D* 74.6 (Sept. 2006), p. 063527. ISSN: 1550-7998, 1550-2368. DOI: 10.1103/PhysRevD.74.063527. arXiv: gr-qc/0511159.

[101] B. Allen and E. P. S. Shellard. "Cosmic-String Evolution: A Numerical Simulation". English. In: *Phys. Rev. Lett.* 64.2 (Jan. 1990), pp. 119–122. ISSN: 0031-9007. DOI: 10.1103/PhysRevLett.64.119.

[102] David P. Bennett and Francois R. Bouchet. "High Resolution Simulations of Cosmic String Evolution. 1. Network Evolution". In: *Phys. Rev.* D41.PUPT-89-1137, UCRL-102446 (1990), p. 2408. DOI: 10.1103/PhysRevD.41.2408.

[103] Jose J. Blanco-Pillado, Ken D. Olum, and Benjamin Shlaer. "The Number of Cosmic String Loops". In: *Phys. Rev.* D89.2 (2014), p. 023512. DOI: 10.1103/PhysRevD.89.023512. arXiv: 1309.6637 [astro-ph.CO].

[104] Neil Turok. "Grand Unified Strings and Galaxy Formation". In: *Nucl. Phys.* B242.UCSB-TH-3-1984 (1984), pp. 520–541. DOI: 10.1016/0550-3213(84)90407-3.

[105] Thibault Damour and Alexander Vilenkin. "Gravitational Wave Bursts from Cosmic Strings". In: *Phys.Rev.Lett.* 85.IHES-P-00-32 (2000), pp. 3761–3764. DOI: 10.1103/PhysRevLett.85.3761. arXiv: gr-qc/0004075.

[106] Thibault Damour and Alexander Vilenkin. "Gravitational Wave Bursts from Cusps and Kinks on Cosmic Strings". In: *Phys. Rev. D* 64.IHES-P-01-15 (2001), p. 064008. DOI: 10.1103/PhysRevD.64.064008. arXiv: gr-qc/0104026.

[107] J. Aasi et al. "Constraints on Cosmic Strings from the LIGO-Virgo Gravitational-Wave Detectors". In: *Phys. Rev. Lett.* 112 (2014), p. 131101. DOI: 10.1103/PhysRevLett.112.131101. arXiv: 1310.2384 [gr-qc].

[108] P. Binetruy et al. "Gravitational Wave Bursts from Cosmic Superstrings with Y-Junctions". In: *Phys. Rev. D* 80 (2009), p. 123510. DOI: 10.1103/PhysRevD.80.123510. arXiv: 0907.4522 [hep-th].

[109] C. J. A. P. Martins and E. P. S. Shellard. "Fractal Properties and Small-Scale Structure of Cosmic String Networks". In: *Phys. Rev.* D73 (2006), p. 043515. DOI: 10.1103/PhysRevD.73.043515. arXiv: astro-ph/0511792.

[110] Graham Vincent, Nuno D. Antunes, and Mark Hindmarsh. "Numerical Simulations of String Networks in the Abelian Higgs Model". In: *Phys. Rev. Lett.* 80.SUSX-TH-97-015 (1998), pp. 2277–2280. DOI: 10.1103/PhysRevLett.80.2277. arXiv: hep-ph/9708427.

[111] J. N. Moore, E. P. S. Shellard, and C. J. A. P Martins. "Evolution of Abelian-Higgs String Networks". In: *Phys. Rev.* D65.2 (Jan. 2001), p. 023503. eprint: hep-ph/0107171.

[112] Mark Hindmarsh, Stephanie Stuckey, and Neil Bevis. "Abelian Higgs Cosmic Strings: Small Scale Structure and Loops". In: *Phys. Rev.* D79.IMPERIAL-TP-08-NB-03 (2009), p. 123504. DOI: 10.1103/PhysRevD.79.123504. arXiv: 0812.1929 [hep-th].

[113] Mark Hindmarsh et al. "Scaling from Gauge and Scalar Radiation in Abelian Higgs String Networks". In: *Phys. Rev.* D96.2 (2017), p. 023525. DOI: 10.1103/PhysRevD.96.023525. arXiv: 1703.06696 [astro-ph.CO].

[114] Jose J. Blanco-Pillado and Ken D. Olum. "Stochastic Gravitational Wave Background from Smoothed Cosmic String Loops". In: *Phys. Rev. D* 96.10 (2017), p. 104046. DOI: 10.1103/PhysRevD.96.104046. arXiv: 1709.02693 [astro-ph.CO].

[115] Jean M. Quashnock and David N. Spergel. "Gravitational Selfinteractions of Cosmic Strings". In: *Phys. Rev.* D42.POP-354 (1990), pp. 2505–2520. DOI: 10.1103/PhysRevD.42.2505.

[116] Thomas Helfer, Josu C. Aurrekoetxea, and Eugene A. Lim. "Cosmic String Loop Collapse in Full General Relativity". In: *Phys. Rev.* D99.KCL-PH-TH/2018-44 (2019), p. 104028. DOI: 10.1103/PhysRevD.99.104028. arXiv: 1808.06678 [gr-qc].

[117] Tanmay Vachaspati and Alexander Vilenkin. "Gravitational Radiation from Cosmic Strings". en. In: *Physical Review D* 31.HUTP-84/A065 (June 1985), pp. 3052–3058. ISSN: 0556-2821. DOI: 10.1103/PhysRevD.31.3052.

[118] Bruce Allen and E.P.S. Shellard. "Gravitational Radiation from Cosmic Strings". In: *Phys. Rev. D* 45.WISC-MILW-91-TH-12 (1992), pp. 1898–1912. DOI: 10.1103/PhysRevD.45.1898.

[119] Jeremy M. Wachter and Ken D. Olum. "Gravitational Backreaction on Piecewise Linear Cosmic String Loops". In: *Phys. Rev.* D95.2 (2017), p. 023519. DOI: 10.1103/PhysRevD.95.023519. arXiv: 1609.01685 [gr-qc].

[120] Jose J. Blanco-Pillado, Ken D. Olum, and Jeremy M. Wachter. "Gravitational Back-Reaction near Cosmic String Kinks and Cusps". In: *Phys. Rev. D* 98.12 (Dec. 2018), p. 123507. ISSN: 2470-0010, 2470-0029. DOI: 10.1103/PhysRevD.98.123507. arXiv: 1808.08254.

[121] David F. Chernoff, Eanna E. Flanagan, and Barry Wardell. "Gravitational Backreaction on a Cosmic String: Formalism". In: *Phys. Rev.* D99.8 (2019), p. 084036. DOI: 10.1103/PhysRevD.99.084036. arXiv: 1808.08631 [gr-qc].

[122] Jorge V. Rocha. "Scaling Solution for Small Cosmic String Loops". In: *Phys. Rev. Lett.* 100 (2008), p. 071601. DOI: 10.1103/PhysRevLett.100.071601. arXiv: 0709.3284 [gr-qc].

[123] Larissa Lorenz, Christophe Ringeval, and Mairi Sakellariadou. "Cosmic String Loop Distribution on All Length Scales and at Any Redshift". In: *JCAP* 10 (2010), p. 003. DOI: 10.1088/1475-7516/2010/10/003. arXiv: 1006.0931 [astro-ph.CO].

[124] Vitaly Vanchurin. "Towards a Kinetic Theory of Strings". In: *Phys.Rev.* D83 (2011), p. 103525. DOI: 10.1103/PhysRevD.83.103525. arXiv: 1103.1593 [hep-th].

[125] Patrick Peter and Christophe Ringeval. "A Boltzmann Treatment for the Vorton Excess Problem". In: *JCAP* 05 (2013), p. 005. DOI: 10.1088/1475-7516/2013/05/005. arXiv: 1302.0953 [astro-ph.CO].

[126] Vitaly Vanchurin. "Kinetic Theory and Hydrodynamics of Cosmic Strings". In: *Phys. Rev. D* 87.6 (2013). [Erratum: Phys.Rev.D 87, 069910 (2013)], p. 063508. DOI: 10.1103/PhysRevD.87.063508. arXiv: 1301.1973 [hep-th].

[127] Daniel Schubring and Vitaly Vanchurin. "Transport Equation for Nambu-Goto Strings". In: *Phys. Rev. D* 89.8 (2014), p. 083530. DOI: 10.1103/PhysRevD.89.083530. arXiv: 1310.6763 [hep-th].

[128] R. R. Caldwell and Bruce Allen. "Cosmological Constraints on Cosmic String Gravitational Radiation". In: *Phys. Rev.* D45.WISC-MILW-91-TH-14 (1992), pp. 3447–3468. DOI: 10.1103/PhysRevD.45.3447.

[129] Matthew R. DePies and Craig J. Hogan. "Stochastic Gravitational Wave Background from Light Cosmic Strings". In: *Phys. Rev.* D75 (2007), p. 125006. DOI: 10.1103/PhysRevD.75.125006. arXiv: astro-ph/0702335.

[130] Tania Regimbau et al. "The Stochastic Background from Cosmic (Super)Strings: Popcorn and (Gaussian) Continuous Regimes". In: *Phys. Rev.* D85 (2012), p. 066001. DOI: 10.1103/PhysRevD.85.066001,10.1103/PhysRevD.85.069902. arXiv: 1111.6638 [astro-ph.CO].

[131] Sachiko Kuroyanagi et al. "Forecast Constraints on Cosmic String Parameters from Gravitational Wave Direct Detection Experiments". In: *Phys. Rev.* D86 (2012), p. 023503. DOI: 10.1103/PhysRevD.86.023503. arXiv: 1202.3032 [astro-ph.CO].

[132] Sophie Henrot-Versille et al. "Improved Constraint on the Primordial Gravitational-Wave Density Using Recent Cosmological Data and Its Impact on Cosmic String Models". In: *Class. Quant. Grav.* 32.4 (2015), p. 045003. DOI: 10.1088/0264-9381/32/4/045003. arXiv: 1408.5299 [astro-ph.CO].

[133] L. Sousa and P. P. Avelino. "Probing Cosmic Superstrings with Gravitational Waves". In: *Phys. Rev.* D94.6 (2016), p. 063529. DOI: 10.1103/PhysRevD.94.063529. arXiv: 1606.05585 [astro-ph.CO].

[134] D. P. Bennett and F. R. Bouchet. "Cosmic-String Evolution". In: *Phys. Rev. Lett.* 63 (Dec. 1989), pp. 2776–2779.

[135] M. Sakellariadou and A. Vilenkin. "Cosmic-String Evolution in Flat Space-Time". In: *Phys. Rev. D* 42 (1990), pp. 349–353. DOI: 10.1103/PhysRevD.42.349.

[136] E. J. Copeland and T. W. B. Kibble. "Kinks and Small-Scale Structure on Cosmic Strings". In: *Phys. Rev.* D80.IMPERIAL-TP-09-TK-02 (2009), p. 123523. DOI: 10.1103/PhysRevD.80.123523. arXiv: 0909.1960 [astro-ph.CO].

[137] Joseph Polchinski and Jorge V. Rocha. "Analytic Study of Small Scale Structure on Cosmic Strings". In: *Phys. Rev.* D74 (2006), p. 083504. arXiv: hep-ph/0606205.

[138] Florian Dubath, Joseph Polchinski, and Jorge V. Rocha. "Cosmic String Loops, Large and Small". In: *Phys. Rev.* D77 (2008), p. 123528. DOI: 10.1103/PhysRevD.77.123528. arXiv: 0711.0994 [astro-ph].

[139] Daiju Matsunami et al. "Decay of Cosmic String Loops Due to Particle Radiation". In: *Phys. Rev. Lett.* 122.20 (2019), p. 201301. DOI: 10.1103/PhysRevLett.122.201301. arXiv: 1903.05102 [hep-ph].

[140] J. J. Blanco-Pillado and Ken D. Olum. "The Form of Cosmic String Cusps". In: *Phys. Rev.* D59 (1999), p. 063508. DOI: 10.1103/PhysRevD.59.063508. arXiv: gr-qc/9810005.

[141] Ken D. Olum and J. J. Blanco-Pillado. "Field Theory Simulation of Abelian Higgs Cosmic String Cusps". In: *Phys. Rev.* D60 (1999), p. 023503. DOI: 10.1103/PhysRevD.60.023503. arXiv: gr-qc/9812040.

[142] Mark Hindmarsh et al. "Loop decay in Abelian-Higgs string networks". In: (Mar. 2021). arXiv: 2103.16248 [astro-ph.CO].

[143] Edward Witten. "Cosmic Superstrings". In: *Phys. Lett. B* 153.PRINT-85-0204 (PRINCETON) (1985), pp. 243–246. DOI: 10.1016/0370-2693(85)90540-4.

[144] George Lazarides, C. Panagiotakopoulos, and Q. Shafi. "Superheavy Superconducting Cosmic Strings from Superstring Models". In: *Phys. Lett. B* 183.NUB-2707 (1987), pp. 289–295. DOI: 10.1016/0370-2693(87)90966-X.

[145] Brandon Carter. "Dilatonic formulation for conducting cosmic string models". In: *Annalen Phys.* 9 (2000). Ed. by G. Neugebauer and R. Collier, pp. 247–257. DOI: 10.1002/(SICI)1521-3889(200005)9:3/5<247::AID-ANDP247>3.0.CO;2-5. arXiv: hep-th/0002162.

[146] Brandon Carter. "Essentials of Classical Brane Dynamics". In: *Int. J. Theor. Phys.* 40 (2001), pp. 2099–2130. DOI: 10.1023/A:1012934901706. arXiv: gr-qc/0012036.

[147] R.L. Davis and E.P.S. Shellard. "Cosmic Vortons". In: *Nucl.Phys.* B323.NSF-ITP-88-167 (1989), pp. 209–224. DOI: 10.1016/0550-3213(89)90594-4.

[148] B. Carter. "Cosmic Rings as a Chump Dark Matter Candidate?" In: *10th Moriond Astrophysics Meeting: The Early Phases of the Universe*. 1990, pp. 213–221.

[149] Robert H. Brandenberger et al. "Cosmic Vortons and Particle Physics Constraints". In: *Phys. Rev. D* 54.BROWN-HET-1036, DAMTP-96-16, MIT-CTP-2515, OBSPM-96014 (1996), pp. 6059–6071. DOI: 10.1103/PhysRevD.54.6059. arXiv: hep-ph/9605382.

[150] C.J.A.P. Martins and E.P.S. Shellard. "Vorton Formation". In: *Phys. Rev. D* 57.DAMTP-R-97-30 (1998), pp. 7155–7176. DOI: 10.1103/PhysRevD.57.7155. arXiv: hep-ph/9804378.

[151] C.J.A.P. Martins and E.P.S. Shellard. "Limits on Cosmic Chiral Vortons". In: *Phys. Lett. B* 445.DAMTP-98-58, DAMTP-1998-58 (1998), pp. 43–51. DOI: 10.1016/S0370-2693(98)01466-X. arXiv: hep-ph/9806480.

[152] Brandon Carter. "Old and New Processes of Vorton Formation". In: *Lect. Notes Phys.* 541 (2000). Ed. by J. Kowalski-Glikman, pp. 71–78. arXiv: hep-ph/9909513.

[153] A. C. Davis et al. "Dynamics and Properties of Chiral Cosmic Strings in Minkowski Space". In: *Phys. Rev. D* 62.DAMTP-2000-46, IMPERIAL-TP-99-00-27 (2000), p. 083516. DOI: 10.1103/PhysRevD.62.083516. arXiv: astro-ph/0005514.

[154] Daniele A. Steer. "Selfintersections and Gravitational Properties of Chiral Cosmic Strings in Minkowski Space". In: *Phys. Rev. D* 63 (2001), p. 083517. DOI: 10.1103/PhysRevD.63.083517. arXiv: astro-ph/0011233.

[155] Y. Lemperiere and E.P.S. Shellard. "Vorton Existence and Stability". In: *Phys. Rev. Lett.* 91 (2003), p. 141601. DOI: 10.1103/PhysRevLett.91.141601. arXiv: hep-ph/0305156.

[156] Richard A. Battye and Paul M. Sutcliffe. "Vorton Construction and Dynamics". In: *Nucl. Phys. B* 814.DCPT-08-69 (2009), pp. 180–194. DOI: 10.1016/j.nuclphysb.2009.01.021. arXiv: 0812.3239 [hep-th].

[157] Julien Garaud, Eugen Radu, and Mikhail S. Volkov. "Stable Cosmic Vortons". In: *Phys. Rev. Lett.* 111 (2013), p. 171602. DOI: 10.1103/PhysRevLett.111.171602. arXiv: 1303.3044 [hep-th].

[158] B. P. Abbott et al. "GW151226: Observation of Gravitational Waves from a 22-Solar-Mass Binary Black Hole Coalescence". In: *Phys. Rev. Lett.* 116.LIGO-P151226 (2016), p. 241103. DOI: 10.1103/PhysRevLett.116.241103. arXiv: 1606.04855 [gr-qc].

[159] Benjamin P. Abbott et al. "GW170104: Observation of a 50-Solar-Mass Binary Black Hole Coalescence at Redshift 0.2". In: *Phys. Rev. Lett.* 118.LIGO-P170104 (2017), p. 221101. DOI: 10.1103/PhysRevLett.118.221101, 10.1103/PhysRevLett.121.129901. arXiv: 1706.01812 [gr-qc].

[160] B.. P.. Abbott et al. "GW170608: Observation of a 19-Solar-Mass Binary Black Hole Coalescence". In: *Astrophys. J.* 851.LIGO-DOCUMENT-P170608-V8 (2017), p. L35. DOI: 10.3847/2041-8213/aa9f0c. arXiv: 1711.05578 [astro-ph.HE].

[161] B. P. Abbott et al. "GW170814: A Three-Detector Observation of Gravitational Waves from a Binary Black Hole Coalescence". In: *Phys. Rev. Lett.* 119.14 (2017), p. 141101. DOI: 10.1103/PhysRevLett.119.141101. arXiv: 1709.09660 [gr-qc].

[162] L. P. Grishchuk. "Amplification of Gravitational Waves in an Istropic Universe". In: *Sov. Phys. JETP* 40 (1975), pp. 409–415.

[163] Alexei A. Starobinsky. "Spectrum of Relict Gravitational Radiation and the Early State of the Universe". In: *JETP Lett.* 30 (1979), pp. 682–685.

[164] V. A. Rubakov, M. V. Sazhin, and A. V. Veryaskin. "Graviton Creation in the Inflationary Universe and the Grand Unification Scale". In: *Phys. Lett.* 115B (1982), pp. 189–192. DOI: 10.1016/0370-2693(82)90641-4.

[165] R. Fabbri and M. d. Pollock. "The Effect of Primordially Produced Gravitons upon the Anisotropy of the Cosmological Microwave Background Radiation". In: *Phys. Lett.* 125B (1983), pp. 445–448. DOI: 10.1016/0370-2693(83)91322-9.

[166] Mohamed M. Anber and Lorenzo Sorbo. "N-Flationary Magnetic Fields". In: *JCAP* 0610 (2006), p. 018. DOI: 10.1088/1475-7516/2006/10/018. arXiv: astro-ph/0606534.

[167] Lorenzo Sorbo. "Parity Violation in the Cosmic Microwave Background from a Pseudoscalar Inflaton". In: *JCAP* 1106 (2011), p. 003. DOI: 10.1088/1475-7516/2011/06/003. arXiv: 1101.1525 [astro-ph.CO].

[168] Enrico Pajer and Marco Peloso. "A Review of Axion Inflation in the Era of Planck". In: *Class. Quant. Grav.* 30 (2013), p. 214002. DOI: 10.1088/0264-9381/30/21/214002. arXiv: 1305.3557 [hep-th].

[169] Peter Adshead, Emil Martinec, and Mark Wyman. "Gauge Fields and Inflation: Chiral Gravitational Waves, Fluctuations, and the Lyth Bound". In: *Phys. Rev.* D88.2 (2013), p. 021302. DOI: 10.1103/PhysRevD.88.021302. arXiv: 1301.2598 [hep-th].

[170] Peter Adshead, Emil Martinec, and Mark Wyman. "Perturbations in Chromo-Natural Inflation". In: *JHEP* 09 (2013), p. 087. DOI: 10.1007/JHEP09(2013)087. arXiv: 1305.2930 [hep-th].

[171] Azadeh Maleknejad. "Axion Inflation with an SU(2) Gauge Field: Detectable Chiral Gravity Waves". In: *JHEP* 07 (2016), p. 104. DOI: 10.1007/JHEP07(2016)104. arXiv: 1604.03327 [hep-ph].

[172] Emanuela Dimastrogiovanni, Matteo Fasiello, and Tomohiro Fujita. "Primordial Gravitational Waves from Axion-Gauge Fields Dynamics". In: *JCAP* 1701.01 (2017), p. 019. DOI: 10.1088/1475-7516/2017/01/019. arXiv: 1608.04216 [astro-ph.CO].

[173] Ryo Namba et al. "Scale-Dependent Gravitational Waves from a Rolling Axion". In: *JCAP* 1601.01 (2016), p. 041. DOI: 10.1088/1475-7516/2016/01/041. arXiv: 1509.07521 [astro-ph.CO].

[174] Ricardo Z. Ferreira et al. "On the Validity of the Perturbative Description of Axions during Inflation". In: *JCAP* 1604.04 (2016), p. 039. DOI: 10.1088/1475-7516/2016/10/E01,10.1088/1475-7516/2016/04/039. arXiv: 1512.06116 [astro-ph.CO].

[175] Marco Peloso, Lorenzo Sorbo, and Caner Unal. "Rolling Axions during Inflation: Perturbativity and Signatures". In: *JCAP* 1609.ACFI-T16-16, UMN–TH–3531-16 (2016), p. 001. DOI: 10.1088/1475-7516/2016/09/001. arXiv: 1606.00459 [astro-ph.CO].

[176] Valerie Domcke, Mauro Pieroni, and Pierre Binétruy. "Primordial Gravitational Waves for Universality Classes of Pseudoscalar Inflation". In: *JCAP* 1606 (2016), p. 031. DOI: 10.1088/1475-7516/2016/06/031. arXiv: 1603.01287 [astro-ph.CO].

[177] R. R. Caldwell and C. Devulder. "Axion Gauge Field Inflation and Gravitational Leptogenesis: A Lower Bound on b Modes from the Matter-Antimatter Asymmetry of the Universe". In: *Phys. Rev.* D97.2 (2018), p. 023532. DOI: 10.1103/PhysRevD.97.023532. arXiv: 1706.03765 [astro-ph.CO].

[178] Nicola Bartolo et al. "Science with the Space-Based Interferometer LISA. IV: Probing Inflation with Gravitational Waves". In: *JCAP* 1612.ACFI-T16-19, UMN-TH-3608-16, CERN-TH-2016-222, KCL-PH-TH-2016-58, IFT-UAM-CSIC-16-104 (2016), p. 026. DOI: 10.1088/1475-7516/2016/12/026. arXiv: 1610.06481 [astro-ph.CO].

[179] Massimo Giovannini. "Gravitational Waves Constraints on Postinflationary Phases Stiffer than Radiation". In: *Phys. Rev.* D58 (1998), p. 083504. DOI: 10.1103/PhysRevD.58.083504. arXiv: hep-ph/9806329.

[180] Massimo Giovannini. "Production and Detection of Relic Gravitons in Quintessential Inflationary Models". In: *Phys. Rev.* D60.TUPT-01-99 (1999), p. 123511. DOI: 10.1103/PhysRevD.60.123511. arXiv: astro-ph/9903004.

[181] Latham A. Boyle and Alessandra Buonanno. "Relating Gravitational Wave Constraints from Primordial Nucleosynthesis, Pulsar Timing, Laser Interferometers, and the CMB: Implications for the Early Universe". In: *Phys. Rev.* D78 (2008), p. 043531. DOI: 10.1103/PhysRevD.78.043531. arXiv: 0708.2279 [astro-ph].

[182] Daniel G. Figueroa and Erwin H. Tanin. "Inconsistency of an Inflationary Sector Coupled Only to Einstein Gravity". In: *JCAP* 1910.10 (2019), p. 050. DOI: 10.1088/1475-7516/2019/10/050. arXiv: 1811.04093 [astro-ph.CO].

[183] Daniel G. Figueroa and Erwin H. Tanin. "Ability of LIGO and LISA to Probe the Equation of State of the Early Universe". In: *JCAP* 1908 (2019), p. 011. DOI: 10.1088/1475-7516/2019/08/011. arXiv: 1905.11960 [astro-ph.CO].

[184] Richard Easther and Eugene A. Lim. "Stochastic Gravitational Wave Production after Inflation". In: *JCAP* 0604 (2006), p. 010. DOI: 10.1088/1475-7516/2006/04/010. arXiv: astro-ph/0601617.

[185] Juan Garcia-Bellido and Daniel G. Figueroa. "A Stochastic Background of Gravitational Waves from Hybrid Preheating". In: *Phys. Rev. Lett.* 98.IFT-UAM-CSIC-06-46 (2007), p. 061302. DOI: 10.1103/PhysRevLett.98.061302. arXiv: astro-ph/0701014.

[186] Juan Garcia-Bellido, Daniel G. Figueroa, and Alfonso Sastre. "A Gravitational Wave Background from Reheating after Hybrid Inflation". In: *Phys. Rev.* D77.IFT-UAM-CSIC-07-38 (2008), p. 043517. DOI: 10.1103/PhysRevD.77.043517. arXiv: 0707.0839 [hep-ph].

[187] Jean Francois Dufaux et al. "Theory and Numerics of Gravitational Waves from Preheating after Inflation". In: *Phys. Rev.* D76 (2007), p. 123517. DOI: 10.1103/PhysRevD.76.123517. arXiv: 0707.0875 [astro-ph].

[188] Jean-Francois Dufaux et al. "Gravity Waves from Tachyonic Preheating after Hybrid Inflation". In: *JCAP* 0903.FTUAM-08-25, IFT-UAM-CSIC-08-90 (2009), p. 001. DOI: 10.1088/1475-7516/2009/03/001. arXiv: 0812.2917 [astro-ph].

[189] Jean-Francois Dufaux, Daniel G. Figueroa, and Juan Garcia-Bellido. "Gravitational Waves from Abelian Gauge Fields and Cosmic Strings at Preheating". In: *Phys. Rev.* D82.IFT-UAM-CSIC-10-38, CERN-PH-TH-2010-121 (2010), p. 083518. DOI: 10.1103/PhysRevD.82.083518. arXiv: 1006.0217 [astro-ph.CO].

[190] Daniel G. Figueroa and Francisco Torrenti. "Gravitational Wave Production from Preheating: Parameter Dependence". In: *JCAP* 1710.CERN-TH-2017-152, IFT-UAM-CSIC-17-069 (2017), p. 057. DOI: 10.1088/1475-7516/2017/10/057. arXiv: 1707.04533 [astro-ph.CO].

[191] Peter Adshead, John T. Giblin, and Zachary J. Weiner. "Gravitational Waves from Gauge Preheating". In: *Phys. Rev.* D98.4 (2018), p. 043525. DOI: 10.1103/PhysRevD.98.043525. arXiv: 1805.04550 [astro-ph.CO].

[192] Shuang-Yong Zhou et al. "Gravitational Waves from Oscillon Preheating". In: *JHEP* 10 (2013), p. 026. DOI: 10.1007/JHEP10(2013)026. arXiv: 1304.6094 [astro-ph.CO].

[193] Stefan Antusch, Francesco Cefala, and Stefano Orani. "Gravitational Waves from Oscillons after Inflation". In: *Phys. Rev. Lett.* 118.1 (2017), p. 011303. DOI: 10.1103/PhysRevLett.120.219901,10.1103/PhysRevLett.118.011303. arXiv: 1607.01314 [astro-ph.CO].

[194] Stefan Antusch, Francesco Cefala, and Stefano Orani. "What Can We Learn from the Stochastic Gravitational Wave Background Produced by Oscillons?" In: *JCAP* 1803.03 (2018), p. 032. DOI: 10.1088/1475-7516/2018/03/032. arXiv: 1712.03231 [astro-ph.CO].

[195] Jing Liu et al. "Gravitational Waves from Oscillons with Cuspy Potentials". In: *Phys. Rev. Lett.* 120.3 (2018), p. 031301. DOI: 10.1103/PhysRevLett.120.031301. arXiv: 1707.09841 [astro-ph.CO].

[196] Mustafa A. Amin et al. "Gravitational Waves from Asymmetric Oscillon Dynamics?" In: *Phys. Rev.* D98 (2018), p. 024040. DOI: 10.1103/PhysRevD.98.024040. arXiv: 1803.08047 [astro-ph.CO].

[197] Marc Kamionkowski, Arthur Kosowsky, and Michael S. Turner. "Gravitational Radiation from First Order Phase Transitions". In: *Phys. Rev.* D49.IASSNS-HEP-93-44, FERMILAB-PUB-93-235-A (1994), pp. 2837–2851. DOI: 10.1103/PhysRevD.49.2837. arXiv: astro-ph/9310044.

[198] Chiara Caprini, Ruth Durrer, and Geraldine Servant. "Gravitational Wave Generation from Bubble Collisions in First-Order Phase Transitions: An Analytic Approach". In: *Phys. Rev.* D77.CERN-PH-TH-2007-206, SACLAY-T07-142 (2008), p. 124015. DOI: 10.1103/PhysRevD.77.124015. arXiv: 0711.2593 [astro-ph].

[199] Stephan J. Huber and Thomas Konstandin. "Gravitational Wave Production by Collisions: More Bubbles". In: *JCAP* 0809 (2008), p. 022. DOI: 10.1088/1475-7516/2008/09/022. arXiv: 0806.1828 [hep-ph].

[200] Mark Hindmarsh et al. "Gravitational Waves from the Sound of a First Order Phase Transition". In: *Phys. Rev. Lett.* 112.HIP-2013-07-TH (2014), p. 041301. DOI: 10.1103/PhysRevLett.112.041301. arXiv: 1304.2433 [hep-ph].

[201] Mark Hindmarsh et al. "Numerical Simulations of Acoustically Generated Gravitational Waves at a First Order Phase Transition". In: *Phys. Rev.* D92.HIP-2015-13-TH (2015), p. 123009. DOI: 10.1103/PhysRevD.92.123009. arXiv: 1504.03291 [astro-ph.CO].

[202] Chiara Caprini et al. "Science with the Space-Based Interferometer eLISA. II: Gravitational Waves from Cosmological Phase Transitions". In: *JCAP* 1604.DESY-15-246 (2016), p. 001. DOI: 10.1088/1475-7516/2016/04/001. arXiv: 1512.06239 [astro-ph.CO].

[203] Daniel Cutting, Mark Hindmarsh, and David J. Weir. "Gravitational Waves from Vacuum First-Order Phase Transitions: From the Envelope to the Lattice". In: *Phys. Rev.* D97.HIP-2018-4-TH (2018), p. 123513. DOI: 10.1103/PhysRevD.97.123513. arXiv: 1802.05712 [astro-ph.CO].

[204] M. Sakellariadou. "Gravitational Waves Emitted from Infinite Strings". In: *Phys. Rev.* D42 (1990), pp. 354–360. DOI: 10.1103/PhysRevD.42.354.

[205] Thibault Damour and Alexander Vilenkin. "Gravitational Radiation from Cosmic (Super)Strings: Bursts, Stochastic Background, and Observational Windows". In: *Phys.Rev.* D 71 (2005), p. 063510. DOI: 10.1103/PhysRevD.71.063510. arXiv: hep-th/0410222.

[206] Daniel G. Figueroa, Mark Hindmarsh, and Jon Urrestilla. "Exact Scale-Invariant Background of Gravitational Waves from Cosmic Defects". In: *Phys. Rev. Lett.* 110.10 (2013), p. 101302. DOI: 10.1103/PhysRevLett.110.101302. arXiv: 1212.5458 [astro-ph.CO].

[207] Heather Audley et al. "Laser Interferometer Space Antenna". In: (2017). arXiv: 1702.00786 [astro-ph.IM].

[208] C. J. Hogan and M. J. Rees. "Gravitational Interactions of Cosmic Strings". In: *Nature* 311 (1984), pp. 109–113. DOI: 10.1038/311109a0.

[209] Frank S. Accetta and Lawrence M. Krauss. "The Stochastic Gravitational Wave Spectrum Resulting from Cosmic String Evolution". In: *Nucl. Phys.* B319.YCTP-P5-88 (1989), pp. 747–764. DOI: 10.1016/0550-3213(89)90628-7.

[210] David P. Bennett and Francois R. Bouchet. "Constraints on the Gravity Wave Background Generated by Cosmic Strings". In: *Phys. Rev.* D43.UCRL-JC-105282 (1991), pp. 2733–2735. DOI: 10.1103/PhysRevD.43.2733.

[211] Xavier Siemens, Vuk Mandic, and Jolien Creighton. "Gravitational Wave Stochastic Background from Cosmic (Super)Strings". In: *Phys. Rev. Lett.* 98 (2007), p. 111101. DOI: 10.1103/PhysRevLett.98.111101. arXiv: astro-ph/0610920.

[212] S. Olmez, V. Mandic, and X. Siemens. "Gravitational-Wave Stochastic Background from Kinks and Cusps on Cosmic Strings". In: *Phys.Rev.* D 81 (2010), p. 104028. DOI: 10.1103/PhysRevD.81.104028. arXiv: 1004.0890 [astro-ph.CO].

[213] S. A. Sanidas, R. A. Battye, and B. W. Stappers. "Constraints on Cosmic String Tension Imposed by the Limit on the Stochastic Gravitational Wave Background from the European Pulsar Timing Array". In: *Physical Review D* 85.12 (June 2012), p. 122003. ISSN: 1550-7998, 1550-2368. DOI: 10.1103/PhysRevD.85.122003. arXiv: 1201.2419.

[214] Sotirios A. Sanidas, Richard A. Battye, and Benjamin W. Stappers. "Projected Constraints on the Cosmic (Super)String Tension with Future Gravitational Wave Detection Experiments". In: *Astrophys. J.* 764 (2013), p. 108. DOI: 10.1088/0004-637X/764/1/108. arXiv: 1211.5042 [astro-ph.CO].

[215] Sachiko Kuroyanagi et al. "Forecast Constraints on Cosmic Strings from Future CMB, Pulsar Timing and Gravitational Wave Direct Detection Experiments". In: *Phys. Rev.* D87.2 (2013), p. 023522. DOI: 10.1103/PhysRevD.87.069903,10.1103/PhysRevD.87.023522. arXiv: 1210.2829 [astro-ph.CO].

[216] L. Sousa and P. P. Avelino. "Stochastic Gravitational Wave Background Generated by Cosmic String Networks: Velocity-Dependent One-Scale Model versus Scale-Invariant Evolution". In: *Phys. Rev.* D88.2 (2013), p. 023516. DOI: 10.1103/PhysRevD.88.023516. arXiv: 1304.2445 [astro-ph.CO].

[217] L. Sousa and P. P. Avelino. "Stochastic Gravitational Wave Background Generated by Cosmic String Networks: The Small-Loop Regime". In: *Phys. Rev.* D89.8 (2014), p. 083503. DOI: 10.1103/PhysRevD.89.083503. arXiv: 1403.2621 [astro-ph.CO].

[218] Yanou Cui et al. "Probing the Pre-BBN Universe with Gravitational Waves from Cosmic Strings". In: *JHEP* 01.KCL-PH-TH/2018-47 (2019), p. 081. DOI: 10.1007/JHEP01(2019)081. arXiv: 1808.08968 [hep-ph].

[219] Alexander C. Jenkins and Mairi Sakellariadou. "Anisotropies in the Stochastic Gravitational-Wave Background: Formalism and the Cosmic String Case". In: *Phys. Rev.* D98.KCL-PH-TH/2018-6, KCL-PH-TH-2018-6 (2018), p. 063509. DOI: 10.1103/PhysRevD.98.063509. arXiv: 1802.06046 [astro-ph.CO].

[220] Geneviève Bélanger et al. "micrOMEGAs5.0 : Freeze-In". In: *Comput. Phys. Commun.* 231 (2018), pp. 173–186. DOI: 10.1016/j.cpc.2018.04.027. arXiv: 1801.03509 [hep-ph].

[221] David P. Bennett and Francois R. Bouchet. "Evidence for a Scaling Solution in Cosmic String Evolution". In: *Phys. Rev. Lett.* 60.FERMILAB-PUB-87-205-A (1988), p. 257. DOI: 10.1103/PhysRevLett.60.257.

[222] David P. Bennett. "The Evolution of Cosmic Strings". In: *Phys. Rev.* D33.SLAC-PUB-3743 (1986), p. 872. DOI: 10.1103/PhysRevD.34.3932.2,10.1103/PhysRevD.33.872.

[223] David P. Bennett. "Evolution of Cosmic Strings. 2." In: *Phys. Rev.* D34.SLAC-PUB-3989 (1986), p. 3592. DOI: 10.1103/PhysRevD.34.3592.

[224] C. J. Burden. "Gravitational Radiation from a Particular Class of Cosmic Strings". In: *Phys. Lett.* 164B.Print-85-0745 (GLASGOW) (1985), pp. 277–281. DOI: 10.1016/0370-2693(85)90326-0.

[225] David Garfinkle and Tanmay Vachaspati. "Radiation from Kinky, Cuspless Cosmic Loops". In: *Phys. Rev.* D36.Print-87-0513 (WASH.U.,ST.LOUIS) (1987), p. 2229. DOI: 10.1103/PhysRevD.36.2229.

[226] C.J.A.P. Martins, J.N. Moore, and E.P.S. Shellard. "A Unified Model for Vortex String Network Evolution". In: *Phys. Rev. Lett.* 92.DAMTP-2000-32 (2004), p. 251601. DOI: 10.1103/PhysRevLett.92.251601. arXiv: hep-ph/0310255.

[227] J. N. Moore, E. P. S. Shellard, and C. J. A. P. Martins. "On the Evolution of Abelian-Higgs String Networks". In: *Phys. Rev.* D65.DAMTP-2001-65 (2002), p. 023503. DOI: 10.1103/PhysRevD.65.023503. arXiv: hep-ph/0107171.

[228] Jean M. Quashnock and Tsvi Piran. "Effects of Gravitational Back Reaction on Small Scale Structure of Cosmic Strings". In: *Phys. Rev.* D43.FERMILAB-PUB-90-179-A (1991), R3785–R3788. DOI: 10.1103/PhysRevD.43.R3785.

[229] T. W. B. Kibble and Edmund J. Copeland. "Evolution of Small Scale Structure on Cosmic Strings". In: *Phys. Scripta* T36.IMPERIAL-TP-89-90-27 (1991), pp. 153–166. DOI: 10.1088/0031-8949/1991/T36/017.

[230] C. J. A. P. Martins, E. P. S. Shellard, and J. P. P. Vieira. "Models for Small-Scale Structure of Cosmic Strings: Mathematical Formalism". English. In: *Physical Review D* 90.4 (Aug. 2014), p. 043518. ISSN: 1550-7998, 1550-2368. DOI: 10.1103/PhysRevD.90.043518. arXiv: 1405.7722 [hep-ph].

[231] E. J. Copeland, João Magueijo, and D. A. Steer. "Cosmological Parameter Dependence in Local String Theories of Structure Formation". en. In: *Physical Review D* 61.DAMTP-1999-34 (Feb. 2000). ISSN: 0556-2821, 1089-4918. DOI: 10.1103/PhysRevD.61.063505. arXiv: astro-ph/9903174.

[232] Joseph Polchinski and Jorge V. Rocha. "Cosmic String Structure at the Gravitational Radiation Scale". In: *Phys. Rev.* D75 (2007), p. 123503. DOI: 10.1103/PhysRevD.75.123503. arXiv: gr-qc/0702055.

[233] R. L. Davis and E. P. S. Shellard. "DO AXIONS NEED INFLATION?" In: *Nucl. Phys.* B324.NSF-ITP-88-195, MIT-CTP-1685, CSR-AT-89-07 (1989), pp. 167–186. DOI: 10.1016/0550-3213(89)90187-9.

[234] Ken D. Olum and J. J. Blanco-Pillado. "Radiation from Cosmic String Standing Waves". In: *Phys. Rev. Lett.* 84 (2000), pp. 4288–4291. DOI: 10.1103/PhysRevLett.84.4288. arXiv: astro-ph/9910354.

[235] David Daverio et al. "Energy-Momentum Correlations for Abelian Higgs Cosmic Strings". In: *Phys. Rev.* D93.8 (2016), p. 085014. DOI: 10.1103/PhysRevD.95.049903,10.1103/PhysRevD.93.085014. arXiv: 1510.05006 [astro-ph.CO].

[236] Steven Weinberg. *Gravitation and Cosmology: Principles and Applications of the General Theory of Relativity*. New York: John Wiley and Sons, 1972. ISBN: 978-0-471-92567-5.

[237] Jose J. Blanco-Pillado, Ken D. Olum, and Benjamin Shlaer. "Cosmic String Loop Shapes". In: *Phys. Rev.* D92.6 (2015), p. 063528. DOI: 10.1103/PhysRevD.92.063528. arXiv: 1508.02693 [astro-ph.CO].

[238] Jose J. Blanco-Pillado, Ken D. Olum, and Jeremy M. Wachter. "Gravitational Backreaction Simulations of Simple Cosmic String Loops". In: *Phys. Rev. D* 100.2 (2019), p. 023535. DOI: 10.1103/PhysRevD.100.023535. arXiv: 1903.06079 [gr-qc].

[239] David F. Chernoff and S. H. Henry Tye. "Detection of Low Tension Cosmic Superstrings". In: *JCAP* 1805.05 (2018), p. 002. DOI: 10.1088/1475-7516/2018/05/002. arXiv: 1712.05060 [astro-ph.CO].

[240] Lawrence M. Krauss. "Gravitational Waves from Global Phase Transitions". In: *Phys. Lett.* B284.YCTP-P33-91 (1992), pp. 229–233. DOI: 10.1016/0370-2693(92)90425-4.

[241] Katherine Jones-Smith, Lawrence M. Krauss, and Harsh Mathur. "A Nearly Scale Invariant Spectrum of Gravitational Radiation from Global Phase Transitions". In: *Phys. Rev. Lett.* 100 (2008), p. 131302. DOI: 10.1103/PhysRevLett.100.131302. arXiv: 0712.0778 [astro-ph].

[242] Elisa Fenu et al. "Gravitational Waves from Self-Ordering Scalar Fields". In: *JCAP* 0910.IFT-UAM-CSIC-09-34, CERN-PH-TH-2009-145 (2009), p. 005. DOI: 10.1088/1475-7516/2009/10/005. arXiv: 0908.0425 [astro-ph.CO].

[243] Wilfried Buchmüller et al. "The Gravitational Wave Spectrum from Cosmological B-L Breaking". In: *JCAP* 1310.DESY-13-050, IPMU-13-0091 (2013), p. 003. DOI: 10.1088/1475-7516/2013/10/003. arXiv: 1305.3392 [hep-ph].

[244] Mark Hindmarsh. "Gravitational Radiation from Kinky Infinite Strings". In: *Phys. Lett.* B251.NCL-90-TP-11 (1990), pp. 28–33. DOI: 10.1016/0370-2693(90)90226-V.

[245] Yuka Matsui and Sachiko Kuroyanagi. "Gravitational Wave Background from Kink-Kink Collisions on Infinite Cosmic Strings". In: (2019). arXiv: 1902.09120 [astro-ph.CO].

[246] Michael Kramer and David J. Champion. "The European Pulsar Timing Array and the Large European Array for Pulsars". In: *Class. Quant. Grav.* 30 (2013), p. 224009. DOI: 10.1088/0264-9381/30/22/224009.

[247] Fazlollah Hajkarim et al. "Effects of the QCD Equation of State and Lepton Asymmetry on Primordial Gravitational Waves". In: (2019). arXiv: 1904.01046 [hep-ph].

[248] Robert R. Caldwell, Tristan L. Smith, and Devin G. E. Walker. "Using a Primordial Gravitational Wave Background to Illuminate New Physics". In: (2018). arXiv: 1812.07577 [astro-ph.CO].

[249] R. A. Battye, R. R. Caldwell, and E. P. S. Shellard. "Gravitational Waves from Cosmic Strings". In: *Topological Defects in Cosmology*. IMPERIAL-TP-95-96-30. 1997, pp. 11–31. arXiv: astro-ph/9706013.

[250] Takeo Moroi and Lisa Randall. "Wino Cold Dark Matter from Anomaly Mediated SUSY Breaking". In: *Nucl. Phys.* B570.IASSNS-HEP-99-54, PUPT-1873, MIT-CTP-2873 (2000), pp. 455–472. DOI: 10.1016/S0550-3213(99)00748-8. arXiv: hep-ph/9906527.

[251] Michael Joyce and Tomislav Prokopec. "Turning around the Sphaleron Bound: Electroweak Baryogenesis in an Alternative Postinflationary Cosmology". In: *Phys. Rev.* D57.CLNS-97-1512, NBI-HE-97-48 (1998), pp. 6022–6049. DOI: 10.1103/PhysRevD.57.6022. arXiv: hep-ph/9709320.

[252] Pierre Salati. "Quintessence and the Relic Density of Neutralinos". In: *Phys. Lett.* B571 (2003), pp. 121–131. DOI: 10.1016/j.physletb.2003.07.073. arXiv: astro-ph/0207396.

[253] Daniel J. H. Chung, Lisa L. Everett, and Konstantin T. Matchev. "Inflationary Cosmology Connecting Dark Energy and Dark Matter". In: *Phys. Rev.* D76.UFIFT-HEP-07-5, MADPH-07-1487 (2007), p. 103530. DOI: 10.1103/PhysRevD.76.103530. arXiv: 0704.3285 [hep-ph].

[254] Vivian Poulin et al. "Cosmological Implications of Ultralight Axionlike Fields". In: *Phys. Rev.* D98.8 (2018), p. 083525. DOI: 10.1103/PhysRevD.98.083525. arXiv: 1806.10608 [astro-ph.CO].

[255] Dario Bettoni, Guillem Domènech, and Javier Rubio. "Gravitational Waves from Global Cosmic Strings in Quintessential Inflation". In: *JCAP* 1902.HIP-2018-21/TH (2019), p. 034. DOI: 10.1088/1475-7516/2019/02/034. arXiv: 1810.11117 [astro-ph.CO].

[256] Nicolás Bernal and Fazlollah Hajkarim. "Primordial Gravitational Waves in Nonstandard Cosmologies". In: *Phys. Rev.* D100.6 (2019), p. 063502. DOI: 10.1103/PhysRevD.100.063502. arXiv: 1905.10410 [astro-ph.CO].

[257] G. S. F. Guedes, P. P. Avelino, and L. Sousa. "Signature of Inflation in the Stochastic Gravitational Wave Background Generated by Cosmic String Networks". In: *Phys. Rev.* D98.12 (2018), p. 123505. DOI: 10.1103/PhysRevD.98.123505. arXiv: 1809.10802 [astro-ph.CO].

[258] Eric Thrane and Joseph D. Romano. "Sensitivity Curves for Searches for Gravitational-Wave Backgrounds". In: *Phys. Rev.* D88.12 (2013), p. 124032. DOI: 10.1103/PhysRevD.88.124032. arXiv: 1310.5300 [astro-ph.IM].

[259] L. Lentati et al. "European Pulsar Timing Array Limits on an Isotropic Stochastic Gravitational-Wave Background". In: *Mon. Not. Roy. Astron. Soc.* 453.3 (2015), pp. 2576–2598. DOI: 10.1093/mnras/stv1538. arXiv: 1504.03692 [astro-ph.CO].

[260] https://www.cosmos.esa.int/web/lisa/lisa-documents.

[261] https://dms.cosmos.esa.int/COSMOS/doc-fetch.php?id=3752747.

[262] Nikolaos Karnesis, Antoine Petiteau, and Marc Lilley. "A Template-Free Approach for Detecting a Gravitational Wave Stochastic Background with LISA". In: (2019). arXiv: 1906.09027 [astro-ph.IM].

[263] Graham R. Vincent, Mark Hindmarsh, and Mairi Sakellariadou. "Correlations in Cosmic String Networks". In: *Phys. Rev.* D55.SUSX-TH-96-008 (1997), pp. 573–581. DOI: 10.1103/PhysRevD.55.573. arXiv: astro-ph/9606137.

[264] G. R. Dvali, Q. Shafi, and S. Solganik. "D-Brane Inflation". In: *4th European Meeting from the Planck Scale to the Electroweak Scale (Planck 2001) La Londe Les Maures, Toulon, France, May 11-16, 2001*. 2001. arXiv: hep-th/0105203.

[265] Nicholas T. Jones, Horace Stoica, and S. H. Henry Tye. "The Production, Spectrum and Evolution of Cosmic Strings in Brane Inflation". In: *Phys. Lett.* B563 (2003), pp. 6–14. DOI: 10.1016/S0370-2693(03)00592-6. arXiv: hep-th/0303269.

[266] Mark G. Jackson, Nicholas T. Jones, and Joseph Polchinski. "Collisions of Cosmic F and D-Strings". In: *JHEP* 0510.CU-TP-1112, CLNS-04-1880, NSF-KITP-04-55 (2005), p. 013. DOI: 10.1088/1126-6708/2005/10/013. arXiv: hep-th/0405229.

[267] Mairi Sakellariadou. "A Note on the Evolution of Cosmic String/Superstring Networks". In: *JCAP* 0504 (2005), p. 003. DOI: 10.1088/1475-7516/2005/04/003. arXiv: hep-th/0410234.

[268] Anastasios Avgoustidis and E. P. S. Shellard. "Effect of Reconnection Probability on Cosmic (Super)String Network Density". In: *Phys. Rev.* D73.DAMTP-2005-133 (2006), p. 041301. DOI: 10.1103/PhysRevD.73.041301. arXiv: astro-ph/0512582.

[269] P. P. Avelino and L. Sousa. "Scaling Laws for Weakly Interacting Cosmic (Super)String and p-Brane Networks". In: *Phys. Rev.* D85 (2012), p. 083525. DOI: 10.1103/PhysRevD.85.083525. arXiv: 1202.6298 [astro-ph.CO].

[270] E. J. Copeland, T. W. B. Kibble, and Daniele A. Steer. "Collisions of Strings with Y Junctions". In: *Phys. Rev. Lett.* 97 (2006), p. 021602. DOI: 10.1103/PhysRevLett.97.021602. arXiv: hep-th/0601153.

[271] E. J. Copeland, T. W. B. Kibble, and Daniele A. Steer. "Constraints on String Networks with Junctions". In: *Phys. Rev.* D75 (2007), p. 065024. DOI: 10.1103/PhysRevD.75.065024. arXiv: hep-th/0611243.

[272] E. J. Copeland et al. "On the Collision of Cosmic Superstrings". In: *Phys. Rev.* D77.IMPERIAL-TP-07-TK-02 (2008), p. 063521. DOI: 10.1103/PhysRevD.77.063521. arXiv: 0712.0808 [hep-th].

[273] A. Avgoustidis and E. P. S. Shellard. "Velocity-Dependent Models for Non-Abelian/Entangled String Networks". In: *Phys. Rev.* D78.UB-ECM-PF-07-11, DAMTP-2007-46 (2008), p. 103510. DOI: 10.1103/PhysRevD.78.103510,10.1103/PhysRevD.80.129907. arXiv: 0705.3395 [astro-ph].

[274] Arttu Rajantie, Mairi Sakellariadou, and Horace Stoica. "Numerical Experiments with p F- and q d-Strings: The Formation of (p,q) Bound States". In: *JCAP* 0711 (2007), p. 021. DOI: 10.1088/1475-7516/2007/11/021. arXiv: 0706.3662 [hep-th].

[275] Mairi Sakellariadou and Horace Stoica. "Dynamics of F/D Networks: The Role of Bound States". In: *JCAP* 0808 (2008), p. 038. DOI: 10.1088/1475-7516/2008/08/038. arXiv: 0806.3219 [hep-th].

[276] Anastasios Avgoustidis and Edmund J. Copeland. "The Effect of Kinematic Constraints on Multi-Tension String Network Evolution". In: *Phys. Rev.* D81 (2010), p. 063517. DOI: 10.1103/PhysRevD.81.063517. arXiv: 0912.4004 [hep-ph].

[277] A. Avgoustidis, Alkistis Pourtsidou, and Mairi Sakellariadou. "Zipping and Unzipping in String Networks: Dynamics of y-Junctions". In: *Phys. Rev.* D91.2 (2015), p. 025022. DOI: 10.1103/PhysRevD.91.025022. arXiv: 1411.7959 [hep-th].

[278] A. Pourtsidou et al. "Scaling Configurations of Cosmic Superstring Networks and Their Cosmological Implications". In: *Phys. Rev.* D83 (2011), p. 063525. DOI: 10.1103/PhysRevD.83.063525. arXiv: 1012.5014 [astro-ph.CO].

[279] Thomas Elghozi, William Nelson, and Mairi Sakellariadou. "Cusps and Pseudocusps in Strings with Y-Junctions". In: *Phys. Rev.* D90.KCL-PH-TH-2014-7 (2014), p. 123517. DOI: 10.1103/PhysRevD.90.123517. arXiv: 1403.3225 [hep-th].

[280] Nicola Bartolo et al. "Probing Non-Gaussian Stochastic Gravitational Wave Backgrounds with LISA". In: *JCAP* 1811.UMN-TH/3720-18, CERN-TH-2018-130, IFT-UAM/CSIC-18-58, DESY 18-086, KCL-PH-TH/2018-22, DESY 18-086, KCL-PH-TH/2018-22, ACFI-T18-08, UMN-TH-3720-18, IFT-UAM-CSIC-18-58, DESY-18-086, KCL-PH-TH-2018-22 (2018), p. 034. DOI: 10.1088/1475-7516/2018/11/034. arXiv: 1806.02819 [astro-ph.CO].

[281] Peter Adshead and Eugene A. Lim. "3-Pt Statistics of Cosmological Stochastic Gravitational Waves". In: *Phys. Rev.* D82.CAS-KITPC-ITP-156 (2010), p. 024023. DOI: 10.1103/PhysRevD.82.024023. arXiv: 0912.1615 [astro-ph.CO].

[282] N. Bartolo et al. "The Primordial Black Hole Dark Matter - LISA Serendipity". In: (2018). arXiv: 1810.12218 [astro-ph.CO].

[283] N. Bartolo et al. "Testing Primordial Black Holes as Dark Matter through LISA". In: (2018). arXiv: 1810.12224 [astro-ph.CO].

[284] Jose J. Blanco-Pillado, Ken D. Olum, and Jeremy M. Wachter. "Energy-Conservation Constraints on Cosmic String Loop Production and Distribution Functions". In: *Phys. Rev. D* 100.12 (2019), p. 123526. DOI: 10.1103/PhysRevD.100.123526. arXiv: 1907.09373 [astro-ph.CO].

[285] Jose J. Blanco-Pillado and Ken D. Olum. "Direct Determination of Cosmic String Loop Density from Simulations". In: *Phys. Rev. D* 101.10 (2020), p. 103018. DOI: 10.1103/PhysRevD.101.103018. arXiv: 1912.10017 [astro-ph.CO].

[286] Matthew R. Adams and Neil J. Cornish. "Detecting a Stochastic Gravitational Wave Background in the Presence of a Galactic Foreground and Instrument Noise". In: *Phys. Rev.* D89.2 (2014), p. 022001. DOI: 10.1103/PhysRevD.89.022001. arXiv: 1307.4116 [gr-qc].

[287] Joseph Polchinski. "Cosmic String Loops and Gravitational Radiation". English. In: *arXiv:0707.0888 [astro-ph, physics:gr-qc, physics:hep-ph, physics:hep-th]* (July 2007). arXiv: 0707.0888 [astro-ph, physics:gr-qc, physics:hep-ph, physics:hep-th].

[288] D. Kirzhnits and A. Linde. "Macroscopic Consequences of the Weinberg Model". In: *Phys. Lett. B* 42 (Dec. 1972), pp. 471–474. DOI: 10.1016/0370-2693(72)90109-8.

[289] G. R. Dvali and S. H. Henry Tye. "Brane Inflation". In: *Phys. Lett.* B450 (1999), pp. 72–82. eprint: hep-ph/9812483.

[290] R. Durrer, M. Kunz, and A. Melchiorri. "Cosmic Structure Formation with Topological Defects". In: *Phys. Rep.* 364 (June 2002), pp. 1–81. eprint: astro-ph/0110348.

[291] Joseph Polchinski. "Introduction to Cosmic F- and D-Strings". In: (2004). arXiv: hep-th/0412244.

[292] Anne-Christine Davis, Philippe Brax, and Carsten van de Bruck. "Brane Inflation and Defect Formation". In: *Phil. Trans. Roy. Soc. Lond.* A366 (2008), pp. 2833–2842. DOI: 10.1098/rsta.2008.0065. arXiv: 0803.0424 [hep-th].

[293] Edmund J. Copeland and T. W. B. Kibble. "Cosmic Strings and Superstrings". In: *Proc. Roy. Soc. Lond.* A466 (2010), pp. 623–657. DOI: 10.1098/rspa.2009.0591. arXiv: 0911.1345 [hep-th].

[294] Mairi Sakellariadou. "Cosmic Strings and Cosmic Superstrings". In: *Nucl. Phys. Proc. Suppl.* 192-193 (2009), pp. 68–90. DOI: 10.1016/j.nuclphysbps.2009.07.046. arXiv: 0902.0569 [hep-th].

[295] Andrei Lazanu and Paul Shellard. "Constraints on the Nambu-Goto Cosmic String Contribution to the CMB Power Spectrum in Light of New Temperature and Polarisation Data". In: *JCAP* 1502.02 (2015), p. 024. DOI: 10.1088/1475-7516/2015/02/024. arXiv: 1410.5046 [astro-ph.CO].

[296] J. D. McEwen et al. "Wavelet-Bayesian Inference of Cosmic Strings Embedded in the Cosmic Microwave Background". In: *Mon. Not. Roy. Astron. Soc.* 472.4 (2017), pp. 4081–4098. DOI: 10.1093/mnras/stx2268. arXiv: 1611.10347 [astro-ph.IM].

[297] A. Vafaei Sadr et al. "Multi-Scale Pipeline for the Search of String-Induced CMB Anisotropies". In: *Mon. Not. Roy. Astron. Soc.* 475.1 (2018), pp. 1010–1022. DOI: 10.1093/mnras/stx3126. arXiv: 1710.00173 [astro-ph.CO].

[298] Razvan Ciuca and Oscar F. Hernández. "Inferring Cosmic String Tension through the Neural Network Prediction of String Locations in CMB Maps". In: *Mon. Not. Roy. Astron. Soc.* 483.4 (2019), pp. 5179–5187. DOI: 10.1093/mnras/sty3478. arXiv: 1810.11889 [astro-ph.CO].

[299] Mark Hindmarsh, Christophe Ringeval, and Teruaki Suyama. "The CMB Temperature Bispectrum Induced by Cosmic Strings". In: *Phys. Rev.* D80 (2009), p. 083501. DOI: 10.1103/PhysRevD.80.083501. arXiv: 0908.0432 [astro-ph.CO].

[300] Mark Hindmarsh, Christophe Ringeval, and Teruaki Suyama. "The CMB Temperature Trispectrum of Cosmic Strings". In: *Phys. Rev.* D81 (2010), p. 063505. DOI: 10.1103/PhysRevD.81.063505. arXiv: 0911.1241 [astro-ph.CO].

[301] T. Vachaspati and A. Vilenkin. "Formation and Evolution of Cosmic Strings". In: *Phys. Rev.* D30 (Nov. 1984), pp. 2036–2045.

[302] I. S. Gradshteyn and I. M. Ryzhik. *Table of Integrals, Series, and Products*. New York and London: Academic Press, 1965.

[303] B. Allen and R. R. Caldwell. "Small-Scale Structure on a Cosmic-String Network". en. In: *Physical Review D* 43.10 (May 1991), pp. 3173–3187. ISSN: 0556-2821. DOI: 10.1103/PhysRevD.43.3173.

[304] B. Allen and R. R. Caldwell. "Kinky Structure on Strings". en. In: *Physical Review D* 43.8 (Apr. 1991), R2457–R2460. ISSN: 0556-2821. DOI: 10.1103/PhysRevD.43.R2457.

[305] J. P. P. Vieira, C. J. A. P. Martins, and E. P. S. Shellard. "Models for Small-Scale Structure on Cosmic Strings: II. Scaling and Its Stability". English. In: *Physical Review D* 94.9 (Nov. 2016), p. 096005. ISSN: 2470-0010, 2470-0029. DOI: 10.1103/PhysRevD.94.096005. arXiv: 1611.06103.

[306] E. Jeong and G. F. Smoot. "Search for Cosmic Strings in CMB Anisotropies". English. In: *The Astrophysical Journal* 624.1 (May 2005), pp. 21–27. ISSN: 0004-637X, 1538-4357. DOI: 10.1086/428921. arXiv: astro-ph/0406432.

[307] Xavier Siemens and Ken D. Olum. "Gravitational Radiation and the Small-Scale Structure of Cosmic Strings". In: *Nucl. Phys.* B611 (2001), pp. 125–145. DOI: 10.1016/S0550-3213(01)00353-4. arXiv: gr-qc/0104085.

[308] Xavier Siemens et al. "Gravitational Wave Bursts from Cosmic (Super)Strings: Quantitative Analysis and Constraints". In: *Phys.Rev.* D 73 (2006), p. 105001. DOI: 10.1103/PhysRevD.73.105001. arXiv: gr-qc/0603115.

[309] Xavier Siemens, Ken D. Olum, and Alexander Vilenkin. "On the Size of the Smallest Scales in Cosmic String Networks". In: *Phys. Rev.* D66 (2002), p. 043501. DOI: 10.1103/PhysRevD.66.043501. arXiv: gr-qc/0203006.

[310] Alexander Vilenkin. "String-Dominated Universe". en. In: *Physical Review Letters* 53.10 (Sept. 1984), pp. 1016–1018. ISSN: 0031-9007. DOI: 10.1103/PhysRevLett.53.1016.

[311] Lara Sousa, Pedro P. Avelino, and Guilherme S.F. Guedes. "Full Analytical Approximation to the Stochastic Gravitational Wave Background Generated by Cosmic String Networks". In: *Phys. Rev. D* 101.10 (2020), p. 103508. DOI: 10.1103/PhysRevD.101.103508. arXiv: 2002.01079 [astro-ph.CO].

[312] P. A. R. Ade et al. "Planck 2015 Results. XIII. Cosmological Parameters". In: *Astron. Astrophys.* 594, A13 (2016), A13. DOI: 10.1051/0004-6361/201525830. arXiv: 1502.01589 [astro-ph.CO].

[313] Izrail Solomonovich Gradshteyn and Iosif Moiseevich Ryzhik. *Table of integrals, series, and products*. Academic press, 2014.

[314] J Aasi et al. "Advanced LIGO". In: *Classical and Quantum Gravity* 32.7 (2015), p. 074001.

[315] F Acernese et al. "Advanced Virgo: A Second-Generation Interferometric Gravitational Wave Detector". In: *Classical and Quantum Gravity* 32.2 (2015), p. 024001.

[316] R. Abbott et al. "Population Properties of Compact Objects from the Second LIGO-Virgo Gravitational-Wave Transient Catalog". In: LIGO-P2000077 (Oct. 2020). arXiv: 2010.14533 [astro-ph.HE].

[317] K. Riles. "Gravitational Waves: Sources, Detectors and Searches". In: *Progress in Particle and Nuclear Physics* 68 (2013), pp. 1–54. ISSN: 0146-6410. DOI: http://dx.doi.org/10.1016/j.ppnp.2012.08.001.

[318] Joseph Polchinski. "Cosmic Superstrings Revisited". In: *AIP Conf. Proc.* 743.1 (2004). Ed. by P. Florides, B. Nolan, and A. Ottewill, pp. 331–340. DOI: 10.1142/S0217751X05026686. arXiv: hep-th/0410082.

[319] Yuka Matsui et al. "Improved Calculation of the Gravitational Wave Spectrum from Kinks on Infinite Cosmic Strings". In: *JCAP* 1611.11 (2016), p. 005. DOI: 10.1088/1475-7516/2016/11/005. arXiv: 1605.08768 [astro-ph.CO].

[320] Matthew J. Stott, Thomas Elghozi, and Mairi Sakellariadou. "Gravitational Wave Bursts from Cosmic String Cusps and Pseudocusps". In: (2016). arXiv: 1612.07599 [hep-th].

[321] Luca Pagano, Laura Salvati, and Alessandro Melchiorri. "New Constraints on Primordial Gravitational Waves from Planck 2015". In: *Phys. Lett.* B760 (2016), pp. 823–825. DOI: 10.1016/j.physletb.2016.07.078. arXiv: 1508.02393 [astro-ph.CO].

[322] Richard H. Cyburt et al. "New BBN Limits on Physics beyond the Standard Model from ^{4}He". In: *Astropart. Phys.* 23.UMN-TH-2316-04, FTPI-MINN-04-28 (2005), pp. 313–323. DOI: 10.1016/j.astropartphys.2005.01.005. arXiv: astro-ph/0408033.

[323] Paul D. Lasky et al. "Gravitational-Wave Cosmology across 29 Decades in Frequency". In: *Phys. Rev.* X6.1 (2016), p. 011035. DOI: 10.1103/PhysRevX.6.011035. arXiv: 1511.05994 [astro-ph.CO].

[324] K. Aggarwal et al. "The NANOGrav 11-Year Data Set: Limits on Gravitational Waves from Individual Supermassive Black Hole Binaries". In: *Astrophys. J.* 880 (2019), p. 2. DOI: 10.3847/1538-4357/ab2236. arXiv: 1812.11585 [astro-ph.GA].

[325] B.P. Abbott et al. "Upper Limits on the Isotropic Gravitational-Wave Background from Advanced LIGO's and Advanced Virgo's Third Observing Run". In: *LIGO-DCC: P2000314* LIGO-P1700272 ().

[326] Nelson Christensen. "Stochastic Gravitational Wave Backgrounds". In: *Rept. Prog. Phys.* 82.1 (2019), p. 016903. DOI: 10.1088/1361-6633/aae6b5. arXiv: 1811.08797 [gr-qc].

[327] Alexander C. Jenkins and Mairi Sakellariadou. "Primordial Black Holes from Cusp Collapse on Cosmic Strings". In: *arXiv:2006.16249 [astro-ph, physics:gr-qc, physics:hep-ph]* KCL-PH-TH/2020-30 (Aug. 2020). arXiv: 2006.16249 [astro-ph, physics:gr-qc, physics:hep-ph].

[328] B.P. Abbott et al. "Prospects for Observing and Localizing Gravitational-Wave Transients with Advanced LIGO, Advanced Virgo and KAGRA". In: *Living Rev. Rel.* 23.LIGO-P1200087, VIR-0288A-12 (2020), p. 3. DOI: 10.1007/s41114-020-00026-9. arXiv: 1304.0670 [gr-qc].

[329] B.P. Abbott et al. "All-Sky Search for Short Gravitational-Wave Bursts in the Second Advanced LIGO and Advanced Virgo Run". In: *Phys. Rev. D* 100.LIGO-P1800308 (2019), p. 024017. DOI: 10.1103/PhysRevD.100.024017. arXiv: 1905.03457 [gr-qc].

[330] Kipp C. Cannon. "A Bayesian Coincidence Test for Noise Rejection in a Gravitational-Wave Burst Search". In: *Class.Quant.Grav.* 25 (2008), p. 105024. DOI: 10.1088/0264-9381/25/10/105024.

[331] B. P. Abbott et al. "Characterization of Transient Noise in Advanced LIGO Relevant to Gravitational Wave Signal GW150914". In: *Class. Quant. Grav.* 33.13 (2016), p. 134001. DOI: 10.1088/0264-9381/33/13/134001. arXiv: 1602.03844 [gr-qc].

[332] Miriam Cabero et al. "Blip Glitches in Advanced LIGO Data". In: *Class. Quant. Grav.* 36.15 (2019), p. 15. DOI: 10.1088/1361-6382/ab2e14. arXiv: 1901.05093 [physics.ins-det].

[333] Patrick R. Brady, Jolien D.E. Creighton, and Alan G. Wiseman. "Upper Limits on Gravitational-Wave Signals Based on Loudest Events". In: *Class.Quant.Grav.* 21 (2004), S1775–S1782. DOI: 10.1088/0264-9381/21/20/020. arXiv: gr-qc/0405044.

[334] V. Mandic et al. "Parameter Estimation in Searches for the Stochastic Gravitational-Wave Background". In: *Physical Review Letters* 109.17 (Oct. 2012). ISSN: 1079-7114. DOI: 10.1103/physrevlett.109.171102.

[335] Despoina Pazouli, Anastasios Avgoustidis, and Edmund J. Copeland. "The Cusp Properties of High Harmonic Loops". In: (Aug. 2020). arXiv: 2008.13693 [hep-th].

[336] Yanou Cui et al. "Cosmic Archaeology with Gravitational Waves from Cosmic Strings". In: *Phys. Rev. D* 97.KCL-PH-TH-2017-51 (2018), p. 123505. DOI: 10.1103/PhysRevD.97.123505. arXiv: 1711.03104 [hep-ph].

[337] Yann Gouttenoire, Géraldine Servant, and Peera Simakachorn. "Beyond the Standard Models with Cosmic Strings". In: *JCAP* 07.DESY-19-204 (2020), p. 032. DOI: 10.1088/1475-7516/2020/07/032. arXiv: 1912.02569 [hep-ph].

[338] J. Urrestilla, A. Achucarro, and A. C. Davis. "D Term Inflation without Cosmic Strings". In: *Phys. Rev. Lett.* 92 (2004), p. 251302. DOI: 10.1103/PhysRevLett.92.251302. arXiv: hep-th/0402032.

[339] Yoichi Aso et al. "Interferometer Design of the KAGRA Gravitational Wave Detector". In: *Phys. Rev. D* 88.4 (Aug. 2013), p. 043007. DOI: 10.1103/PhysRevD.88.043007.

[340] Pijushpani Bhattacharjee. "Cosmic Strings and Ultrahigh-Energy Cosmic Rays". In: *Phys. Rev.* D40.PRINT-89-0793 (FERMILAB), FERMILAB-PUB-89-196-A (1989), p. 3968. DOI: 10.1103/PhysRevD.40.3968.

[341] A. A. Abdo et al. "The Spectrum of the Isotropic Diffuse Gamma-Ray Emission Derived from First-Year Fermi Large Area Telescope Data". In: *Phys. Rev. Lett.* 104.SLAC-PUB-13940 (2010), p. 101101. DOI: 10.1103/PhysRevLett.104.101101. arXiv: 1002.3603 [astro-ph.HE].

[342] Jane H. MacGibbon and Robert H. Brandenberger. "High-Energy Neutrino Flux from Ordinary Cosmic Strings". In: *Nucl. Phys.* B331.BROWN-HET-697 (1990), pp. 153–172. DOI: 10.1016/0550-3213(90)90020-E.

[343] Jane H. MacGibbon and Robert H. Brandenberger. "Gamma-Ray Signatures from Ordinary Cosmic Strings". In: *Phys. Rev.* D47.BROWN-HET-765 (1993), pp. 2283–2296. DOI: 10.1103/PhysRevD.47.2283. arXiv: astro-ph/9206003.

[344] Robert H. Brandenberger, A. T. Sornborger, and M. Trodden. "Gamma-Ray Bursts from Ordinary Cosmic Strings". In: *Phys. Rev.* D48.BROWN-HET-896 (1993), pp. 940–942. DOI: 10.1103/PhysRevD.48.940. arXiv: hep-ph/9302254.

[345] Yanou Cui and David E. Morrissey. "Non-Thermal Dark Matter from Cosmic Strings". In: *Phys. Rev.* D79.MCTP-08-09, NSF-KITP-08-17 (2009), p. 083532. DOI: 10.1103/PhysRevD.79.083532. arXiv: 0805.1060 [hep-ph].

[346] H. F. Santana Mota and Mark Hindmarsh. "Big-Bang Nucleosynthesis and Gamma-Ray Constraints on Cosmic Strings with a Large Higgs Condensate". In: *Phys. Rev.* D91.4 (2015), p. 043001. DOI: 10.1103/PhysRevD.91.043001. arXiv: 1407.3599 [hep-ph].

[347] Jean-Francois Dufaux. "Cosmic Super-Strings and Kaluza-Klein Modes". In: *JCAP* 1209 (2012), p. 022. DOI: 10.1088/1475-7516/2012/09/022. arXiv: 1201.4850 [hep-th].

[348] M. Punturo et al. "The Einstein Telescope: A Third-Generation Gravitational Wave Observatory". In: *Proceedings, 14th Workshop on Gravitational Wave Data Analysis (GWDAW-14): Rome, Italy, January 26-29, 2010*. Vol. 27. Class. Quant. Grav. 2010, p. 194002. DOI: 10.1088/0264-9381/27/19/194002.

[349] S. Hild et al. "Sensitivity Studies for Third-Generation Gravitational Wave Observatories". In: *Class. Quant. Grav.* 28 (2011), p. 094013. DOI: 10.1088/0264-9381/28/9/094013. arXiv: 1012.0908 [gr-qc].

[350] T.W.B. Kibble. "Phase Transitions in the Early Universe". In: *Acta Phys. Polon. B* 13.ICTP-81-82-19 (1982), p. 723.

[351] Nicholas T. Jones, Horace Stoica, and S.H.Henry Tye. "Brane Interaction as the Origin of Inflation". In: *JHEP* 07 (2002), p. 051. DOI: 10.1088/1126-6708/2002/07/051. arXiv: hep-th/0203163.

[352] Saswat Sarangi and S.H.Henry Tye. "Cosmic String Production towards the End of Brane Inflation". In: *Phys. Lett. B* 536.CLNS-02-1786 (2002), pp. 185–192. DOI: 10.1016/S0370-2693(02)01824-5. arXiv: hep-th/0204074.

[353] Jon Urrestilla and Alexander Vilenkin. "Evolution of Cosmic Superstring Networks: A Numerical Simulation". In: *JHEP* 02 (2008), p. 037. DOI: 10.1088/1126-6708/2008/02/037. arXiv: 0712.1146 [hep-th].

[354] B. Carter. "Covariant Mechanics of Simple and Conducting Strings and Membranes". In: *The Formation and Evolution of Cosmic Strings. Proceedings, Workshop, Cambridge, UK, July 3-7, 1989*. Ed. by G.W. Gibbons, S.W. Hawking, and T. Vachaspati. 1990, pp. 143–178.

[355] Brandon Carter and Patrick Peter. "Supersonic String Models for Witten Vortices". In: *Phys.Rev.* D52.DAMTP-R-94-56 (1995), pp. 1744–1748. DOI: 10.1103/PhysRevD.52.1744. arXiv: hep-ph/9411425.

[356] Silvano Bonazzola and Patrick Peter. "Can High-Energy Cosmic Rays Be Vortons?" In: *Astropart. Phys.* 7 (1997), pp. 161–172. DOI: 10.1016/S0927-6505(97)00015-7. arXiv: hep-ph/9701246.

[357] B. Carter. "Duality Relation between Charged Elastic Strings and Superconducting Cosmic Strings". In: *Phys. Lett.* B224 (1989), pp. 61–66. DOI: 10.1016/0370-2693(89)91051-4.

[358] B. Carter. "Basic Brane Theory". In: *Class. Quant. Grav.* 9 (1992), S19–S33. DOI: 10.1088/0264-9381/9/S/002.

[359] Arif Babul, Tsvi Piran, and David N. Spergel. "Bosonic Superconducting Cosmic Strings. 1. Classical Field Theory Solutions". In: *Phys. Lett. B* 202.IASSNS-AST-87/4 (1988), pp. 307–314. DOI: 10.1016/0370-2693(88)90476-5.

[360] P. Peter. "Superconducting Cosmic String: Equation of State for Space - like and Time - like Current in the Neutral Limit". In: *Phys. Rev.* D45 (1992), pp. 1091–1102. DOI: 10.1103/PhysRevD.45.1091.

[361] Brandon Carter and Patrick Peter. "Dynamics and Integrability Property of the Chiral String Model". In: *Phys. Lett.* B466 (1999), pp. 41–49. DOI: 10.1016/S0370-2693(99)01070-9. arXiv: hep-th/9905025.

[362] Christophe Ringeval. "Equation of State of Cosmic Strings with Fermionic Current-Carriers". In: *Phys. Rev.* D63 (2001), p. 063508. DOI: 10.1103/PhysRevD.63.063508. arXiv: hep-ph/0007015.

[363] Christophe Ringeval. "Fermionic Massive Modes along Cosmic Strings". In: *Phys. Rev.* D64 (2001), p. 123505. DOI: 10.1103/PhysRevD.64.123505. arXiv: hep-ph/0106179.

[364] P. Peter. "Equation of State of Cosmic Strings in the Presence of Charged Particles". In: *Class. Quant. Grav.* 9 (1992), S197–S206. DOI: 10.1088/0264-9381/9/S/013.

[365] P. Peter. "Influence of the Electric Coupling Strength in Current Carrying Cosmic Strings". In: *Phys. Rev. D* 46 (1992), pp. 3335–3349. DOI: 10.1103/PhysRevD.46.3335.

[366] B. Carter. "Mechanics of Cosmic Rings". In: *Phys. Lett. B* 238 (1990), pp. 166–171. DOI: 10.1016/0370-2693(90)91714-M. arXiv: hep-th/0703023.

[367] Stephen C. Davis, Anne-Christine Davis, and Mark Trodden. "N=1 Supersymmetric Cosmic Strings". In: *Phys. Lett. B* 405.DAMTP-96-107, MIT-CTP-2612 (1997), pp. 257–264. DOI: 10.1016/S0370-2693(97)00642-4. arXiv: hep-ph/9702360.

[368] B. Carter and D. A. Steer. "Symplectic Structure for Elastic and Chiral Conducting Cosmic String Models". In: *Phys. Rev.* D69 (2004), p. 125002. DOI: 10.1103/PhysRevD.69.125002. arXiv: hep-th/0307161.

[369] Mark Hindmarsh and Owe Philipsen. "WIMP Dark Matter and the QCD Equation of State". In: *Phys. Rev.* D71.MS-TP-05-1 (2005), p. 087302. DOI: 10.1103/PhysRevD.71.087302. arXiv: hep-ph/0501232.

[370] Jonathan Rocher and Mairi Sakellariadou. "Constraints on Supersymmetric Grand Unified Theories from Cosmology". In: *JCAP* 2005.3, 004 (Mar. 2005), p. 004. DOI: 10.1088/1475-7516/2005/03/004. arXiv: hep-ph/0406120.

[371] Arttu Rajantie. "Formation of Topological Defects in Gauge Field Theories". In: *Int. J. Mod. Phys. A* 17.DAMTP-2001-78 (2002), pp. 1–44. DOI: 10.1142/S0217751X02005426. arXiv: hep-ph/0108159.

[372] R.J. Rivers, F.C. Lombardo, and F.D. Mazzitelli. "The Formation of Classical Defects after a Slow Quantum Phase Transition". In: *Phys. Lett. B* 539 (2002), pp. 1–7. DOI: 10.1016/S0370-2693(02)02044-0. arXiv: hep-ph/0205337.

[373] Christophe Ringeval et al. "Large Scale CMB Anomalies from Thawing Cosmic Strings". In: *JCAP* 2016.2, 033 (Feb. 2016), p. 033. DOI: 10.1088/1475-7516/2016/02/033. arXiv: 1510.01916 [astro-ph.CO].

[374] Christophe Ringeval and Francois R. Bouchet. "All Sky CMB Map from Cosmic Strings Integrated Sachs-Wolfe Effect". In: *Phys.Rev.* D86 (2012), p. 023513. DOI: 10.1103/PhysRevD.86.023513. arXiv: 1204.5041 [astro-ph.CO].

[375] Joanes Lizarraga et al. "Constraining Topological Defects with Temperature and Polarization Anisotropies". In: *Phys.Rev.* D90.10 (2014), p. 103504. DOI: 10.1103/PhysRevD.90.103504. arXiv: 1408.4126 [astro-ph.CO].

[376] Andrei Lazanu, E. P. S. Shellard, and Martin Landriau. "CMB Power Spectrum of Nambu-Goto Cosmic Strings". In: *Phys. Rev.* D91.8 (2015), p. 083519. DOI: 10.1103/PhysRevD.91.083519. arXiv: 1410.4860 [astro-ph.CO].

[377] Yi-Fu Cai, Eray Sabancilar, and Tanmay Vachaspati. "Radio Bursts from Superconducting Strings". In: *Phys. Rev. D* 85 (2012), p. 023530. DOI: 10.1103/PhysRevD.85.023530. arXiv: 1110.1631 [astro-ph.CO].

[378] Yi-Fu Cai et al. "Radio Broadcasts from Superconducting Strings". In: *Phys. Rev. D* 86 (2012), p. 043521. DOI: 10.1103/PhysRevD.86.043521. arXiv: 1205.3170 [astro-ph.CO].

[379] Chiara Arina, Jan Hamann, and Yvonne Y.Y. Wong. "A Bayesian View of the Current Status of Dark Matter Direct Searches". In: *JCAP* 09 (2011), p. 022. DOI: 10.1088/1475-7516/2011/09/022. arXiv: 1105.5121 [hep-ph].

[380] Chiara Arina. "Bayesian Analysis of Multiple Direct Detection Experiments". In: *Phys. Dark Univ.* 5-6 (2014), pp. 1–17. DOI: 10.1016/j.dark.2014.03.003. arXiv: 1310.5718 [hep-ph].

[381] Stephen Hawking. "Gravitationally collapsed objects of very low mass". In: *Mon. Not. Roy. Astron. Soc.* 152 (1971), p. 75.

[382] Bernard J. Carr and S. W. Hawking. "Black Holes in the Early Universe". In: *Mon. Not. Roy. Astron. Soc.* 168 (1974), pp. 399–415.

[383] B. J. Carr. "The Primordial Black Hole Mass Spectrum". In: *ApJ* 201 (Oct. 1975), pp. 1–19. DOI: 10.1086/153853.

[384] George F. Chapline. "Cosmological Effects of Primordial Black Holes". In: *Nature* 253.5489 (1975), pp. 251–252. DOI: 10.1038/253251a0.

[385] P. Meszaros. "Primeval Black Holes and Galaxy Formation". In: *Astron. Astrophys.* 38 (1975), pp. 5–13.

[386] N. Afshordi, P. McDonald, and D.N. Spergel. "Primordial Black Holes as Dark Matter: The Power Spectrum and Evaporation of Early Structures". In: *Astrophys. J. Lett.* 594 (2003), pp. L71–L74. DOI: 10.1086/378763. arXiv: astro-ph/0302035.

[387] Bernard J. Carr and M.J. Rees. "How Large Were the First Pregalactic Objects?" In: (Jan. 1984).

[388] Rachel Bean and Joao Magueijo. "Could Supermassive Black Holes Be Quintessential Primordial Black Holes?" In: *Phys. Rev. D* 66 (2002), p. 063505. DOI: 10.1103/PhysRevD.66.063505. arXiv: astro-ph/0204486.

[389] B.P. Abbott et al. "GWTC-1: A Gravitational-Wave Transient Catalog of Compact Binary Mergers Observed by LIGO and Virgo during the First and Second Observing Runs". In: *Phys. Rev. X* 9.LIGO-P1800307 (2019), p. 031040. DOI: 10.1103/PhysRevX.9.031040. arXiv: 1811.12907 [astro-ph.HE].

[390] Misao Sasaki et al. "Primordial Black Hole Scenario for the Gravitational-Wave Event GW150914". In: *Phys. Rev. Lett.* 117.RESCEU-17-16, RUP-16-7, YITP-16-43 (2016), p. 061101. DOI: 10.1103/PhysRevLett.121.059901, 10.1103/PhysRevLett.117.061101. arXiv: 1603.08338 [astro-ph.CO].

[391] R. Abbott et al. "Properties and Astrophysical Implications of the 150 Msun Binary Black Hole Merger GW190521". In: *Astrophys. J. Lett.* 900.LIGO-P2000021 (2020), p. L13. DOI: 10.3847/2041-8213/aba493. arXiv: 2009.01190 [astro-ph.HE].

[392] Misao Sasaki et al. "Primordial black holes—perspectives in gravitational wave astronomy". In: *Class. Quant. Grav.* 35.6 (2018), p. 063001. DOI: 10.1088/1361-6382/aaa7b4. arXiv: 1801.05235 [astro-ph.CO].

[393] Bernard Carr et al. "Constraints on Primordial Black Holes". In: RESCEU-03/20; KEK-Cosmo-249; KEK-TH-2199; IPMU20-0024 (Feb. 2020). arXiv: 2002.12778 [astro-ph.CO].

[394] Bernard Carr and Florian Kuhnel. "Primordial Black Holes as Dark Matter: Recent Developments". In: *Ann. Rev. Nucl. Part. Sci.* 70 (2020), pp. 355–394. DOI: 10.1146/annurev-nucl-050520-125911. arXiv: 2006.02838 [astro-ph.CO].

[395] Anne M. Green and Bradley J. Kavanagh. "Primordial Black Holes as a dark matter candidate". In: *J. Phys. G* 48.4 (2021), p. 4. DOI: 10.1088/1361-6471/abc534. arXiv: 2007.10722 [astro-ph.CO].

[396] S. W. Hawking. "Particle Creation by Black Holes". In: *Commun. Math. Phys.* 43 (1975). Ed. by G. W. Gibbons and S. W. Hawking. [Erratum: Commun.Math.Phys. 46, 206 (1976)], pp. 199–220. DOI: 10.1007/BF02345020.

[397] James M. Bardeen, B. Carter, and S. W. Hawking. "The Four laws of black hole mechanics". In: *Commun. Math. Phys.* 31 (1973), pp. 161–170. DOI: 10.1007/BF01645742.

[398] Don N. Page. "Particle Emission Rates from a Black Hole: Massless Particles from an Uncharged, Nonrotating Hole". In: *Phys. Rev. D* 13 (1976), pp. 198–206. DOI: 10.1103/PhysRevD.13.198.

[399] Jane H. MacGibbon. "Quark and gluon jet emission from primordial black holes. 2. The Lifetime emission". In: *Phys. Rev. D* 44 (1991), pp. 376–392. DOI: 10.1103/PhysRevD.44.376.

[400] Jane H. MacGibbon, Bernard J. Carr, and Don N. Page. "Do Evaporating Black Holes Form Photospheres?" In: *Phys. Rev. D* 78 (2008), p. 064043. DOI: 10.1103/PhysRevD.78.064043. arXiv: 0709.2380 [astro-ph].

[401] B. V. Vainer and P. D. Naselskii. "Cosmological implications of the process of primordial black hole evaporation". In: *Soviet Astronomy* 55 (Apr. 1978), p. 231.

[402] Ia. B. Zeldovich et al. "Primordial black holes and the deuterium problem". In: *Soviet Astronomy Letters* 3 (June 1977), pp. 110–112.

[403] D. Lindley. "Primordial black holes and the cosmic baryon number". In: *Mon. Not. R. Astron. Soc.* 196 (July 1981), pp. 317–338. DOI: 10.1093/mnras/196.2.317.

[404] Don N. Page and S. W. Hawking. "Gamma rays from primordial black holes". In: *Astrophys. J.* 206 (1976), pp. 1–7. DOI: 10.1086/154350.

[405] Jane H. MacGibbon and Bernard J. Carr. "Cosmic rays from primordial black holes". In: *Astrophys. J.* 371 (1991), pp. 447–469. DOI: 10.1086/169909.

[406] P. N. Okele and M. J. Rees. "Observational consequences of positron production by evaporating black holes". In: *Astron. Astrophys.* 81 (1980), pp. 263–264.

[407] William DeRocco and Peter W. Graham. "Constraining Primordial Black Hole Abundance with the Galactic 511 keV Line". In: *Phys. Rev. Lett.* 123.25 (2019), p. 251102. DOI: 10.1103/PhysRevLett.123.251102. arXiv: 1906.07740 [astro-ph.CO].

[408] Mathieu Boudaud and Marco Cirelli. "Voyager 1 $e^{\pm}$ Further Constrain Primordial Black Holes as Dark Matter". In: *Phys. Rev. Lett.* 122.4 (2019), p. 041104. DOI: 10.1103/PhysRevLett.122.041104. arXiv: 1807.03075 [astro-ph.HE].

[409] Edward L. Wright. "On the density of pbh's in the galactic halo". In: *Astrophys. J.* 459 (1996), p. 487. DOI: 10.1086/176910. arXiv: astro-ph/9509074.

[410] R. Lehoucq et al. "New constraints on the primordial black hole number density from Galactic gamma-ray astronomy". In: *Astron. Astrophys.* 502 (2009), p. 37. DOI: 10.1051/0004-6361/200911961. arXiv: 0906.1648 [astro-ph.HE].

[411] B. J. Carr et al. "Constraints on primordial black holes from the Galactic gamma-ray background". In: *Phys. Rev. D* 94.4 (2016), p. 044029. DOI: 10.1103/PhysRevD.94.044029. arXiv: 1604.05349 [astro-ph.CO].

[412] Bohdan Paczynski. "Gravitational microlensing by the galactic halo". In: *Astrophys. J.* 304 (1986), pp. 1–5. DOI: 10.1086/164140.

[413] Hiroko Niikura et al. "Microlensing constraints on primordial black holes with Subaru/HSC Andromeda observations". In: *Nature Astron.* 3.6 (2019), pp. 524–534. DOI: 10.1038/s41550-019-0723-1. arXiv: 1701.02151 [astro-ph.CO].

[414] R. Benton Metcalf and Joseph Silk. "New Constraints on Macroscopic Compact Objects as a Dark Matter Candidate from Gravitational Lensing of Type Ia Supernovae". In: *Phys. Rev. Lett.* 98 (2007), p. 071302. DOI: 10.1103/PhysRevLett.98.071302. arXiv: astro-ph/0612253.

[415] Andrew Gould. "Femtolensing of Gamma-Ray Bursters". In: ApJ 386 (Feb. 1992), p. L5. DOI: 10.1086/186279.

[416] Andrey Katz et al. "Femtolensing by Dark Matter Revisited". In: *JCAP* 12 (2018), p. 005. DOI: 10.1088/1475-7516/2018/12/005. arXiv: 1807.11495 [astro-ph.CO].

[417] Peter W. Graham, Surjeet Rajendran, and Jaime Varela. "Dark Matter Triggers of Supernovae". In: *Phys. Rev. D* 92.6 (2015), p. 063007. DOI: 10.1103/PhysRevD.92.063007. arXiv: 1505.04444 [hep-ph].

[418] Fabio Capela, Maxim Pshirkov, and Peter Tinyakov. "Constraints on primordial black holes as dark matter candidates from capture by neutron stars". In: *Phys. Rev. D* 87.12 (2013), p. 123524. DOI: 10.1103/PhysRevD.87.123524. arXiv: 1301.4984 [astro-ph.CO].

[419] Jaiyul Yoo, Julio Chaname, and Andrew Gould. "The end of the MACHO era: limits on halo dark matter from stellar halo wide binaries". In: *Astrophys. J.* 601 (2004), pp. 311–318. DOI: 10.1086/380562. arXiv: astro-ph/0307437.

[420] C. G. Lacey and J. P. Ostriker. "Massive black holes in galactic halos ?" In: ApJ 299 (Dec. 1985), pp. 633–652. DOI: 10.1086/163729.

[421] B. J. Carr. "On the cosmological density of black holes." In: *Comments on Astrophysics* 7.5 (Jan. 1978), pp. 161–173.

[422] B. J. Carr. "Pregalactic black hole accretion and the thermal history of the universe". In: MNRAS 194 (Feb. 1981), pp. 639–668. DOI: 10.1093/mnras/194.3.639.

[423] Massimo Ricotti, Jeremiah P. Ostriker, and Katherine J. Mack. "Effect of Primordial Black Holes on the Cosmic Microwave Background and Cosmological Parameter Estimates". In: *Astrophys. J.* 680 (2008), p. 829. DOI: 10.1086/587831. arXiv: 0709.0524 [astro-ph].

[424] Daniele Gaggero et al. "Searching for Primordial Black Holes in the radio and X-ray sky". In: *Phys. Rev. Lett.* 118.24 (2017), p. 241101. DOI: 10.1103/PhysRevLett.118.241101. arXiv: 1612.00457 [astro-ph.HE].

[425] B. J. Carr. "Cosmological gravitational waves - Their origin and consequences". In: A&A 89.1-2 (Sept. 1980), pp. 6–21.

[426] Ryo Saito and Jun'ichi Yokoyama. "Gravitational wave background as a probe of the primordial black hole abundance". In: *Phys. Rev. Lett.* 102 (2009). [Erratum: Phys.Rev.Lett. 107, 069901 (2011)], p. 161101. DOI: 10.1103/PhysRevLett.102.161101. arXiv: 0812.4339 [astro-ph].

[427] Karsten Jedamzik, Martin Lemoine, and Jerome Martin. "Collapse of Small-Scale Density Perturbations during Preheating in Single Field Inflation". In: *JCAP* 1009 (2010), p. 034. DOI: 10.1088/1475-7516/2010/09/034. arXiv: 1002.3039 [astro-ph.CO].

[428] Richard Easther, Raphael Flauger, and James B. Gilmore. "Delayed Reheating and the Breakdown of Coherent Oscillations". In: *JCAP* 1104 (2011), p. 027. DOI: 10.1088/1475-7516/2011/04/027. arXiv: 1003.3011 [astro-ph.CO].

[429] J. Kevorkian and J. D. Cole. *Multiple Scale and Singular Perturbation Methods*. Springer New York, 1996. DOI: 10.1007/978-1-4612-3968-0. URL: https://doi.org/10.1007%2F978-1-4612-3968-0.

[430] Jérôme Martin, Theodoros Papanikolaou, and Vincent Vennin. "Primordial Black Holes from the Preheating Instability in Single-Field Inflation". In: *JCAP* 01 (2020), p. 024. DOI: 10.1088/1475-7516/2020/01/024. arXiv: 1907.04236 [astro-ph.CO].

[431] Anne M. Green and Karim A. Malik. "Primordial Black Hole Production Due to Preheating". In: *Phys. Rev. D* 64 (2001), p. 021301. DOI: 10.1103/PhysRevD.64.021301. arXiv: hep-ph/0008113.

[432] Theodoros Papanikolaou, Vincent Vennin, and David Langlois. "Gravitational Waves from a Universe Filled with Primordial Black Holes". In: (Oct. 2020). arXiv: 2010.11573 [astro-ph.CO].

[433] Karsten Jedamzik, Martin Lemoine, and Jerome Martin. "Generation of Gravitational Waves during Early Structure Formation between Cosmic Inflation and Reheating". In: *JCAP* 04 (2010), p. 021. DOI: 10.1088/1475-7516/2010/04/021. arXiv: 1002.3278 [astro-ph.CO].

[434] Jérôme Martin et al. "Metric Preheating and Radiative Decay in Single-Field Inflation". In: *JCAP* 05 (2020), p. 003. DOI: 10.1088/1475-7516/2020/05/003. arXiv: 2002.01820 [astro-ph.CO].

[435] Viatcheslav F. Mukhanov and G. V. Chibisov. "Quantum Fluctuations and a Nonsingular Universe". In: *JETP Lett.* 33 (1981), pp. 532–535.

[436] Hideo Kodama and Misao Sasaki. "Cosmological Perturbation Theory". In: *Prog. Theor. Phys. Suppl.* 78 (1984), pp. 1–166. DOI: 10.1143/PTPS.78.1.

[437] Viatcheslav F. Mukhanov, H. A. Feldman, and Robert H. Brandenberger. "Theory of Cosmological Perturbations. Part 1. Classical Perturbations. Part 2. Quantum Theory of Perturbations. Part 3. Extensions". In: *Phys. Rept.* 215.BROWN-HET-796, BROWN-HET-800, BROWN-HET-780 (1992), pp. 203–333. DOI: 10.1016/0370-1573(92)90044-Z.

[438] F. Finelli and Robert H. Brandenberger. "Parametric Amplification of Gravitational Fluctuations during Reheating". In: *Phys. Rev. Lett.* 82.BROWN-HET-1142 (1999), pp. 1362–1365. DOI: 10.1103/PhysRevLett.82.1362. arXiv: hep-ph/9809490.

[439] Sergio M.C.V. Goncalves. "Black Hole Formation from Massive Scalar Field Collapse in the Einstein-de Sitter Universe". In: *Phys. Rev. D* 62 (2000), p. 124006. DOI: 10.1103/PhysRevD.62.124006. arXiv: gr-qc/0008039.

[440] Andreas Albrecht et al. "Reheating an Inflationary Universe". In: *Phys. Rev. Lett.* 48.UPR-0189T, EFI-82-09-CHICAGO (1982), p. 1437. DOI: 10.1103/PhysRevLett.48.1437.

[441] L.F. Abbott, Edward Farhi, and Mark B. Wise. "Particle Production in the New Inflationary Cosmology". In: *Phys. Lett. B* 117.MIT-CTP-983 (1982), p. 29. DOI: 10.1016/0370-2693(82)90867-X.

[442] Lev Kofman, Andrei D. Linde, and Alexei A. Starobinsky. "Towards the Theory of Reheating after Inflation". In: *Phys. Rev. D* 56.IFA-97-28, SU-ITP-97-18 (1997), pp. 3258–3295. DOI: 10.1103/PhysRevD.56.3258. arXiv: hep-ph/9704452.

[443] W.˜H. Press and P Schechter. "Formation of Galaxies and Clusters of Galaxies by Self-Similar Gravitational Condensation". In: *apj* 187 (1974), pp. 425–438. DOI: 10.1086/152650.

[444] J.A. Peacock and A.F. Heavens. "Alternatives to the Press-Schechter Cosmological Mass Function". In: *Mon. Not. Roy. Astron. Soc.* 243 (1990), pp. 133–143.

[445] Richard G. Bower. "The Evolution of Groups of Galaxies in the Press-Schechter Formalism". In: *Mon. Not. Roy. Astron. Soc.* 248 (1991), p. 332.

[446] J.R. Bond et al. "Excursion Set Mass Functions for Hierarchical Gaussian Fluctuations". In: *Astrophys. J.* 379.CFPA-TH-90-015 (1991), p. 440. DOI: 10.1086/170520.

[447] Marcello Musso and Ravi K. Sheth. "The Importance of Stepping up in the Excursion Set Approach". In: *Mon. Not. Roy. Astron. Soc.* 438.3 (2014), pp. 2683–2693. DOI: 10.1093/mnras/stt2387. arXiv: 1306.0551 [astro-ph.CO].

[448] Farnik Nikakhtar et al. "The Excursion Set Approach: Stratonovich Approximation and Cholesky Decomposition". In: *Mon. Not. Roy. Astron. Soc.* 478.4 (2018), pp. 5296–5300. DOI: 10.1093/mnras/sty1415. arXiv: 1802.04207 [astro-ph.CO].

[449] Cedric G. Lacey and Shaun Cole. "Merger Rates in Hierarchical Models of Galaxy Formation". In: *Mon. Not. Roy. Astron. Soc.* 262 (1993), pp. 627–649.

[450] Jun Zhang and Lam Hui. "On Random Walks with a General Moving Barrier". In: *Astrophys. J.* 641 (2006), pp. 641–646. DOI: 10.1086/499802. arXiv: astro-ph/0508384.

[451] A. Buonocore et al. "On the Two-Boundary First-Crossing-Time Problem for Diffusion Processes". In: *Journal of Applied Probability* 27.1 (1990), 102?114. DOI: 10.2307/3214598.

[452] S. P. Bhavsar and J. D. Barrow. "First Ranked Galaxies in Groups and Clusters". In: *Mon. Not. Roy. Astron. Soc.* 213 (Apr. 1985), pp. 857–869. DOI: 10.1093/mnras/213.4.857.

[453] Azadeh Moradinezhad Dizgah, Gabriele Franciolini, and Antonio Riotto. "Primordial Black Holes from Broad Spectra: Abundance and Clustering". In: *JCAP* 11.11 (2019), p. 001. DOI: 10.1088/1475-7516/2019/11/001. arXiv: 1906.08978 [astro-ph.CO].

[454] James M. Bardeen et al. "The Statistics of Peaks of Gaussian Random Fields". In: *Astrophys. J.* 304.FERMILAB-PUB-85-148-A, NSF-ITP-85-93 (1986), pp. 15–61. DOI: 10.1086/164143.

[455] Aseem Paranjape and Ravi K. Sheth. "Peaks Theory and the Excursion Set Approach". In: *Mon. Not. Roy. Astron. Soc.* 426 (2012), pp. 2789–2796. DOI: 10.1111/j.1365-2966.2012.21911.x. arXiv: 1206.3506 [astro-ph.CO].

[456] Andrew D. Gow et al. "The Power Spectrum on Small Scales: Robust Constraints and Comparing PBH Methodologies". In: (Aug. 2020). arXiv: 2008.03289 [astro-ph.CO].

[457] Karsten Jedamzik. "The Cloud in Cloud Problem in the Press-Schechter Formalism of Hierarchical Structure Formation". In: *Astrophys. J.* 448 (1995), pp. 1–17. DOI: 10.1086/175936. arXiv: astro-ph/9408080.

[458] T. Yano, M. Nagashima, and N. Gouda. "Limitation of the Press-Schechter Formalism". In: *Astrophys. J.* 466.OU-TAP-20 (1996), p. 1. DOI: 10.1086/177488. arXiv: astro-ph/9504073.

[459] Masahiro Nagashima. "A Solution to the Missing Link in the Press-Schechter Formalism". In: *Astrophys. J.* 562.NAOJ-TH-AP-2001-44 (2001), p. 7. DOI: 10.1086/323490. arXiv: astro-ph/0108480.

[460] Matthew W. Choptuik. "Universality and Scaling in Gravitational Collapse of a Massless Scalar Field". In: *Phys. Rev. Lett.* 70.FPRINT-92-33 (1993), pp. 9–12. DOI: 10.1103/PhysRevLett.70.9.

[461] Charles R. Evans and Jason S. Coleman. "Observation of Critical Phenomena and Selfsimilarity in the Gravitational Collapse of Radiation Fluid". In: *Phys. Rev. Lett.* 72.TAR-039-UNC (1994), pp. 1782–1785. DOI: 10.1103/PhysRevLett.72.1782. arXiv: gr-qc/9402041.

[462] Tatsuhiko Koike, Takashi Hara, and Satoshi Adachi. "Critical Behavior in Gravitational Collapse of Radiation Fluid: A Renormalization Group (Linear Perturbation) Analysis". In: *Phys. Rev. Lett.* 74.TIT-HEP-284, COSMO-53, TIT-HEP-284-COSMO-53 (1995), pp. 5170–5173. DOI: 10.1103/PhysRevLett.74.5170. arXiv: gr-qc/9503007.

[463] Carsten Gundlach. "Critical Phenomena in Gravitational Collapse". In: *Living Rev. Rel.* 2 (1999), p. 4. arXiv: gr-qc/0001046.

[464] Carsten Gundlach. "Critical Phenomena in Gravitational Collapse". In: *Phys. Rept.* 376 (2003), pp. 339–405. DOI: 10.1016/S0370-1573(02)00560-4. arXiv: gr-qc/0210101.

[465] Jens C. Niemeyer and K. Jedamzik. "Near-Critical Gravitational Collapse and the Initial Mass Function of Primordial Black Holes". In: *Phys. Rev. Lett.* 80 (1998), pp. 5481–5484. DOI: 10.1103/PhysRevLett.80.5481. arXiv: astro-ph/9709072.

[466] Ilia Musco, John C. Miller, and Alexander G. Polnarev. "Primordial Black Hole Formation in the Radiative Era: Investigation of the Critical Nature of the Collapse". In: *Class. Quant. Grav.* 26 (2009), p. 235001. DOI: 10.1088/0264-9381/26/23/235001. arXiv: 0811.1452 [gr-qc].

[467] Ilia Musco and John C. Miller. "Primordial Black Hole Formation in the Early Universe: Critical Behaviour and Self-Similarity". In: *Class. Quant. Grav.* 30 (2013), p. 145009. DOI: 10.1088/0264-9381/30/14/145009. arXiv: 1201.2379 [gr-qc].

[468] Christian T. Byrnes et al. "Primordial Black Holes with an Accurate QCD Equation of State". In: *JCAP* 08 (2018), p. 041. DOI: 10.1088/1475-7516/2018/08/041. arXiv: 1801.06138 [astro-ph.CO].

[469] Ilia Musco. "Threshold for Primordial Black Holes: Dependence on the Shape of the Cosmological Perturbations". In: *Phys. Rev. D* 100.12 (2019), p. 123524. DOI: 10.1103/PhysRevD.100.123524. arXiv: 1809.02127 [gr-qc].

[470] Sam Young. "The Primordial Black Hole Formation Criterion Re-Examined: Parameterisation, Timing, and the Choice of Window Function". In: *Int. J. Mod. Phys. D* 29.02 (2019), p. 2030002. DOI: 10.1142/S0218271820300025. arXiv: 1905.01230 [astro-ph.CO].

[471] Sam Young and Marcello Musso. "Application of Peaks Theory to the Abundance of Primordial Black Holes". In: *arXiv:2001.06469 [astro-ph, physics:gr-qc, physics:hep-th]* (Jan. 2020). arXiv: 2001.06469 [astro-ph, physics:gr-qc, physics:hep-th].

[472] Teruaki Suyama and Shuichiro Yokoyama. "A Novel Formulation of the PBH Mass Function". In: *PTEP* 2020.2 (2020), 023E03. DOI: 10.1093/ptep/ptaa011. arXiv: 1912.04687 [astro-ph.CO].

[473] Cristiano Germani and Ravi K. Sheth. "Nonlinear Statistics of Primordial Black Holes from Gaussian Curvature Perturbations". In: *Phys. Rev. D* 101.ICCUB-19-021 (2020), p. 063520. DOI: 10.1103/PhysRevD.101.063520. arXiv: 1912.07072 [astro-ph.CO].

[474] Karim A. Malik and David Wands. "Cosmological Perturbations". In: *Phys. Rept.* 475 (2009), pp. 1–51. DOI: 10.1016/j.physrep.2009.03.001. arXiv: 0809.4944 [astro-ph].

[475] David Wands et al. "A New Approach to the Evolution of Cosmological Perturbations on Large Scales". In: *Phys. Rev.* D62 (2000), p. 043527. DOI: 10.1103/PhysRevD.62.043527. arXiv: astro-ph/0003278.

[476] Sam Young, Christian T. Byrnes, and Misao Sasaki. "Calculating the Mass Fraction of Primordial Black Holes". In: *JCAP* 1407 (2014), p. 045. DOI: 10.1088/1475-7516/2014/07/045. arXiv: 1405.7023 [gr-qc].

[477] Tomohiro Harada et al. "Cosmological Long-Wavelength Solutions and Primordial Black Hole Formation". In: *Phys. Rev. D* 91.RUP-15-5, RESCEU-4-15 (2015), p. 084057. DOI: 10.1103/PhysRevD.91.084057. arXiv: 1503.03934 [gr-qc].

[478] Tomohiro Harada, Chul-Moon Yoo, and Kazunori Kohri. "Threshold of Primordial Black Hole Formation". In: *Phys. Rev. D* 88.RUP-13-9, KEK-COSMO-129, KEK-TH-1668 (2013), p. 084051. DOI: 10.1103/PhysRevD.88.084051. arXiv: 1309.4201 [astro-ph.CO].

[479] Viatcheslav F. Mukhanov. "Gravitational Instability of the Universe Filled with a Scalar Field". In: *JETP Lett.* 41 (1985), pp. 493–496.

[480] Viatcheslav F. Mukhanov. "Quantum Theory of Gauge Invariant Cosmological Perturbations". In: *Sov.Phys.JETP* 67 (1988), pp. 1297–1302.

[481] Jerome Martin, Christophe Ringeval, and Vincent Vennin. "Encyclopædia Inflationaris". In: *Phys. Dark Univ.* 5-6 (2014), pp. 75–235. DOI: 10.1016/j.dark.2014.01.003. arXiv: 1303.3787 [astro-ph.CO].

[482] David Polarski and Alexei A. Starobinsky. "Semiclassicality and Decoherence of Cosmological Perturbations". In: *Class. Quant. Grav.* 13.LMPM-95-4 (1996), pp. 377–392. DOI: 10.1088/0264-9381/13/3/006. arXiv: gr-qc/9504030.

[483] J. Lesgourgues, David Polarski, and Alexei A. Starobinsky. "Quantum to Classical Transition of Cosmological Perturbations for Nonvacuum Initial States". In: *Nucl. Phys.* B497.LMPT-10-96 (1997), pp. 479–510. DOI: 10.1016/S0550-3213(97)00224-1. arXiv: gr-qc/9611019.

[484] Claus Kiefer and David Polarski. "Why Do Cosmological Perturbations Look Classical to Us?" In: *Adv. Sci. Lett.* 2 (2009), pp. 164–173. DOI: 10.1166/asl.2009.1023. arXiv: 0810.0087 [astro-ph].

[485] Jerome Martin and Vincent Vennin. "Quantum Discord of Cosmic Inflation: Can We Show That CMB Anisotropies Are of Quantum-Mechanical Origin?" In: *Phys. Rev.* D93.2 (2016), p. 023505. DOI: 10.1103/PhysRevD.93.023505. arXiv: 1510.04038 [astro-ph.CO].

[486] Tomohiro Harada et al. "Primordial Black Hole Formation in the Matter-Dominated Phase of the Universe". In: *Astrophys. J.* 833.RUP-16-25, OCU-PHYS-454, AP-GR-134, KEK-TH-1929, KEK-COSMO-197 (2016), p. 61. DOI: 10.3847/1538-4357/833/1/61. arXiv: 1609.01588 [astro-ph.CO].

[487] Edward Witten. "Cosmic Separation of Phases". In: *Phys. Rev. D* 30 (1984), pp. 272–285. DOI: 10.1103/PhysRevD.30.272.

[488] C.J. Hogan. "Gravitational radiation from cosmological phase transitions". In: *MNRAS* 218 (1986), pp. 629–636. DOI: https://doi.org/10.1093/mnras/218.4.629.

[489] Michael S. Turner and Frank Wilczek. "Relic gravitational waves and extended inflation". In: *Phys. Rev. Lett.* 65 (1990), pp. 3080–3083. DOI: 10.1103/PhysRevLett.65.3080.

[490] Arthur Kosowsky, Michael S. Turner, and Richard Watkins. "Gravitational radiation from colliding vacuum bubbles". In: *Phys. Rev. D* 45 (1992), pp. 4514–4535. DOI: 10.1103/PhysRevD.45.4514.

[491] Arthur Kosowsky and Michael S. Turner. "Gravitational radiation from colliding vacuum bubbles: envelope approximation to many bubble collisions". In: *Phys. Rev. D* 47 (1993), pp. 4372–4391. DOI: 10.1103/PhysRevD.47.4372. arXiv: astro-ph/9211004.

[492] K. Kajantie et al. "Is there a hot electroweak phase transition at m(H) larger or equal to m(W)?" In: *Phys. Rev. Lett.* 77 (1996), pp. 2887–2890. DOI: 10.1103/PhysRevLett.77.2887. arXiv: hep-ph/9605288.

[493] Chiara Caprini et al. "Detecting gravitational waves from cosmological phase transitions with LISA: an update". In: *JCAP* 03 (2020), p. 024. DOI: 10.1088/1475-7516/2020/03/024. arXiv: 1910.13125 [astro-ph.CO].

[494] Daniel Cutting et al. "Gravitational waves from vacuum first order phase transitions II: from thin to thick walls". In: *Phys. Rev. D* 103.2 (2021), p. 023531. DOI: 10.1103/PhysRevD.103.023531. arXiv: 2005.13537 [astro-ph.CO].

[495] Thomas Konstandin. "Gravitational radiation from a bulk flow model". In: *JCAP* 03 (2018), p. 047. DOI: 10.1088/1475-7516/2018/03/047. arXiv: 1712.06869 [astro-ph.CO].

[496] Ryusuke Jinno and Masahiro Takimoto. "Gravitational waves from bubble collisions: An analytic derivation". In: *Phys. Rev. D* 95.2 (2017), p. 024009. DOI: 10.1103/PhysRevD.95.024009. arXiv: 1605.01403 [astro-ph.CO].

[497] Ryusuke Jinno and Masahiro Takimoto. "Gravitational waves from bubble dynamics: Beyond the Envelope". In: *JCAP* 01 (2019), p. 060. DOI: 10.1088/1475-7516/2019/01/060. arXiv: 1707.03111 [hep-ph].

[498] Mark Hindmarsh et al. "Shape of the acoustic gravitational wave power spectrum from a first order phase transition". In: *Phys. Rev.* D96.10 (2017), p. 103520. DOI: 10.1103/PhysRevD.96.103520. arXiv: 1704.05871 [astro-ph.CO].

[499] Ryusuke Jinno, Thomas Konstandin, and Henrique Rubira. "A hybrid simulation of gravitational wave production in first-order phase transitions". In: *JCAP* 04 (2021), p. 014. DOI: 10.1088/1475-7516/2021/04/014. arXiv: 2010.00971 [astro-ph.CO].

[500] John Ellis, Marek Lewicki, and José Miguel No. "Gravitational waves from first-order cosmological phase transitions: lifetime of the sound wave source". In: *JCAP* 07 (2020), p. 050. DOI: 10.1088/1475-7516/2020/07/050. arXiv: 2003.07360 [hep-ph].

[501] John Ellis et al. "Gravitational wave energy budget in strongly supercooled phase transitions". In: *JCAP* 06 (2019), p. 024. DOI: 10.1088/1475-7516/2019/06/024. arXiv: 1903.09642 [hep-ph].

[502] Ue-Li Pen and Neil Turok. "Shocks in the Early Universe". In: *Phys. Rev. Lett.* 117.13 (2016), p. 131301. DOI: 10.1103/PhysRevLett.117.131301. arXiv: 1510.02985 [astro-ph.CO].

[503] Daniel Cutting, Mark Hindmarsh, and David J. Weir. "Vorticity, kinetic energy, and suppressed gravitational wave production in strong first order phase transitions". In: (June 2019). arXiv: 1906.00480 [hep-ph].

[504] Chiara Caprini and Ruth Durrer. "Gravitational waves from stochastic relativistic sources: Primordial turbulence and magnetic fields". In: *Phys. Rev. D* 74 (2006), p. 063521. DOI: 10.1103/PhysRevD.74.063521. arXiv: astro-ph/0603476.

[505] Grigol Gogoberidze, Tina Kahniashvili, and Arthur Kosowsky. "The Spectrum of Gravitational Radiation from Primordial Turbulence". In: *Phys. Rev. D* 76 (2007), p. 083002. DOI: 10.1103/PhysRevD.76.083002. arXiv: 0705.1733 [astro-ph].

[506] Tina Kahniashvili et al. "Gravitational Radiation from Primordial Helical Inverse Cascade MHD Turbulence". In: *Phys. Rev. D* 78 (2008). [Erratum: Phys.Rev.D 79, 109901 (2009)], p. 123006. DOI: 10.1103/PhysRevD.78.123006. arXiv: 0809.1899 [astro-ph].

[507] Tina Kahniashvili, Grigol Gogoberidze, and Bharat Ratra. "Gravitational Radiation from Primordial Helical MHD Turbulence". In: *Phys. Rev. Lett.* 100 (2008), p. 231301. DOI: 10.1103/PhysRevLett.100.231301. arXiv: 0802.3524 [astro-ph].

[508] Chiara Caprini, Ruth Durrer, and Geraldine Servant. "The stochastic gravitational wave background from turbulence and magnetic fields generated by a first-order phase transition". In: *JCAP* 12 (2009), p. 024. DOI: 10.1088/1475-7516/2009/12/024. arXiv: 0909.0622 [astro-ph.CO].

[509] Chiara Caprini, Ruth Durrer, and Elisa Fenu. "Can the observed large scale magnetic fields be seeded by helical primordial fields?" In: *JCAP* 11 (2009), p. 001. DOI: 10.1088/1475-7516/2009/11/001. arXiv: 0906.4976 [astro-ph.CO].

[510] Peter Niksa, Martin Schlederer, and Günter Sigl. "Gravitational Waves produced by Compressible MHD Turbulence from Cosmological Phase Transitions". In: *Class. Quant. Grav.* 35.14 (2018), p. 144001. DOI: 10.1088/1361-6382/aac89c. arXiv: 1803.02271 [astro-ph.CO].

[511] Robert H. Kraichnan. "Kolmogorov's Hypotheses and Eulerian Turbulence Theory". In: *The Physics of Fluids* 7.11 (1964), pp. 1723–1734. DOI: 10.1063/1.2746572. eprint: https://aip.scitation.org/doi/pdf/10.1063/1.2746572. URL: https://aip.scitation.org/doi/abs/10.1063/1.2746572.

[512] Alberto Roper Pol et al. "The timestep constraint in solving the gravitational wave equations sourced by hydromagnetic turbulence". In: *Geophys. Astrophys. Fluid Dynamics* 114.1-2 (2020), pp. 130–161. DOI: 10.1080/03091929.2019.1653460. arXiv: 1807.05479 [physics.flu-dyn].

[513] Alberto Roper Pol et al. "Numerical simulations of gravitational waves from early-universe turbulence". In: *Phys. Rev. D* 102.8 (2020), p. 083512. DOI: 10.1103/PhysRevD.102.083512. arXiv: 1903.08585 [astro-ph.CO].

[514] Tina Kahniashvili et al. "Circular polarization of gravitational waves from early-Universe helical turbulence". In: *Phys. Rev. Res.* 3.1 (2021), p. 013193. DOI: 10.1103/PhysRevResearch.3.013193. arXiv: 2011.05556 [astro-ph.CO].

[515] Axel Brandenburg et al. "The scalar, vector, and tensor modes in gravitational wave turbulence simulations". In: (Mar. 2021). arXiv: 2103.01140 [gr-qc].

[516] Chiara Caprini et al. "General Properties of the Gravitational Wave Spectrum from Phase Transitions". In: *Phys. Rev. D* 79 (2009), p. 083519. DOI: 10.1103/PhysRevD.79.083519. arXiv: 0901.1661 [astro-ph.CO].

[517] Axel Brandenburg et al. "Evolution of hydromagnetic turbulence from the electroweak phase transition". In: *Phys. Rev. D* 96.12 (2017), p. 123528. DOI: 10.1103/PhysRevD.96.123528. arXiv: 1711.03804 [astro-ph.CO].

[518] Guo-Wei He, Meng Wang, and Sanjiva K. Lele. "On the computation of space-time correlations by large-eddy simulation". In: *Physics of Fluids* 16.11 (2004), pp. 3859–3867. DOI: 10.1063/1.1779251. eprint: https://doi.org/10.1063/1.1779251. URL: https://doi.org/10.1063/1.1779251.

[519] P. Olesen. "On inverse cascades in astrophysics". In: *Phys. Lett. B* 398 (1997), pp. 321–325. DOI: 10.1016/S0370-2693(97)00235-9. arXiv: astro-ph/9610154.

[520] Axel Brandenburg and Tina Kahniashvili. "Classes of hydrodynamic and magnetohydrodynamic turbulent decay". In: *Phys. Rev. Lett.* 118.5 (2017), p. 055102. DOI: 10.1103/PhysRevLett.118.055102. arXiv: 1607.01360 [physics.flu-dyn].

[521] Marc G. Genton. "Classes of Kernels for Machine Learning: A Statistics Perspective". In: *J. Mach. Learn. Res.* 2 (Mar. 2002), pp. 299–312. ISSN: 1532-4435.

[522] K. Enqvist et al. "Nucleation and bubble growth in a first order cosmological electroweak phase transition". In: *Phys.Rev.* D45 (1992), pp. 3415–3428. DOI: 10.1103/PhysRevD.45.3415.

[523] Axel Brandenburg, Kari Enqvist, and Poul Olesen. "Large scale magnetic fields from hydromagnetic turbulence in the very early universe". In: *Phys. Rev. D* 54 (1996), pp. 1291–1300. DOI: 10.1103/PhysRevD.54.1291. arXiv: astro-ph/9602031.

[524] J.R. Wilson and G.J. Matthews. *Relativistic Numerical Hydrodyamics*. Cambridge: Cambridge University Press, 2003.

[525] Bram Van Leer. "Towards the ultimate conservative difference scheme. IV. A new approach to numerical convection". In: *Journal of Computational Physics* 23.3 (1977), pp. 276–299. ISSN: 0021-9991. DOI: https://doi.org/10.1016/0021-9991(77)90095-X. URL: https://www.sciencedirect.com/science/article/pii/002199917790095X.

[526] Peter Anninos and P. Chris Fragile. "Non-oscillatory central difference and artificial viscosity schemes for relativistic hydrodynamics". In: *Astrophys. J. Suppl.* 144 (2003), p. 243. DOI: 10.1086/344723. arXiv: astro-ph/0206265.

[527] P. A. Davidson. *Turbulence: An Introduction for Scientists and Engineers*. en. Oxford, UK ; New York: Oxford University Press, 2004. ISBN: 978-0-19-852948-4.

[528] T. von Karman. "Progress in the Statistical Theory of Turbulence". en. In: *Proceedings of the National Academy of Sciences* 34.11 (Nov. 1948), pp. 530–539. ISSN: 0027-8424, 1091-6490. DOI: 10.1073/pnas.34.11.530.

[529] Yukio Kaneda. "Lagrangian and Eulerian Time Correlations in Turbulence". en. In: *Physics of Fluids A: Fluid Dynamics* 5.11 (Nov. 1993), pp. 2835–2845. ISSN: 0899-8213. DOI: 10.1063/1.858747.

[530] Yu-Hong Dong and Pierre Sagaut. "A Study of Time Correlations in Lattice Boltzmann-Based Large-Eddy Simulation of Isotropic Turbulence". en. In: *Physics of Fluids* 20.3 (Mar. 2008), p. 035105. ISSN: 1070-6631, 1089-7666. DOI: 10.1063/1.2842381.

[531] M. Wilczek and Y. Narita. "Wave-Number–Frequency Spectrum for Turbulence from a Random Sweeping Hypothesis with Mean Flow". en. In: *Phys. Rev. E* 86.6 (Dec. 2012), p. 066308. ISSN: 1539-3755, 1550-2376. DOI: 10.1103/PhysRevE.86.066308.

[532] T. Sanada and V. Shanmugasundaram. "Random Sweeping Effect in Isotropic Numerical Turbulence". en. In: *Physics of Fluids A: Fluid Dynamics* 4.6 (June 1992), pp. 1245–1250. ISSN: 0899-8213. DOI: 10.1063/1.858242.

[533] Yukio Kaneda and Toshiyuki Gotoh. "Lagrangian Velocity Autocorrelation in Isotropic Turbulence". en. In: *Physics of Fluids A: Fluid Dynamics* 3.8 (Aug. 1991), pp. 1924–1933. ISSN: 0899-8213. DOI: 10.1063/1.857922.

[534] J. Mercer. "Functions of Positive and Negative Type, and their Connection with the Theory of Integral Equations". In: *Philosophical Transactions of the Royal Society of London Series A* 209 (Jan. 1909), pp. 415–446. DOI: 10.1098/rsta.1909.0016.

[535] Salomon Bochner and T Teichmann. "Harmonic analysis and the theory of probability". In: *Physics Today* 9.3 (1956), p. 22.

[536] R. Silverman. "Locally stationary random processes". In: *IRE Transactions on Information Theory* 3.3 (1957), pp. 182–187. DOI: 10.1109/TIT.1957.1057413.

[537] Dave Higdon, Jenise Swall, and J Kern. "Non-stationary spatial modeling". In: *Bayesian statistics* 6.1 (1999), pp. 761–768.

[538] G. Peter Lepage. "A new algorithm for adaptive multidimensional integration". In: *Journal of Computational Physics* 27.2 (May 1978), pp. 192–203. DOI: 10.1016/0021-9991(78)90004-9.